

THE DYNAMICS AND  
THERMODYNAMICS OF  
**COMPRESSIBLE  
FLUID FLOW**

---

ASCHER H. SHAPIRO

RONALD

ASCHER H. SHAPIRO is Professor of Mechanical Engineering at the Massachusetts Institute of Technology where he received his S.B. and his Sc.D. For various periods he served on the Subcommittee on Turbines, the Subcommittee on Internal Flow, and the Subcommittee on Compressors and Turbines of the National Advisory Committee for Aeronautics. Beginning with the Lexington Project he has been associated with studies of the use of nuclear energy for aircraft propulsion. An inventor and a consulting engineer for many industrial firms, Professor Shapiro is a Fellow of the American Academy of Arts and Sciences.

The Dynamics  
and Thermodynamics of  
COMPRESSIBLE FLUID  
FLOW

By  
**ASCHER H. SHAPIRO**  
*Professor of Mechanical Engineering  
Massachusetts Institute of Technology*

IN TWO VOLUMES

VOLUME II

THE RONALD PRESS COMPANY , NEW YORK

Copyright, 1954, by  
THE RONALD PRESS COMPANY

*All Rights Reserved*

The text of this publication or any part  
thereof may not be reproduced in any  
manner whatsoever without permission in  
writing from the publisher.

10MP

To

SYLVIA

*who gave meaning to this effort*

Library of Congress Catalog Card Number: 53-8869

PRINTED IN THE UNITED STATES OF AMERICA

## PREFACE

During the past two decades a rapid growth of interest in the motion of compressible fluids has accompanied developments in high-speed flight, jet engines, rockets, ballistics, combustion, gas turbines, ram jets and other novel propulsive mechanisms, heat transfer at high speeds, and blast-wave phenomena. My purpose in writing this book is to make available to students, engineers, and applied physicists a work on compressible fluid motion which would be suitable as an introductory text in the subject as well as a reference work for some of its more advanced phases. The choice of subject matter has not been dictated by any particular field of engineering, but rather includes topics of interest to aeronautical engineers, mechanical engineers, chemical engineers, applied mechanicians, and applied physicists.

In selecting material from the vast literature of the field the basic objective has been to make the book of practical value for engineering purposes. To achieve this aim, I have followed the philosophy that the most practical approach to the subject of compressible fluid mechanics is one which combines theoretical analysis, clear physical reasoning, and empirical results, each leaning on the other for mutual support and advancement, and the whole being greater than the sum of the parts.

The analytical developments of this book comprise two types of treatments: those leading to design methods and those leading to exemplary methods. The design methods are direct and rapid, and easily applied to a variety of problems. Therefore, they are suited for use in the engineering office. The discussions of these design methods are detailed and illustrative examples are often given. The exemplary methods, on the other hand, comprise those theoretical analyses which are time consuming, which generally require mathematical invention, and which are not easily applied to a variety of problems. Such methods are primarily of value for yielding detailed answers to a small number of typical problems. Although they are not in themselves suitable for the engineering office, the examples which they permit to be worked out often provide important information about the behavior of fluids in typical situations. Thus they serve as guides to the designer in solving the many complex problems where even the so-called design methods are not sufficient. The treatment of exemplary methods in this book usually consists of a brief outline of the method, together with a presentation of those results obtained by the method which illuminate significant questions concern-

ing fluid motion and which help to form the vital "feel" so desired by designers.

In keeping with the spirit of the several foregoing remarks, all the important results of the book have been reduced to the form of convenient charts and tables. Unless otherwise specified, the charts and tables are for a perfect gas with a ratio of specific heats ( $k$ ) of 1.4.

In those parts of the book dealing with fundamentals, emphasis is placed on the introduction of new concepts in an unambiguous manner, on securing a clear physical understanding before the undertaking of an analysis, on the rigorous application of physical laws, and on showing fruitful avenues of approach in analytical thinking. The remaining part of the work proceeds at a more rapid pace befitting the technical maturity of advanced students and professionals.

The work is organized in eight parts. Part I sets forth the basic concepts and principles of fluid dynamics and thermodynamics from which the remainder of the book proceeds and also introduces some fundamental concepts peculiar to compressible flows. In Part II is a discussion of problems accessible by the most simple picture of fluid motion—the one-dimensional analysis. Part III constitutes a summary of the basic ideas and concepts necessary for the succeeding chapters on two- and three-dimensional flow. Parts IV, V, and VI then present in order comprehensive surveys of subsonic flows, of supersonic flows (including hypersonic flow), and of mixed subsonic-supersonic flows. In Part VII is an exposition of unsteady one-dimensional flows. Part VIII is an examination of the viscous and heat conduction effects in laminar and turbulent boundary layers, and of the interaction between shock waves and boundary layers. For those readers not already familiar with it, the mathematical theory of characteristic curves is briefly developed in Appendix A. Appendix B is a collection of tables which facilitate the numerical solution of problems.

The "References and Selected Bibliography" at the end of each chapter will, it is hoped, be a helpful guide for further study of the voluminous subject. Apart from specific references cited in each chapter, the lists include general references appropriate to the subject matter of each chapter. The choice of references has been based primarily on clarity, on completeness, and on the desirability of an English text, rather than on historical priority.

My first acknowledgment is to Professor Joseph H. Keenan, to whom I owe my first interest in the subject, and who, as teacher, friend, and colleague, has been a source of inspiration and encouragement.

In an intangible yet real way I am indebted to my students, who have made teaching a satisfying experience, and to my friends and colleagues

at the Massachusetts Institute of Technology who contributed the climate of constructive criticism so conducive to creative effort.

Many individuals and organizations have been cooperative in supplying me with helpful material and I hope that I have not failed to acknowledge any of these at the appropriate place in the text. The National Advisory Committee for Aeronautics and the M.I.T. Gas Turbine Laboratory have been especially helpful along these lines.

I was fortunate in being able to place responsibility for the important work of the drawings in the competent hands of Mr. Percy H. Lund, who, with Miss Prudence Santoro, has been most cooperative in this regard.

For help with the final revision and checking of the manuscript I wish to give thanks to Dr. Bruce D. Gavril and Dr. Ralph A. Burton.

Finally, but by no means least, I must express a word of appreciation to Sylvia, and to young Peter, Mardi, and Bunny, who, one and all, made it possible for me to escape from the office into the somewhat less trying atmosphere of the home, and there to carry this work forward to its completion.

ASCHER H. SHAPIRO

Arlington, Mass.

## C O N T E N T S

---

### V O L U M E I I

#### *Part V. Supersonic Flow (Continued)*

CHAPTER	PAGE
17 AXIALLY SYMMETRIC SUPERSONIC FLOW . . . . .	651
Exact Solution for Flow Past a Cone. Linear Theory for Slender Bodies of Revolution. Method of Characteristics. Miscellaneous Experimental Results.	
18 SUPERSONIC FLOW PAST WINGS OF FINITE SPAN . . . . .	703
Preliminary Considerations of Finite Wings. Sweptback Wings. Similarity Rule for Supersonic Wings. The Method of Supersonic Source and Doublet Distributions. The Method of Conical Fields. Typical Theoretical Results for Finite Wings. Comparison of Theory with Experiment.	
19 HYPERSONIC FLOW . . . . .	745
Similarity Laws for Hypersonic Flow. Oblique Shock Relations for Hypersonic Flow. Simple-Wave Expansion Relations for Hypersonic Flow. Hypersonic Performance of Two-Dimensional Profiles. Hypersonic Performance of Bodies of Revolution. Experimental Results.	

#### *Part VI. Mixed Flow*

20 THE HODOGRAPH METHOD FOR MIXED SUBSONIC-SUPERSONIC FLOW . . . . .	773
Equations of the Hodograph Method. Source-Vortex Flow. Compressible Flow with 180° Turn. The Limit Line. Solution of Hodograph Equations by Hypergeometric Functions.	
21 TRANSONIC FLOW . . . . .	800
The Transonic Similarity Law. Applications of the Transonic Similarity Law. Flow in Throat of Converging-Diverging Nozzle. Relaxation Method. Transonic Flow Past a Wavy Wall. Flow at Mach Number Unity. Slopes of Force Coefficients at $M_\infty = 1$ . Transonic Flow Past Wedge Nose.	

## CONTENTS

CHAPTER	PAGE
22 DRAG AND LIFT AT TRANSONIC SPEEDS . . . . .	857

Experimental Validity of Transonic Similarity Law. Characteristics of Wing Profiles. Characteristics of Wings. Transonic Drag of Bodies of Revolution. Detached Shocks. Theoretical Consideration of Transonic Flow Without Shocks. Interaction Between Boundary Layer and Shock Wave.

*Part VII. Unsteady Motion in One Dimension*

23 UNSTEADY WAVE MOTION OF SMALL AMPLITUDE . . . . .	907
--	-----

Equations of Motion. Waves of Small Amplitude. Simplified Physical Analysis of Pressure Pulse. Characteristic Curves. Application of Theory. Development of Wave Forms. Effects of Gradual Changes in Area.

24 UNSTEADY, ONE-DIMENSIONAL, CONTINUOUS FLOW . . . . .	930
---	-----

Extension of Linearized Theory. Method of Characteristics. Simple Waves. Waves of Both Families. Unit Operations and Boundary Conditions. Unsteady, One-Dimensional Flow with Area Change, Friction, and Heat Transfer or Combustion. Remarks on Details of Working Out the Method of Characteristics. Some Examples.

25 UNSTEADY, ONE-DIMENSIONAL SHOCK WAVES . . . . .	992
--	-----

Analysis in Terms of Stationary Shock Formulas. Analysis of Moving Shocks. The Shock Tube—Riemann's Problem. Weak Shock Waves. Modified Calculation Procedure for Weak Shocks. End Conditions and Interaction Effects for Strong Shocks. Comparison Between Experimental and Theoretical Results.

*Part VIII. Flow of Real Gases with Viscosity and Heat Conductivity*

26 THE LAMINAR BOUNDARY LAYER . . . . .	1033
---	------

Differential Equations of the Laminar Boundary Layer. Flow With Prandtl Number Unity. Flow With Arbitrary Prandtl Number. Integral Equations of the Laminar Boundary Layer. Laminar Boundary Layer for Axi-Symmetric Flow. Experimental Results for Laminar Boundary Layers. Stability of the Laminar Boundary Layer.

27 THE TURBULENT BOUNDARY LAYER . . . . .	1080
---	------

Differential Equations of the Turbulent Boundary Layer. Integral Equations of the Turbulent Boundary Layer. Analyses of Recovery Factor, Skin Friction, and Heat Transfer for Turbulent Flow Past a Flat Plate with Turbulent Prandtl Number of Unity. Theoretical and Experimental Results for Skin Friction on Flat Plates. Recovery Factor for Turbulent Flow. Turbulent Boundary Layer on Bodies of Revolution.

## CONTENTS

## CHAPTER

CHAPTER	PAGE
28 BOUNDARY LAYERS IN TUBES AND IN THE PRESENCE OF SHOCK WAVES . . . . .	1130

Flow in Tubes. Shock-Boundary Layer Interactions in Supersonic Flow. Shock-Boundary Layer Interactions in Transonic Flow. Normal Shocks in Ducts. Boundary-Layer Separation Produced by Shock Waves.

INDEX FOR VOLUMES I AND II . . . . .	1161
--------------------------------------	------

PART V  
SUPERSONIC FLOW (Continued)

## Chapter 17

### AXIALLY SYMMETRIC SUPERSONIC FLOW

#### 17.1. Introductory Remarks

Important practical examples of axially symmetric supersonic flow are (i) the flow past the fuselages of supersonic aircraft, rockets, and ram jets, (ii) the flow past projectiles, and (iii) internal flow in ducts, nozzles, and diffusers of round cross section.

Even though there are only two space coordinates in an axially symmetric flow, the mathematical problems prove to be more difficult than for two-dimensional flow because an axi-symmetric flow is essentially a space flow, whereas a two-dimensional flow is essentially a plane flow. Likewise, the physical natures of the two types of flows are quite different.

The important analytical methods which have been developed and which are outlined in this chapter are (i) the classical Taylor-Maccoll exact solution for the flow past a cone, (ii) the approximate linearized theory, first proposed by von Kármán and Moore, and based on the elementary solution for an infinitesimal "source" in a uniform, parallel supersonic flow, and (iii) the method of characteristics, a procedure for stepwise construction applicable to any flow pattern, time permitting its use.

These analyses are based on the assumption of a frictionless, steady flow, isentropic along each streamline. The flow is taken to be axi-symmetric. In some cases, the flow is assumed irrotational, but in others it is necessary to take account of the vorticity in the fluid.

A final section in the chapter summarizes some typical experimental results.

**Hypersonic Similarity Law.** In Chapter 19 there is derived a *hypersonic similarity law* for flow with small perturbations at high supersonic speeds. The law is applicable when the *hypersonic similarity parameter*  $K \equiv M_\infty \tau$  ( $\tau$  = thickness ratio) is of the order of magnitude of unity or larger. It states that for a given class of affinely related axi-symmetric bodies the distribution of  $C_p M_\infty^2$  on the surface depends only on the parameter  $K$ .

This result is relevant to the present chapter because various investigations (see Chapter 19) have shown that the similarity law often prevails at Mach Numbers which are usually considered to be super-

sonic rather than hypersonic. In the present chapter several methods are presented for determining the pressure distribution on bodies of revolution. For the range in which the similarity law is valid, it is necessary to carry out these calculations (which are often tedious) only for a few values of  $M_\infty \tau$ . Then the similarity law gives, with little effort, the pressure distributions on members of the particular family of affinely related shapes investigated for all combinations of  $M_\infty$  and  $\tau$  falling within the range of validity of the law.

### NOMENCLATURE

$c$	speed of sound	$\mathbf{V}$	vector velocity
$C_p$	pressure coefficient	$x, y, z$	Cartesian coordinates
$F$	see Eq. 17.34; also fineness ratio	$\alpha$	Mach angle
$G$	see Eq. 17.34	$\beta$	$\sqrt{M_\infty^2 - 1}$
$i$	$\sqrt{-1}$	$\delta$	semi-angle of cone; thickness ratio of body of revolution
$K$	similarity parameter, $M_1 \tau = M_1/F$	$\theta$	flow direction
$k$	ratio of specific heats	$\xi$	$x$ -coordinate of source
$M$	Mach Number	$\rho$	mass density
$n$	direction normal to streamline	$\sigma$	shock angle
$p$	pressure	$\tau$	thickness ratio; $\tau = 1/F$
$Q$	source strength; also see Eq. 17.34a	$\phi$	perturbation velocity potential
$r$	radius in spherical coordinates; also radius in cylindrical coordinates	$\Phi$	velocity potential
$R$	see Eq. 17.11; also radius in spherical coordinates; also radius to surface of axi-symmetric body	$\omega$	angle in spherical coordinates
$s$	entropy per unit mass	$(\cdot)_1$	signifies conditions upstream of conical shock
$S$	cross-sectional area of axi-symmetric body in plane normal to axis of symmetry	$(\cdot)_2$	signifies conditions downstream of conical shock
$u$	$x$ -component of perturbation velocity	$(\cdot)_s$	signifies conditions at surface of cone
$U_\infty$	free-stream velocity	$(\cdot)_r$	signifies component in $r$ -direction
$v$	$r$ -component of perturbation velocity	$(\cdot)_\omega$	signifies component in $\omega$ -direction
$V$	velocity	$(\cdot)_0$	signifies stagnation state
$V_{\max}$	maximum velocity for adiabatic flow	$(\cdot)_\infty$	signifies free-stream conditions
		$(\cdot)_{I,II}$	signifies conditions on characteristic curves

### 17.2. Exact Solution for Flow Past a Cone

In plane supersonic flow a class of *simple-wave* solutions (Prandtl-Meyer flow, Chapter 15) was found, defined by the property that the two velocity components should be functions of each other. In the corresponding flow pattern all stream properties are uniform on straight lines in the physical plane, and these straight lines are identical with the Mach lines. If a simple-wave flow pattern defined by the same property is sought for an axi-symmetric flow, it is found again that all stream properties are uniform on straight lines in the physical plane. These lines are no longer the Mach lines, however, and the solution requires that these straight lines pass through a common point. Thus, because of the axial symmetry, all stream properties are constant on cones having a common vertex. The resulting flow pattern is in fact a special variety of the general class of *conical flows* discussed in Chapter 18.

**General Nature of Flow Pattern.** The type of simple-wave flow outlined above could be bounded only by a cone. By assuming that fluid properties are constant on cones having a common vertex, therefore, we obtain the flow pattern past a cone (Fig. 17.1a). The practical

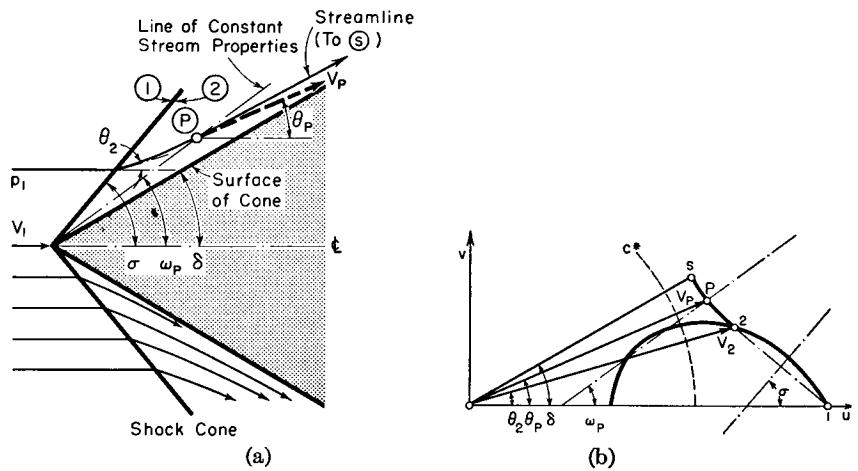


FIG. 17.1. Flow past cone.

(a) Shock cone and typical streamline.  
(b) Hodograph image of streamline.

importance of this flow pattern is not limited to cones, however, since the solutions for a cone will be applicable to the region near the tip of any sharp-nosed body of revolution.

A continuous variation of fluid properties from free-stream conditions,

$p_1$  and  $V_1$ , to the surface of the cone, conditions  $p_s$  and  $V_s$ , proves to be impossible.<sup>(3)</sup> A shock is therefore necessary. But, since the flow downstream of the shock is by assumption conical, it follows that the shock itself must be conical and of uniform strength, and must be attached to the tip of the cone.

Consider a typical streamline (Fig. 17.1a) and its image in the hodograph plane (Fig. 17.1b). Across the shock cone there is a discontinuous change in direction and velocity from 1 to 2; points 1 and 2 therefore lie on a common hodograph shock polar originating at point 1. Between 2 and  $s$  is a region of conical flow in which all stream properties vary continuously, the streamline reaching point  $s$  on the surface of the cone only in infinite distance. The velocity vector to point  $s$  in the hodograph plane makes the cone semi-angle  $\delta$  with the axis. A typical point  $P$ , with its corresponding angle  $\omega_P$  is shown, together with its image point in the hodograph plane. All stream properties are constant on the cone  $\omega_P$ , and hodograph point  $P$  is the image of the entire cone  $\omega_P$ . Likewise, the line 1-2- $P$ - $s$  is the hodograph image of all streamlines. Since all streamlines experience the same entropy jump across the shock, the flow between the shock and the cone is isentropic and irrotational.

**Governing Physical Equations.** Let us use spherical coordinates  $r$  and  $\omega$ , with corresponding velocity components  $V_r$  and  $V_\omega$  (see Fig. 17.2a). Then, considering the toroidal-shaped control volume of Fig. 17.2b, for which the *in-going* mass flows are indicated, the equation of continuity states that the *net* outflux of mass is zero:

$$\frac{\partial}{\partial r} (2\pi\rho V_r r^2 \cdot d\omega \cdot \sin \omega) dr + \frac{\partial}{\partial \omega} (2\pi\rho V_\omega r \cdot dr \cdot \sin \omega) d\omega = 0$$

Simplifying, and noting that all stream properties are independent of  $r$ , i.e.,  $\partial/\partial r = 0$  and  $\partial/\partial \omega = d/d\omega$ , we have

$$2\rho V_r + \rho V_\omega \cot \omega + \rho \frac{dV_\omega}{d\omega} + V_\omega \frac{d\rho}{d\omega} = 0 \quad (17.1)$$

Now, considering the velocity components of Fig. 17.2c, the condition of irrotationality is introduced by setting the circulation around the boundary of the control volume equal to zero:

$$V_r dr + \left( V_\omega + \frac{\partial V_\omega}{\partial r} dr \right) (r + dr) d\omega - \left( V_r + \frac{\partial V_r}{\partial \omega} d\omega \right) dr - V_\omega r d\omega = 0$$

which reduces to

$$V_\omega = \frac{dV_r}{d\omega} \quad (17.2)$$

Euler's equation, the velocity of sound, and the energy equation are, respectively,

$$dp = -\rho V dV = -\rho (V_r dV_r + V_\omega dV_\omega) \quad (17.3)$$

$$dp/d\rho = c^2 \quad (17.4)$$

$$c^2 = \frac{k-1}{2} (V_{\max}^2 - V^2) \quad (17.5)$$

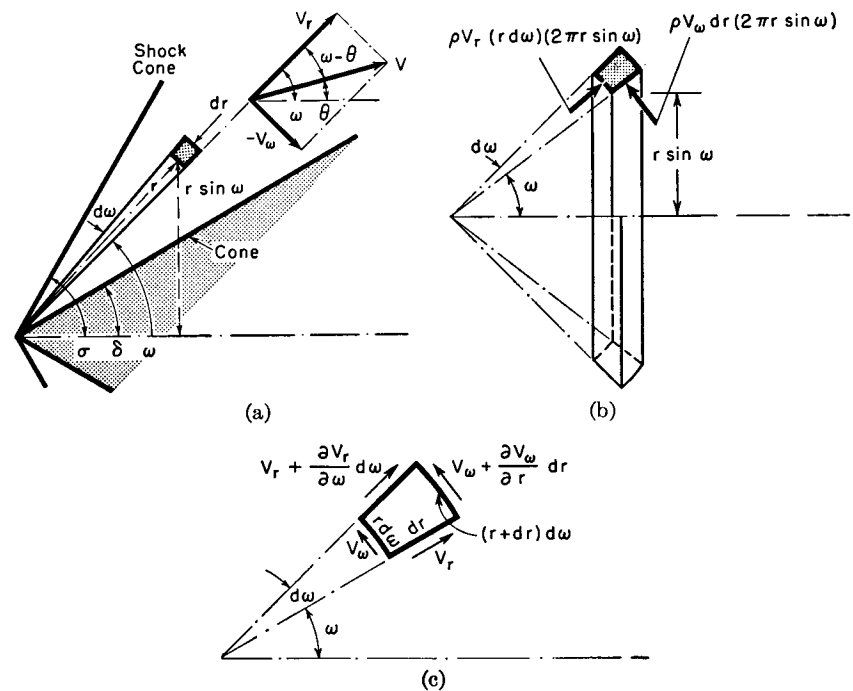


FIG. 17.2. Analysis of cone flow.

(a) Nomenclature.

(b) Continuity equation.

(c) Equation of irrotationality.

Combining Eqs. 17.3, 17.4, and 17.5 to eliminate the pressure, we get

$$\begin{aligned} V_r dV_r + V_\omega dV_\omega &= -\frac{dp}{\rho} = -\frac{dp}{\rho} \frac{dp}{d\rho} = -c^2 \frac{dp}{\rho} \\ &= -\frac{k-1}{2} (V_{\max}^2 - V^2) \frac{d\rho}{\rho} \end{aligned}$$

whence

$$\frac{d\rho}{\rho} = -\frac{2}{k-1} \frac{V_r dV_r + V_\omega dV_\omega}{V_{\max}^2 - V^2}$$

Inserting this expression into Eq. 17.1, and rearranging, we obtain

$$\begin{aligned} \frac{k-1}{2} \left( 2V_r + V_\omega \cot \omega + \frac{dV_\omega}{d\omega} \right) (V_{\max}^2 - V_\omega^2 - V_r^2) \\ = \left( V_r \frac{dV_r}{d\omega} + V_\omega \frac{dV_\omega}{d\omega} \right) V_\omega \quad (17.6) \end{aligned}$$

But, from Eq. 17.2,

$$V_\omega = \frac{dV_r}{d\omega}, \quad \text{whence} \quad \frac{dV_\omega}{d\omega} = \frac{d^2V_r}{d\omega^2}$$

With these it is now possible to eliminate terms in  $V_\omega$  from Eq. 17.6. Thus we obtain, after rearrangement, an ordinary, nonlinear differential equation of second order for  $V_r$  in terms of  $\omega$ :

$$\begin{aligned} -\frac{d^2V_r}{d\omega^2} \left[ \frac{k+1}{2} \left( \frac{dV_r}{d\omega} \right)^2 - \frac{k-1}{2} (V_{\max}^2 - V_r^2) \right] - \frac{k-1}{2} \left( \frac{dV_r}{d\omega} \right)^3 \cot \omega \\ - kV_r \left( \frac{dV_r}{d\omega} \right)^2 + \frac{k-1}{2} (V_{\max}^2 - V_r^2) \frac{dV_r}{d\omega} \cot \omega \\ + (k-1)V_r(V_{\max}^2 - V_r^2) = 0 \quad (17.7) \end{aligned}$$

The integration of this equation was first done by Busemann<sup>(3)</sup> with a clever graphical construction in the hodograph plane, and subsequently by Taylor and MacColl<sup>(4)</sup> by straightforward numerical integration. Let us consider the latter method first.

**Numerical Integration of Taylor and MacColl.** The general procedure for arriving at solutions to Eq. 17.7 is indicated by the following schedule of operations:

- (i) Select a value of  $\delta$  (cone angle) and of  $(V_r/V_{\max})_s$ , corresponding to the Mach Number at the cone surface.
- (ii) Begin with  $\omega = \delta$ , at which  $V_r = (V_r)_s$  and  $V_\omega = 0$ .
- (iii) Integrate Eq. (17.7) stepwise, for small steps in  $\omega$ , by replacing the differential equation by a finite-difference equation.
- (iv) Having found the value of  $V_r/V_{\max}$  corresponding to each value of  $\omega$ ,  $V_\omega/V_{\max}$  may be found by differentiation, using Eq. 17.2.
- (v) The final step is to determine the appropriate shock angle  $\sigma$  and free-stream velocity  $V_1/V_{\max}$ . This is done by cut-and-try. For each value of  $\omega$  during the integration there is a corresponding flow angle  $\theta$  and Mach Number  $M$ . Corresponding to each point of the integration the downstream Mach Number of a shock having a shock angle  $\sigma = \omega$  and turning angle  $\theta$  is compared with the Mach Number  $M$  of the integration. When these two Mach Numbers are found to be alike, the limit of integration has been reached and the correct shock strength has been found.
- (vi) From the shock tables the approach Mach Number  $M_1$  may then be found. Flow properties in the conical-flow region are finally computed by using

the shock relations for the shock, the isentropic relations for the conical-flow region, and the values of  $V_r/V_{\max}$  and  $V_\omega/V_{\max}$  as functions of  $\omega$  found by the previous integration.

**Graphical Construction of Busemann.** A geometrical solution to the cone equations, leading to *apple curves* analogous to the hodograph shock polars for plane shocks, is due to Busemann.<sup>(3)</sup> The governing equations must first be put into a form involving only the hodograph variables  $V$  and  $\theta$ .

**HODOGRAPH EQUATIONS.** From the geometry of Fig. 17.2a,

$$V_r = V \cos(\omega - \theta); \quad V_\omega = -V \sin(\omega - \theta) \quad (17.8)$$

or, differentiating with respect to  $\omega$ ,

$$\frac{dV_r}{d\omega} = -V \left( 1 - \frac{d\theta}{d\omega} \right) \sin(\omega - \theta) + \frac{dV}{d\omega} \cos(\omega - \theta) \quad (17.9a)$$

$$\frac{dV_\omega}{d\omega} = -V \left( 1 - \frac{d\theta}{d\omega} \right) \cos(\omega - \theta) - \frac{dV}{d\omega} \sin(\omega - \theta) \quad (17.9b)$$

From Eqs. 17.2 and 17.8, however,

$$\frac{dV_r}{d\omega} = V_\omega = -V \sin(\omega - \theta) \quad (17.9c)$$

When this is substituted into Eq. 17.9a, we obtain

$$\frac{d\theta}{d\omega} = -\frac{dV/d\omega}{V \tan(\omega - \theta)} \quad (17.9d)$$

Eliminating  $d\theta/d\omega$  from Eq. 17.9b, and substituting the expressions for  $V_r$ ,  $V_\omega$ ,  $dV_r/d\omega$ , and  $dV_\omega/d\omega$  given by Eqs. 17.8, 17.9b, and 17.9c into Eq. 17.6, we get, after rearrangement,

$$\frac{dV}{d\omega} = \frac{V \sin(\omega - \theta) \frac{\sin \theta}{\sin \omega}}{1 - \frac{2V^2 \sin^2(\omega - \theta)}{(k-1)(V_{\max}^2 - V^2)}} \quad (17.10)$$

The geometrical relations for two neighboring points,  $P$  and  $P'$ , on the same streamline in the hodograph plane are shown in Fig. 17.3. From Eq. 17.9d, it is evident that the tangent to the hodograph streamline makes the angle  $(\omega - \theta)$  with the normal to the velocity vector. From the geometry of the figure, this may be interpreted as meaning that the vector change in velocity,  $dV$ , must be normal to the line of constant  $\omega$ . This result might have been reached on physical grounds since (i) the cones of constant  $\omega$  are surfaces of constant pressure, (ii) the velocity gradient is normal to these cones, and therefore (iii) the vector change in  $V$  must lie normal to the line of constant  $\omega$ .

Also seen from Fig. 17.3 is that the normal to the hodograph streamline makes the angle  $\omega$  with the axis. This is illustrated further in Fig. 17.1b.

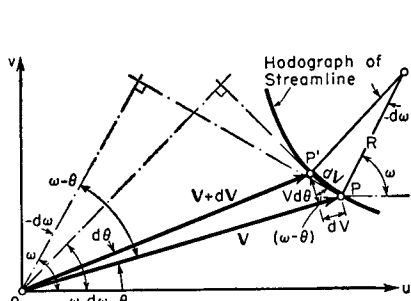


FIG. 17.3. Geometry of hodograph streamline.

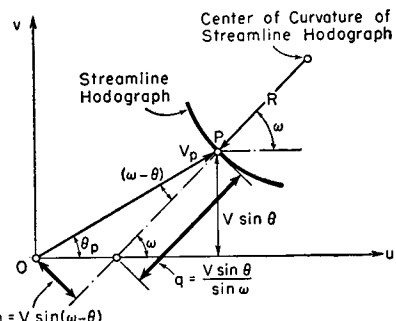


FIG. 17.4. Graphical aid to construction of hodograph streamline.

If  $R$  is the radius of curvature of the hodograph streamline at point  $P$ , then, from Fig. 17.3,

$$R = - \frac{|dV|}{d\omega} = \frac{dV}{\sin(\omega - \theta) d\omega} \quad (17.11)$$

which, when combined with Eq. 17.10, gives

$$R = \frac{V \frac{\sin \theta}{\sin \omega}}{1 - \frac{2V^2 \sin^2(\omega - \theta)}{(k-1)(V_{\max}^2 - V^2)}} = \frac{q}{1 - \frac{2h^2}{(k-1)(V_{\max}^2 - V^2)}} \quad (17.12)$$

where  $q$  and  $h$  are defined by Eq. 17.12 and have the geometrical significance shown by Fig. 17.4.

**GRAPHICAL SOLUTION.** The graphical construction of the solution now begins with the choice of free-stream Mach Number  $M_1$  and shock-wave angle  $\sigma$ , thus defining points 1 and 2 of the hodograph shock polar (Fig. 17.5) as well as the velocity  $V_2$  and streamline angle  $\theta_2$  at the beginning of the region of conical flow. Using Eq. 17.12 and the graphical construction of Fig. 17.4, the radius of curvature  $R_2$  of the hodograph streamline at point 2 is computed and the corresponding center of curvature  $2'$  is laid off graphically. A short arc  $2-3$  is then drawn with the radius  $R_2$  about the center  $2'$ , thus giving, at least approximately, point 3 on the hodograph streamline. Using the fluid properties at 3 together with Eq. 17.12, the value of  $R_3$  is found, and another short arc laid off with radius  $R_3$  about the center  $3'$ . This procedure is continued until the normal to the hodograph streamline passes through the origin, thus indicating that the surface of the cone passes through the origin, thus indicating that the surface of the cone has been reached, since Fig. 17.1a shows that  $\theta_s = \omega_s = \delta$ .

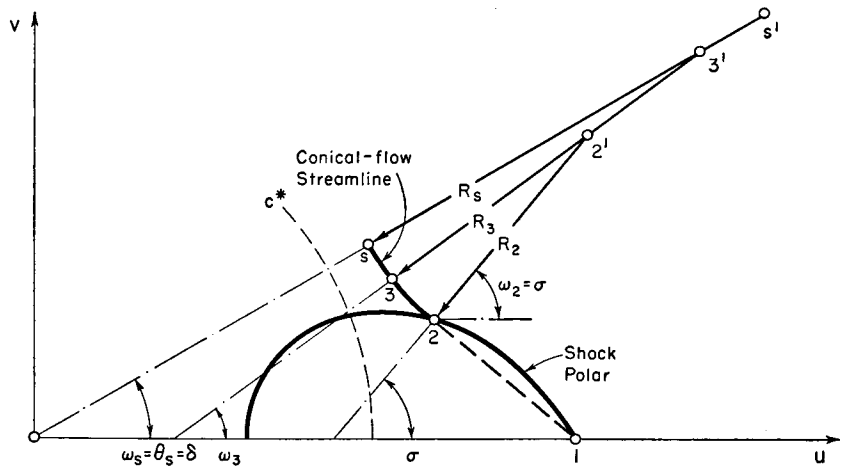


FIG. 17.5. Graphical construction of cone flow.

Point  $s$  on the hodograph streamline is thus established and yields the velocity at the surface of the cone, together with the cone angle  $\delta$  corresponding to the initially chosen values of  $M_1$  and  $\sigma$ . The physical streamlines may also be drawn inasmuch as the streamline direction  $\theta$  is known for each polar angle  $\omega$ .

If the procedure outlined above is repeated for the same value of  $M_1$ , but with different values of shock angle  $\sigma$ , a corresponding point  $s$  is found for each such angle, giving a family of solutions for cones of various angles  $\delta$  in a stream of fixed Mach Number  $M_1$ . The locus of such points  $s$  forms the type of curve shown in Fig. 17.6, aptly named by Busemann an *apple curve*.

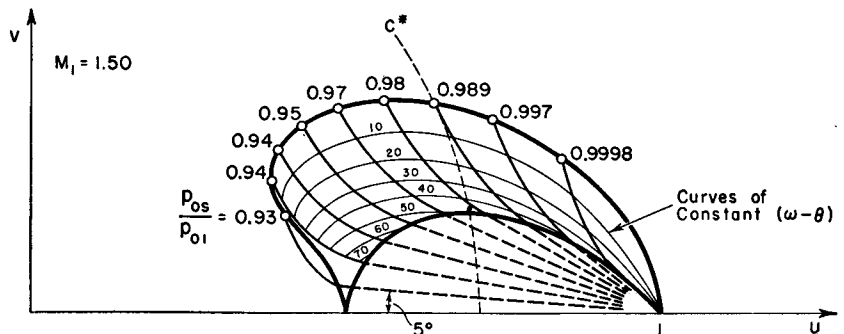


FIG. 17.6. Apple curves for flow past cone with  $M_1 = 1.50$  (after Hantsche and Wendt).

**APPLE CURVES.** Fig. 17.6<sup>(5)</sup> shows a typical apple curve, for  $M_1 = 1.50$ . Several hodograph streamlines are shown, corresponding to different cone angles. The stagnation-pressure ratio across the shock for each such cone angle is also indicated. For convenience in graphical

construction, lines of constant  $(\omega - \theta)$  are shown, the apple curve itself being such a curve with the value zero for  $(\omega - \theta)$ .

**Charts and Tables for Flow Past Cones.** The graphical construction is obviously limited in accuracy. Accordingly, the apple curves are useful primarily for showing general orders of magnitude and for comparative and illustrative purposes.

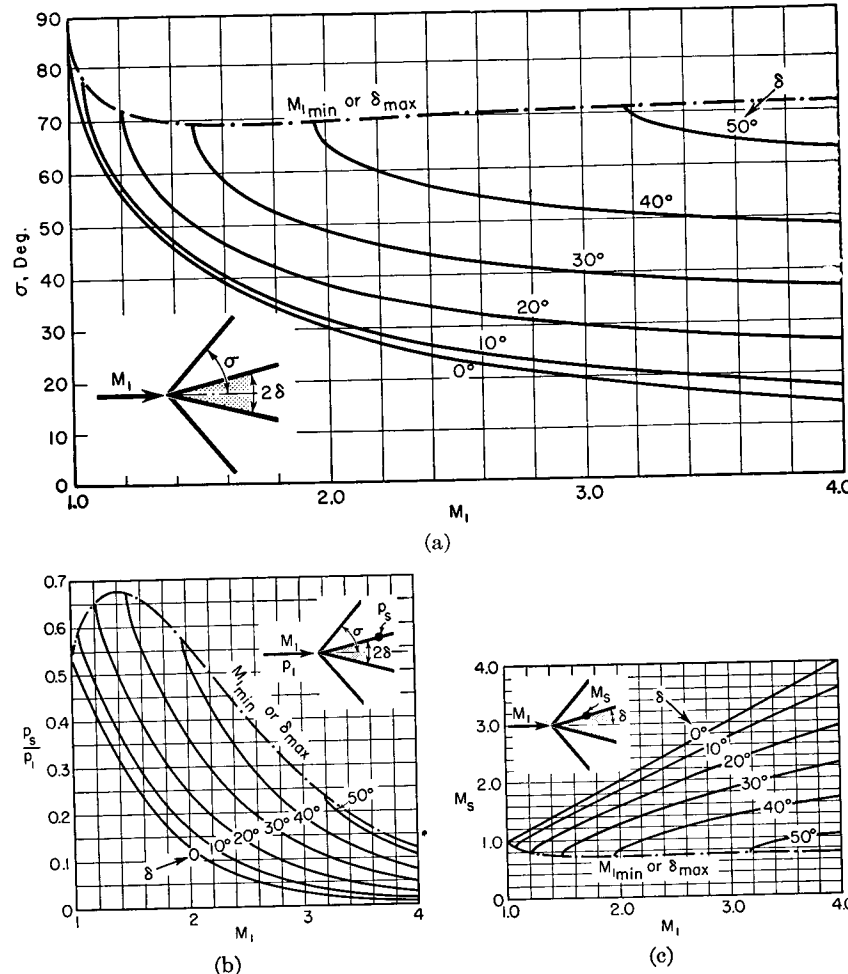


FIG. 17.7. Theoretical results for flow past cone.

- (a) Shock angle versus approach Mach Number, with cone angle as parameter.
- (b) Ratio of surface stagnation pressure to free-stream stagnation pressure versus free-stream Mach Number, with cone angle as parameter.
- (c) Surface Mach Number versus free-stream Mach Number, with cone angle as parameter.

Kopal<sup>(6)</sup> has prepared extensive tables of theoretical results, based on the integration of Eq. 17.7 by means of a differential analyser. Many of these results have been put into convenient graphical form in Reference 7. Small-scale charts showing the most important practical results are given in Figs. 17.7a to 17.7f.

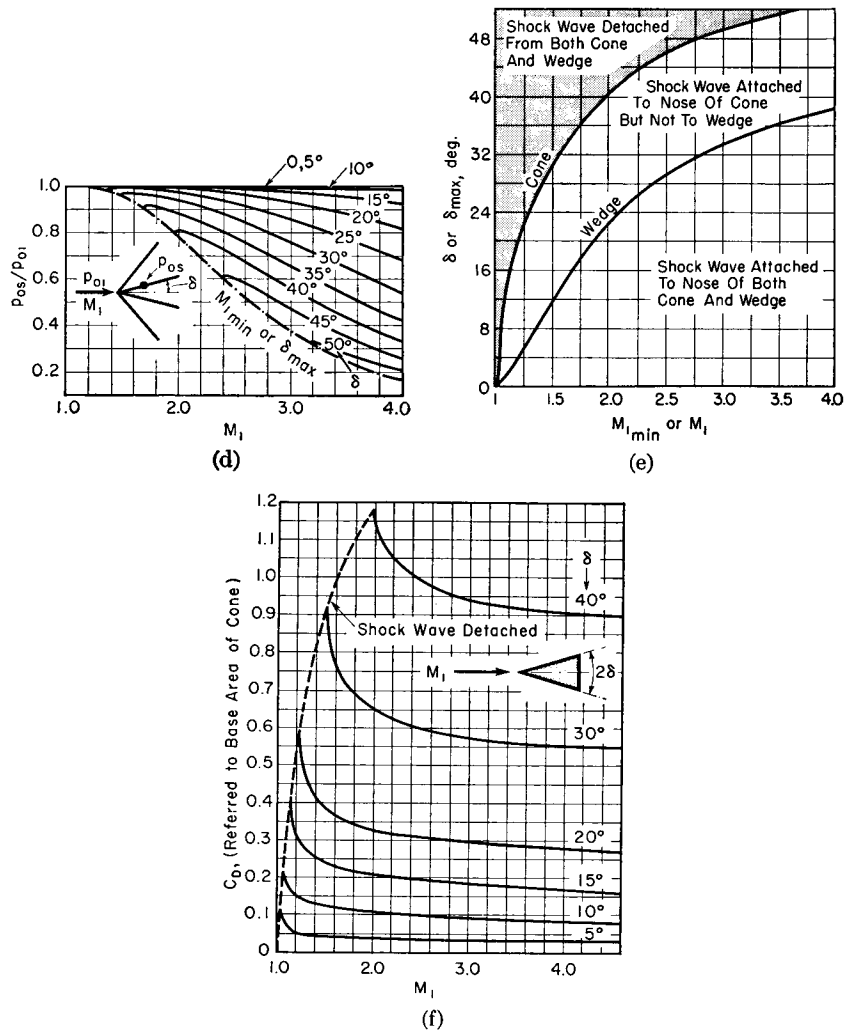


FIG. 17.7. (Continued)

- (d) Ratio of surface stagnation pressure to free-stream stagnation pressure, with cone angle as parameter.
- (e) Regions of shock attachment and detachment for cone and wedge.
- (f) Pressure-drag coefficient based on projected frontal area.

**Special Features of Flow Past Cones.** It may be noted from the apple curves, Fig. 17.6, that for each value of  $M_1$  there is a maximum value of  $\delta$  for which there exists a solution to conical flow; and, conversely, for each value of  $\delta$ , there is a minimum  $M_1$ . Furthermore, for a given  $M_1$ , and for a cone angle less than  $\delta_{\max}$ , there appear to be two possible solutions. Similar results were obtained in Chapter 16 for wedges.

**STRONG AND WEAK SOLUTIONS.** The *strong solution*, i.e., the solution with the larger shock angle, is never observed in photographs of flow past cones. In practice the cone is never infinite. Since the flow behind the "strong" shock is always subsonic, and since a subsonic flow cannot have conical properties, it is impossible for the "strong" solution to exist physically. The occurrence of the *weak solution* is possible with finite cones in supersonic flow because cutting off the downstream part of the cone cannot affect the upstream flow.

In Fig. 17.7, accordingly, only curves for the weak solution are presented, and these are all bounded by a line labeled " $M_{1\min}$  or  $\delta_{\max}$ " beyond which the shock is detached.

**ATTACHED AND DETACHED SHOCKS.** Fig. 17.7e shows the regions of attached and detached shocks for cones, together with the corresponding regions for two-dimensional wedges. For a given Mach Number cones may have considerably larger angles than wedges before detachment occurs.

**PRESSURE DRAG.** The wave-drag coefficient of conical tips, based on frontal projected area, is shown in Fig. 17.7f. It may be seen that supersonic aircraft and projectiles must have sharp noses if the wave drag is not to be excessive.

**COMPARISON OF CONES WITH WEDGES.** As compared with two-dimensional wedges, cones produce less disturbance in the flow because the flow may deviate from a conelike obstacle in three dimensions, whereas for a wedgelike obstacle the deviation can be in only two dimensions. For equal cone and wedge angles, therefore, the surface pressure rise and shock angle are greater for wedges. Thus, a wedge of given angle is a more sensitive instrument than a cone for determining the Mach Number of a stream by measuring the Mach angle or pressure rise; but, on the other hand, cones of larger angle than wedges may be used with a given Mach Number.

**USE OF CONE FOR SUPERSONIC DIFFUSION.** Inspection of Fig. 17.6 shows that there are many instances where the flow between the shock cone and the solid cone passes from supersonic speeds to subsonic speeds without shocks. Streamlines and Mach lines for such a case are illustrated in Fig. 17.8a. That this actually occurs in practice has

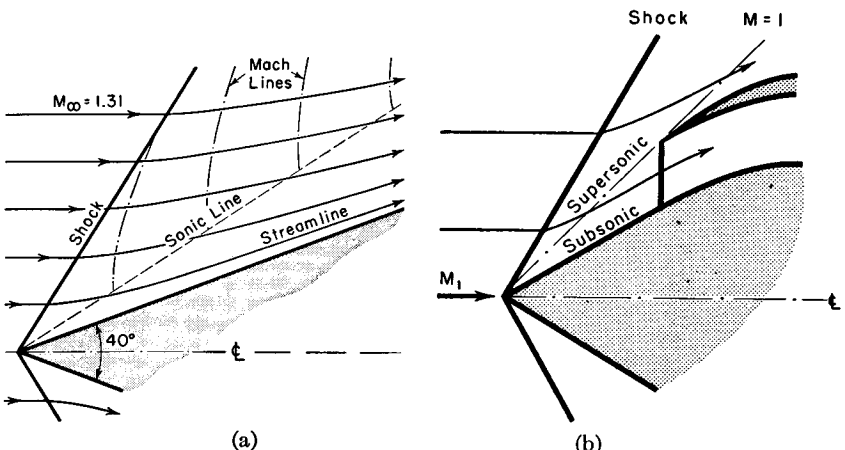


FIG. 17.8. (a) Typical streamlines and Mach lines for cone flow.  
(b) Application of flow past cone to design of supersonic inlet.

been confirmed by experiment, thus providing a direct refutation to the idea that passage from supersonic to subsonic speeds must necessarily be accompanied by shocks. This result also suggests the use of supersonic diffusers like that of Fig. 17.8b, where a portion of the supersonic deceleration occurs without losses downstream of the shock.

**Comparison with Experiment.** Photographs of the waves attached to cones<sup>(29)</sup> verify beautifully the theory as here outlined. Corresponding measurements of the shock angle are shown in Fig. 17.9e and are seen to agree almost perfectly with the analytical predictions. The measured pressure coefficient at the surface of the cone is also in good accord with the theory provided that the pressure taps are sufficiently far from the vertex to avoid the distorting effects of boundary layers. Since the effects produced by cones can be so accurately predicted, cone-shaped probes are often used for measuring the local Mach Number of a supersonic stream.

**Flow Past Yawing Cones.** The important aerodynamic features of supersonic flow past yawing cones, such as yaw angle of shock, drag coefficient, and lift coefficient, have been calculated in great detail by Kopal based on theories by Stone. Both the theory and the results are too extensive to be given here, and the reader is referred to References 8 and 9 for details.

### 17.3. Linear Theory for Slender Bodies of Revolution

Although, by the method of characteristics, it is possible to work out exactly the frictionless supersonic flow pattern for any body of

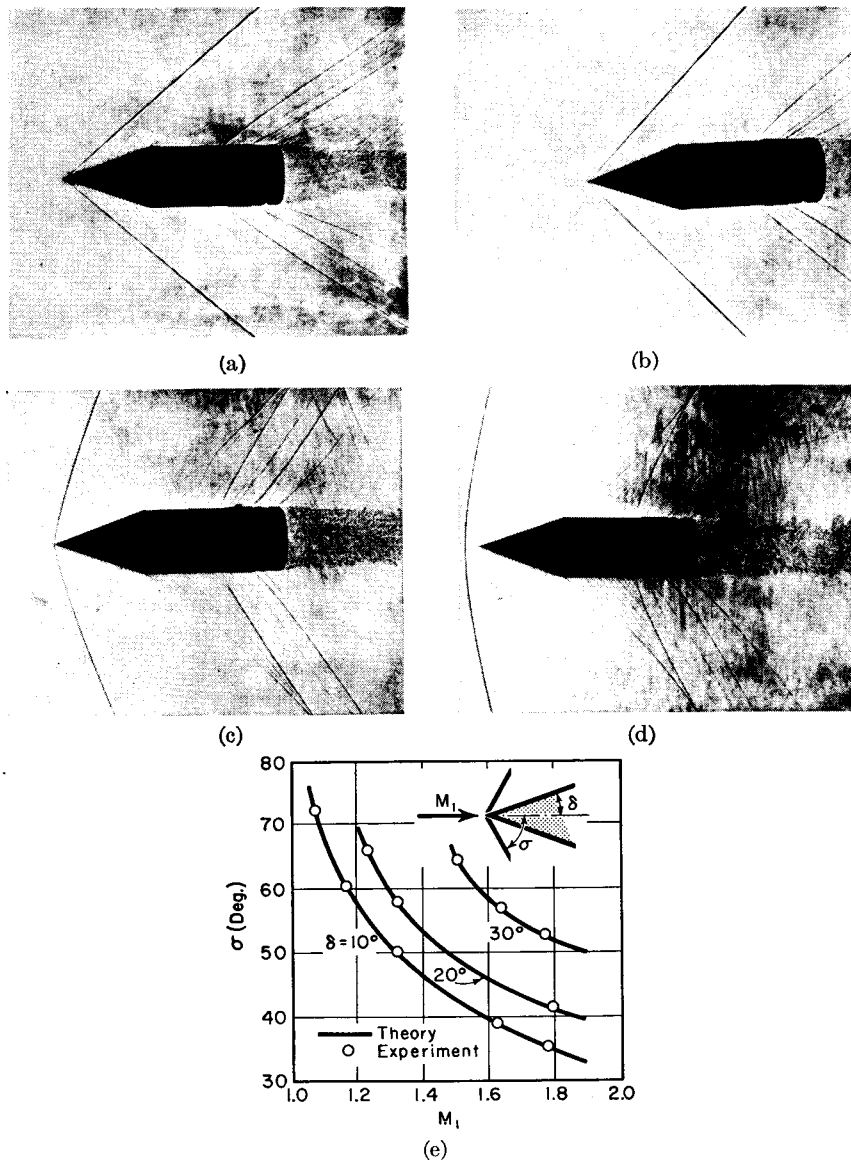


FIG. 17.9. Experimental results for cones (after MacColl).

- Shadowgraph,  $M_1 = 1.794$ . Shock is attached.
- Shadowgraph,  $M_1 = 1.576$ . Shock is attached but has larger angle than in (a). Note Mach lines produced by slight roughnesses on the surface.
- Shadowgraph,  $M_1 = 1.160$ . The Mach Number is too low to permit of conical flow. The shock is not conical and is about to detach from the nose.
- Shadowgraph,  $M_1 = 1.090$ . Shock is detached and curved. Flow is subsonic behind shock as far as the sharp corner at the shoulder of the projectile.
- Comparison of measured wave angles with theoretical results.

revolution, the exact method is laborious and does not give answers in analytical form, but rather requires each case to be worked out individually on a numerical basis. The method of small perturbations,<sup>(10)</sup> on the other hand, yields only approximate results, but has the great advantage of being an analytic method, so that formulas showing the effects of the different variables entering into a problem may readily be obtained.

**Linearized Equations of Motion.** We shall assume that a slender body of revolution is placed in an otherwise uniform, parallel supersonic flow with properties  $M_\infty$ ,  $\rho_\infty$ ,  $U_\infty$ , etc. The axis of the body is parallel to the free-stream direction, and hence there is complete axial symmetry. The body is furthermore assumed to be very slender, so that the perturbations from the free-stream velocity are very small compared with the free-stream velocity. By writing the velocity potential as

$$\Phi = U_\infty x + \varphi$$

where  $\varphi$  is the perturbation velocity potential, the derivatives of which give the perturbation velocity components  $u$ ,  $v$ , and  $w$ , and by following the line of argument employed for two-dimensional flow (Chapter 10), the equation for the velocity potential in three dimensions is reduced to the following linear differential equation for the perturbation velocity potential:

$$(1 - M_\infty^2) \frac{\partial^2 \varphi}{\partial x^2} + \frac{\partial^2 \varphi}{\partial y^2} + \frac{\partial^2 \varphi}{\partial z^2} = 0 \quad (17.13)$$

The local pressure coefficient has the approximate linearized form

$$C_p = -2 \frac{u}{U_\infty} = -\frac{2}{U_\infty} \frac{\partial \varphi}{\partial x} \quad (17.14)$$

**Compressible Sources and Sinks.** For incompressible flow it is well known that the flow pattern around a body of revolution may be synthesized by imagining sources and sinks to be placed on the axis of the body. The linearized method for supersonic flow is based on an extension of this concept.

**INCOMPRESSIBLE SOURCE.** When the flow is incompressible,  $M_\infty = 0$ , and Eq. 17.13 becomes

$$\frac{\partial^2 \varphi}{\partial x^2} + \frac{\partial^2 \varphi}{\partial y^2} + \frac{\partial^2 \varphi}{\partial z^2} = 0 \quad (17.15a)$$

A particular solution of Eq. 17.15a is

$$\varphi = -\frac{Q}{4\pi \sqrt{x^2 + y^2 + z^2}} = -\frac{Q}{4\pi R} \quad (17.15b)$$

where  $Q$  is a constant and  $R$  is the radius from the origin. That this is indeed a solution may be verified by direct differentiation and substitution. The equipotential lines are concentric spheres around the origin and hence the streamlines are straight radial lines and represent the flow from a point source or sink placed at the origin. The radial velocity is

$$V_r = \frac{\partial \varphi}{\partial R} = \frac{Q}{4\pi R^2}$$

and thus  $Q$  is seen to represent the *strength* of the source in terms of the volume rate of flow issuing from the source. The source velocities and potential lines are shown in Fig. 17.10a.

**SUBSONIC SOURCE.** When  $M_\infty < 1$ , we rearrange Eq. 17.13 in the form

$$\frac{\partial^2 \varphi}{\partial x^2} + \frac{\partial^2 \varphi}{\partial [ \sqrt{1 - M_\infty^2} y ]^2} + \frac{\partial^2 \varphi}{\partial [ \sqrt{1 - M_\infty^2} z ]^2} = 0 \quad (17.16a)$$

By comparing this with Eq. 17.15, we immediately see that a particular solution is

$$\varphi = -\frac{Q}{4\pi \sqrt{x^2 + (1 - M_\infty^2)(y^2 + z^2)}} \quad (17.16b)$$

which may be rearranged in the form

$$\left( \frac{x}{Q/4\pi\varphi} \right)^2 + \left( \frac{y}{\sqrt{1 - M_\infty^2} Q/4\pi\varphi} \right)^2 + \left( \frac{z}{\sqrt{1 - M_\infty^2} Q/4\pi\varphi} \right)^2 = 1 \quad (17.16c)$$

The equipotential lines of this *subsonic compressible source* are ellipsoids of revolution. Both the equipotential lines and the perturbation streamlines are as shown in Fig. 17.10b.

**SUPERSONIC SOURCE.** When  $M_\infty > 1$ , we write Eq. 17.13 in the form

$$\frac{\partial^2 \varphi}{\partial x^2} + \frac{\partial^2 \varphi}{\partial [ i\sqrt{M_\infty^2 - 1} y ]^2} + \frac{\partial^2 \varphi}{\partial [ i\sqrt{M_\infty^2 - 1} z ]^2} = 0 \quad (17.17a)$$

where  $i = \sqrt{-1}$ . By analogy with Eq. 17.15, a particular solution is

$$\varphi = -\frac{Q}{4\pi \sqrt{x^2 - (M_\infty^2 - 1)(y^2 + z^2)}} \quad (17.17b)$$

which may be rearranged in the form

$$\left( \frac{x}{Q/4\pi\varphi} \right)^2 - \left( \frac{y}{\sqrt{M_\infty^2 - 1} Q/4\pi\varphi} \right)^2 - \left( \frac{z}{\sqrt{M_\infty^2 - 1} Q/4\pi\varphi} \right)^2 = 1 \quad (17.17c)$$

From this it is evident that the equipotential lines of the *supersonic compressible source* are hyperboloids of revolution in the upstream and downstream Mach cones (Fig. 17.10c). Or course, only the part of the flow pattern lying in the downstream Mach cone is physically

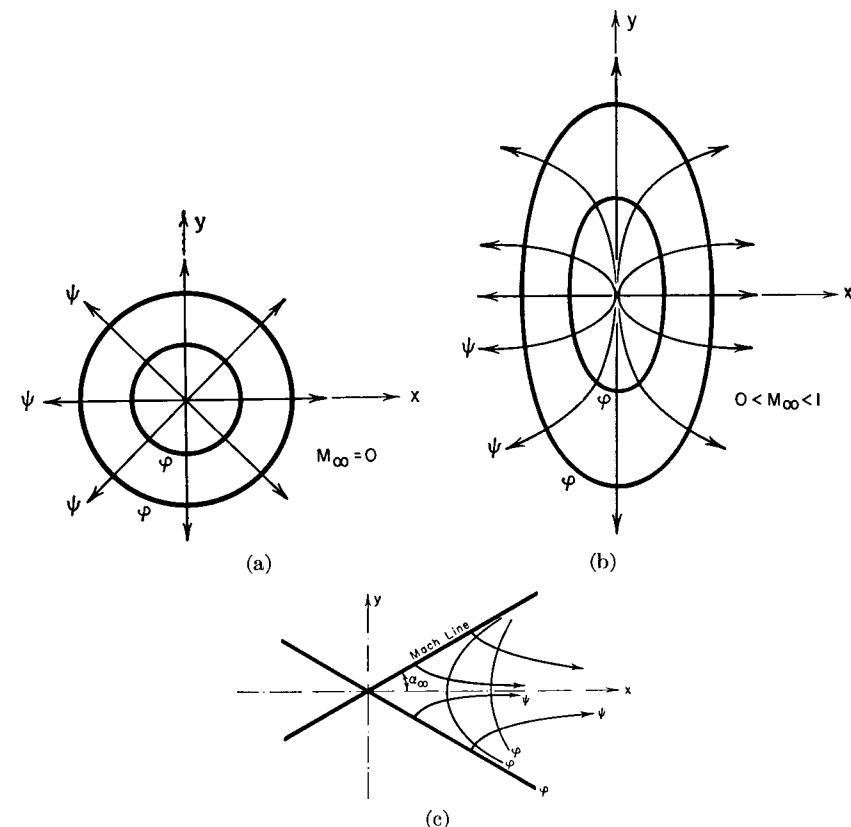


FIG. 17.10. Equipotential lines and perturbation streamlines for point source.

- (a) Incompressible.
- (b) Subsonic.
- (c) Supersonic.

significant. In Fig. 17.10c only the perturbation streamlines for this region are shown.

It must be emphasized that Eqs. 17.16 and 17.17 do not truly represent source flows, but acquire this title in a conceptual sense because of the formal analogy with Eq. 17.15. The important result is that Eqs. 17.16b and 17.17b represent elementary solutions of the differential equation. Likewise, Fig. 17.10 shows only the perturbation streamlines; the true streamlines are nearly straight parallel lines and are

found by adding vectorially the perturbation velocity at each point to the free-stream velocity.

**Superposition of Sources.** Since Eq. 17.13 is linear, and since Eq. 17.17b is an elementary solution to Eq. 17.13, we may construct more complex solutions of Eq. 17.13 merely by adding together the velocity potentials for several sources or sinks. This is most conveniently done by imagining the sources and sinks to be continuously distributed along the axis of the body.

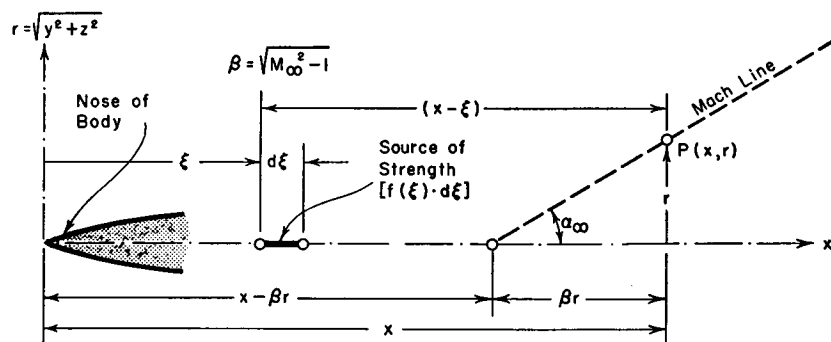


FIG. 17.11. Nomenclature for Kármán-Moore theory.

Referring to the meridian plane of Fig. 17.11, let  $\xi$  represent the  $x$ -coordinate of an elementary source lying on the axis of the body, and let the sharp nose of the body be at  $x = 0$ . The strength of the distributed source per unit length is called  $f(\xi)$ ; thus the strength of the elementary source lying between  $\xi$  and  $\xi + d\xi$  is  $f(\xi) d\xi$ . Now let us consider the potential at the point  $P(x, r)$ , owing to the source of strength  $f(\xi) d\xi$  at the location  $(\xi, 0)$ . By comparison with the expression of Eq. 17.17b for the potential of a source at the origin, we may write

$$\frac{f(\xi) d\xi}{4\pi \sqrt{(x-\xi)^2 - \beta^2 r^2}}; \quad \beta = \sqrt{M_\infty^2 - 1}$$

for the potential in question. Now the total potential at  $P(x, r)$  is due to all the sources lying between  $\xi = 0$  and  $\xi = x - \beta r$ ; these limits are chosen because the sources cannot begin upstream of the tip of the body, and because the effect of a given element of source is felt only in the Mach cone downstream of the source.\* Thus, the perturbation potential at  $P(x, r)$ , may be written

$$\varphi(x, r) = \int_0^{x-\beta r} \frac{f(\xi) d\xi}{4\pi \sqrt{(x-\xi)^2 - \beta^2 r^2}} \quad (17.18)$$

\*Mathematically, the upper limit of integration may be interpreted as the limiting value of  $\delta$  for which the integrand of Eq. 17.18 is real.

This is a definite integral from which  $\xi$  vanishes after the integration is performed. Our problem now is to determine the form of  $f(\xi)$  which will give us the flow pattern for a body of selected shape.

It is necessary to calculate the perturbation velocity components. Omitting the algebraic steps, we get

$$u = \frac{\partial \varphi}{\partial x} = \int_0^{x-\beta r} \frac{f'(\xi)}{4\pi} \frac{d\xi}{\sqrt{(x-\xi)^2 - \beta^2 r^2}} \quad (17.19)$$

$$v = \frac{\partial \varphi}{\partial r} = - \int_0^{x-\beta r} \frac{f'(\xi)}{4\pi} \left( \frac{x-\xi}{r} \right) \frac{d\xi}{\sqrt{(x-\xi)^2 - \beta^2 r^2}} \quad (17.20)$$

where  $v$  is now taken to be the perturbation velocity component in the  $r$ -direction, and  $f'(\xi)$  denotes  $d[f(\xi)]/d\xi$ . It should be mentioned here that in taking the derivatives of Eq. 17.18 due account must be taken of the fact that the upper limit of integration is a variable.

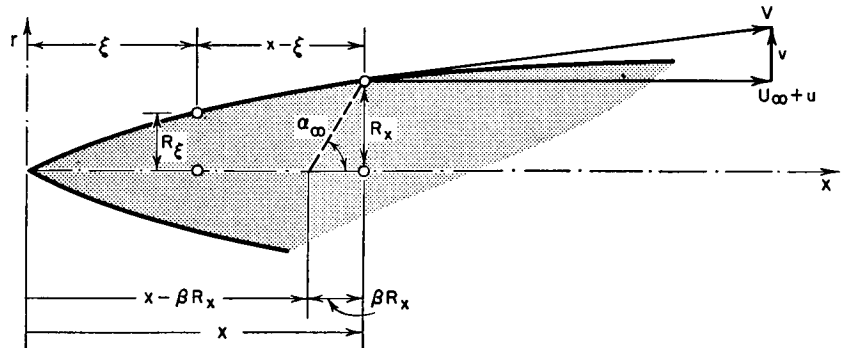


FIG. 17.12. Boundary condition at surface

**Source Distribution.** Referring to Fig. 17.12, the boundary condition at the body may be written

$$\frac{dR_x}{dx} = \left( \frac{v}{U_\infty + u} \right)_{r=R_x} \leq \frac{(v)_{r=R_x}}{U_\infty}$$

Furthermore, if, as assumed, the body is very slender, we may write

$$\beta R_x \ll (x - \xi); \quad \beta R_x \ll x$$

With the help of Eq. 17.20, therefore, the boundary condition may be written approximately

$$\frac{dR_x}{dx} = -\frac{1}{U_\infty} \int_0^x \frac{f'(\xi) d\xi}{4\pi R_x} = -\frac{1}{4\pi U_\infty R_x} \int_0^x d[f(\xi)]$$

This may be immediately integrated to give

$$\frac{dR_x}{dx} = -\frac{f(x)}{4\pi U_\infty R_x}$$

where the lower limit of integration is found by setting  $f(0) = 0$ , since if the source strength did not start with zero at the tip there would be a blunt leading edge and consequently a detached shock wave. The analysis is, therefore, limited to slender bodies with pointed tips. Inasmuch as the foregoing equation is valid, within the assumptions, for all values of  $x$ , we may write it in the form

$$\frac{dR_\xi}{d\xi} = \frac{-f(\xi)}{4\pi U_\infty R_\xi}$$

or,

$$f(\xi) = -4\pi U_\infty R_\xi \frac{dR_\xi}{d\xi} = -2U_\infty \frac{dS_\xi}{d\xi} \quad (17.21)$$

where  $S_\xi = \pi R_\xi^2$ , and represents the cross-sectional area of the body. Eq. 17.21 thus gives the desired function  $f(\xi)$  corresponding to a body of given shape.

**Working Formulas.** Finally, substituting Eq. 17.21 into Eqs. 17.19, 17.20, and 17.14, we get the following working formulas for the method:

$$\varphi(x, r) = - \int_0^{x-\beta r} \frac{U_\infty}{2\pi} \frac{dS_\xi}{d\xi} \frac{d\xi}{\sqrt{(x-\xi)^2 - \beta^2 r^2}} \quad (17.22)$$

$$u(x, r) = - \int_0^{x-\beta r} \frac{U_\infty}{2\pi} \frac{d^2 S_\xi}{d\xi^2} \frac{d\xi}{\sqrt{(x-\xi)^2 - \beta^2 r^2}} \quad (17.23)$$

$$v(x, r) = - \int_0^{x-\beta r} \frac{U_\infty}{2\pi} \frac{d^2 S_\xi}{d\xi^2} \left( \frac{x-\xi}{r} \right) \frac{d\xi}{\sqrt{(x-\xi)^2 - \beta^2 r^2}} \quad (17.24)$$

$$C_p(x, r) = \int_0^{x-\beta r} \frac{1}{\pi} \frac{d^2 S_\xi}{d\xi^2} \frac{d\xi}{\sqrt{(x-\xi)^2 - \beta^2 r^2}} \quad (17.25)$$

For axi-symmetric bodies of arbitrary shape, these equations can always be solved by graphical or numerical differentiation and integration. This procedure is of course fairly lengthy, since the integrations must be repeated for each set of values of  $x$  and  $r$  where the pressure coefficient is desired, but nevertheless the method for arbitrary bodies is considerably more rapid than the method of characteristics. A modification of the calculation method outlined here, using a finite number of sources and sinks, is outlined in Reference 11, and reduces the labor of calculation considerably.

For axi-symmetric bodies having shapes which can be described by simple functions, the working equations can be integrated to give analytic solutions in closed form. Two such examples will now be discussed.

**Flow Past a Cone.** It is of special interest to apply the linear theory to flow past a cone, because the exact solution for this case was found

in Art. 17.2, and thus it is possible to estimate the accuracy of the linear theory by comparison.

Using the nomenclature of Fig. 17.1a and assuming, within the approximations of the linear theory, that  $\tan \delta \cong \delta$ , we have

$$S_\xi = \pi \xi^2 \delta^2; \quad dS_\xi/d\xi = 2\pi \delta^2 \xi; \quad d^2 S_\xi/d\xi^2 = 2\pi \delta^2$$

We are particularly interested in the pressure coefficient at the surface of the cone. Substituting into Eq. 17.25, setting  $r = R$ , and carrying out the integration, we obtain

$$C_{ps} = -2\delta^2 \int_0^{x-\beta r} \frac{d\xi}{\sqrt{(x-\xi)^2 - \beta^2 r^2}} = -2\delta^2 \ln \frac{\beta R}{x + \sqrt{x^2 - \beta^2 R^2}}$$

But  $\beta R \ll x$ , and hence, to the degree of approximation of the method,

$$C_{ps} = -2\delta^2 \ln \frac{\beta R}{2x} = 2\delta^2 \ln \frac{2}{\delta \sqrt{M_\infty^2 - 1}} \quad (17.26)$$

Fig. 17.13 indicates the type of agreement which may be expected from the first-order theory. From Fig. 17.13a it appears that the error in calculating  $C_{ps}$  is very small for cone semi-vertex angles up to about  $10^\circ$ , but for larger angles the error becomes very large. A generalized comparison is shown in Fig. 17.13b <sup>(33)</sup> in terms of the hypersonic similarity parameter discussed in Chapter 19. The close grouping of the several curves for the different cone angles illustrates the utility of working with this parameter. From this chart it may be seen that, with semi-vertex angles up to  $15^\circ$ , the first-order theory is accurate within 10 per cent as long as  $M_\infty \tan \delta$  is less than 0.3.

**Flow Past a Parabolic Body of Revolution.** Consider the flow past a body of revolution <sup>(12)</sup> with the meridian curve

$$R = \frac{1}{2F} (1 - 4x^2)$$

where the body extends from  $x = -0.5$  to  $x = +0.5$ ,  $F$  is the length-diameter ratio, and the maximum diameter is  $1/F$ . Substituting into Eq. 17.25, and noting that the lower limit of integration is now  $-0.5$ , there results for the surface pressure coefficient,

$$C_{ps} = \frac{4}{F^2} \left\{ [12x^2 - 1 + 6\beta^2 R^2] \cosh^{-1} \left( \frac{x+0.5}{\beta R} \right) + 6[(x+0.5) - 4x] \sqrt{(x+0.5)^2 - \beta^2 R^2} \right\} \quad (17.27)$$

This equation is plotted in Fig. 17.14 for a length-diameter ratio of 10 at  $M_\infty = 1.4$ . For comparison there are shown also the pressure

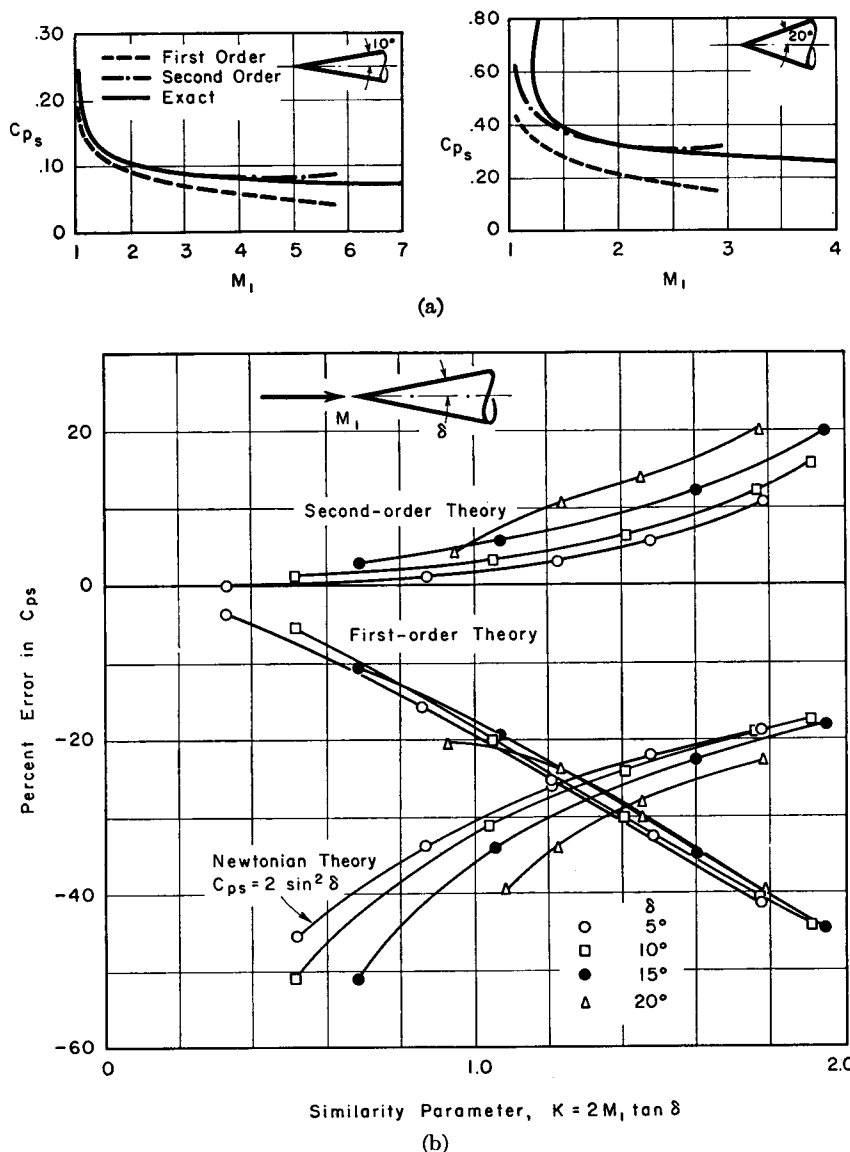


FIG. 17.13. (a) Calculated surface pressure coefficient on cone versus free-stream Mach Number according to (i) first-order (Kármán-Moore) theory, (ii) second-order (Van Dyke) theory, and (iii) exact (Taylor-Maccoll) theory.

(b) Accuracy of several approximate procedures for calculating surface pressure coefficient on cone, correlated by means of hypersonic similarity parameter (after Ihret).

distributions over the same body for incompressible flow and over a two-dimensional body with the same profile for  $M_\infty = 1.4$ .

For incompressible flow over the body of revolution the pressure distribution is symmetrical fore and aft, and there is no drag. For supersonic flow, on the other hand, the pressures acting on the rearward half of the body are generally lower than those acting over the forward half, and there is a resultant wave drag.

For two-dimensional supersonic flow over the same profile (ignoring vorticity), the surface pressure depends only on the local slope and continually decreases. Because of the pressure recovery near the tail of the axi-symmetric body, the wave drag in three-dimensional flow is smaller than in two-dimensional flow. Within the approximations of the linear theory, no wake is left by this profile in two-dimensional flow, whereas for the body of revolution there is a wake which extends to infinity.

Fig. 17.15 illustrates the difference in wave drag (based on maximum

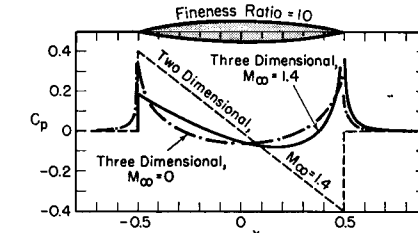


FIG. 17.14. Comparison of pressure distributions on two- and three-dimensional bodies having parabolic contours (after Jones).

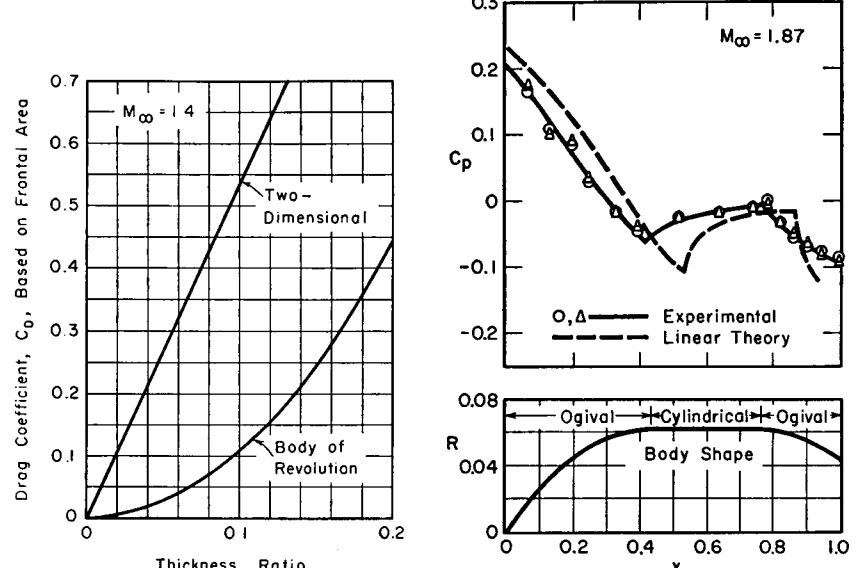


FIG. 17.15. Comparison of pressure drags of two- and three-dimensional bodies having parabolic contours (after Jones).

FIG. 17.16. Comparison of measured pressure distribution on A-4 missile at  $M_\infty = 1.87$  with results of linear theory (after Thompson).

frontal area) between a wing section of parabolic profile and a fuselage of parabolic profile. The difference in magnitudes is striking. Although the wave drag of the wing increases with the first power of thickness ratio, whereas that of the fuselage increases as the square of the thickness ratio, this does not reverse the relative magnitudes for practicable thickness ratios.

**Comparison of Linear Theory with Measured Pressure Distribution on Projectile.** Fig. 17.16 shows how the pressure distribution calculated by the linearized theory<sup>(11)</sup> compares with the experimental pressure distribution on a typical projectile shape. It is seen that the linear theory gives a fair approximation to the measured results. The method of characteristics<sup>(11)</sup> gives somewhat better agreement.

**Projectiles of Minimum Wave Drag.** Because the linear theory gives results in analytic form, it may be used to solve such variational problems as the determination of projectile shapes for fixed length and volume having minimum wave drag.<sup>(13)</sup> The shape of such a projectile is illustrated in Fig. 17.17.

**Open-Nosed Bodies of Revolution.** The linearized theory outlined here may also be extended to open-nosed bodies, such as ram-jet fuselages. For details the reader is referred to References 14 and 15.

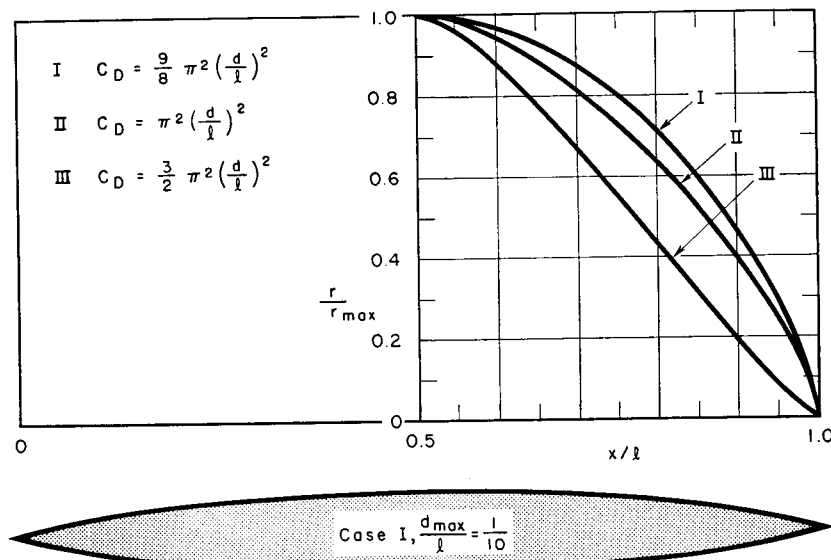


FIG. 17.17. Shapes of bodies of revolution of minimum pressure drag under various restraints (after Jones).

- I. Body with minimum pressure drag for given length and volume.
- II. Body with minimum pressure drag for given length and diameter.
- III. Body with minimum pressure drag for given diameter and volume.

**Inclined Bodies of Revolution.** For an extension of the linear theory to inclined bodies of revolution, the reader is referred to References 16 and 30.

**Second-Order Theory.** The results of this article are based on the linear, or first-order terms in the equation of motion. A significant improvement in the method, taking account of second-order terms, has been developed by Van Dyke.<sup>(30)</sup>

Although the numerical calculations required are not lengthy, the analytical formulation of the method is too lengthy to be given here, and the reader is referred to Reference 30 for full details of the analysis and of convenient calculation procedures based on specially prepared tables.

The degree of accuracy to be expected from the second-order theory is illustrated by Fig. 17.13. The second-order theory is markedly superior to the first-order theory, and, for values of  $M_1 \tan \delta$  less than 0.5, is in almost perfect agreement with the exact solution.

**Comparison of Several Approximate Methods.** Ehret<sup>(33)</sup> has made an illuminating comparison of various approximate methods of solution (requiring calculation times of a few hours) with the exact method of characteristics (requiring calculation times of a few weeks). Each of the approximate methods turns out to be fairly accurate in a certain range of the similarity parameter  $K$ , and very inaccurate in other ranges of  $K$ .

The various approximate methods considered for determining the surface pressure distribution include

- (i) The *first-order theory* discussed in Art. 17.3.
- (ii) The *second-order theory* of Van Dyke referred to above.
- (iii) The *tangent-cone method*, using the exact solutions for cones whose slopes correspond to the local slopes of the body surface.
- (iv) The *conical-shock-expansion theory* of Eggers and Savin,<sup>(34)</sup> based on the observation that the equations for the variation of surface Mach Number with surface slope downstream of the vertex of a pointed body of revolution are approximately the same as the Prandtl-Meyer equations for two-dimensional flow when  $K$  is greater than unity.

(v) The *Newtonian theory* of corpuscular flow (see Chapter 19) based on the assumption that the nose shock wave lies very near to the body surface, a condition which becomes valid as  $M_1 \rightarrow \infty$ . This assumption leads to the results that the component of velocity normal to the surface is destroyed and that the tangential component is unaltered; it is then readily shown from momentum considerations that the surface pressure coefficient is given by  $2 \sin^2 \delta$ .

Fig. 17.18a shows a comparison of the computed surface pressure distributions for a tangent-ogive body of revolution with a fineness

ratio of 6 at  $M_1 = 3$ , corresponding to a value of the similarity parameter of  $K = 0.5$ . The accuracy of each approximate method is seen to vary considerably along the length of the body.

A summary of the errors in computing the pressure drag coefficient by the several approximate methods, found by carrying out detailed calculations for a variety of typical bodies of revolution, is shown in Fig. 17.18b. The first-order theory and second-order theory are seen to be most accurate for values of  $K$  less than 0.8. For values of  $K$

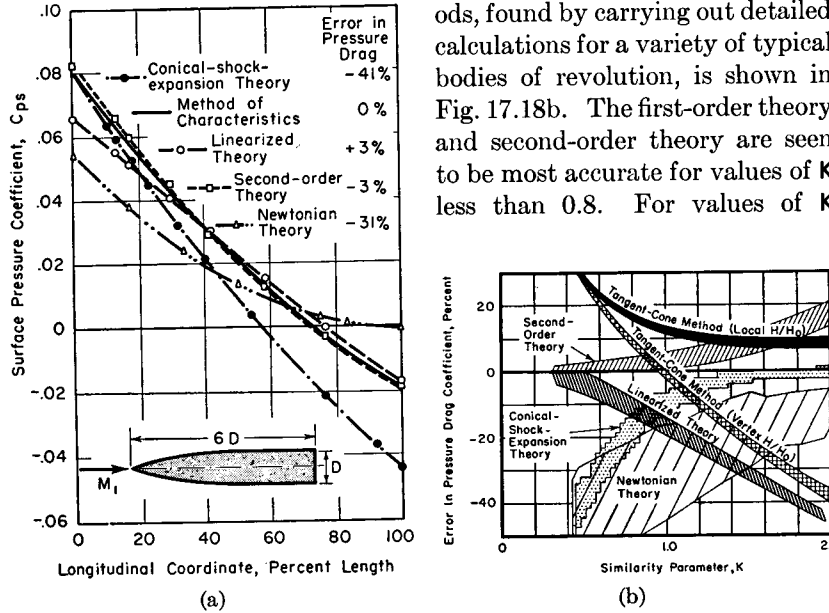


FIG. 17.18. Accuracy of various approximate methods for computing surface pressure distribution on bodies of revolution (after Ehret).

- (a) Comparison of approximate methods with exact method of characteristics for tangent-ogive body with  $M_1 = 3$ ,  $F = 6$ ,  $K = 0.5$ .  
 (b) Zones of error in pressure drag coefficient for various typical body shapes.

greater than about 1.6, however, the conical-shock-expansion theory, the Newtonian theory, and the tangent-cone method are the most accurate. It should be noted, however, that Fig. 17.18b is not a good guide for estimating the error in local surface pressure coefficients, as is evident from Fig. 17.18a.

#### 17.4. Method of Characteristics

Because the governing differential equation is hyperbolic in nature, the method of characteristics may be used for the exact stepwise numerical calculation of axi-symmetric supersonic flows.

**Characteristic Equations for Axi-Symmetric Irrotational Flow.** When the flow is axi-symmetric, steady, and irrotational, the differential

equation for the complete velocity potential, in terms of cylindrical coordinates  $x$  and  $r$  (Fig. 17.19), is (see Chapter 9):

$$\left(1 - \frac{u^2}{c^2}\right)\Phi_{xx} - 2\frac{uv}{c^2}\Phi_{xr} + \left(1 - \frac{v^2}{c^2}\right)\Phi_{rr} + \frac{\Phi_r}{r} = 0 \quad (17.27)$$

where

$$c^2 = c_0^2 - \frac{k-1}{2}V^2 = c_0^2 - \frac{k-1}{2}(u^2 + v^2) \quad (17.28)$$

and

$$u = \partial\Phi/\partial x = \Phi_x; \quad v = \partial\Phi/\partial r = \Phi_r \quad (17.29)$$

Following the procedure of Appendix A, we note, by comparison of Eq. 17.27 with Eq. A.11, and using the symbol  $r$  in place of  $y$ , that the coefficients of the latter equation are, in this instance:  $A = c^2 - u^2$ ;  $B = -uv$ ;  $C = c^2 - v^2$ ;  $D = -c^2v/r$ . Substituting these into Eqs. A.17 and A.18, we get the following differential equations for the characteristic curves of Eq. 17.27:

$$\left(\frac{dr}{dx}\right)_{I,II} = \frac{-uv \pm c\sqrt{u^2 + v^2 - c^2}}{c^2 - u^2} \quad (17.30a)$$

$$\left(\frac{dv}{du}\right)_{I,II} = \frac{uv \pm c\sqrt{u^2 + v^2 - c^2}}{c^2 - v^2} - \frac{c^2v}{c^2 - v^2} \frac{1}{r} \left(\frac{dr}{du}\right)_{I,II} \quad (17.31)$$

where the upper sign refers to family  $I$ , and the lower sign to family  $II$ .

These equations are more convenient to handle when written in terms of the velocity components  $V$  and  $\theta$  (Fig. 17.19). Setting

$$u = V \cos \theta; \quad v = V \sin \theta$$

and noting that  $\sin \alpha = c/V$ , Eqs. 17.30 and 17.31 are transformed into

$$(dr/dx)_{I,II} = \tan(\theta \mp \alpha) \quad (17.30b)$$

$$\frac{1}{V} \left(\frac{dV}{d\theta}\right)_{I,II} = \mp \tan \alpha + \frac{\sin \alpha \tan \alpha \sin \theta}{\sin(\theta \mp \alpha)} \frac{1}{r} \left(\frac{dr}{d\theta}\right)_{I,II} \quad (17.32)$$

The curves of Eq. 17.30b are projections on the physical plane of curves lying in the  $\varphi$ ,  $x$ ,  $r$ -surface representing the solution to Eq. 17.27. Likewise, the curves of Eq. 17.32 are the corresponding projections on the hodograph plane of the corresponding curves lying in the  $\varphi$ ,  $u$ ,  $v$ -surface representing the solution to Eq. 17.27. Thus, the simultaneous

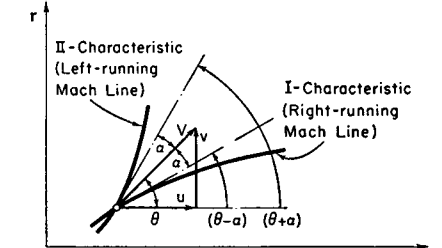


FIG. 17.19. Relation between streamlines and characteristics.

solution of the ordinary differential equations of Eqs. 17.30b and 17.32 for given initial conditions is equivalent to solving the original partial differential equation, Eq. 17.27.

Eqs. 17.30b and 17.32 are seen to be similar to the corresponding expressions for two-dimensional flow except for the presence of the last term in Eq. 17.32. From Eq. 17.30b and Fig. 17.19 it is evident that the physical characteristics of family I are the *right-running Mach lines* and those of family II are the *left-running Mach lines*.

Since Eqs. 17.30b and 17.32 each contain terms in both velocity and physical coordinates, it is necessary that they be solved simultaneously. That is, both the physical and hodograph characteristics must be constructed at the same time. This is in contrast to the two-dimensional problem, where the last term of Eq. 17.32 is absent, thus making it possible to construct the hodograph characteristics independently of the physical characteristics.

**Calculation Procedure.** To construct the two families of characteristic curves in the physical and hodograph planes, we replace the system of continuous characteristic curves by a system of straight-line chords connecting the intersection points of the two curves of the two families. Of course the accuracy of this procedure depends on the fineness of the net which is chosen. Corresponding to the replacement of a continuous curve by a series of chords, we replace Eqs. 17.30b and 17.32 by finite-difference equations.

**UNIT PROCESS.** The unit step of the entire procedure may be summed up thus: Given in Fig. 17.20 the locations of two points 1 and 2 in

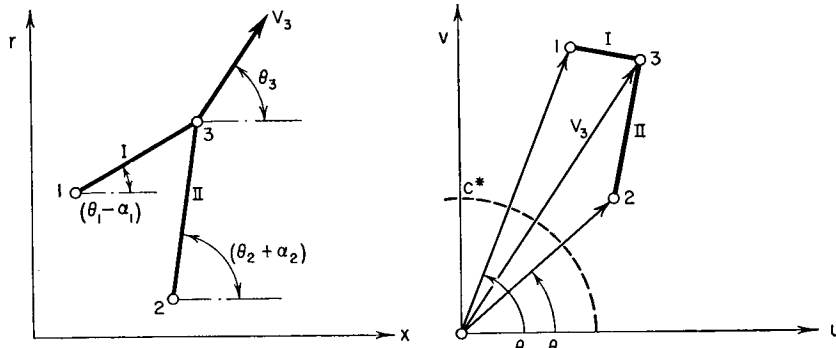


FIG. 17.20. Unit process of characteristics method.

both the physical and hodograph planes; to find the location in both planes of a point 3 lying at the intersection of the two characteristics passing through points 1 and 2.

As a first approximation, we may assume the average fluid properties

on the chord 2-3 to be substantially the same as at 2; and, similarly, we may take the conditions at 1 as an approximation to the average properties on the chord 1-3.

Then Eqs. 17.30b may be written approximately as

$$r_3 - r_1 = (x_3 - x_1) \tan(\theta_1 - \alpha_1) \quad (17.33a)$$

$$r_3 - r_2 = (x_3 - x_2) \tan(\theta_2 + \alpha_2) \quad (17.33b)$$

and, since  $\theta_1$ ,  $\theta_2$ ,  $\alpha_1$  and  $\alpha_2$  are all known,  $r_3$  and  $x_3$  may be solved for graphically or by simultaneous solution of the two equations.

Now, multiplying Eq. 17.32 by  $d\theta \cot \alpha$ , we put it into the form

$$(d\theta)_{I,II} \pm \frac{\cot \alpha}{V} (dV)_{I,II} \mp \frac{\sin \theta \sin \alpha}{\sin(\theta \mp \alpha)} \frac{(dr)_{I,II}}{r} = 0 \quad (17.32a)$$

Let us introduce the abbreviations,

$$Q \equiv (\cot \alpha)/V \quad (17.34a)$$

$$F \equiv (\sin \theta \sin \alpha)/\sin(\theta + \alpha) \quad (17.34b)$$

$$G \equiv (\sin \theta \sin \alpha)/\sin(\theta - \alpha) \quad (17.34c)$$

Note that  $Q$ ,  $F$ , and  $G$  depend only on the hodograph coordinates of the point. Applying Eq. 17.32a in finite-difference form to the chords 1-3 and 2-3, we have

$$\theta_3 - \theta_1 + Q_1(V_3 - V_1) - \frac{G_1}{r_1}(r_3 - r_1) = 0 \quad (17.35a)$$

$$\theta_3 - \theta_2 - Q_2(V_3 - V_2) + \frac{F_2}{r_2}(r_3 - r_2) = 0 \quad (17.35b)$$

Given all conditions at 1 and 2, and having previously found  $r_3$ , this pair of equations may be solved simultaneously for  $\theta_3$  and  $V_3$ , thus completing the first approximation to the unit step.

The approximate results already found may now be improved by a rapidly convergent iteration procedure which rests on the use of average conditions between 1-2 and 2-3. Having found tentative values of  $r_3$ ,  $x_3$ ,  $V_3$ , and  $\theta_3$  from the first approximation, we may repeat the entire computation, using this time mean values of the coefficients of the derivatives. Thus, in Eq. 17.33a, we would employ  $\bar{\theta}_{1-3} = (\theta_1 + \theta_3)/2$  in place of  $\theta_1$ ; and  $\bar{\alpha}_{1-3} = (\alpha_1 + \alpha_3)/2$  in place of  $\alpha_1$ . Likewise, in Eq. 17.35a, we would employ the mean values  $\bar{Q}_{1-3}$  and  $\bar{G}_{1-3}/\bar{r}_{1-3}$ . This process may be repeated as many times as seems necessary, each successive approximation making use of the results of the preceding one. Generally two or three trials are sufficient to give a degree of convergence consistent with the errors inherent in the use of a finite number of net points. The iteration procedure is especially important at small

Mach Numbers. Although the improvement in accuracy obtained by iteration appears to be small for each new point determined, it must be remembered that the conditions at a newly determined point become the initial conditions for the next succeeding point, so that small errors are cumulative and may in the end become quite large.

**POINT ON AXIS OF SYMMETRY.** When a point such as 2 lies on the axis of symmetry, then  $r_2$  and  $\theta_2$  are simultaneously zero, and  $F_2/r_2$  is indeterminate. Its limiting form may be found, remembering that we are working along the chord 2-3, as

$$\begin{aligned} \lim_{\substack{r_2 \rightarrow 0 \\ \theta_2 \rightarrow 0}} \frac{\sin \theta_2 \sin \alpha_2}{r_2 \sin(\theta_2 + \alpha_2)} &= \lim \frac{\sin \theta_2 \sin \alpha_2}{r_2(\cos \theta_2 \sin \alpha_2 + \sin \theta_2 \cos \alpha_2)} \\ &= \lim \frac{\sin \theta_2}{r_2} = \lim \left( \frac{d\theta}{dr} \right)_{II} \cong \frac{\theta_3}{r_3} \end{aligned}$$

and with this form Eq. 17.35b may be solved directly.

If point 3, i.e., the point to be found, lies on the axis of symmetry, so that  $r_3 = 0$  and  $\theta_3 = 0$ , no difficulties arise, as either of Eqs. 17.35 may be solved immediately for  $V_3$ .

**POINT ON SOLID BOUNDARY.** When point 3 lies on a solid boundary,  $\theta_3$  is known from the slope of the boundary, and point 3 in the physical plane is found from the intersection of the boundary curve with *one* of the characteristic curves. Thus the appropriate equation of Eqs. 17.35 is used for finding  $V_3$  at such a boundary point.

**POINT ON CONSTANT-PRESSURE BOUNDARY.** When point 3 lies on the boundary of a free jet, where the pressure and velocity are known, point 3 in the physical plane is found from the intersection of *one* of the characteristics with the jet boundary. Thus the appropriate equation of Eqs. 17.35 is used for finding  $\theta_3$  at such a free-boundary point.

There is of course a great similarity between the calculations described here and those described in Chapter 15 for two-dimensional flow. The discussions in that chapter relative to initial-value situations, numerical versus graphical procedures, field method versus net method, organization of the numerical solution, etc., are all applicable here.

**Example of Method.** Fig. 17.21 shows the results of an example<sup>(19)</sup> describing the flow at Mach Number 2.047 past a conical-nosed body. The conical nose, with a semi-vertex angle of  $30^\circ$ , is joined at point 1 ( $x = 3$ ) by a circular arc of radius 10 in the meridian plane.

The flow in the neighborhood of the tip is found from the results of the exact Taylor-Maccoll method for a cone, thus establishing the fluid properties on the cones marked  $30^\circ$ ,  $40^\circ$ ,  $45^\circ$ , and on the downstream side of the shock cone  $47.4^\circ$ .

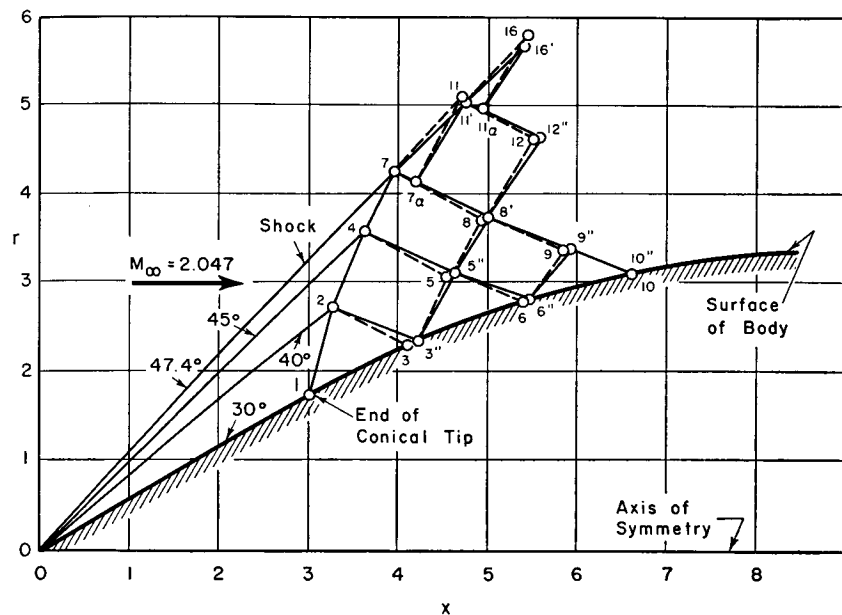


FIG. 17.21. Example of construction of characteristics net (after Cronvich).

All fluid properties are constant on these lines up to the intersection of the *II*-characteristic originating at point 1. In passing, it may be noted that even with a sharp-nosed body not having a conical tip, the exact cone solution is applicable in a limited region near the nose, and is always used to get a set of initial values downstream of the shock for use with the method of characteristics.

Point 2 is located by applying Eqs. 17.33b and 17.35b to the chord 1-2, and finding the intersection of the latter with the line marked  $40^\circ$ . Of course the fluid properties at 2 are known from the cone solution. Points 4 and 7 are located similarly.

Point 3 is found by applying Eqs. 17.33a and 17.35a to the chord 2-3, and finding the intersection of this chord with the surface of the body. The iteration procedure is necessary here, since  $V_3$  is at first not known, and  $\theta_3$  is known only after the location of point 3 is found. The dashed chord 2-3 represents the first approximation, whereas the solid chord 2-3'' represents the third approximation. Similar notation is used for the remainder of the characteristics net.

Point 5 is now found from points 3 and 4, this being a direct application of the unit process previously described. Proceeding in this way, the flow in the entire region 1-7-10 is established.

Downstream of this region the flow is no longer irrotational, because the Mach waves originating at the body weaken the shock where they intersect the latter, and the curvature of the shock in turn produces entropy variations which make the flow rotational.

Often, however, the vorticity created by curvature in the shock wave is small, and a good approximation is obtained by continuing the calculation beyond 7-10 with the assumption that the flow remains irrotational. Using this assumption,

we must now construct the curved portion of the shock simultaneously with the characteristics net.

By straight-line interpolation we choose arbitrarily an intermediate point 7a on the  $I$ -characteristic 7-8'. The point 11' on the downstream side of the shock wave is now found by satisfying simultaneously Eqs. 17.33b and 17.35b for the chord 7a-11, and the oblique shock equations for the direction of 7-11, and the changes in flow properties across the shock at point 11. To accomplish this solution requires the use of the iteration procedure. The position chosen for point 7a is seen to determine the length 7a-11' along the curved part of the shock wave. By continuing this procedure the entire flow downstream of the curved shock and of the line 7-10 may be calculated.

**Graphical Method of de Haller.** An ingenious graphical method, using in part the two-dimensional hodograph characteristics, has been described by de Haller.<sup>(23)</sup> Eq. 17.32 may be rearranged in the form

$$\begin{aligned} (dV)_{I,II} &= \frac{V}{\cot \alpha} [\mp (d\theta)_{I,II} + (\delta\theta)_{I,II}] \\ &= \mp \frac{V}{\cot \alpha} (d\theta)_{I,II} + (\delta V)_{I,II} \end{aligned} \quad (17.36a)$$

where, by definition,

$$(\delta\theta)_{I,II} \equiv \frac{\sin \theta \sin \alpha}{\sin(\theta \mp \alpha)} \frac{dr}{r}; \quad (\delta V)_{I,II} \equiv \frac{V}{\cot \alpha} (\delta\theta)_{I,II} \quad (17.36b)$$

If the flow were two-dimensional, the term  $\delta\theta$  would be zero, and Eq. 17.36a would be the equation of the familiar two-dimensional epicycloid hodograph characteristics (Chapter 15). Referring to Fig. 17.22, we may thus obtain a first approximation to point 3 lying at the intersection of the characteristics passing through the known points 1 and 2 by using the simple graphical construction for the two-dimensional characteristics. The next step is to bring in the correction term  $\delta\theta$  owing to the three-dimensional nature of the flow. Having established point 3 approximately,  $\delta\theta_I$  and  $\delta\theta_{II}$  may be calculated approximately from Eq. 17.36b. Then, because of the form of Eq. 17.36a, we may determine  $\delta V$  by laying out  $\delta\theta$  along the two-dimensional hodograph characteristics. Thus, in Fig. 17.22a, we lay off the angle  $\delta\theta_I$  from point 1 along either of the two-dimensional characteristics passing through 1, thus establishing point 4, and then, by swinging an arc through 4, we determine point 5. The distance 1-5 then represents  $\delta V_I$ . Similarly we construct the chord 2-7 representing  $\delta V_{II}$ . We now complete the hodograph construction by finding the corrected point 3' at the intersection of the two-dimensional characteristics passing through points 5 and 7. Finally, the corrected physical point 3' (Fig. 17.22b) is found by laying off 2-3' at the corresponding mean value of  $(\theta + \alpha)$ , and 1-3' at the corresponding mean value of  $(\theta - \alpha)$ .

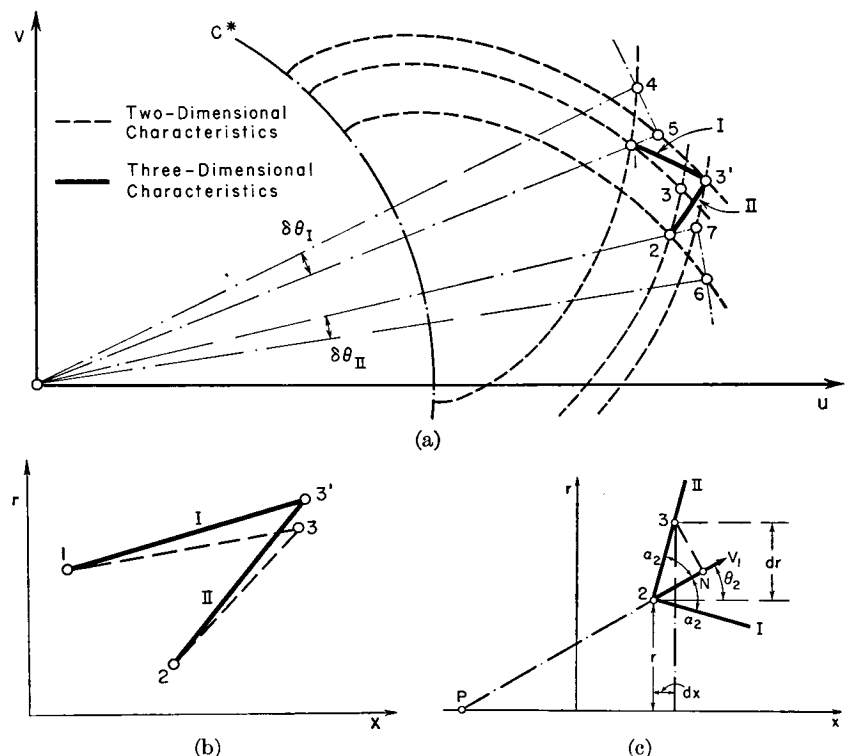


FIG. 17.22. De Haller's graphical method of characteristics.

(a) Hodograph plane.

(b) Physical plane.

(c) Graphical aid to construction.

Fig. 17.22c illustrates a graphical construction for  $\delta\theta_{II}$ . Draw the velocity vector through point 2, and extend it backward to point  $P$ . Draw the normal 3-N. Then, from the geometry of the figure,

$$\frac{r}{\sin \theta} = \overline{P - 2}$$

$$dr = \overline{2 - 3} \sin(\theta + \alpha) = \frac{\overline{3 - N}}{\sin \alpha} \sin(\theta + \alpha)$$

so that, comparing with Eq. 17.36b,

$$(\delta\theta)_{II} = \frac{\overline{3 - N}}{\overline{P - 2}} \quad (17.37)$$

A similar construction may be used for  $\delta\theta_I$ .

The accuracy of the method is illustrated in Fig. 17.22, showing, for a spherical source beginning at the sonic speed, the hodograph

diagram (Fig. 17.23a), the physical plane with Mach waves (Fig. 17.23b), and a chart of  $M^*$  versus location in nozzle (Fig. 17.23c). This chart shows excellent agreement between the stepwise results of the method of characteristics and the exact one-dimensional formula

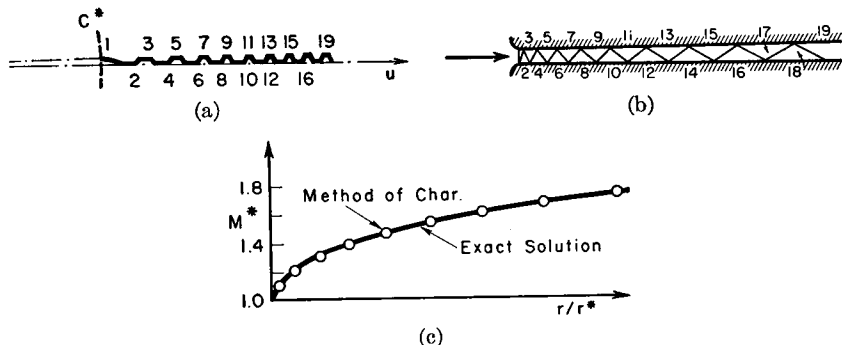


FIG. 17.23. Application of de Haller's method to point source flow.

(a) Hodograph plane.

(b) Physical plane, showing Mach lines.

(c) Comparison of characteristics solution with exact solution.

for isentropic flow. Note that, because of the symmetry of the flow from a point source, it was necessary to investigate only the region of flow in a cone of small vertex angle.

Further applications of the method to flow past a cone and to the design of axi-symmetric nozzles are given in Reference 23.

**Flow with Rotation.** Most supersonic flow patterns with axial symmetry have curved shock waves in important regions of the flow, and hence it is necessary to take account of vorticity in the flow more often than is the case with two-dimensional flow.

Using methods similar to that worked out for two-dimensional rotational flow in Chapter 16, the differential equations of the characteristics are found to be (see References 1, 17, and 20 for details)

$$(dr/dx)_{I,II} = \tan(\theta \mp \alpha) \quad (17.38)$$

$$(d\theta)_{I,II} \pm \frac{\cot \alpha}{V} (dV)_{I,II} \mp \frac{\sin \theta \sin \alpha}{\sin(\theta \mp \alpha)} \frac{(dr)_{I,II}}{r} \pm \frac{\sin \alpha \cos \alpha}{Rk} (ds)_{I,II} = 0 \quad (17.39)$$

where  $R$  is the gas constant and  $s$  is the entropy.

The physical characteristics are, as usual, the Mach lines of the flow. The equation for the hodograph characteristics is similar to that for irrotational flow, except for the addition of the last term, involving the change in entropy  $(ds)$  along the characteristics. In the case under

consideration, for which the stagnation enthalpy is assumed the same everywhere, the entropy remains constant on each streamline, but varies from streamline to streamline. This suggests that we write

$$(ds)_{I,II} = (ds/dn)(dn)_{I,II}$$

where  $n$  is distance normal to the streamline. For the wave of family  $II$ , the geometry of Fig. 17.24 shows that

$$dn_{II} = \frac{\sin \alpha}{\sin(\theta + \alpha)} (dr)_{II}$$

and there is a similar relation for  $(dn)_I$ . Thus, the last term of Eq. 17.39 may be written

$$\pm \frac{\sin^2 \alpha \cos \alpha}{Rk \sin(\theta \mp \alpha)} \left( \frac{ds}{dn} \right) (dn)_{I,II}$$

If the variation of entropy normal to the streamlines is not large, we may, from the geometry of Fig. 17.24, write further

$$\frac{ds}{dn} \cong \frac{s_1 - s_2}{n_2 - n_1} = \frac{s_1 - s_2}{(x_3 - x_2) \frac{\sin \alpha_2}{\cos(\theta_2 + \alpha_2)} + (x_3 - x_1) \frac{\sin \alpha_1}{\cos(\theta_1 - \alpha_1)}}$$

With the help of these expressions, Eqs. 17.38 and 17.39 may be solved in finite-difference form in a manner similar to that already described for irrotational flow.

**Example of Flow Past Projectile.** As an example of the results obtained by the method of characteristics, Fig. 17.25b shows the pressure distribution obtained at  $M_\infty = 3.24$  on the surface of the German rocket projectile of Fig. 17.25a. <sup>(18)</sup> In this particular case there is little error in the calculations as the result of ignoring vorticity behind the curved shock wave. Similar calculations at  $M_\infty = 8$ , however, show that vorticity cannot be ignored in the latter case. Fig. 17.25c shows, for the same body, a comparison of the calculated pressure distributions at three different Mach Numbers. The agreement between the calculated and measured pressure distributions, shown by Fig. 17.25d, is seen to be quite good.

**Example of Flow Past Double-Cone Body.** <sup>(18)</sup> The wave pattern and some of the streamlines for the flow at  $M_\infty = 1.587$  past a body composed of two cones, back to back, is shown in Fig. 17.26a. The corresponding velocity distribution is shown in Fig. 17.26b. The "small mesh" is that of Fig. 17.26a, while the results labeled "large

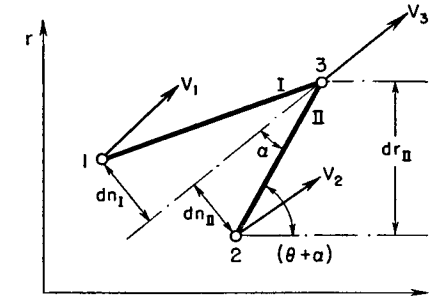


FIG. 17.24. Nomenclature for characteristics method in rotational flow.

mesh" were based on about one-third as many mesh points. There is very little difference in the two sets of calculations except very near the trailing edge.

At the sharp corner near the middle of the body, the flow in the immediate neighborhood of the corner is given exactly by the two-

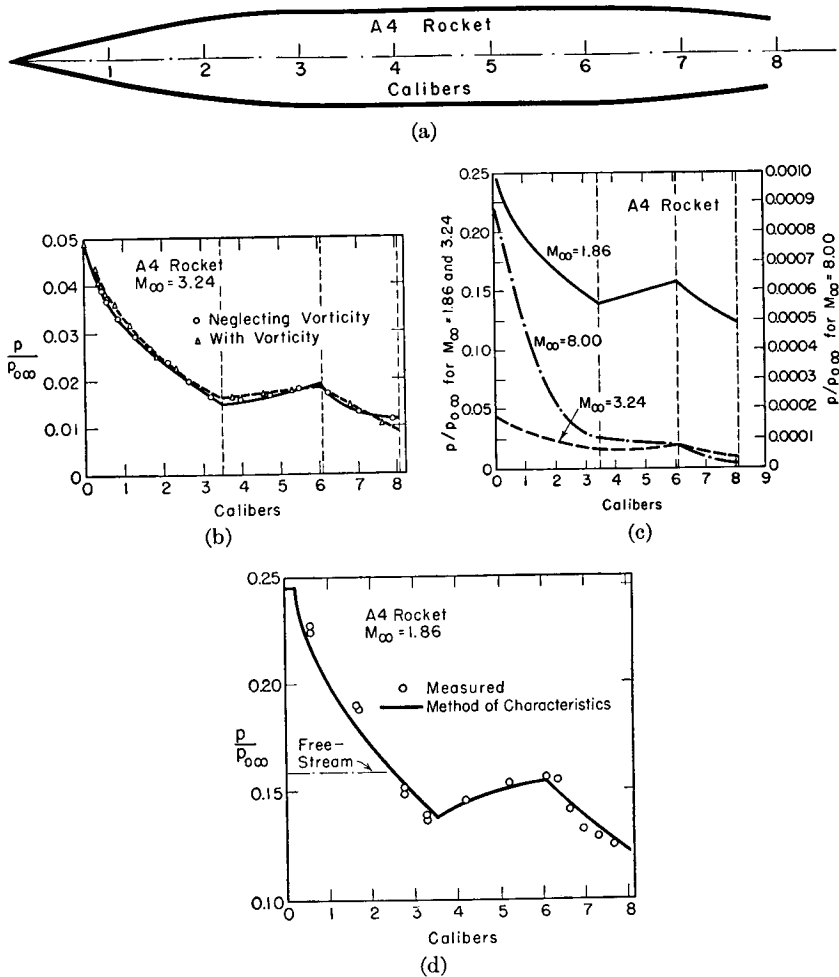


FIG. 17.25. Flow past A-4 rocket (after Isenberg).

- Profile.
- Theoretical pressure distribution at  $M_{\infty} = 3.24$ , as found by method of characteristics. Pressure distribution found by Van Dyke's approximate second-order theory is in almost perfect agreement with curves of this chart.
- Theoretical pressure distributions, as found by method of characteristics, for several Mach Numbers.
- Comparison of measured with theoretical pressure distributions.

dimensional relations for Prandtl-Meyer flow. In this small region changes in radius are negligible compared with the radius itself, and thus the flow may be considered plane. This is a situation frequently encountered with axi-symmetric flow.

**Example of External Flow Around Open-Nosed Body.**<sup>(20)</sup> The wave pattern for the external flow past an open-nosed body, such as a ram jet, is illustrated in Fig. 17.27a, and the corresponding streamline pattern is shown in Fig. 17.27b. The latter figure also indicates that the calculated shock wave shape is in excellent agreement with the observed shape. The corresponding pressure distribution is shown in Fig. 17.27c.

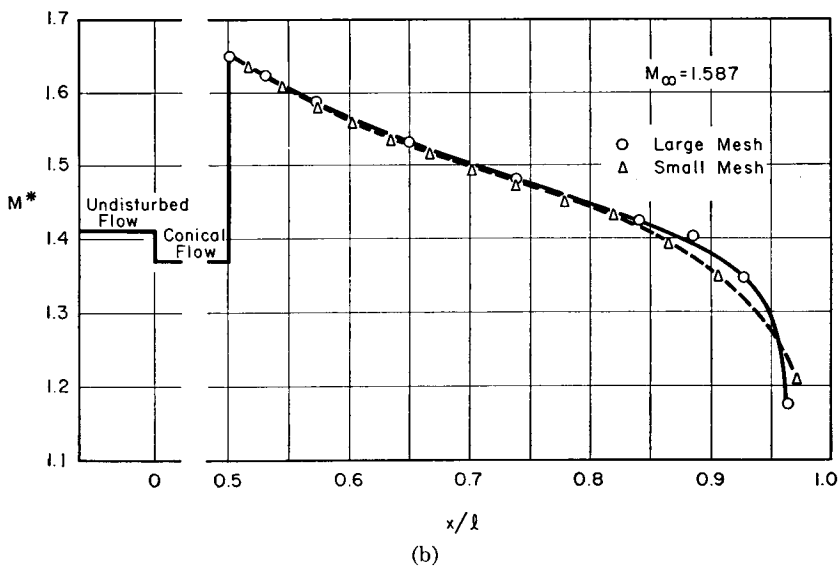
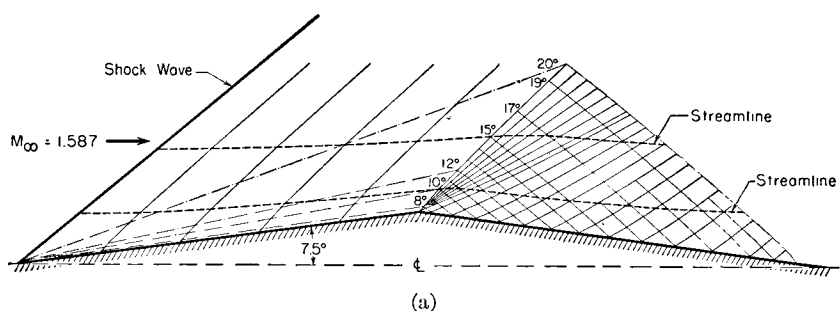


FIG. 17.26. Flow past double-cone body (after Isenberg).

- Streamlines and Mach lines.
- Pressure distributions as found by fine mesh and coarse mesh.

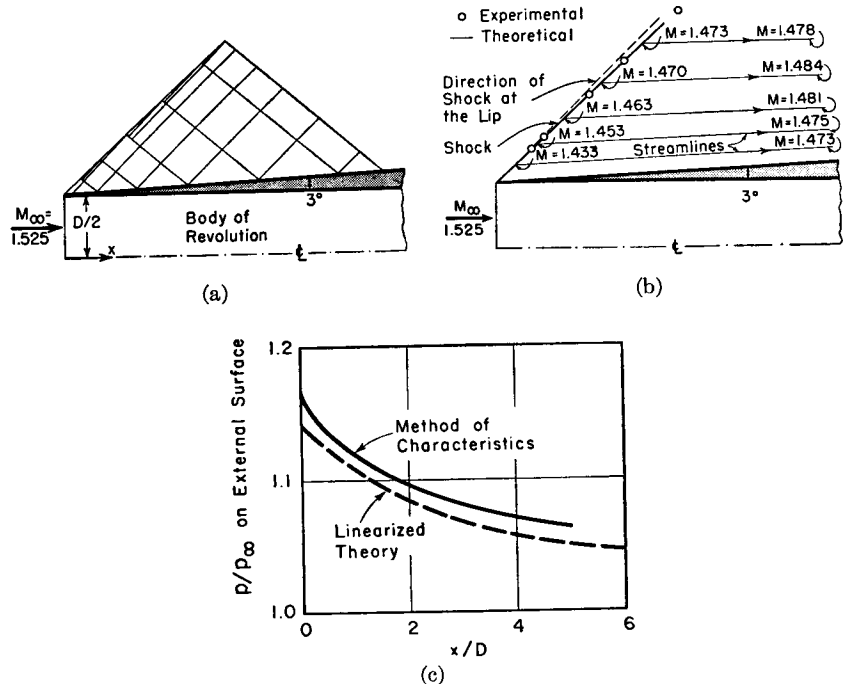


FIG. 17.27. External flow past open-nosed body (after Ferri).

- (a) Characteristics net.  
 (b) Streamlines and shock wave.  
 (c) Surface pressure distribution.

**Example of Internal Flow for Open-Nosed Body.** <sup>(20)</sup> The wave pattern and streamlines for the internal flow near the entrance of a supersonic inlet of revolution are shown in Figs. 17.28a and b. It is found that the shock originating at the lip is strengthened as it moves toward the center line, and, as a result, beyond a certain point the flow is subsonic behind the shock. The extent of subsonic flow for  $M_\infty = 1.6$  is shown in Fig. 17.28c as a function of the lip angle.

Note that the internal and external flows of Figs. 17.27 and 17.28 may be calculated independently of each other as long as the shocks are attached to the lip of the inlet.

**Example of Axially Symmetric Body with Low Pressure Drag.** <sup>(20)</sup> Fig. 17.29 shows the wave pattern and streamlines for the flow through a body of revolution consisting of a central plug and a surrounding cylinder. This body is designed so that no waves are produced externally to the body, and, therefore, the body has only the small amount of pressure drag occasioned by the shock attached to the 10°-inlet cone. Indeed, this drag could be reduced to zero if the plug were properly

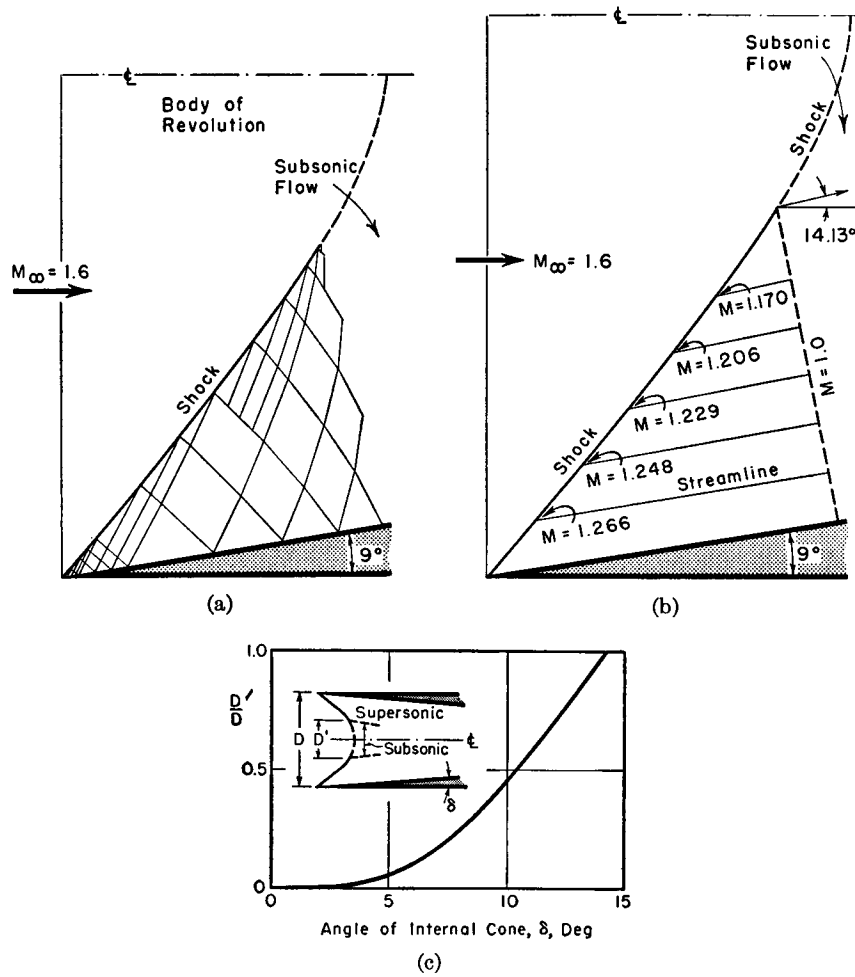


FIG. 17.28. Internal flow through open-nosed body (after Ferri).

- (a) Characteristics net.  
 (b) Streamlines and shock wave.  
 (c) Extent of subsonic flow behind shock.

tapered to zero angle at the inlet. This flow arrangement will be recognized as similar to the Busemann biplane for two-dimensional flow.

**Supersonic Inlets.** For air-breathing propulsion engines at supersonic speeds, it is very important to have supersonic diffusers of high efficiency, and, because of the shape of supersonic aircraft and missiles, it is often convenient to make such diffusers axi-symmetric. A converging-diverging passage, such as is discussed in Chapter 5, comes to

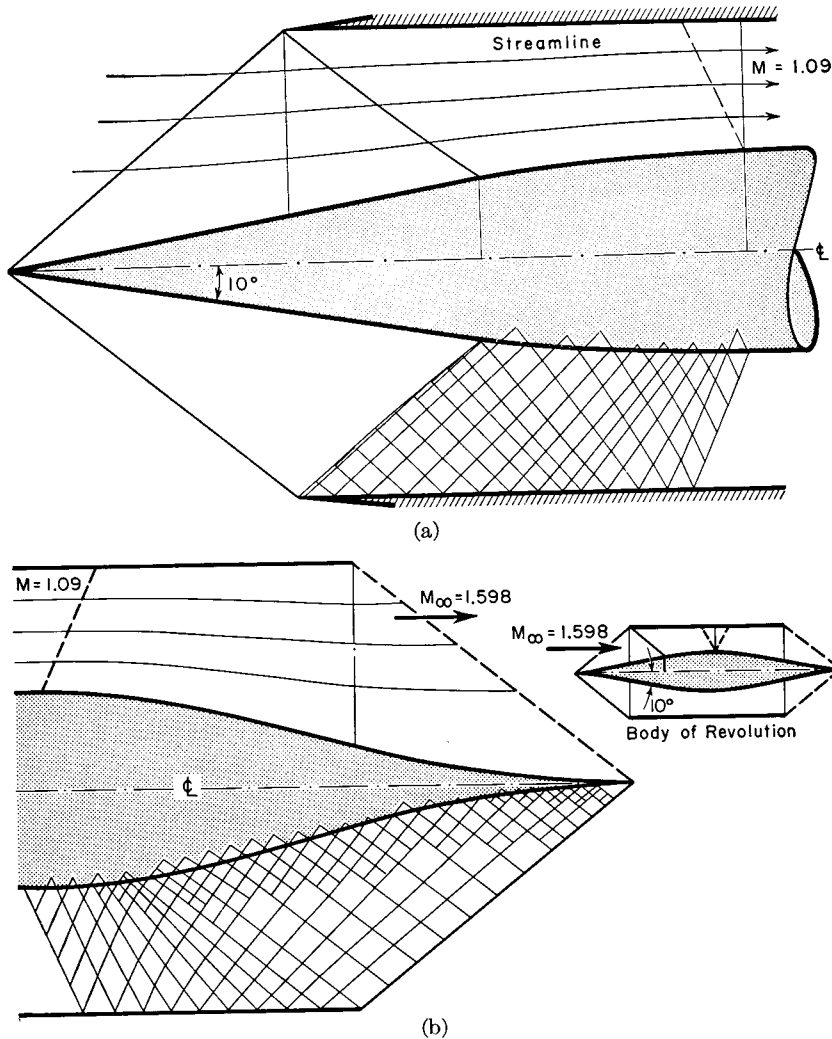


FIG. 17.29. Axi-symmetric body with low pressure drag (after Ferri).

- (a) Mach lines and streamlines for forward half.  
 (b) Mach lines and streamlines for aft half.

mind as the first possibility, but Oswatitsch<sup>(28)</sup> has proposed a type of diffuser with a central plug which has the advantages of providing more usable volume in an aircraft and withal a better efficiency. Figs. 17.8b and 17.29 show inlet diffusers based on this general idea.

In Fig. 17.30 are shown several additional types proposed by Oswatitsch. Fig. 17.30a shows a diffuser with one conical oblique shock and one weak normal shock. The cone may have a rather large included angle, and yet the conical shock is rather weak: at the same time the

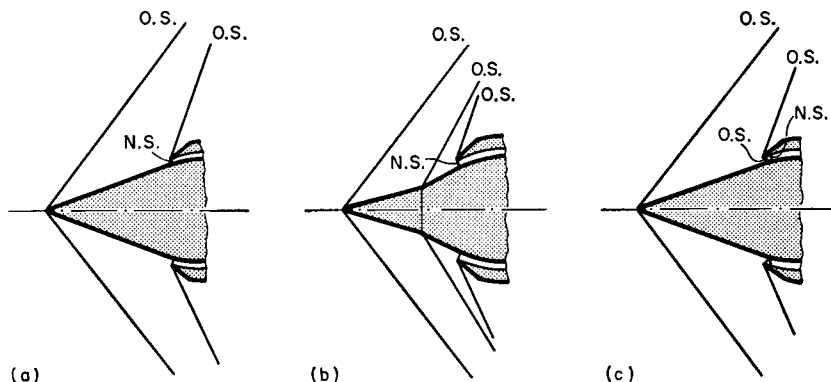
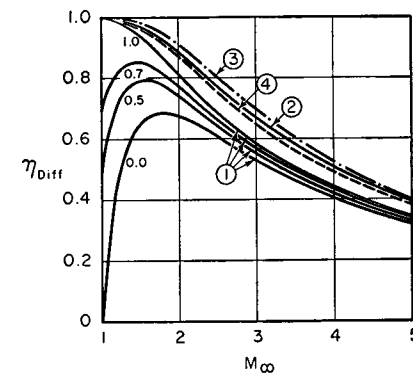


FIG. 17.30. Oblique shock supersonic inlets (after Oswatitsch).

O.S.: Oblique shock.  
 N.S.: Normal shock.

efficient compression downstream of the conical shock reduces the Mach Number to the point where the losses across the normal shock are very small. An extension of this scheme is shown in Fig. 17.30b, where two oblique shocks precede the normal shock. A variant of the latter scheme is illustrated in Fig. 17.30c, where the second oblique shock is generated at the outer rim of the annular intake.

In Fig. 17.31 the efficiency of single-shock conical diffusers<sup>(35)</sup> like that of Fig. 17.8b is compared with that of other types. The conical-

FIG. 17.31. Efficiency of single-shock diffusers for  $k = 1.4$  (after Lukasiewicz).

- Curves 1: Normal shock followed by subsonic diffuser of indicated efficiency.  
 Curve 2: Oblique or conical shock with sonic velocity behind shock, followed by isentropic subsonic compression.  
 Curve 3: Conical shock with sonic velocity at cone surface, followed by isentropic subsonic compression.  
 Curve 4: One-dimensional, fixed-geometry, converging-diverging diffuser with maximum allowable contraction for starting, followed by isentropic subsonic compression.

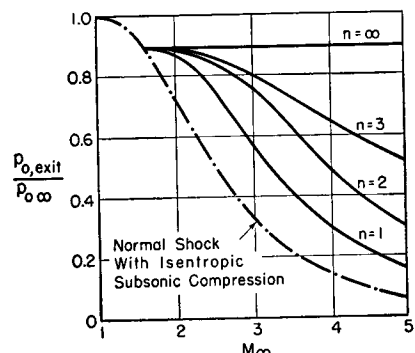


FIG. 17.32. Pressure recovery of multi-shock two-dimensional diffusers for  $k = 1.4$ . There are  $n$  oblique shocks, each with the same stagnation-pressure ratio. Following the last shock, where the Mach Number is 1.6, the stream is further decelerated by a normal shock and then by an isentropic subsonic compression (after Lukasiewicz).

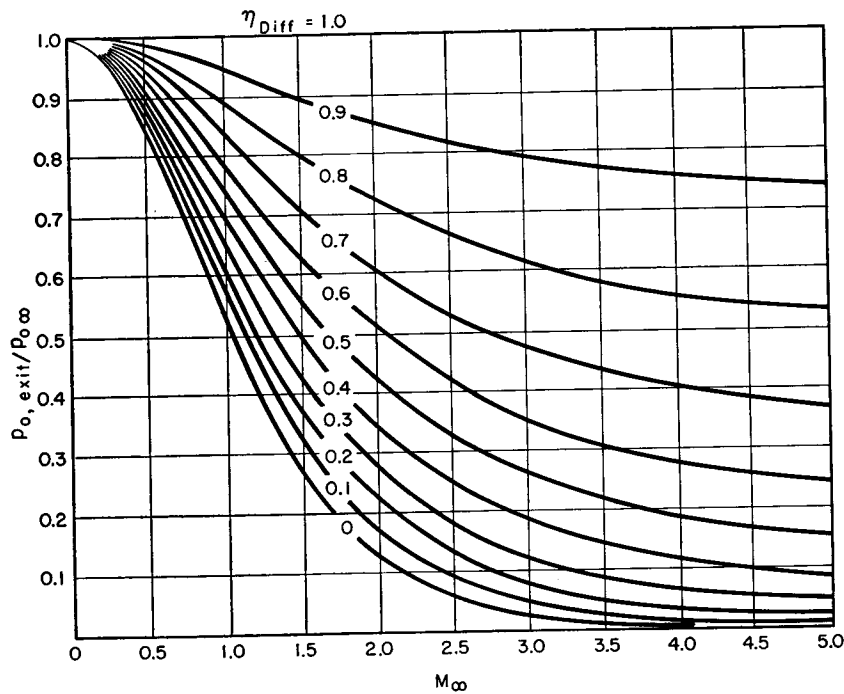


FIG. 17.33. Relation between diffuser efficiency and stagnation-pressure ratio, for  $k = 1.4$ . Based on formulas of Chapter 5, leading to

$$\frac{p_{0,\text{exit}}}{p_{0,\infty}} = \left[ \frac{1 + \eta_{\text{diff}} \frac{k-1}{2} M_{\infty}^2}{1 + \frac{k-1}{2} M_{\infty}^2} \right]^{\frac{1}{k-1}}$$

shock diffuser is seen to be considerably more efficient than a normal-shock diffuser, and is comparable in efficiency with the optimum design of a fixed-geometry, converging-diverging one-dimensional diffuser.

Two practical points to be kept in mind here are (i) the ready adaptability of the plug-type diffuser for variable-geometry applications, and (ii) the frequent need for boundary-layer control in order to prevent the desired flow configuration from being ruined by shock-boundary layer interactions.

The increase in efficiency realizable by substituting a number of weak shocks for a single strong shock is not easily calculated for a plug-type diffuser. Some notion of this improvement may be gained, however, by carrying out the corresponding (and comparatively simple) calculations for a two-dimensional diffuser with a series of oblique shocks. As seen from Fig. 17.32, there is considerable improvement in going from 1 to 2 or 3 shocks, especially at high Mach Numbers.

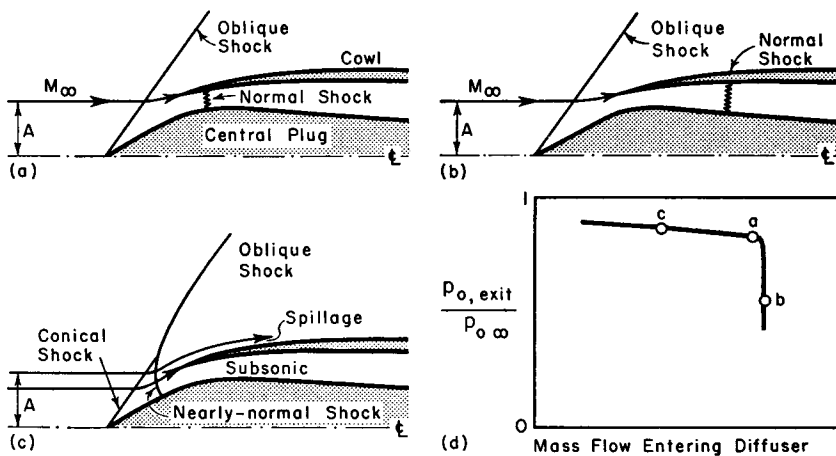


FIG. 17.34. Operation of plug-type diffuser with constant approach conditions but variable discharge pressure.

- (a) Optimum conditions. Maximum mass flow and high pressure recovery.
- (b) Discharge pressure too low. High mass flow but low pressure recovery.
- (c) Discharge pressure too high. High pressure recovery but low mass flow.
- (d) Corresponding curve of pressure recovery versus mass flow.

It may be noted that the performance is expressed in terms of diffuser efficiency (see Chapter 5) in Fig. 17.31, whereas in Fig. 17.32 it is expressed in terms of stagnation-pressure recovery. Since both these measures of performance are used frequently, there is given in Fig. 17.33 a chart for passing quickly from one to the other.

Fig. 17.34 shows the typical performance of a plug-type diffuser at constant approach Mach Number when the discharge pressure of the

diffuser is varied (for example, by means of a throttle valve or by the operation of an engine downstream of the diffuser). Fig. 17.34a represents the design condition, with the maximum mass flow entering the diffuser, and with a high efficiency because the normal shock is at the minimum area. When the back pressure is too low, as in Fig. 17.34b, the flow is still the maximum, but the normal shock occurs at a higher Mach Number, thus producing a larger loss in stagnation pressure. When the back pressure is too high, a normal shock stands ahead of the cowl lip and allows some flow to spill over the cowl lip (Fig. 17.34c), thus reducing the mass rate of flow. The curve of pressure recovery versus mass flow (Fig. 17.34d) is composed of a nearly horizontal part, corresponding to spillage operation with a nearly normal shock, and a vertical portion, corresponding to operation with a swallowed normal shock and with the maximum possible mass rate of flow.

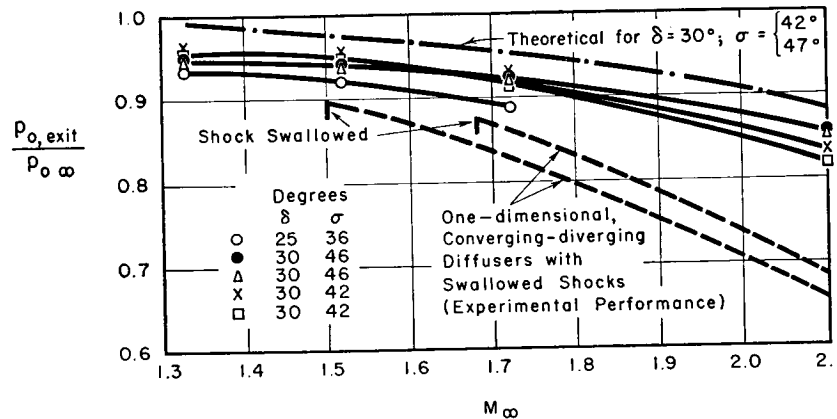


FIG. 17.35. Experimental performance of plug-type diffusers with several cowl designs. Comparison with theoretical performance and with experimental performance of normal shock, converging-diverging diffusers (after Ferri and Nucci).

Fig. 17.35<sup>(36)</sup> shows experimental values of pressure recovery for the optimum conditions of operation (point *a* of Fig. 17.34d) as a function of free-stream Mach Number for several diffusers of the type shown in Fig. 17.34. The measured efficiency is considerably higher than the values attainable with fixed-geometry normal-shock diffusers. One reason for the comparatively high "theoretical" performance is the neglect of viscosity in the theoretical analysis, but it is clear that the measured performance generally follows the theoretical curve.

**Supersonic Nozzle Design.** The design of an axi-symmetric nozzle to produce a uniform, parallel, supersonic flow is somewhat different from the design of a two-dimensional nozzle.

Referring to Fig. 17.36, suppose that along the line *AB* near the throat the distribution of the velocity vector is known. Several points

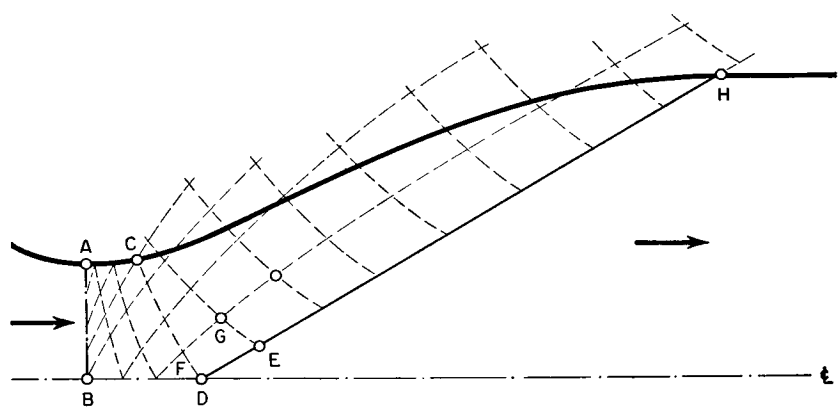


FIG. 17.36. Design of nozzle for parallel, supersonic flow.

on this line are chosen as starting points for the characteristics net. The wall is curved outward from point *A* for some distance, in a manner at the disposal of the designer. The characteristics net is then constructed stepwise in the region downstream of *AB* and bounded by the wall on one side and by the center line of symmetry on the other. This procedure is continued until the design Mach Number of the nozzle is reached along the axis. Let the point at which it is reached be called *D*, and let *C* be the point on the wall lying on the same characteristic as point *D*.

The entire flow pattern is thus far known in the region *A-C-D-B*. The wall contour *A-C* was selected arbitrarily, but beyond *C* the wall must be so shaped as to give the desired uniform parallel flow at exit. The Mach line extending downstream from *D* must be straight because it bounds the uniform, parallel flow of the test section, and so it may be drawn in. Along this line several points are chosen as the end points of *I*-characteristics. If *E* is one of these points, then a point such as *G* may be found from the known data at *F* and *E*. Proceeding in this way the characteristics net is constructed in the region above the characteristic *C-D* and the characteristic *D-E-H*. Once the characteristics are drawn, the velocity is known at each point, and so the streamlines may be drawn.

The particular streamline of interest is the one passing through *C*, for this gives the desired nozzle contour, *C-H*, to produce a uniform, parallel flow at exit. To find this boundary streamline requires, in general, an interpolation for the stream direction  $\theta$  between the net points. As a check on accuracy, the area ratio found by this construction may be compared with the exact area ratio based on one-dimensional isentropic flow.

An approximate analytical method for determining nozzle contours is given in Reference 22.

**Rapid Approximate Method for Pressure Distribution on Circular-Arc Ogives.**<sup>(37)</sup> By examining the results of exact applications of the method of characteristics to a large number of examples, Zienkiewicz<sup>(37)</sup> discovered an empirical rule which greatly reduces the labor of computing the surface pressure distribution on the nose portion of a body of revolution having a circular-arc ogive for a nose. Comparing the actual pressure distribution with that for two-dimensional Prandtl-Meyer flow (which is easily calculated as in Chapter 15) over the same profile, it was found that

$$p_n - p = \lambda(p_n - p_t)$$

where  $\lambda$  remains virtually constant along a given ogive at a given free-stream Mach Number;  $p_n$  is the pressure at the nose just downstream of the attached shock in axi-symmetric flow;  $p$  is the local pressure at point  $P$  on the surface in axi-symmetric flow; and  $p_t$  is the local pressure at  $P$  for a two-dimensional simple-wave expansion from  $p_n$  at the nose. The table below shows how  $\lambda$  depends on the free-stream Mach Number  $M_\infty$  upstream of the nose shock and on the fineness ratio  $L/D$  of the nose ( $L$  is the axial length of the circular-arc ogive from the tip to where it becomes tangent to the cylindrical portion of the body, and  $D$  is the diameter where this tangency occurs).

$L/D$	$M_\infty$						
	1.5	1.6	1.8	2.0	2.5	3.0	3.5
2.0.....		0.820	0.869	0.914			
2.5.....	0.748	.775	.817	.861	0.942		
3.0.....	.713	.738	.781	.821	.906	0.962	
3.5.....			.750	.786	.870	.928	0.968
4.0.....				.762	.840	.899	.938
4.5.....					.813	.870	.911
5.0.....					.795	.845	.887
5.5.....						.826	.864
6.0.....						.810	.844
6.5.....							.827
7.0.....							.814

## 17.5. Miscellaneous Experimental Results

In this article we present some experimental results for practical problems not easily accessible to analysis.

**Static Pressure Probes.**<sup>(24)</sup> Typical results of an experimental investigation of the static pressure on probes having spherical and conical heads are shown in Fig. 17.37. After some 10 diameters downstream

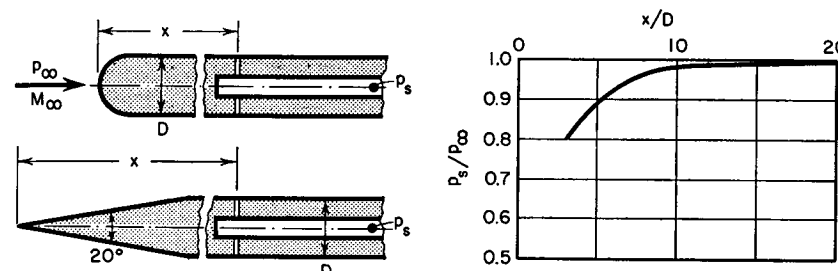


FIG. 17.37. Static pressure at various distances aft of nose of static pressure probe (after Cronvich).

of the tip the static pressure is within one or 2 per cent of free-stream pressure for either type of probe. This instrument is, therefore, useful for measuring static pressures in a supersonic stream. Extensive data are given in Reference 24.

**Drag of Projectiles.**<sup>(25)</sup> Typical measurements of the drag of projectiles are shown in Fig. 17.38. The drag coefficient is seen to decrease

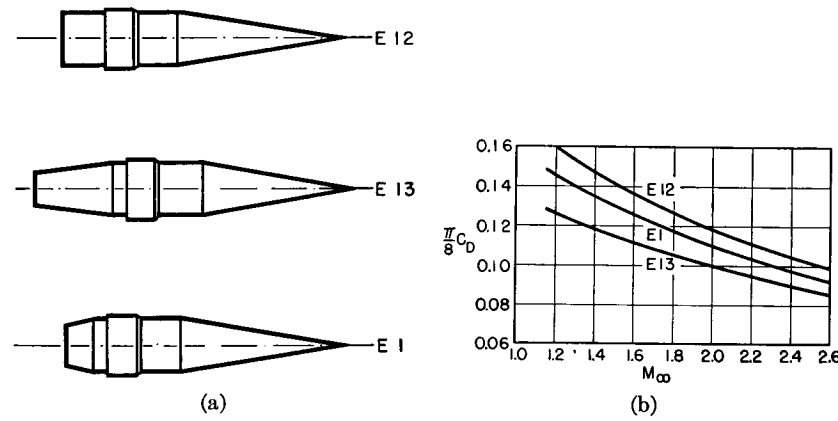


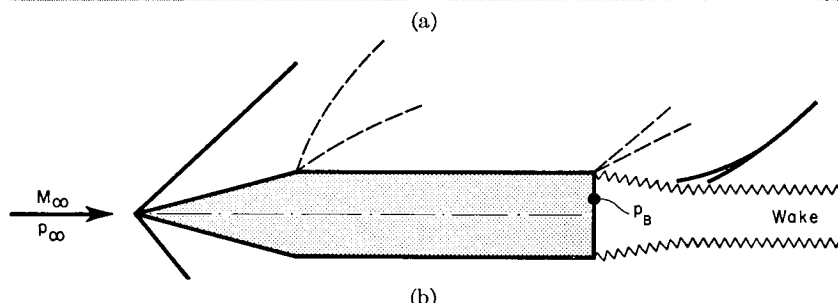
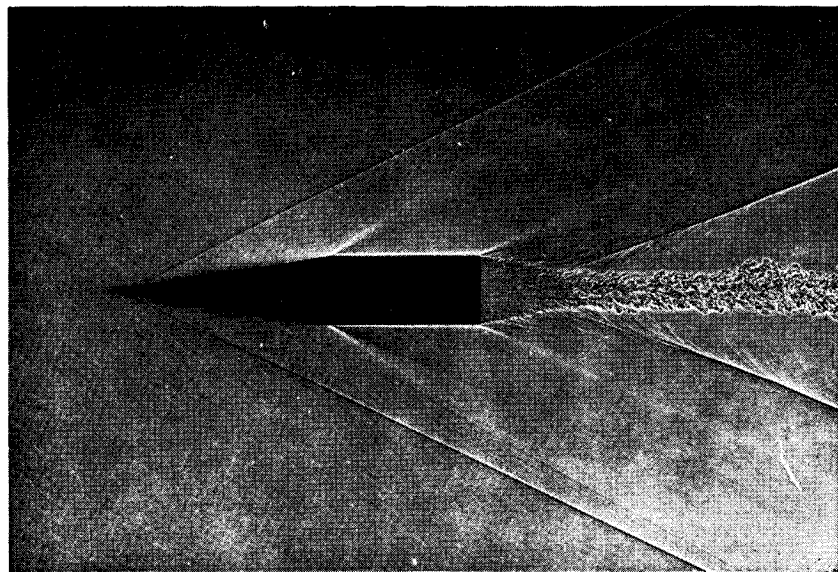
FIG. 17.38. Drag of projectiles (after Charters).

(a) Projectile shapes.

(b) Drag coefficient versus Mach Number.

with Mach Number, but the rate of decrease is small at high Mach Numbers. The drag coefficient at supersonic speeds is generally far greater than that at subsonic speeds.

**Base Pressure on Projectiles.**<sup>(31,32)</sup> Most supersonic projectiles, missiles, and aircraft have a flat base, either circular or annular. The pressures on this base contribute in either a positive or negative way to the drag of the body.



(a) Schlieren photograph of cone-cylinder at  $M_\infty = 2.33$ , with turbulent boundary layer on cylindrical part of projectile (Ballistic Research Laboratories, Aberdeen).  
 (b) Nomenclature.  
 (c) Summary of measurements of base pressure versus Mach Number (after Kurzweg).

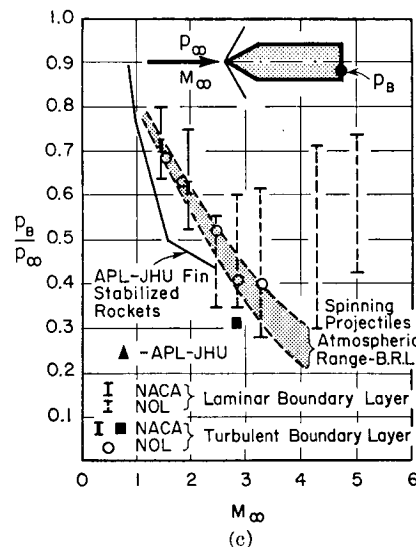


FIG. 17.39. Base pressure on projectiles.

Using the nomenclature of Fig. 17.39b, the *base drag* is defined as

$$D_{\text{base}} \equiv (p_\infty - p_B) A_b$$

where  $A_b$  is the area of the flat base on which the base pressure  $p_B$  acts.

Fig. 17.39a is a typical schlieren photograph of the flow near the base of a projectile. Near the end of the cylindrical portion the surface pressure is not very different from  $p_\infty$ . As the flow leaves the projectile it expands around the edge in a Prandtl-Meyer expansion. The base pressure is therefore smaller than  $p_\infty$  and, consequently, the base drag is positive. When a jet issues from the rear end (as in a rocket) the situation may of course be different.

Fig. 17.39c is a summary of many tests on cone-cylinder projectiles. In a general way the base drag is seen to increase with Mach Number, but the base drag coefficient ( $2D_{\text{base}}/kp_\infty M_\infty^2 A_b$ ) decreases with Mach Number.

The nature of the boundary-layer flow at the aft end of the cylinder is found by experiment to be all-important in the determination of the base pressure. The effects of variations in Reynolds Number are extremely large for a laminar boundary layer, but are quite small for a fully developed turbulent layer. It is accordingly difficult to predict the base drag with good accuracy unless it is known that the boundary layer is turbulent.

When the Reynolds Number is increased, the Mach Number being maintained constant, the base pressure decreases as long as the boundary layer is laminar. As the Reynolds Number reaches the point where transition to turbulence occurs, the base pressure rises, thus reducing the base drag. At very high Reynolds Numbers  $p_B/p_\infty$  is nearly independent of Reynolds Number. From Fig. 17.39c it may be seen that the base pressure for a turbulent boundary layer lies between the maximum and minimum values which are attained with a laminar boundary layer.

Apart from the effects mentioned above, other aspects of the experimental measurements may be summarized as follows: <sup>(32)</sup>

- Large changes in surface temperature can significantly alter the base pressure.
- The effect of body shape is great for length-diameter ratios less than about 4 but is small for length-diameter ratios greater than about 6.
- The presence of tail fins can considerably change the base drag.

#### REFERENCES AND SELECTED BIBLIOGRAPHY

- FERRI, A. *Elements of Aerodynamics of Supersonic Flows*. New York: The Macmillan Co., 1949.
- SAUER, R. *Introduction to Theoretical Gas Dynamics*. Ann Arbor: J. W. Edwards, 1947.

3. BUSEMANN, A. Drucke auf Kegelformige Spitzen bei Bewegung mit Überschallgeschwindigkeit, *Z.a.M.M.*, Vol. 9 (1929), p. 496.
4. TAYLOR, G. I., and MACCOLL, J. W. The Air Pressure on a Cone Moving at High Speed, *Proc. Roy. Soc. (A)*, Vol. 139 (1933), p. 278.
5. HANTZSCHE, W., and WENDT, H. Cones in Supersonic Flow, *NACA Tech. Memo.*, No. 1157 (1947).
6. KOPAL, Z. *Tables of Supersonic Flow Around Cones*, M.I.T. Center of Analysis, Tech. Report No. 1, M.I.T., 1947.
7. DAILEY, C. L., and WOOD, F. C. *Computation Curves for Compressible Fluid Problems*, New York: John Wiley & Sons, Inc., 1949.
8. KOPAL, Z. *Tables of Supersonic Flows Around Yawing Cones*, M.I.T. Center of Analysis, Tech. Report No. 3, M.I.T., 1947.
9. KOPAL, Z. *Supersonic Flow Around Cones of Large Yaw*, M.I.T. Center of Analysis, Tech. Report No. 5, M.I.T., 1947.
10. VON KÁRMÁN, T., and MOORE, N. B. The Resistance of Slender Bodies Moving with Supersonic Velocities with Special Reference to Projectiles, *Trans. A.S.M.E.*, Vol. 54 (1932), pp. 303-10.
11. THOMPSON, J. R. A Rapid Graphical Method for Computing the Pressure Distribution at Supersonic Speeds on a Slender Body of Revolution, *NACA Tech. Note*, No. 1768 (1949).
12. JONES, R. T., and MARGOLIS, K. Flow Over a Slender Body of Revolution at Supersonic Velocities, *NACA Tech. Note*, No. 1768 (1949).
13. SEARS, W. R. On Projectiles of Minimum Wave Drag, *Quarterly App. Math.*, Vol. 4, No. 4 (1947), p. 361.
14. LUDLOFF, H. F., and REICHE, F. Linearized Treatment of Supersonic Flow Through Ducts, *Jour. Aero. Sci.*, Vol. 16, No. 1 (1949), p. 5.
15. MOORE, F. Linearized Supersonic Axially Symmetric Flow About Open-Nosed Bodies Obtained by Use of Stream Function, *NACA Tech. Note*, No. 2116 (1950).
16. LAITONE, E. V. The Linearized Subsonic and Supersonic Flow About Inclined Slender Bodies of Revolution, *Jour. Aero. Sci.*, Vol. 14, No. 11 (1947), p. 631.
17. ISENBERG, J. S., and LIN, C. C. The Method of Characteristics in Compressible Flow, Part I (Steady Supersonic Flow), *Air Materiel Command Report*, No. F-TR-1173A-ND (Dec., 1947).
18. ISENBERG, J. S. The Method of Characteristics in Compressible Flow, Part IB (Numerical Examples), *Air Materiel Command Report*, No. F-TR-1173C-ND (Dec., 1947).
19. CRONVICH, L. L. A Numerical-Graphical Method of Characteristics for Axially Symmetric Isentropic Flow, *Jour. Aero. Sci.*, Vol. 15, No. 3 (1948), p. 155.
20. FERRI, A. Application of the Method of Characteristics to Supersonic Rotational Flow, *NACA Tech. Note*, No. 1135 (1946).
21. FERRI, A. The Method of Characteristics for the Determination of Supersonic Flow Over Bodies of Revolution at Small Angles of Attack, *NACA Tech. Note*, No. 1809 (1949).
22. FOELSCH, K. The Analytic Design of an Axially Symmetric Laval Nozzle for a Parallel and Uniform Jet, *Jour. Aero. Sci.*, Vol. 16, No. 3 (1949), p. 161.
23. DE HALLER, P. The Application of a Graphic Method to Some Dynamic Problems in Gases, *Sulzer Technical Review*, No. 1 (1945), p. 6.
24. CRONVICH, L. L. *Pressure Distributions Over a Cylinder with Conical or Hemispherical Head*, Report No. CM-528 of the Applied Physics Lab. of Johns Hopkins Univ., 1949.
25. CHARTERS, A. C. Some Ballistic Contributions to Aerodynamics, *Jour. Aero. Sci.*, Vol. 14, No. 3 (1947), p. 155.
26. HILL, F. K. Base Pressure at Supersonic Velocities, *Jour. Aero. Sci.*, Vol. 17, No. 3 (1950), p. 185.
27. HEBERLE, J. W., WOOD, G. P., and GOODERUM, P. B. Data on Shape and Location of Detached Shock Waves on Cones and Spheres, *NACA Tech. Note*, No. 2000 (1950).

28. OSWATITSCH, K. Pressure Recovery for Missiles with Reaction Propulsion at High Supersonic Speeds, *NACA Tech. Memo.*, No. 1140 (1947).
29. MACCOLL, J. W. The Conical Shock Wave Formed by a Cone Moving at a High Speed, *Proc. Roy. Soc. (A)*, Vol. 159 (1937), p. 459.
30. VAN DYKE, M. D. First- and Second-Order Theory of Supersonic Flow Past Bodies of Revolution, *Jour. Aero. Sci.*, Vol. 18, No. 3 (1951), p. 161. See also: VAN DYKE, M. D. Practical Calculation of Second-Order Supersonic Flow Past Nonlifting Bodies of Revolution, *NACA Tech. Note*, No. 2744 (1952). See also: VAN DYKE, M. D. A Study of Second-Order Supersonic Flow Theory, *NACA Report*, No. 1081 (1952).
31. KURZWEG, H. H. Interrelationship Between Boundary Layer and Base Pressure, *Jour. Aero. Sci.*, Vol. 18, No. 11 (1951), p. 743.
32. CHAPMAN, D. R. Note on Base Pressure Measurements, *Jour. Aero. Sci.*, Vol. 17, No. 12 (1950), p. 812.
33. EHRET, D. M. Accuracy of Approximate Methods for Predicting Pressure on Pointed Nonlifting Bodies of Revolution in Supersonic Flow, *NACA Tech. Note*, No. 2764 (1952).
34. EGGRERS, A. J., JR., and SAVIN, R. C. Approximate Methods for Calculating the Flow About Nonlifting Bodies of Revolution at High Supersonic Speeds, *NACA Tech. Note*, No. 2579 (1951).
35. LUKASIEWICZ, J. Supersonic Diffusers, *British A.R.C.*, R & M No. 2501 (1952).
36. FERRI, A., and NUCCI, L. M. Preliminary Investigation of a New Type of Supersonic Inlet, *NACA Tech. Note*, No. 2286 (1951).
37. ZIENKIEWICZ, H. K. A Method for Calculating Pressure Distributions on Circular Arc Ogives at Zero Incidence at Supersonic Speeds, Using the Prandtl-Meyer Flow Relations, *British A.R.C.*, C. P. No. 114 (1953).

## PROBLEMS

**17.1.** Demonstrate, for the axi-symmetric flow past a cone, that the condition of irrotationality is  $dV_r/d\omega = V_\infty$ . Employ a geometrical interpretation based on the facts that (i) the pressure is constant on rays emanating from the origin, and (ii) the vector change in velocity is in the direction of the pressure gradient.

**17.2.** Demonstrate by simple physical reasoning that the type of flow typified by plane flow past a wedge, i.e., with all changes in stream properties occurring exclusively across the oblique shock, is impossible for flow past a cone.

**17.3.** Demonstrate that, for the region of flow between a conical shock wave and a cone, the hodograph of the streamline has the differential equation

$$v \frac{d^2v}{du^2} = 1 + \left( \frac{dv}{du} \right)^2 - \left( \frac{u + v \frac{dv}{du}}{c} \right)^2$$

**17.4.** Demonstrate that in an axi-symmetric supersonic flow, if the  $x$ - and  $r$ -components of velocity are unique functions of each other, then the only possible flow pattern is one in which the surfaces of constant fluid properties are cones having a common vertex.

**17.5.** Investigate the supersonic flow past a cone for isothermal flow ( $k = 1$ ) and demonstrate that

$$\frac{V_r}{(V_r)_{\omega=\delta}} = \cos(\omega - \delta)$$

Determine the shape of the streamlines, and other properties of the flow pattern.

**17.6.** Find, for a cone, a relation between the surface pressure coefficient,  $C_p$ , and the drag coefficient based on the base area of the cone.

**17.7.** (a) Find the equation of the perturbation streamlines in the  $x$ ,  $y$ -meridian plane for a "supersonic source" placed in a uniform, parallel stream. Demonstrate that these perturbation streamlines are equilateral hyperbolas for  $M_\infty = \sqrt{2}$ .

(b) Determine the pressure coefficient produced by the source at each point on the streamline, and express the pressure coefficient in terms of the  $x$ -coordinate of the streamline.

**17.8.** Investigate the shape of the streamlines for the linearized solution of flow past a cone, and compare with the exact solution.

Show that for this approximate solution all fluid properties are uniform on cones having a common vertex.

**17.9.** Using the linearized theory, determine the surface pressure distribution and the wave-drag coefficient for a body with fineness ratio 10 at speed  $M_\infty = \sqrt{2}$  having the form

$$\frac{R}{R_{\max}} = \sin \pi \frac{x}{L}$$

**17.10.** Determine the pressure distribution on the body of Fig. 17.25a by the linearized theory, and compare the results with Fig. 17.25b.

**17.11.** Develop the characteristic equations for axi-symmetric, irrotational flow, assuming that the perturbation velocities are sufficiently small to make the linearized equations applicable.

## Chapter 18

### SUPERSONIC FLOW PAST WINGS OF FINITE SPAN

#### 18.1. Introductory Remarks

In Chapters 14, 15, and 16 it was shown how two-dimensional supersonic flows past any profile could be solved with relative ease. The methods presented there lead to the aerodynamic properties of untapered wings of infinite span having rectangular planforms.

In all practical situations, however, we must deal with wings of finite span, and so it is important to understand the effects produced by the ends of such wings. Furthermore, it is of interest to determine whether the aerodynamic properties of supersonic wings may be improved or controlled through changes in planform effected through sweepback or sweepforward of the leading and trailing edges, or of raking the wing tip.

In this chapter we shall outline the methods available for treating such problems, and shall summarize those results of greatest practical importance.

Because of the great mathematical difficulties attached to three-dimensional flows, it is necessary, except in the discussion of the infinite sweepback wing, to employ the method of small perturbations. This is tantamount to the assumption that the wing is very thin in one of the directions lateral to the flow, and, correspondingly, that only first-order changes in all fluid properties are significant. As supersonic wings must be thin in order to escape the penalty of large drag, the restriction to small perturbations is not necessarily of serious consequence.

In addition to neglecting second-order perturbations, we shall ignore viscous effects and shall assume the flow irrotational and isentropic. The net consequence of making these assumptions is that for most aerodynamically desirable wings we get a good approximation to the pressure distribution at the wing surface unless the boundary layer either separates or exhibits rapid rates of growth.

The significance and validity of the non-viscous theory are examined in the final part of the chapter through a comparison with experimental results.

## NOMENCLATURE

$\alpha$	angle of attack	$U_\infty$	free-stream velocity
$\mathcal{R}$	aspect ratio	$x, y, z$	Cartesian coordinates
$b$	span; also chordwise position of maximum thickness position	$\alpha_\infty$	free-stream Mach angle
$c$	speed of sound	$\beta$	$\sqrt{M_\infty^2 - 1}$
$d$	see Figs. 18.17a and 18.19a	$\delta$	thickness ratio
$C_p$	pressure coefficient	$\eta$	$y$ -coordinate of source
$C_L$	lift coefficient	$\theta$	cylindrical coordinate
$C_D$	pressure drag coefficient	$\lambda$	$\tan \Lambda$
$C_f$	skin-friction coefficient	$\Lambda$	sweepback angle of leading edge
$C_{D,\text{tot}}$	sum of coefficients of pressure drag and skin friction	$\Lambda_{\frac{1}{2}}$	sweepback angle of mid-chord line
$D$	drag	$\mu$	$(\pi/2) - \Lambda$
$e$	see Figs. 18.17a and 18.19a	$\xi$	$x$ -coordinate of source
$L$	lift	$\tau$	slope of surface in $y, z$ -plane
$l$	chord	$\varphi$	perturbation velocity potential
$M$	Mach Number	$\Phi$	defined by Eq. 18.38
$n$	$\lambda/\beta$	$(\cdot)_\infty$	signifies free-stream conditions; also signifies aerodynamic properties of unswept wing of infinite span
$p$	pressure	$(\cdot)_n$	signifies component normal to leading edge
$q$	intensity of source distribution; also conical-flow parameter (Eq. 18.32)	$(\cdot)_t$	signifies component tangential to leading edge
$r$	radius in cylindrical coordinates	$(\cdot)_e$	signifies equivalent two-dimensional, for swept wing
$\mathfrak{R}$	real part of a complex variable		
$s$	transformed $q$ -variable (see Eq. 18.35)		
$t$	thickness of wing; also $\lambda y/x$		
$u, v, w$	Cartesian velocity components		

## 18.2. Preliminary Considerations of Finite Wings

Certain rules useful to the understanding of finite wings may be derived from our general knowledge of the behavior of supersonic flows and of flows with small perturbations.

**Regions of Two-Dimensional Flow on Finite Wings.** Because of the rule that in supersonic flow a disturbance is felt only within the Mach cone extending downstream from the source of disturbance, certain portions of finite wings behave as though they were in a two-dimensional flow. To illustrate this point, consider (Fig. 18.1a) a wing of infinite span with a thin profile at a small angle of incidence. Any disturbances

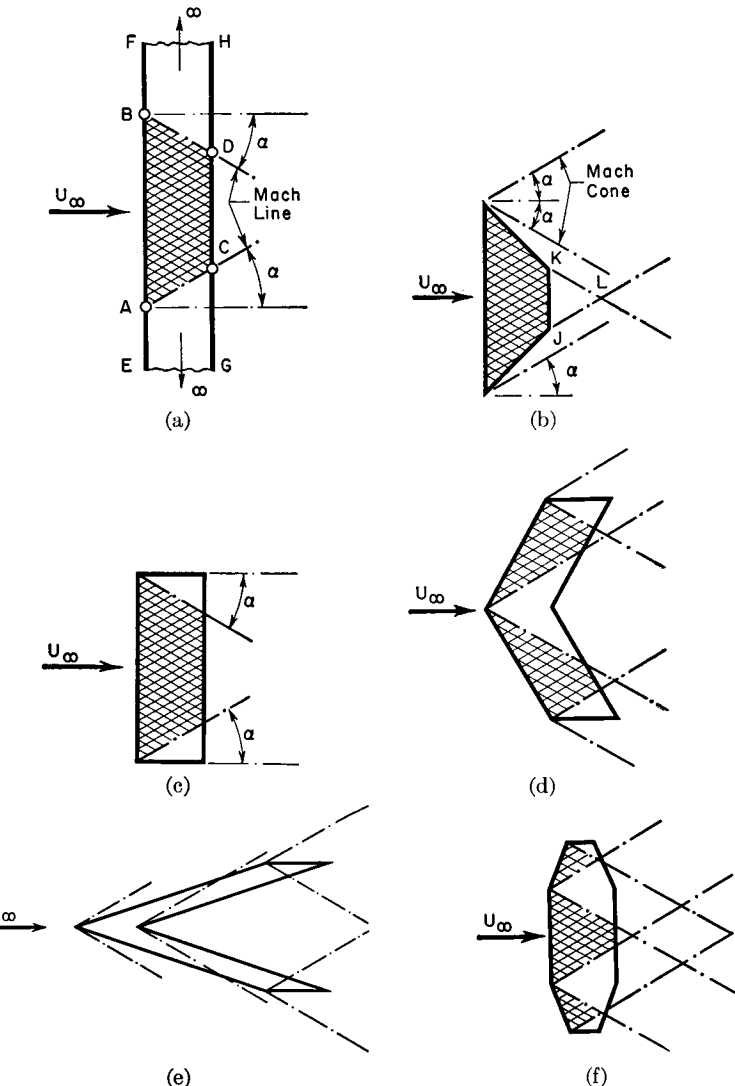


FIG. 18.1. Illustrates regions where two-dimensional flow prevails on three-dimensional wings. Shaded zones signify two-dimensional flow.

produced in the regions  $E-A-C-G$  or  $B-F-H-D$  cannot influence the flow in  $A-B-D-C$ . Therefore, if the infinite wing is cut along  $A-C$  and  $B-D$ , and if all except the finite wing  $A-B-D-C$  is removed, this finite wing will produce the same two-dimensional flow that it would if it were part of an infinite wing. The downwash pattern behind the wing, however, will not be completely two-dimensional.

By applying the same reasoning to the other planforms of Fig. 18.1,

it may be shown that two-dimensional flow exists in those regions which are shaded.

When the wing is unswept, but the wing ends are raked inside the Mach cones emanating from the ends of the leading edge, as in Fig. 18.1b, the flow over the entire planform is two-dimensional. The downwash in the plane of the wing, however, is two-dimensional only in the region  $J-K-L$ . With an unswept wing having its ends within the tip Mach cones, as in Fig. 18.1c, the flow is two-dimensional except within the tip Mach cones.

If a wing of infinite span were swept back, the flow past it would appear two-dimensional to an observer moving along the span at such a speed that in the observer's coordinate system the oncoming flow was normal to the spanwise direction. Such a wing may be calculated by the methods of two-dimensional flow, using the simple corrections outlined in Art. 18.3. With this in mind, it follows that the arrowhead wing of Fig. 18.1d will have two-dimensional flow except within the tip Mach cones and the Mach cone originating at the forward point. If the leading edges of such a wing were swept behind the Mach line from the forward point, however, as in Fig. 18.1e, no part of the flow would be two-dimensional.

The shaded portions of Fig. 18.1 indicate only those portions in the plane of the wing where the flow is two-dimensional. To determine which portions of the flow away from the wing surface are two-dimensional, it must be recalled that the disturbances of the wing tips, etc., are propagated within the Mach cones.

From these considerations it is clear that, for a given wing planform, whether or not an element of the wing surface has two-dimensional or three-dimensional flow over it depends in part on the free-stream Mach Number.

**Supersonic and Subsonic Leading and Trailing Edges.** Consider a swept wing of infinite span, as in Fig. 18.2. The free-stream velocity  $U_\infty$  may be resolved into components along the span ( $U_{\infty n}$ ) and normal to the span ( $U_{\infty t}$ ). An observer moving along the span with the uniform speed  $U_{\infty t}$  sees a two-dimensional flow with the free-stream velocity  $U_{\infty n}$  past an unswept wing. Whether this equivalent two-dimensional flow is supersonic or subsonic depends on whether  $U_{\infty n}$  is, respectively, greater or less than  $c_\infty$ . Since  $c_\infty = U_\infty \sin \alpha_\infty$ , and  $U_{\infty n} = U_\infty \sin \mu$ , it follows that

$$M_{\infty n} = U_{\infty n}/c_\infty = \sin \mu / \sin \alpha_\infty$$

Hence the equivalent two-dimensional flow is supersonic if  $\mu$  exceeds the Mach angle (Fig. 18.2a) but is subsonic if  $\mu$  is less than  $\alpha_\infty$  (Fig. 18.2b). In the former case we say that the leading edge is supersonic, and in the latter that it is subsonic. Identical considerations apply to

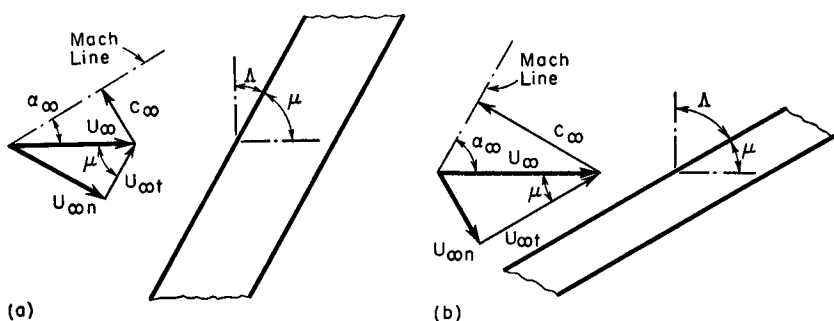


FIG. 18.2. Swept leading edges.

(a) Supersonic leading edge ( $U_{\infty n} > c_\infty$ ).  
(b) Subsonic leading edge ( $U_{\infty n} < c_\infty$ ).

the trailing edge. Thus, in Fig. 18.1d both the leading and trailing edges are supersonic, whereas in Fig. 18.1e both the leading and trailing edges are subsonic.

The significance of the natures of the leading and trailing edges may be illustrated by considering the details of the mechanism by which lift is produced on a flat plate of infinite span. Fig. 18.3 shows schem-

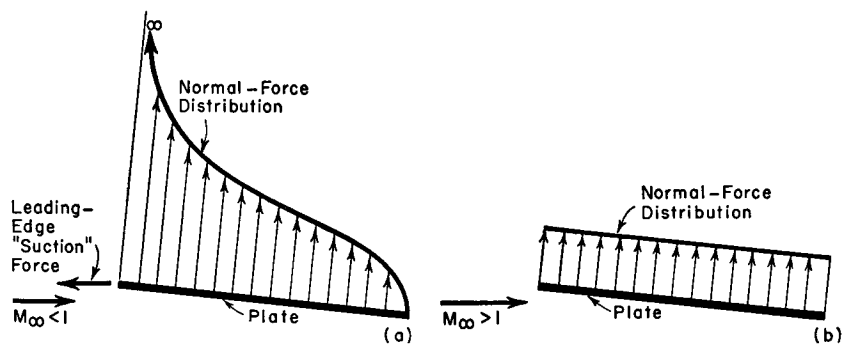


FIG. 18.3. Chordwise distribution of pressure force on flat plate at angle of attack.

(a) Subsonic.  
(b) Supersonic.

atically the lift distributions over the chord of such a wing in subsonic and supersonic flow.

In the starting instant of subsonic flow, the motion around the wing is both irrotational and without circulation, and hence produces no lift. However, this flow has infinite velocity around the sharp trailing edge, and, as a result of viscosity, no matter how small the latter may be, the flow separates near the trailing edge and produces a vortex. In accordance with Kelvin's Theorem, the shedding of this "starting vortex" has as a reaction the production of circulation around the profile,

the magnitude of the circulation being determined by the Kutta-Joukowski condition that the rearward stagnation point be at the trailing edge. From this it follows that the fluid pressures acting on the upper and lower surfaces of the airfoil at the trailing edge are equal, and the trailing-edge lift per unit area is zero (Fig. 18.3a).

In supersonic flow the trailing-edge lift per unit area, in consequence of the rule of forbidden signals, need not be zero. Indeed, since in supersonic simple-wave flow the local pressure depends only on the local inclination of the surface, the lift distribution of the flat plate is constant over the chord (Fig. 18.3b).

Near the leading edge in incompressible flow the lift per unit area tends toward infinity, in accordance with the infinite fluid velocity at the sharp corner. It may be argued that this infinite velocity necessarily leads to boundary-layer separation. This difficulty is eliminated, however, by allowing a small rounding of the leading edge, a change which does not alter the essential character of the flow over most of the profile. The very low pressures at the leading edge produce a "suction force" which cancels the drag component of the normal force, and leads to zero net drag, skin friction excepted (d'Alembert's Paradox). In supersonic flow, this "suction force" is not present, and there results an "induced drag due to lift."

We may summarize the foregoing considerations as follows: (i) supersonic leading and trailing edges have finite lift loadings, (ii) a subsonic leading edge tends to have a very high lift loading and a negative drag force, and (iii) a sharp subsonic trailing edge has zero lift loading.

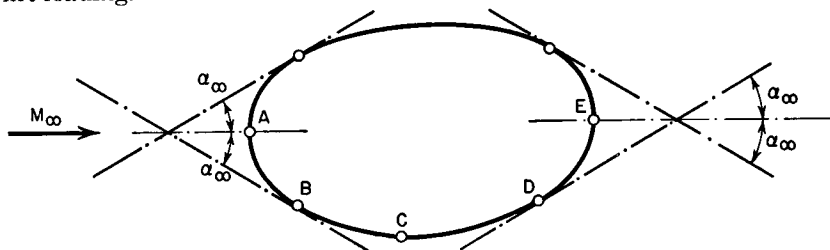


FIG. 18.4. Wing planform having leading and trailing edges with partially supersonic and partially subsonic flow.

AB, supersonic leading edge.

BC, subsonic leading edge.

CD, subsonic trailing edge.

DE, supersonic trailing edge.

Consider the arbitrary planform of Fig. 18.4. The curve A-B is called a supersonic leading edge because the flow in this neighborhood is like that near the leading edge of a supersonic normal wing with infinite span. For like reasons, the line D-E is called a supersonic trailing edge.

The boundary B-C, on the other hand, is called a subsonic leading edge because the velocity component normal to the edge is less than the sonic speed, and the flow is typically subsonic in character. Between C and D the boundary is called a subsonic trailing edge. Note that disturbances propagated from points along C-D cover part of the planform, and thus the flow can adjust itself so as to satisfy the Kutta-Joukowski condition at the trailing edge.

A practical rule which follows from these considerations is that the portion of the boundary of the planform which constitutes a subsonic leading edge should have a rounded nose so as to avoid a large form drag owing to separation at the leading edge. Conversely, supersonic leading edges should be sharp so as to avoid the large pressure drags associated with detached shock waves.

With planforms of general shape, the simultaneous presence of portions having both supersonic and subsonic properties leads understandably to analytical problems of considerable difficulty.

**Superposition of Effects.** Since we are considering flows with small perturbations, the governing equations are linear. Thus it is possible to study separately the effects of thickness, camber, and angle of incidence, and to determine by linear addition the flow pattern for a combination of these effects. Thus, the perturbation pressure distribution on the profile of Fig. 18.5d may be found by adding the perturbation pressure distributions for the flows of Figs. 18.5a, b, and c.

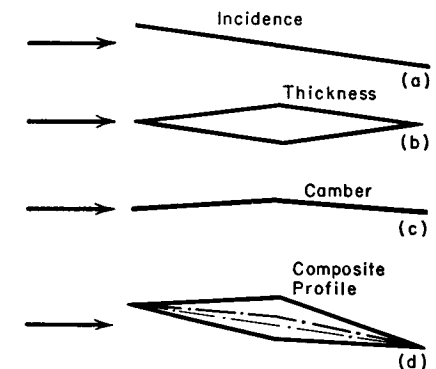


FIG. 18.5. Illustrating linear superposition of effects of incidence, thickness, and camber.

### 18.3. Sweptback Wings

We shall now investigate the properties of infinite sweptback wings, but it is important to remember that the results we obtain are applicable also to such cases as the shaded areas of Fig. 18.1d.

Two separate cases may be distinguished, corresponding to Figs. 18.2a and b. In the latter case, where the leading edge is swept behind the Mach line, the flow normal to the leading edge is subsonic, and that part of the flow pattern not influenced by viscosity will behave as though the flow were subsonic. This problem was treated in detail in Art. 13.7, and will not be discussed here.

The former case, where the leading edge is swept ahead of the Mach line, has a supersonic normal component of velocity, and is the subject of our present attention.

**Equivalent Two-Dimensional Flow.** Consider a wing of infinite span swept at an angle  $\Lambda$  and set at an angle of attack  $a$  (Fig. 18.6). We

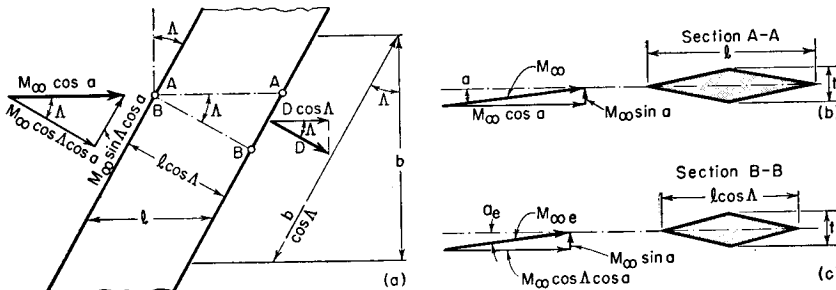


FIG. 18.6. Analysis of infinite sweptback wing.

- (a) View in plane of wing.
- (b) View in plane parallel to direction of flight.
- (c) View in plane normal to leading edge.

may resolve the free-stream Mach Number  $M_\infty$  into three components: (i) the Mach Number  $M_\infty \cos \Lambda \cos a$  in the plane of the wing and normal to the leading edge, (ii) the velocity  $M_\infty \sin a$  normal to the plane of the wing, and (iii) the velocity  $M_\infty \sin \Lambda \cos a$  in the plane of the wing and tangential to the leading edge. To an observer moving along the span with the last-named tangential speed, the flow appears two-dimensional, and may be so treated (except for the boundary-layer flow). Let us use the subscript  $e$  to denote quantities seen by the moving observer. With the help of Fig. 18.6c, we may write

$$M_{\infty e} = \sqrt{(M_\infty \sin a)^2 + (M_\infty \cos a \cos \Lambda)^2} = M_\infty \sqrt{1 - \sin^2 \Lambda \cos^2 a} \quad (18.1)$$

$$a_e = \arctan \frac{M_\infty \sin a}{M_\infty \cos a \cos \Lambda} = \arctan \frac{\tan a}{\cos \Lambda} \quad (18.2)$$

$$\delta_e = \frac{t}{l \cos \Lambda} = \frac{\delta}{\cos \Lambda} \quad (18.3)$$

where  $\delta$  is the thickness ratio in the plane parallel to  $U_\infty$ . Since the lift is not changed by the observer's motion, we may write

$$C_L \equiv \frac{L}{\frac{1}{2} p_\infty M_\infty^2 l b}; \quad C_{L e} \equiv \frac{L}{\frac{1}{2} p_\infty M_{\infty e}^2 (l \cos \Lambda) (b / \cos \Lambda)}$$

With the help of Eq. 18.1, we obtain, therefore,

$$C_L = C_{L e} (M_{\infty e} / M_\infty)^2 = C_{L e} (1 - \sin^2 \Lambda \cos^2 a) \quad (18.4)$$

Since, for the present, we are ignoring viscous drag, the tangential component of velocity does not contribute to the drag, and the pressure drag is normal to the leading edge. Thus, if  $D$  is the total pressure drag, the component of this in the  $M_\infty$  direction is only  $D \cos \Lambda$ . Accordingly, we write

$$C_D = \frac{D \cos \Lambda}{\frac{1}{2} p_\infty M_\infty^2 l b}; \quad C_{D e} = \frac{D}{\frac{1}{2} p_\infty M_{\infty e}^2 (l \cos \Lambda) (b / \cos \Lambda)}$$

or

$$C_D = C_{D e} \cos \Lambda (M_{\infty e} / M_\infty)^2 = C_{D e} \cos \Lambda (1 - \sin^2 \Lambda \cos^2 a) \quad (18.5)$$

**Calculation of Properties of Swept Wing.** These equations take exact account of the geometrical relationships and are correct even for large angles of attack. For any given profile shape with given values of  $M_\infty$ ,  $\Lambda$ ,  $a$ , and  $\delta$ , the corresponding values of  $M_{\infty e}$ ,  $a_e$ , and  $\delta_e$  may be found from Eqs. 18.1 to 18.3. The corresponding force coefficients  $C_{L e}$  and  $C_{D e}$  may then be found from two-dimensional theory. Finally, the values of  $C_L$  and  $C_D$  for the swept wing, based on the free-stream velocity and direction, may be calculated from Eqs. 18.4 and 18.5.

**Effect of Skin Friction.** Since the skin friction depends primarily on the free-stream velocity and direction, the total drag coefficient may be found merely by adding the skin-friction coefficient,  $C_f$ , to the pressure drag coefficient:

$$C_{D, \text{tot}} = C_D + C_f \quad (18.6)$$

**Approximate Formulas for Small Angles of Attack.** When the angle of attack is small, we may write

$$\cos a \cong 1; \quad \tan a \cong a; \quad \tan^{-1} a_e \cong a_e$$

Then Eqs. 18.1 and 18.2 may be written, with good accuracy, as

$$M_{\infty e} \cong M_\infty \cos \Lambda \quad (18.7)$$

$$a_e \cong a / \cos \Lambda \quad (18.8)$$

Similarly, Eqs. 18.4, 18.5, and 18.6 become

$$C_L \cong C_{L e} \cos^2 \Lambda \quad (18.9)$$

$$C_{D, \text{tot}} \cong C_{D e} \cos^2 \Lambda + C_f \quad (18.10)$$

**Thin Profiles at Small Angle of Attack.** If, in addition to the assumption of small angles of attack, we assume that the profile is thin, the linearized theory of Chapter 14 yields

$$C_{L\epsilon} = \frac{4a_\epsilon}{\sqrt{M_\infty^2 - 1}}; \quad C_{D\epsilon} = \frac{4}{\sqrt{M_\infty^2 - 1}} (a_\epsilon^2 + K\delta_\epsilon^2)$$

where the coefficient  $K$  depends only on the thickness distribution of the profile as seen in a plane normal to the leading edge.

Combining these relations with Eqs. 18.7 to 18.10, we get

$$C_L = \frac{4 \cos \Lambda}{\sqrt{M_\infty^2 \cos^2 \Lambda - 1}} a \quad (18.11)$$

$$C_{D,\text{tot}} = \frac{4 \cos \Lambda}{\sqrt{M_\infty^2 \cos^2 \Lambda - 1}} a^2 + \frac{4 \cos^3 \Lambda}{\sqrt{M_\infty^2 \cos^2 \Lambda - 1}} K\delta_\epsilon^2 + C_f \quad (18.12)$$

A plot of Eq. 18.11 shows that the lift-curve slope  $dC_L/da$  increases with sweepback angle  $\Lambda$  for all values of  $M_\infty$ . Thus there is actually a gain from sweepback on this score.

The first term on the right-hand side of Eq. 18.12 represents the induced drag due to lift. It may be seen by comparison with Eq. 18.11 that this part of the drag increases in proportion to the lift.

The second term on the right-hand side of Eq. 18.12 represents the wave drag due to thickness. This term was intentionally left in terms of  $\delta_\epsilon$  rather than  $\delta$  because structural considerations would dictate that  $\delta_\epsilon$  be kept more nearly constant than  $\delta$  as the sweepback  $\Lambda$  was changed. With  $\delta_\epsilon$  constant, the thickness drag at first decreases as the sweepback is increased, but when the leading edge begins to approach the Mach line (i.e.,  $M_\infty \cos \Lambda \rightarrow 1$ ) the thickness drag begins to rise.

**DIAMOND PROFILE.** Another important result may be simply illustrated by taking the case of a symmetrical double-wedge profile with no skin friction, in which case  $C_f = 0$  and  $K = 1$ . Then, by setting equal to zero the derivative  $\partial(D/L)/\partial a$ , we get

$$\left(\frac{D}{L}\right)_{\min} = \frac{\cos \Lambda}{2\delta_\epsilon}$$

$$a' = \delta_\epsilon \cos \Lambda$$

$$C_{L'} = \frac{4\delta_\epsilon \cos^2 \Lambda}{\sqrt{M_\infty^2 \cos^2 \Lambda - 1}}$$

where  $a'$  and  $C_{L'}$  are respectively the incidence and lift coefficient at the condition of maximum lift-drag ratio. These relations show that sweepback increases the maximum lift-drag ratio but that this condition occurs at a smaller angle of attack and, within the restrictions of the paragraph which follows, at a slightly smaller lift coefficient.

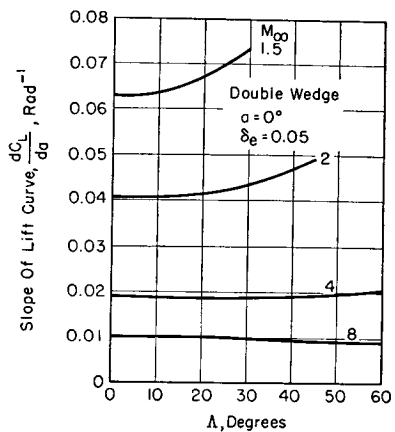


FIG. 18.7. Effect of sweepback on lift-curve slope of wing with double-wedge profile (after Ivey and Bowen, NACA).

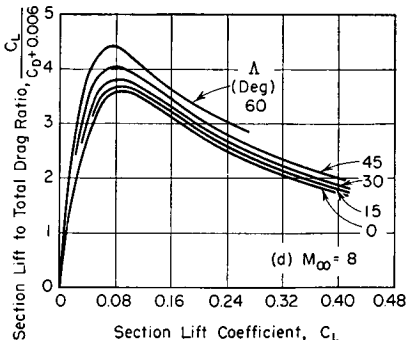
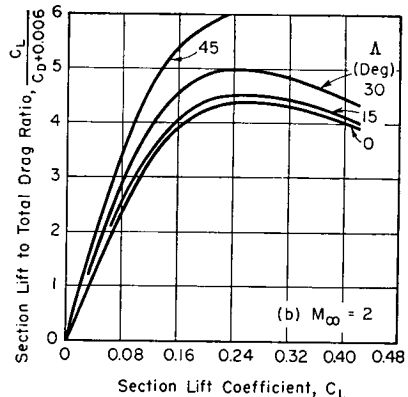
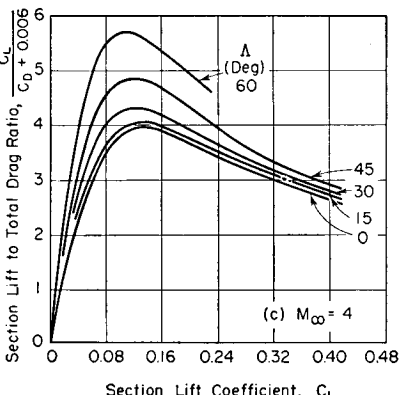
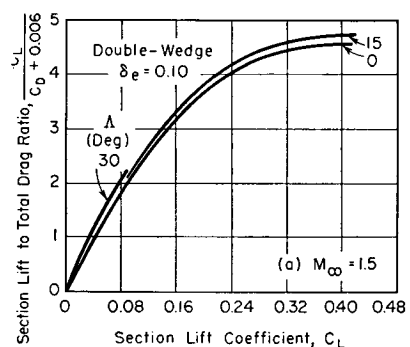


FIG. 18.8. Effect of sweepback on lift-drag ratio of wing with double-wedge profile (after Ivey and Bowen, NACA).

It should be noted that Eqs. 18.11 and 18.12 are valid only within the approximations of the linear theory, and that they are further restricted to combinations of  $\Lambda$  and  $M_\infty$  such that the leading-edge shock wave is attached.

**Typical Effect of Sweepback.** The foregoing discussion is amplified by the illustrative curves of Figs. 18.7 and 18.8. These curves give a more accurate picture than is provided by the linear theory, inasmuch as they are based upon (i) the exact geometrical relations of Eqs. 18.1 to 18.5; (ii) the calculation of the pressure drag for a 10% symmetrical double wedge, using the exact expansion wave and shock theory for a frictionless fluid; and (iii) a skin-friction coefficient of 0.006.

Sweepback is seen to yield substantial improvements in performance.

#### 18.4. Similarity Rule for Supersonic Wings

In Chapter 13 we discussed Gothert's rule for linearized flow, by means of which the flow pattern around any wing in subsonic flow could be related to the incompressible flow past an affinely related wing.

Using the same approach we shall now derive a rule by which the flow pattern around any thin wing at small incidence in a supersonic flow may be related to the flow past an affinely related wing at  $M_\infty = \sqrt{2}$ .

**Similarity Transformation.** For supersonic flow with only small perturbations from a uniform, parallel flow along the  $x$ -axis, the equation of the perturbation velocity potential (Eq. 13.1) is

$$-\beta^2 \frac{\partial^2 \varphi}{\partial x^2} + \frac{\partial^2 \varphi}{\partial y^2} + \frac{\partial^2 \varphi}{\partial z^2} = 0 \quad (18.13a)$$

where

$$\beta \equiv \sqrt{M_\infty^2 - 1} \quad (18.13b)$$

We now introduce the transformation

$$x' \equiv x; \quad y' \equiv \beta y; \quad z' \equiv \beta z; \quad \varphi'(x', y', z') \equiv \beta^2 \varphi(x, y, z) \quad (18.14)$$

In terms of these variables Eq. 18.13a takes the form

$$-\frac{\partial^2 \varphi'}{\partial x'^2} + \frac{\partial^2 \varphi'}{\partial y'^2} + \frac{\partial^2 \varphi'}{\partial z'^2} = 0 \quad (18.15)$$

It may be further verified by the methods of Chapter 13 that the boundary conditions of the original flow at infinity and at the profile surface give, in the transformed flow, uniform parallel flow at infinity together with flow past a new profile whose ordinates are related to that of the original profile by Eq. 18.14.

A comparison of Eq. 18.13a with Eq. 18.15 shows that the latter is

#### Art. 18.4 SIMILARITY RULE FOR SUPERSONIC WINGS

the same as the equation of the perturbation potential  $\varphi$  when  $M_\infty = \sqrt{2}$ . From Eq. 18.14 it may also be seen that the flow  $\varphi'(x', y', z')$  refers to a body all of whose lateral dimensions are greater by the factor  $\beta$  than the corresponding dimensions of the original body.

The linearized pressure coefficients at corresponding points in the two flows are related by

$$C_p' = -\frac{2}{U_\infty} \frac{\partial \varphi'}{\partial x'} = -\frac{2}{U_\infty} \beta^2 \frac{\partial \varphi}{\partial x} = \beta^2 C_p \quad (18.16)$$

where  $C_p'$  may be thought of as the pressure coefficient at  $M_\infty = \sqrt{2}$  for a body whose lateral dimensions are  $\beta$  times larger than the corresponding lateral dimensions of the body whose corresponding pressure coefficient is  $C_p$  at Mach Number  $M_\infty = \sqrt{2}$ .

**Similarity Rule.** If  $\delta$ ,  $\mathcal{R}$ , and  $a$  denote respectively the thickness ratio, aspect ratio, and incidence, and  $l$ ,  $t$ , and  $b$  denote respectively the characteristic body dimensions in the  $x$ -,  $y$ -, and  $z$ -directions, the similarity rule may be expressed symbolically in the form

$$(C_p)_{M_\infty, \delta, a, \mathcal{R}, x/l, y/t, z/b} = \frac{1}{\beta^2} (C_p)_{\sqrt{2}, \beta\delta, \beta a, \beta \mathcal{R}, x/l, y/t, z/b} \quad (18.17)$$

Within the assumptions of the linear theory, the pressure coefficient for supersonic flow is proportional to either the angle of attack or the thickness ratio if these two variables are changed simultaneously and in proportion to each other. Applying this rule to the right-hand side of Eq. 18.17, we may obtain the more useful form

$$(C_p)_{M_\infty, \delta, a, \mathcal{R}, x/l, y/t, z/b} = \frac{1}{\beta} (C_p)_{\sqrt{2}, \delta, a, \beta \mathcal{R}, x/l, y/t, z/b} \quad (18.18)$$

which states that *the pressure coefficient at a given point for flow at  $M_\infty$  past a given wing is greater by the factor  $1/\beta$  than the pressure coefficient at a corresponding point for flow at Mach Number  $\sqrt{2}$  past a wing which is alike in all respects except that its aspect ratio is greater by the factor  $\beta$  than that of the original wing.*

By integration, the lift coefficients will accordingly be related by

$$(C_L)_{M_\infty, \delta, a, \mathcal{R}} = \frac{1}{\beta} (C_L)_{\sqrt{2}, \delta, a, \beta \mathcal{R}} \quad (18.19)$$

Identical rules will hold for the moment coefficient and the pressure drag coefficient.

The forms of these rules yield a further rule, namely: the linearized theory for supersonic wings must depend on  $M_\infty$  and  $\mathcal{R}$  in such a way that these variables always appear in the combination  $\sqrt{M_\infty^2 - 1} \mathcal{R}$ .

**GEOMETRICAL INTERPRETATION.** The similarity rules are essentially the result of dimensional reasoning.

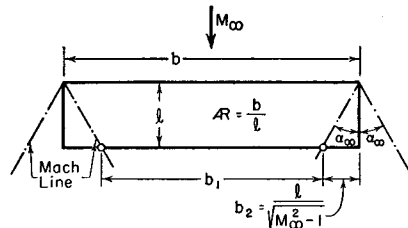


FIG. 18.9. Illustrating that the proportion of two-dimensional flow depends on the factor  $\mathcal{R} \sqrt{M_\infty^2 - 1}$ .

$$\frac{b_1}{b} = \frac{b - \frac{2l}{\sqrt{M_\infty^2 - 1}}}{b} = 1 - \frac{2l}{b\sqrt{M_\infty^2 - 1}} = 1 - \frac{2}{\mathcal{R} \sqrt{M_\infty^2 - 1}}$$

As a result of Eq. 18.19, it is sufficient to solve for the supersonic flow past thin wings for the special case  $M_\infty = \sqrt{2}$ , after which the general result is obtained by replacing the term  $\mathcal{R}$ , wherever it appears, by the term  $\sqrt{M_\infty^2 - 1} \mathcal{R}$ .

### 18.5. The Method of Supersonic Source and Doublet Distributions

In Chapter 17 it was shown that an elementary solution to the linearized differential equation, Eq. 18.13, is that corresponding to a *supersonic source*, and that by a distribution of such sources along the axis of symmetry the flow patterns past bodies of revolution might be established.

By distributing sources on the planform of a thin finite wing lying in the  $x, y$ -plane, it is possible similarly to calculate the flow past wings having symmetry about the  $z$ -axis at zero angle of attack. Such a calculation leads to a determination of the thickness drag.<sup>(5)</sup>

A further extension of this principle is to distribute in the plane of the wing *supersonic doublets*. Such a distribution has the same effect as a circulation around the wing and gives rise to a lifting force. By means of an appropriate doublet distribution the lift and the drag due to lift of finite wings at an angle of attack may be calculated.<sup>(6)</sup>

The calculation of the pressure distribution for wings at angles of incidence is much more tedious than that for wings at zero incidence. Moreover, the method of conical fields is often better adapted to the lift problem. Accordingly, we shall discuss here only the method of source distributions.

**Supersonic Source Distribution.** Suppose that the profile lies in the  $x, y$ -plane, that the free-stream velocity  $U_\infty$  is in the  $x$ -direction, and that the profile is very thin in the  $z$ -direction. Then, within the approximations of the linear theory, the boundary condition at the profile may be written

$$\tau = w/U_\infty = \varphi_z/U_\infty \quad (18.20)$$

where  $\tau$  is the slope of the profile measured in the  $y, z$ -plane. Since the airfoil is assumed to be very thin, Eq. 18.20 may be evaluated approximately in the plane  $z = 0$ .

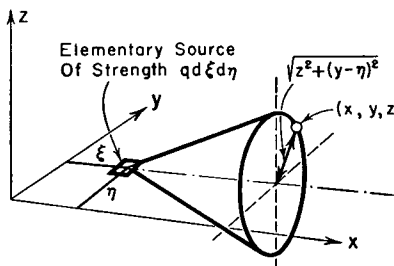


FIG. 18.10. Elementary source  $q d\xi d\eta$  at the coordinates  $(\xi, \eta, 0)$ .

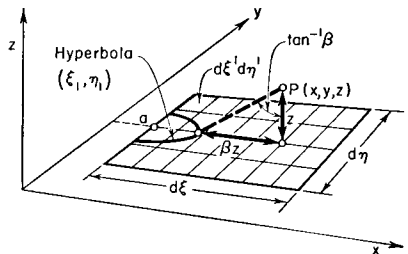


FIG. 18.11. Only those source elements  $q d\xi' d\eta'$  lying forward of the hyperbola  $\xi_1, \eta_1$  contribute to the potential at  $P$ .

Referring to Fig. 18.10, consider an elementary source in the  $x, y$ -plane, and let the  $x$ - and  $y$ -coordinates of the source be  $\xi$  and  $\eta$ , respectively. If  $q$  is the strength of the source per unit area, the infinitesimal perturbation potential at the point  $(x, y, z)$  owing to the infinitesimal source at  $(\xi, \eta, 0)$  is, according to Art. 17.3, given by

$$d\varphi = - \frac{q d\xi d\eta}{\sqrt{(x - \xi)^2 - \beta^2[(y - \eta)^2 + z^2]}} \quad (18.21)$$

where  $q$  is in general a function of  $\xi$  and  $\eta$ . To find the  $z$ -component of velocity at  $(x, y, z)$  owing to this source element, we compute

$$\frac{\partial}{\partial z} (d\varphi) = - \frac{q \beta^2 z d\xi d\eta}{[(x - \xi)^2 - \beta^2[(y - \eta)^2 + z^2]]^{3/2}}$$

This shows that the  $w$ -velocity due to this source element is zero everywhere in the  $x, y$ -plane except on the area  $d\xi d\eta$ . That is, it is everywhere zero when  $z = 0$  except where  $(x - \xi)$  is small compared with  $d\xi$  and  $(y - \eta)$  is small compared with  $d\eta$ , and in this region it is indeterminate. Hence, to find the  $w$ -velocity at  $\xi, \eta$  we must subdivide  $d\xi d\eta$  into smaller elements and sum the effects of these elements at a point  $P$  lying slightly above  $d\xi d\eta$  (Fig. 18.11) and then allow  $z$  to

approach zero. However, only those elements of  $d\xi d\eta$  which lie in the forward Mach cone extending from  $P(x, y, z)$  should be included. This forward Mach cone intersects  $d\xi d\eta$  in a hyperbola with coordinates  $\eta_1$  and  $\xi_1$ . The equation of the hyperbola may be shown to be

$$(x - \xi_1)^2 = \beta^2[(y - \eta_1)^2 + z^2]$$

The potential at  $P$  owing to a constant source intensity  $q$  over  $d\xi d\eta$  may thus be written

$$\varphi(P) = -q \int_a^{x-\beta z} d\xi' \int_{-\eta_1}^{+\eta_1} \frac{d\eta'}{\sqrt{(x - \xi')^2 - \beta^2[(y - \eta')^2 + z^2]}}$$

Note that the limits of integration, defined by the forward Mach cone, are also such as to include only the regions where the radical in the integrand has real values.

By integrating and inserting the indicated limits it may be shown<sup>(5)</sup> that

$$\varphi = -\frac{\pi q}{\beta} (x - \beta z - a)$$

and, therefore,

$$w = \partial\varphi/\partial z = \pi q; \quad q = w/\pi \quad (18.22)$$

This result remains valid as  $z \rightarrow 0$  and  $a \rightarrow x$ . Previously we found that there is no contribution to  $w$  at  $z = 0$  except from the source element directly at the point in question, and thus it follows that Eq. 18.22 gives the total  $w$ -velocity at the point  $\xi, \eta$ . In other words, the  $w$ -component of velocity at the surface depends only on the local source intensity. The  $u$ - and  $v$ -components of velocity, on the other hand,

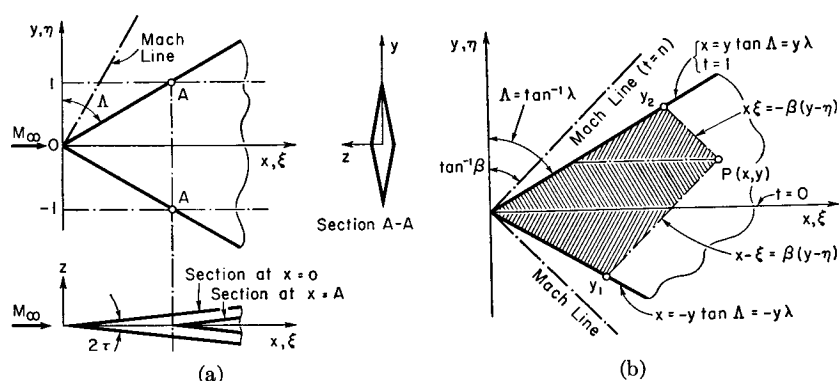


FIG. 18.12. Single-wedge delta with subsonic leading edge.

(a) Illustrates nomenclature.

(b) Potential at  $P$  is the sum of the potentials produced by the source distributions in the three-shaded regions.

are affected by all source elements lying in the Mach cones upstream of the point in question.

**Application to Simple Delta Wing with Subsonic Leading Edge.** Let us consider a delta wing (point foremost) with constant  $q$  over the surface. From Eq. 18.22, therefore,  $w$  is also constant at the surface. Since this source distribution gives complete symmetry about  $z$ , these conditions yield a wedge-shaped profile in the  $z$ -plane (Fig. 18.12a). Referring to Fig. 18.12b, the potential at  $P$  is the sum of the potentials owing to the source elements in the three shaded areas. Remembering that  $q$  is constant, and using Eqs. 18.21 and 18.22, we may write, assuming that  $\lambda > \beta$

$$\begin{aligned} \varphi(x, y, 0) = & -\frac{w}{\pi} \int_{y_1}^0 d\eta \int_{-\lambda\eta}^{x-\beta(y-\eta)} f(\xi, \eta) d\xi \\ & -\frac{w}{\pi} \int_0^y d\eta \int_{\lambda\eta}^{x-\beta(y-\eta)} f(\xi, \eta) d\xi \\ & -\frac{w}{\pi} \int_y^{y_2} d\eta \int_{\lambda\eta}^{x+\beta(y-\eta)} f(\xi, \eta) d\xi \end{aligned} \quad (18.23)$$

where

$$f(\xi, \eta) = [(x - \xi)^2 - \beta^2(y - \eta)^2]^{-1/2} \quad (18.23a)$$

and, from the geometry of the figure,

$$y_1 = \frac{\beta y - x}{\beta + \lambda}, \quad \text{and} \quad y_2 = \frac{x + \beta y}{\beta + \lambda}$$

Omitting the details of the integration<sup>(5)</sup> the important end result is that

$$u = \varphi_x = -\frac{w}{\pi} \frac{2}{\beta \sqrt{n^2 - 1}} \cosh^{-1} n \sqrt{\frac{1 - (t/n)^2}{1 - t^2}} \quad (18.24a)$$

which holds for values

$$0 < t < 1; \quad n > 1 \quad (18.24b)$$

where the symbols  $t$  and  $n$  are defined by

$$n \equiv \lambda/\beta \quad (18.25a)$$

$$t \equiv \lambda y/x \quad (18.25b)$$

Note that, for  $n > 1$ , the leading edge is swept behind the Mach line, and the leading edge is subsonic; while, for  $n < 1$ , the leading edge is supersonic. The variable  $t$  is constant on straight lines through the vertex, and is zero on the axis and unity on the leading edge. Eq. 18.24b signifies that Eq. 18.24a is valid in the region occupied by the wing.

It is seen from Eq. 18.24a that  $\varphi_x$ , and hence

$$C_p \cong -2\varphi_x/U_\infty$$

is constant along straight lines through the vertex.

By means of a similar analysis, the following additional result is obtained for the flow between the Mach line and the leading edge, at  $z = 0$ :

When

$$1 < t < n; \quad n > 1 \quad (18.26a)$$

then

$$\varphi_x = u = -\frac{w}{\pi} \frac{2}{\beta \sqrt{n^2 - 1}} \cosh^{-1} \sqrt{\frac{n^2 - 1}{t^2 - 1}} \quad (18.26b)$$

Recalling that the wing has no effect ahead of the Mach lines emanating from the apex (i.e., for  $t > n$ ), it is evident that Eqs. 18.24a and 18.26b give the entire pressure distribution in the plane of the wing.

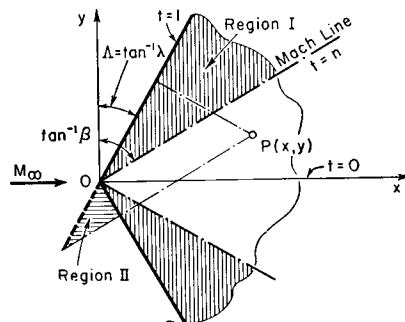


FIG. 18.13. Single-wedge delta with supersonic leading edge.

**Simple Delta Wing with Supersonic Leading Edge.** In this case, for which the leading edge is supersonic (Fig. 18.13), we have  $\lambda < \beta$ , or  $n < 1$ . Two-dimensional flow exists at any point in Region I ( $n < t < 1$ ) by virtue of the reasoning of Art. 18.3. Using the analysis for an infinite sweptback wing, the incremental velocity in Region I may be shown to have the constant value

$$u = \varphi_x = -\frac{w}{\beta \sqrt{1 - n^2}} \quad (18.27a)$$

for

$$n < t < 1; \quad n < 1 \quad (18.27b)$$

For a point  $P(x, y)$  lying behind the Mach line, the incremental velocity may be thought of as the sum of (i) that of Eq. 18.27a, corresponding to an infinite swept wing, plus (ii) that due to a source distribution of magnitude  $(-w/\pi)$  in Region II. When the infinitely swept wing is cut off along  $OB$  to form the delta wing, Region II is the only part of the cutoff portion which affects conditions at  $P$ . By adding the source distribution  $(-w/\pi)$  in Region II to the source distribution  $(w/\pi)$  of the infinitely swept wing, the net effect is to make the flow in Region II identical with the undisturbed free-stream flow,

thus yielding the desired boundary condition. Carrying through the details of this calculation, it is found that <sup>(5)</sup>

$$u = \varphi_x = -\frac{w}{\beta \sqrt{1 - n^2}} \left[ 1 - \frac{2}{\pi} \sin^{-1} n \sqrt{\frac{1 - (t/n)^2}{1 - t^2}} \right] \quad (18.28a)$$

for

$$0 < t < n; \quad n < 1 \quad (18.28b)$$

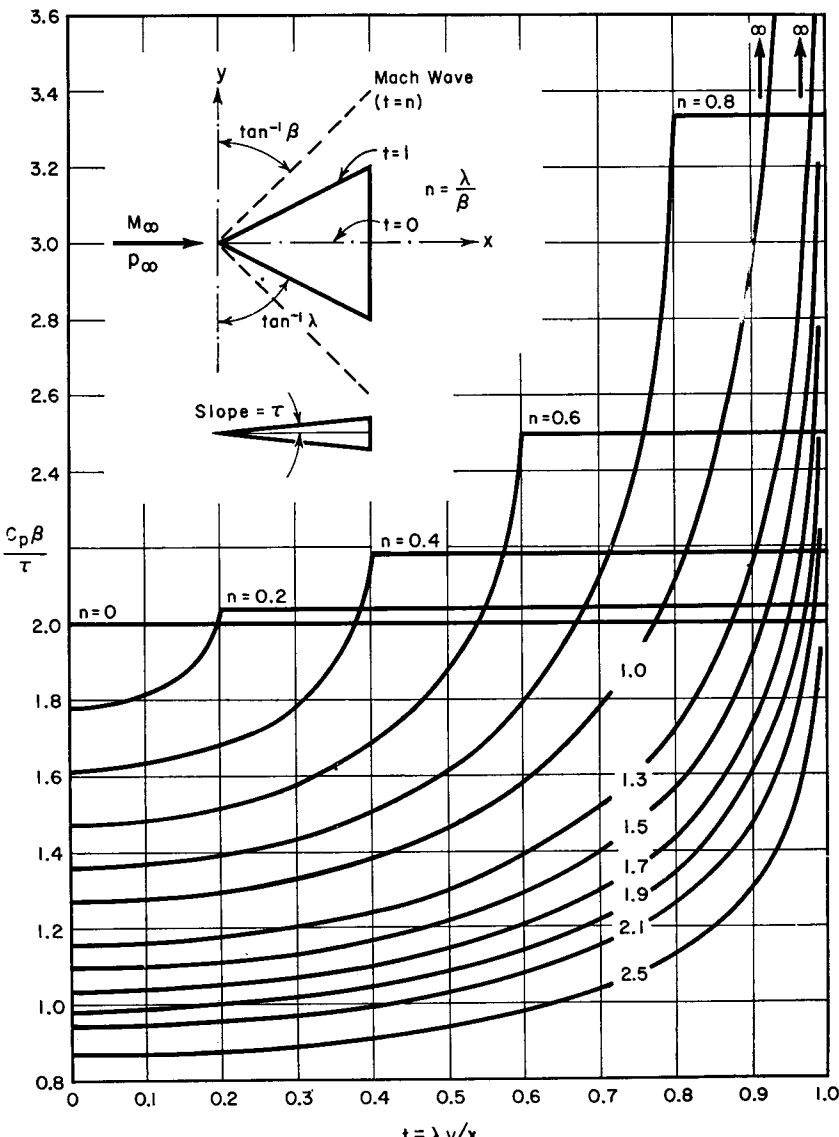


FIG. 18.14. Pressure-coefficient parameter for single-wedge delta (after Puckett).

**Pressure Distribution for Single-Wedge Deltas.** It is convenient to form the parameter

$$\frac{C_p \beta}{\tau} \cong \left( -2 \frac{\varphi_x}{U_\infty} \right) \beta \left( \frac{U_\infty}{w} \right) = -2 \frac{\varphi_x \beta}{w} \quad (18.29)$$

for it will be noted from Eqs. 18.24 to 18.28 that this parameter depends only on  $t$  and  $n$ . Fig. 18.14 shows how this pressure-coefficient parameter varies with the location parameter  $t$  for various values of the shape parameter  $n$ .

For supersonic leading edges ( $n < 1$ ), the pressure is constant in the region between the leading edge and the Mach line ( $n < t < 1$ ), and falls off to lower values in the region between the Mach line and the axis ( $0 < t < n$ ). An interesting result when  $n < 1$  is obtained by integrating the pressure over the entire surface (between  $t = 0$  and  $t = 1$ ), for it turns out that this integral is independent of  $n$ ; from which it is concluded that the pressure drag of a single-wedge delta is independent of sweepback angle provided that the leading edge is supersonic.

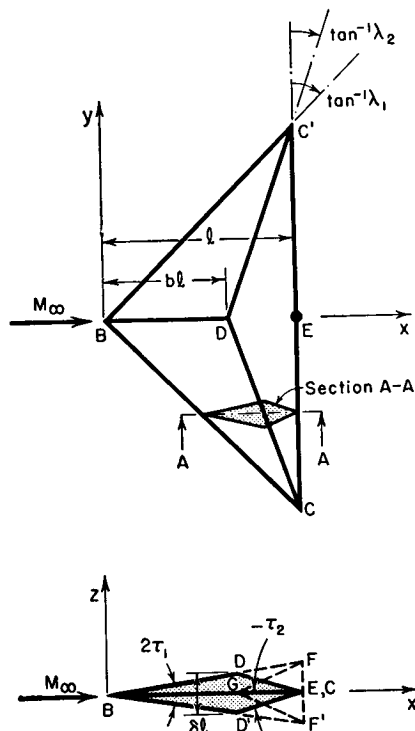


FIG. 18.15. Double-wedge delta wing.

at  $B$  and with constant slope  $\tau_1$ ; and (ii) a single-wedge delta (profile  $G-F-F'$ ) with vertex at  $G$  and constant slope  $(-\tau_1 + \tau_2)$ , where  $\tau_2$  is a negative number. In region  $B-D-C$  (see planform) the source strength is

$$q = \frac{w}{\pi} = \frac{\tau_1 U_\infty}{\pi}$$

while in region  $D-C'-C$  (see planform) the source strength is

$$q = \frac{\Sigma w}{\pi} = \frac{\tau_1 U_\infty}{\pi} + \frac{(-\tau_1 + \tau_2) U_\infty}{\pi} = \frac{\tau_2 U_\infty}{\pi}$$

Thus the boundary conditions are satisfied over the entire planform.

The detailed calculations<sup>(1,5)</sup> are too lengthy to be given here, but the results are of practical interest. When the Mach line lies behind both the leading edge and the maximum-thickness line, the pressure drag coefficient is given in Fig. 18.16a. <sup>(5)</sup>

When the Mach line lies ahead of the maximum-thickness line or ahead of both the maximum-thickness line and the leading edge, the pressure drag coefficient is given by Fig. 18.16b. <sup>(5)</sup> In both charts the curve  $n_1 = 0$ , corresponding to two-dimensional flow for a wing of infinite span, is inserted for comparison.

It may be seen from Figs. 18.16a and 18.16b that the thickness drag coefficient of the delta wing is larger than that of a two-dimensional wing if the leading edge is supersonic. By sweeping the leading edge well behind the Mach line and by simultaneously putting the point of

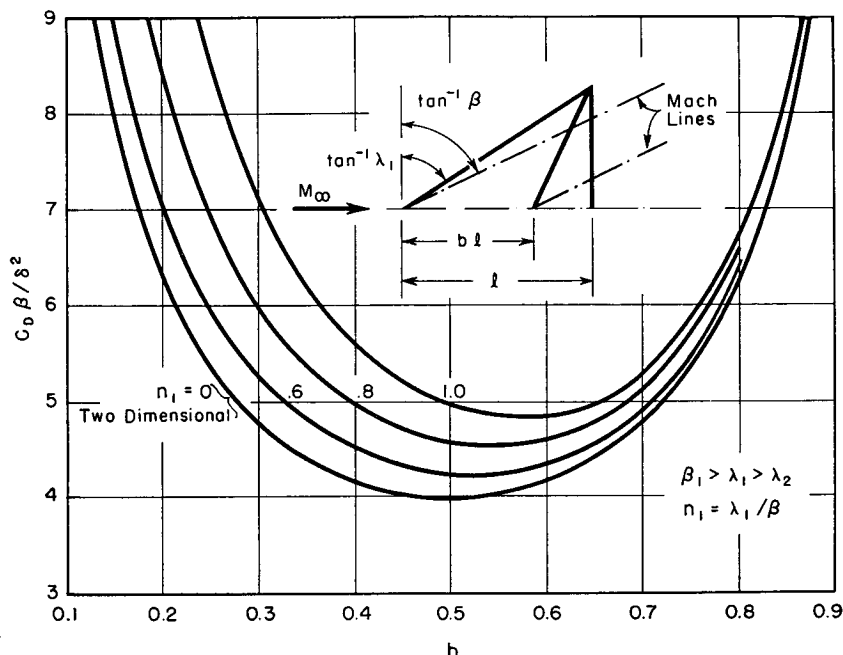


FIG. 18.16(a). Thickness drag of double-wedge delta—supersonic leading edge and supersonic line of maximum thickness (after Puckett)

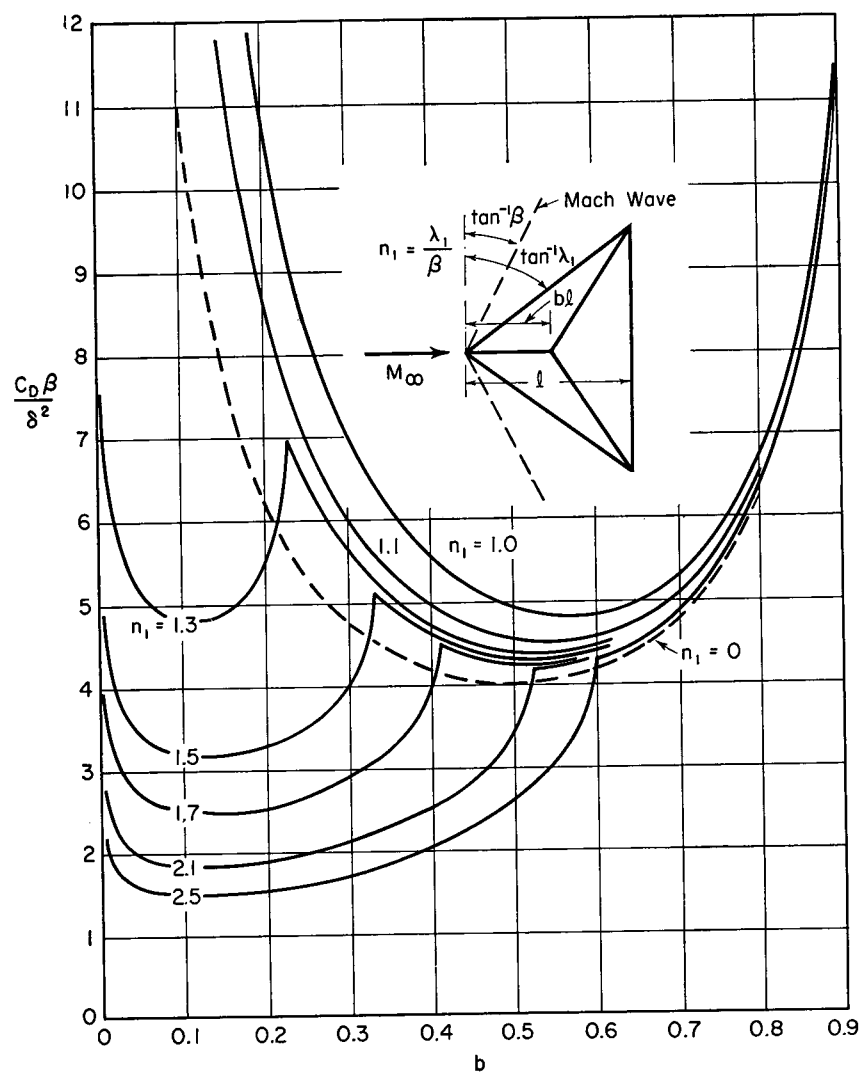


FIG. 18.16(b). Thickness drag of double-wedge delta—subsonic line of maximum thickness (after Puckett).

maximum thickness far enough forward so that the line of maximum thickness is also behind the Mach line, very substantial decreases in pressure drag may be obtained as compared with the two-dimensional wing, unless viscous effects act to produce considerable changes in pressure distribution.

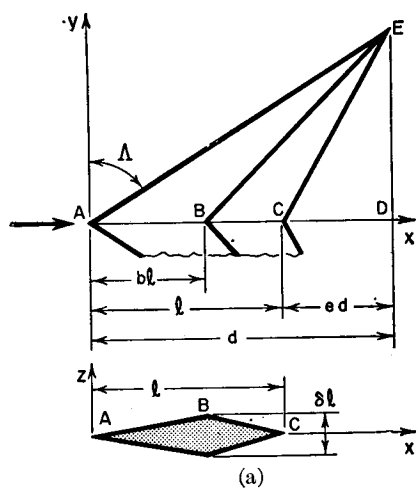
Corresponding results for wings with biconvex sections are given in Reference 17.

**Sweptback Arrowhead Wings.** The method of approach outlined previously may be extended to such planforms as that of Fig. 18.17a, where the complete solution is found by superposing three constant source distributions: one in the area  $A-D-E$ , the second in the area  $B-D-E$ , and the third in the area  $C-D-E$ . If the profile is not made up of straight line segments, as, for example, in the case of a biconvex profile, similar results may be obtained<sup>(17)</sup> by superposing an infinite number of source distributions, each of which is constant in a triangular region; the chordwise rate of change of total source intensity is then proportional to the rate of change of slope of the profile.

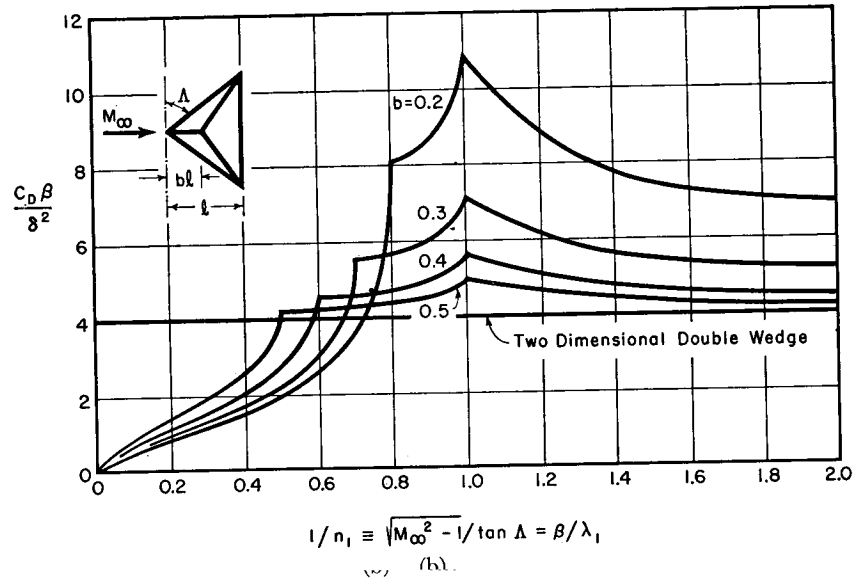
The thickness drag of planforms for which both the leading and trailing edges are swept<sup>(8)</sup> is shown in Figs. 18.17b, c, and d. Fig. 18.17b gives the same results as Figs. 18.16a and 18.16b in a form which brings out clearly the importance of having the location of maximum thickness close to the leading edge. Fig. 18.17c, by comparison with the previous figure, shows the effect of sweeping the trailing edge, and illustrates that in the range where the delta wing has less drag than the two-dimensional wing, sweeping the trailing edge reduces the thickness drag still further. The same result is shown even more strikingly in Fig. 18.17d.

**Arrowhead Wing with Constant Chord.** The arrowhead wing with constant chord of Fig. 18.18a is analyzed by superposing source distributions in triangles with sides parallel to the leading edge. The first triangle begins at the leading edge and has a source intensity to produce the slope of the profile at the leading edge. An infinitesimal distance behind the leading edge, an infinitesimal source distribution (which is in fact negative) is superposed, of such magnitude as to produce the necessary changes in profile slope; and so on, until the trailing edge is reached. The details of this calculation have been carried through in Reference 7 for a biconvex profile of 10% thickness ratio (normal to leading edge), at  $M_\infty = \sqrt{2}$ , with 60°-sweepback. Fig. 18.18b shows the pressure distribution at various stations along the span. On the axis of symmetry the pressure distribution is that of a two-dimensional supersonic wing, for reasons of symmetry. At spanwise distances greater than two chord lengths, the pressure distribution is very much like that of a subsonic flow, corresponding approximately to an infinitely swept wing with subsonic leading edge. Fig. 18.18c shows how the drag coefficient drops very rapidly in the spanwise direction, demonstrating that the thickness drag may be drastically reduced by sharp sweepback.

**Systematic Representation of Pressure Drag of Swept Wings.** Lawrence<sup>(18)</sup> has made a comprehensive survey of the various source-type solutions for the pressure (wave) drag of thin, nonlifting wings, and has



(a)



$$l/n_1 \equiv \sqrt{M_\infty^2 - 1} / \tan \Delta = \beta / \lambda_1$$

FIG. 18.17. Arrowhead wings with double-wedge profile at zero incidence (after Puckett and Stewart).

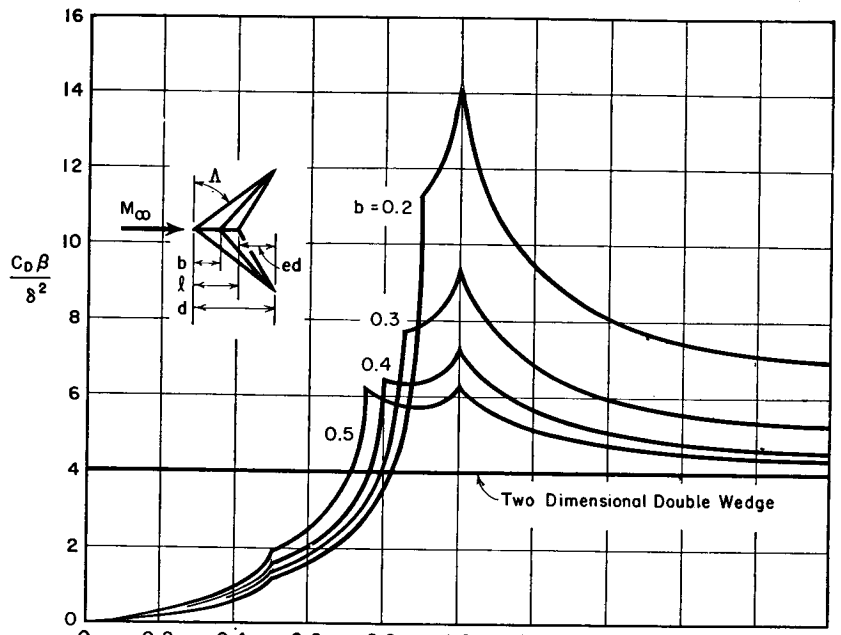
(a) Nomenclature.

(b) Thickness drag for  $e = 0$ .

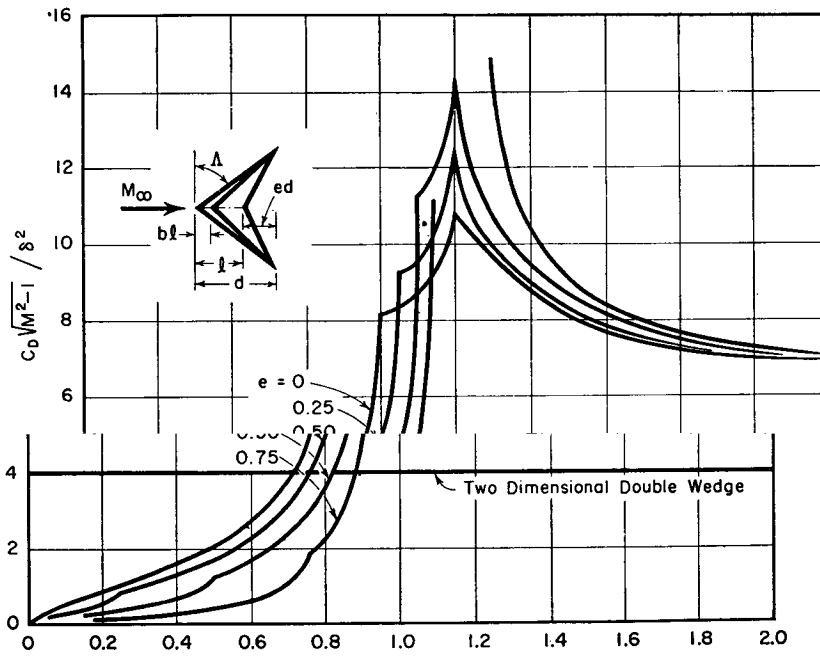
(c) Thickness drag for  $e = 0.5$ .

(d) Thickness drag for  $b = 0.2$ .

(See opposite page.)



(c)



(d)

FIG. 18.17. (Continued)

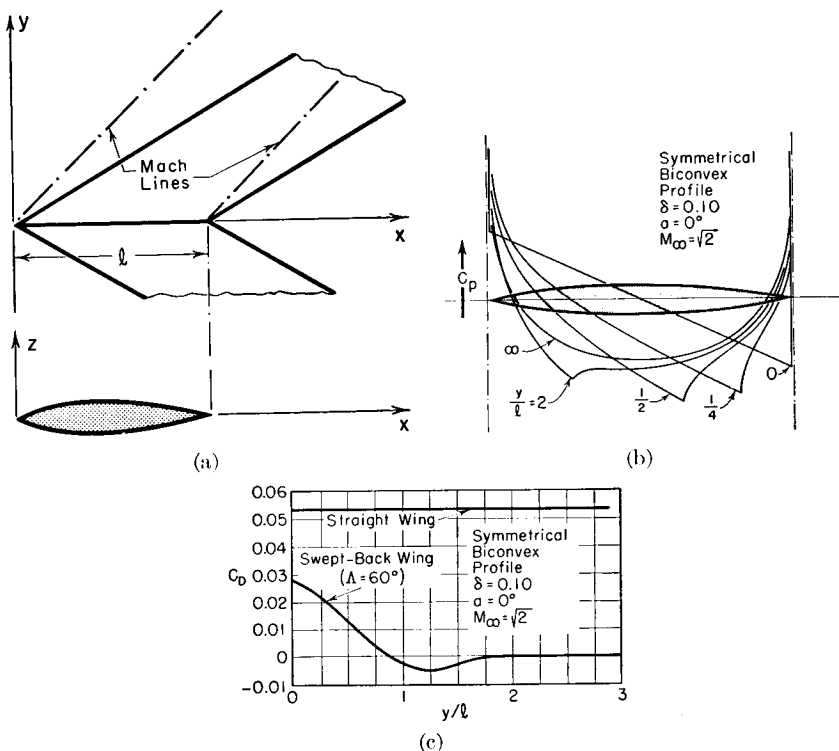


FIG. 18.18. Arrowhead wing with constant chord, biconvex profile, and subsonic leading edge (after Jones).

- (a) Planform.
- (b) Pressure distribution at various spanwise stations.
- (c) Thickness drag coefficient at various spanwise stations.

digested them in a series of charts of uniform style which facilitate practical computations and which make comparisons easy. The wings are all assumed to have straight leading and trailing edges, straight maximum-thickness lines, and the same dimensionless airfoil profile in each chordwise plane. Fig. 18.19a shows the nomenclature employed and the applicable geometrical relationships.

The various solutions in the literature have been rearranged so that they are in the form

$$\frac{C_d}{\mathcal{R} \delta^2} = f(\mathcal{R} \sqrt{M_\infty^2 - 1}, \mathcal{R} \tan \Lambda_i, \gamma, b, \text{profile})$$

On each chart of Fig. 18.19 the profile shape and the values of  $\gamma$  (taper ratio) and of  $b$  (chordwise position of maximum thickness) are maintained constant, and  $C_d/\mathcal{R} \delta^2$  is plotted against  $\mathcal{R} \sqrt{M_\infty^2 - 1}$  for constant values of  $\mathcal{R} \tan \Lambda_i$ . The latter depends only on  $\gamma$  and  $e$ ,

and therefore a curve of constant  $\mathcal{R} \tan \Lambda_i$  represents a family of wings having a constant ratio of tip chord to root chord and a constant ratio of root chord to the effective distance  $d$  from the apex  $A$  to the projected tip  $B$  (note that  $e$  is negative if  $C$  lies aft of  $B$ ). For a given wing the curves of Fig. 18.19 are basically curves of  $C_d$  versus  $\sqrt{M_\infty^2 - 1}$ .

The values of  $\gamma$  and  $b$  for the various charts permit comparisons showing the effects of taper ratio and of the position of maximum thickness. Of the charts presented, all but Fig. 18.19h are for double-wedge profiles, and the latter is for a biconvex parabolic arc profile.

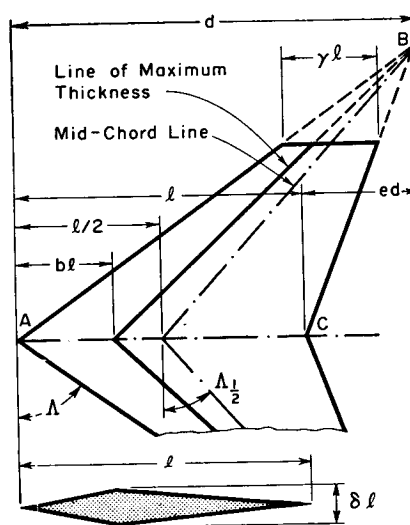
**Computation of Lift by Doublet Distributions.** For methods by which the lift of finite wings may be calculated in terms of the velocity potential produced by a doublet distribution in the plane of the wing, the reader is referred to References 1 and 8.

## 18.6. The Method of Conical Fields

One of the interesting features of the flow past a cone (Chapter 17) is its "conical" nature—all flow properties are uniform on cones having their vertexes at the vertex of the solid cone. In Art. 18.5, it was seen further that with delta wings at zero incidence the surface pressure is uniform on straight lines passing through the apex of the delta.

Busemann<sup>(9)</sup> conceived the general idea of the *conical field*, that is, a flow in which all fluid properties are uniform on rays through a common vertex. The only irrotational flow fitting this specification exactly is the supersonic flow past a cone. However, conical fields are also applicable to the perturbation fluid properties of a linearized supersonic flow provided that the boundary conditions in these perturbation properties satisfy the conical condition. This can hardly be the case for subsonic flows because the boundary conditions to infinity influence the flow. However, in supersonic flow disturbances are propagated only in the downstream Mach cone, and thus conical fields in limited regions have practical significance.

**Regions of Conical Flow.** To illustrate this concept, consider the three wing planforms of Fig. 18.20, all of which have flat-plate profiles at an angle of incidence. The regions of conical flow on each planform are filled by dashed straight lines passing through a common vertex. The delta of Fig. 18.20a, with leading edges swept behind the Mach lines, has boundary conditions of the conical type, and thus may be treated by the method of conical fields. Likewise, the portion of the tip of the rectangular wing of Fig. 18.20b lying within the Mach cone may be treated by the method of conical fields because it has a conical boundary condition. The polygonal planform of Fig. 18.20c has three regions of conical flow with separate vertexes; in the regions where the



$$e \equiv 1 - (l/d); -1 \leq e \leq 1$$

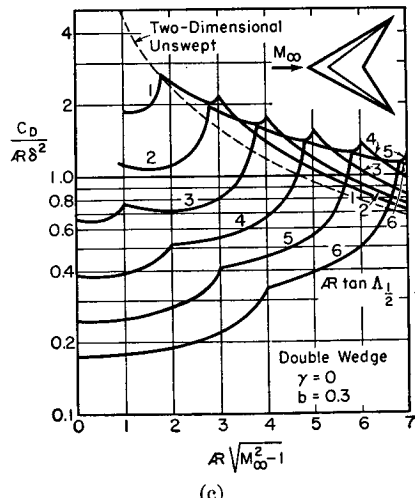
$$AR \equiv (\text{span})^2 / \text{planform area}$$

$$AR \tan \frac{\Delta_1}{2} = 2 \frac{1-\gamma}{1+\gamma} \cdot \frac{1+e}{1-e}$$

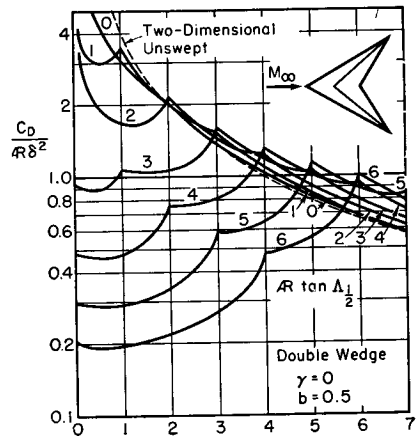
$$\tan \frac{\Delta_1}{2} / \tan \Delta = (1+e)/2$$

$$\frac{\sqrt{M_{\infty}^2 - 1}}{\tan \Delta} = \frac{\beta}{\lambda_1} = \frac{AR \sqrt{M_{\infty}^2 - 1}}{AR \tan \Delta} = (AR \sqrt{M_{\infty}^2 - 1}) \cdot \frac{1-e}{4} \frac{1+\gamma}{1-\gamma}$$

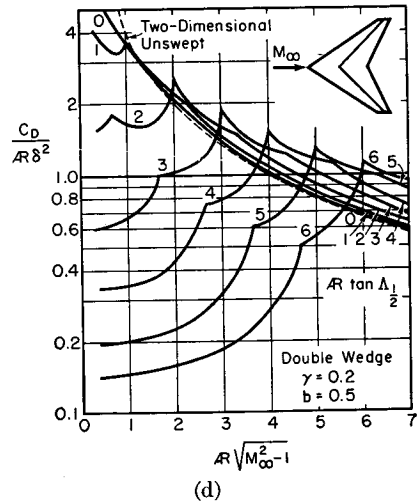
(a)



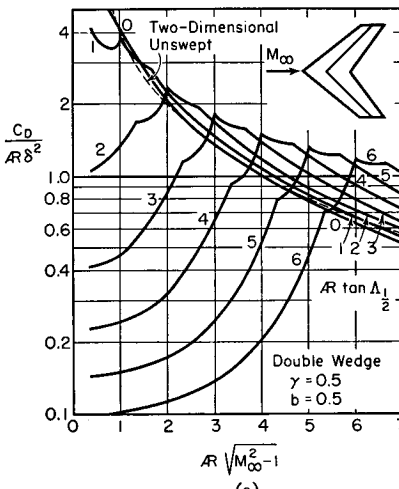
(c)



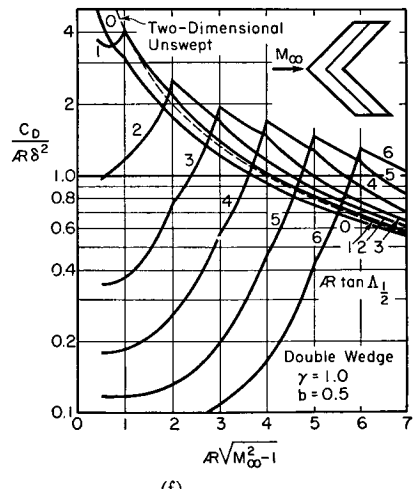
(b)



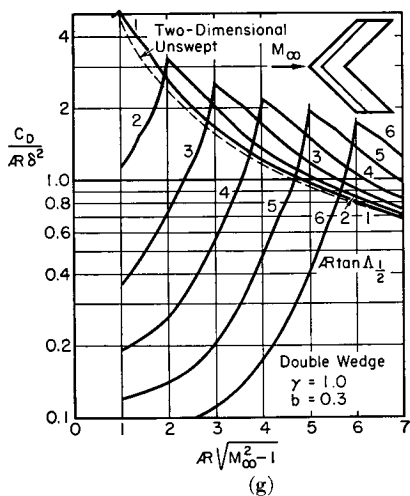
(d)



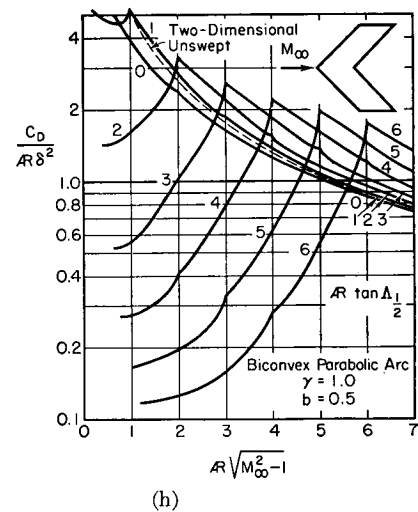
(e)



(f)



(g)



(h)

FIG. 18.19. Systematic presentation of wave drag of thin, nonlifting wings having straight leading and trailing edges and the same dimensionless profile in all chordwise planes (after Lawrence).

(a) Nomenclature and geometrical relationships. Note that  $e$  is negative if  $C$  lies aft of  $B$ .

(b), (c), (d), (e), (f), (g) Wings with double-wedge profiles.

(h) Wings with biconvex parabolic arc profile.

FIG. 18.19. (See opposite page.)

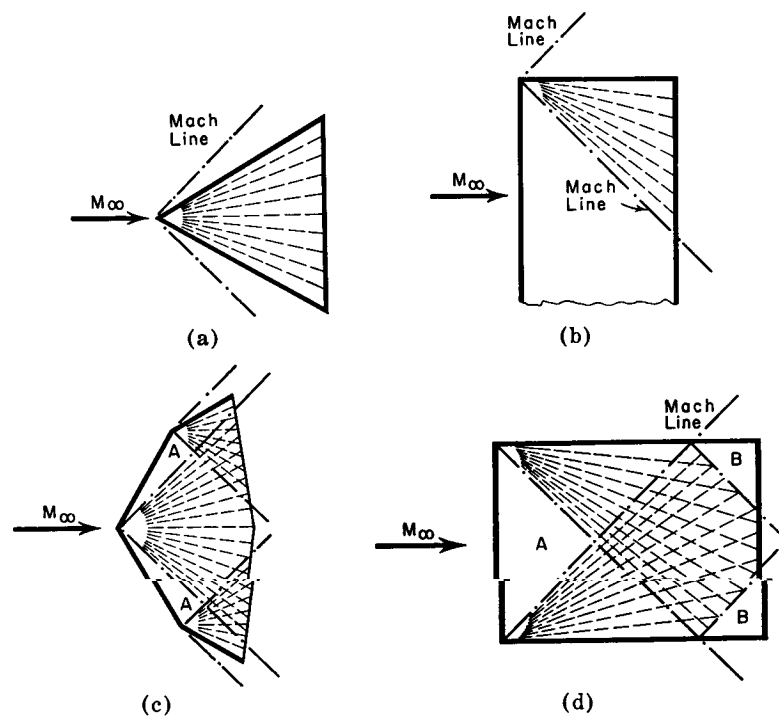


FIG. 18.20. Dashed lines indicate zones of conical flow.

conical flows overlap, the perturbation velocities may be added because of the linear nature of the flow. Regions *A* have flows corresponding to two-dimensional, infinitely swept wings. In Fig. 18.20d, showing a wing of rectangular planform, it is to be noted that regions *B* are not conical because the conical boundary conditions corresponding to the Mach lines leaving the leading-edge tips end where these Mach lines cross the opposite wing tips.

**Equations of Conical Field.** With the origin placed at the vertex of the conical field (Fig. 18.21), and with the free-stream flow in the *x*-direction, the linearized equation for the perturbation potential may be written as

$$-\beta^2 \frac{\partial^2 \varphi}{\partial x^2} + \frac{\partial^2 \varphi}{\partial y^2} + \frac{\partial^2 \varphi}{\partial z^2} = 0; \quad \beta = \sqrt{M_\infty^2 - 1} \quad (18.29)$$

Differentiating partially with respect to *x*, and noting that  $u = \partial \varphi / \partial x$ , we get

$$(\partial / \partial x)(\partial v / \partial y) = (\partial / \partial y)(\partial v / \partial x) = (\partial / \partial y)(\partial u / \partial y), \text{ etc.,}$$

$$-\beta^2 \frac{\partial^2 u}{\partial x^2} + \frac{\partial^2 u}{\partial y^2} + \frac{\partial^2 u}{\partial z^2} = 0 \quad (18.30)$$

From this it is evident that a solution of Eq. 18.29 for  $\varphi(x, y, z)$  is also a solution for  $u(x, y, z)$ . Similarly it may be shown to be also a solution for  $v(x, y, z)$ ,  $w(x, y, z)$ , and  $C_v(x, y, z)$ .

It is convenient to work in the cylindrical coordinate system  $r, \theta, x$  (Fig. 18.21), in terms of which Eq. 18.29 becomes

$$-\beta^2 \frac{\partial^2 \varphi}{\partial r^2} + \frac{\partial^2 \varphi}{\partial \theta^2} + \frac{1}{r} \frac{\partial \varphi}{\partial r} + \frac{1}{r^2} \frac{\partial^2 \varphi}{\partial \theta^2} = 0 \quad (18.31)$$

Following the treatment of Reference 10, we introduce a conical coordinate system in terms of the variable *q*, defined by

$$q = \frac{r \sqrt{M_\infty^2 - 1}}{x} = \frac{\tan \sigma}{\tan \alpha_\infty} \quad (18.32)$$

Note that *q* is constant on coaxial cones with vertexes at the origin, and that it has the value zero on the *x*-axis and the value unity on the

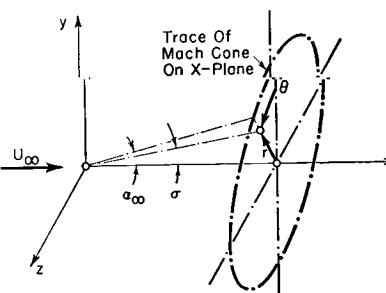


FIG. 18.21. Cylindrical coordinate system.

Mach cone. Considering  $\varphi$  to be a function of *q*,  $\theta$ , and *x*, we get, by the usual methods of interchanging of variables,

$$\frac{\partial \varphi}{\partial r} = \frac{\beta}{x} \varphi_\theta \quad (18.33a)$$

$$\frac{\partial \varphi}{\partial \theta} = \varphi_r \quad (18.33b)$$

$$\frac{\partial \varphi}{\partial x} = \varphi_z - \frac{q}{x} \varphi_\theta \quad (18.33c)$$

Taking second derivatives in like manner, and substituting into Eq. 18.31, we find

$$(1 - q^2) \varphi_{\theta\theta} + \frac{1}{q} (1 - 2q^2) \varphi_\theta + \frac{1}{q^2} \varphi_{rr} + 2qx\varphi_{r\theta} - x^2 \varphi_{zz} = 0$$

As explained previously, a similar equation may be written for *u*, with which it is more convenient to work because the boundary conditions in *u* are relatively simple. Then, using the fact that in conical flows *u* does not depend on *x*, but only on *q* and  $\theta$ , the equation reduces to

$$(1 - q^2) u_{\theta\theta} + \frac{1}{q} (1 - 2q^2) u_\theta + \frac{1}{q^2} u_{rr} = 0 \quad (18.34)$$

**Transformation of Chaplygin.** A fortunate transformation, attributed to Chaplygin,

$$q \equiv \frac{2s}{1 + s^2} \quad (18.35)$$

transforms Eq. 18.34 into the familiar Laplace equation in the polar coordinates  $s$  and  $\theta$ :

$$u_{ss} + \frac{1}{s} u_s + \frac{1}{s^2} u_{\theta\theta} = 0 \quad (18.36)$$

Note that the transformation given by Eq. 18.35 yields real values of  $s$  only when  $0 \leq q \leq 1$ , that is, only within the Mach cone. Within this region, therefore, solutions of elliptical type may be expected. Outside the Mach cone, Eq. 18.35 gives meaningless results, and the method of characteristics must be used.

**Solution by Means of Functions of a Complex Variable.** Either the real or imaginary part of any analytic function of the complex variable  $se^{i\theta}$  will satisfy Eq. 18.36. Thus, within the Mach cone, the problem may be reduced to that of finding the real part of an analytic function

$$u = \Re[f(se^{i\theta})] \quad (18.37)$$

such that  $u$ , as given by this relation, satisfies the boundary conditions on the Mach cone ( $s = 1$ ) and also on the surfaces of bodies lying within the Mach cone.

Assuming that the required function of Eq. 18.37 may be found, it remains to find the other velocity components. This is done by first integrating to find  $\varphi$ . Because of the conical nature of the flow, the potential  $\varphi$  must be expressible in the form

$$\varphi = x \cdot \Phi(q, \theta) \quad (18.38)$$

Combining this with Eq. 18.33c, we get

$$u = \frac{\partial \varphi}{\partial x} = \Phi - q \Phi_u = -q^2 \frac{\partial}{\partial q} \left( \frac{\Phi}{q} \right)$$

Then, integrating at constant  $\theta$ , and using Eq. 18.38 again, we find

$$\varphi = -xq \left[ \int_1^q \frac{u}{q^2} dq + g(\theta) \right] \quad (18.39)$$

where the integration is performed with constant  $\theta$ , and  $g(\theta)$  is an arbitrary function of  $\theta$ .

The radial component of velocity, denoted by  $v$ , is next found from Eqs. 18.33a and 18.39 as

$$v = \frac{\partial \varphi}{\partial r} = \frac{\beta}{x} \varphi_u = -\beta \left[ \int_1^q \frac{u}{q^2} dq + \frac{u}{q} + g(\theta) \right]$$

which becomes, after integration by parts,

$$v = -\beta \left[ \int_1^q \frac{u_a}{q} dq + (u)_{q=1} + g(\theta) \right] \quad (18.40)$$

The tangential component of velocity, denoted by  $w$ , may also be found from Eqs. 18.33b and 18.39 as

$$w = \frac{1}{r} \frac{\partial \varphi}{\partial \theta} = \frac{\beta}{xq} \frac{\partial \varphi}{\partial \theta} = -\beta \left[ \int_1^q \frac{u_{\theta}}{q^2} dq + g'(\theta) \right] \quad (18.41)$$

The details of applying the method are too laborious to be given here; for these the reader is referred to References 8 through 13.

### 18.7. Typical Theoretical Results for Finite Wings

We shall now summarize some important theoretical results of a practical nature found with the methods of this chapter, and drawn from References 3, 6, 8, 9, 11, 12, 14, and 15.

**Rectangular Wings.** Because of the assumed linearity of the perturbation velocities, the effects due to thickness and due to incidence may be treated separately, and then superposed for the complete wing.

For the rectangular wing of finite span (Fig. 18.22a), the flow is

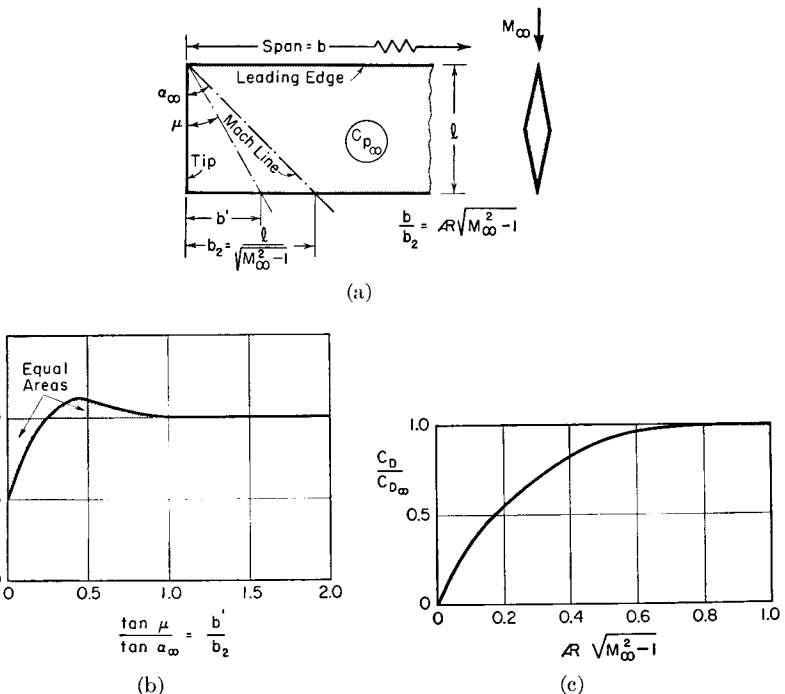


FIG. 18.22. Rectangular wing of finite span at zero incidence (after Bonney).

(a) Configuration near tip.

(b) Pressure distribution near tip.

(c) Effect of aspect ratio on thickness drag.

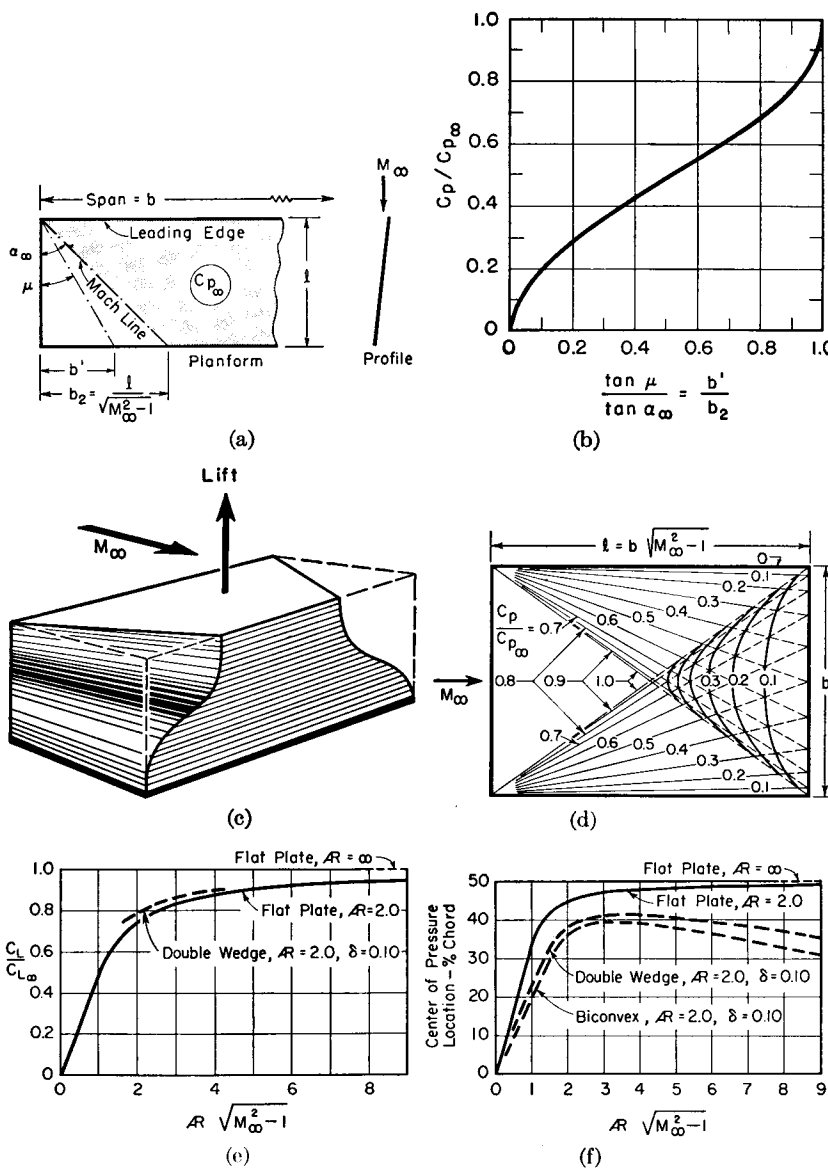


FIG. 18.23. Rectangular flat plate of finite span at angle of attack (after Bonney).

- Configuration near tip.
- Pressure distribution near tip.
- Three-dimensional view of lift distribution.
- Superposition of three pressure coefficients in the region where both regions of conical flow overlap the two-dimensional flow. For this purpose a value of  $C_p/C_{p\infty}$  of 0.7, say, on one of the radial lines is best thought of as the sum of (i) 1.0, corresponding to the two-dimensional flow, and (ii) -0.3, corresponding to the effects of the conical flow near the tip.
- Effect of aspect ratio on lift coefficient.
- Effect of aspect ratio on center of pressure.

two-dimensional except for the portions of the wing tips lying within the Mach cones generated at the tips of the leading edge. Within these tip regions the perturbation velocities are conical.

**THICKNESS DRAG.** Assuming no interaction between the tip Mach cones, the spanwise distribution of pressure coefficient at a fixed chord position is shown in Fig. 18.22b for a symmetrical profile at zero incidence. At the outboard tip, the pressure coefficient is exactly one-half the two-dimensional value ( $C_{p\infty}$ ), while at the Mach line it is equal to the two-dimensional value. In between, the variation of  $C_p$  is such that the average value over the tip area is exactly equal to  $C_{p\infty}$ . Consequently, the thickness drag is independent of aspect ratio, and is given by the two-dimensional value, as long as  $AR\sqrt{M_\infty^2 - 1} > 2$ .

When  $AR\sqrt{M_\infty^2 - 1} < 2$ , the conical fields from the two tips cross, and the superposition of effects is such that the total thickness drag is not changed until  $AR\sqrt{M_\infty^2 - 1} < 1$ , after which there is a reduction as compared with the two-dimensional value, as shown in Fig. 18.22c.

**LIFT AND INDUCED DRAG.** The spanwise pressure distribution in the tip region for an inclined plate with zero thickness is shown in Fig. 18.23b. It is seen that the flow around the tip reduces the pressure coefficient (and the lift intensity) there to zero, and that  $C_p$  takes on the two-dimensional value at the Mach line. Because of the symmetry of the curve, the average value of  $C_p$  at any chordwise station for the part of the span lying within the tip region is exactly half the two-dimensional value. Consequently the coefficients of lift and induced drag for the tip triangle are half the corresponding two-dimensional values, and the center of pressure of the tip triangle is at 2/3 chord.

Fig. 18.23c shows a three-dimensional perspective of the lift distribution when the tip triangles do not intersect. When the tip triangles do intersect the pressure coefficient of the two-dimensional flow is added to the pressure-loss coefficients of the two conical flows at a point in the region of intersection to give the pressure coefficient at the point in question. This procedure is valid of course only to the point where the Mach line from one tip intersects the other tips, i.e., only for  $AR\sqrt{M_\infty^2 - 1} > 1$ . Lines of constant pressure coefficient for this limiting case are shown, based on the superposition principle, in Fig. 18.23d. This diagram is universally valid for any value of  $l$  less than  $b\sqrt{M_\infty^2 - 1}$ , because in supersonic flow a reduction in chord obtained by cutting off the downstream part of the chord cannot affect the upstream pressure distribution. If the chord is made larger than the limiting value of Fig. 18.23d, the pressure distribution over the added region is difficult to predict, but it is likely that the amount of additional lift obtained is negligible or perhaps even negative.

When these considerations are applied to wings of various aspect

ratios, the ratio of lift coefficient to the two-dimensional  $C_{L\infty}$  takes the form of Fig. 18.23e, while the center of pressure is as shown in Fig. 18.23f. The reduction in lift owing to tip loss is small until  $R\sqrt{M_\infty^2 - 1}$  is less than 5. The effect of tip loss is to move the center of pressure slightly forward.

**Lift of Straight Wing with Raked Tips.** When the leading and trailing edges are normal to  $M_\infty$ , and when the tip is raked within the Mach cone so that it is a subsonic trailing edge, as in Fig. 18.24, the spanwise distribution of pressure coefficient (owing to angle of attack) along a line such as A-A is as shown in Fig. 18.23b. From this it follows that the average value of  $C_p/C_{p\infty}$  in the tip region is 0.50. With this rule

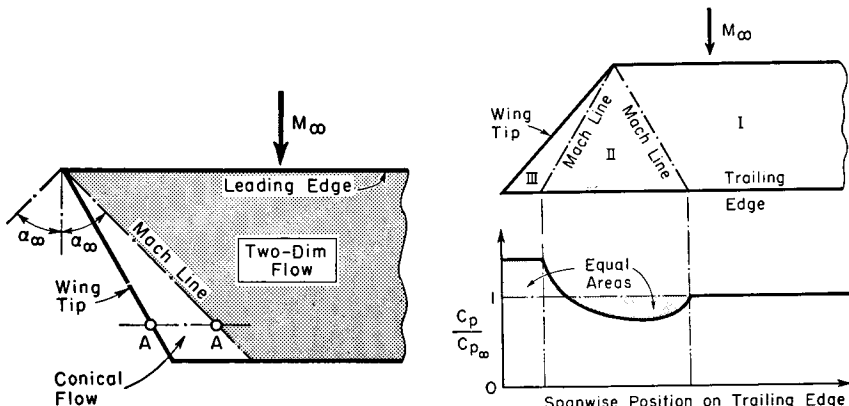


FIG. 18.24. Rectangular flat plate with raked tip lying within Mach cone.

FIG. 18.25. Rectangular flat plate with supersonic raked tip.

it is easy to determine the lift coefficient and center of pressure for wings with such tips.

When the wing has the shape of Fig. 18.25, with raked tips outside the Mach cone and acting as supersonic leading edges, three types of regions may be identified: (i) Region I, with two-dimensional, uniform flow, (ii) Region II, with conical flow, and (iii) Region III with the uniform, parallel flow typical of infinite sweptback wings. The spanwise pressure distribution is as shown in the diagram. When integrated, this curve leads to the surprising results that the lift coefficient and induced drag coefficient are the same as if the wing were subject to the uniform pressure distribution of an infinite-span airfoil. This conclusion applies also when the regions of conical flow overlap to any extent whatsoever.

**Lift of Delta with Supersonic Leading Edge.** The forward-pointing triangle, Fig. 18.26d, is a special case of Fig. 18.25. Thus, the thin

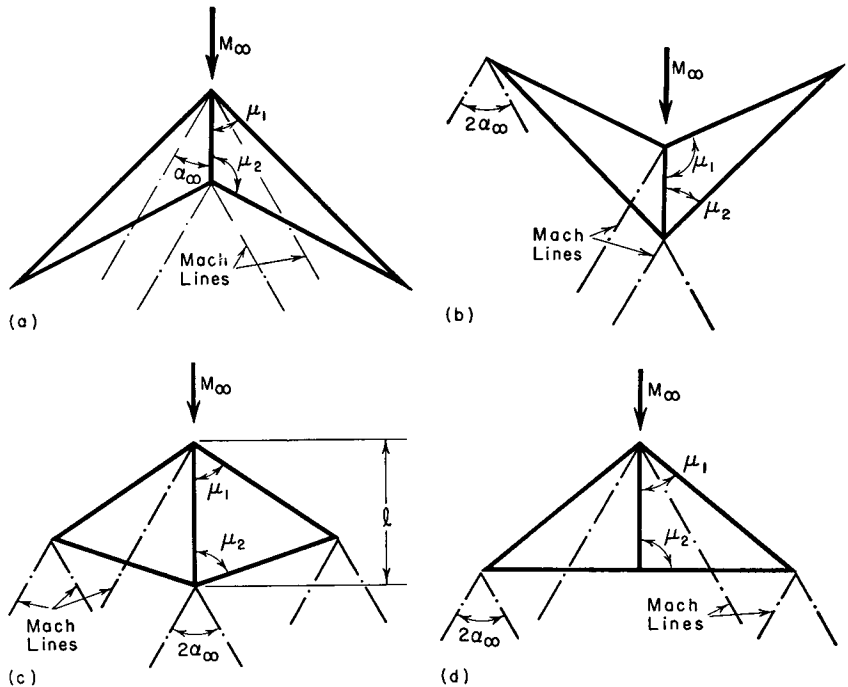


FIG. 18.26. Several planforms with symmetry about fore-and-aft diagonal.

delta wing with supersonic leading edge has the same  $C_L$  as an infinite-span airfoil, and has its center of pressure  $2/3$  of the chord aft of the apex.

**Lift of Thin Quadrilateral Wings with Supersonic Leading and Trailing Edges.** Consider thin quadrilaterals which are symmetrical about a diagonal in the direction of flow, and with supersonic leading and trailing edges. Various possibilities are shown in Fig. 18.26. Then, if we define

$$\cos \epsilon \equiv \tan \alpha_\infty / \tan \mu$$

the lift coefficient, as compared with the two-dimensional lift coefficient, is given by <sup>(12)</sup>

$$\frac{C_L}{C_{L\infty}} = \frac{2}{\pi} \frac{\epsilon_2 \sin 2\epsilon_1 - \epsilon_1 \sin 2\epsilon_2}{\sin \epsilon_2 \sin 2\epsilon_1 - \sin \epsilon_1 \sin 2\epsilon_2}$$

Reference 12 also gives expressions for the center of pressure.

**Lift of Thin Diamond Planform with Supersonic Leading and Trailing Edges.** A special case of Fig. 18.26c occurs when  $\mu_1 = \mu_2$ , in which case the planform is diamond-shaped. The main results are given in the

following table, where  $x_{c.p.}$  is the distance aft of the leading apex to the center of pressure: <sup>(12)</sup>

$\tan \mu / \tan \alpha_\infty$	1.000	1.556	2.000	$\infty$
$C_L / C_{L\infty}$	0.849	0.912	0.938	1.000
$x_{c.p.} / l$	0.467	0.479	0.484	0.500

It is seen that there is little difference between such a diamond and a wing of infinite span.

**Lift of Delta Wings.** <sup>(8)</sup> The lift of thin delta wings having the planform of Fig. 18.17a is shown in Fig. 18.27. For values of the abscissa greater than 1, i.e., for supersonic leading edges, the curves represent graphically the formula given previously for symmetrical quadrilateral planforms.

On comparing with Fig. 18.8c it is seen that planforms with  $e \leq 0.5$  and  $\sqrt{M_\infty^2 - 1} / \tan \Lambda \leq 0.6$  are of practical interest because, as compared with the two-dimensional case, there is a large decrease in thickness drag with little loss of lift.

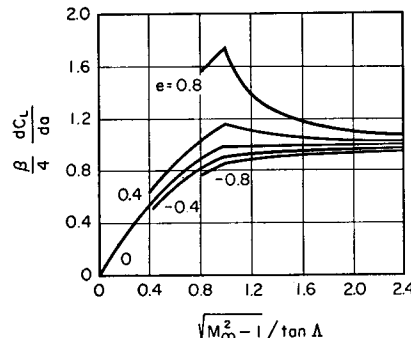


FIG. 18.27. Effect of sweepback on lift-curve slope of arrowhead wing of Fig. 18.17a (after Puckett and Stewart).

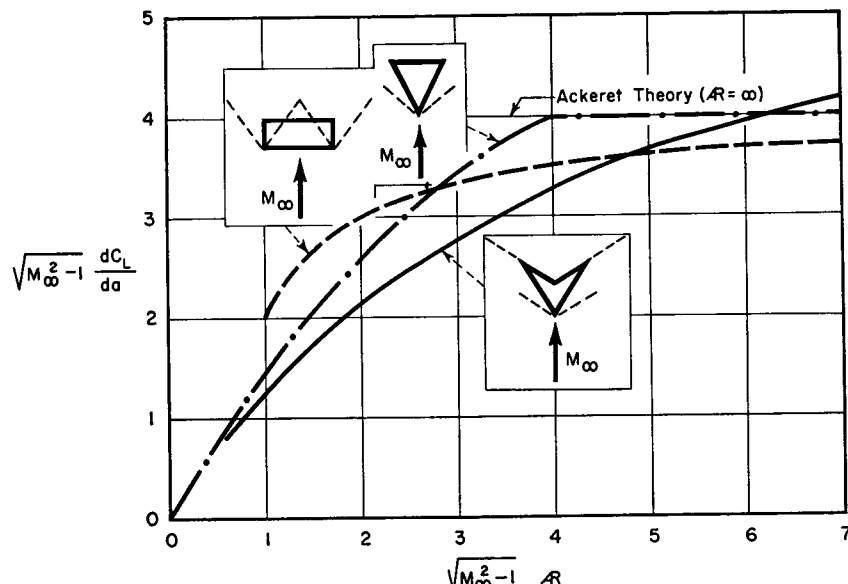


FIG. 18.28. Lifting properties of three planforms (after Jones).

**Comparison of Wing Planforms.** Fig. 18.28 <sup>(15)</sup> shows a comparison between the lift-curve slopes of three planforms. For  $M_\infty \leq 1.4$ , the rectangular wing gives the highest  $C_L$  for  $AR < 3$ . Between  $3 < AR < 6$ , the delta with straight trailing edge gives the highest  $C_L$ ; and, for  $AR > 6$ , the arrowhead delta has the highest  $dC_L/d\alpha$ .

A further comparison between these three planforms is shown in

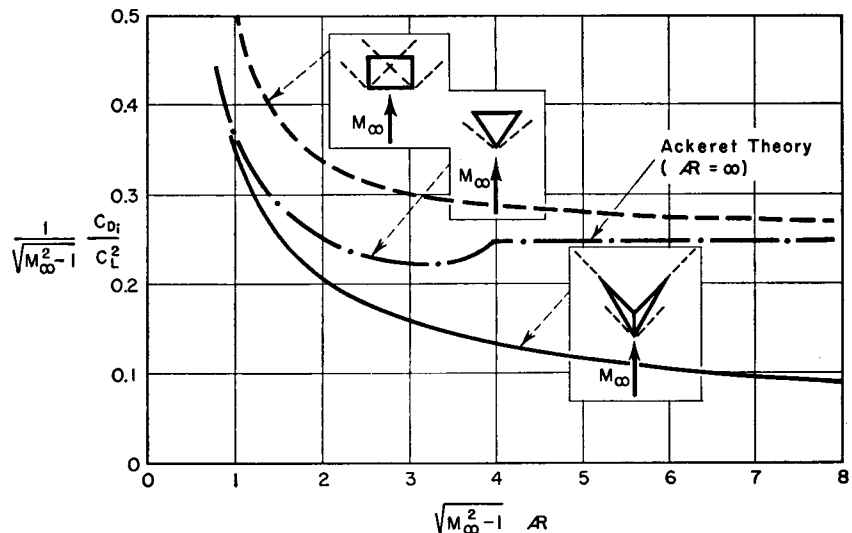


FIG. 18.29. Induced drag of three planforms (after Jones).

Fig. 18.29, <sup>(15)</sup> where it is seen that there are significant differences in induced drag due to lift, the delta arrowhead showing the least induced drag, and the rectangular wing the most.

### 18.8. Comparison of Theory with Experiment

A systematic comparison of the foregoing theoretical predictions with experimental results is given in Reference 16, from which the following results are drawn.

**Lift-Curve Slope.** Fig. 18.30 shows that the linear theories predict remarkably well the effect of aspect ratio on the lift-curve slope of unswept wings. Similarly good agreement is indicated in Fig. 18.31 for the effect of sweep angle on lift-curve slope, except where the Mach line is nearly coincident with the leading edge.

**Center of Pressure.** As might be expected, the linear theory gave erroneous results as to the center-of-pressure location, and is not reliable for this purpose (the experimental results are not shown here).

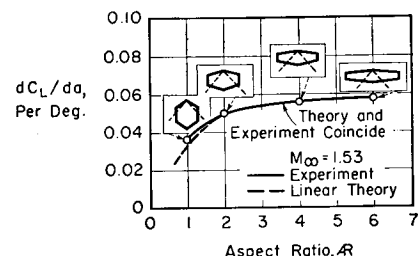


Fig. 18.30. Comparison of experiment and theory for lift-curve slope of unswept wings (after Vincenti).

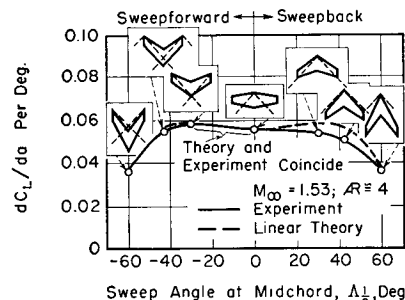


Fig. 18.31. Comparison of experiment and theory for lift-curve slope of swept wings (after Vincenti).

**Thickness Drag.** The effect of sweep angle on the thickness plus skin-friction drag is shown in Fig. 18.32. Over most of the range the difference between the measured  $C_D$  and that computed by the linear theory is consistent with a turbulent skin-friction coefficient of about 0.006. In the region where the flow normal to the leading edge is transonic the linear theory, as might be expected, overestimates the pressure drag.

An unexpected result is shown in Fig. 18.33. For double-wedge delta wings with subsonic leading edges the linear theory suggests that the thickness drag may be considerably reduced by placing the line of

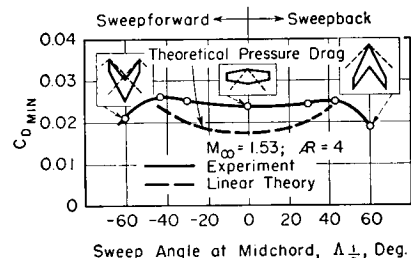


Fig. 18.32. Thickness plus skin-friction drag as a function of sweep angle (after Vincenti).

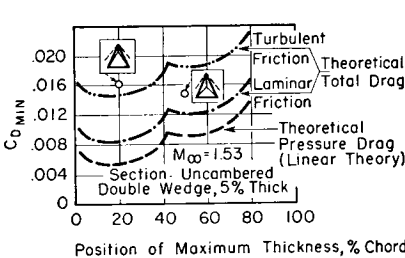


Fig. 18.33. Thickness plus skin-friction drag as a function of position of maximum thickness (after Vincenti).

maximum thickness near the leading edge. In the experiments the effect was found to be opposite, and it was established in various ways that the difference was due to a change in skin-friction coefficient. The reduction in pressure drag when the line of maximum thickness is far forward is brought about by a rise in pressure over the surface aft of this line. This apparently causes the boundary layer in this region to become turbulent, and thus increases the skin-friction drag to such an extent that the total drag is increased rather than decreased.

**Induced Drag.** The induced drag for a delta wing with a subsonic leading edge and with several profiles is shown in Fig. 18.34. Two curves based on the linear theory are shown: (i) the lower line includes the *leading-edge suction* connected with the extremely high negative pressure at a subsonic leading edge; (ii) the upper line omits the "leading-edge suction" on the grounds that in practice it would not exist because of boundary-layer separation. It is seen that the profiles with sharp

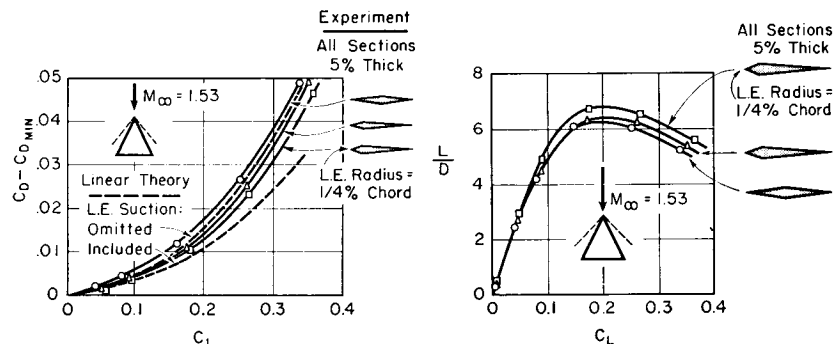


Fig. 18.34. Effect of radius of subsonic leading edge on pressure drag due to lift (after Vincenti).

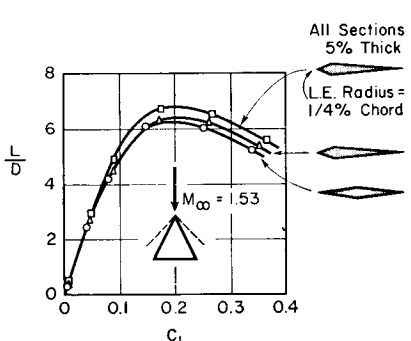


Fig. 18.35. Effect of radius of subsonic leading edge on lift-drag ratio (after Vincenti).

leading edges have induced drags which agree well with the upper curve, while the profile with the rounded leading edge achieves part of the leading-edge suction and thereby has a lower drag.

Finally, the experimental results of Fig. 18.34 are replotted in Fig. 18.35 and show convincingly that it is desirable to have a slight rounding of the leading edge when the leading edge is subsonic. A different set of experiments, not shown here, demonstrated that it was equally bad to round the leading edge if the latter were supersonic.

## REFERENCES AND SELECTED BIBLIOGRAPHY

1. FERRI, A. *Elements of Aerodynamics of Supersonic Flows*. New York: The Macmillan Co., 1949.
2. BONNEY, E. A. *Engineering Supersonic Aerodynamics*. New York: McGraw-Hill Book Co., Inc., 1950.
3. VON KÁRMÁN, T. Supersonic Aerodynamics—Principles and Applications, *Jour. Aero. Sci.*, Vol. 14, No. 7 (1947), p. 373.
4. IVEY, H. R., and BOWEN, E. N., JR. Theoretical Supersonic Lift and Drag Characteristics of Symmetrical Wedge-Shape-Airfoil Sections as Affected by Sweepback Outside the Mach Cone, *NACA Tech. Note*, No. 1223 (1947).
5. PUCKETT, A. E. Supersonic Wave Drag of Thin Airfoils, *Jour. Aero. Sci.*, Vol. 13, No. 9 (1946), p. 475.
6. LIGHTHILL, M. J. The Supersonic Theory of Wings of Finite Span, *British A.R.C. R & M No. 2001* (1944).
7. JONES, R. T. Thin Oblique Airfoils at Supersonic Speeds, *NACA Tech. Note*, No. 1107 (1946).

8. PUCKETT, A. E., and STEWART, H. J. Aerodynamic Performance of Delta Wings at Supersonic Speeds, *Jour. Aero. Sci.*, Vol. 14, No. 10 (1947), p. 567.
9. BUSEMANN, A. Infinitesimal Kegele Überschallstromung, *Schriften den deutschen Akademie der Luftfahrtforschung*, 7B (1943), p. 105.
10. HAYES, W. D. Linearized Theory of Conical Supersonic Flow with Application to Triangular Wings, *North American Aviation Co. Report NA-46-818* (1946).
11. STEWART, H. J. The Lift of a Delta Wing at Supersonic Speeds, *Quarterly App. Math.*, Vol. 4, No. 3 (1946), p. 246.
12. SNOW, R. M. Aerodynamics of Thin Quadrilateral Wings at Supersonic Speeds, *Quarterly App. Math.*, Vol. 5, No. 4 (1948), p. 417.
13. BESKIN, L. Supersonic Flow Past Airfoil Tips, *Jour. App. Mech.*, Paper No. 48-A-23.
14. BONNEY, E. A. Aerodynamic Characteristics of Rectangular Wings at Supersonic Speeds, *Jour. Aero. Sci.*, Vol. 14, No. 2 (1947), p. 111.
15. JONES, R. T. Estimated Lift-Drag Ratios at Supersonic Speed, *NACA Tech. Note*, No. 1350 (1947).
16. VINCENTI, W. G. Comparison Between Theory and Experiment for Wings at Supersonic Speeds, *NACA Tech. Note*, No. 2100 (1950).
17. BEANE, B. The Characteristics of Supersonic Wings Having Biconvex Sections, *Jour. Aero. Sci.*, Vol. 18, No. 1 (1951), p. 7.
18. LAWRENCE, T. Charts of the Wave Drag of Wings at Zero Lift, *British A.R.C. Tech. Rept.*, C.P. No. 116 (1953).

## Chapter 19

### HYPersonic FLOW

#### 19.1. Introductory Remarks

The various exact theories for supersonic flow which have been discussed previously are of course applicable at large Mach Numbers as well as small. However, when the Mach Number is very large, the flow exhibits a special behavior which is worth studying separately. It is then called *hypersonic flow*. A more precise definition of hypersonic flow will be given later.

It may be recalled that the linearized equations for the velocity potential are not valid for very large Mach Numbers, thus making invalid for hypersonic flow the Ackeret approximation for two-dimensional profiles (Chapter 14) and the source-sink method of Kármán and Moore for bodies of revolution (Chapter 17). Indeed, it will be seen that for hypersonic flow the pressure coefficient varies nonlinearly with thickness ratio and angle of incidence, as compared with the familiar linear laws for thin two-dimensional bodies at moderate supersonic speeds.

The principal applications of the theory of hypersonic flow are, at present, to the flight of rockets and guided missiles at very high speeds. Often such flight is feasible only at very high altitudes where the air density is relatively small and the drag is not prohibitive. Hence hypersonic flow may sometimes occur under conditions for which the fluid may no longer be treated as a continuum. Such flows lie in the so-called realm of "super-aerodynamics," for which kinetic theory rather than continuum dynamics must be employed for analysis. Having made these precautionary remarks, we shall confine our attention to a study of hypersonic flows from the continuum viewpoint.

Some of the general features of hypersonic flow may be grasped from a qualitative examination of the exact relations for isentropic flow, Prandtl-Meyer flow, and oblique shock waves. When the Mach Number is very large, the speed is very near the maximum speed corresponding to the stagnation temperature. If the flow is disturbed by a body the speed of the fluid remains almost unchanged, but the local speed of sound undergoes large changes. The Mach angle is extremely small, and hence the Mach waves tend to follow the surface of the body. Likewise, oblique shock waves make a very small angle with the flow and thus

tend also to follow the surface of the body. Referring to the flat plate at incidence (Fig. 19.1a) these considerations give rise to the concept of a *hypersonic boundary layer* near the surface; within this layer there is confined all the fluid which has been affected by the presence of the body. The similarity with the *viscous boundary layer* is obvious.

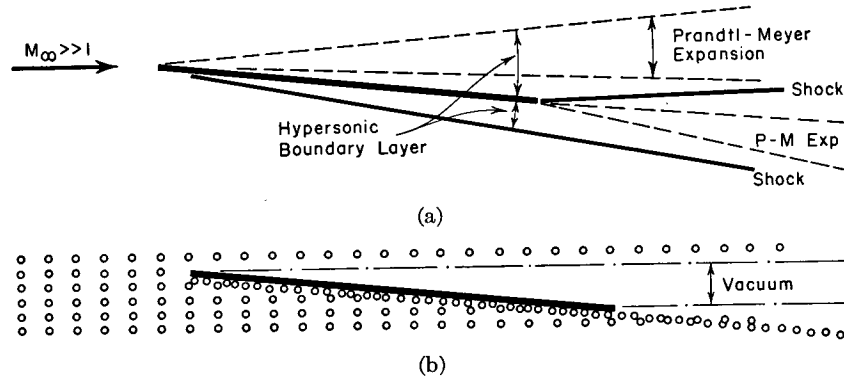


FIG. 19.1. (a) Hypersonic boundary layer.  
(b) Newton's corpuscular theory of fluid dynamics.

Since the pressure rise across the shock at high  $M$  is very much larger than the pressure decrease across the Prandtl-Meyer expansion, as an approximation it may be assumed that there is a vacuum on the upper side of the plate. On the lower side the oblique shock nearly coincides with the plate surface. Therefore the flow of Fig. 19.1a conforms approximately to *Newton's corpuscular theory* of fluid dynamics, which for the flat plate gives the flow of Fig. 19.1b. From momentum considerations alone, and assuming that the magnitude of the fluid velocity is substantially unchanged, Newton's theory yields  $C_L \cong 2 \sin^2 a$  and  $C_D \cong 2 \sin^3 a$ , where  $a$  is the angle of incidence.

Since exact methods are in fact available for hypersonic flow in the form of the method of characteristics, the main discussion of this chapter will center around similarity laws for hypersonic flow. These laws (i) illustrate general rules of behavior of such flows, (ii) permit the most general extension of analytical results, and (iii) may be used for correlating and extending experimental data at hypersonic speeds. In order to arrive at similarity laws of reasonably simple form, it will be necessary to assume that there are only small perturbations from a uniform, parallel flow. This is not a serious restriction because at hypersonic speeds the drag of a thick body is so enormous that only thin bodies are of practical interest.

## NOMENCLATURE

$a$	angle of attack	$t$	maximum thickness
$c$	speed of sound	$u, v$	Cartesian velocity components
$C_p$	pressure coefficient	$U_\infty$	free-stream velocity
$C_{ps}$	pressure coefficient of shock	$x, y$	Cartesian coordinates
$C_L$	lift coefficient	$\delta$	thickness ratio
$C_D$	drag coefficient	$\eta$	$y/t$
$\mathcal{D}$	similarity function for $C_D$	$\theta_s$	deflection angle across shock
$f$	function of $\xi$ and $\eta$ (Eq. 19.6)	$\theta_e$	deflection angle of simple-wave expansion
$h$	dimensionless thickness distribution	$\xi$	$x/l$
$k$	ratio of specific heats	$\sigma$	shock angle
$K$	hypersonic similarity parameter, $M_\infty \delta$	$\varphi$	perturbation velocity potential
$K_s$	similarity parameter for shock, $M_1 \theta_s$	$\omega$	angle of turn through a wave; positive for compressions, negative for expansions
$K_e$	similarity parameter for simple-wave expansion, $M_1 \theta_e$	$(\ )_\infty$	signifies free-stream conditions
$l$	chord	$(\ )_0$	signifies stagnation state
$\mathcal{L}$	similarity function for $C_L$	$(\ )_1$	signifies condition before shock
$M$	Mach Number	$(\ )_2$	signifies condition after shock
$\mathcal{M}$	similarity function for $C_M$	$(\ )_i$	signifies conditions at beginning of simple-wave expansion
$p$	pressure		
$\mathcal{P}$	similarity function for $C_p$ , see Eq. 19.24		
$\mathcal{P}_s$			

19.2. Similarity Laws for Hypersonic Flow <sup>(1,7)</sup>

We shall derive the similarity law for two-dimensional flow in detail and shall subsequently state the analogous forms for axi-symmetric flow and for wings of finite span.

**Approximate Differential Equation for Hypersonic Flow.** Consider a two-dimensional, irrotational motion past a thin profile. If the stream is initially uniform and parallel, and is of magnitude  $U_\infty$  in the  $x$ -direction, the exact expression for the perturbation velocity potential  $\varphi$  is, as shown in Chapter 10, given by

$$\left(1 - \frac{u^2}{c^2}\right) \frac{\partial^2 \varphi}{\partial x^2} - 2 \frac{uv}{c^2} \frac{\partial^2 \varphi}{\partial x \partial y} + \left(1 - \frac{v^2}{c^2}\right) \frac{\partial^2 \varphi}{\partial y^2} = 0 \quad (19.1)$$

where the velocity components are

$$u = U_\infty + \frac{\partial \varphi}{\partial x}; \quad v = \frac{\partial \varphi}{\partial y} \quad (19.2)$$

and the local speed of sound is related to the free-stream speed of sound by

$$\begin{aligned} c^2 &= c_\infty^2 - \frac{k-1}{2} [(u^2 + v^2) - U_\infty^2] \\ &= c_\infty^2 - \frac{k-1}{2} \left[ 2U_\infty \frac{\partial \varphi}{\partial x} + \left( \frac{\partial \varphi}{\partial x} \right)^2 + \left( \frac{\partial \varphi}{\partial y} \right)^2 \right] \quad (19.3) \end{aligned}$$

For hypersonic flow over a thin profile, the speeds  $c_\infty$ ,  $\partial \varphi / \partial x$ , and  $\partial \varphi / \partial y$  are all small compared with  $U_\infty$ . Keeping this in mind when substituting Eqs. 19.2 and 19.3 into Eq. 19.1, and retaining only terms of first order in  $c_\infty / U_\infty$ , etc., we obtain

$$\begin{aligned} &\left[ 1 - (k+1) \frac{M_\infty \partial \varphi}{c_\infty \partial x} - \frac{k-1}{2} \frac{1}{c_\infty^2} \left( \frac{\partial \varphi}{\partial y} \right)^2 - M_\infty^2 \right] \frac{\partial^2 \varphi}{\partial x^2} - 2 \frac{M_\infty}{c_\infty} \frac{\partial \varphi}{\partial y} \frac{\partial^2 \varphi}{\partial x \partial y} \\ &+ \left[ 1 - (k-1) \frac{M_\infty \partial \varphi}{c_\infty \partial x} - \frac{k+1}{2} \frac{1}{c_\infty^2} \left( \frac{\partial \varphi}{\partial y} \right)^2 \right] \frac{\partial^2 \varphi}{\partial y^2} = 0 \quad (19.4) \end{aligned}$$

**Affine Transformation.** Tsien<sup>(1)</sup> has shown that Eq. 19.4 can be put into a form which relates the flows about affinely connected profiles if the coordinate transformations

$$\xi \equiv x/l; \quad \eta \equiv \frac{y/l}{\delta} = \frac{y}{t} \quad (19.5)$$

are employed, where  $l$  is the chord and  $\delta$  is the thickness ratio of the profile. Note that the  $\eta$  parameter represents a magnification of the coordinate normal to the surface of the body, thus making it possible to investigate more easily the velocity variation in the hypersonic boundary layer. The nondimensional form employed for the velocity potential  $\varphi$  is

$$\varphi \equiv \frac{c_\infty l}{M_\infty} f(\xi, \eta) \quad (19.6)$$

Substituting Eqs. 19.5 and 19.6 into Eq. 19.4 by the usual mathematical methods for interchange of variables, and assuming (i) that  $\delta^2 \ll 1$ , and (ii) that the product  $M_\infty \delta$  is at least of the order of magnitude of unity, the resulting equation when small-order terms are neglected is

$$\left[ 1 - (k-1) \frac{\partial f}{\partial \xi} - \frac{k+1}{2(M_\infty \delta)^2} \left( \frac{\partial f}{\partial \eta} \right)^2 \right] \frac{\partial^2 f}{\partial \eta^2} = (M_\infty \delta)^2 \frac{\partial^2 f}{\partial \xi^2} + 2 \frac{\partial f}{\partial \eta} \frac{\partial^2 f}{\partial \xi \partial \eta} \quad (19.7)$$

The boundary conditions are:

$$\text{at } x = -\infty: \quad \frac{\partial \varphi}{\partial x} = 0; \quad \frac{\partial \varphi}{\partial y} = 0 \quad (19.8a)$$

$$\text{at profile surface: } \left( \frac{\partial \varphi}{\partial y} \right)_s = U_\infty \delta h(\xi) \quad (19.8b)$$

where the function  $h(\xi)$  represents the ratio of the local surface slope to the thickness ratio  $\delta$ . Note that  $h(\xi)$  depends only on the form of the thickness distribution of a family of affinely related profiles and not on the thickness ratio itself. In terms of the transformed variables  $\xi$ ,  $\eta$ , and  $f$ , these boundary conditions become:

$$\text{at } \xi = -\infty: \quad \frac{\partial f}{\partial \xi} = 0; \quad \frac{\partial f}{\partial \eta} = 0 \quad (19.9a)$$

$$\text{at profile surface: } \left( \frac{\partial f}{\partial \eta} \right)_s = M_\infty^2 \delta^2 h(\xi) \quad (19.9b)$$

**Similarity Rule.** By examination of the forms of Eqs. 19.7 and 19.9 the following similarity rule may be seen to hold for hypersonic flow:

If a series of profiles having the same thickness distribution but different thickness ratios are placed in flows of different Mach Numbers such that the product  $M_\infty \delta$  is the same for all the profiles, then the flow patterns are similar in the sense that they are governed by the same function  $f(\xi, \eta)$ . This is true because the functions  $f(\xi, \eta)$  for the various profiles are determined by the same differential equation (Eq. 19.7) and the same boundary conditions (Eqs. 19.9). From this it follows further that the function  $f(\xi, \eta)$  depends only on the ratio of specific heats  $k$ , the hypersonic similarity parameter  $K$ , and the thickness distribution  $h(\xi)$ .

The product  $M_\infty \delta$  is called the *hypersonic similarity parameter* and is represented by the symbol  $K \equiv M_\infty \delta$ .

In arriving at Eq. 19.7 it was assumed that  $K$  is at least of the order of magnitude of unity. We may now define hypersonic flow more precisely as a supersonic flow with small perturbations for which  $M_\infty \delta$  is of the order of unity or greater.

**Force Coefficients.** From the exact isentropic relations we may obtain

$$\frac{p}{p_\infty} = \frac{p/p_0}{p_\infty/p_0} = \frac{\left( 1 + \frac{k-1}{2} \frac{u^2 + v^2}{c^2} \right)^{-k/(k-1)}}{\left( 1 + \frac{k-1}{2} M_\infty^2 \right)^{-k/(k-1)}}$$

This, together with Eqs. 19.2, 19.3, 19.5, and 19.6, is now substituted into the formula for the pressure coefficient,

$$C_p \equiv \frac{p - p_\infty}{\frac{1}{2} \rho_\infty U_\infty^2} = \frac{2}{k M_\infty^2} \left( \frac{p}{p_\infty} - 1 \right)$$

After expanding the resultant expression for  $C_p$  in a power series and discarding higher-order terms according to the assumptions previously made, we obtain for the pressure coefficient corresponding to a given thickness distribution  $h(\xi)$ ,

$$C_p = \delta^2 \mathcal{P}(\mathbf{K}, k, \xi, \eta) = \frac{1}{M_\infty^2} \mathbf{K}^2 \mathcal{P}(\mathbf{K}, k, \xi, \eta) \quad (19.10a)$$

where the function  $\mathcal{P}(\mathbf{K}, k, \xi, \eta)$  is given by

$$\mathcal{P}(\mathbf{K}, k, \xi, \eta) \equiv \frac{2}{k\mathbf{K}^2} \left[ \left\{ 1 - (k-1) \frac{\partial f}{\partial \xi} - \frac{k-1}{2\mathbf{K}^2} \left( \frac{\partial f}{\partial \eta} \right)^2 \right\}^{\frac{k}{k-1}} - 1 \right] \quad (19.10b)$$

But it has already been shown that  $f(\xi, \eta)$  depends only on  $k$ ,  $\mathbf{K}$ , and  $h(\xi)$ . Accordingly, for profiles having the same thickness distribution (and whose camber and angle of attack are proportional to  $\delta$ ), the quantities  $C_p/\delta^2$  and  $C_p M_\infty^2$  are functions only of the single parameter  $\mathbf{K}$ , provided of course that the pressure coefficients are all evaluated at the same values of  $\xi$  and  $\eta$  and that gases with the same ratio of specific heats are used.

Within the approximations of thin-profile theory the lift, drag, and moment coefficients of a family of affinely related profiles are therefore expressible concisely as

$$C_L = \frac{1}{l} \oint C_p dx = \delta^2 \mathcal{L}(\mathbf{K}, k) = \frac{1}{M_\infty^2} \mathbf{K}^2 \mathcal{L}(\mathbf{K}, k) \quad (19.11)$$

$$C_D = \frac{1}{l} \oint C_p \frac{dy}{dx} dx = \delta^3 \mathcal{D}(\mathbf{K}, k) = \frac{1}{M_\infty^3} \mathbf{K}^2 \mathcal{D}(\mathbf{K}, k) \quad (19.12)$$

$$C_M = \frac{1}{l^2} \oint C_p x dx = \delta^2 \mathcal{M}(\mathbf{K}, k) = \frac{1}{M_\infty^2} \mathbf{K}^2 \mathcal{M}(\mathbf{K}, k) \quad (19.13)$$

where the functions  $\mathcal{L}$ ,  $\mathcal{D}$ , and  $\mathcal{M}$  depend, for a given thickness distribution, only on  $k$  and  $\mathbf{K}$ . These rules show that when air flows hypersonically past different profiles having the same thickness distribution, with the camber and angle of attack being made proportional to  $\delta$ , the quantities  $C_L/\delta^2$ ,  $C_L M_\infty^2$ ,  $C_D/\delta^3$ ,  $C_D M_\infty^3$ ,  $C_M/\delta^2$ , and  $C_M M_\infty^2$  are all functions of the single parameter  $M_\infty \delta$ .

**Illustration of Similarity Law.** The meaning of the similarity laws as stated above may be clarified by means of a specific example.

Suppose that a symmetrical profile with thickness ratio  $\delta = 0.10$  is tested at  $M_\infty = 5$  and angle of attack  $a_1 = 5^\circ$ ; the measurements yield corresponding values of  $C_{L1}$  and  $C_{D1}$ .

What conclusions can we draw concerning the performance of a geometrically similar profile with thickness ratio  $\delta_2 = 0.05$ ? In order to apply the similarity

law, we must set  $M_\infty \delta_1 = M_\infty \delta_2$ , and hence information concerning the second profile can be drawn from the data for the first profile only at  $M_\infty = 10$ . In addition, the two profiles will be affinely related only if  $a_2/a_1 = \delta_2/\delta_1$ ; hence we must also set  $a_2 = 2.5^\circ$ .

Eqs. 19.11 and 19.12 accordingly state that the lift and drag coefficients corresponding to  $\delta_2 = 0.05$ ,  $M_\infty = 10$ , and  $a_2 = 2.5^\circ$  are related to those corresponding to  $\delta_1 = 0.10$ ,  $M_\infty = 5$ , and  $a_1 = 5^\circ$  by the ratios

$$C_{L2}/C_{L1} = (\delta_2/\delta_1)^2 = 1/4$$

$$C_{D2}/C_{D1} = (\delta_2/\delta_1)^3 = 1/8$$

**Infinite Mach Number.** When  $M_\infty$  becomes infinite,  $\mathbf{K}$  also becomes infinite. The functions  $\mathcal{P}$ ,  $\mathcal{L}$ ,  $\mathcal{D}$ , and  $\mathcal{M}$  then are independent of the thickness ratio  $\delta$ . Consequently it is concluded from Eqs. 19.10, 19.11, 19.12, and 19.13 that, at infinite Mach Number,  $C_p$  varies as  $\delta^2$ ,  $C_L$  varies as  $\delta^2$ ,  $C_D$  varies as  $\delta^3$ , and  $C_M$  varies as  $\delta^2$ .

This result conforms with Newton's corpuscular theory of fluid dynamics.

**Comparison with Ackeret Linearized Theory.** The linearized theory for supersonic flow past thin profiles (Chapter 14) shows that, for affinely related profiles,

$$C_L \sim \frac{\delta}{\sqrt{M_\infty^2 - 1}}; \quad C_D \sim \frac{\delta^2}{\sqrt{M_\infty^2 - 1}}$$

For hypersonic flow,  $M_\infty^2 \gg 1$ , and thus these may be written

$$C_L \sim \frac{\delta^2}{M_\infty \delta}; \quad C_D \sim \frac{\delta^3}{M_\infty \delta}$$

It is seen that these agree with Eqs. 19.11 and 19.12 if we set  $\mathcal{L} = 1/\mathbf{K}$  and  $\mathcal{D} = 1/\mathbf{K}$ . The rules of the linear theory therefore fit into the hypersonic similarity laws. The latter are more general, however, inasmuch as they apply to very high supersonic speeds whereas the Ackeret theory does not.

**Similarity Law for Bodies of Revolution.**<sup>(1,7)</sup> By following the procedure outlined above for two-dimensional flows, the hypersonic similarity parameter for axi-symmetric flow is found also to be  $\mathbf{K} = M_\infty \delta$ . The similarity laws for the pressure coefficient and drag coefficient (referred to the maximum cross-sectional area of the body) are

$$C_p = \delta^2 \mathcal{P}(\mathbf{K}, k, \xi) = \frac{1}{M_\infty^2} \mathbf{K}^2 \mathcal{P}(\mathbf{K}, k, \xi) \quad (19.14)$$

$$C_D = \delta^2 \mathcal{D}(\mathbf{K}, k) = \frac{1}{M_\infty^2} \mathbf{K}^2 \mathcal{D}(\mathbf{K}, k) \quad (19.15)$$

Corresponding results for inclined bodies of revolution are presented in References 6 and 7.

**Similarity Laws for Wings of Finite Span.**<sup>(8)</sup> Following the same line of reasoning as for two-dimensional flow, the following similarity rules may be shown to apply to affinely related wings of finite span, where it is to be understood that the affinity relations require the camber, angle of incidence, and aspect ratio all to vary in proportion to  $\delta$ :

$$C_p = \delta^2 \mathcal{P}(\mathbf{K}, k) = \frac{1}{M_\infty^2} \mathbf{K}^2 \mathcal{P}(\mathbf{K}, k) \quad (19.16)$$

$$C_L = \delta^2 \mathcal{L}(\mathbf{K}, k) = \frac{1}{M_\infty^2} \mathbf{K}^2 \mathcal{L}(\mathbf{K}, k) \quad (19.17)$$

$$C_D = \delta^3 \mathcal{D}(\mathbf{K}, k) = \frac{1}{M_\infty^3} \mathbf{K}^3 \mathcal{D}(\mathbf{K}, k) \quad (19.18)$$

$$C_m = \delta^2 \mathcal{M}(\mathbf{K}, k) = \frac{1}{M_\infty^2} \mathbf{K}^2 \mathcal{M}(\mathbf{K}, k) \quad (19.19)$$

The pressure coefficients are to be compared, of course, at corresponding points of the affinely related wings under consideration.

If the aspect ratio is of the order of magnitude of unity or greater, the tip Mach cones cover a negligibly small fraction of the planform area. Consequently the flow may with good accuracy be treated as two-dimensional.

**Rotational Flows.** An important conclusion reached by Hayes<sup>(2)</sup> is that the hypersonic similarity laws as given above apply to flows with rotation as well as to irrotational flows. This is especially significant because of the large entropy increases which occur across oblique shocks at hypersonic speeds.

**Combined Supersonic-Hypersonic Similarity Law.**<sup>(13)</sup> It has been shown on page 751 that the small-disturbance theories of supersonic flow and hypersonic flow yield equivalent results for plane flow at very high Mach Numbers. Van Dyke<sup>(13)</sup> has shown that the two small-disturbance theories may be artificially combined for three-dimensional as well as plane flows merely by reinterpreting the solutions of the hypersonic theory. In brief, the foregoing hypersonic similarity laws of Eqs. 19.10, 19.11, 19.12, 19.13, 19.14, 19.15, 19.16, 19.17, 19.18, and 19.19 are modified by replacing  $M_\infty$  wherever it occurs by  $\sqrt{M_\infty^2 - 1}$ . Thus the similarity parameter would become  $\mathbf{K} \equiv \sqrt{M_\infty^2 - 1} \delta$ , and Eq. 19.10a, for example, would take the form

$$C_p = \delta^2 \mathcal{P}(\mathbf{K}, k, \xi, \eta) = \frac{\mathbf{K}^2}{M_\infty^2 - 1} \mathcal{P}(\mathbf{K}, k, \xi, \eta)$$

It is evident that these modified forms are virtually equivalent to the original hypersonic forms as  $M_\infty$  grows large. What Van Dyke has shown is that the modified forms embrace the similarity laws of supersonic flow with small disturbances (see Chapter 14, for example), and yield a single correlation rule valid from the upper limit of the transonic range up to and including hypersonic flows.

**Optimum Use of Hypersonic Small-Disturbance Theory for Large Disturbances.**<sup>(13)</sup> The error in hypersonic small-disturbance theory is only of order  $\delta^2$ , as compared with order  $\delta$  for supersonic linearized theory and  $\delta^{2/3}$  for transonic small-disturbance theory. Hence the need to correct for higher order terms in the thickness ratio is less in the hypersonic range than at lower speeds. Nevertheless, the accuracy of hypersonic small-disturbance theory can be strikingly improved simply by interpreting its results in conformity with the Newtonian corpuscular (or impact) theory. The latter assumes that fluid particles striking the surface of a body lose the normal component of their free-stream momentum, with the result that the surface  $C_p$  is proportional to the square of the sine of the streamwise inclination. This suggests that the pressure distribution predicted by hypersonic small-disturbance theory might best be extrapolated to thick shapes by assuming a sine-squared variation. Van Dyke<sup>(13)</sup> has shown that this is indeed true. For example, the surface  $C_p$  for cones of semi-vertex angle  $\gamma$  is much better correlated at high values of  $\gamma$  if one plots  $C_p/\sin^2 \gamma$  vs.  $M_\infty \tan \gamma$  instead of  $C_p/\tan^2 \gamma$  vs.  $M_\infty \tan \gamma$ . It has also been shown by Van Dyke that the accuracy of correlating lift forces at hypersonic speeds may be increased manyfold by this interpretation of the similarity law.

### 19.3. Oblique Shock Relations for Hypersonic Flow

Starting with the exact shock relations of Chapter 16, we shall find special relations for large values of the initial Mach Number  $M_1$  and small values of the turning angle  $\theta_s$ . These special formulas will be useful for working out the pressure distributions over thin airfoils and fuselages in hypersonic flow.<sup>(14)</sup>

**Exact Shock Equations.** The pressure ratio across the shock, in terms of the shock angle  $\sigma$ , is

$$\frac{p_2}{p_1} = \frac{2k}{k+1} M_1^2 \sin^2 \sigma - \frac{k-1}{k+1}$$

Previously we have found the pressure coefficient to be given by

$$C_p = \frac{2}{k M_1^2} \left( \frac{p_2}{p_1} - 1 \right); \text{ whence } \frac{p_2}{p_1} = 1 + \frac{k M_1^2}{2} C_p \quad (19.20a)$$

Thus, the pressure coefficient for the shock,  $C_{ps}$ , is

$$C_{ps} = \frac{4}{k+1} \left( \sin^2 \sigma - \frac{1}{M_1^2} \right) \quad (19.20b)$$

Now, the relation between shock angle, turning angle, and initial Mach Number for an oblique shock may be written

$$\frac{1}{M_1^2} = \sin^2 \sigma - \frac{k+1}{2} \frac{\sin \sigma \sin \theta_s}{\cos(\sigma - \theta_s)}$$

Combining this with the preceding relation, we get, after some trigonometric rearrangement,

$$\frac{1}{4} C_{ps}^2 \cos^2 \sigma = \left[ 1 - \frac{C_{ps}}{2} \right]^2 \sin^2 \sigma \tan^2 \theta_s \quad (19.21)$$

**Similarity Form of Shock Relations.** Eqs. 19.20 and 19.21 are exact. We now introduce assumptions consistent with the assumptions of large  $M_1$  and small  $\theta_s$ . These assumptions require  $C_{ps}$  to be small compared with unity and  $\sigma$  and  $\theta_s$  to be small also in the sense that  $\cos \sigma \cong 1$  and  $\tan \theta_s \cong \theta_s$ . Inserting these approximations into Eq. 19.21, and using Eq. 19.20b, we get

$$\frac{1}{4} C_{ps}^2 = \theta_s^2 \sin^2 \sigma = \theta_s^2 \left( \frac{k+1}{4} C_{ps} + \frac{1}{M_1^2} \right) \quad (19.22)$$

We now put this into a form suggested by the hypersonic similarity relations. The thickness ratio of an oblique shock is represented by the turning angle  $\theta_s$ , and the hypersonic similarity parameter by  $K_s \equiv M_1 \theta_s$ . Accordingly we postulate that

$$C_{ps} = \theta_s^2 \varphi_s(K_s, k); \quad K_s \equiv M_1 \theta_s \quad (19.23)$$

where  $\varphi_s$  is the form of the function for the special geometry of an oblique shock. Eliminating  $C_{ps}$  and  $M_1$  from Eq. 19.22 with the help of Eq. 19.23 and the definition of  $K_s$ , we obtain

$$\varphi_s^2 - (k+1)\varphi_s - \frac{4}{K_s^2} = 0$$

The only valid solution to this quadratic is

$$\varphi_s = \frac{k+1}{2} + \sqrt{\left( \frac{k+1}{2} \right)^2 + \left( \frac{2}{K_s} \right)^2} \quad (19.24)$$

because only the positive sign before the radical gives a positive value for  $\varphi_s$ .

Similarly, the Mach Number  $M_2$  after the shock may, on the basis of the same approximations, be shown to be given by

$$\frac{M_2}{M_1} \cong \frac{1}{\sqrt{1 + \frac{k}{2} K_s^2 \varphi_s^2}} \quad (19.25)$$

**Limiting Case of Infinite Mach Number.** When  $M_1$  becomes infinite,  $K_s \rightarrow \infty$ , and thus Eqs. 19.23 and 19.24 take the form

$$C_{ps} \rightarrow (k+1)\theta_s^2 \quad (19.26)$$

Considering the flat plate of Fig. 19.1a, and assuming zero pressure on the upper surface (the validity of this assumption is proved later), the lift and drag coefficients are seen to be

$$C_L \cong (k+1)\theta_s^2; \quad C_D \cong C_L \theta_s \cong (k+1)\theta_s^3 \quad (19.27)$$

where  $\theta_s$  in this case is equal to the angle of incidence. These results, if we set  $k = 1$ , are in accord with Newton's corpuscular theory for small angles of incidence.

Considering a symmetrical profile of finite thickness at zero incidence, the Ackeret linear theory indicates that the pressure drag varies with Mach Number according to  $C_D \sim \delta^2 / \sqrt{M_\infty^2 - 1}$ , which suggests that the pressure drag coefficient tends to vanish at very high Mach Numbers. Eq. 19.27, however, shows that this is not so, and that the pressure drag coefficient tends rather to reach a limiting finite value as  $M_\infty$  increases indefinitely.

As  $M_1$  tends to infinity, Eq. 19.25, together with Eqs. 19.23 and 19.26, show that

$$M_2 \rightarrow \frac{1}{\theta_s} \frac{2}{\sqrt{k(k+1)}} \quad (19.28)$$

Hence, for small values of  $\theta_s$ ,  $M_2$  is also large compared with unity when  $M_1$  is very large.

#### 19.4. Simple-Wave Expansion Relations for Hypersonic Flow <sup>(4)</sup>

The flow over the surface of thin two-dimensional profiles may be approximated by a simple-wave expansion. This expansion starts either with the free-stream conditions or with the conditions which follow an oblique shock attached to the leading edge. In either case the starting Mach Number for the simple-wave flow is very large (see Eq. 19.28) compared with unity, and grows even larger during the expansion.

According to the exact relations of Chapter 15, the turning angle  $\theta_e$  of a simple-wave expansion may be written

$$\begin{aligned}\theta_e = & \sqrt{\frac{k+1}{k-1}} \left( \arctan \sqrt{\frac{k-1}{k+1}} \sqrt{M^2 - 1} \right. \\ & - \arctan \sqrt{\frac{k-1}{k+1}} \sqrt{M_i^2 - 1} \left. \right) \\ & - (\arctan \sqrt{M^2 - 1} - \arctan \sqrt{M_i^2 - 1}) \quad (19.29)\end{aligned}$$

where  $M$  is the local Mach Number, and  $M_i$  is the Mach Number at the beginning of the expansion. For hypersonic flow, we may employ the approximations

$$\sqrt{M^2 - 1} \cong M; \quad \sqrt{M_i^2 - 1} \cong M_i$$

Making these substitutions, and expanding Eq. 19.29 in an infinite series, we obtain

$$\theta_e = \frac{2}{k-1} \left( \frac{1}{M_i} - \frac{1}{M} \right) - \frac{1}{3} \left[ \left( \frac{k+1}{k-1} \right)^2 - 1 \right] \left( \frac{1}{M_i^3} - \frac{1}{M^3} \right) + \dots \quad (19.30)$$

The pressure ratio for the expansion may be taken approximately as

$$\frac{p}{p_i} = \frac{p/p_0}{p_i/p_0} = \frac{\left( 1 + \frac{k-1}{2} M_i^2 \right)^{\frac{k}{k-1}}}{\left( 1 + \frac{k-1}{2} M^2 \right)} \cong \left( \frac{M_i}{M} \right)^{\frac{2k}{k-1}} \quad (19.31)$$

Substituting  $M$  as found from Eq. 19.31 into Eq. 19.30, we find

$$\begin{aligned}M_i \theta_e = & \frac{2}{k-1} \left[ 1 - \left( \frac{p}{p_i} \right)^{\frac{k-1}{2k}} \right] \\ & - \frac{1}{3M_i^2} \left[ \left( \frac{k+1}{k-1} \right)^2 - 1 \right] \left[ 1 - \left( \frac{p}{p_i} \right)^{\frac{3(k-1)}{2k}} \right] + \dots \quad (19.32)\end{aligned}$$

Since  $M_i$  is very large compared with unity, we shall retain only the first term on the right-hand side. Then, since the appropriate hypersonic similarity parameter for the expansion is

$$K_e \equiv M_i \theta_e \quad (19.33)$$

we get

$$\frac{p}{p_i} = \left( 1 - \frac{k-1}{2} K_e \right)^{\frac{2k}{k-1}} \quad (19.34a)$$

and

$$\begin{aligned}C_{p_e} = & \frac{2}{kM_i^2} \left( \frac{p}{p_i} - 1 \right) = \frac{2}{kM_i^2} \left[ \left( 1 - \frac{k-1}{2} K_e \right)^{\frac{2k}{k-1}} - 1 \right] \\ = & \frac{2}{kK_e^2} \left[ \left( 1 - \frac{k-1}{2} K_e \right)^{\frac{2k}{k-1}} - 1 \right] \theta_e^2 \quad (19.34b)\end{aligned}$$

Note that when  $K_e$  becomes equal to  $2/(k-1)$ , the local pressure goes to zero, thus indicating that the local Mach Number has become infinite. If the surface of the profile curves still further so that  $K_e$  exceeds this limiting value, the flow can deflect no further, and there exists a cavitated region near the profile. Accordingly, Eq. 19.34 is valid if  $K_e \leq 2/(k-1)$ , but for larger values of  $K_e$  it must be assumed that  $p = 0$ , at least within the postulate of a continuum.

### 19.5. Hypersonic Performance of Two-Dimensional Profiles

The force and moment coefficients for a thin profile are found by first determining the pressure coefficient at each point on the surface and then integrating over the entire profile according to Eqs. 19.11 to 19.13.

To illustrate the procedure, we shall suppose that the angle of incidence of a given profile is such that there is no leading-edge shock for the upper surface. In that case there must necessarily be a leading-edge shock for the lower surface. The free-stream conditions are denoted by  $M_\infty$  and  $p_\infty$ .

**Pressure Coefficient on Upper Surface with No Leading-Edge Shock.** For the upper surface the relations of Art. 19.4 may be applied directly, provided that  $M_i = M_\infty$ ,  $p_i = p_\infty$ , and that  $\theta_e$  is interpreted as the angle between the free-stream direction and the local tangent to the surface. Then, using Eq. 19.34 and the definition of the pressure coefficient, we obtain, for the upper surface,

$$C_p = \frac{2}{kM_\infty^2} \left( \frac{p}{p_\infty} - 1 \right) = \frac{2}{kM_\infty^2} \left[ \left( 1 - \frac{k-1}{2} K_e \right)^{\frac{2k}{k-1}} - 1 \right]$$

If the similarity parameter for the entire profile is  $K = M_\infty \delta$ , where  $\delta$  is the thickness ratio and it is understood that for affinely related profiles the angle of attack and camber are proportional to  $\delta$ , the foregoing expression may be written as

$$\frac{C_p}{\delta^2} = \frac{2}{kK^2} \left[ \left( 1 - \frac{k-1}{2} K_e \right)^{\frac{2k}{k-1}} - 1 \right] \quad (19.35)$$

**Pressure Coefficient on Lower Surface with Leading-Edge Shock.** To determine  $C_p$  for the lower surface, we first find conditions just behind the leading-edge shock by using the relations of Art. 19.3 with  $M_1 = M_\infty$ ,  $p_1 = p_\infty$ ,  $M_2 = M_i$ ,  $p_2 = p_i$ , and with  $\theta_s$  taken as the angle between the free-stream direction and the tangent to the surface at the leading edge. From these relations it is possible to find  $p_i$  and  $M_i$  as the starting conditions for the simple-wave expansion on the lower surface.

The next step is to employ the relations of Art. 19.4 for the simple-wave flow, using the values of  $p_i$  and  $M_i$  downstream of the shock, and taking  $\theta_e$  as the angle between the tangent to the surface at the leading edge and the local tangent to the surface.

For the local pressure coefficient, we form

$$C_p = \frac{2}{kM_\infty^2} \left( \frac{p}{p_\infty} - 1 \right) = \frac{2}{kM_\infty^2} \left( \frac{p_i p_2}{p_i p_1} - 1 \right)$$

We then substitute for  $p/p_i$  according to Eq. 19.34, for  $p_2/p_1$  according to Eqs. 19.20a and 19.23, and introduce  $K \equiv M_\infty \delta$ . Thus we obtain

$$\frac{C_p}{\delta^2} = \left( \frac{K_s^2}{K^2} \sigma_s + \frac{2}{kK^2} \right) \left( 1 - \frac{k-1}{2} K_e \right)^{\frac{2k}{k-1}} - \frac{2}{kK^2} \quad (19.36)$$

Detailed considerations for a family of affinely related profiles having a particular ratio of angle of incidence to thickness ratio show that  $K_s$  and  $K_e$  are uniquely related to  $K$ . The right-hand sides of Eqs. 19.35 and 19.36 may therefore be evaluated in terms of  $K$ ,  $k$ , and  $a/\delta$ . Integrations of the type of Eqs. 19.11, 19.12, and 19.13 may then be carried out in terms of the dimensionless parameters  $\xi$  and  $\eta$ . For given values of  $K$  and of  $a/\delta$  the calculations lead to numerical values of  $C_L/\delta^2$ ,  $C_D/\delta^3$ , and  $C_m/\delta^2$ . Full details of the calculation procedure are given in convenient form in Reference 4. We shall now examine some typical results of the calculations.

**Flat Plate Airfoil.** If  $a$  is the angle of attack, then  $K \equiv M_\infty a$ . Then, for the upper surface, Eq. 19.35 is applicable, with  $\delta = a$ , and  $K_e = K$ . For the lower surface, Eq. 19.36 is applicable, with  $\delta = a$  and  $K_s = K$ . By making these substitutions we obtain

$$\begin{aligned} \frac{C_L}{a^2} &= \frac{C_D}{a^3} = \frac{k+1}{2} + \sqrt{\left( \frac{k+1}{2} \right)^2 + \frac{4}{K^2}} \\ &\quad + \frac{2}{kK^2} \left[ 1 - \left( 1 - \frac{k-1}{2} K \right)^{\frac{2k}{k-1}} \right] \quad (19.37) \end{aligned}$$

except that when  $K \geq 2/(k-1)$  the last term becomes simply  $2/k K^2$ .

Fig. 19.2 shows in solid lines  $C_L$  and  $C_D/a$  versus angle of incidence

for  $M_\infty$  from 3 to  $\infty$ , as computed from this formula. For finite values of  $M_\infty$ , the lift curve starts as a straight line, but rapidly becomes parabolic. As  $M_\infty$  becomes very large, however, it is seen that  $C_L \rightarrow$

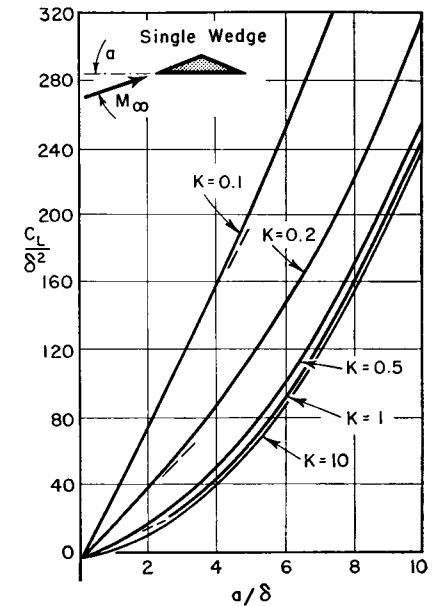
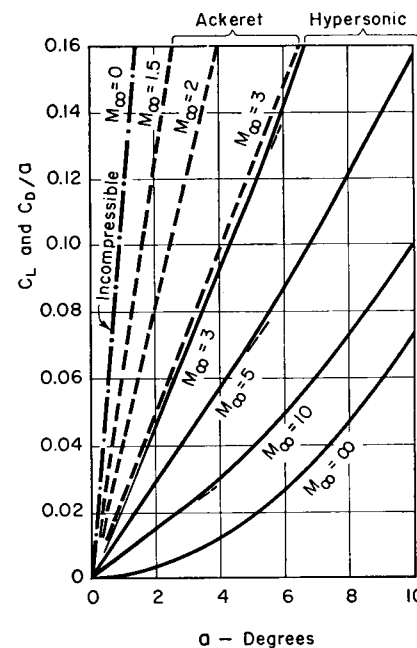


FIG. 19.2. Lift and drag of flat plate. Solid curves indicate hypersonic theory; dashed curves indicate linear theory of supersonic flow (after Linnell).

FIG. 19.3. Lift of single-wedge profile (after Linnell).

$(k+1)a^2$ , indicating an exactly parabolic relation. The point of transition from a linear relation approaches the origin as  $M_\infty$  approaches infinity.

The dashed curves of Fig. 19.2 show the results of the Ackeret linear theory [ $C_L = C_D/a = 4/\sqrt{M_\infty^2 - 1}$ ]. At  $M_\infty = 3$ , the Ackeret theory begins to underestimate the forces by an appreciable amount, and for larger  $M_\infty$  the Ackeret theory is increasingly inaccurate.

The uppermost curve shows for comparison the lift coefficient in incompressible flow [ $C_L = 2\pi a$ ].

**Profiles with Thickness.** Fig. 19.3 shows in generalized form the lift curve of a single-wedge profile with a flat bottom. The curves on this chart are similar to those of Fig. 19.2, since, for a particular value of  $\delta$ , they may be regarded as plots of  $C_L$  versus  $a$  for constant  $M_\infty$ . These generalized curves may also be used for finding the effects of  $\delta$  and of  $M_\infty$  on the lift coefficient.

Fig. 19.4 is a comparison between the lift-drag polars of (i) the double-wedge profile, (ii) the single-wedge profile, and (iii) the single circular-arc profile. For large values of  $K$ , i.e., for hypersonic flow, the single-wedge shows the best performance, and the double-wedge the worst. This may be explained as follows. In hypersonic flow the algebraic pressure rise across a shock of given turning angle is very much greater than across an expansion wave of equal turning angle. The aerodynamic forces are, therefore, influenced mostly by the pressures on those surfaces upstream of which the flow has passed through a shock. It is always desirable, therefore, to operate with angles of attack sufficiently large to avoid a leading-edge shock on the upper

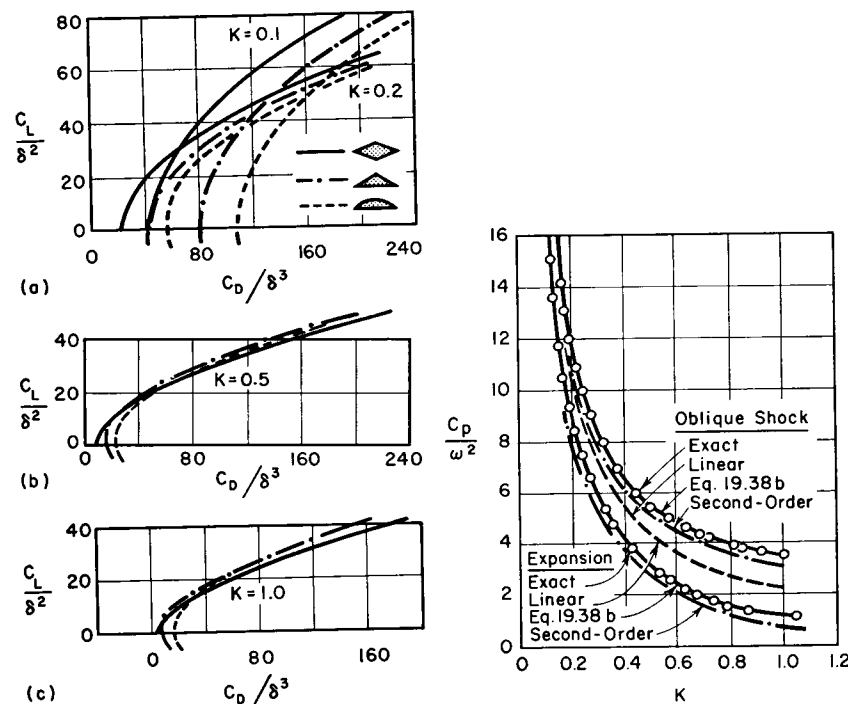


FIG. 19.4. Lift-drag polars of double-wedge, single-wedge, and single-convex profile (after Linnell).

FIG. 19.5. Pressure coefficient for oblique shocks and for Prandtl-Meyer waves. "Second-order" refers to first two terms in Eq. 19.38b; "first-order" refers to first term in Eq. 19.38b (after Dorrance).

surface of the profile, for otherwise there is a loss of lift owing to the positive  $C_p$  on the upper surface. Assuming that this condition is met, the contribution of the upper surface to the lift is increasingly negligible as  $M_\infty$  increases. Since most of the lift is, therefore, furnished by the lower surface, it follows that expansions on the lower surface reduce

the lift and are undesirable. Consequently, the best profiles in hypersonic flow have flat lower surfaces.

**Approximate Method of Calculation by Expanding the Pressure Coefficient as a Power Series in the Similarity Parameter.** The calculation procedure outlined previously loses in simplicity because the regions of compression and of expansion must be treated separately, and thus it is not possible to obtain closed formulas for the profile force coefficients. By introducing a small approximation, this difficulty is removed, as explained below.<sup>(12)</sup>

Let  $\omega$  be the angle of turn through a wave, taken as positive for compressions and negative for expansions. Then

$$\theta_s = \omega; \quad K_s = M_s \omega$$

$$\theta_e = -\omega; \quad K_e = -M_e \omega$$

Using this nomenclature, Eq. 19.24 is expanded as a power series in  $K_s$ , thus yielding

$$\frac{C_{ps}}{\omega^2} = \frac{2}{K_s} + \frac{k+1}{2} + \frac{(k+1)^2}{16} K_s + [\text{Order}] K_s^3 + \dots \quad (19.38a)$$

Similarly, Eq. 19.34b is expanded as a power series in  $K_e$ , thus yielding

$$\frac{C_{pe}}{\omega^2} = \frac{2}{K_e} + \frac{k+1}{2} + \frac{k+1}{6} K_e + [\text{Order}] K_e^2 + \dots \quad (19.38b)$$

It is evident that these equations are identical up through the second term. Furthermore, the third terms differ by only 10 per cent for  $K < 1.66$ . The approximation adopted here is to assume that Eq. 19.38b applies to compressions as well as to expansions. The accuracy of the method is shown in Fig. 19.5 to be excellent.

With this approximation, analytical formulas for two-dimensional profiles may be worked out in a manner exactly like that of the linear Ackeret theory (Chapter 14). Dorrance<sup>(12)</sup> gives these in simple tabular form for virtually every profile shape. For example, the properties of the symmetrical double-wedge in hypersonic flow are given by

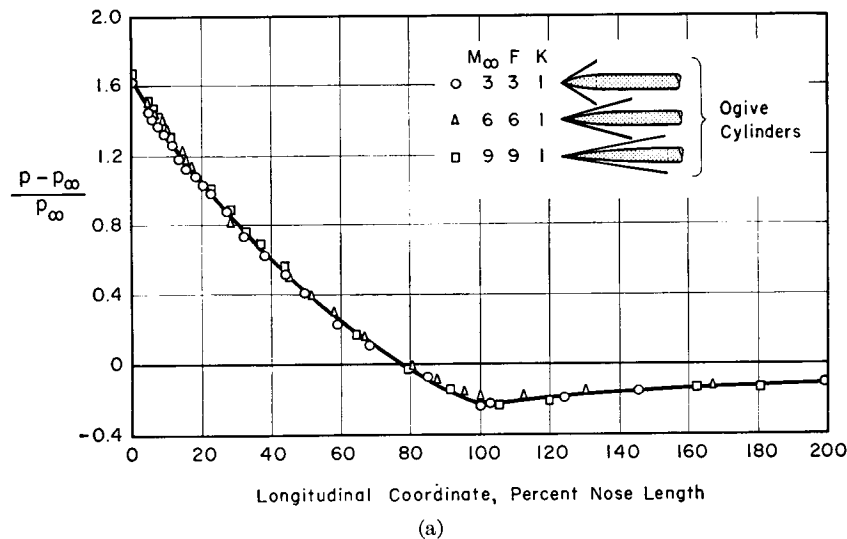
$$\frac{C_L}{\delta^2} = 2 \frac{a}{\delta} \left[ \frac{2}{M_\infty \delta} + \frac{k+1}{6} M_\infty \delta \left( 3 + \frac{a^2}{\delta^2} \right) \right]$$

$$\frac{C_D}{\delta^3} = \frac{4}{M_\infty \delta} \left( 1 + \frac{a^2}{\delta^2} \right) + \frac{k+1}{3} M_\infty \delta \left[ \left( \frac{a}{\delta} \right)^4 + 6 \left( \frac{a}{\delta} \right)^2 + 1 \right]$$

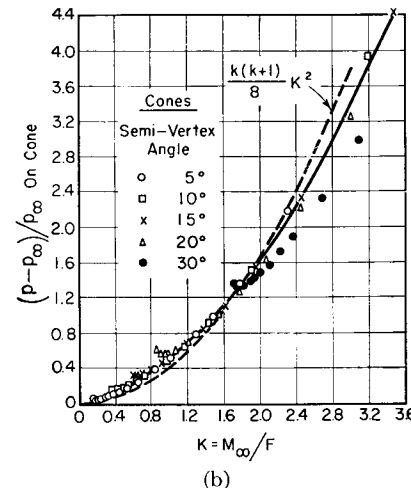
## 19.6. Hypersonic Performance of Bodies of Revolution

A careful appraisal of the hypersonic similarity law has been carried out in References 5 and 8, based on comparisons with exact solutions

for the pressure distributions on cylindrical bodies having either a conical nose or an ogival nose. The fineness ratio  $F$  of such bodies is for the present purpose defined as the ratio of the length of the nose section to the maximum diameter of the nose section. The appropriate hypersonic similarity parameter is  $K \equiv M_\infty/F$ . The exact solutions, all of which are for zero angle of attack, were found by the method of characteristics together with the Taylor-Maccoll solution for a cone.



(a)



(b)

FIG. 19.6. Pressure distribution plotted according to hypersonic similarity law (after Ehret *et al.*).

- (a) Three ogive-cylinders with  $K = 1$ .
- (b) Five cones with different vertex angles.

**Correlation of Pressure Distributions.** Fig. 19.6a shows the pressure distributions on three ogive cylinders of different fineness ratios but at such Mach Numbers that  $K = 1$  for all three. The agreement in the three pressure distributions is striking, thus illustrating the utility and accuracy of the similarity concept.

**Correlation of Vertex Pressure Coefficient.** Fig. 19.6b indicates that the pressure coefficients for cones are well correlated by the  $K$  parameter over a wide range of fineness ratios and Mach Numbers. An approximate formula for the cone may be found as follows. If  $M_\infty$  is very large, and if we assume the turning angle across the conical shock to be equal to the semi-vertex angle of the cone,  $\theta$ , Eq. 19.26 yields

$$C_p = \frac{2}{kM_\infty^2} \left( \frac{p}{p_\infty} - 1 \right) = (k+1)\theta^2 \quad (19.39a)$$

Furthermore, for small vertex angles,

$$F \cong 1/2\theta$$

It follows, therefore, that

$$\frac{p - p_\infty}{p_\infty} \cong \frac{k(k+1)}{8} K^2 \quad (19.39b)$$

This formula is represented by a dashed line in Fig. 19.6b.

**Range of Applicability of Similarity Law.** Using curves like those of Fig. 19.6 as a guide, Ehret *et al.*<sup>(5)</sup> and Rossow<sup>(8)</sup> have constructed

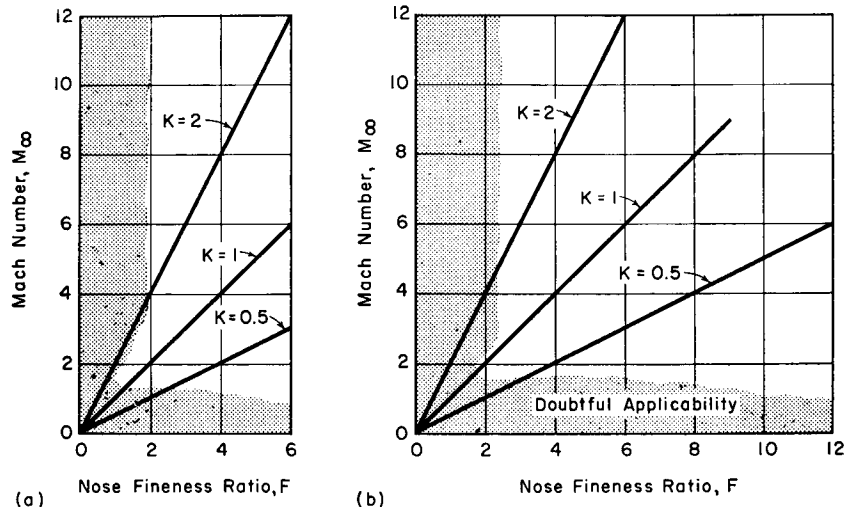


FIG. 19.7. Range of applicability of similarity law (after Ehret *et al.*).

- (a) Cone-cylinders.
- (b) Ogive-cylinders.

Fig. 19.7, in which is shown the range of variables for which the hypersonic similarity law is valid in the sense that it will predict the pressure coefficient on the body with an error not exceeding 5 per cent. The range of applicability is astonishingly large, considering the nature of the assumptions underlying the similarity law.

**Generalized Pressure Distribution on Ogive-Cylinder Bodies.** Fig. 19.8, based on crossplots of a number of exact solutions of the flow for representative values of  $K$ , may be used for determining the pressure distribution over any ogive cylinder falling within the range of the hypersonic similarity law. Fig. 19.8a refers to the ogival nose section, and Fig. 19.8b to the cylindrical section. This generalized chart is in excellent agreement with individual cases worked out by the method of characteristics.

Similar generalized curves are presented in Reference 8 for cone-cylinder bodies.

When applied to the German V-2 missile, the theoretical generalization of Fig. 19.8 leads to excellent agreement with wind tunnel measurements, as shown by Fig. 19.9.

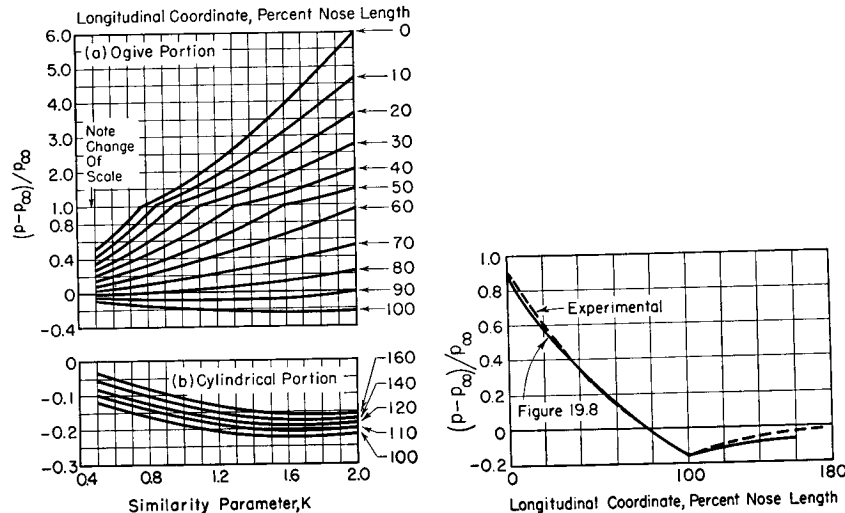


FIG. 19.8. Generalized charts for pressure distribution on cylinders with ogival nose, taking account of vorticity behind curved shock (after Rossow).

**Effects of Nose-Fineness Ratio and Mach Number on Pressure Distribution.** The curves of Fig. 19.8, which seem to be quite reliable, are replotted in Fig. 19.10 to show the effects of fineness ratio and Mach

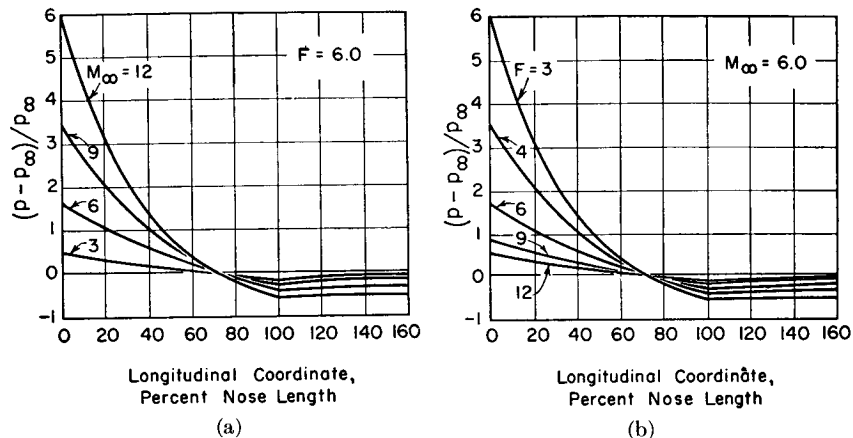


FIG. 19.10. Pressure distribution on ogive-cylinders (after Ehret *et al.*).

- (a) Nose-fineness ratio = 6.0, showing effect of Mach Number.  
(b)  $M_{\infty} = 6.0$ , showing effect of nose-fineness ratio.

Number on the pressure distribution of ogive-cylinders. From this figure it is concluded that: (i) As either the Mach Number or bluntness is increased, the pressure coefficient at the vertex is increased. (ii) The pressure coefficient goes to zero at approximately 75 per cent of nose length for all values of  $F$  and  $M_{\infty}$ . (iii) The negative pressure coefficient on the cylinder increases in magnitude with increasing Mach Number or bluntness. (iv) With increasing Mach Number or bluntness the rate of pressure recovery along the cylinder decreases. The last-named item is important for the design of static-pressure probes.

The pressure distributions on ogives were found<sup>(5)</sup> to give straight lines when plotted as  $\log p$  versus per cent of nose length, provided that  $K$  exceeds 0.5. Thus, for an ogival nose, an empirical law for the surface pressure is

$$\frac{p}{p_{\infty}} = \left( \frac{p}{p_{\infty}} \right)_{\text{vertex}} 10^{m(x/l)} \quad (19.40a)$$

where  $x$  is distance aft of the vertex,  $l$  is the length of the nose,  $(p/p_{\infty})_{\text{vertex}}$  is the pressure ratio at the vertex as given by tables of the exact solution for a cone tangent to the vertex, and  $m$  has the following values, dependent only on  $K$ :

$K$	0.5	0.7	1.0	1.5	2.0
$m$	-0.25	-0.36	-0.55	-0.86	-1.17

A simpler but more approximate expression is

$$\log_{10} \frac{p}{p_{\infty}} = m \left( \frac{x}{l} - 0.75 \right) \quad (19.40b)$$

**Nose Drag Coefficients.** The drag coefficients of cone-cylinders and ogive cylinders, based on the maximum frontal area, and as found by integration of the exact pressure distribution, are plotted in Fig. 19.11 according to the similarity form suggested by Eq. 19.15. It was found that within the unshaded zones of Fig. 19.7 the hypersonic similarity law permits the drag coefficient for each type of body to be correlated by a single curve. The curve for cones is of course identical with the curve of Fig. 19.6b.

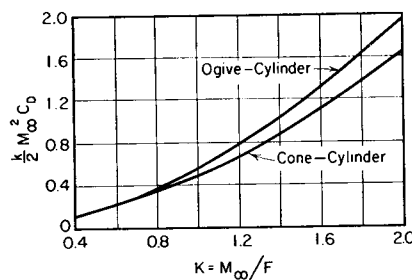


FIG. 19.11. Nose drag coefficients for cone-cylinders and ogive-cylinders (after Rossow).

**Approximate Pressure Distribution for Bodies of Revolution.** <sup>(13)</sup> An approximate but extremely simple method of estimating the pressure distribution on pointed bodies has been advanced by Eggers and by Zienkiewicz. This "cone-expansion" method consists in applying the two-dimensional Prandtl-Meyer relations behind the tip of a pointed body. Thus, for a body of revolution, the surface pressure and Mach Number at the tip are taken from the solution for a cone, and the subsequent surface pressure distribution is calculated according to a two-dimensional simple-wave expansion. This approximation yields surprising accuracy at high Mach Numbers. At lower Mach Numbers, Zienkiewicz has obtained good accuracy by introducing certain empirical factors (see Chapter 17, page 696).

## 19.7. Experimental Results

**Wings.** The experimental lift and drag characteristics at  $M_\infty = 6.9$  of a delta wing and of a rectangular wing with  $\mathcal{R} = 1$ , both having double-wedge profiles, are shown in Fig. 19.12. <sup>(9)</sup>

All the theoretical curves of this figure are based on two-dimensional flow, an assumption which is justified because the region of three-dimensional flow is so small at  $M_\infty = 6.9$ . In the case of the delta wing the two-dimensional flow is appropriately corrected (as described in Chapter 18) for the sweptback leading edges.

Fig. 19.12a shows clearly the nonlinear nature of the lift-curve slope although the linear theory is surprisingly adequate up to angles of attack of 5°.

Only the pressure drag is included in Fig. 19.12b. The agreement with theory is, consequently, good at large angles of attack but poor at low angles. If a skin-friction drag coefficient of 0.0028 (corresponding

to laminar flow at the test Reynolds Number) is added to the theoretical pressure drag, the total is in good agreement with the measurements at both low and high angles of attack.

A similar result is shown in Fig. 19.12c. The experimental lift-drag ratio based on the measured pressure distribution is in good accord with the inviscid theory. The experimental force measurements agree with the theory, however, only when the skin-friction coefficient is added to the latter.

**Shock Angles on Cones.** Fig. 19.13 <sup>(10)</sup> illustrates strikingly the rule of thumb that at hypersonic speeds the flow affected by a body lies within a hypersonic boundary layer.

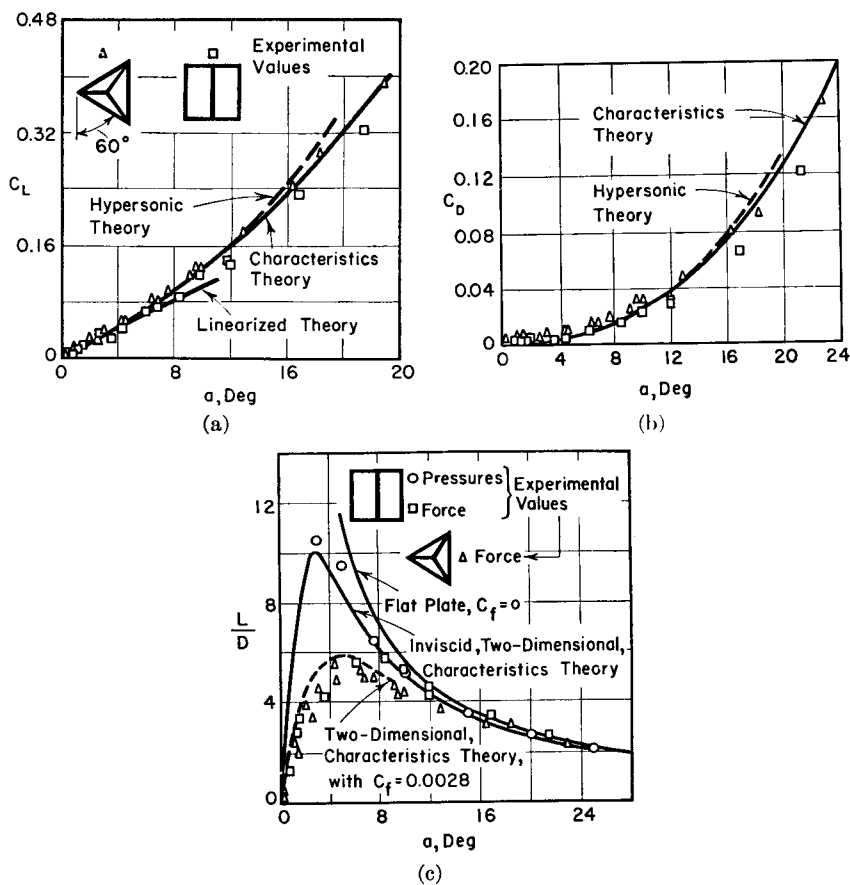


FIG. 19.12. Experimental lift and drag of wings with double-wedge profiles and with delta and square planforms ( $M_\infty = 6.9$ ) (after McLellan).

- (a) Lift coefficient.
- (b) Drag coefficient.
- (c) Lift-drag ratio.

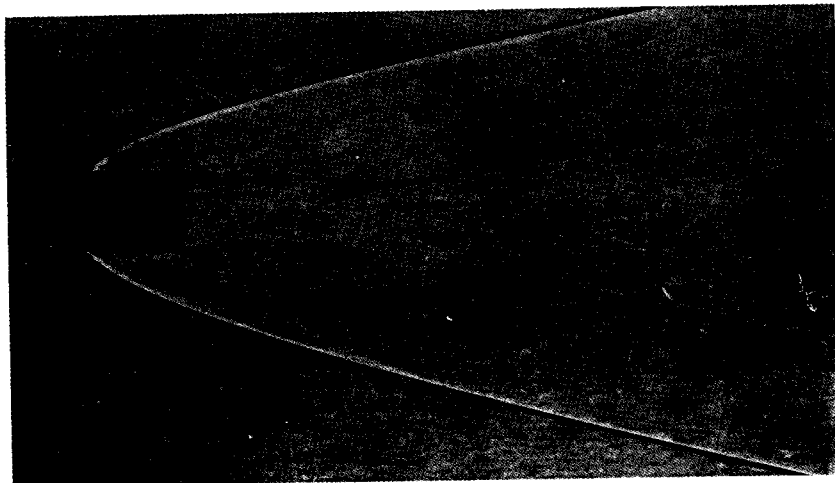


FIG. 19.13. Shadowgraph of flow past  $60^\circ$  cone (included angle) at  $M_\infty = 6.7$ . Note that nose shock is straight up to the point where it is intersected by the first Mach wave from the shoulder (after Soule and Sabol).

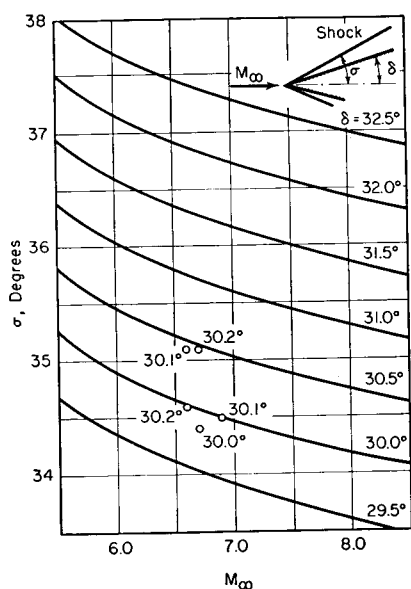


FIG. 19.14. Experimental and theoretical shock wave angles for cones. Curves indicate theoretical solutions. Points indicate shock angle measured from shadowgraphs; the number next to each point shows the semi-angle of the cone (after Soule and Sabol).

Measurements of shock angles from shadowgraphs like Fig. 19.13 yield values which differ from the theoretical values by only a small fraction of one degree, as shown by Fig. 19.14. <sup>(10)</sup>

**Pressure Distribution on Cone-Cylinder.** Fig. 19.15 <sup>(9)</sup> shows generally good agreement between the theoretical and measured pressure distributions on a cone-cylinder of  $20^\circ$  included angle at  $M_\infty = 6.9$ .

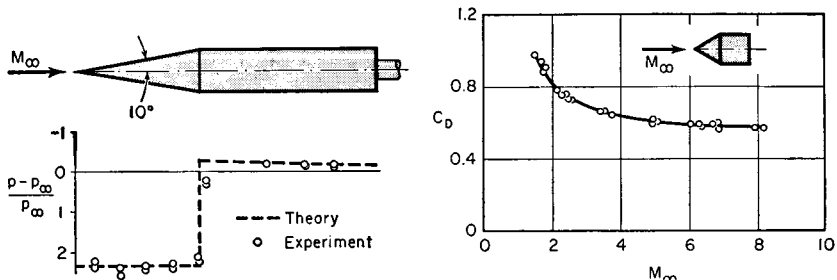


FIG. 19.15. Experimental and theoretical pressure distributions on cone-cylinder at  $M_\infty = 6.9$  (after McLellan).

FIG. 19.16. Drag coefficient of cone-cylinder (based on frontal area) versus Mach Number (after Stevens).

**Drag of Cone-Cylinder.** The drag curve of a cone-cylinder is seen from Fig. 19.16 to level off at hypersonic speeds. <sup>(11)</sup> The value at very high Mach Numbers is about half the value of unity predicted by the Newtonian corpuscular theory.

**Sphere at Hypersonic Speeds.** Fig. 19.17 is a schlieren picture of the flow past a sphere at a Mach Number of 12.1. Despite the bluntness of the sphere, the bow shock is nearly attached. Also of interest is the

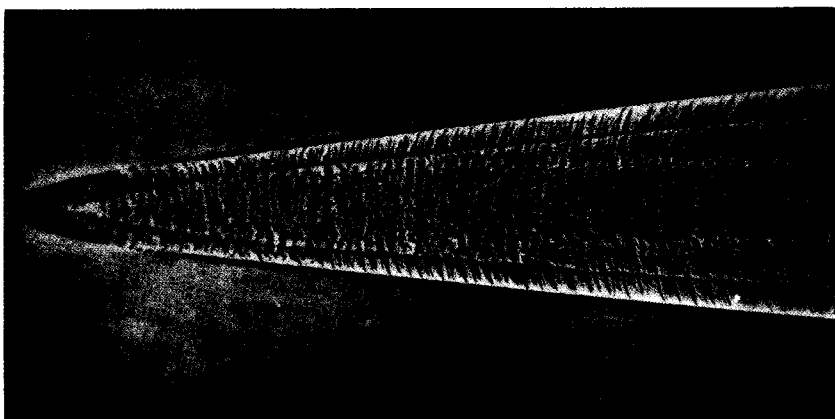


FIG. 19.17. Schlieren photograph of flow past sphere at  $M_\infty = 12.1$  (New Mexico School of Mines).

highly turbulent wake. Between the wake and the bow shock wave is a zone containing curious but unexplained striations.

#### REFERENCES AND SELECTED BIBLIOGRAPHY

1. TSIEN, H. S. Similarity Laws of Hypersonic Flows, *Jour. Math. and Phys.*, Vol. 25, No. 3 (1946), p. 247.
2. HAYES, W. D. On Hypersonic Similitude, *Quarterly App. Math.*, Vol. 5, No 1. (1947), p. 105.
3. FALKOVICH, S. V. Two-Dimensional Motion of a Gas at Large Supersonic Velocities, *NACA Tech. Memo.*, No. 1239 (1949).
4. LINNELL, R. D. Two-Dimensional Airfoils in Hypersonic Flows, *Jour. Aero. Sci.*, Vol. 16, No. 1 (1949), p. 22.
5. EHRET, D. M., ROSSOW, V. J., and STEVENS, V. I. An Analysis of the Applicability of the Hypersonic Similarity Law to the Study of Flow About Bodies of Revolution at Zero Angle of Attack, *NACA Tech. Note*, No. 2250 (1950).
6. NEICE, S. E., and EHRET, D. M. Similarity Laws for Slender Bodies of Revolution in Hypersonic Flows, *Jour. Aero. Sci.*, Vol. 18, No. 8 (1951), p. 527.
7. HAMAKER, F. M., NEICE, S. E., and EGGERS, A. J., JR. The Similarity Law for Hypersonic Flow About Slender Three-Dimensional Shapes, *NACA Tech. Note*, No. 2443 (1951).
8. ROSSOW, V. J. Applicability of the Hypersonic Similarity Rule to Pressure Distributions Which Include the Effects of Rotation for Bodies of Revolution at Zero Angle of Attack, *NACA Tech. Note*, No. 2399 (1951).
9. MCLELLAN, C. M. Exploratory Investigation of Wings and Bodies at  $M = 6.9$ , *Jour. Aero. Sci.*, Vol. 18, No. 10 (1951), p. 641.
10. SOULE, H. V., and SABOL, A. P. Development and Preliminary Investigation of a Method of Obtaining Hypersonic Aerodynamic Data by Firing Models Through Highly Cooled Gases, *NACA Tech. Note*, No. 2120 (1950).
11. STEVENS, V. I. Hypersonic Research Facilities at the Ames Aeronautical Laboratory, *Jour. App. Phys.*, Vol. 21 (1950), p. 1150.
12. DORRANCE, W. H. Two-Dimensional Airfoils at Moderate Hypersonic Velocities, *Jour. Aero. Sci.*, Vol. 19, No. 9 (1952), p. 593.
13. VAN DYKE, M. D. Applications of Hypersonic Small-Disturbance Theory, *Jour. Aero. Sci.*, Vol. 21, No. 3 (1954), p. 179.
14. FRAENKEL, L. E. Curves for Estimating the Wave Drag of Some Bodies of Revolution, Based on Exact and Approximate Theories, *British A.R.C.*, Tech. Rep. C.P. No. 136 (1953).
15. EGGERS, A. J., JR., SYVERTSON, C. A., and KRAUS, S. A Study of Inviscid Flow About Airfoils at High Supersonic Speeds, *NACA Report*, No. 1123 (1953).

#### PART VI

#### MIXED FLOW

## Chapter 20

### THE HODOGRAPH METHOD FOR MIXED SUBSONIC-SUPERSONIC FLOW

#### 20.1. Introductory Remarks

Because of the profound differences between subsonic and supersonic flows, both mathematical and physical, some early investigators doubted whether steady mixed flows (i.e., flows containing both subsonic and supersonic regions) could exist stably. It is now known that these doubts were ill-founded, since we have many illustrations, both experimental and analytical, of mixed steady flows.

In practice it seems relatively easy to obtain a smooth and continuous transition from subsonic to supersonic speeds, the simplest example being the converging-diverging nozzle. The reverse process, that is, a smooth and continuous transition from supersonic to subsonic speeds, has proved extremely difficult to realize. Indeed, deceleration through the speed of sound is, with a few exceptions, invariably accompanied by shock waves with their attendant losses and boundary-layer disturbances.

In this chapter we shall investigate by the *hodograph method* certain mixed flow patterns which are interesting as illustrations of the general features of mixed flows. In addition, some of the questions concerning the possible existence of shockless transition from supersonic to subsonic speeds will be discussed, in particular as they relate to the so-called *limit line*.

The hodograph method is particularly well adapted to the study of mixed flows. Because of the linearity of the hodograph equations a few elementary solutions may be superposed to yield more complex solutions.

Many of the practical problems of high-speed flight are related to mixed flows. Flight in the important range of Mach Numbers between 0.75 and 1.3 is certain to involve regions of both supersonic and subsonic flow. Similar problems exist in the design of **compressors** and turbines and indeed often represent the chief limitations on performance. In these several cases the reduction of the large drag which usually occurs at transonic speeds represents one of the fruitful avenues of research.

The analyses of this chapter are based on the assumptions of two-

dimensional, steady, irrotational, isentropic motion of a perfect gas. No assumptions as to small perturbations are made, however, and the results are exact within the foregoing premises. This is in distinction to the manner in which the hodograph method was applied in Chapter 11, where the use of the "tangent-gas" approximation led to the Kármán-Tsien method for subsonic flow.

Additional material relevant to the subject matter of this chapter may be found in Chapter 21.

### NOMENCLATURE

$a$	fluid acceleration	$u, v$	Cartesian velocity components
$c$	speed of sound	$V$	velocity
$J$	function of $\gamma$ (see p. 778)	$w$	mass rate of flow
$k$	ratio of specific heats	$x, y$	Cartesian coordinates
$K_1, K_2, \text{etc.}$	constants of integration		
$l$	characteristic length dimension	$\alpha$	Mach angle
$L$	function of $\gamma$ (see Eq. 20.18)	$\gamma$	$(\rho/\rho_0)^{1/5}$
$M$	Mach Number	$\Gamma$	circulation
$M^*$	$V/c^*$	$\theta$	flow direction
$n$	a constant	$\rho$	mass density
$P$	a function of $V$	$\varphi$	velocity potential
$Q$	volume flow at density $\rho_0$ ; also a function of $\theta$	$\psi$	stream function
$r$	$\sqrt{x^2 + y^2}$	$(\ )_0$	signifies stagnation condition
$R$	radius of curvature of streamline; also see Eq. 20.10	$(\ )^*$	signifies condition where $M = 1$
$s$	distance along streamline	$(\ )_\psi$	signifies "along a streamline"
$t$	time		

### 20.2. Equations of the Hodograph Method

The point of view of the hodograph method was given in Chapter 11, together with the derivation of the hodograph equations.

**Differential Equation.** It may be recalled that  $V$  and  $\theta$ , the polar velocity coordinates, are taken as independent variables, and either the stream function  $\psi$  or the potential function  $\varphi$  as dependent variable. The resulting differential equation in terms of  $\psi$  is

$$V^2\psi_{vv} + V\left(1 + \frac{V^2}{c^2}\right)\psi_v + \left(1 - \frac{V^2}{c^2}\right)\psi_{\theta\theta} = 0 \quad (20.1a)$$

where

### Art. 20.2 EQUATIONS OF THE HODOGRAPH METHOD

$$c^2 = c_0^2 - \frac{k-1}{2} V^2 \quad (20.1b)$$

If  $c^2$  is eliminated from these equations, we get

$$V^2\left(1 - \frac{k-1}{2} \frac{V^2}{c_0^2}\right)\psi_{vv} + V\left(1 - \frac{k-3}{2} \frac{V^2}{c_0^2}\right)\psi_v + \left(1 - \frac{k+1}{2} \frac{V^2}{c_0^2}\right)\psi_{\theta\theta} = 0 \quad (20.1c)$$

**Calculation Procedure.** Mathematically, it is necessary to find functions  $\psi(V, \theta)$  which satisfy Eq. 20.1c. Assuming that some such function has been found, the physical streamlines and pressure distribution may then be computed as described below.

Since  $\psi(V, \theta)$  is assumed known, the derivatives  $\psi_v$  and  $\psi_\theta$  may be calculated. Next, the following relations, derived in Chapter 11, are used for finding  $\varphi_v$  and  $\varphi_\theta$  as functions of  $V$  and  $\theta$  (note that  $\rho_0/\rho$  depends only on  $V/c_0$ ):

$$\varphi_\theta = \frac{\rho_0}{\rho} V\psi_v; \quad \varphi_v = -\frac{\rho_0}{\rho} \frac{1}{V} \left(1 - \frac{V^2}{c^2}\right)\psi_\theta \quad (20.2)$$

The following formulas, also derived in Chapter 11, are then employed for finding  $x_v$ ,  $x_\theta$ ,  $y_v$ , and  $y_\theta$  as functions of  $V$  and  $\theta$ :

$$x_v = \frac{\cos \theta}{V} \varphi_v - \frac{\rho_0 \sin \theta}{\rho} \frac{1}{V} \psi_v \quad (20.3a)$$

$$x_\theta = \frac{\cos \theta}{V} \varphi_\theta - \frac{\rho_0 \sin \theta}{\rho} \frac{1}{V} \psi_\theta \quad (20.3b)$$

$$y_v = \frac{\sin \theta}{V} \varphi_v + \frac{\rho_0 \cos \theta}{\rho} \frac{1}{V} \psi_v \quad (20.3c)$$

$$y_\theta = \frac{\sin \theta}{V} \varphi_\theta + \frac{\rho_0 \cos \theta}{\rho} \frac{1}{V} \psi_\theta \quad (20.3d)$$

Having these four derivatives,  $x$  and  $y$  may by integration be expressed in terms of  $V$  and  $\theta$ . Since  $\psi$  is known originally in terms of  $V$  and  $\theta$ , it follows that the physical streamlines and velocity distribution are also known.

**Superposition of Solutions.** Eq. 20.1c is linear in the dependent variable  $\psi$ . Hence, if  $\psi_1(V, \theta)$  and  $\psi_2(V, \theta)$  are each solutions to the differential equation, it follows that  $A_1\psi_1 + A_2\psi_2$  is also a solution,  $A_1$  and  $A_2$  being arbitrary constants. This makes it possible by linear superposition to construct complex solutions from elementary solutions, the elementary solutions being weighted according to the factors  $A_1$  and  $A_2$ . The linearity extends to the remaining equations of the method,

for it will be noted that Eqs. 20.2 and 20.3 are all linear in the dependent variables. Therefore, if the functions  $x_1(V, \theta)$ ,  $x_2(V, \theta)$ ,  $y_1(V, \theta)$ , and  $y_2(V, \theta)$  correspond to the original solutions  $\psi_1$  and  $\psi_2$ , the functions  $(A_1x_1 + A_2x_2)$  and  $(A_1y_1 + A_2y_2)$  correspond to the combined solution  $A_1\psi_1 + A_2\psi_2$ . Note, however, that the linear superposition is allowable only when  $\psi$ ,  $x$ , and  $y$  are expressed in terms of the hodograph coordinates  $V$  and  $\theta$ .

### 20.3. Source-Vortex Flow

As a simple example of the hodograph method, we shall consider the combination of a line source (or sink) with a potential vortex. This flow is of practical importance in the diffusers of centrifugal compressors, is of potential importance as a possibly efficient form of supersonic diffuser, and approximates the flow in vortex-type dust collectors.

**Source Flow.** Although the relations for the compressible line source or sink are easily found from one-dimensional considerations, the very simplicity of this flow makes it an instructive example of the procedure used in the hodograph method.

**INTEGRATION OF EQUATIONS.** Let us seek a particular solution of Eq. 20.1c in which  $\psi$  depends on  $\theta$  only. Then  $\psi_v = \psi_{vv} = 0$ , and the differential equation reduces to

$$\psi_{\theta\theta} = d^2\psi/d\theta^2 = 0$$

The general solution to this is  $\psi = K_1\theta + K_2$ , where  $K_1$  and  $K_2$  are constants of integration. The streamlines are lines of constant flow direction and must therefore be straight lines passing through the origin.

Differentiation of this solution yields  $\psi_\theta = K_1$ . Then Eq. 20.2 yields

$$\varphi_\theta = 0; \quad \varphi_v = -K_1 \frac{\rho_0}{\rho} \frac{1}{V} \left( 1 - \frac{V^2}{c^2} \right)$$

Substituting these into Eq. 20.3b, and integrating with respect to  $\theta$  at constant  $V$ , we obtain

$$x_\theta = -K_1 \frac{\rho_0}{\rho} \frac{\sin \theta}{V}; \quad x = K_1 \frac{\rho_0}{\rho} \frac{\cos \theta}{V} + f(V)$$

Differentiating the latter expression with respect to  $V$ , and recalling that  $d(\rho_0/\rho)/dV = (\rho_0/\rho)(V/c^2)$ , we get

$$x_v = -K_1 \frac{\rho_0}{\rho} \frac{\cos \theta}{V^2} + K_1 \frac{\rho_0}{\rho} \frac{\cos \theta}{c^2} + f'(V)$$

Comparing this expression with the expression for  $x_v$  which is found when  $\varphi_v$  and  $\psi_v$  are substituted into Eq. 20.3a, we see that  $f'(V) = 0$ . It follows that  $f(V) = K_3$ , and, finally, that

$$x = K_1 \frac{\rho_0}{\rho} \frac{\cos \theta}{V} + K_3$$

Similarly, integration of Eqs. 20.3c and 20.3d yields

$$y = K_1 \frac{\rho_0}{\rho} \frac{\sin \theta}{V} + K_4$$

The constants  $K_2$ ,  $K_3$ , and  $K_4$  merely involve displacements of the entire streamline pattern in the hodograph and physical planes. Since such shifts are unimportant, we set these constants equal to zero.

**STREAMLINE PATTERN.** By dividing the expression for  $x$  by that for  $y$ , it may be seen that lines of constant flow direction  $\theta$  are also lines of constant  $x/y$ . But the latter are radial lines through the origin, and the former were previously shown to be lines of constant  $\psi$ . Therefore the physical streamlines are those of a *two-dimensional source or sink*.

For reasons which are evident from the final solution we let  $K_1$  have the value  $(\rho^*/\rho_0)c^*r^*$ , where  $r^*$  is the radius where the Mach Number is unity. Then, since the radial distance in the physical plane is  $r = \sqrt{x^2 + y^2}$ , the foregoing expressions for  $x$  and  $y$  may be combined to give

$$\frac{r}{r^*} = \left( \frac{\rho^*}{\rho} \right) \left( \frac{c^*}{V} \right)$$

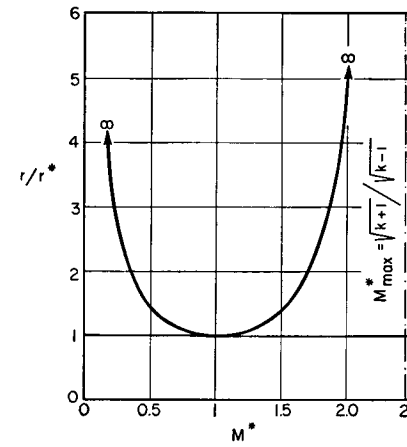
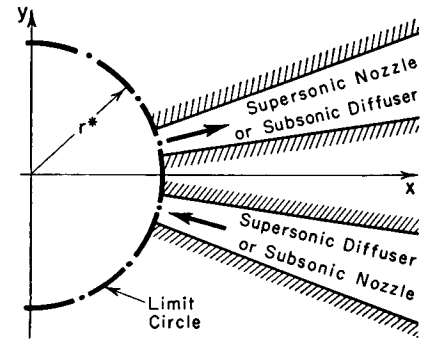


Fig. 20.1. Two-dimensional source or sink.



(a) Radius versus dimensionless speed.  
(b) Physical flow pattern.

This may be recognized as the continuity equation, since  $r/r^*$  represents the isentropic area ratio  $A/A^*$  for a line source or sink.

**LIMIT LINE.** Fig. 20.1a shows  $r/r^*$  as a function of the local Mach Number, and indicates that the source-sink flow cannot exist inside the radius  $r^*$ . In other words, there is a *forbidden region* to the flow. Outside the *limit line* formed by the radius  $r^*$ , the streamlines are radial lines (Fig. 20.1b), and the field of flow may be regarded as two-sheeted, with the two sheets joined on  $r^*$  as a branch line; one sheet has only supersonic flow, and the other only subsonic flow. This is of course the mathematical interpretation of the solution; physically it is absurd, since at a given physical location there can be instantaneously only one value of the velocity vector, pressure, density, etc. Only one sheet of the plane at a time is acceptable for physical reasons. This means that in a source or sink flow the velocity may be either subsonic or supersonic, but not both. In order for the flow to pass from subsonic to supersonic speeds, or vice versa, the passage must therefore be converging-diverging.

**FLUID ACCELERATION.** Another interesting feature of this flow which we shall later investigate in more general form is the particle acceleration along a streamline in the neighborhood of the limit line. The acceleration of a fluid particle in the streamline direction  $r$  is

$$a = V \frac{dV}{dr} = \frac{V}{dr/dV} = \pm \frac{\rho}{\rho^* c^* r} \frac{V^3}{\left(\frac{V^2}{c^2} - 1\right)}$$

from which it is seen that the particle acceleration is infinite at the limit line.

**Vortex Flow.** Let us now seek a particular solution of Eq. 20.1c in which  $\psi$  depends on  $V$  only. Then  $\psi_\theta = \psi_{\theta\theta} = 0$ , and the differential equation becomes

$$V^2 \left(1 - \frac{k-1}{2} \frac{V^2}{c_0^2}\right) \frac{d^2\psi}{dV^2} + V \left(1 - \frac{k-3}{2} \frac{V^2}{c_0^2}\right) \frac{d\psi}{dV} = 0$$

This ordinary differential equation cannot be integrated in closed form except for certain values of  $k$ . Fortunately a closed solution is possible for  $k = 1.4$ . It may be shown to be

$$\psi = K_1 J + K_2$$

where  $J$  is a function of the dimensionless velocity  $V/c_0$ :

$$J \equiv \frac{1}{2} \ln \frac{1-\gamma}{1+\gamma} + \gamma + \frac{1}{3} \gamma^3 + \frac{1}{5} \gamma^5; \gamma \equiv \sqrt{1 - 0.2(V^2/c_0^2)} = \left(\frac{\rho}{\rho_0}\right)^{1/5}$$

From this and Eqs. 20.2 it may be shown that

$$\psi_V = \frac{K_1}{V} \gamma^5; \quad \psi_\theta = 0$$

$$\varphi_V = 0; \quad \varphi_\theta = K_1 \frac{\rho_0}{\rho} \gamma^5$$

Then, substituting these into Eqs. 20.3, we find

$$x_V = -K_1 \frac{\sin \theta}{V^2}; \quad x_\theta = K_1 \frac{\cos \theta}{V}$$

$$y_V = K_1 \frac{\cos \theta}{V^2}; \quad y_\theta = K_1 \frac{\sin \theta}{V}$$

Integrating these, and omitting unessential additive constants, we get  $x$  and  $y$  in terms of  $V$  and  $\theta$ :

$$x = K_1 \frac{\sin \theta}{V}; \quad y = K_1 \frac{\cos \theta}{V}$$

Letting  $K_1 \equiv r^* c^*$ , where  $r^*$  is the radius corresponding to  $M = 1$ , we may rewrite these in the form

$$\frac{x}{r^*} = \frac{\sin \theta}{V/c^*}; \quad \frac{y}{r^*} = \frac{\cos \theta}{V/c^*}; \quad \frac{r}{r^*} = \frac{1}{V/c^*}$$

Previously it was shown that the streamlines of this flow are lines of constant velocity. Now it is seen that the lines of constant velocity are also concentric circles in the physical plane. It follows, therefore,

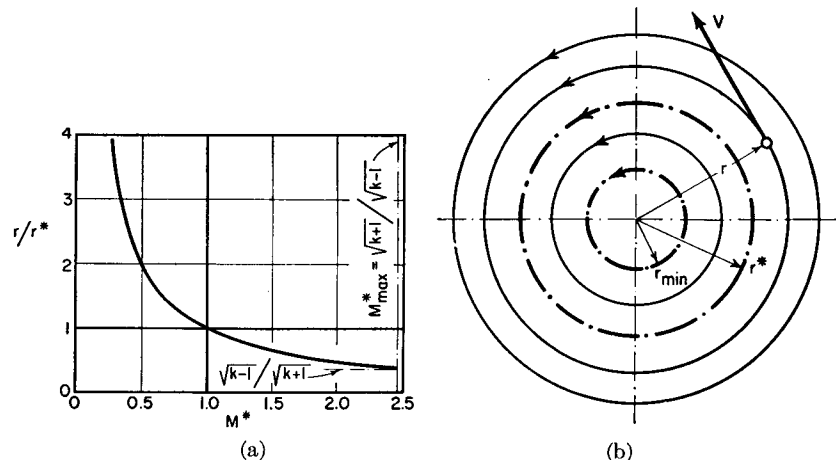


FIG. 20.2. Compressible potential vortex.

(a) Radius versus dimensionless speed.  
(b) Physical flow pattern.

that the physical streamlines are concentric circles. It may also be seen that the velocity variation is that of a *potential vortex*, i.e.,  $V_r$  is constant.

The essential features of the flow pattern are illustrated in Fig. 20.2.

The only peculiarity in this flow is that there is a minimum radius corresponding to the maximum possible velocity:

$$\frac{r_{\min}}{r^*} = \frac{c^*}{V_{\max}} = \sqrt{\frac{k-1}{k+1}} = \frac{1}{\sqrt{6}}$$

Inside of  $r_{\min}$  there is an absolute vacuum, at least within the assumptions of this analysis. It should be remembered, however, that near  $r_{\min}$  the assumption of a continuous fluid breaks down, and so the solution is not valid in this neighborhood.

**Source-Vortex.** We are now ready to examine the source-vortex or sink-vortex. For this it is convenient to express the constants of the elementary flows in a somewhat different form.

**SOURCE FLOW.** For the line source we may write, from continuity,

$$\rho^* c^* r^* = w = \rho_0 Q$$

where  $w$  is the mass rate of flow generated per unit length of source, and  $Q$  is the corresponding volume rate of flow at the density  $\rho_0$ . Then the several results for the source flow may be expressed as follows:

$$\psi = \frac{Q}{2\pi} \theta \quad (20.4)$$

$$x = \frac{Q}{2\pi c_0} \frac{\cos \theta}{(\rho/\rho_0)(V/c_0)}; \quad y = \frac{Q}{2\pi c_0} \frac{\sin \theta}{(\rho/\rho_0)(V/c_0)}; \quad r = \frac{Q}{2\pi c_0} \frac{1}{(\rho/\rho_0)(V/c_0)} \quad (20.5)$$

**VORTEX FLOW.** For the vortex flow we note that  $2\pi r^* c^* = \Gamma$ , where  $\Gamma$  is the circulation for any closed curve enclosing the origin. Then the formulas for the line vortex may be written as

$$\psi = \frac{\Gamma}{2\pi} J \quad (20.6)$$

$$x = \frac{\Gamma}{2\pi c_0} \frac{\sin \theta}{(V/c_0)}; \quad y = -\frac{\Gamma}{2\pi c_0} \frac{\cos \theta}{(V/c_0)}; \quad r = \frac{\Gamma}{2\pi c_0} \frac{1}{(V/c_0)} \quad (20.7)$$

**SUPERPOSITION OF SOURCE AND VORTEX.** The constants  $Q$  and  $\Gamma$  may respectively be regarded as the strengths of the source and vortex. A convenient measure of the strength of the combined flow is  $\sqrt{Q^2 + \Gamma^2}$ , and either the ratio  $Q/\Gamma$  or  $\Gamma/Q$  may be taken to represent the relative

strengths of the source and vortex. We therefore combine the elementary solutions in the following manner:

$$\psi = \frac{Q}{2\pi} \theta + \frac{\Gamma}{2\pi} J$$

which may be rearranged in the form

$$\frac{2\pi\psi}{\sqrt{Q^2 + \Gamma^2}} = \frac{\theta}{\sqrt{1 + (\Gamma/Q)^2}} + \frac{J}{\sqrt{1 + (Q/\Gamma)^2}} \quad (20.8)$$

and

$$x = \frac{Q}{2\pi c_0} \frac{\cos \theta}{(\rho/\rho_0)(V/c_0)} + \frac{\Gamma}{2\pi c_0} \frac{\sin \theta}{(V/c_0)}$$

which may be rearranged in the form

$$\frac{2\pi c_0}{\sqrt{Q^2 + \Gamma^2}} x = \frac{\cos \theta}{\left(\frac{\rho}{\rho_0}\right)\left(\frac{V}{c_0}\right)\sqrt{1 + \left(\frac{\Gamma}{Q}\right)^2}} + \frac{\sin \theta}{\left(\frac{V}{c_0}\right)\sqrt{1 + \left(\frac{Q}{\Gamma}\right)^2}} \quad (20.9a)$$

Similarly, we obtain

$$\frac{2\pi c_0}{\sqrt{Q^2 + \Gamma^2}} y = \frac{\sin \theta}{\left(\frac{\rho}{\rho_0}\right)\left(\frac{V}{c_0}\right)\sqrt{1 + \left(\frac{\Gamma}{Q}\right)^2}} - \frac{\cos \theta}{\left(\frac{V}{c_0}\right)\sqrt{1 + \left(\frac{Q}{\Gamma}\right)^2}} \quad (20.9b)$$

$$R \equiv \frac{2\pi c_0}{\sqrt{Q^2 + \Gamma^2}} r = \frac{1}{(V/c_0)} \sqrt{\left(\frac{\rho}{\rho_0}\right)^2 \left[1 + \left(\frac{\Gamma}{Q}\right)^2\right]} + \frac{1}{1 + \left(\frac{Q}{\Gamma}\right)^2} \quad (20.10)$$

**CONSTRUCTION OF STREAMLINES.** To plot a physical streamline for selected values of  $Q$  and  $\Gamma$ , a value of  $\psi$  is chosen and corresponding pairs of values of  $V/c_0$  and  $\theta$  are solved for from Eq. 20.8. These are then substituted into Eq. 20.9 to determine corresponding values of  $x$  and  $y$  on the streamline.

Fig. 20.3a shows a typical streamline of the compressible vortex-source. The physical plane is mathematically covered twice by the streamline pattern, but of course only one set of streamlines at a time is physically allowable. A limit line, within which there is no flow, is present. At the limit line ( $r_{\min}$ ) the two superimposed streamlines meet in a cusp. The minimum radius  $r_{\min}$  lies inside of the radius  $r^*$  where  $M = 1$ . One set of physical streamlines is purely supersonic, whereas the other set has both subsonic and supersonic portions.

It may be shown that at the limit line the fluid acceleration is infinite and that the component of velocity in the radial direction is equal to the local sound velocity. In consequence of the latter fact, one Mach

line at the cusp is tangent to the limit line, a result which we shall prove more generally in Art. 20.5.

The streamline pattern as a whole is rotationally symmetric, as may be seen from the complete diagram of the physical streamlines (Fig. 20.3b).

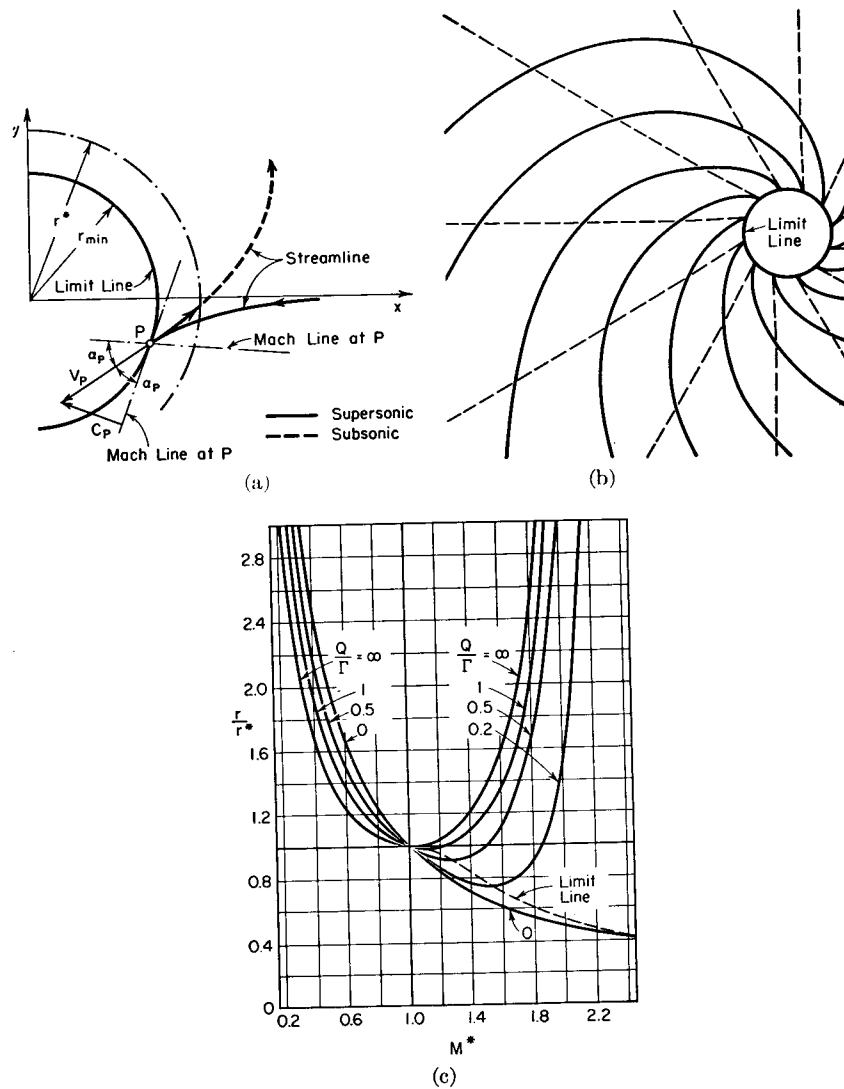


FIG. 20.3. Compressible source-vortex.

- Typical streamline.
- Complete streamline pattern.
- Radius versus dimensionless speed for various strengths of source and vortex.

It is striking that in this flow pattern a deceleration from supersonic speeds to subsonic speeds is possible without shocks. This is of potential significance for supersonic diffusers and centrifugal compressors.

**QUANTITATIVE RESULTS.** The relation between radius and  $M^*$  for various strength ratios  $Q/\Gamma$  is shown in Fig. 20.3c. This shows that  $Q/\Gamma$  must be small compared with unity in order to have smooth deceleration from high supersonic speeds.

Additional features of this flow are summarized in Fig. 20.3d, where, for various values of  $Q/\Gamma$ , there are plotted (i) the critical radius parameter  $R^*$ , (ii) the minimum radius parameter  $R_{\min}$ , (iii)  $R_{\min}/R^*$ , and (iv) the values of  $M^*$  and  $M$  corresponding to the minimum radius.

#### 20.4. Compressible Flow with 180°-Turn

Ringleb <sup>(1)</sup> has explored a simple yet highly instructive example of mixed flow which we shall study in detail.

**Product-Type Solution of Differential Equations.** A standard method for finding solutions to partial differential equations is to seek product-type solutions which reduce the problem to that of solving ordinary

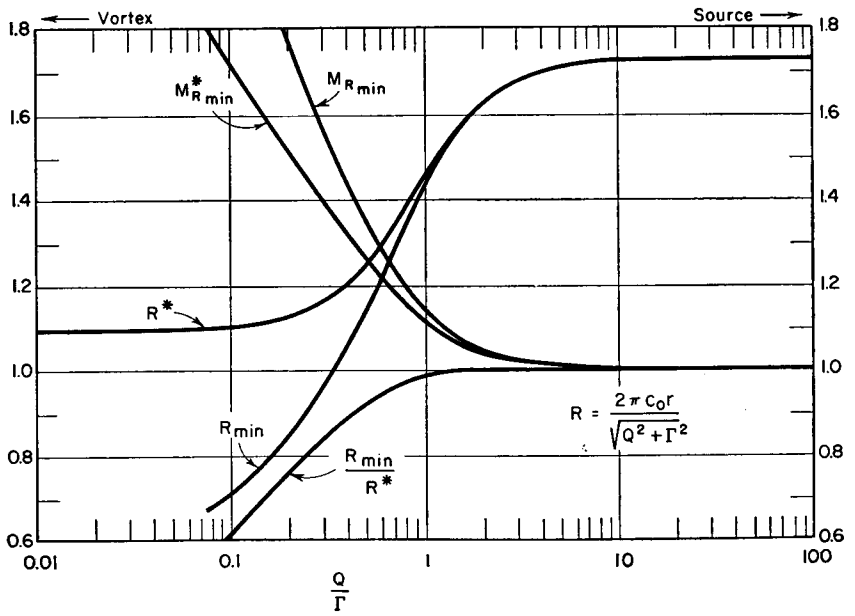


FIG. 20.3. (Continued)

- Parameters at limit line and at sonic line.

differential equations. Accordingly, we seek solutions to Eq. 20.1c of the form

$$\psi = P(V) \cdot Q(\theta) \quad (20.11)$$

where  $P$  is a function only of  $V$ , and  $Q$  is a function only of  $\theta$ . Then, in the usual notation, where  $P' = dP/dV$ ,  $P'' = d^2P/dV^2$ , etc., we have

$$\psi_v = QP'; \quad \psi_{vv} = QP''; \quad \psi_{\theta\theta} = PQ''$$

Substituting these into Eq. 20.1c, and rearranging, we get

$$V^2 \frac{1 - \frac{k-1}{2} \frac{V^2}{c_0^2} P''}{1 - \frac{k+1}{2} \frac{V^2}{c_0^2} P} + V \frac{1 - \frac{k-3}{2} \frac{V^2}{c_0^2} P'}{1 - \frac{k+1}{2} \frac{V^2}{c_0^2} P} + \frac{Q''}{Q} = 0$$

Now, since  $V$  and  $\theta$  are independent, this equation may be satisfied for all values of  $V$  and  $\theta$  only if

$$Q''/Q = -n^2 \quad (20.12)$$

$$V^2 \frac{1 - \frac{k-1}{2} \frac{V^2}{c_0^2} P''}{1 - \frac{k+1}{2} \frac{V^2}{c_0^2} P} + V \frac{1 - \frac{k-3}{2} \frac{V^2}{c_0^2} P'}{1 - \frac{k+1}{2} \frac{V^2}{c_0^2} P} = n^2 \quad (20.13)$$

where  $n^2$  is an arbitrary constant.

Eq. 20.12 is the differential equation of simple harmonic motion, and its general solution may be written as

$$Q(\theta) = K_1 \sin n\theta + K_2 \cos n\theta \quad (20.14)$$

Eq. 20.13 may be solved by analysis in a few special cases, but in general it must be solved through numerical integration or with a differential analyzer.

**Ringleb's Example.** A particular solution of Eq. 20.13, when  $n = 1$ , is  $P = 1/V$ . That this is indeed a solution may be verified by direct substitution into Eq. 20.13.

We shall investigate the particular case for which, corresponding to  $n = 1$ ,

$$\psi = \frac{c_0^2 l}{V} \sin \theta \quad (20.15)$$

where  $l$  is any characteristic length dimension, and  $c_0^2 l$  is used in place of  $K$  for the sake of dimensional homogeneity.

**INTEGRATION OF STREAMLINES.** Differentiating Eq. 20.15, we obtain

$$\psi_v = -\frac{c_0^2 l}{V^2} \sin \theta; \quad \psi_\theta = \frac{c_0^2 l}{V} \cos \theta$$

Substituting these into Eqs. 20.2, we get

$$\varphi_v = -c_0^2 l \frac{\rho_0}{\rho} \frac{1}{V^2} \left( 1 - \frac{V^2}{c^2} \right) \cos \theta; \quad \varphi_\theta = -c_0^2 l \frac{\rho_0}{\rho} \frac{1}{V} \sin \theta$$

Inserting these into Eqs. 20.3, and simplifying, there is obtained

$$x_v = c_0^2 l \frac{\rho_0}{\rho} \left( -\frac{\cos 2\theta}{V^3} + \frac{\cos^2 \theta}{V c^2} \right) \quad (20.16a)$$

$$x_\theta = -c_0^2 l \frac{\rho_0}{\rho} \frac{\sin 2\theta}{V^2} \quad (20.16b)$$

$$y_v = c_0^2 l \frac{\rho_0}{\rho} \left( -\frac{\sin 2\theta}{V^3} + \frac{\sin \theta \cos \theta}{V c^2} \right) \quad (20.16c)$$

$$y_\theta = c_0^2 l \frac{\rho_0}{\rho} \frac{\cos 2\theta}{V^2} \quad (20.16d)$$

With the help of Eq. 20.16b, we may now write

$$x = \int x_\theta d\theta + f(V) = \frac{c_0^2 l}{2} \frac{\rho_0}{\rho} \frac{\cos 2\theta}{V^2} + f(V)$$

Differentiating this with respect to  $V$  (and noting that  $\rho_0/\rho$  depends upon  $V$ ), we get

$$x_v = \frac{c_0^2 l}{2} \cos 2\theta \left[ -\frac{\rho_0}{\rho} \frac{2}{V^3} + \frac{1}{V^2} \left( \frac{\rho_0}{\rho} \frac{V}{c^2} \right) \right] + f'(V)$$

Comparison of this with Eq. 20.16a indicates that

$$\frac{df}{dV} = f'(V) = \frac{c_0^2 l}{2} \frac{\rho_0}{\rho} \frac{1}{V c^2}$$

Integrating, and ignoring an unimportant additive constant of integration, we write

$$f(V) = \frac{c_0^2 l}{2} \int \frac{\rho_0}{\rho} \frac{dV}{V c^2} = \frac{l}{2} L \quad (20.17)$$

where the integral  $L$  is found by expressing  $c^2/c_0^2$  and  $\rho_0/\rho$  in terms of  $V$ . Eq. 20.17 is integrable in closed form only for special values of  $k$ . For  $k = 1.4$ ,  $L$  has the value

$$L \equiv - \left[ \frac{1}{2} \ln \frac{1+\gamma}{1-\gamma} - \frac{1}{\gamma} - \frac{1}{3\gamma^3} - \frac{1}{5\gamma^5} \right]; \quad \gamma \equiv \sqrt{1 - 0.2 \frac{V^2}{c_0^2}} = \left( \frac{\rho}{\rho_0} \right)^{1/5} \quad (20.18)$$

Inserting Eq. 20.17 into the previous expression for  $x$ , we have

$$\frac{x}{l} = \frac{1}{2} \left[ \frac{\rho_0}{\rho} \left( \frac{c_0}{V} \right)^2 \cos \theta + L \right] \quad (20.19a)$$

By means of similar integrations we get, ignoring immaterial additive constants,

$$\frac{y}{l} = \frac{1}{2} \frac{\rho_0}{\rho} \left( \frac{c_0}{V} \right)^2 \sin 2\theta \quad (20.19b)$$

Eqs. 20.19, together with Eq. 20.15, are the parametric equations of the streamlines in terms of  $\theta$  and  $V/c_0$ . By eliminating  $\theta$  between Eq. 20.15 and Eqs. 20.19 we get a useful pair of parametric equations of the streamlines in terms of  $\psi$  and  $V/c_0$ :

$$\frac{x}{l} = \frac{1}{2} \frac{\rho_0}{\rho} \left( \frac{c_0}{V} \right)^2 - 2 \frac{\psi^2}{l^2 c_0^2} + \frac{L}{2} \quad (20.20a)$$

$$\frac{y}{l} = \pm \frac{\rho_0}{\rho} \frac{c_0}{V} \frac{\psi}{c_0 l} \sqrt{1 - \frac{V^2}{c_0^2} \left( \frac{\psi}{l c_0} \right)^2} \quad (20.20b)$$

**THE INCOMPRESSIBLE CASE.** Since these results are rather complex, it is helpful to begin by analyzing them for the limiting case of incompressible flow. For this we set  $\rho = \rho_0$ , and we note that  $L$  becomes an unimportant constant which may be omitted without altering the shape of the flow pattern. Then Eqs. 20.20 become

$$\frac{x}{l} = \frac{1}{2} \left( \frac{c_0^2}{V^2} - 2 \frac{\psi^2}{l^2 c_0^2} \right); \quad \frac{y}{l} = \pm \frac{c_0}{V} \frac{\psi}{c_0 l} \sqrt{1 - \frac{V^2}{c_0^2} \left( \frac{\psi}{l c_0} \right)^2} \quad (20.21)$$

where  $c_0$  is now interpreted as some reference velocity, since it was originally introduced merely as a dimensional constant.

To find the shape of the streamlines, we eliminate  $V/c_0$  from this pair of equations, and thus obtain

$$\left( \frac{y}{l} \right)^2 = \left( \frac{\psi}{l c_0} \right)^2 \left[ 2 \frac{x}{l} + \left( \frac{\psi}{l c_0} \right)^2 \right] \quad (20.22)$$

Similarly, by eliminating  $\psi/c_0 l$  from Eqs. 20.21, we get the equation of the lines of constant velocity, and thus of constant pressure:

$$\left( \frac{x}{l} \right)^2 + \left( \frac{y}{l} \right)^2 = \left( \frac{r}{l} \right)^2 = \frac{1}{4} \left( \frac{c_0}{V} \right)^4 \quad (20.23)$$

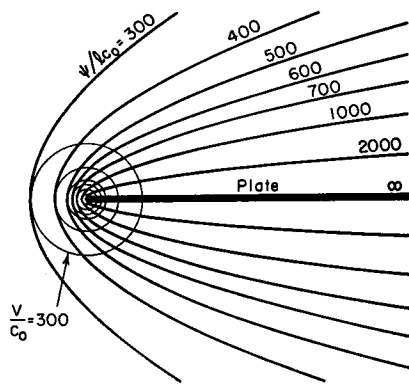


FIG. 20.4. Incompressible flow around the edge of a plate.

The streamlines, according to Eq. 20.22, are confocal parabolas, symmetrical with respect to the  $x$ -axis. Therefore the flow pattern is that of a 180°-turn around a semi-infinite plane lying along the  $x$ -axis (Fig. 20.4). Inspection of Eq. 20.23 shows that the lines of constant pressure are circles concentric with the origin, also as shown in Fig. 20.4. It is evident from Eq. 20.15 that on any given streamline, either for compressible or incompressible flow, the maximum speed is reached when  $\theta = \pm\pi/2$ . For reasons of symmetry, this condition must occur on the  $x$ -axis. At the edge of the plate the velocity is, of course, infinite for the incompressible case.

**THE COMPRESSIBLE CASE.** For compressible flow the streamlines may be plotted from Eqs. 20.20. For any selected value of the streamline constant  $\psi/lc_0$  the corresponding values of  $x/l$  and  $y/l$  at various points on the streamline may be computed by choosing various values of the parameter  $V/c_0$ .

For small values of  $\psi/lc_0$  the maximum Mach Number on the streamline is so small that the flow is essentially incompressible, and such streamlines are virtually identical with those of Fig. 20.4. See, for example, the streamline labeled 300 in Fig. 20.5a. Eq. 20.15 shows that the hodograph streamlines are circles all tangent to the horizontal axis at the origin. As seen from Fig. 20.5b, the streamline 300 is everywhere subsonic.

As  $\psi/lc_0$  increases parts of the flow become supersonic. The streamlines become flattened near their apex, in accordance with the area-ratio requirements for isentropic flow.

The streamline 550 has a point of infinite acceleration (Fig. 20.5c) at  $V/c_0 = 1.2$ , and reaches a maximum speed of  $V/c_0 = 1.67$ .

All streamlines with  $\psi/c_0 l$  larger than 550 show a peculiar behavior. For example, considering the streamline 650, the behavior is regular as the streamline approaches the edge until point  $F$  is reached, at which point the acceleration becomes infinite. The streamline then doubles back on itself until, at point  $G$ , there is again an infinite acceleration and a cusp, and the streamline for the second time doubles back on itself. The loci of the cusp points (such as  $F$  and  $G$ ) for various streamlines form the limit line of this flow. To the right of the limit line three flow planes are superposed and are branched at the limit curves. Of course only one such flow plane at a time is physically possible.

**LIMIT LINE.** To learn more about the limit line in this case, it is helpful to compute the curvature of the streamlines, for at the cusps the streamlines have infinite curvature. With the help of Eqs. 20.21,

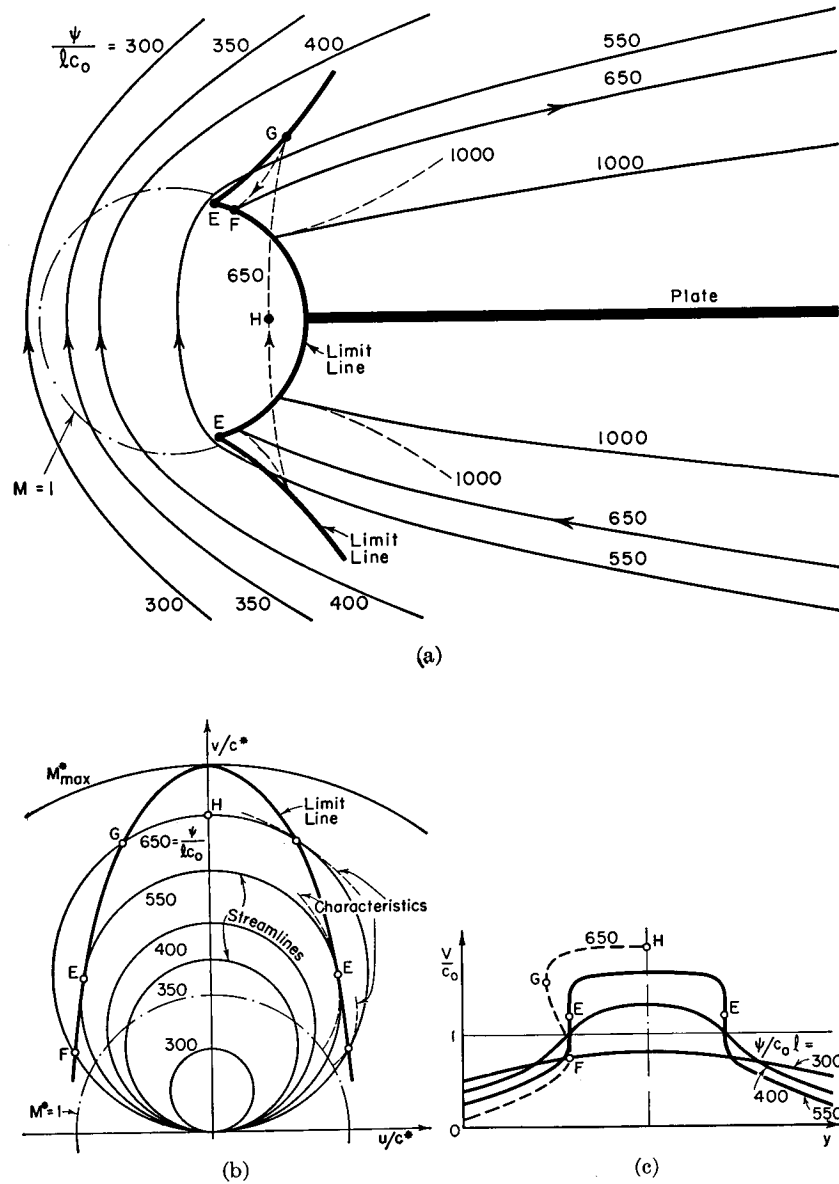


FIG. 20.5. Compressible flow around the edge of a plate (after Ringleb).

- (a) Streamlines and limit line.
- (b) Streamlines and limit line in hodograph plane.
- (c) Velocity distribution on several streamlines of (a).

we may compute the radius of curvature,  $R$ , of the physical streamlines, as

$$\begin{aligned} \frac{l}{R} &= \frac{l(d^2y/dx^2)_{\psi}}{[1 + (dy/dx)_{\psi}]^{3/2}} \\ &= \frac{l \left( \frac{dV}{dx} \frac{d}{dV} \left[ \frac{dy}{dx} \right] \right)_{\psi}}{1 + \left( \frac{dy}{dx} \right)_{\psi}^{3/2}} \\ &= \pm \frac{\frac{\rho_0}{\rho} \frac{V}{c_0} \frac{\psi}{lc_0}}{\frac{c_0^2}{c^2} \left[ 1 - \left( \frac{V}{c_0} \right)^2 \left( \frac{\psi}{lc_0} \right)^2 \right] - \frac{c_0^2}{V^2}} \end{aligned}$$

At the limit line the denominator of this expression is zero, and the "limit-line condition" may be expressed as

$$\frac{c^2}{V^2} = 1 - \left( \frac{V}{c_0} \right)^2 \left( \frac{\psi}{lc_0} \right)^2 \quad (20.24)$$

Eliminating  $c^2$  with the help of the energy equation,

$$c^2 = c_0^2 - \frac{k-1}{2} V^2$$

we get

$$\left( \frac{V}{c_0} \right)^2 = \frac{k+1}{2} \left( \frac{lc_0}{\psi} \right)^2 \pm \frac{lc_0}{\psi} \sqrt{\frac{k+1}{4} \left( \frac{lc_0}{\psi} \right)^2 - 1}$$

as the value of  $V/c_0$  at the limit line for a streamline with a given value of  $\psi/lc_0$ . It is evident that this expression is real only when

$$\left( \frac{k+1}{4} \right)^2 \left( \frac{lc_0}{\psi} \right)^2 - 1 \geq 0$$

that is, only when

$$\frac{lc_0}{\psi} \geq \frac{4}{k+1} \quad (= 1.667 \text{ for } k = 1.4)$$

Eq. 20.15 shows, however, that  $lc_0/\psi$  is also the maximum value of  $V/c_0$  on the streamline. We conclude, therefore, that no difficulties in the flow arise on any streamline for which the maximum speed is less than  $1.67c_0$  (corresponding to a maximum local Mach Number of 2.50).

Historically, this example had an important influence on the thinking of investigators in this field. The experimental facts until recently seemed to indicate that when a stream flowing over a curved surface

became supersonic locally the deceleration to subsonic speeds was always accompanied by shocks. The example given here shows at least that there is no natural law forbidding the efficient deceleration of supersonic flows.

### 20.5. The Limit Line

The examples of the vortex-source and of the Ringleb 180°-turn both contain the remarkable feature of the *limit line*. In both cases the streamlines are cusped at the limit line and turn back upon themselves; and, moreover, the fluid acceleration and pressure gradient are each infinite at the limit line. If the Mach lines of these flows were to be drawn, it would be found that the Mach lines of one family intersect and have an envelope, the envelope being the limit line itself. From this it follows that the component of velocity normal to the limit line is equal to the local speed of sound.

Many other examples of particular solutions to the equations of motion containing limit lines are to be found in the literature, and all exhibit the features outlined above. A particularly revealing example was touched upon in Chapter 15, and will now be discussed from a different point of view because it illuminates in a simple manner the typical behavior of streamlines in the vicinity of a limit line.

**Compression Prandtl-Meyer Flow.** Consider the two-dimensional supersonic flow past the concave wall of Fig. 20.6a. The influence of the wall is propagated along straight left-running Mach lines, on each of which all stream properties are uniform. Near the wall a streamline such as  $AB$  is quite regular, and is a transformation of the wall streamline. At a considerable distance from the wall, however, the Mach lines cross and form an envelope. A typical streamline far from the wall, such as  $CDEF$ , has two cusps and doubles back upon itself twice. Between the two branches of the limit line the flow plane is covered thrice with streamlines. Clearly the flow depicted in Fig. 20.6a must in practice be modified beyond the limit line. The nature of this modification is suggested by the fact that at the beginning of the limit line the spacing between successive Mach lines goes to zero, and thus the velocity gradient along a streamline becomes infinite. Viscous and heat conduction effects must, consequently, come into play and so the flow near the limit line cannot in fact be irrotational. Schlieren photographs of flows like that of Fig. 20.6a show that shock waves appear approximately in the position of the envelope of the shock waves.

A still more pronounced example, where it is well known that shocks appear, is that of Fig. 20.6b, in which the entire turning of the wall is concentrated at a sharp bend. The dotted streamline is based on the assumption of isentropic flow, for which the simple-wave (Prandtl-

Meyer) solution is applicable. This leads to two cusps, at  $A$  and  $B$ , on each streamline. In practice it is well known that the actual streamline undergoes a sharp turn across an oblique shock which lies somewhat upstream of the first cusp in the Prandtl-Meyer streamline.

**Criterion of Limit Line.** We shall now define the limit line as the locus of points in the flow where the fluid acceleration is infinite, and we shall proceed to determine a criterion for the appearance of a limit line.

The fluid particle acceleration along a streamline may be written,

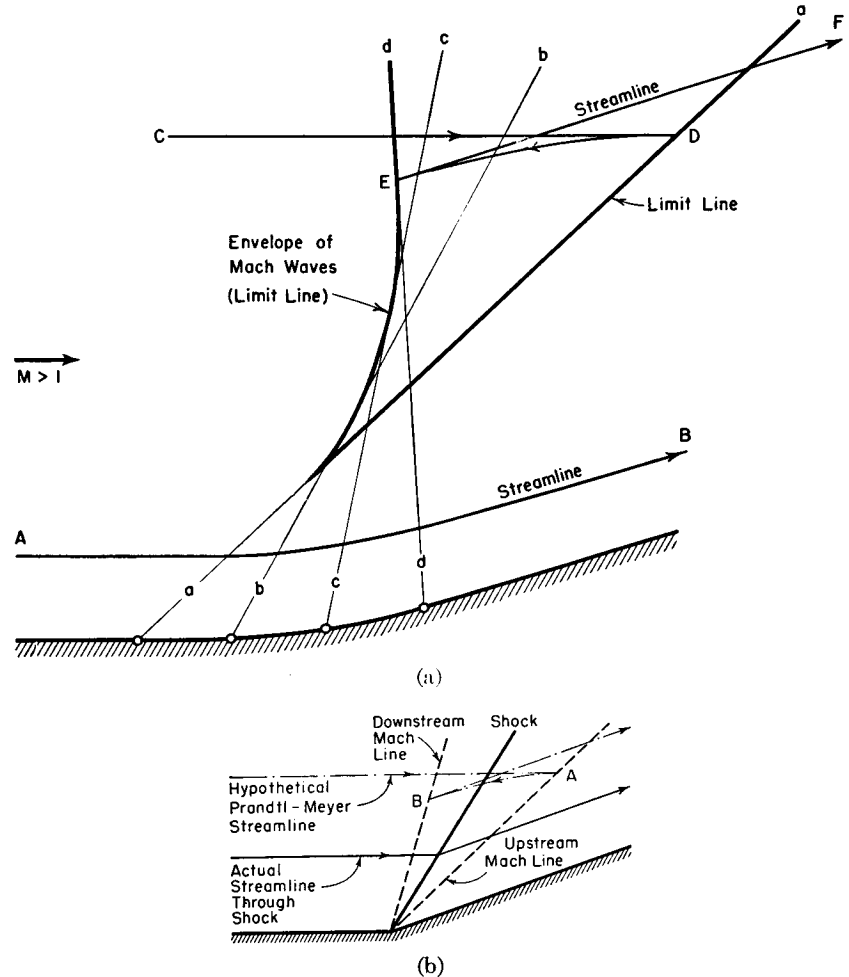


Fig. 20.6. Formation of limit lines in compressive Prandtl-Meyer flow

- (a) Wall with continuous curvature.
- (b) Wall with sharp bend.

using the symbol  $D/dt$  for the substantial derivative and  $s$  for distance along the streamline, as

$$a_\psi = \left( \frac{DV}{dt} \right)_\psi = \left( \frac{Ds}{dt} \right)_\psi \left( \frac{d\varphi}{ds} \right)_\psi \left( \frac{dV}{d\varphi} \right)_\psi$$

Or, since  $(Ds/dt)_\psi = V$ , and  $(d\varphi/ds)_\psi = V$ , it may also be written as

$$a_\psi = V^2 \left( \frac{dV}{d\varphi} \right)_\psi \quad (20.25)$$

In order to find the conditions for which  $(dV/d\varphi)_\psi$  might be infinite, we write the following relations, based on the assumptions that  $\varphi$  and  $\psi$  are continuous functions of  $V$  and  $\theta$ :

$$d\varphi = \varphi_v dV + \varphi_\theta d\theta \quad (20.26a)$$

$$d\psi = \psi_v dV + \psi_\theta d\theta \quad (20.26b)$$

Regarding these as a pair of simultaneous equations in  $dV$  and  $d\theta$ , and solving for  $dV$ , we obtain

$$dV = \frac{\psi_\theta d\varphi - \varphi_\theta d\psi}{\varphi_v \psi_\theta - \varphi_\theta \psi_v}$$

from which it follows that

$$\left( \frac{dV}{d\varphi} \right)_\psi = \frac{\psi_\theta}{\varphi_v \psi_\theta - \varphi_\theta \psi_v} = \frac{\psi_\theta}{\partial(\varphi, \psi)/\partial(V, \theta)} \quad (20.27)$$

where the denominator is the Jacobian of Eqs. 20.26. Referring back to Eq. 20.25, we see that the fluid acceleration becomes infinite either when this Jacobian vanishes or when  $\psi_\theta$  becomes infinite. The former possibility proves to be the one of greater significance. Setting the Jacobian equal to zero, and employing Eqs. 20.2 for  $\varphi_v$  and  $\varphi_\theta$ , we get as the criterion of the limit line that

$$(1 - M^2)\psi_\theta^2 + V^2\psi_v^2 = 0 \quad (20.28)$$

Inspection of this equation shows that under no circumstances may it be satisfied unless  $M > 1$ , that is, unless the flow is supersonic. Limit lines may occur, therefore, only in supersonic regions of the flow.

**Behavior of Streamlines Near the Limit Line.** To prove that cusps in the streamlines appear at the limit line, let us consider an arbitrary increment  $ds$  along the streamline. Along the streamline,  $ds = d\varphi/V$ , and  $d\psi = 0$ , and so we may write

$$ds = \left( \frac{d\varphi}{V} \right)_\psi = \left( \frac{d\varphi}{dV} \right)_\psi \frac{dV}{V}$$

Combining this with Eq. 20.25, we get

$$ds = \frac{V dV}{a_\psi} \quad (20.29)$$

This shows that, when the fluid acceleration becomes infinite,  $ds$  goes to zero. If successive increments  $dV$  of the same sign are chosen along a streamline, it is evident that  $ds$  generally changes sign when the streamline reaches the limit line. Accordingly, a cusp is formed at the limit line.

The curvature of the streamlines also becomes infinite at the limit line. To prove this, we may note from the graphical construction of Fig. 20.7 that the streamline radius of curvature is  $R \equiv (ds/d\theta)_\psi$ . This may be rewritten as

$$R \equiv \left( \frac{ds}{d\theta} \right)_\psi = \left( \frac{ds}{d\varphi} \right)_\psi \left( \frac{d\varphi}{dV} \right)_\psi \left( \frac{dV}{d\theta} \right)_\psi = \frac{1}{V} \left( \frac{d\varphi}{dV} \right)_\psi \left( \frac{dV}{d\theta} \right)_\psi$$

Comparing this with Eq. 20.25, we see that

$$R = \frac{V}{a_\psi} \left( \frac{dV}{d\theta} \right)_\psi \quad (20.30)$$

The radius of curvature therefore goes to zero as the acceleration becomes infinite, thus indicating either a sharp corner or a cusp in the streamline at the limit line. But it is known that, except at singular points, a sharp bend in the streamline can occur only with oblique shocks. Since the latter are not allowable in the present analysis of continuous flows, it follows that *the physical streamline must have a cusp at the limit line*. A more detailed proof of this point is given in Reference 4.

**Limit Line in Hodograph Plane.** The criterion of the limit line, Eq. 20.28, may be rewritten in the form

$$\frac{1}{1 - M^2} = - \frac{\psi_\theta^2}{V^2 \psi_v^2} = - \left[ \frac{(d\psi/d\theta)_v}{V(d\psi/dV)_\theta} \right]^2$$

Eliminating  $(d\psi/dV)_\theta$  with the help of the mathematical relation

$$\left( \frac{d\psi}{d\theta} \right)_v \left( \frac{d\theta}{dV} \right)_\psi \left( \frac{dV}{d\psi} \right)_\theta = -1$$

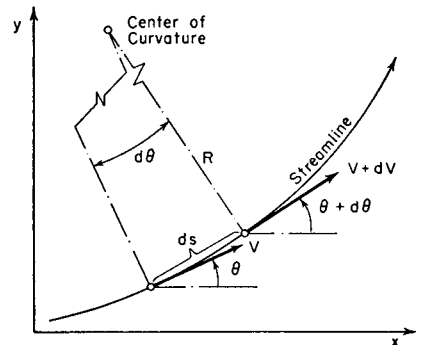


FIG. 20.7. Geometry of streamline.

it may be shown that

$$\frac{1}{V} \left( \frac{dV}{d\theta} \right)_\psi = \pm \frac{1}{\sqrt{M^2 - 1}}$$

The left-hand side of this relation has a simple geometric meaning in the hodograph plane. As seen from Fig. 20.8a, the left-hand side

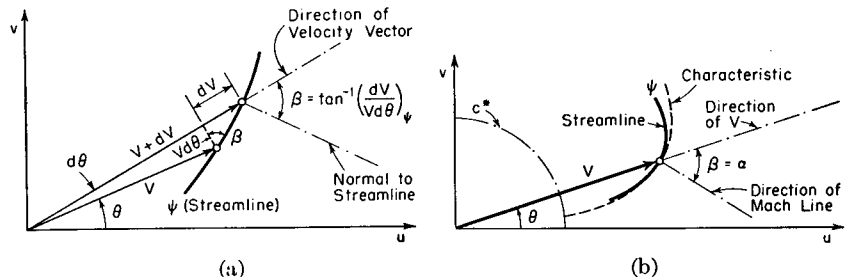


FIG. 20.8. At the limit line the hodograph streamline is tangent to the hodograph characteristic.

represents the tangent of the angle  $\beta$  between the velocity vector and the normal to the two-dimensional hodograph characteristic.

By definition, however,

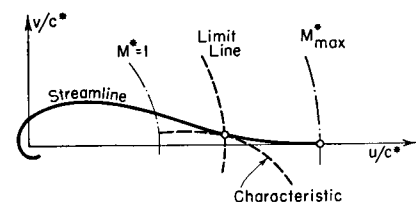
$$\frac{1}{\sqrt{M^2 - 1}} = \tan \alpha$$

where  $\alpha$  is the local Mach angle. Therefore it follows that  $\beta = \pm \alpha$ . But the Mach angle is, geometrically, the angle between the velocity vector and the normal to the two-dimensional hodograph characteristic. Therefore, as shown in Fig. 20.8b, *at a point on the hodograph limit line the hodograph streamline is locally tangent to the hodograph characteristic of one family*.

If the limit line exists, therefore, its hodograph image is defined by the locus of points where the hodograph characteristics of one family are tangent to the hodograph streamlines. This result is illustrated in Fig. 20.5b for Ringleb's example. In the source flow of Fig. 20.1 the hodograph streamlines are radial lines which are tangent to the hodograph characteristics at  $M = 1$ ; as shown previously, the sonic line is in this case also the limit line. Fig. 20.9 shows the relation between the streamlines, characteristics, and limit line in the hodograph plane for the vortex-source of Fig. 20.3.

FIG. 20.9. Hodograph streamline for the flow of Fig. 20.3.

Since the physical limit line is tangent to a Mach line, and since the component of velocity normal to the Mach line is equal to the local speed of sound, it follows further that at the limit line the component of velocity normal to the limit line is equal to the local speed of sound (see Fig. 20.3a).



It appears from these considerations, therefore, that if solutions to the hodograph equation (Eq. 20.1) are found for which the hodograph streamlines are nowhere tangent to the hodograph characteristics, then limit lines cannot appear in the physical flow.

**Limit Line as Envelope of Mach Waves.** The physical characteristics for two-dimensional, irrotational, supersonic flow were shown in Chapter 15 to be defined by the differential equation

$$(c^2 - u^2)(dy)^2 - 2uv dy dx + (c^2 - v^2)(dx)^2 = 0 \quad (20.31)$$

Since  $x$  and  $y$  are assumed to be continuous functions of  $V$  and  $\theta$ , we may write

$$dx = x_v dV + x_\theta d\theta; \quad dy = y_v dV + y_\theta d\theta$$

Substituting in these relations the expressions for  $x_v$ ,  $x_\theta$ ,  $y_v$ , and  $y_\theta$  given by Eqs. 20.3,  $dx$  and  $dy$  may each be expressed in terms of  $\theta$ ,  $V$ ,  $d\theta$ ,  $dV$ , and the derivatives  $\varphi_v$ ,  $\varphi_\theta$ ,  $\psi_v$ ,  $\psi_\theta$ . When these expressions for  $dx$  and  $dy$  are placed in Eq. 20.31, and when  $\varphi_v$  and  $\varphi_\theta$  are further eliminated by means of Eq. 20.2, the transformed equations of the physical characteristics are obtained in the form

$$[V^2(d\theta)^2 - (M^2 - 1)(dV)^2][V^2\psi_v^2 + (1 - M^2)\psi_\theta^2] = 0$$

The term in the second set of square brackets is seen, by comparison with Eq. 20.28, to be equal to zero at the hodograph limit line. This means that an element of the hodograph limit line, when transferred to the physical plane, will have its slope equal to that of one family of Mach waves.

The question now arises whether the hodograph limit line is identical with a hodograph characteristic. It may be proved<sup>(4,5)</sup> that the limiting hodograph can never be a characteristic in the hodograph plane. In the physical plane, therefore, the limiting line cannot be a Mach line. But, as shown before, the limit line is everywhere tangent to one family of Mach lines. It is concluded, therefore, that *the physical limit line must be the envelope of one family of Mach waves*.

This geometric property, with its simple physical interpretation, is illustrated in Fig. 20.6a.

Since the physical limit line is tangent to a Mach line, and since the component of velocity normal to the Mach line is equal to the local speed of sound, it follows further that at the limit line the component of velocity normal to the limit line is equal to the local speed of sound (see Fig. 20.3a).

**Forbidden Regions of the Flow.** Having discovered the possibility of limit lines in the flow, we now inquire as to whether the flow up to the

limit line may be employed and joined at that line to another flow pattern.

One type of joining of the two flows would be by means of a shock discontinuity. However, the limit line makes the Mach angle with the velocity vector, whereas the angle of an oblique shock is larger than the Mach angle. On these elementary grounds it is seen that the original flow cannot be continued across a shock at the limit line.

As to the possibility of joining a new solution at the limit line without discontinuities, the argument is lengthy, but it has been shown<sup>(4,5)</sup> that this cannot be done.

The region beyond the limit line is therefore truly forbidden within the limits of these statements. If physical flow boundaries corresponding to two streamlines of the theoretical flow are constructed up to the limit line, and then continued beyond the limit line, it is therefore to be expected that the flow will differ from the theoretical flow even before the limit line is reached. Whether shocks then appear, or whether no steady-state flow pattern is then possible, cannot be stated in general.

**Axially Symmetric and Three-Dimensional Flows.** All the theorems proved in this section concerning limit lines have been generalized by Tsien<sup>(5)</sup> and shown to be valid also for axially symmetric flows and for three-dimensional flows in terms of limiting surfaces, stream surfaces, and characteristic surfaces.

**Geometric Interpretation of Limit-Line Occurrence.** The potential, steady motion of a gas is governed by the continuity equation, Euler's

equations, and the condition of irrotationality. Each of these has a geometrical interpretation.

For example, consider the mixed flow over the curved surface of Fig. 20.10, with an embedded supersonic region present. For the flow to be irrotational there is a tendency for the streamlines nearer the wall to have more curvature than those far from the wall. However, in following a stream, tube continuity requires the spacing between two adjacent streamlines to decrease as the

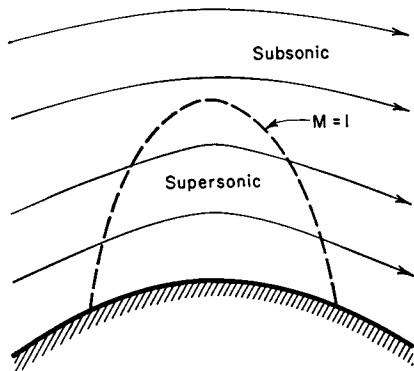


FIG. 20.10. Supersonic zone near a curved surface.

sonic line is approached and subsequently to increase in the supersonic region until the peak Mach Number on the streamline is reached. This requirement tends to make the streamlines flatter as the wall is approached.

These two geometric demands on the streamlines, one based on continuity and the other based on irrotationality, can sometimes act oppositely and even be incompatible. If so, one of the physical requirements must be relaxed, which means that either (i) the flow becomes unsteady, or (ii) viscous effects appear in the form of shock waves.

**Physical Interpretation of the Limit Line.** To evaluate what might ensue when a limit line appears in a theoretical solution, we must re-examine the fundamental assumptions of the solution. These assumptions are (i) steady flow (ii) irrotationality, (iii) zero viscous and heat conduction effects. One possibility is that no steady-state flow patterns are possible, in which case the first assumption would fail. A second possibility is that shock waves appear, which would make the latter two assumptions invalid.

In the case of supersonic flow past a concave corner, Fig. 20.6b, it is known that the theoretical flow pattern having limit lines is replaced by a steady flow with an oblique shock wave. This shows that in at least one case the assumption of irrotationality fails. The original solution is, in this case, valid up to the shock wave.

If the theoretical flow is replaced by an unsteady-state flow, no part of the steady theoretical solution is, of course, valid.

**Upper and Lower Critical Mach Numbers.** Shock waves cannot appear in subsonic regions of the flow. For bodies immersed in a flowing stream the *lower critical Mach Number* is therefore defined as the minimum free-stream Mach Number for which the sonic velocity is first reached somewhere in the flow field.

If limit lines appear in the irrotational flow past a body, the evidence is strong that either steady or moving shock waves will appear in the flow pattern. The imminence of a limit line may also produce large adverse pressure gradients in the viscous boundary layer and, because of thickening or separation of the latter, may effect changes in the irrotational flow which bring the limit-line phenomenon even nearer. Therefore the free-stream Mach Number at which the limit line first appears in the irrotational flow may be regarded as an *upper critical Mach Number*.

Tsien<sup>(5)</sup> has suggested that the actual critical Mach Number for the appearance of shock waves and compressibility burble must lie between the limits of these two critical Mach Numbers.

**Limit Lines for Flow Past Given Profiles.** All the previous discussions of the limit line referred to solutions of the equations of motion which are regular in the hodograph plane but exhibit irregularities in the physical plane. In many ways this is an unsatisfactory approach, since we are very much more interested in whether limit lines can appear in the flow

past a given profile than we are in whether completely regular physical streamlines are obtained from particular solutions of the hodograph equations.

This problem will be discussed more fully in Chapter 22.

## 20.6. Solution of Hodograph Equations by Hypergeometric Functions

As a result of the linearity of Eqs. 20.1, and the existence of product-type solutions as shown by Eqs. 20.11, 20.12, 20.13, and 20.14, the general solution of the hodograph differential equation may be expressed as

$$\psi = \sum_{n=0}^{n=\infty} [P_n(V)] [A_n \cos n\theta + B_n \sin n\theta] \quad (20.32)$$

where  $P_n(V)$  is the solution to Eq. 20.13 corresponding to a specific value of  $n$ , and  $A_n$  and  $B_n$  are constants to be determined by the boundaries of the flow.

For incompressible flow the differential equation of the function  $P$  is (since  $c_0 = \infty$ )

$$V^2 P'' + VP' - n^2 P = 0 \quad (20.33)$$

It may be verified by substitution that the solution to this equation is

$$P_n = V^n$$

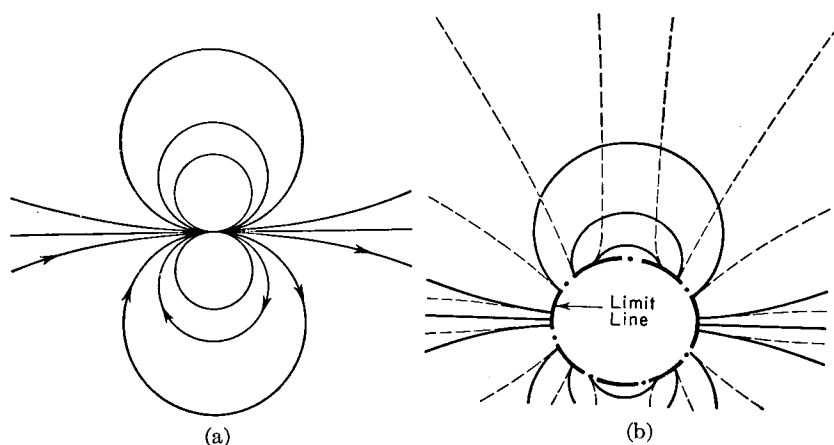


Fig. 20.11. Two-dimensional doublet (after Ringleb).

- (a) Incompressible flow.
- (b) Compressible generalization of (a).

The general solution to the hodograph equations for incompressible flow may accordingly be written

$$\psi_{\text{incomp}} = \Sigma V^n (A_n \cos n\theta + B_n \sin n\theta) \quad (20.34)$$

The streamline patterns defined by Eq. 20.34 are those of well-known elementary solutions for incompressible potential flow. They may also be regarded as the limiting forms of the streamline patterns corresponding to Eq. 20.32 as the Mach Number goes to zero. Unfortunately, the physical streamlines thus found alter in shape as the Mach Number changes, and so this attack on the problem does not provide a convenient method for determining the effect of Mach Number on a profile of given shape.

The compressible generalization of a doublet was found in this way by Ringleb <sup>(1)</sup> by setting all the constants  $A_n$  and  $B_n$  equal to zero, except  $A_{1/2} = 1$ . This leads to the flow pattern of Fig. 20.11, which is seen to have a limit line when the fluid is compressible.

More general methods for obtaining solutions like that of Eq. 20.32 involve the use of hypergeometric functions. For details of this method the reader is referred to References 6, 8, and 9.

## REFERENCES AND SELECTED BIBLIOGRAPHY

1. RINGLEB, F. Exakte Lösungen der Differentialgleichungen einer adiabatischen Gassstromung, *Z.a.M.M.*, Vol. 20, No. 4 (1940), pp. 185-98.
2. KRAFT, H., and DIBBLE, C. G. Some Two-Dimensional Adiabatic Compressible Flow Patterns, *Jour. Aero. Sci.*, Vol. 11, No. 4 (1944), p. 283.
3. VON KÁRMÁN, T. Compressibility Effects in Aerodynamics, *Jour. Aero. Sci.*, Vol. 8, No. 9 (1941), p. 337.
4. DALITZ, R. H. Some Mathematical Aspects of Compressible Flow, *Australian Council for Aeronautics Report*, ACA-20 (1946).
5. TSIEN, H. S. The "Limiting Line" in Mixed Subsonic and Supersonic Flow of Compressible Fluids, *NACA Tech. Note*, No. 961 (1944).
6. GARRICK, I. E., and KAPLAN, C. On the Flow of a Compressible Fluid by the Hodograph Method: II—Fundamental Set of Particular Flow Solutions of the Chaplygin Differential Equation, *NACA Tech. Rep.*, No. 790 (1944).
7. TSIEN, H. S., and KUO, Y. H. Two-Dimensional Irrotational Mixed Subsonic and Supersonic Flow of a Compressible Fluid and the Upper Critical Mach Number, *NACA Tech. Note*, No. 995 (1946).
8. HUCKEL, VERA. Tables of Hypergeometric Functions for Use in Compressible-Flow Theory, *NACA Tech. Note*, No. 1716 (1948).
9. LIGHTHILL, M. J. The Hodograph Transformation in Trans-sonic Flow, *Proc. Roy. Soc. (A)*, Vol. 191 (1947), p. 323; Vol. 191 (1947), p. 341; Vol. 191 (1947), p. 352; Vol. 192 (1947), p. 135.

## Chapter 21

### TRANSonic FLOW

#### 21.1. Introductory Remarks

The term *transonic* implies flows with speeds near the local speed of sound. Such flows may be either subsonic or supersonic, or, more commonly, may contain both subsonic and supersonic regions.

Both the theoretical and the experimental approaches to such problems are difficult. The theoretical treatment owes its difficulties to the different nature of the mathematical solutions for subsonic flows (elliptical solutions) and for supersonic flows (hyperbolic solutions). Experimental investigations in wind tunnels are handicapped by the undue influence caused by the boundaries of the wind tunnel stream (either walls or the free surface of a jet) near Mach Number unity, thus tending to make wind tunnel tests unreliable. Recent trends point toward the use of porous or slotted test-section walls as a means of overcoming such difficulties, the objective being to produce a condition midway between that of wave reflection in like sense from a fixed wall and reflection in unlike sense from a constant-pressure boundary.

The extreme lateral influence produced by an obstacle in a stream near Mach Number unity is illustrated by an examination of the linearized equation for two-dimensional flow with small perturbations:

$$(1 - M_\infty^2) \frac{\partial u''}{\partial x} + \frac{\partial v''}{\partial y} = 0 \quad (21.1)$$

where  $u''$  and  $v''$  are the perturbation velocities. This shows that when  $M_\infty = 1$ ,  $\partial v''/\partial y = 0$ , and, therefore, that  $v''$  depends only on  $x$ . In other words, the disturbance produced by the body is propagated laterally with undiminished strength, as shown in Fig. 21.1. This result is in accord with the solutions for subsonic and supersonic flow past a wavy wall derived previously in Chapters 10 and 14. Since the curvature of the streamlines remains finite as  $y$  increases, it follows that infinite pressure differences can exist between the surface of the body and points at great lateral distances from the body.

Of course this picture of the flow is not physically plausible. Equally implausible are other results of the linear theory, such as that (i) the drag in an inviscid fluid is zero for  $M_\infty$  slightly less than unity, but infinite for  $M_\infty$  slightly greater than unity, and (ii) the lift coefficient is

infinite at Mach Number unity. The answer to these seeming paradoxes is that one of the assumptions of the theory of small perturbations underlying Eq. 21.1 is invalid for transonic flow; that assumption is that the local velocity is not close to the local speed of sound.

Despite the imperfection of the theory underlying Fig. 21.1, it is surely indicative that at Mach Number unity the influence of boundaries very far from the obstacle may not be negligible. This effect, as suggested before, renders difficult the interpretation of wind tunnel data.

In this chapter we shall consider a number of analytical methods of studying transonic flows and shall discuss some typical theoretical results from the point of view of their practical significance. The study of transonic flow will be rounded out in Chapter 22 by an examination of experimental results and by a theoretical consideration of the possibility of obtaining transonic flows without shocks.

In proportion to its importance, the understanding of transonic flows is smaller than for any other phase of high-speed compressible flow. Much work therefore remains to be done in this field.

Additional material relevant to the subject matter of the present chapter may be found in Chapter 22.

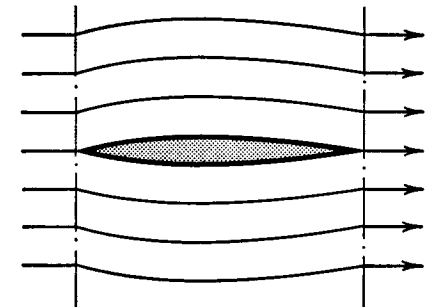


FIG. 21.1. Flow past thin profile at  $M_\infty = 1$ , as predicted by linearized theory of supersonic flow.

#### NOMENCLATURE

$a$	angle of attack	to height at throat;
$a_0, a_2, a_4, \dots$	coefficients of power series (Eq. 21.67)	also transformed velocity potential (Eq. 21.11)
$A$	aspect ratio	$h$ ratio of slope of profile to thickness ratio
$b$	span of wing	$k$ ratio of specific heats
$b_1, b_3, \dots$	coefficients of power series (Eq. 21.67)	$K$ transonic similarity parameter for two-dimensional flow (Eqs 21.14a and 21.17)
$c$	speed of sound	$K'$ transonic similarity parameter for axi-symmetric flow (Eq. 21.23)
$C_p$	pressure coefficient	
$C_D$	drag coefficient	
$C_L$	lift coefficient	
$C_m$	moment coefficient	
$\mathcal{D}$	similarity function for $C_D$	
$f$	ratio of nozzle height	

## NOMENCLATURE—Continued

$K''$	transonic similarity parameter for three-dimensional flow (Eq. 21.26)	$w$	mass rate of flow
$l$	chord	$x, y, z$	Cartesian coordinates
$C_L$	similarity function for $C_L$	$\delta$	thickness ratio; also turning angle
$m, n$	exponents (Eq. 21.10)	$\xi$	transformed $x$ -coordinate
$M$	Mach Number	$\eta$	transformed $y$ -coordinate
$M^*$	$V/c^*$	$\theta$	flow direction
$\mathfrak{M}$	similarity function for $C_{\mathfrak{M}}$	$\xi$	transformed $x$ -coordinate
$p$	pressure	$\rho$	mass density
$\varphi$	similarity function for $C_p$	$\sigma$	shock angle
$R$	radius of curvature of nozzle wall	$\Phi$	velocity potential
$t$	thickness of profile	$\varphi$	perturbation velocity potential (Eq. 21.5)
$u, v, w$	Cartesian velocity components	$\psi$	stream function
$u', v'$	perturbation velocity components from a condition of uniform, parallel flow at speed $c^*$	$( )_{\infty}$	signifies free-stream conditions
$u'', v''$	perturbation velocity components from a condition of uniform, parallel flow at speed $U_{\infty}$	$( )^*$	signifies sonic conditions
$\tilde{u}, \tilde{v}$	$u'/c^*$ and $v'/c^*$ , respectively	$( )_1$	signifies state upstream of shock or at beginning of simple-wave expansion
$U_{\infty}$	free-stream velocity	$( )_2$	signifies state downstream of shock
$V$	velocity	$( )_0$	signifies isentropic stagnation state
$V_{\max}$	maximum velocity for adiabatic flow	$( )_s$	signifies sonic point on wall
		$( )_{sh}$	refers to oblique shock
		$( )_{P-M}$	refers to simple-wave expansion

## 21.2. The Transonic Similarity Law

The Prandtl-Glauert rule for subsonic flow and the Ackeret small-perturbation method for supersonic flow, both of which are based on Eq. 21.1, may be thought of as similarity rules connecting the performance of affinely related thin profiles at different free-stream Mach Numbers. Although these rules fail near Mach Number unity because of the invalidity of Eq. 21.1, it is possible to construct analogous rules

for transonic flow, based on the premise that all velocities are in the neighborhood of the critical velocity. The *transonic similarity law* which is thus found is, like the hypersonic similarity law, of considerable use (i) for extrapolation of experimental data beyond the range of measured variables, and (ii) for reaching generalizations concerning the flow behavior at transonic speeds.

**General Remarks Concerning Similarity Laws.** All the similarity laws outlined in this book, namely, those for subsonic, transonic, supersonic, and hypersonic flows with small perturbations, may be considered as forms of dimensional analysis.

In its most general form dimensional analysis constitutes a recognition that when two different physical experiments are described by identical differential equations and that when the experiments are such as to give identical boundary conditions for the differential equations, then the solutions of the equations must be identical.

Consider, for example, the well-known case of incompressible, steady flow under the action of viscous stresses, pressure gradients, and inertia effects. By rearranging the governing Navier-Stokes equations so that the variables are dimensionless lengths (based on some reference length), dimensionless velocity components (based on some reference velocity), and dimensionless pressures (based on the reference velocity and on the fluid density), it is found that the differential equations are identical in form for different flows provided that the latter have equal Reynolds Numbers. If, in addition, the different flows considered have boundaries which are geometrically similar, the boundary conditions (expressed in the dimensionless variables) are identical. Accordingly, the solutions of the equations are identical for the flows past geometrically similar bodies at the same Reynolds Number, and, therefore, the dimensionless velocity distribution, dimensionless pressure distribution, and dimensionless shear stress distribution are respectively equal for the flows considered.

The type of similitude discussed in the foregoing paragraph is one based on geometrically similar models. The several similarity rules discussed in this book for inviscid, compressible flow illustrate a form of similitude which is sometimes called the *theory of distorted models*. That is, the similarity laws relate flows at different Mach Numbers past bodies which are not geometrically similar but which are rather affinely related by means of lateral contractions or elongations. The similarity laws take such a form because the differential equations and boundary conditions can be made identical for flows with different Mach Numbers only when the physical boundaries are related by certain stretching factors.

Spreiter<sup>(23)</sup> has formulated a generalized version of the transonic rule

which shows that, properly interpreted, it includes the similarity rules for subsonic and supersonic (but not hypersonic) flow.

We shall now derive in detail the transonic similarity law for two-dimensional flow past thin profiles. Subsequently we shall briefly consider axi-symmetric flow and flow past wings of finite span.

**Approximate Differential Equation for Transonic Flow.** Two-dimensional, steady, irrotational, isentropic motions may be described by the exact differential equation (Eqs. 9.34 and 9.35)

$$(c^2 - u^2) \frac{\partial u}{\partial x} - 2uv \frac{\partial u}{\partial y} + (c^2 - v^2) \frac{\partial v}{\partial y} = 0 \quad (21.2a)$$

$$c^2 = \frac{k+1}{2} c^{*2} - \frac{k-1}{2} (u^2 + v^2) \quad (21.2b)$$

where  $u$  and  $v$  are the respective velocity components along  $x$  and  $y$ .

**ASSUMPTIONS.** We suppose that we are dealing with thin profiles placed in an otherwise uniform stream at transonic speed. This leads us to assume (i) that there are only small perturbations from the free-stream velocity  $U_\infty$ , and (ii) that the fluid velocity is near the local sound velocity, and, therefore, near the critical sound velocity. Mathematically, these assumptions may be stated in the forms

$$(c^* - U_\infty)/c^* \ll 1$$

$$(c^* - u)/c^* \ll 1$$

$$v/c^* \ll 1$$

**PERTURBATIONS ABOUT THE CRITICAL VELOCITY.** These assumptions suggest that for transonic flow the appropriate perturbation velocity is  $(c^* - u)$ , i.e., the deviation from the critical speed. In subsonic and supersonic flow, it may be recalled parenthetically, the appropriate perturbation velocity was the deviation from  $U_\infty$ . We therefore develop the coefficients of Eq. 21.2a in terms of  $(c^* - u)$ , etc., employing Eq. 21.2b for  $c^2$ . Dropping quadratic terms of quantities small compared with unity, according to the assumptions stated above, we obtain

$$\begin{aligned} c^2 - u^2 &= \frac{k+1}{2} c^{*2} - \frac{k-1}{2} (u^2 + v^2) - u^2 \\ &= \frac{k+1}{2} (c^{*2} - u^2) - \frac{k-1}{2} v^2 \\ &= \frac{k+1}{2} (c^* - u)(-c^* + u + 2c^*) - \frac{k-1}{2} v^2 \\ &= -\frac{k+1}{2} (c^* - u)^2 + (k+1)(c^* - u)c^* - \frac{k-1}{2} v^2 \\ &\cong (k+1)c^*(c^* - u) \end{aligned} \quad (21.3a)$$

$$uv = -v(c^* - u) + vc^* \cong vc^* \quad (21.3b)$$

$$\begin{aligned} c^2 - v^2 &= \frac{k+1}{2} c^{*2} - \frac{k-1}{2} (u^2 + v^2) - v^2 \\ &= \frac{k-1}{2} (c^{*2} - u^2) - \frac{k+1}{2} v^2 + c^{*2} \\ &\cong c^{*2} + (k-1)c^*(c^* - u) \end{aligned} \quad (21.3c)$$

Substituting these into Eq. 21.2a, we get the approximate equation

$$-(k+1)(u - c^*) \frac{\partial u}{\partial x} - 2v \frac{\partial u}{\partial y} + c^* \frac{\partial v}{\partial y} = 0 \quad (21.4a)$$

where the term  $(k-1)c^*(c^* - u)(\partial v/\partial y)$  has been neglected in comparison with the remaining terms because, in transonic flow, the small lateral decay of disturbances causes  $\partial v/\partial y$  to be of smaller order than  $\partial u/\partial x$  (see, for example, Eq. 21.1).

**PERTURBATION VELOCITY POTENTIAL.** We now introduce the total velocity potential  $\Phi$  as the sum of two parts: (i)  $c^*x$ , representing a uniform parallel flow at the critical speed, and (ii)  $(1 - M_\infty^*)\varphi$ , representing the perturbation potential:

$$\Phi = c^*x + (1 - M_\infty^*)\varphi; \quad M_\infty^* \equiv U_\infty/c^* \quad (21.5)$$

Then

$$u = \partial\Phi/\partial x = c^* + (1 - M_\infty^*)(\partial\varphi/\partial x) \equiv c^* + u' \quad (21.6a)$$

$$v = \partial\Phi/\partial y = (1 - M_\infty^*)(\partial\varphi/\partial y) \equiv v', \quad \text{etc.} \quad (21.6b)$$

Substituting these derivatives into Eq. 21.4a, we obtain

$$-(k+1)(1 - M_\infty^*) \frac{\partial\varphi}{\partial x} \frac{\partial^2\varphi}{\partial x^2} - 2(1 - M_\infty^*) \frac{\partial\varphi}{\partial y} \frac{\partial^2\varphi}{\partial x \partial y} + c^* \frac{\partial^2\varphi}{\partial y^2} = 0 \quad (21.7)$$

**BOUNDARY CONDITIONS.** The boundary condition at infinity requires that the velocity components there be  $u = U_\infty$  and  $v = 0$ . From Eqs. 21.6, therefore,

$$\text{at } x = y = \pm\infty: \quad \begin{cases} \frac{\partial\varphi}{\partial x} = -c^* \\ \frac{\partial\varphi}{\partial y} = 0 \end{cases} \quad (21.8)$$

Referring to Fig. 21.2, let  $l$  and  $t$  be respectively the chord and maximum thickness of the profile, and let  $\delta \equiv t/l$  be the thickness ratio. Also, let  $h$  represent the ratio of the local surface slope to the thickness ratio. Then the local slope of the surface may be expressed as

$$(dy/dx)_{\text{surf}} = \delta h$$

where it is understood that  $h$  is a nondimensional function of the dimensionless abscissa  $x/l$ . The boundary condition at the surface of the body, assuming that the flow follows the contour, is, within the assumption of small perturbations,

$$\frac{v}{u} = \frac{v}{c^*} = \delta h$$

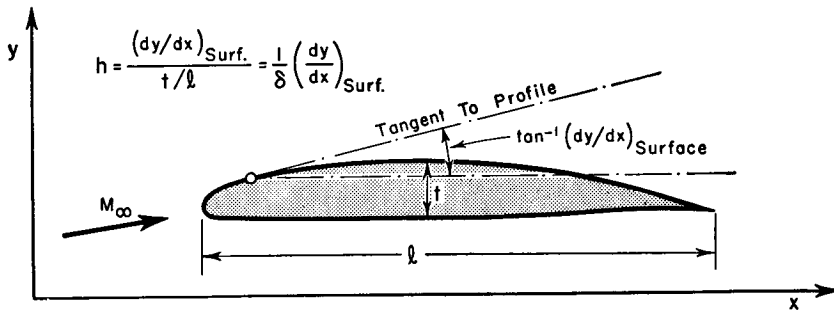


FIG. 21.2. Nomenclature.

Then, using Eq. 21.6b, and noting that this boundary condition may be evaluated on the  $x$ -axis because the profile is assumed very thin (this approximation is appraised later), we may write

$$\text{at } \left\{ \begin{array}{l} y = 0 \\ 0 \leq x/l \leq 1 \end{array} \right\} : (1 - M_\infty) \frac{\partial \varphi}{\partial y} = c^* \delta h \quad (21.9)$$

**TRANSONIC DIFFERENTIAL EQUATION.** Employing the nomenclature of Eqs. 21.6, where the primed quantities signify perturbations from a uniform, parallel flow with speed  $c^*$ , Eq. 21.4a may alternatively be written in the form

$$(k + 1)u' \frac{\partial u'}{\partial x} + 2v' \frac{\partial u'}{\partial y} - c^* \frac{\partial v'}{\partial y} = 0$$

Now  $u'$  and  $v'$  are of the same order and are very much less than  $c^*$ . However, because the lateral decay of disturbances is so small at transonic speeds,  $\partial v'/\partial y$  and  $\partial u'/\partial y$  are considerably smaller than  $\partial u'/\partial x$ . Then, considering the orders of magnitudes of the products in this equation, it is seen that the second term is negligible compared with the remaining terms. Therefore the differential equation for transonic flow with small perturbations may be written as

$$(k + 1)u' \frac{\partial u'}{\partial x} - c^* \frac{\partial v'}{\partial y} = 0 \quad (21.4b)$$

This equation, which is seen to be essentially nonlinear, is justified in a different manner in connection with Eq. 21.15a.

**Derivation of Similarity Conditions.** Despite the relative simplicity of Eq. 21.7, explicit solutions cannot easily be obtained. As in the case of subsonic flow, supersonic flow, and hypersonic flow, therefore, we attempt to extract information from the equations of motion without actually solving them. This is done by transforming the governing differential equation in such a way as to point to similarity laws. Such a similarity law gives the solution for a whole class of related bodies at related conditions if the solution for only one of these bodies at one set of conditions is known.

**TRANSFORMED VARIABLES.** We now seek a similarity rule which will relate the pressure distributions on affinely related profiles of different thickness ratios and operating at different transonic Mach Numbers. That is, we try to find a form of the equations which will involve only a single parameter of the thickness ratio and Mach Number, rather than these two variables separately.

Accordingly, we introduce the nondimensional coordinates

$$\xi \equiv x/l \quad (21.10a)$$

$$\eta \equiv (y/l)(k + 1)^{-m} \delta^{-n} \quad (21.10b)$$

where  $m$  and  $n$  are exponents to be determined in such a way that both the governing differential equation and its boundary conditions contain the same combined parameter of thickness ratio and  $M_\infty^*$ . We further suppose that the perturbation potential  $\varphi$  depends on the dimensionless coordinates according to the nondimensional form

$$\varphi = lc^* f(\xi, \eta) \quad (21.11)$$

**TRANSFORMED DIFFERENTIAL EQUATION.** Now we transform from the  $x, y$ -system of coordinates to the  $\xi, \eta$ -system by means of the usual mathematical forms:

$$\frac{\partial \varphi}{\partial x} = \frac{\partial \varphi}{\partial \xi} \frac{d\xi}{dx} = c^* \frac{\partial f}{\partial \xi}$$

$$\frac{\partial}{\partial x} \frac{\partial \varphi}{\partial x} = \left( \frac{\partial}{\partial \xi} \frac{\partial \varphi}{\partial x} \right) \frac{d\xi}{dx} = \frac{c^*}{l} \frac{\partial^2 f}{\partial \xi^2}$$

$$\frac{\partial}{\partial y} \frac{\partial \varphi}{\partial x} = \left( \frac{\partial}{\partial \eta} \frac{\partial \varphi}{\partial x} \right) \frac{d\eta}{dy} = \frac{c^*}{l(k + 1)^m \delta^n} \frac{\partial^2 f}{\partial \eta \partial \xi}$$

$$\frac{\partial \varphi}{\partial y} = \frac{\partial \varphi}{\partial \eta} \frac{d\eta}{dy} = \frac{c^*}{(k + 1)^m \delta^n} \frac{\partial f}{\partial \eta}$$

$$\frac{\partial}{\partial y} \frac{\partial \varphi}{\partial y} = \left( \frac{\partial}{\partial \eta} \frac{\partial \varphi}{\partial y} \right) \frac{d\eta}{dy} = \frac{c^*}{l(k + 1)^{2m} \delta^{2n}} \frac{\partial^2 f}{\partial \eta^2}$$

Substituting these into Eq. 21.7, and simplifying, we obtain

$$-(k+1)^{2m+1}(1-M_\infty^*)\delta^{2n}\frac{\partial f}{\partial \xi}\frac{\partial^2 f}{\partial \xi^2} + \frac{\partial^2 f}{\partial \eta^2} = 2(1-M_\infty^*)\frac{\partial f}{\partial \eta}\frac{\partial^2 f}{\partial \eta \partial \xi} \quad (21.12)$$

TRANSFORMED BOUNDARY CONDITIONS. Applying the transformation relations to the boundary conditions of Eqs. 21.8 and 21.9, we obtain:

$$\text{at } \xi = \eta = \pm\infty: \begin{cases} \frac{\partial f}{\partial \xi} = -1 \\ \frac{\partial f}{\partial \eta} = 0 \end{cases} \quad (21.13a)$$

$$\text{at } \eta = 0; 0 \leq \xi \leq 1: \frac{\partial f}{\partial \eta} = \frac{(k+1)^m \delta^{n+1}}{1-M_\infty^*} [h(\xi)] \quad (21.13b)$$

KÁRMÁN TRANSONIC SIMILARITY PARAMETER. Now, comparing the first term of Eq. 21.12 with Eq. 21.13b, we see that a parameter common to the differential equation and the boundary condition, and involving  $(1-M_\infty^*)$ ,  $(k+1)$ , and  $\delta$ , may be constructed if we set

$$2m+1 = -m; \quad m = -1/3$$

$$2n = -(n+1); \quad n = -1/3$$

The parameter so defined is the *Kármán transonic similarity parameter*, and is denoted by  $2K$ :

$$2K \equiv \left(\frac{k+1}{2}\right)^{1/3} (1-M_\infty^*) \delta^{-2/3} \quad (21.14a)$$

Equation 21.10b must now be written as

$$\eta = (y/l)[(k+1)\delta]^{1/3} \quad (21.14b)$$

The differential equation, Eq. 21.12, and the boundary conditions, Eqs. 21.13, when written in terms of  $K$  have the forms

$$-2K \frac{\partial f}{\partial \xi} \frac{\partial^2 f}{\partial \xi^2} + \frac{1}{(2)^{1/3}} \frac{\partial^2 f}{\partial \eta^2} = 4K(k+1)^{-1/3} \delta^{2/3} \frac{\partial f}{\partial \eta} \frac{\partial^2 f}{\partial \eta \partial \xi} \quad (21.15a)$$

$$\text{at } \xi = \eta = \pm\infty: \quad \frac{\partial f}{\partial \xi} = -1; \quad \frac{\partial f}{\partial \eta} = 0 \quad (21.16a)$$

$$\text{at } \eta = 0; 0 \leq \xi \leq 1: \quad 2K \frac{\partial f}{\partial \eta} = \frac{1}{(2)^{1/3}} h(\xi) \quad (21.16b)$$

ORDER OF MAGNITUDE OF  $K$ . In order to formulate a transonic similarity rule, it is necessary to assume that  $\delta$  and  $M_\infty^*$  are of such

magnitudes that the parameter  $K$  is not greater in order of magnitude than unity. This assumption is not very stringent inasmuch as for most practical cases it follows from the assumptions previously made. Since, for thin profiles,  $\delta$  is at least one order of magnitude less than unity, the last term of Eq. 21.15a may be ignored compared with the first two terms. Accordingly, the equation may be written as

$$-(2)^{4/3}K \frac{\partial f}{\partial \xi} \frac{\partial^2 f}{\partial \xi^2} + \frac{\partial^2 f}{\partial \eta^2} = 0 \quad (21.15b)$$

provided that  $K$  is not large compared with unity.

TRANSONIC SIMILARITY LAW. Equations 21.15b and 21.16 do not contain  $M^*$  and  $\delta$  explicitly, but rather only in terms of the *transonic similarity parameter*,  $K$ . Inspection of these equations leads to the transonic similarity law:

If a series of affine bodies having the same dimensionless thickness distribution  $h(\xi)$  are placed in flows of different free-stream Mach Number and different values of  $k$ , such that the parameter  $K$  remains constant, then the flow patterns are similar in the sense that the same function  $f(\xi, \eta)$  describes the several flows. For affinely related profiles, it is to be understood that the camber and the angle of incidence are adjusted in proportion to  $\delta$ .

ALTERNATE FORM OF TRANSONIC SIMILARITY PARAMETER.<sup>†</sup> Thus far  $K$  has been expressed in terms of  $M_\infty^*$ . For a more useful expression in terms of  $M_\infty$ , we form

$$\begin{aligned} 1 - M_\infty^* &= 1 - \frac{U_\infty}{c^*} = 1 - \frac{U_\infty c_\infty}{c_\infty c^*} \\ &= 1 - M_\infty \frac{c_\infty}{c^*} = (1 - M_\infty) \frac{c_\infty}{c^*} + \left(1 - \frac{c_\infty}{c^*}\right) \end{aligned}$$

<sup>†</sup>Within the approximations of transonic theory, several forms of the transonic similarity law may be devised, all of them being equivalent at  $M_\infty = 1$  but differing somewhat at Mach Numbers above and below unity. Spreiter<sup>(25)</sup> has shown that the most satisfactory form, from the point of view of agreeing with experiments and with exact theoretical solutions, is slightly different from the one presented in this chapter. In Spreiter's formulation, the transonic similarity parameter, instead of Eq. 21.17, is given by

$$K \equiv \frac{1 - M_\infty^2}{2 \left[ \frac{k+1}{2} M_\infty^2 \delta \right]^{2/3}}$$

and the similarity laws are identical with Eqs. 21.19, 21.20, 21.21, 21.22, 21.23, 21.24, 21.25, 21.30, 21.31, and 21.32, provided that the term  $(k+1)$  is everywhere replaced by  $(k+1)M_\infty^2$ .

Then, using Eq. 21.2b, we obtain  $c_\infty/c^*$  in terms of  $(M_\infty - 1)$ :

$$\begin{aligned} c_\infty^2 &= \frac{k+1}{2} c^{*2} - \frac{k-1}{2} U_\infty^2 \\ \frac{c_\infty}{c^*} &= \sqrt{\frac{\frac{k+1}{2}}{1 + \frac{k-1}{2} M_\infty^2}} \\ &= \sqrt{\frac{1}{1 + 2 \frac{k-1}{k+1} (M_\infty - 1) + \frac{k-1}{k+1} (M_\infty - 1)^2}} \end{aligned}$$

Using the binomial theorem, this is expanded in terms of  $(M_\infty - 1)$ . Retaining only first-order terms, we get

$$\frac{c_\infty}{c^*} \cong 1 + \frac{k-1}{k+1} (1 - M_\infty)$$

Substituting this into the previous expression, we obtain, if terms up to  $(1 - M_\infty)$  are retained,

$$1 - M_\infty^* \cong \frac{2}{k+1} (1 - M_\infty)$$

Therefore the transonic similarity parameter (Eq. 21.14a) may be written as

$$\kappa \equiv \left[ \frac{1 - M_\infty}{\left( \frac{k+1}{2} \right) \delta} \right]^{2/3} \cong \frac{1 - M_\infty^2}{2 \left[ \left( \frac{k+1}{2} \right) \delta \right]^{2/3}} \quad (21.17)$$

Note that this parameter includes not only the effects of  $M_\infty$  and  $\delta$ , as originally intended, but also the effect of the specific-heat ratio  $k$ .

**Force Coefficients.** Without actually obtaining solutions to Eq. 21.15b, several useful conclusions may be drawn concerning the forces on airfoils in the transonic range.

**PRESSURE COEFFICIENT.** With the assumptions of small perturbations and of transonic flow, the pressure coefficient may be written as

$$C_p = \frac{p - p_\infty}{\frac{1}{2} \rho_\infty U_\infty^2} \cong -2 \frac{(u - U_\infty)}{U_\infty} \cong -2 \left( \frac{u}{c^*} \frac{c^*}{U_\infty} - 1 \right)$$

We have previously found that

$$\frac{u}{c^*} = \frac{1}{c^*} \left[ c^* + (1 - M_\infty^*) \frac{\partial \varphi}{\partial x} \right] = 1 + (1 - M_\infty^*) \frac{\partial f}{\partial \xi}$$

Noting that  $U_\infty/c^* \equiv M_\infty^*$ , and that  $M_\infty^* \cong 1$ , we obtain

$$C_p \cong -2(1 - M_\infty^*) \frac{\partial f}{\partial \xi} = -\frac{4}{k+1} (1 - M_\infty) \frac{\partial f}{\partial \xi} \quad (21.18)$$

The solution  $f(\xi, \eta)$  to the governing differential relations, Eqs. 21.15b and 21.16, depends only on  $h$  and  $\kappa$ . That is, it depends only on the thickness distribution of the particular family of affinely related profiles under consideration and on the value of the transonic similarity parameter  $\kappa$  under consideration. The derivative  $\partial f/\partial \xi$  therefore depends only on the profile shape, on  $\kappa$ , and on the dimensionless coordinates  $\xi, \eta$  of the point considered. The pressure coefficient may, therefore, be expressed implicitly as

$$C_p = \frac{1 - M_\infty}{(k+1)/2} \varphi(\kappa, \xi, \eta) = \frac{\delta^{2/3}}{[(k+1)/2]^{1/3}} \kappa \varphi(\kappa, \xi, \eta) \quad (21.19)$$

where  $\varphi$  is a function only of the arguments  $\kappa, \xi, \eta$ , and the form of the function  $\varphi$  is determined by the dimensionless thickness distribution of the family of profiles.

**EXAMPLE OF TRANSONIC SIMILARITY RULE.** To illustrate the meaning of Eq. 21.19, suppose that a profile of 5% thickness has a peak negative pressure coefficient of 0.3 at  $M_\infty = 0.95$ . Then, at  $M_\infty = 0.90$ , an affinely-related profile with  $\delta = 0.141$  would be transonically similar, inasmuch as  $\kappa$  is then the same for both profiles. From Eq. 21.19 it follows further that the function  $\varphi$  has the same numerical magnitude for both profiles, whence it is concluded that the peak negative pressure coefficient of the second profile is 0.6.

**LIFT COEFFICIENT.** The lift coefficient is found by integrating the vertical component of the pressure coefficient around the contour of the profile. With the help of Eq. 21.19, and assuming the profile to be very thin, we may write

$$\begin{aligned} C_L &= \frac{1}{l} \oint C_p dx = \oint C_p d\xi = \frac{\delta^{2/3}}{[(k+1)/2]^{1/3}} \mathcal{L}(\kappa) \\ &= \frac{1 - M_\infty}{(k+1)/2} \frac{\mathcal{L}(\kappa)}{\kappa} \end{aligned} \quad (21.20)$$

**MOMENT COEFFICIENT.** Similarly, the moment coefficient is given approximately by

$$\begin{aligned} C_m &= \frac{1}{l^2} \oint C_p x dx = \oint C_p \xi d\xi = \frac{\delta^{2/3}}{[(k+1)/2]^{1/3}} \mathcal{M}(\kappa) \\ &= \frac{1 - M_\infty}{(k+1)/2} \frac{\mathcal{M}(\kappa)}{\kappa} \end{aligned} \quad (21.21)$$

**PRESSURE DRAG COEFFICIENT.** The pressure drag coefficient is found by integrating the horizontal component of the pressure coefficient around the contour of the airfoil. We may therefore write, approximately,

$$\begin{aligned} C_D &= \frac{1}{l} \oint C_p dy = \frac{1}{l} \oint C_p \left( \frac{dy}{dx} \right)_{\text{surf}} dx = \oint C_p \delta h d\xi \\ &= \frac{\delta^{5/3}}{[(k+1)/2]^{1/3}} \mathfrak{D}(K) = \frac{(1 - M_\infty)^{5/2}}{[(k+1)/2]^2} \frac{\mathfrak{D}(K)}{K^{5/2}} \end{aligned} \quad (21.22)$$

In all these expressions the functions  $\mathfrak{L}$ ,  $\mathfrak{M}$ , and  $\mathfrak{D}$  are functions only of the parameter  $K$  and of the dimensionless thickness distribution  $h(\xi)$  of the family of profiles.

**FLOW AT  $M_\infty = 1$ .** When  $M_\infty = 1$ , the parameter  $K$  is zero irrespective of the thickness ratio. Hence the functions  $\mathfrak{L}$ ,  $\mathfrak{M}$ , and  $\mathfrak{D}$  depend on the thickness distribution but not on the thickness ratio. Therefore it follows that at Mach Number unity the lift and moment coefficients of affinely similar profiles vary as  $\delta^{2/3}$ , whereas the pressure drag coefficient varies as  $\delta^{5/3}$ . Thus the drag-lift ratio at the sonic speed is proportional to  $\delta$ . The importance of using thin profiles for transonic speeds is therefore obvious.

**Axially Symmetric Flow.** By means of an analysis similar to that for plane flows <sup>(1)</sup> a transonic similarity law may be derived for such axi-symmetric flows as that past a projectile or fuselage at zero yaw.

The similarity parameter for this case is

$$K' \equiv 2 \frac{1 - M_\infty}{(k+1)\delta^2} \quad (21.23)$$

and the pressure coefficient and pressure drag coefficient are, using notation similar to that employed previously, given implicitly by

$$C_p = \delta^2 \mathfrak{P}(K', \xi, \eta) = \frac{1 - M_\infty}{(k+1)/2} \frac{\mathfrak{P}(K', \xi, \eta)}{K'} \quad (21.24)$$

$$C_D = \delta^2 \mathfrak{D}(K') = \frac{1 - M_\infty}{(k+1)/2} \frac{\mathfrak{D}(K')}{K'} \quad (21.25)$$

At Mach Number unity, where  $K = 0$  irrespective of the thickness ratio, it is seen that the pressure drag coefficient varies as the square of the thickness ratio. For affine bodies of fixed length, the total drag then varies as the fourth power of the maximum diameter, thus emphasizing the importance of slenderness in order to avoid excessive drag.

**Wings of Finite Span.** Let us consider now the transonic flow past affine wings of finite span, with chord  $l$ , thickness  $t$ , and span  $b$ . The

span lies in the  $z$ -direction. Then the dimensionless coordinates corresponding to Eq. 21.10 are

$$\xi = x/l; \quad \eta = \frac{y}{l} (k+1)^{1/3} \delta^{1/3}; \quad \zeta = \frac{z}{l} (k+1)^{1/3} \delta^{1/3}$$

where the exponents  $1/3$  are entered immediately because of the previous results for plane flow. The perturbation velocity potential takes the form

$$\varphi = lc^* f(\xi, \eta, \zeta)$$

and Eq. 21.15b, with the inclusion of the third dimension, becomes

$$-(2)^{4/3} K \frac{\partial f}{\partial \xi} \frac{\partial^2 f}{\partial \xi^2} + \frac{\partial^2 f}{\partial \eta^2} + \frac{\partial^2 f}{\partial \zeta^2} = 0$$

The boundary conditions are the same as for plane flow, but the slope function of course depends not only on  $\xi$  but also on the spanwise location  $\zeta$ .

As a result of these considerations, which are entirely parallel to those for plane flow, it may be shown that the transonic similarity parameter is

$$K'' \equiv \frac{1 - M_\infty}{\left[ \frac{k+1}{2} \frac{\delta}{b} \right]^{2/3}} \quad (21.26)$$

In comparing pressure coefficients by means of Eq. 21.18, the profiles must be affinely related at corresponding values of  $\zeta$  and must at corresponding values of  $\xi$  have the camber and angle of incidence adjusted in proportion to the thickness ratio,  $\delta$ . In addition, the aspect ratios must also be related according to the coordinate transformation. This requires that

$$AR \sim \frac{b}{l} = \frac{b}{z} \cdot \frac{z}{l} = \frac{\zeta}{z/b} (k+1)^{-1/3} \delta^{-1/3}$$

from which it is seen that, in order to make comparisons at corresponding values of  $\zeta$  and  $z/b$ , the  $AR$  must be made proportional to  $[(k+1)\delta]^{-1/3}$ .

To state the transonic similarity rule concretely, let us suppose that there are two wings 1 and 2 with affinely related profiles and which operate at such Mach Numbers and incidence and with such aspect ratios that

$$\left. \begin{aligned} \frac{1 - M_{\infty 1}}{[(k_1 + 1)\delta_1]^{2/3}} &= \frac{1 - M_{\infty 2}}{[(k_2 + 1)\delta_2]^{2/3}} \\ \alpha_1/\delta_1 &= \alpha_2/\delta_2 \\ \frac{AR_1}{[(k_1 + 1)\delta_1]^{-1/3}} &= \frac{AR_2}{[(k_2 + 1)\delta_2]^{-1/3}} \end{aligned} \right\} \quad (21.27)$$

Then it follows from the similarity law that, at corresponding points,

$$\frac{C_{p1}}{C_{p2}} = \left( \frac{\delta_1}{\delta_2} \right)^{2/3} \left( \frac{k_2 + 1}{k_1 + 1} \right)^{1/3} = \frac{1 - M_\infty k_2 + 1}{1 - M_\infty k_1 + 1} \quad (21.28)$$

This rule may be stated succinctly as

$$\begin{aligned} [C_p]_{\alpha/\delta; R(k+1)^{1/3}\delta^{1/3}} &= \frac{K'' \delta^{2/3}}{(k+1)^{1/3}} \mathcal{P}(K'', \xi, \eta, \zeta, z/b) \\ &= \frac{1 - M_\infty}{k+1} \mathcal{P}(K'', \xi, \eta, \zeta, z/b) \end{aligned} \quad (21.29)$$

Integrating the pressure coefficient over the surface of the wing, and assuming that the surface pressure coefficient for thin profiles may be evaluated at  $\eta = 0$ , it may be shown that the force coefficients of transonically similar wings are expressible as

$$[C_L]_{\alpha/\delta; R(k+1)^{1/3}\delta^{1/3}} = \frac{\delta^{2/3}}{(k+1)^{1/3}} \mathcal{L}(K'') = \frac{1 - M_\infty}{k+1} \frac{\mathcal{L}(K'')}{K''} \quad (21.30)$$

$$[C_M]_{\alpha/\delta; R(k+1)^{1/3}\delta^{1/3}} = \frac{\delta^{2/3}}{(k+1)^{1/3}} \mathcal{M}(K'') = \frac{1 - M_\infty}{k+1} \frac{\mathcal{M}(K'')}{K''} \quad (21.31)$$

$$[C_D]_{\alpha/\delta; R(k+1)^{1/3}\delta^{1/3}} = \frac{\delta^{5/3}}{(k+1)^{1/3}} \mathcal{D}(K'') = \frac{(1 - M_\infty)^{5/2}}{(k+1)^2} \frac{\mathcal{D}(K'')}{(K'')^{5/2}} \quad (21.32)$$

**Flows with Rotation.** The transonic similarity law as derived above is based on the assumption of potential flow, thus barring from consideration regions having vorticity. It is well known, however, that shocks usually occur in transonic flow. On the other hand, these shocks are in regions of only slightly supersonic flow where the entropy change across the shock is negligible. Moreover, the shocks usually are only slightly curved, and, therefore, the variations in entropy from one streamline to the next are very small. The vorticity induced by curved shocks in transonic flow does not, therefore, significantly affect the transonic similarity laws.

Under certain conditions, on the other hand, the effects of viscosity, which are usually confined to thin boundary layers, may be greatly exaggerated by shock waves owing to the well-known phenomenon of interaction between shock waves and boundary layers. Whether or not the transonic similarity laws then hold depends in part, consequently, on the degree to which the character of the shock-boundary layer interaction is altered by the changes in  $M_\infty$  and  $\delta$  required for transonic similarity.

**Effect of Violating Boundary Conditions on Validity of Transonic Similarity Law.** The Prandtl-Glauert rule for subsonic flow, it may be recalled, is based on an approximate application of the boundary

condition at the profile; that is, it is applied not at the surface of the profile but rather on the  $x$ -axis. Historically, this at first led to fortuitously correct results for plane flow, but to quite erroneous results for axi-symmetric flow. The significance of this approximation was not explored until some twenty years after the statement of the rule.

**PLANE FLOW.** A similar approximation of the boundary condition underlies the transonic similarity law, and the question naturally arises to what degree this assumption is justified. This question has been investigated for plane flow <sup>(4)</sup> by an iteration procedure combining the features of the Prandtl-Glauert and Rayleigh-Janzen methods (Chapter 12), wherein the total velocity potential is expressed as a power series in a parameter which contains  $\delta$ ,  $M_\infty$  and  $k$ . Without going into details here, the significant results of this study may be stated as follows:

- (i) As  $\delta \rightarrow 0$  and  $M_\infty \rightarrow 1$  simultaneously, the exact solution to the flow may be expressed in terms of a series involving a single parameter, that parameter being the transonic similarity parameter  $K$ .
- (ii) A comparison of the exact with the approximate boundary condition shows that the approximation is justified for plane transonic flow.
- (iii) For transonic flow with small perturbations the limiting form of an exact solution of the governing differential equations is the same as the solution of the limiting form (Eq. 21.15b) of the differential equation. This conclusion leads to a comparatively convenient method of working out series solutions.

**Axi-SYMMETRIC FLOW.** A similar investigation for axi-symmetric transonic flow <sup>(5)</sup> led to the following results:

- (i) For regions of the flow field not close to the body, the similarity law of Eqs. 21.23 to 21.25 applies approximately.
- (ii) In the neighborhood of the body, a similarity law exists only if the body is extremely slender, and in this case involves a different similarity parameter, namely,

$$J \equiv \delta^2 \log [\sqrt{2} \delta (1 - M_\infty)]$$

### 21.3. Applications of the Transonic Similarity Law

We shall now consider several practical applications of the transonic similarity law.

**Oblique Shocks.** <sup>(3)</sup> All the oblique shock relations of Chapter 16 are valid so long as the approach flow is supersonic. However, for shocks with  $M_1$  nearly equal to unity, the transonic similarity law suggests that

the exact shock relations may be put into an explicit algebraic form which brings out clearly the way in which the physical variables depend upon each other.

**EXACT SHOCK RELATIONS.** For transonic flow through an oblique shock, with approach Mach Number  $M_1$  and turning angle  $\delta$ , a convenient and appropriate form of the similarity parameter defined by Eq. 21.17 is

$$K_{sh} \equiv \frac{1}{2} \frac{M_1^2 - 1}{\left[ \left( \frac{k+1}{2} \right) \delta \right]^{2/3}}; \quad K_{sh} \geq 0 \quad (21.33)$$

If  $\sigma$  is the shock angle, and subscripts 1 and 2 denote, respectively, conditions upstream of and downstream of the shock, the exact shock relations of Chapter 16 may be written as

$$\frac{p_2}{p_1} = \frac{2k}{k+1} M_1^2 \sin^2 \sigma - \frac{k-1}{k+1} \quad (21.34)$$

$$\frac{\tan(\sigma - \delta)}{\tan \sigma} = \frac{k-1}{k+1} + \frac{2}{k+1} \frac{1}{M_1^2 \sin^2 \sigma} \quad (21.35)$$

The pressure coefficient of the shock is defined as

$$C_p \equiv \frac{p_2 - p_1}{\frac{1}{2} \rho_1 V_1^2} = \frac{p_1}{\frac{1}{2} \rho_1 V_1^2} \left( \frac{p_2}{p_1} - 1 \right) = \frac{2}{k M_1^2} \left( \frac{p_2}{p_1} - 1 \right) \quad (21.36)$$

With Eqs. 21.34 and 21.36 it is possible to eliminate  $\sigma$  and  $p_2/p_1$  from Eq. 21.35. The latter may then be shown to be

$$\tan \delta \left( 1 - \frac{C_p}{2} \right) \sqrt{\frac{k+1}{4} C_p + \frac{1}{M_1^2}} = \frac{C_p}{2} \sqrt{1 - \frac{k+1}{4} C_p} - \frac{1}{M_1^2} \quad (21.37)$$

**TRANSONIC SIMILARITY FORM OF SHOCK RELATIONS.** We now attempt to modify this exact relation to an approximate form corresponding to the transonic similarity law. If such a form exists, then it may be written according to Eq. 21.19 as

$$C_p = \left( \frac{2}{k+1} \right)^{1/3} \delta^{2/3} \varphi_{sh}(K_{sh}) = \frac{M_1^2 - 1}{(k+1)K_{sh}} \varphi_{sh}(K_{sh}) \quad (21.38)$$

To find the function  $\varphi_{sh}(K_{sh})$  for the shock, we note first that, since  $M_1$  is near unity and since  $\delta$  is assumed small, Eq. 21.33 may be expressed approximately as the series

$$\frac{1}{M_1^2} = 1 - 2K_{sh} \left( \frac{k+1}{2} \delta \right)^{2/3} + \dots \quad (21.39)$$

Substituting  $C_p$  from Eq. 21.38 and  $1/M_1^2$  from Eq. 21.39 into Eq. 21.37, and approximating  $\tan \delta$  as  $\delta$ , the exact relation of Eq. 21.37

may be shown to have the following approximate form when only the lowest order terms are retained:

$$1 = \frac{\varphi_{sh}^2}{4} \left( 2K_{sh} - \frac{\varphi_{sh}}{2} \right) \quad (21.40)$$

The fact that  $M_1$ ,  $\delta$ , and  $k$  do not appear explicitly here indicates the validity of the concept of transonic similarity.

The character of the roots of this cubic equation may be shown to depend on the algebraic sign of the quantity

$$E = \frac{1}{4} - \frac{8}{27} K_{sh}^3$$

(i) *Positive Values of E.* If  $E$  is positive, there are two complex roots and one real root. The complex roots are physically meaningless, and the real root is negative. The latter corresponds to a rarefaction discontinuity, and may also be dismissed as physically impossible. Therefore, positive values of  $E$  are of no interest.

(ii) *Zero Value of E; Limiting Case of Attached Shock.* When  $E$  is zero, we obtain the minimum value of  $K_{sh}$  which is physically meaningful, namely

$$(K_{sh})_{min} = (27/32)^{1/3} = 0.945 \quad (21.41a)$$

There are three roots, of which two are identical, thus giving two distinct roots, of which only one is positive and thus physically possible:

$$(\varphi_{sh})_{\delta_{max}} = 2^{4/3} = 2.502 \quad (21.41b)$$

The minimum value of 0.945 for  $K_{sh}$  corresponds to the maximum value of  $\delta$  for a given  $M_1$  (or to a minimum value of  $M_1$  for a given  $\delta$ ) for which there is a solution to the oblique shock relations. It corresponds, therefore, to the limiting case of an *attached shock*. Thus we obtain the beautifully simple result that, for  $M_1$  near unity, and  $k = 1.4$ ,

$$\delta_{max} \cong 0.908(M_1 - 1)^{3/2} \quad (21.42)$$

(iii) *Negative Values of E.* For negative values of  $E$ , corresponding to values of  $K_{sh}$  greater than  $(K_{sh})_{min}$ , there are two physically meaningful roots, corresponding to the weak and strong shocks for given values of  $M_1$  and  $\delta$ . These roots are, respectively,

$$\varphi_{sh,w} = \left[ \sqrt{\frac{2}{3}} K_{sh} \cos \frac{\pi - \gamma}{3} \right]^{-1} \quad (21.43)$$

$$\varphi_{sh,s} = \left[ \sqrt{\frac{2}{3}} K_{sh} \cos \frac{\pi + \gamma}{3} \right]^{-1} \quad (21.44)$$

where

$$\cos \gamma = \sqrt{\frac{27}{32}} \frac{1}{K_{sh}^3} \quad (21.45)$$

It will be recalled that the *strong shock* is usually met with only when there are detached shock waves, and that the *weak shock* otherwise seems to occur in practice, except for confined flows in ducts.

An algebraic approximation to Eq. 21.43 is <sup>(3)</sup> given by

$$\varphi_{sh,w} = \sqrt{\frac{2}{K_{sh}}} + \frac{1}{4K_{sh}^2} + \frac{0.11048}{K_{sh}^{7/2}} + \frac{0.06250}{K_{sh}^3} + \dots \quad (21.46)$$

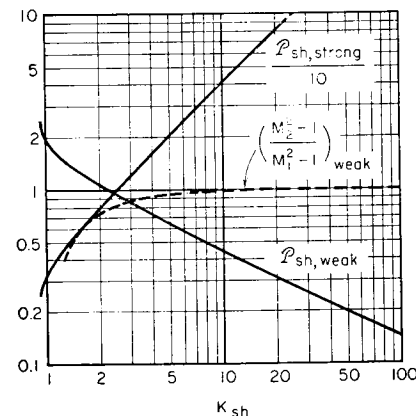


FIG. 21.3. Transonic similarity functions for oblique shock (after Tsien and Baron).

The function  $\varphi_{sh}(K_{sh})$  is plotted in Fig. 21.3 for both the weak and strong shock.

MACH NUMBER DOWNSTREAM OF SHOCK. In connection with the calculation of the flow past thin, sharp airfoils at slightly supersonic speeds, it is necessary to know the Mach Number after the shock. Since we are dealing with shocks for which  $(M_1 - 1)$  is small compared with unity, and since the entropy increase across the shock is of third order in  $(M_1 - 1)$ , no great error is involved in using the isentropic relations for this purpose. With this assumption the pressure ratio across the shock may be written as

$$\frac{p_2}{p_1} = \left[ \frac{1 + \frac{k-1}{2} M_1^2}{1 + \frac{k-1}{2} M_2^2} \right]^{\frac{k}{k-1}} = \left[ \frac{1 + \frac{k-1}{k+1} (M_1^2 - 1)}{1 + \frac{k-1}{k+1} (M_2^2 - 1)} \right]^{\frac{k}{k-1}}$$

Noting that both  $(M_1^2 - 1)$  and  $(M_2^2 - 1)$  are small compared with unity, this expression may be expanded by the binomial theorem and substituted into Eq. 21.36. Neglecting higher-order terms, we obtain

$$C_p = \frac{2}{k+1} (M_1^2 - 1) \left( 1 - \frac{M_2^2 - 1}{M_1^2 - 1} \right)$$

Using this to eliminate  $C_p$  from Eq. 21.38, we get the desired relation for  $M_2$ :

$$\frac{M_2^2 - 1}{M_1^2 - 1} = 1 - \frac{\varphi_{sh}}{2K_{sh}} \quad (21.47)$$

The curve of  $(M_2^2 - 1)/(M_1^2 - 1)$  in Fig. 21.3 is for a weak shock. It is calculated by combining Eq. 21.47 with Eqs. 21.43 and 21.45.

CONDITION OF SONIC FLOW DOWNSTREAM OF SHOCK. Eq. 21.47 allows us immediately to determine when the downstream flow is exactly sonic, for, if we set  $M_2 = 1$ , we get

$$\varphi_{sh}^* = 2K_{sh}^* \quad (21.48)$$

where the asterisk denotes sonic conditions downstream of the shock.

If Eq. 21.40 is divided by  $K_{sh}^3$ , there is obtained

$$\frac{1}{K_{sh}^3} = \left( \frac{\varphi_{sh}}{2K_{sh}} \right)^2 \left( 2 - \frac{\varphi_{sh}}{2K_{sh}} \right)$$

Combining this with Eq. 21.48, we obtain the interesting result that

$$K_{sh}^* = 1; \quad \varphi_{sh}^* = 2 \quad (21.49)$$

This result applies only to the weak shock, for with a strong shock  $M_2$  is always less than unity. Therefore we may say that, if  $K_{sh} < 1$ , the flow after a weak shock is subsonic; whereas, if  $K_{sh} > 1$ , the flow after a weak shock is supersonic.

Prandtl-Meyer Expansion. <sup>(3)</sup> Just as the oblique shock relations may be put into transonic similarity form, so may the exact relations for a simple-wave expansion be put into transonic similarity form when it is assumed that  $M$  is near unity and that the turning angles are small.

EXACT RELATIONS. Letting  $V$  denote the local velocity, and  $\theta$  the streamline direction, the relation between  $V$  and  $\theta$  in a simple-wave expansion (Chapter 15) is given by

$$\sqrt{M^2 - 1} dV = V d\theta$$

where  $d\theta$  is taken as always positive for an expansion. Eliminating  $dV$  by means of Euler's equation,

$$dp = -\rho V dV$$

we obtain

$$d\left(\frac{p}{p_1}\right) = -\left(\frac{\rho_1}{p_1}\right)\left(\frac{\rho}{\rho_1}\right) \frac{V^2}{\sqrt{M^2 - 1}} d\theta \quad (21.50)$$

where subscript 1 denotes conditions at the beginning of the turn. For a perfect gas, we may write

$$c_1^2 = kp_1/\rho_1; \quad \rho_1/p_1 = k/c_1^2 \quad (21.51)$$

The energy equation for adiabatic flow may be written in terms of  $c$  and  $V$ ,

$$c^2 + \frac{k-1}{2} V^2 = c_1^2 + \frac{k-1}{2} V_1^2$$

and, eliminating  $c^2$  by means of the isentropic relation between  $c^2$  and  $p$ , we may form

$$\frac{V^2}{c_1^2} = \frac{2}{k-1} \left[ 1 + \frac{k-1}{2} M^2 - \left( \frac{p}{p_1} \right)^{\frac{k-1}{k}} \right] \quad (21.52)$$

Noting further that

$$M^2 = \frac{V^2 c_1^2}{c_1^2 c^2} = \frac{V^2}{c_1^2} \left( \frac{p_1}{p} \right)^{\frac{k-1}{k}}$$

Eq. 21.52 may be put in the form

$$M^2 - 1 = \left( \frac{2}{k-1} + M_1^2 \right) \left( \frac{p_1}{p} \right)^{\frac{k-1}{k}} - \frac{k+1}{k-1} \quad (21.53)$$

The pressure coefficient of the turn is defined as

$$C_p = \frac{2}{kM_1^2} \left( \frac{p}{p_1} - 1 \right); \quad \therefore \quad \frac{p}{p_1} = 1 + \frac{kM_1^2}{2} C_p \quad (21.54)$$

Now, substituting Eqs. 21.51, 21.52, 21.53, and 21.54 into Eq. 21.50, and using the isentropic laws, we may arrive at the following exact differential relation connecting  $C_p$  and  $\theta$ :

$$\frac{dC_p}{d\theta} = \quad (21.55)$$

$$-\frac{2}{M_1^2} \frac{\left( 1 + \frac{kM_1^2}{2} C_p \right)^{\frac{1}{k}} \left[ \frac{2}{k-1} + M_1^2 - \frac{2}{k-1} \left( 1 + \frac{kM_1^2}{2} C_p \right)^{\frac{k-1}{k}} \right]}{\sqrt{\left( \frac{2}{k-1} + M_1^2 \right) \left( 1 + \frac{kM_1^2}{2} C_p \right)^{-\frac{k-1}{k}}}} - \frac{k+1}{k-1}$$

**TRANSONIC SIMILARITY FORM OF EXPANSION FORMULA.** Our next task is to find an approximate form of this equation fitting into the form of the transonic similarity relation. The latter is appropriately written for a simple-wave expansion as

$$C_p = \frac{\theta^{2/3}}{[(k+1)/2]^{1/3}} \Phi_{P-M}(K_{P-M}) = \frac{M_1^2 - 1}{k+1} \frac{\Phi_{P-M}}{K_{P-M}} \quad (21.56)$$

where

$$K_{P-M} \equiv \frac{M_1^2 - 1}{2 \left( \frac{k+1}{2} \theta \right)^{2/3}} \quad (21.57)$$

Expanding the right-hand terms of Eq. 21.55 in a power series of  $C_p$ , and retaining only the leading terms on the assumptions that both  $C_p$  and  $(M_1^2 - 1)$  are small compared with unity, it may be shown that

$$\frac{dC_p}{d\theta} \cong - \frac{2}{\sqrt{(M_1^2 - 1) \left( 1 - \frac{k+1}{M_1^2 - 1} \frac{C_p}{2} \right)}} \quad (21.58)$$

Next, using Eqs. 21.56 and 21.57, we form

$$\begin{aligned} \frac{dC_p}{d\theta} &= \frac{dC_p}{dK_{P-M}} \cdot \frac{dK_{P-M}}{d\theta} \\ &= \left[ \left( \frac{M_1^2 - 1}{k+1} \right) \frac{d}{dK_{P-M}} \left( \frac{\Phi_{P-M}}{K_{P-M}} \right) \right] \left[ \frac{M_1^2 - 1}{2 \left( \frac{k+1}{2} \right)^{2/3}} \left( -\frac{2}{3} \theta^{-5/3} \right) \right] \end{aligned}$$

Eliminating  $dC_p/d\theta$  by means of Eq. 21.58, and simplifying with the help of Eqs. 21.56 and 21.57, we get

$$\frac{1}{3} K_{P-M}^{5/2} \frac{d}{dK_{P-M}} \left( \frac{\Phi_{P-M}}{K_{P-M}} \right) = \frac{1}{\sqrt{2 - \Phi_{P-M}/K_{P-M}}} \quad (21.59)$$

This is an ordinary differential equation between  $\Phi_{P-M}$  and  $K_{P-M}$ , which, when integrated, yields

$$\left( 2 - \frac{\Phi_{P-M}}{K_{P-M}} \right)^{3/2} = \left( \frac{3}{K_{P-M}} \right)^{3/2} + B$$

The constant of integration,  $B$ , is evaluated by noting that when  $\theta = 0$ ,  $C_p$  is also zero since there is no turning of the stream. Correspondingly, when  $K_{P-M} = \infty$ ,  $\Phi_{P-M} = 0$ , whence  $B = (2)^{3/2}$ . Thus, we finally get

$$\Phi_{P-M} = 2K_{P-M} - [(2K_{P-M})^{3/2} + 3]^{2/3} \quad (21.60)$$

One case of special interest is a Prandtl-Meyer expansion beginning with  $M_1 = 1$ . Then, from Eq. 21.57,  $K_{P-M} = 0$ , and Eqs. 21.60 and 21.56 show that

$$(C_p)_{M_1=1} = - \frac{(3\theta)^{2/3}}{[(k+1)/2]^{1/3}} \quad (21.61)$$

This indicates that in transonic flow  $C_p$  is nonlinear with  $\theta$ , as contrasted with the linear result of the small-perturbation theory for supersonic flow ( $C_p = 2\theta/\sqrt{M_1^2 - 1}$ ). Note also that the latter relation would

indicate that  $C_p$  becomes infinite in the neighborhood of the sonic speed, whereas Eq. 21.61 proves that this is far from true.

The pressure function for Prandtl-Meyer flow, as given by Eq. 21.60, is plotted in Fig. 21.4.

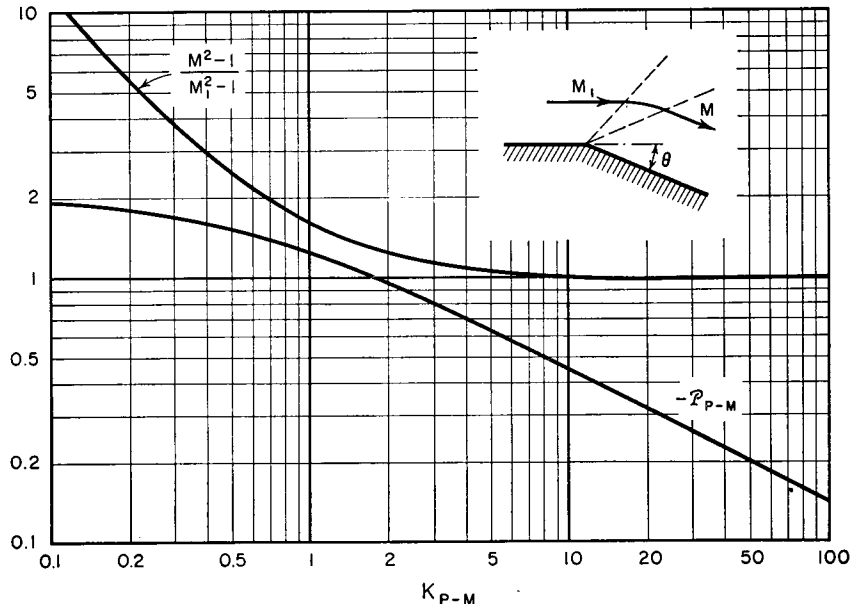


FIG. 21.4. Transonic similarity functions for simple-wave expansion (after Tsien and Baron).

By recalling that Eq. 21.47 for the Mach Number downstream of a shock was based on the assumption of isentropic flow, it is immediately evident that the same relation holds for Prandtl-Meyer flow. Then, with the help of Eq. 21.60, we get

$$\frac{M^2 - 1}{M_1^2 - 1} = 1 - \frac{\Phi_{P-M}}{K_{P-M}} = -1 + \left[ (2)^{3/2} + \frac{3}{K_{P-M}^{3/2}} \right]^{2/3} \quad (21.62)$$

This relation is also plotted in Fig. 21.4.

**Flat-Plate Airfoil.** <sup>(3)</sup> We may now easily find the aerodynamic characteristics of a flat plate at a small angle of incidence,  $\alpha$  (Fig. 21.5a). Applying the oblique shock theory to the lower surface and the Prandtl-Meyer theory to the upper surface, and noting that for this case

$$K = K_{sh} = K_{P-M} = \frac{M_\infty^2 - 1}{2 \left( \frac{k+1}{2} a \right)^{2/3}}$$

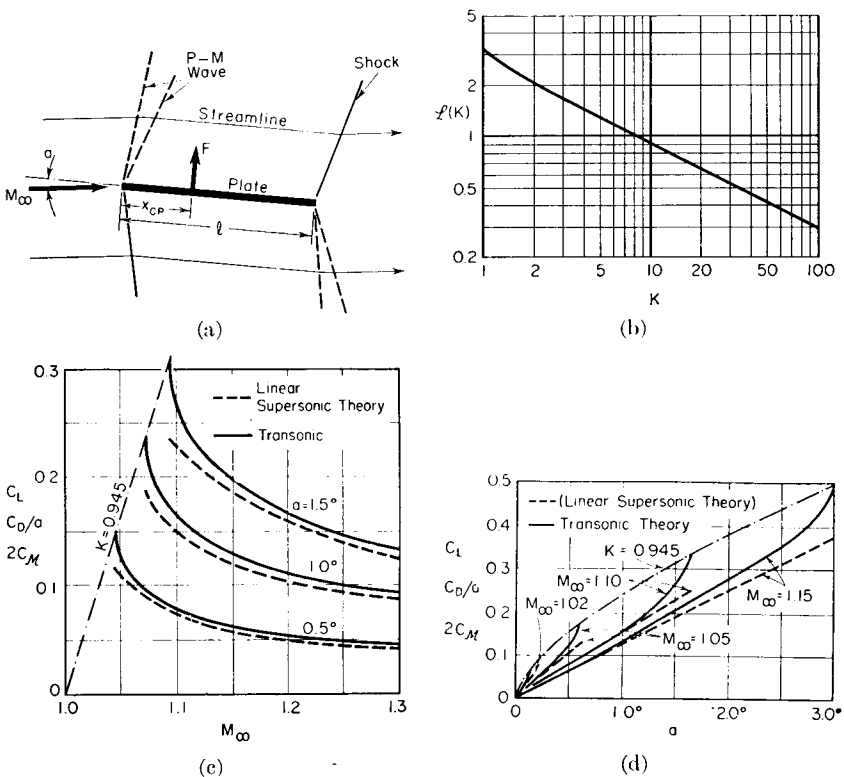


FIG. 21.5. Transonic flow over flat plate (after Tsien and Baron).

(a) Nomenclature.

(b) Lift function versus similarity parameter.

(c) Effect of Mach Number on force characteristics.

(d) Effect of angle of incidence on force characteristics.

we get

$$C_L = \frac{1}{l} \int_0^l (C_{p_{lower}} - C_{p_{upper}}) dx = \left( \frac{2}{k+1} \right)^{1/3} a^{2/3} \mathcal{L}(K) \quad (21.63)$$

$$C_D = \frac{1}{l} \int_0^l (C_{p_{lower}} - C_{p_{upper}}) \frac{dy}{dx} dx = \left( \frac{2}{k+1} \right)^{1/3} a^{5/3} \mathcal{L}(K) \quad (21.64)$$

$$C_M = \frac{1}{l^2} \int_0^l (C_{p_{lower}} - C_{p_{upper}}) x dx = \left( \frac{2}{k+1} \right)^{1/3} a^{2/3} \frac{\mathcal{L}(K)}{2} \quad (21.65)$$

where

$$\mathcal{L}(K) \equiv \Phi_{sh} - \Phi_{P-M} \quad (21.66)$$

The function  $\mathcal{L}(K)$  in Eq. 21.66 is evaluated by means of Figs. 21.3 and 21.4, and is plotted in Fig. 21.5b, thus giving a generalized representation of the force coefficients. To give a better picture of the

aerodynamic characteristics, the curve of Fig. 21.5b is used together with Eqs. 21.63 to 21.65 for constructing a chart of  $C_L$  versus  $M_\infty$  at constant incidence (Fig. 21.5c) and a chart of  $C_L$  versus  $\alpha$  at constant Mach Number (Fig. 21.5d). For comparative purposes, these charts show also the results of the Ackeret linear theory. It is seen that for very small incidence the lift-curve slope agrees well with the linear theory. As the incidence increases, however, the lift-curve slope does not remain constant but instead increases very rapidly, and the pre-

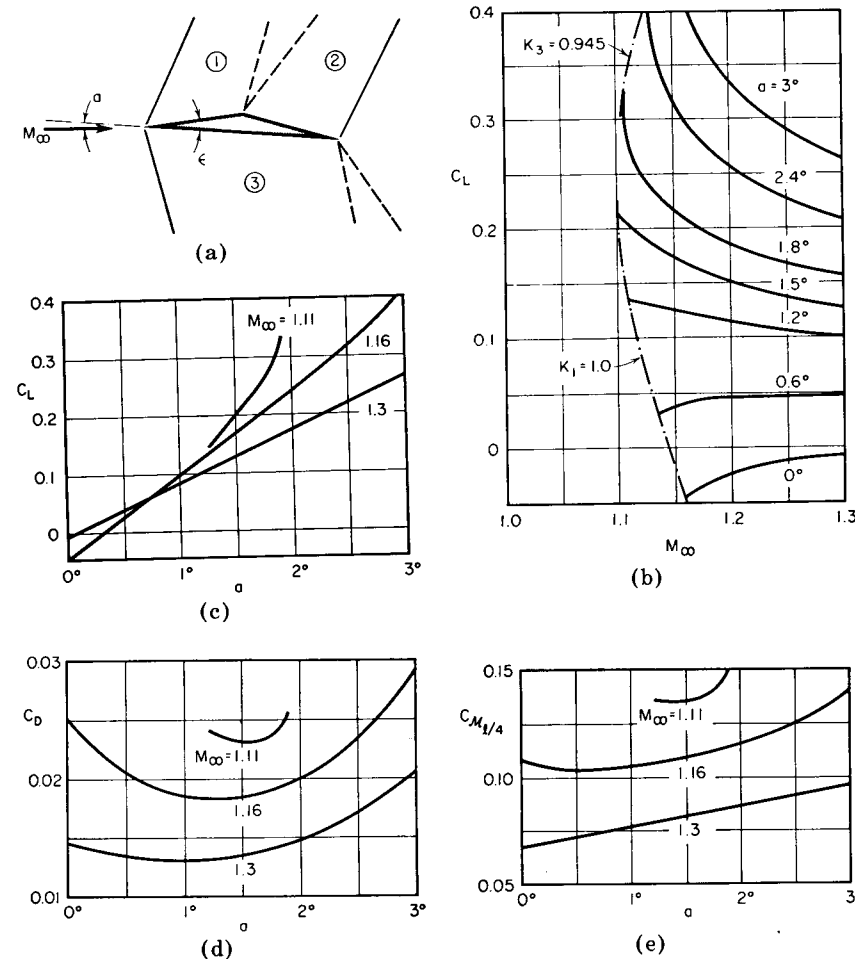


FIG. 21.6. Transonic flow over single wedge with  $\epsilon = 3^\circ$  (after Tsien and Baron).

- Nomenclature.
- Lift coefficient versus Mach Number.
- Lift coefficient versus incidence.
- Drag coefficient versus incidence.
- Moment coefficient versus incidence.

dicted lift is always greater than the lift given by the linear theory, at least up to the point where the oblique shock on the lower surface detaches itself.

**Asymmetric Wedge Airfoil.**<sup>(3)</sup> The results of the oblique shock theory and the Prandtl-Meyer theory may easily be applied to find the section force characteristics of any profile for which the flow near the surface is composed of oblique shocks and simple-wave expansions.

For example, considering the asymmetric double wedge of Fig. 21.6a, the shock theory may be used for finding  $C_p$  in regions 1 and 3 and the Mach Number in region 1; then the Prandtl-Meyer theory gives  $C_p$  in region 2. Integrating the pressure coefficient over the surface gives the several force coefficients.

Generalized lift, drag, and moment similarity curves have been thus computed<sup>(3)</sup> for the profile of Fig. 21.6a. The aerodynamic properties of a profile with thickness are illustrated in the charts of Fig. 21.6 for the particular profile with  $\epsilon = 3^\circ$ .

Fig. 21.6b shows that for small incidence,  $C_L$  increases slightly with an increase in  $M_\infty$ , whereas at large incidence  $C_L$  decreases as  $M_\infty$  increases. The latter trend is of course familiar for supersonic flow.

Fig. 21.6c shows that whereas the lift curve is linear at high transonic

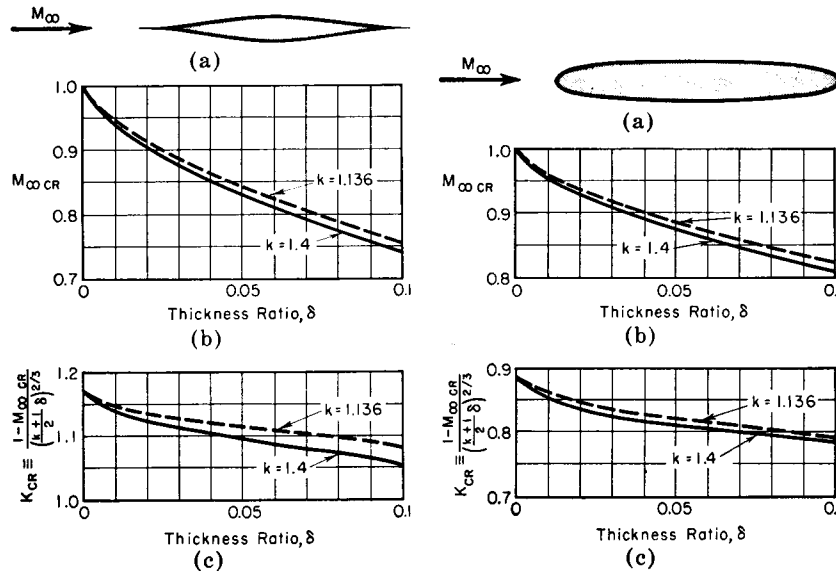


FIG. 21.7. Transonic flow past Kaplan (cusped) profile (after Kaplan).

- Profile shape.
- Lower critical Mach Number.
- Critical value of transonic similarity parameter.

FIG. 21.8. Transonic flow past elliptical profile (after Kaplan).

- Profile shape.
- Lower critical Mach Number.
- Critical value of transonic similarity parameter.

Mach Numbers (as might be expected from the linearized theory of supersonic flow), for  $M_\infty$  of about 1.1 it is strongly concave upward.

The curves of  $C_D$  versus  $a$  (Fig. 21.6d) at first decrease to a minimum at about  $a \approx 1.5^\circ$ , after which they increase. For supersonic flow with small perturbations, it may be recalled in contrast that the drag is the sum of two parts: (i) a constant portion due to thickness, and (ii) an "induced drag due to lift" which varies with the square of  $a$ .

**Critical Mach Number for Subsonic Flow.** Kaplan<sup>(2)</sup>, by means of series expansions, has computed the lower critical Mach Number (corresponding to the first appearance of local supersonic zones) for the cusped profile of Fig. 21.7 and the elliptical profile of Fig. 21.8. The curves show the computed value of  $M_{\infty,cr}$  versus thickness ratio  $\delta$ , and the corresponding "critical" value  $K_{cr}$  of the transonic similarity parameter versus  $\delta$ .

It is seen that as  $\delta \rightarrow 0$ ,  $M_{\infty,cr} \rightarrow 1$ , thus making the flow near the lower critical Mach Number fit well with the assumptions of transonic similarity. Accordingly, the curve of  $K_{cr}$  is quite flat for small values of  $\delta$ , and the limiting value of  $K_{cr}$  as  $\delta \rightarrow 0$  is independent of specific-heat ratio, all in accordance with the law of transonic similarity.

From Figs. 21.7 and 21.8 it may be concluded that the lower critical Mach Number for transonic flow past thin profiles can be computed approximately by the rough rule that  $K_{cr} \approx 1$ .

#### 21.4. Flow in Throat of Converging-Diverging Nozzle

Some of the earliest attempts to study mixed subsonic and supersonic flows near the sound velocity were formulated by means of power

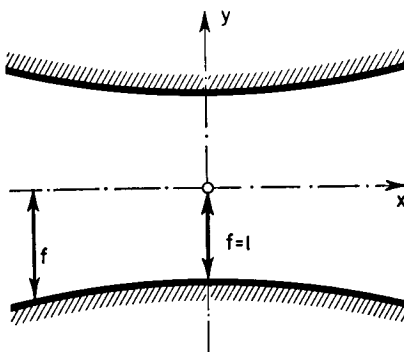
series solutions to the equations of motion, and were applied particularly to the flow in the throat of a converging-diverging nozzle. Apart from the instructive value of such results, they are of practical utility in the design of supersonic nozzles for wind tunnels.

##### Solution by Power Series.<sup>(6)</sup>

Referring to Fig. 21.9, let the nozzle axis lie along  $x$ , and let the flow be two-dimensional, with the  $y$ -axis at the narrowest cross section.

FIG. 21.9. Throat of nozzle.

The shape of the nozzle is given by  $y = f(x)$  where  $f$  denotes the ratio of the half-height to the half-height at the throat. It is convenient to make the half-height at the throat equal to unity.



It is assumed that the velocity components  $u$  and  $v$  may be expressed as power series in  $y$ , with the coefficients of the series depending upon  $x$ . Since the flow is symmetrical about the  $x$ -axis, the series for  $u$  must contain only even powers of  $y$ , whereas that for  $v$  must contain only odd powers. We therefore formulate the expressions

$$\left. \begin{aligned} u(x, y) &= a_0 + \frac{1}{2!} a_2 y^2 + \frac{1}{4!} a_4 y^4 + \dots \\ v(x, y) &= b_1 y + \frac{1}{3!} b_3 y^3 + \dots \end{aligned} \right\} \quad (21.67)$$

where the coefficients  $a$  and  $b$  are functions of  $x$ . Our task now is to determine these coefficients so that the flow satisfies the governing physical relations.

**EQUATION OF IRROTATIONALITY.** Since the flow is assumed irrotational, it is necessary that

$$\partial u / \partial y = \partial v / \partial x$$

and, using Eq. 21.67, this results in

$$a_2 y + \frac{1}{3!} a_4 y^3 = b_1' y + \frac{1}{3!} b_3' y^3$$

where  $b' = db/dx$ . Since this relation must prevail for all values of  $y$ , the coefficients of like powers of  $y$  must be equal. Hence

$$a_2 = b_1'; \quad a_4 = b_3' \quad (21.68)$$

**EQUATION OF CONTINUITY.** For isentropic, two-dimensional, irrotational flow, the equation of continuity may be written in the form (Chapter 9)

$$(c^2 - u^2) \frac{\partial u}{\partial x} - 2uv \frac{\partial u}{\partial y} + (c^2 - v^2) \frac{\partial v}{\partial y} = 0$$

where

$$c^2 = \frac{k-1}{2} (V_{\max}^2 - V^2)$$

Taking derivatives of Eq. 21.67, substituting these into the continuity relation, and equating the terms independent of  $y$ , there results

$$b_1 = - \frac{V_{\max}^2 - \frac{k+1}{k-1} a_0^2}{V_{\max}^2 - a_0^2} a_0' \quad (21.69)$$

**BOUNDARY CONDITION.** At the wall of the nozzle, the condition that the gas follows the wall may be written in the form

$$v_r / u_r = dy / dx = df / dx = f'$$

where  $u_f$  and  $v_f$  denote the velocity components at the wall. When this condition is combined with Eqs. 21.67, we obtain

$$b_1 f + \frac{1}{6} b_3 f^3 = f' \left( a_0 + \frac{1}{2} a_2 f^2 + \frac{1}{24} b_3' f^4 \right) \quad (21.70)$$

Now, suppose that the nozzle contour is given, that is to say,  $f(x)$  and the derivative  $f'(x)$  are known. Then, if  $a_0(x)$  were known (corresponding to the velocity distribution on the  $x$ -axis) it would be possible (i) to compute  $b_1(x)$  from Eq. 21.69; (ii) to compute  $a_2(x)$  from Eq. 21.68a; (iii) to integrate Eq. 21.70 numerically and thus find  $b_3(x)$ ; and (iv) to determine  $a_4(x)$  from Eq. 21.68b. With all the coefficients of Eqs. 21.67 known the entire flow pattern is determined, at least to the fourth power in  $y$ .

**CONSERVATION OF TOTAL MASS FLOW.** In order to determine  $a_0(x)$ , it is necessary to satisfy the equation of continuity for the entire flow passing through any section of the nozzle. This conservation principle may be written

$$\int_0^f u \rho \, dy = w = \text{constant}$$

where

$$\frac{\rho}{\rho_0} = \left( 1 - \frac{V^2}{V_{\max}^2} \right)^{\frac{1}{k-1}}$$

The details of the calculation procedure, including the introduction of many approximations in order to get rapid convergence, are described in Reference 6.

**Typical Results.** Two general types of steady flow without shocks through a converging passage are possible. As is well known from one-dimensional considerations, the flow may be symmetrical about the minimum cross section with subsonic velocities on both sides; or it may be asymmetric, with subsonic speed on one side and supersonic speed on the other side of the throat.

**SYMMETRIC SOLUTION.** Fig. 21.10 shows curves of constant speed for the symmetric solution of a plane nozzle with a hyperbolic wall, the radius of curvature of the wall at the throat being five times the throat half-height. The maximum speed reached on the wall is greater than that reached on the center line, and in Fig. 21.10b there is a sizable supersonic zone near the wall even though from a one-dimensional viewpoint the flow is entirely subsonic. As in the one-dimensional case, there are an infinite number of continuous, symmetrical solutions, each with a different maximum Mach Number in the throat. Corresponding to the choking effect in one-dimensional flow, there is a limit to this maximum

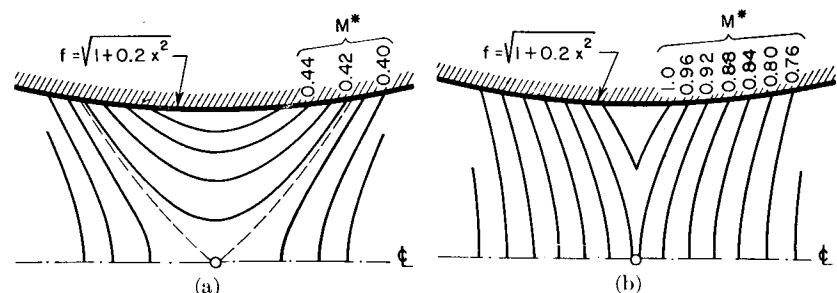
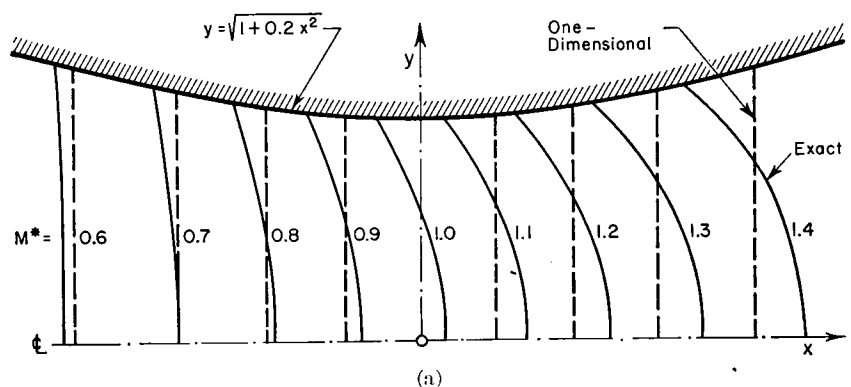


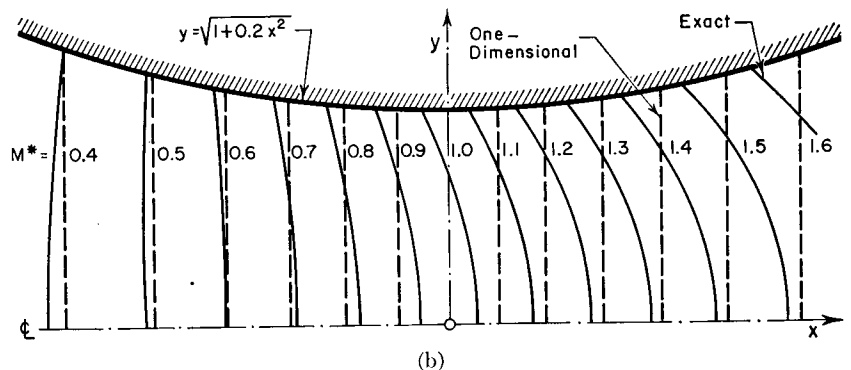
FIG. 21.10. Contours of constant speed for symmetric flow through throat of two-dimensional nozzle. Wall contour is hyperbolic; the wall radius of curvature at the throat is five times the throat half-height (after Oswatitsch and Rothstein).

(a) Low Mach Number at throat.

(b) Maximum Mach Number for which continuous solution is possible.



(a)



(b)

FIG. 21.11. Contours of constant speed for asymmetric flow through throat of nozzle. Wall contour is hyperbolic; the wall radius of curvature is five times the throat half-height (after Oswatitsch and Rothstein).

(a) Two-dimensional flow.

(b) Axi-symmetric flow.

Mach Number for which such continuous, symmetrical flows are possible. The limiting case of symmetrical flow is shown in Fig. 21.10b.

**ASYMMETRIC SOLUTION.** The asymmetric case is illustrated in Fig. 21.11 for both plane flow and axi-symmetric flow. The sonic speed is reached at the wall upstream of the throat, and at the center line downstream of the throat. Fig. 21.11 shows also how far from accurate the one-dimensional solution is, especially at high supersonic speeds. As in the case of one-dimensional flow, however, there is a single unique flow pattern for continuous, asymmetrical flow. In other words, downstream of the throat the Mach Number at a given point is uniquely determined by the geometry if no shocks are present.

**Approximate Solution for Shape of Sonic Line.** By combining the concept of a series solution with the concept of a special form of the differential equation for transonic flow, Sauer<sup>(7)</sup> has succeeded in obtaining approximate but general rules for the shape of the sonic line in a nozzle when the flow passes from subsonic to supersonic speeds.

**APPROXIMATE DIFFERENTIAL EQUATION.** Let us define  $\tilde{u}$  and  $\tilde{v}$  by

$$\frac{u}{c^*} = 1 + \tilde{u}; \quad \frac{v}{c^*} = \tilde{v} \quad (21.71)$$

where  $\tilde{u}$  and  $\tilde{v}$ , which are assumed to be small compared with unity for transonic flow with small perturbations, represent dimensionless disturbance velocities from a condition of uniform, parallel flow at the sonic speed. With this notation, Eq. 21.4b has the form

$$(k + 1)\tilde{u} \frac{\partial \tilde{u}}{\partial x} - \frac{\partial \tilde{v}}{\partial y} = 0 \quad (21.72)$$

**SERIES FORMULATION.** Following the line of thought underlying Eqs. 21.67, the perturbation velocity potential corresponding to the disturbance velocities  $\tilde{u}$  and  $\tilde{v}$  is now written in the form

$$\frac{1}{c^*} \varphi = f_0(x) + y^2 f_2(x) + y^4 f_4(x) + \dots$$

By differentiation, the dimensionless perturbation velocities are then found to be

$$\tilde{u} = \frac{1}{c^*} \frac{\partial \varphi}{\partial x} = f_0' + y^2 f_2' + y^4 f_4' + \dots \quad (21.73a)$$

$$\tilde{v} = \frac{1}{c^*} \frac{\partial \varphi}{\partial y} = 2y f_2 + 4y^3 f_4 \quad (21.73b)$$

where the primes signify differentiation with respect to  $x$ . Taking the derivatives  $\partial \tilde{u} / \partial x$  and  $\partial \tilde{v} / \partial y$  in Eqs. 21.73, substituting these into

Eq. 21.72, and equating coefficients of like powers of  $y$ , we obtain the following relations among the coefficients:

$$2f_2 = (k + 1)f_0' f_2'' \quad (21.74a)$$

$$12f_4 = (k + 1)(f_0' f_2'' + f_0'' f_2') \quad (21.74b)$$

Now  $f_0'$  represents, according to Eq. 21.73a, the velocity distribution on the  $x$ -axis. For a short distance along the axis, the velocity on the axis may be approximated by a straight line. Restricting our considera-

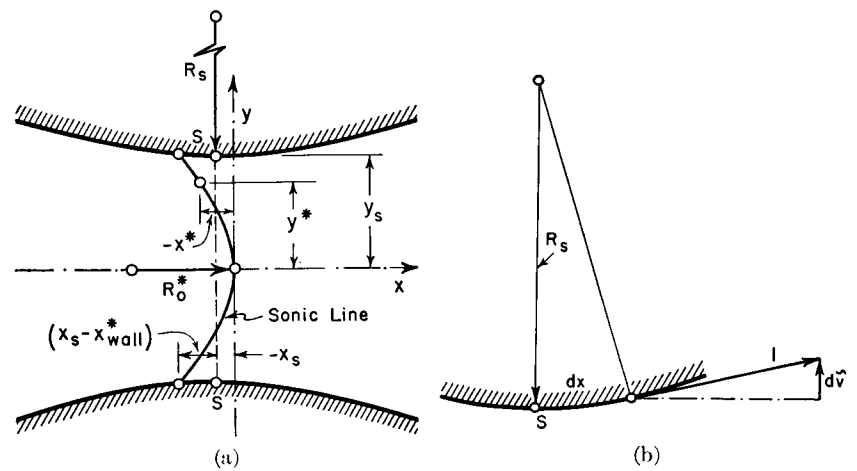


FIG. 21.12. Throat of nozzle.

- (a) Nomenclature for sonic line.  
(b) Curvature of wall.

tions to the neighborhood of the sonic line, and setting  $x = 0$  where the sonic line crosses the  $x$ -axis (Fig. 21.12a), we write, accordingly,

$$f_0' = [\tilde{u}(x)]_{y=0} \cong \left( \frac{d\tilde{u}}{dx} \right)_0 x \quad (21.75a)$$

where  $(d\tilde{u}/dx)_0$  denotes the velocity gradient on the axis near  $x = 0$ . Then, from Eqs. 21.74, we may evaluate the remaining coefficients as

$$f_2 = \frac{k + 1}{2} \left( \frac{d\tilde{u}}{dx} \right)_0^2 x; \quad f_4 = \frac{(k + 1)^2}{24} \left( \frac{d\tilde{u}}{dx} \right)_0^3 \quad (21.75b)$$

The velocity distribution, Eqs. 21.73, may now be expressed as

$$\tilde{u} = \left( \frac{d\tilde{u}}{dx} \right)_0 x + \frac{k + 1}{2} \left( \frac{d\tilde{u}}{dx} \right)_0^2 y^2 + \dots \quad (21.76a)$$

$$\tilde{v} = (k + 1) \left( \frac{d\tilde{u}}{dx} \right)_0^2 x y + \frac{(k + 1)^2}{6} \left( \frac{d\tilde{u}}{dx} \right)_0^3 y^3 + \dots \quad (21.76b)$$

**SONIC LINE.** To obtain the equation of the sonic line, we first set down the definition of the sonic line as

$$u^2 + v^2 = c^*{}^2; \text{ or } (1 + \tilde{u})^2 + \tilde{v}^2 = 1$$

Within the assumptions of the present theory, this may be approximated by  $\tilde{u} \cong 0$ , and thus we get from Eq. 21.76a,

$$x^* = -\frac{k+1}{2} \left( \frac{d\tilde{u}}{dx} \right)_0 y^{*2} \quad (21.77)$$

where the asterisk denotes the sonic condition, and Fig. 21.12 illustrates the notation. The sonic curve is, therefore, a parabola, and its curvature on the  $x$ -axis may be shown to be given by

$$\frac{1}{R_0^*} = \frac{d^2 x^* / dy^{*2}}{\sqrt{1 + (dx^* / dy^*)^2}} = (k+1) \left( \frac{d\tilde{u}}{dx} \right)_0 \quad (21.78)$$

We next wish to relate the location of the sonic curve to the throat section of the nozzle, signified by point  $S$  on the wall. Since  $\tilde{v}_s = 0$ , we find from Eq. 21.76b that

$$-x_s = \frac{k+1}{6} \left( \frac{d\tilde{u}}{dx} \right)_0 y_s^2 \quad (21.79)$$

and we note from Fig. 21.12 that  $(-x_s)$  is the maximum distance of the sonic line downstream of the throat.

To find where the sound speed is first reached on the wall, we note that at the wall near the throat it is a good approximation to write  $y^* \cong y_s$ . Using this approximation, Eqs. 21.77 and 21.79 may be combined to yield

$$x_s - x_{\text{wall}}^* = \frac{k+1}{3} \left( \frac{d\tilde{u}}{dx} \right)_0 y_s^2 = 2(-x_s) \quad (21.80)$$

The wall curvature near the throat is evaluated, employing the approximate geometry of Fig. 21.12b, as

$$\frac{1}{R_s} \cong \frac{\partial \tilde{v}}{\partial x}$$

Then, using Eq. 21.76b, we get

$$\frac{1}{R_s} = (k+1) \left( \frac{d\tilde{u}}{dx} \right)_0^2 y_s = \frac{1}{R_0^*} \left( \frac{d\tilde{u}}{dx} \right)_0 y_s \quad (21.81)$$

**SONIC-LINE PARAMETERS FOR GIVEN NOZZLE SHAPE.** Thus far we have thought in terms of the velocity distribution on the axis,  $(d\tilde{u}/dx)_0$ , as being known. In practice, however, it is the shape of the nozzle

which is known. If we regard the nozzle shape near the throat as being defined by  $y_s$  and  $R_s$ , Eqs. 21.78 through 21.81 may be inverted to give the following sonic-line parameters in terms of nozzle shape:

$$\left[ \frac{d\tilde{u}}{d(x/y_s)} \right]_0 = \sqrt{\frac{1}{k+1} \frac{y_s}{R_s}} \quad (21.82a)$$

$$\frac{R_0^*}{y_s} = \sqrt{\frac{1}{k+1} \frac{R_s}{y_s}} \quad (21.82b)$$

$$\frac{x_s - x_{\text{wall}}^*}{y_s} = 2 \frac{(-x_s)}{y_s} = \sqrt{\frac{k+1}{9} \frac{y_s}{R_s}} \quad (21.82c)$$

The sonic line is a parabola determined by Eq. 21.77 in conjunction with Eq. 21.82a.

**AXI-SYMMETRIC NOZZLES.** Similar considerations for axi-symmetric nozzles<sup>(7)</sup> lead to the following results:

$$\frac{x^*}{y_s} = -\frac{k+1}{4} \left[ \frac{d\tilde{u}}{d(x/y_s)} \right]_0 \left( \frac{y^*}{y_s} \right)^2 \quad (21.83a)$$

$$\left[ \frac{d\tilde{u}}{d(x/y_s)} \right]_0 = \sqrt{\frac{2}{k+1} \frac{y_s}{R_s}} \quad (21.83b)$$

$$\frac{R_0^*}{y_s} = \sqrt{\frac{2}{k+1} \frac{R_s}{y_s}} \quad (21.83c)$$

$$\frac{x_s - x_{\text{wall}}^*}{y_s} = \frac{(-x_s)}{y_s} = \sqrt{\frac{k+1}{32} \frac{y_s}{R_s}} \quad (21.83d)$$

**COMPARISON OF PLANE AND AXI-SYMMETRIC NOZZLES.** The relative contours of the sonic line for plane and axi-symmetric nozzles having the same profile are shown in Fig. 21.13, in accordance with the comparative values in Eqs. 21.82 and Eqs. 21.83, respectively. Note that the rate of velocity increase on the axis for the round nozzle is  $\sqrt{2}$  times greater than that for the flat nozzle, which is the same result as would be given by a one-dimensional analysis.

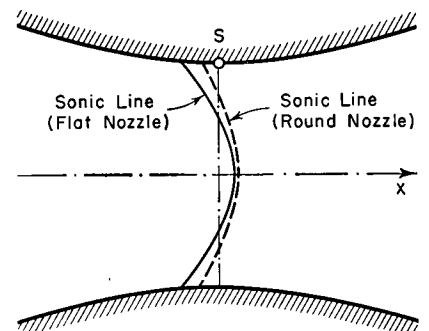


FIG. 21.13. Comparison of sonic lines in plane and axi-symmetric nozzles having same wall contours (after Sauer).

**COMPARISON WITH EXACT RESULTS.** The accuracy of the approximate formulas may be checked against the more exact results of Fig. 21.11a

and 21.11b, where  $R_s/y_s = 5$ . The comparison, which follows, shows the approximation formulas to be quite accurate.

	Flat		Round	
	Exact	Approx.	Exact	Approx.
$\left[ \frac{d\bar{u}}{d(x/y_s)} \right]_0$	0.27	0.29	0.37	0.41
$(-x_s)/y_s$	0.12	0.12	0.14	0.12
$(x_s - x^*_{\text{wall}})/y_s$	0.23	0.23	0.12	0.12

**APPLICATION TO WIND TUNNEL DESIGN.** An important practical application of these results is to the design of supersonic nozzles for wind tunnels. In using the method of characteristics, it is necessary to begin the calculations at an initial line in the supersonic region on which the velocity is known. The results in Reference 6 (typified by Fig. 21.11) give such information for hyperbolic contours near the throat, and those of References 8 and 9 for several other contours. The approximate formulas of Eqs. 21.82 and 21.83 may be employed for contours near the throat when the exact solution is not known.

**Transition from Purely Subsonic Flow to Subsonic-Supersonic Flow.** The one-dimensional theory of the way in which the flow in a converging-diverging nozzle changes from a purely subsonic flow (symmetrical solution) to a subsonic-supersonic flow without discontinuities (asymmetric solution) is summarized in Fig. 21.14. For high exhaust pressures, the flow is subsonic throughout and the passage behaves like a conventional venturi. As the exhaust pressure is reduced, the speeds increase but there are no changes in the general character of the flow until the speed of sound is reached in the throat. Further reductions in exhaust pressure cause a normal shock to grow and to proceed downstream; a typical pattern

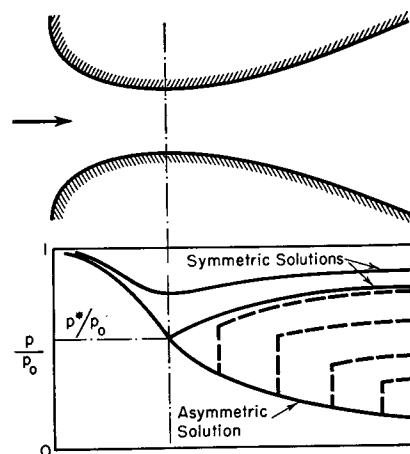


FIG. 21.14. One-dimensional theory of development of supersonic flow in nozzle.

comprises subsonic flow to the throat, supersonic flow between the throat and the shock, and subsonic flow downstream of the shock. When the exhaust pressure is sufficiently low, all the flow downstream of the throat is supersonic, corresponding to the unique asymmetric solution.

Taking account of two-dimensional effects, Fig. 21.10b shows a

typical continuous symmetrical solution with the highest local Mach Number for which such a solution is possible. Similarly, Fig. 21.11a shows the unique continuous asymmetric solution for the same nozzle. There is no hint from these two patterns as to how the transition from one to the other takes place. It has been suggested by Emmons<sup>(10)</sup>

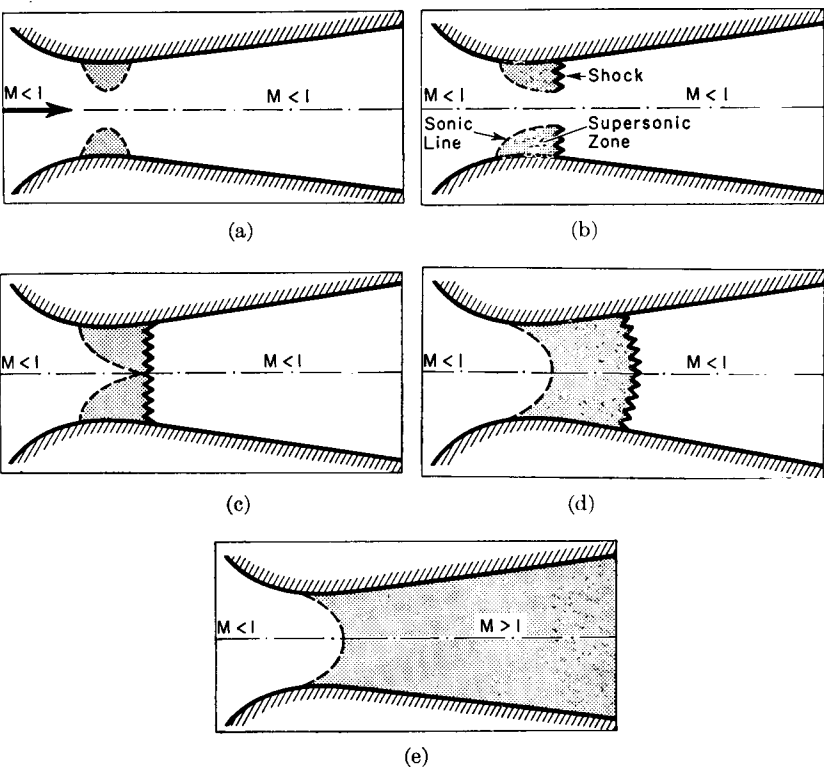


FIG. 21.15. Two-dimensional effects in development of supersonic flow through nozzle. Shaded zones are supersonic, and dashed lines are sonic lines (after Emmons).

- (a) Lowest back pressure for which continuous venturi-type flow is possible. Note supersonic zones.
- (b, c, d) Shocks appear, grow, and move downstream as back pressure is reduced. Condition (d) is similar to one-dimensional flow.
- (e) Shock-free flow through entire nozzle.

that the intermediate stages are as sketched in Fig. 21.15, where sketches (a) and (e) indicate the continuous solutions already discussed. Sketch (d) indicates a phase which is very similar to the one-dimensional flow of Fig. 21.14, but sketches (b) and (c) incorporate essentially two-dimensional effects, indicating as they do the initiation of a shock on the wall near the end of the supersonic zone, and the growth of this shock until it extends across the entire passage.

In attempting to study the transition phases analytically, it is to be expected that any mathematically continuous solution would involve limit lines and the overlapping of streamlines. This would of course lead to physical discontinuities in the form of shocks. Consequently, to obtain analytical solutions to the transition problem requires that viscous terms be retained in the equations of motion, and this probably leads to hopeless difficulties unless numerical solutions are sought with the aid of high-speed computing machines.

Apart from the last-named possibility, the only way in which combined subsonic-supersonic flows containing shocks can be handled is through the use of numerical relaxation methods, with the shock treated as a discontinuity. This method is discussed in the next article together with its application to the transition flow in a nozzle.

## 21.5. Relaxation Method

The relaxation method <sup>(11)</sup> is unique in that it may be used not only for obtaining theoretical solutions to incompressible, subsonic, transonic, supersonic, or hypersonic flow, or to combined fields of flow, with given physical boundaries, but it allows solutions to be obtained even when there are shocks in the flow. It is based on finding numerical solutions to the equations of motion. Consequently, it requires a great deal of labor, and individual solutions are obtained rather than general solutions or families of particular solutions. Therefore, the method is not suitable as a tool for making design calculations. Its importance lies rather in yielding exemplary solutions to typical cases, thus giving the designer a general understanding or "feel" for the important features of typical flow patterns.

**Equations of Motion.** To obtain a systematic method for arriving at numerical solutions, we put the equations of motion into finite-difference form.

Assuming that we are dealing with plane, steady, isentropic, and irrotational flow, the equation of continuity,

$$\frac{\partial}{\partial x}(\rho u) + \frac{\partial}{\partial y}(\rho v) = 0$$

is identically satisfied through the use of the stream function  $\psi$ , defined by

$$\frac{\rho}{\rho_0} u = \frac{\partial \psi}{\partial y} = \psi_y; \quad \frac{\rho}{\rho_0} v = -\frac{\partial \psi}{\partial x} = -\psi_x$$

where  $\rho_0$  is the stagnation density. Since we are dealing with an irrotational flow, we may write

$$\frac{\partial v}{\partial x} - \frac{\partial u}{\partial y} = 0$$

Differentiating the velocity components, and inserting the derivatives into the equation of irrotationality, we obtain

$$\psi_{xx} + \psi_{yy} - \psi_x \left( \ln \frac{\rho}{\rho_0} \right)_x - \psi_y \left( \ln \frac{\rho}{\rho_0} \right)_y = 0 \quad (21.84)$$

**Equations of Motion in Finite-Difference Form.** Let us imagine the  $x, y$ -plane (Fig. 21.16) to be covered by a square grid with spacing  $h$ . If a certain flow pattern  $\psi = \psi(x, y)$  satisfied Eq. 21.84, there would be a value of  $\psi$  corresponding to each net point of the grid, and these values would be so related as to satisfy Eq. 21.84 in every small region of the flow. This condition may be expressed approximately in finite-difference form by relating the value  $\psi_0$  at a point 0 to the values of  $\psi_1, \psi_2, \psi_3$ , and  $\psi_4$  at the surrounding net points. The relevant derivatives may be written in the following finite-difference forms:

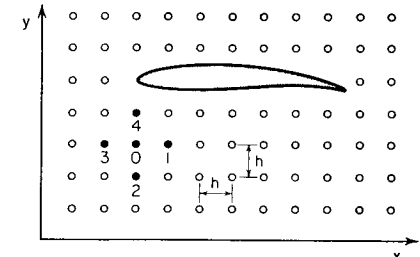


FIG. 21.16. Square grid used for relaxation method.

$$\psi_x \cong \frac{\psi_1 - \psi_0}{h} \cong \frac{\psi_1 - \psi_3}{2h}$$

$$\psi_{xx} \cong \frac{1}{h} \left[ \frac{\psi_1 - \psi_0}{h} - \frac{\psi_0 - \psi_3}{h} \right] = \frac{\psi_1 - 2\psi_0 + \psi_3}{h^2}$$

$$\psi_y \cong \frac{\psi_4 - \psi_0}{h} \cong \frac{\psi_4 - \psi_2}{2h}$$

$$\psi_{yy} \cong \frac{1}{h} \left[ \left( \frac{\psi_4 - \psi_0}{h} \right) - \left( \frac{\psi_0 - \psi_2}{h} \right) \right] = \frac{\psi_4 - 2\psi_0 + \psi_2}{h^2}$$

$$(\ln \frac{\rho}{\rho_0})_x = \frac{(\ln \frac{\rho}{\rho_0})_1 - (\ln \frac{\rho}{\rho_0})_3}{2h}$$

$$(\ln \frac{\rho}{\rho_0})_y = \frac{(\ln \frac{\rho}{\rho_0})_4 - (\ln \frac{\rho}{\rho_0})_2}{2h}$$

When these are introduced into Eq. 21.84, we get the finite-difference form of the differential equation,

$$\begin{aligned} \psi_1 + \psi_2 + \psi_3 + \psi_4 - 4\psi_0 - \frac{1}{4}(\psi_1 - \psi_3)[(\ln \frac{\rho}{\rho_0})_1 - (\ln \frac{\rho}{\rho_0})_3] \\ - \frac{1}{4}(\psi_1 - \psi_3)[(\ln \frac{\rho}{\rho_0})_4 - (\ln \frac{\rho}{\rho_0})_2] = 0 \quad (21.85a) \end{aligned}$$

The density ratio,  $\rho/\rho_0$ , is connected with the local speed and thus with the local derivatives of the stream function, inasmuch as

$$V^2 = u^2 + v^2 = \left(\frac{\rho_0}{\rho}\right)^2 (\psi_x^2 + \psi_y^2)$$

There are many important details in using the relaxation method, described fully in References 10 and 11. A brief outline of the method of attack to indicate its potentialities and limitations is given below.

**Incompressible Flow.** To illustrate the approach, suppose to begin with that the flow were incompressible. Then Eq. 21.85a would take the simple form

$$\psi_1 + \psi_2 + \psi_3 + \psi_4 - 4\psi_0 = 0 \quad (21.85b)$$

To obtain a solution for flow past given boundaries, the values of  $\psi$  are first guessed at each point of the net, based on the known boundary conditions and on the computer's judgment and intuition. Then it is seen whether Eq. 21.85b is satisfied at every net point. In general, the right-hand side of Eq. 21.85b will not equal zero for any point, and its magnitude is termed the *residual*. The residual is a measure of the amount by which the differential equation,  $\psi_{xx} + \psi_{yy} = 0$ , is violated at each point with the assumed distribution of  $\psi$ . The residuals are then "relaxed" by systematically adjusting the values of  $\psi$  at each point in such a manner as to reduce the residuals. When all the residuals have been completely relaxed, the distribution of  $\psi$  represents a solution to the Laplace equation with the assumed boundary conditions.

**Compressible Flow.** With compressible irrotational flow, the situation differs from incompressible flow through the presence of the last two terms in Eq. 21.85a. While these terms generally do not vary greatly throughout the field of flow, they enormously complicate the otherwise simple pattern of calculations. This suggests that these terms need be calculated accurately only a few times during the relaxation procedure, and that between such accurate calculations they be taken as constant in order to hasten the calculations.

**Rotational Flow.** Although the method has been outlined for irrotational flow, it may easily be extended to rotational flow<sup>(11)</sup>, an extension which is important when there are curved shock waves in the flow.

**Shock Waves.** It sometimes happens that when there are regions of both subsonic and supersonic flow it is impossible to relax all the residuals in the field of flow. This result signifies that there is no steady, continuous flow with the assumed boundary conditions, and it is probably equivalent to the appearance of limit lines in analytical solutions. Experiment results then suggest that shocks will be present.

When this situation occurs, the relaxation solution is modified by assuming a location and shape for the shock wave. The shock line is then treated as a boundary in the flow, and the relaxation method is employed to solve for the flow patterns upstream and downstream of the shock. When this has been done, the correctness of the assumed shock is tested by seeing whether the flow conditions on the two sides of the discontinuity satisfy the oblique shock relations. If they do not, the shock shape and location are modified and the procedure repeated until both the relaxation equation and the shock relations are everywhere satisfied. Note that when shocks are present, the problem is in part one of determining the location of an initially unknown boundary.

**Application to Two-Dimensional Nozzle with Hyperbolic Walls.** We now return to the question of how the flow in the throat section of a nozzle develops as the exhaust pressure is reduced. This problem has been worked out in detail<sup>(10)</sup> by the relaxation method.

The continuous solutions are substantially the same as those of Figs. 21.10 and 21.11. What is of interest here is the typical solution with

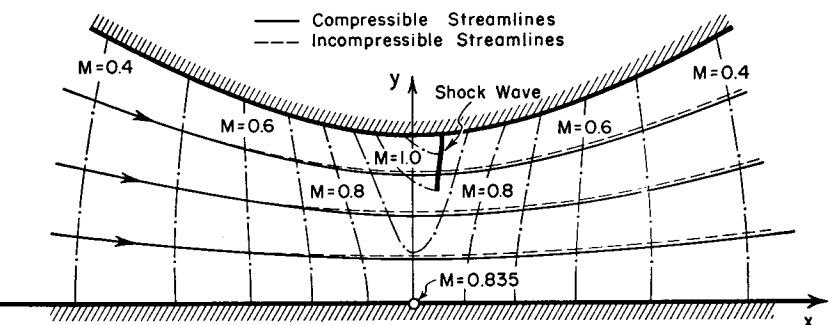


FIG. 21.17. Flow in two-dimensional nozzle with hyperbolic wall contour. The zone of supersonic flow near the throat wall is terminated by a shock (after Emmons).

shock waves of Fig. 21.17. Two facts are striking: (i) the shock wave curves upstream, and (ii) the shock first originates *upstream* of the  $M = 1$  line of the supersonic zone of the highest-speed, continuous, symmetrical solution, which suggests that the shock may appear quite suddenly with a finite length.

Aside from these unexpected results, the development of the shock wave, as summarized in Fig. 21.18 for the relaxation solutions, is in accord with the speculations of Fig. 21.15. However, photographs of the flow through a nozzle of the shape under consideration here (wall radius of curvature at throat is about twice the half-height) show shock patterns somewhat different from those of Fig. 21.18. This suggests that the viscous boundary layer and the shock-boundary layer inter-

action are very important, especially in the sensitive zone near  $M = 1$ .

A final point of interest is the actual amount of mass flow through the nozzle as compared with the amount which would be determined from one-dimensional isentropic theory in conjunction with measurements of

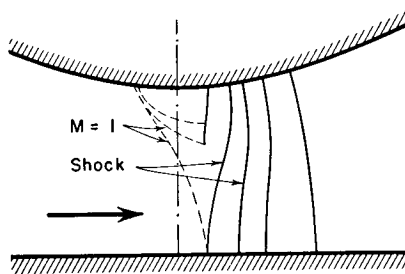


FIG. 21.18. Development of zone of supersonic flow and of terminating shock as back pressure is reduced. Nozzle is two-dimensional, with hyperbolic wall contour (after Emmons).

the upstream stagnation pressure and of the wall static pressure at the throat. This comparison is shown in Fig. 21.19. The actual flow, even disregarding friction, is as much as 5 per cent less than that predicted by one-dimensional calculations, and the choking flow is about

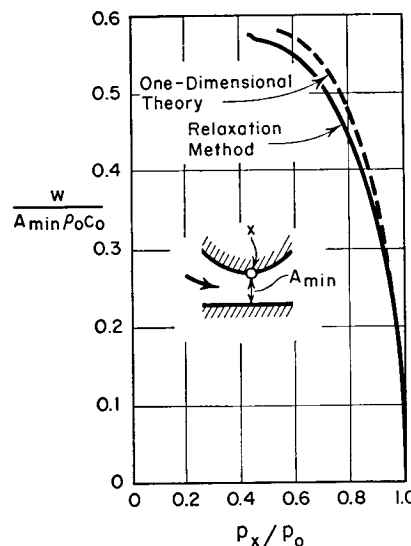


FIG. 21.19. Mass flow through two-dimensional nozzle with hyperbolic wall contour (radius of curvature at throat is about twice the throat height from axis of symmetry to wall). Solid curve shows flow computed by relaxation method, taking account of two-dimensional effects. Dashed curve is based on assumption of one-dimensional flow at the throat. Left-hand end of each curve represents choking condition (after Emmons).

0.7 per cent less than that predicted by one-dimensional theory. These figures, of course, would vary according to the shape of the nozzle.

**Transonic Flow Past Two-Dimensional Profiles.** Another application of the relaxation method to transonic flow with shock waves, it may be recalled, was discussed in Chapter 12 in connection with the flow past a symmetrical airfoil.

## 21.6. Transonic Flow Past a Wavy Wall

In Chapters 10 and 14, respectively, the subsonic and supersonic flows along a wavy wall (Fig. 21.20) were studied with the aim of observing some general features of subsonic and supersonic flow.

These linearized solutions have been extended to transonic flow <sup>(13)</sup>, where the nonlinear terms are essential, by using the Prandtl-Busemann method (Chapter 12) of expanding the velocity potential in a power series of the thickness ratio. The mathematical details are too lengthy to be given here, but the results are of practical interest.

The maximum velocity in the flow occurs at the crest of the wall ( $x = 0$ ), and the minimum at the trough ( $x = 180^\circ$ ). The pressure distribution at the wall, expressed in transonic similarity fashion, is

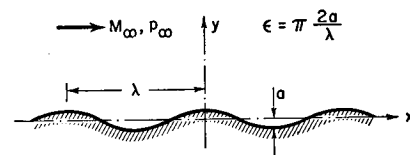


FIG. 21.20. Nomenclature for flow past wave-shaped wall.

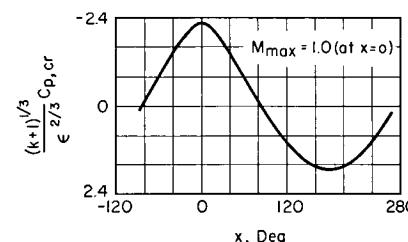


FIG. 21.21. Pressure distribution on wave-shaped wall of Fig. 21.20, expressed in transonic similarity fashion, for critical case where the maximum Mach Number in the flow is unity. The pressure coefficient is referred to the free-stream conditions  $p_\infty$  and  $M_\infty$  (after Kaplan).

shown in Fig. 21.21 for the special case where the Mach Number on the wall at  $x = 0$  is exactly unity. This condition corresponds to the maximum free-stream Mach Number for which the flow is everywhere subsonic.

The form of the results shows that the pressure coefficient at the wall is proportional to the  $2/3$ -power of the thickness ratio. Sample calculations show that the disturbance produced by the wall at transonic speeds is very considerable. For example, if the wall has a thickness ratio  $(2a/l)$  of only 0.01, Fig. 21.21 leads to the conclusion that the critical condition is reached at the wall when  $M_\infty \approx 0.91$  and that the peak negative pressure coefficient is then approximately 0.17.

### 21.7. Flow at Mach Number Unity

As might be expected, the analytical determination of flow patterns when  $M_\infty$  is exactly unity involves formidable difficulties. Several specific examples have been worked out, however, and although the calculations are too lengthy to be given here, the results are very instructive. Moreover, they may be extended to values of  $M_\infty$  above and below unity by the method of Art. 21.8.

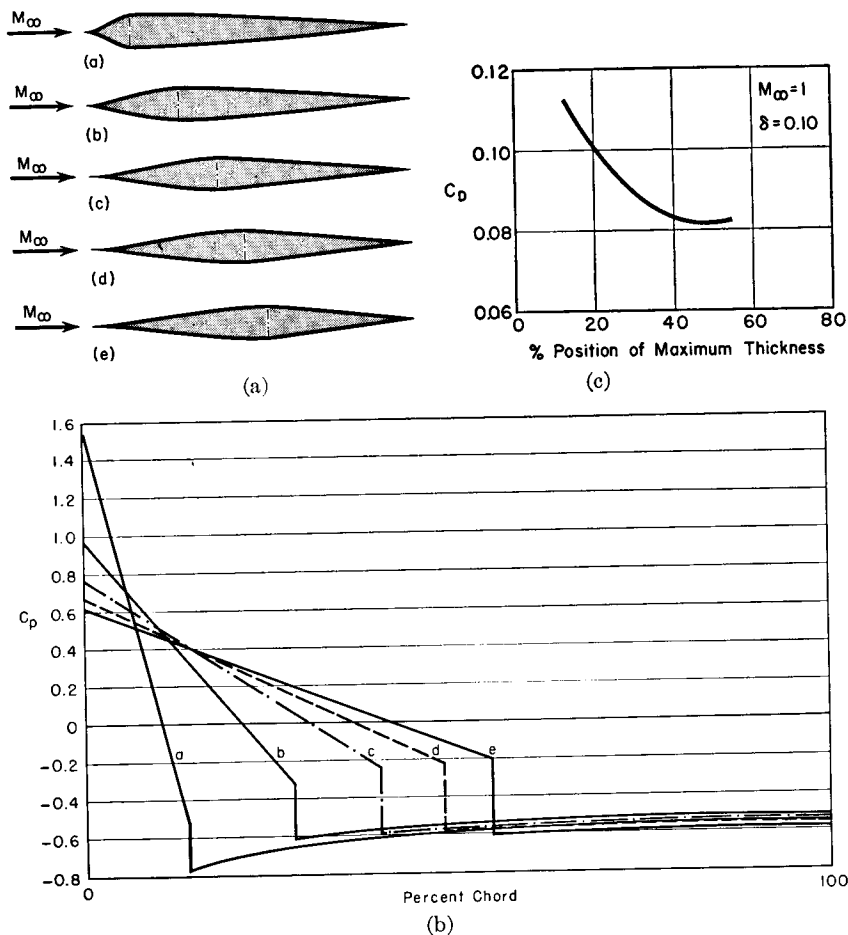


FIG. 21.22. Two-dimensional profiles of 10% thickness ratio having different positions of maximum thickness and affinely related cusped noses. The rear part of each profile is shaped so as to give minimum total pressure drag at  $M_\infty = 1$  (after Guderley).

- (a) Profile shapes.
- (b) Pressure distributions for  $M_\infty = 1$ .
- (c) Total pressure drag versus position of maximum thickness, for  $M_\infty = 1$ .

**Drag of Two-Dimensional Symmetrical Profiles.** <sup>(14)</sup> Fig. 21.22a shows a series of profiles which have affinely related noses, and, for each nose, a rear portion such as to give minimum pressure drag. The corresponding pressure distributions are given in Fig. 21.22b, and the drag coefficient (referred to the chord) is shown in Fig. 21.22c as a function of the position of maximum thickness.

Minimum pressure drag is obtained with the profile whose maximum thickness is at about 50% chord.

Perhaps the most interesting and important feature of these results is that at transonic speeds with thin profiles there is a finite pressure drag which, although considerable in magnitude, is nonetheless not nearly so large as would be predicted by extrapolating subsonic or supersonic theories into the transonic range.

**Two-Dimensional Profiles with Wedge-Shaped Nose.** <sup>(15)</sup> The pressure distribution over the nose of a profile having a wedge-shaped fore portion is shown in transonic similarity form in Fig. 21.23. With such a profile the sonic line in the flow field must start at the sharp shoulders of the profile, at which point there is a Prandtl-Meyer corner flow starting with Mach Number unity. Thus it is possible to establish the pressure distribution over the fore portion without considering the shape of the aft portion of the profile. Because of the Prandtl-Meyer corner flow, the pressure coefficient passes discontinuously through zero at the shoulder (see Fig. 21.24b).

The shapes and pressure distributions for three profiles of 10% thickness ratio and with wedge-shaped noses are shown in Figs. 21.24a and b. One of the profiles is the conventional double-wedge or diamond, and, for comparison, there are two other profiles with rear parts such as to give minimum total pressure drag.

The drag coefficients of 10% profiles with wedge noses and rear parts of minimum drag are shown in Fig. 21.24c as functions of the position of maximum thickness. For comparison, this chart shows also the pressure drag of the diamond profile and of the cusped-nose profiles of Fig. 21.22. From the chart it is again observed that the

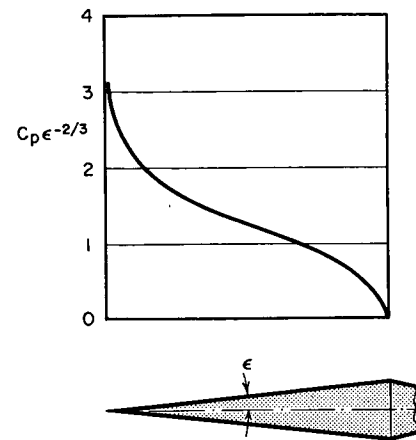


FIG. 21.23. Pressure distribution at  $M_\infty = 1$  over wedge-shaped nose terminated by sharp-corner shoulders (after Guderley and Yoshihara).

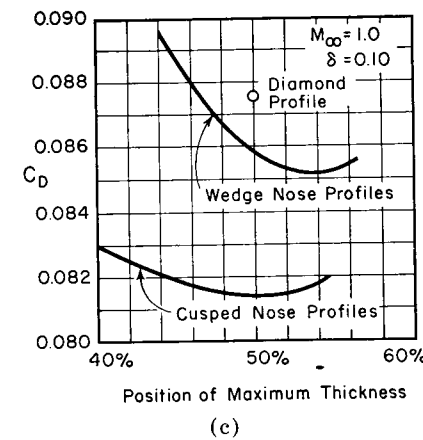
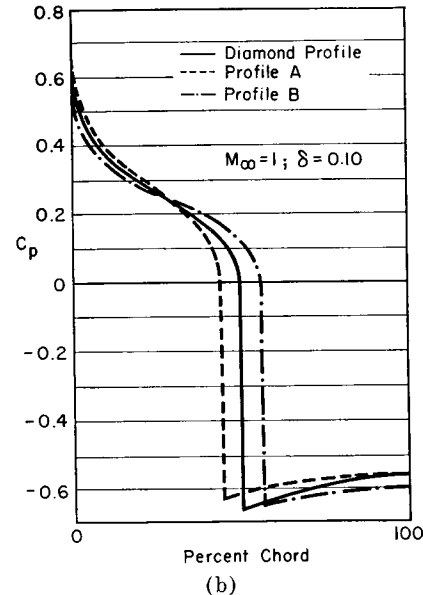
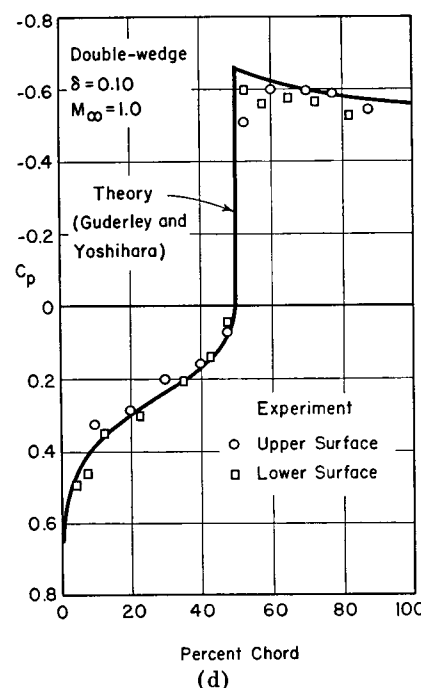
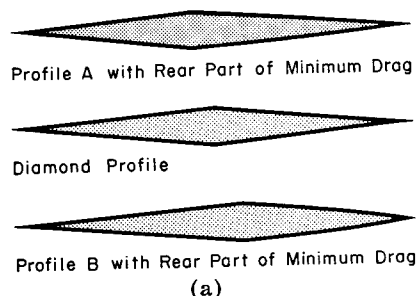


FIG. 21.24. Flow at  $M_\infty = 1$  past profiles with wedge-shaped noses and sharp-corner shoulders (after Guderley and Yoshihara).

- Profile shapes.
- Theoretical pressure distributions on profiles of (a).
- Theoretical pressure drag coefficient versus position of maximum thickness when rear part is such as to give minimum total pressure drag. Also shown is result for diamond profile and cusped-nose profiles of Fig. 21.22.
- Comparison of theoretical and experimental pressure distribution on 10% double-wedge at  $M_\infty = 1$  (after Habel and Henderson).

pressure drag is a minimum when the maximum thickness is at about 50% chord. Although the cusped-nose profile has a lower drag than the wedge-shaped profile, an important conclusion to be drawn from Fig. 21.24c is that at  $M_\infty = 1$  the pressure drag is not very sensitive to profile shape.

Experimental measurements <sup>(21)</sup> on a 10% double-wedge profile at  $M_\infty = 1$  (Fig. 21.24d) are in good accord with the theory, especially over the forward half of the profile. Viscous effects are undoubtedly significant in a small region aft of the shoulder.

**Lift of Symmetrical Double Wedge.** <sup>(24)</sup> The theoretical lift-curve slope at zero lift and  $M_\infty = 1$  is shown by the following table to decrease as the thickness ratio increases:

$\delta$	0.04	0.05	0.06	0.07	0.08	0.09	0.10
$(dC_L/d\alpha)_{a=0, M_\infty=1}$	7.24	6.76	6.35	6.02	5.76	5.53	5.35

Of further interest is that the lift-curve slope at zero lift does not vary with Mach Number at  $M_\infty = 1$ , i.e.,

$$\left[ \frac{d}{dM_\infty} \left( \frac{dC_L}{da} \right) \right]_{M_\infty=1} = 0$$

For the range of supersonic speeds in which the shock is attached,  $(dC_L/d\alpha)_{a=0}$  decreases rapidly as  $M_\infty$  increases (as illustrated strikingly

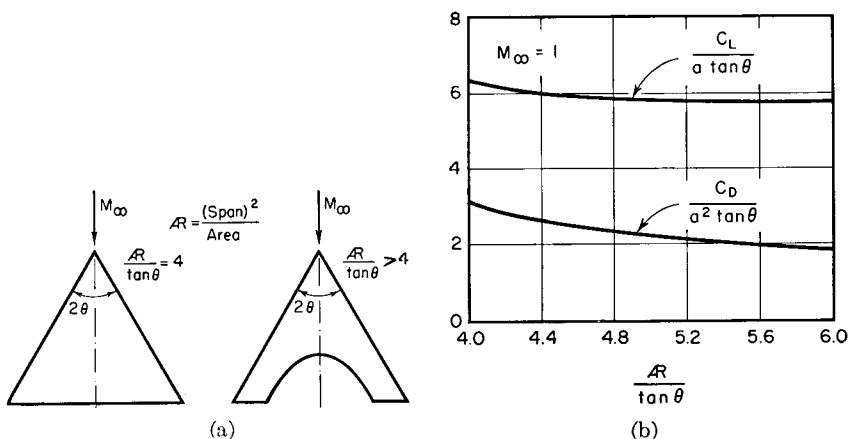


FIG. 21.25. Flow at  $M_\infty = 1$  past family of flat-plate sweptback wings (after Heaslet, Lomax, and Spreiter).

- Planform.
- Lift and induced drag versus planform parameter.

by the linear supersonic theory). It follows that the lift-curve slope must undergo rapid alterations in the range of Mach Numbers from unity to that for shock attachment, particularly because the lift-curve slope at the point of shock attachment is considerably greater than at  $M_\infty = 1$ .

**Lift and Drag of Flat-Plate, Sweptback Wing.**<sup>(16)</sup> The lift and induced drag coefficients of the family of sweptback wings shown in Fig. 21.25a are summarized in Fig. 21.25b.

All other things remaining unchanged, the lift is proportional to angle of incidence,  $\alpha$ , and the induced drag to  $\alpha^2$ , as in supersonic flow. Note that the values of  $C_L/a \tan \theta$  and  $C_D/a^2 \tan \theta$  for the sweptback wing are always less than for the triangular wing (for which  $\pi \tan \theta = 4$ ).

### 21.8. Slopes of Force Coefficients at $M_\infty = 1$

By a simple and intuitive consideration<sup>(17)</sup> it is possible to determine the slopes of the several curves of force coefficient versus Mach Number at  $M_\infty = 1$ .

**Pressure Distribution on Body is Independent of  $M_\infty$  near Mach Number Unity.** For supersonic free-stream Mach Numbers slightly greater than unity, a detached shock stands ahead of the body (Fig.

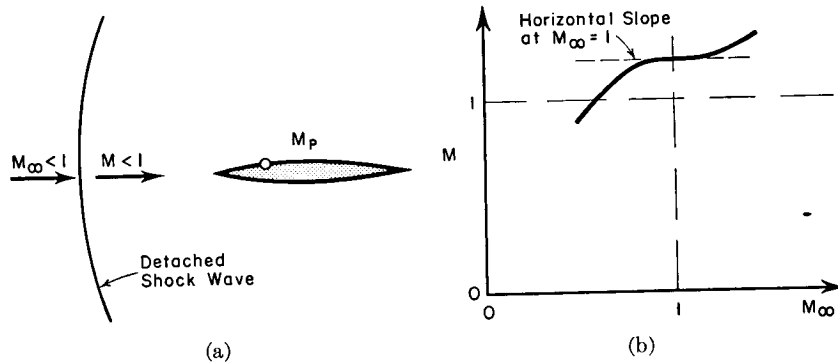


FIG. 21.26. Flow past body when  $M_\infty \approx 1$ .

- (a) Detached shock wave is nearly normal and stands far ahead of body.  
 (b) Local fluid properties do not change with  $M_\infty$  when  $M_\infty = 1$ .

21.26a). As  $M_\infty$  decreases and approaches unity, the detached shock becomes very nearly normal and stands very far ahead of the body and, in addition, the Mach Number just downstream of the normal shock is barely below unity. Indeed, according to the familiar Prandtl formula, the Mach Number downstream of a weak normal shock is as

much below unity as the approach Mach Number is above unity. When  $M_\infty$  is slightly greater than unity, the flow far ahead of the body (but downstream of the shock wave) is uniform and slightly subsonic. Consequently the flow pattern near the body for subsonic flow with  $M_\infty$  a little less than unity is the same as that for supersonic flow with  $M_\infty$  slightly greater than unity. Hence, if  $M$  denotes the local Mach Number at some particular point for a free-stream Mach Number of  $M_\infty$ , the curve of  $M$  versus  $M_\infty$  should have a horizontal slope at  $M_\infty = 1$  (Fig. 21.26b). This conclusion may be expressed as

$$(dM/dM_\infty)_{M_\infty=1} \rightarrow 0 \quad (21.86)$$

**Variation of  $C_p$  with  $M_\infty$ .** Neglecting entropy changes, and assuming flow with small perturbations, we may employ for the pressure coefficient the relation preceding Eq. 21.47. If  $C_p$  is the local pressure coefficient corresponding to the local Mach Number  $M$  and the free-stream Mach Number  $M_\infty$ , we may write,

$$C_p = \frac{2}{k+1} [(M_\infty^2 - 1) - (M^2 - 1)] \quad (21.87)$$

By differentiation of Eq. 21.87 we obtain

$$\frac{dC_p}{dM_\infty} = \frac{2}{k+1} \left[ 2M_\infty - 2M \frac{dM}{dM_\infty} \right]$$

When  $M_\infty \rightarrow 1$ , Eq. 21.86 is applicable, and thus we obtain the surprisingly simple result that

$$\left( \frac{dC_p}{dM_\infty} \right)_{M_\infty=1} = \frac{4}{k+1} \quad (21.88)$$

This may be put into the transonic similarity form suggested by Eq. 21.19, by means of a simple rearrangement based on the definition of  $K$ :

$$\frac{d \left[ \frac{C_p}{\delta^{2/3}} \left( \frac{k+1}{2} \right)^{1/3} \right]}{dK} = \frac{\left( \frac{k+1}{2} \right)^{1/3} \frac{1}{\delta^{2/3}} dC_p}{\frac{1}{2} \left( \frac{2}{k+1} \right)^{2/3} \frac{1}{\delta^{2/3}} (-2 dM_\infty)} = -2 \quad (21.89)$$

**FLOW WITH LARGE PERTURBATIONS.** If the flow is isentropic but has appreciable perturbations, then the relation following Eq. 21.46 must be used for determining the pressure coefficient. In this case it may be shown that

$$\left( \frac{dC_p}{dM_\infty} \right)_{M_\infty=1} = \frac{4}{k+1} - \frac{2}{k+1} (C_p)_{M_\infty=1} \quad (21.90)$$

Often the value of  $C_p$  at  $M_\infty = 1$  is large enough so that the last term of Eq. 21.90 must be taken into account.

**Lift Coefficient.** The value of  $C_L$  is found by integration of  $C_p$  with respect to the chord,

$$C_L = \int_0^1 (C_{pl} - C_{pu}) d\left(\frac{x}{l}\right)$$

where the subscripts  $l$  and  $u$  refer respectively to the lower and upper surfaces. Differentiating this expression with respect to  $M_\infty$ , and evaluating the results at  $M_\infty = 1$ , we have

$$\left(\frac{dC_L}{dM_\infty}\right)_{M_\infty=1} = \int_0^1 \left(\frac{dC_{pl}}{dM_\infty} - \frac{dC_{pu}}{dM_\infty}\right)_{M_\infty=1} d\left(\frac{x}{l}\right)$$

Writing the integrand in the form given by Eq. 21.90, and carrying out the indicated integration, we obtain

$$\left(\frac{dC_L}{dM_\infty}\right)_{M_\infty=1} = \frac{4}{k+1} - \frac{2}{k+1} (C_L)_{M_\infty=1} \quad (21.91)$$

**Drag Coefficient at Zero Lift.** Assuming that we are dealing with profiles symmetrical about the chord line, the pressure drag coefficient at zero lift is most conveniently expressed as the sum of two parts: (i)  $C_{Df}$  for the forward part, i.e., the part forward of the position of maximum thickness, and (ii)  $C_{Dr}$  for the rear part.

For the forward part we may write

$$C_{Df} = \int_{-\delta/2}^{+\delta/2} C_p d\left(\frac{y}{l}\right)$$

where the integration is carried out over the forward surface. Differentiating with respect to  $M_\infty$ , substituting Eq. 21.90 for the integrand, and integrating, we get

$$\left(\frac{dC_{Df}}{dM_\infty}\right)_{M_\infty=1} = \frac{4}{k+1} \delta - \frac{2}{k+1} (C_{Df})_{M_\infty=1} \quad (21.92a)$$

For the rear part we obtain, in similar fashion,

$$\left(\frac{dC_{Dr}}{dM_\infty}\right)_{M_\infty=1} = -\frac{4}{k+1} \delta - \frac{2}{k+1} (C_{Dr})_{M_\infty=1} \quad (21.92b)$$

Addition of these two equations yields, for the entire profile,

$$\left(\frac{dC_D}{dM_\infty}\right)_{M_\infty=1} = -\frac{2}{k+1} (C_D)_{M_\infty=1} \quad (21.92c)$$

**Curves of Force Coefficients.** Eqs. 21.88, 21.90, 21.91, and 21.92 serve as useful guides for fairing in and extrapolating experimental

results. One immediate result of interest is that although thin profiles with equal thickness ratios may have different values of  $C_L$  at  $M_\infty = 1$ , the slopes of the curves of  $C_L$  versus  $M_\infty$  are nearly the same for these different profiles.

Another interesting and important result for thin profiles which is evident from Eqs. 21.88 and 21.91 is that the curves of  $C_p$  and  $C_L$  are all rising with Mach Number at  $M_\infty = 1$ . Since it is known that at supersonic speeds the values of  $C_p$  and  $C_L$  decrease as  $M_\infty$  increases, it follows that there must be a peak in the curves at a value of  $M_\infty$  somewhat in excess of unity, as suggested by Fig. 21.27. This conclusion is generally confirmed by experimental data, although shock wave-boundary layer interactions can sometimes modify it.

The pressure drag coefficient for zero lift, on the other hand, is shown by Eq. 21.92c to decrease with Mach Number in the vicinity of Mach Number unity. Accordingly the curve of  $C_D$  (zero-lift pressure drag) versus  $M_\infty$  must peak at a value slightly less than unity, as suggested by Fig. 21.27.

**Implications for Wind-Tunnel Testing.** The difficulties of making wind tunnel tests near Mach Number unity have already been elaborated. By using the results outlined in this article the need for such tests may be partially eliminated. If tests are performed at Mach Numbers both above and below the troublesome range near Mach Number unity, the performance in the latter range may be estimated with the help of Eqs. 21.90, 21.91, and 21.92, together with similar formulas which may be derived for three-dimensional flows.

**Application to Biconvex Profile.** Fig. 21.28 shows the application of these ideas to a 12% biconvex profile.<sup>(19)</sup> Pressure distributions on the surface were measured for subsonic Mach Numbers up to 0.94 and for supersonic Mach Numbers of 1.29 and 1.42. Integration of the surface pressures yielded the data points of the chart, in which the separate drags of the forward and rear portions are shown in addition to the total drag. The drag coefficient for values of  $M_\infty$  between 0.96 and 1.20 was interpolated for by assuming a constant surface pressure distribution in this range. This constant pressure distribution was taken as the

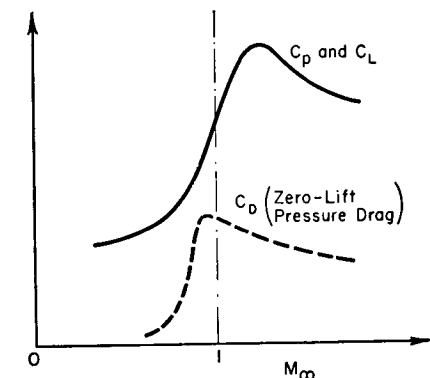


FIG. 21.27. Maxima in curves of  $C_p$  and  $C_L$  occur at supersonic free-stream Mach Number. Maximum for  $C_D$  occurs for  $M_\infty < 1$ .

mean of that for  $M_\infty = 0.94$  and that for  $M_\infty = 1.42$ , a procedure entailing little error because the two latter distributions were so nearly alike. The drag curves interpolated in this manner (shown by dashed lines) were faired into the experimental curves. For values of  $M_\infty$  greater than 1.42 the experimental curves were faired into curves calculated

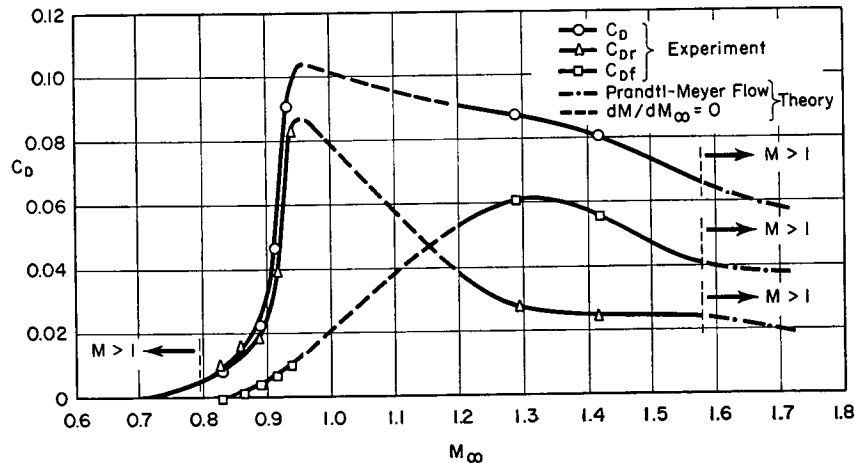


FIG. 21.28. Drag coefficient versus  $M_\infty$  for 12% biconvex circular-arc profile, illustrating interpolation in the transonic range by means of the assumption that  $(dM/dM_\infty)_{M_\infty=1} = 0$  (after Bryson).

by means of oblique shock theory and simple-wave theory. The latter curves begin at  $M_\infty = 1.58$ , corresponding to the point where the flow behind the attached shock is exactly sonic.

The interpolation procedure in the transonic range is seen to give a fairly consistent picture. As predicted by Eq. 21.92a,  $C_{Df}$  reaches a maximum at supersonic speeds, whereas  $C_{Dr}$  and  $C_D$  have maxima at subsonic speeds. The curve of  $C_D$  has a slightly negative slope as it passes through Mach Number unity (Eq. 21.92c). Up to Mach Number unity the fore drag is small compared with the rear drag, but in the range of fully supersonic flow ( $M_\infty > 1.58$ ) the fore drag constitutes about two-thirds of the total.

### 21.9. Transonic Flow Past Wedge Nose

In Art. 21.7 results were presented for the flow at  $M_\infty = 1$  past a profile having a wedge-shaped nose terminated by sharp-corner shoulders. For such profiles, it was pointed out, the pressure distribution on the wedge must, in the absence of viscous effects, be independent of the shape of the profile aft of the shoulders.

The problem of flow at high subsonic speeds past a wedge-shaped

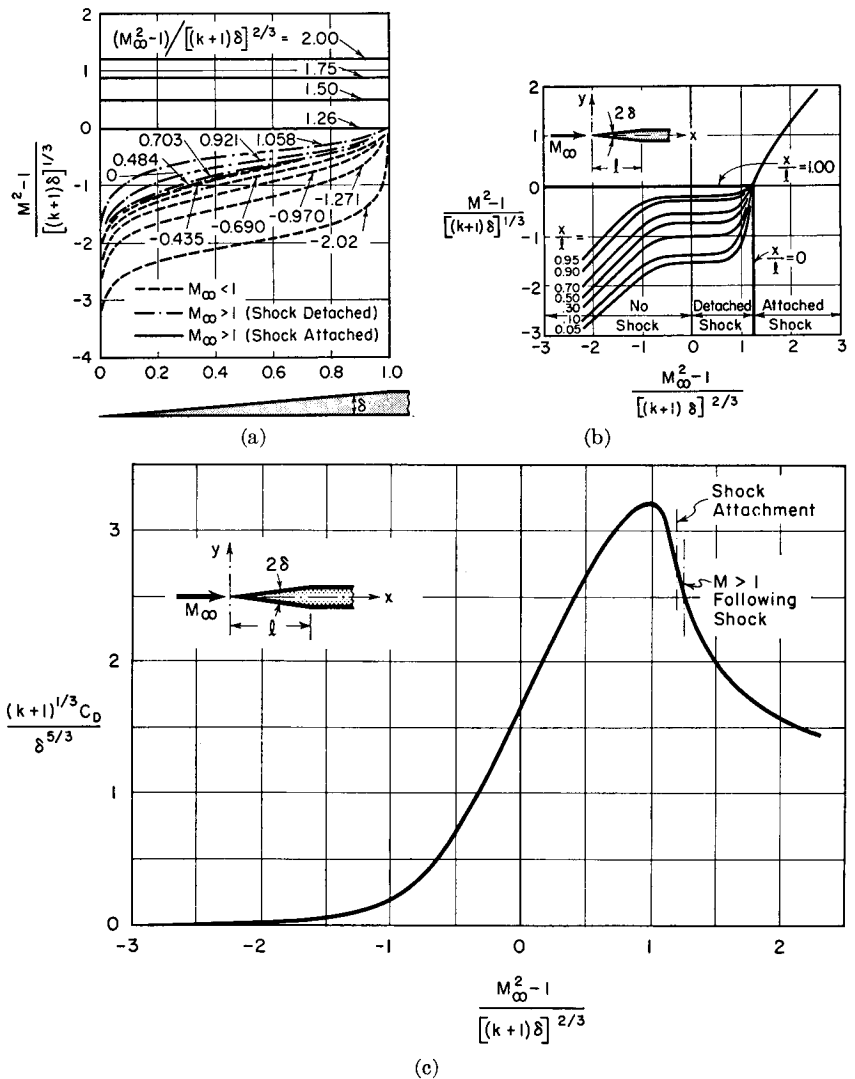


FIG. 21.29. Theoretical results at surface of wedge-shaped nose terminated by sharp-corner shoulders (after Bryson). Results are compiled from following references:

Range	Investigator	Reference
$M_\infty < 1$	Cole	20
$M_\infty = 1$	Guderley and Yoshihara	15
$M_\infty > 1$ , detached shock	Vincenti and Waggoner	18
$M_\infty > 1$ , attached shock	Tsien and Baron	3
(a) Chordwise distribution of Mach Number for various free-stream Mach Numbers.		
(b) Variation of local Mach Number with free-stream Mach Number for various chordwise stations.		
(c) Pressure drag coefficient versus free-stream Mach Number.		

nose has been explored analytically by Cole<sup>(20)</sup> and, at supersonic speeds with detached shocks, by Vincenti and Wagoner.<sup>(18)</sup> For supersonic speeds with attached shocks, the method of Tsien and Baron (Art. 21.3) has already been discussed.

By combining the results of the several investigations mentioned above, Bryson<sup>(19)</sup> has given a picture of the theoretical flow past a wedge-shaped nose for the entire transonic region. The results are presented in Fig. 21.29 in generalized forms consistent with the transonic similarity laws.

Fig. 21.29a shows that at low subsonic Mach Numbers the distribution of Mach Number on the surface is typically that of a subsonic flow, with a stagnation point at the apex. At sufficiently high supersonic Mach Numbers, the leading-edge shock is attached, and the Mach Number is constant on the surface. In the range of low supersonic Mach Numbers there is a detached shock and the flow near the surface is essentially subsonic in character. For flow with no shocks and also for flow with a detached shock the flow becomes sonic at the sharp shoulder. It may be noted for reference purposes that the parameter on the curves is 1.19 at the point of shock attachment, and is 1.26 when the flow downstream of the attached shock is exactly sonic. The change from completely subsonic flow to supersonic flow with an attached shock is seen to be gradual in character, and no such phenomenon as a "sonic barrier" is present. The curves for  $M_\infty < 1$  and for  $M_\infty > 1$  are very closely grouped in the neighborhood of  $M_\infty = 1$ , thus substantiating our previous conclusion that  $(dM/dM_\infty)_{M_\infty=1} = 0$ .

The latter result is even more strikingly evident from Fig. 21.29b, where the local Mach Number is plotted against free-stream Mach Number for various stations on the wedge.

The integrated pressure drag coefficient, based on the length  $l$ , is shown in Fig. 21.29c as a function of free-stream Mach Number. The curve is in accord with the rule expressed by Eq. 21.92a, and has a shape like that of the curve of  $C_p$  versus  $M_\infty$  (Fig. 21.27).

These theoretical results are compared with experimental measurements in Chapter 22.

#### REFERENCES AND SELECTED BIBLIOGRAPHY

1. VON KÁRMÁN, T. Similarity Law of Transonic Flow, *Jour. Math. and Phys.*, Vol. 26 (1947), p. 182.
2. KAPLAN, C. On Similarity Rules for Transonic Flows, *NACA Tech. Note*, No. 1527 (1948).
3. TSIEN, H. S., and BARON, J. R. Airfoils in Slightly Supersonic Flow, *Jour. Aero. Sci.*, Vol. 16, No. 1 (1949), p. 55.
4. PERL, W., and KLEIN, M. M. Theoretical Investigation and Application of Transonic Similarity Law for Two-Dimensional Flow, *NACA Tech. Note*, No. 2191 (1950).

5. PERL, W., and KLEIN, M. M. Theoretical Investigation of Transonic Similarity for Bodies of Revolution, *NACA Tech. Note*, No. 2239 (1950).
6. OSWATITSCH, K., and ROTHSTEIN, W. Flow Pattern in a Converging-Diverging Nozzle, *NACA Tech. Memo.*, No. 1215 (1949).
7. SAUER, R. General Characteristics of the Flow Through Nozzles at Near Critical Speeds, *NACA Tech. Memo.*, No. 1147 (1947).
8. MEYER, T. Über zweidimensional Bewegungsvorgänge in einem Gas, das mit Überschallgeschwindigkeit strömt, *Forschung a. d. Geb. d. Ing.*, 62 (1908).
9. TAYLOR, G. I. The Flow of Air at High Speeds Past Curved Surfaces, *British A.R.C.*, R & M No. 1381 (1930).
10. EMMONS, H. W. The Theoretical Flow of a Frictionless, Adiabatic, Perfect Gas Inside of a Two-Dimensional Hyperbolic Nozzle, *NACA Tech. Note*, No. 1003 (1946).
11. EMMONS, H. W. The Numerical Solution of Compressible Fluid Flow Problems, *NACA Tech. Note*, No. 932 (1944).
12. EMMONS, H. W. Flow of a Compressible Fluid Past a Symmetrical Airfoil in a Wind Tunnel and in Free Air, *NACA Tech. Note*, No. 1746 (1948).
13. KAPLAN, C. On a Solution of the Nonlinear Differential Equation for Transonic Flow Past a Wave-Shaped Wall, *NACA Tech. Note*, No. 2383 (1951).
14. GUDERLEY, K. G. Singularities at the Sonic Velocity, *U.S. Air Force Technical Report*, F-TR-1171-ND (1948).
15. GUDERLEY, G., and YOSHIHARA, H. The Flow Over a Wedge Profile at Mach Number One, *Jour. Aero. Sci.*, Vol. 17, No. 11 (1950), p. 723.
16. HEASLET, M. A., LOMAX, H., and SPREITER, J. R. Linearized Compressible-Flow Theory for Sonic Flight Speeds, *NACA Tech. Note*, No. 1824 (1949).
17. LIEPMANN, H. W., and BRYSON, A. E., Jr. Transonic Flow Past Wedge Sections, *Jour. Aero. Sci.*, Vol. 17, No. 12 (1950), p. 745.
18. VINCENTI, W. G., and WAGONER, C. B. Transonic Flow Past a Wedge Profile with Detached Bow Wave—General Analytical Method and Final Calculated Results, *NACA Tech. Note*, No. 2339 (1951).
19. BRYSON, A. E., Jr. An Experimental Investigation of Transonic Flow Past Two-Dimensional Wedge and Circular-Arc Sections Using a Mach-Zehnder Interferometer, *NACA Tech. Note*, No. 2560 (1951).
20. COLE, J. D. Drag of a Finite Wedge at High Subsonic Speeds, *Jour. Math. and Phys.*, Vol. 30, No. 2 (1951), p. 79.
21. HABEL, L. W., and HENDERSON, J. H. Preliminary Investigation of Airfoil Characteristics in the Langley Annular Transonic Tunnel, *NACA R.M.*, No. L50E18 (1950).
22. GRIFFITH, W. Shock-Tube Studies of Transonic Flow Over Wedge Profiles, *Jour. Aero. Sci.*, Vol. 19, No. 4 (1952), p. 249.
23. SPREITER, J. R. On the Application of Transonic Similarity Rules, *NACA Tech. Note*, No. 2726 (1952).
24. GUDERLEY, G., and YOSHIHARA, H. Two-Dimensional Unsymmetric Flow Patterns at Mach Number 1, *Jour. Aero. Sci.*, Vol. 20, No. 11 (1953), p. 757.
25. SPREITER, J. R. On Alternative Forms for the Basic Equations of Transonic Flow Theory, *Jour. Aero. Sci.*, Vol. 21, No. 1 (1954), p. 70.

- 21.1. The two-dimensional transonic similarity rule of Eq. 21.19 states that, at *corresponding points* of the flow past affinely related profiles operating with the same values of  $K$ ,  $C_p$  is proportional to  $\delta^{2/3}/(k+1)^{1/3}$ .  
(a) Show that the corresponding points are not at geometrically similar locations, but are rather connected by the rules that

$$x_1/l_1 = x_2/l_2; \quad \frac{y_1/l_1}{y_2/l_2} = \frac{\delta_2^{4/3}(k_2+1)^{1/3}}{\delta_1^{4/3}(k_1+1)^{1/3}}$$

where  $l$  is the chord,  $t$  is the maximum thickness, and subscripts 1 and 2 refer to affine profiles which are transonically similar.

(b) Compare the corresponding locations for the cases where  $M_{\infty 1} = 0.95$  and  $M_{\infty 2} = 0.90$ .

(c) What do you conclude from the above formulas regarding the comparison of lift and drag coefficients for the profile?

(d) Determine what is meant by corresponding points in the transonic similarity rule for wings of finite span.

**21.2.** Suppose experimental data were available giving the lift and drag coefficients versus Mach Number for a 10% profile in the transonic range. Explain how you would derive from these data curves showing  $C_L$  and  $C_D$  versus  $M_{\infty}$  for a 5% profile in the transonic range.

**21.3.** Demonstrate that if  $\mathcal{P} \sim K^{-3/2}$ , then Eq. 21.19 leads to the same conclusions as the linearized theory of supersonic flow.

What is the significance, if any, of this?

**21.4.** (a) Using the exact results for oblique shock waves, plot, for the shock corresponding to the limiting case of shock attachment,  $K$  versus wedge angle and initial Mach Number. Determine the range of Mach Numbers and wedge angles for which the transonic similarity law is accurate to within 5 per cent in this respect.

(b) Carry out a corresponding inquiry for the value of  $K$  corresponding to sonic velocity downstream of the shock.

**21.5.** (a) Using the results of the exact oblique shock relations, plot  $(k+1)C_p/(M_1 - 1)$  versus  $K$  for several values of  $\delta$ , where  $C_p$  is the pressure coefficient across the shock,  $\delta$  is the turning angle, and  $M_1$  is the approach Mach Number. From this chart, construct a chart of  $M_1$  versus  $\delta$  which indicates the range of parameters for which the transonic similarity law can be relied upon with an error in  $C_p$  of not more than 5 per cent.

(b) Derive a similar range of parameters for transonic flow past a cone.

**21.6.** Formulate expressions for Prandtl-Meyer *compressions* based on the assumptions of transonic similarity.

**21.7.** Employing the exact equations for a Prandtl-Meyer expansion beginning with  $M = 1$ , plot the exact value of

$$C_p \frac{[(k+1)/2]^{1/3}}{(3\theta)^{2/3}}$$

versus  $\theta$  for such an expansion, and compare this exact result with the value of  $(-1)$  predicted by the transonic similarity theory. Determine the range of values of  $\theta$  and  $M$  for which the approximate theory predicts  $C_p$  within 5 per cent.

**21.8.** (a) Consider the supersonic flow past a cone of half-angle  $\delta$  at the minimum free-stream Mach Number,  $M_{1,\min}$ , for which the shock remains attached. Plot  $(M_{1,\min} - 1)$  versus  $\delta^2$  in radians, and show that this curve approaches a straight line as  $M_{1,\min}$  approaches unity.

(b) Explain this in terms of the transonic similarity law.

(c) Determine the value of the transonic similarity parameter corresponding to shock detachment. Compare with the value of  $-0.945$  for the two-dimensional similarity parameter in the case of shock detachment for the flow past a wedge.

**21.9.** (a) Compare the laws of variation of lift and drag coefficients with thickness ratio for two-dimensional flow in the subsonic, transonic, supersonic, and hypersonic regimes.

(b) Make similar comparisons for the drag of slender bodies of revolution in the four regimes.

(c) Repeat the comparisons to show the effects of maximum thickness on total lift and drag for bodies of fixed length.

**21.10.** Consider a flat-plate profile operating at an angle of incidence of  $5^\circ$ . Neglecting viscous effects, plot  $C_L$ ,  $C_D$ , and  $C_M$  versus  $M_{\infty}$  for this profile over a range of speeds from incompressible to hypersonic flow. Plot also  $C'_L$ ,  $C'_D$ , and  $C'_M$  versus  $M_{\infty}$ , where the primed coefficients are based on  $c_{\infty}$  rather than on  $V_{\infty}$ .

**21.11.** Consider a slender body of revolution of fineness ratio 20 and having a parabolic profile in the meridian plane, with a sharp nose and tail. Neglecting viscous effects, plot  $C_D$  versus  $M_{\infty}$  over a range of speeds from incompressible to hypersonic flow. Plot also  $C'_D$  versus  $M_{\infty}$ , where  $C'_D$  is based on  $c_{\infty}$  rather than on  $V_{\infty}$ , as a measure of total drag.

**21.12.** Demonstrate that the Mach Number at the wall of a nozzle throat is approximately

$$M_{\infty s} \cong 1 + \frac{1}{3} \frac{y_s}{R_s}$$

**21.13.** Demonstrate that, within the approximations of transonic flow with small perturbations, the physical characteristics are defined by

$$\frac{dy}{dx} = \pm \sqrt{\frac{c^*}{(k+1)u'}}$$

where  $u'$  is the perturbation speed in the  $x$ -direction, referred to  $c^*$ .

When are the characteristics real and when are they imaginary?

Determine the corresponding differential equation for the hodograph characteristics expressed in terms of  $u'$  and  $v'$ , and also in terms of the polar velocity coordinates corresponding to  $u'$  and  $v'$ .

**21.14.** By interchanging dependent and independent variables, show that the transonic perturbation equation (Eq. 21.72) and the equation of irrotationality take the respective hodograph forms

$$(k+1) \frac{\partial y}{\partial \tilde{v}} + \frac{\partial x}{\partial \tilde{u}} = 0$$

$$\frac{\partial x}{\partial \tilde{v}} - \frac{\partial y}{\partial \tilde{u}} = 0$$

Note that these equations are linear, and that, after elimination of  $x$  by differentiation, there is obtained the Tricomi equation:

$$(k + 1) \frac{\partial^2 y}{\partial \tilde{v}^2} = \frac{\partial^2 y}{\partial \tilde{u}^2}$$

**21.15.** Show that if the flow is isentropic, but has perturbations which are not necessarily small, the variation of  $C_p$  with  $M_\infty$  at the condition where the latter is unity is given by Eq. 21.90.

Using this result, investigate the shape of the curve of  $C_p$  versus  $M_\infty$  near Mach Number unity.

**21.16.** Show that the equation of the hodograph shock polar for transonic flow is given approximately by

$$\frac{2}{k + 1} \tilde{v}^2 = (\tilde{u}_1 - \tilde{u})^2 (\tilde{u}_1 + \tilde{u})$$

where  $\tilde{u}_1$  is equal to  $(U_1 - c^*)/c^*$  and  $U_1$  is the velocity approaching the shock.

From this find the transonic similarity forms of the conditions for a detached shock and for sonic flow behind the shock, as expressed by Eqs. 21.41 and 21.49.

**21.17.** Show that the results of the linearized supersonic theory for flow past a wedge of turning angle  $\delta$  may be put into the following transonic similarity form:

$$\frac{(k + 1)^{1/3} C_p}{\delta^{2/3}} = 2 \sqrt{\frac{[(k + 1) \delta]^{2/3}}{M_\infty^2 - 1}}$$

## Chapter 22

### DRAG AND LIFT AT TRANSONIC SPEEDS

#### 22.1. Introductory Remarks

In the preceding two chapters various theoretical considerations concerning mixed flows and transonic flows were outlined.

In this chapter we shall concern ourselves principally with outlining typical experimental results at transonic speeds. Apart from the intrinsic value of experimental data, such data serve to illuminate the various analytical approaches, and thus make it possible to plan future experiments more intelligently. The experiments will be discussed with this in mind.

Because of the great lateral influence of profiles at transonic speeds, models must be made extremely small compared with the wind tunnel in which they are tested, and this introduces great experimental difficulties. Consequently, the body of data at transonic speeds is considerably smaller and less reliable than at either subsonic or supersonic speeds. In recent years, fortunately, sufficient experimental results at transonic speeds have become available to indicate the principal features of the flow past profiles, three-dimensional wings, and bodies of revolution. These will be outlined.

Experimentally, the drag coefficient at transonic speeds is higher than at either subsonic or supersonic speeds. We shall discuss some of the theoretical thinking on the question of whether such high drags are in fact unavoidable or whether they may be eliminated by proper design.

Finally, we shall examine the main features of the shock-boundary layer interaction at transonic speeds. This interaction often plays such a major part in determining the flow pattern, especially at transonic speeds, that even a discussion of "potential" transonic flow can scarcely omit considerations of this effect.

## NOMENCLATURE

$A$	cross-sectional area for flow	$x, y$	Cartesian coordinates
$c^*$	critical sound velocity	$\alpha_s$	Mach angle at surface
$C_D$	drag coefficient	$\beta$	$\sqrt{M_\infty^2 - 1}$
$C_L$	lift coefficient	$\delta$	thickness ratio; also wedge semi-angle
$C_p$	pressure coefficient	$\eta$	see Fig. 22.27
$D$	drag	$\theta$	turning angle
$h$	height of supersonic zone	$\theta_s$	flow direction at surface
$k$	ratio of specific heats	$\rho$	mass density
$l$	chord	$\sigma$	shock angle
$L$	lift; also see Fig. 22.27	$(\ )_\infty$	signifies free-stream conditions
$M$	Mach Number	$(\ )_0$	signifies stagnation state
$M_s^*$	$V/c^*$ at surface	$(\ )_s$	signifies point of intersection of sonic line with detached shock
$M_{cr}$	lower critical $M_\infty$	$(\ )_{SB}$	signifies sonic point on body
$p$	pressure		
$u'$	perturbation velocity in $x$ -direction, referred to $U_\infty$		
$U_\infty$	free-stream velocity		
$V$	velocity		

## 22.2. Experimental Validity of Transonic Similarity Law

We shall now discuss several systematic collections of experimental data which will serve to indicate the reliability with which experimental data may be extended through the use of the similarity law. In addition, the measured data are of interest for themselves.

**Flow Past Biconvex Circular Arc Profiles.** <sup>(1)</sup> The results of wind tunnel measurements made at transonic speeds past biconvex profiles are shown in Fig. 22.1.

In Fig. 22.1b is shown, for a 6% profile, the way in which the Mach Number  $M_y$  above the point of maximum thickness decays with increasing distance  $y/l$  from the profile. Examination of the faired curves shows that the lateral influence of the profile (as measured by the distance  $y/l$  required for  $M_y$  to approach  $M_\infty$ ) increases as  $M_\infty$  approaches unity, thus verifying in this respect the predictions of the crude linearized theory.

Similar results are given in Fig. 22.1c for a 12% profile. In addition to the experimental points on this chart, there are shown four predicted curves, corresponding to  $\delta = 0.12$ , which are derived by the similarity law from the faired curves of Fig. 22.1b for  $\delta = 0.06$ . These are derived by the argument which follows. If the similarity parameter  $K_y$  is defined in terms of a point ( $x = l/2, y = y$ ) having a local  $M_y$ , then  $C_{py} = 0$  if the latter is referred to  $p_y$  and  $M_y$ . It follows from Eq. 21.19 that for fixed values of  $K_y$  and  $\xi$  there can be only one value of  $\eta$ . We

are considering here only points for which  $\xi = 0.5$ . Then, if  $\delta_1 = 0.06$  and  $\delta_2 = 0.12$ , it follows from Eqs. 21.17 and 21.14b that if

$$\frac{1 - M_{y1}^2}{1 - M_{y2}^2} = \left(\frac{\delta_1}{\delta_2}\right)^{2/3} = \left(\frac{1}{2}\right)^{2/3} = 0.630$$

then

$$\frac{(y/l)_1}{(y/l)_2} = \left(\frac{\delta_2}{\delta_1}\right)^{1/3} = (2)^{1/3} = 1.260$$

For each curve of Fig. 22.1b, pairs of values of  $M_{y1}$  and  $(y/l)_1$  may be selected; then, using the formulas given immediately above, the cor-

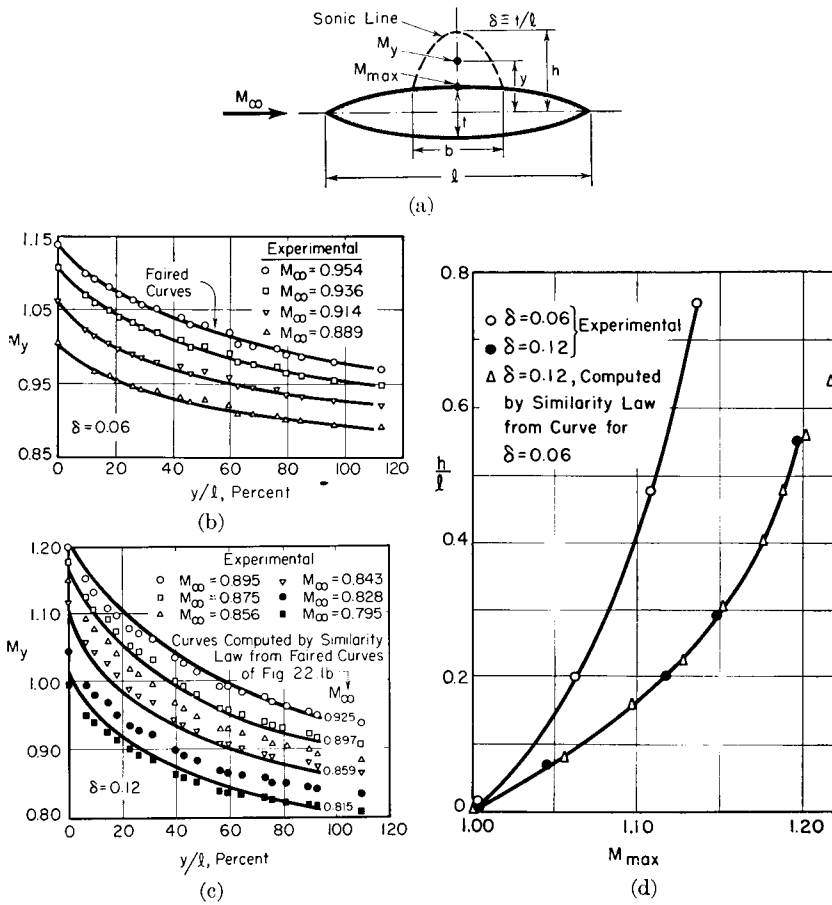


FIG. 22.1. Flow past biconvex profile (after Liepmann, Ashkenas, and Cole).

(a) Nomenclature.

(b) Lateral decay of local Mach Number for  $\delta = 0.06$ .

(c) Lateral decay of local Mach Number for  $\delta = 0.12$ . Curves are computed by applying similarity law to faired curves of (b).

(d) Height of supersonic zone.

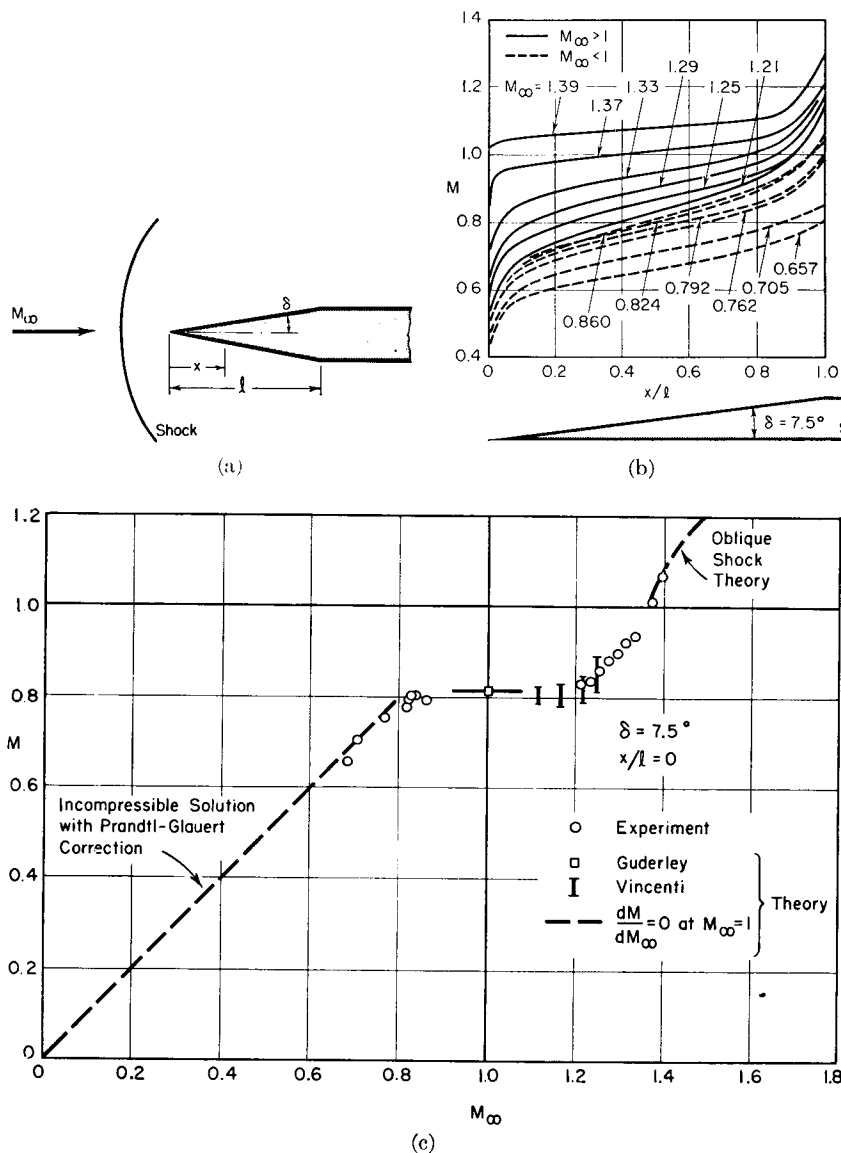


FIG. 22.2. Experimental results for flow past wedge-shaped nose (after Liepmann and Bryson).

- (a) Nomenclature.
- (b) Surface Mach Number versus per cent chord.
- (c) Surface Mach Number versus free-stream Mach Number, at  $x/l = 0.5$ .

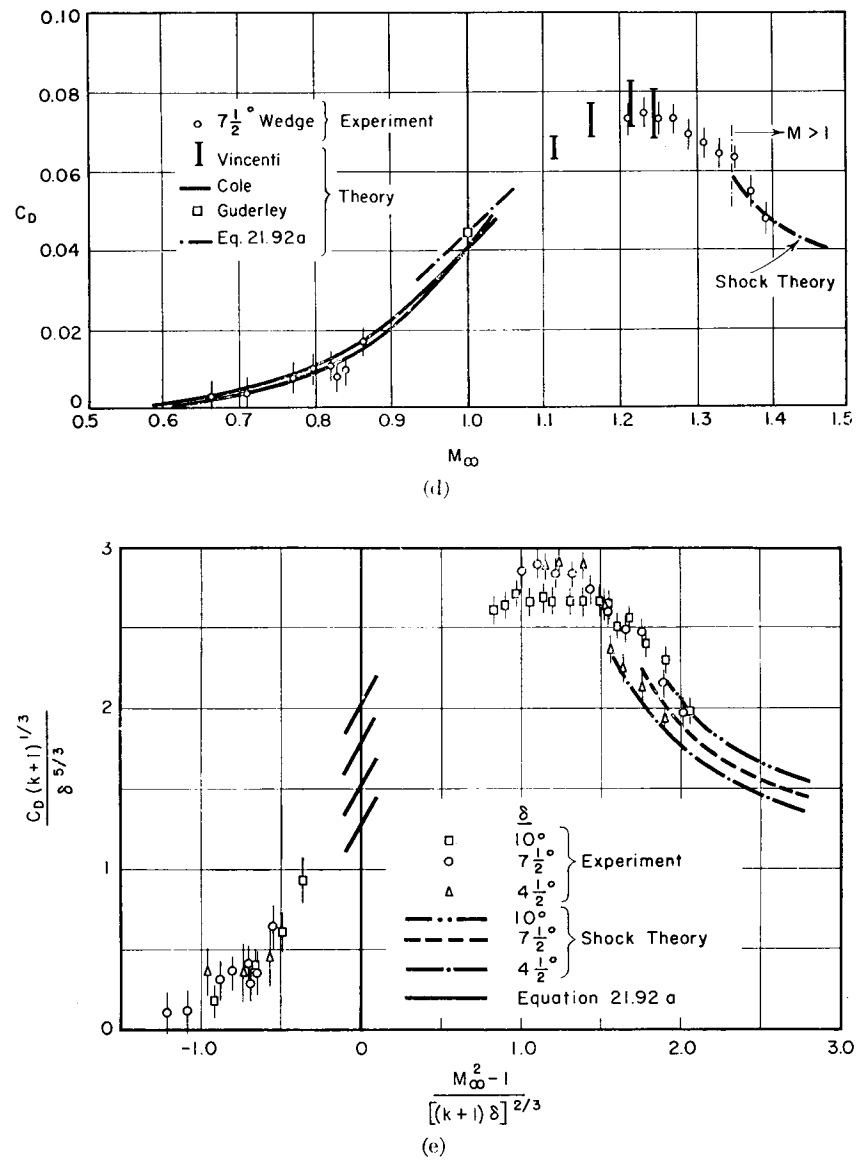


FIG. 22.2 (Continued)

- (d) Drag coefficient versus  $M_\infty$  for  $\delta = 7.5^\circ$ . Vertical lines through data points indicate experimental accuracy.
- (e) Transonic similarity correlation of  $C_D$  with  $M_\infty$ . Vertical lines through data points indicate experimental accuracy.

responding pairs of values for  $\delta_2 = 0.12$  may be computed. In this way the curves of Fig. 22.1c are drawn. The appropriate value of  $M_\infty$  is attached to each curve by using the same calculation procedure and by noting that  $M_\infty \rightarrow M_\infty$  as  $y \rightarrow \infty$ .

From Fig. 22.1c it is evident that in this instance the transonic similarity law is quite good except for values of  $M_\infty$  very close to unity. The discrepancies are in part due to interference between the model and the tunnel walls; this interference is especially pronounced near  $M_\infty$  equal to unity, and, moreover, tends to make  $M_\infty$  a somewhat ambiguous quantity. If the computed curves of Fig. 22.1c are thought of as representing the decay of  $M$  beginning with some particular value of  $M_{max}$  at the point of maximum thickness, then only the shapes of the curves are important, and in this respect the agreement with the experimental data for  $\delta = 0.12$  is seen to be good.

A further check on the transonic similarity law, based on the same data, is illustrated by Fig. 22.1d, where the height of the supersonic zone is plotted against  $M_{max}$ , the latter being the surface Mach Number at mid-chord. Apart from the experimental results for  $\delta = 0.06$  and  $\delta = 0.12$ , there is shown also the predicted result for  $\delta = 0.12$ , based on a combination of the transonic similarity law with the experimental data for  $\delta = 0.06$ . The similarity law states that if

$$\frac{1 - M_{max,1}^{-2}}{1 - M_{max,2}^{-2}} = \left(\frac{\delta_1}{\delta_2}\right)^{2/3} = 0.630$$

then

$$\frac{(h/l)_1}{(h/l)_2} = \left(\frac{\delta_2}{\delta_1}\right)^{1/3} = 1.260$$

In this case the predictions of the similarity law are in remarkable agreement with the measurements.

**Flow Past Wedge-Shaped Nose.** <sup>(2)</sup> Figs. 22.2b, c, d, e show the results of measurements on a wedge-nose of the shape shown in Fig. 22.2a, and may be compared with Fig. 21.29. Since the Mach Number at the shoulder corner must be unity as long as  $M_\infty$  is less than the value required for an attached shock at the nose, the pressure distribution over the wedge-shaped nose is, in this range of  $M_\infty$ , independent of the shape of the afterbody, provided of course that boundary-layer effects are negligible.

The distribution of Mach Number along the wedge surface is shown in Fig. 22.2b. For high Mach Numbers, there is an attached shock, and the Mach Number on the surface is constant except for the influence of the marked changes in boundary-layer thickness near the apex and near the shoulder, changes which are felt to a considerable distance along the wedge. As  $M_\infty$  decreases, the Mach Number distribution changes slowly and regularly until it takes the typical subsonic form.

Note that because of the rounding effect of the boundary layer at the corner, the Mach Number at the corner is considerably different from unity, even for the flows with detached shock. These results are in good agreement with Fig. 21.29a, except in the vicinity of the corner.

Fig. 22.2b reveals that over the range of  $M_\infty$  from 0.82 to 1.2, the distribution of Mach Number on the wedge is almost independent of  $M_\infty$ , thus confirming the theoretical prediction of Art. 21.8 that  $(dM/dM_\infty)_{M_\infty=1} = 0$ .

The same result is shown even more clearly in Fig. 22.2c, where  $M$  is cross-plotted versus  $M_\infty$  at mid-chord ( $x/l = 0.50$ ) for  $\delta = 7.5^\circ$ . Besides indicating that  $dM/dM_\infty \cong 0$  over a surprisingly wide range of values of  $M_\infty$  in the neighborhood of unity, this chart shows a number of interesting comparisons with theory (see also Fig. 21.29b). In the low range of  $M_\infty$ , there is shown the incompressible theory corrected by the Prandtl-Glauert rule. At  $M_\infty = 1$ , there is shown the theoretical result of Guderley <sup>(3)</sup> together with the theoretical prediction that  $(dM/dM_\infty)_{M_\infty=1} = 0$ . In the low supersonic range are shown the theoretical predictions of Vincenti and Wagoner; <sup>(4)</sup> these are shown as horizontal bars, the upper end corresponding to the approximation that  $C_p \cong -2u'/c^*$  and the lower to  $C_p \cong -2u'/U_\infty$  (these two methods of calculating  $C_p$  are equally correct within the approximations of the transonic theory). When  $M_\infty$  is high enough so that a shock is attached to the nose, the oblique shock theory is used for finding  $M$  versus  $M_\infty$ .

In sum, the experimental data of Fig. 22.2c are in excellent accord with the theories for the several ranges of Mach Number shown. At a given point on the wedge  $M$  at first increases almost linearly with  $M_\infty$  in the low subsonic range; in the transonic range  $M$  remains nearly constant; and in the supersonic range  $M$  again increases with  $M_\infty$ .

By integrating the measured pressure coefficients over the surface of the wedge, the drag of the *nose* of the wedge up to the shoulder may be found, and may be reckoned as a drag coefficient based on the chord length  $l$ :

$$C_D = 2 \tan \delta \int_0^1 C_p d(x/l)$$

The measured drag coefficients as so found are plotted versus  $M_\infty$  in Fig. 22.2d for  $\delta = 7.5^\circ$ . As in the previous chart, there are shown also (i) the theoretical drag based on oblique shock theory for values of  $M_\infty$  large enough to yield an attached nose shock; (ii) the theoretical drag for slightly supersonic speeds with detached shock, shown as a range corresponding to the two different definitions of  $C_p$ ; (iii) the theoretical drag at  $M_\infty = 1$  as computed by Guderley and Yoshihara; <sup>(5)</sup> (iv) the theoretical drag slope at  $M_\infty = 1$  based on Eq. 21.92a; and (v) the theoretical drag for subsonic speeds as computed by Cole, <sup>(6)</sup> and also given as a range of values corresponding to the two definitions

of  $C_D$ . The agreement between the various theories and the measurements is generally good. It is seen that the pressure drag coefficient rises rapidly with  $M_\infty$  at high subsonic Mach Numbers and reaches a maximum at  $M_\infty \approx 1.2$  to 1.3, after which it decreases, at first quite rapidly and then more slowly, as is usual in the supersonic range.

The data of Fig. 22.2d, together with similar data for two other wedge angles, are replotted in Fig. 22.2e according to the form of the transonic similarity law. It is seen that the similarity principle is quite successful in bringing all the data within a rather narrow band, notwithstanding that the range of wedge angles makes the assumption of

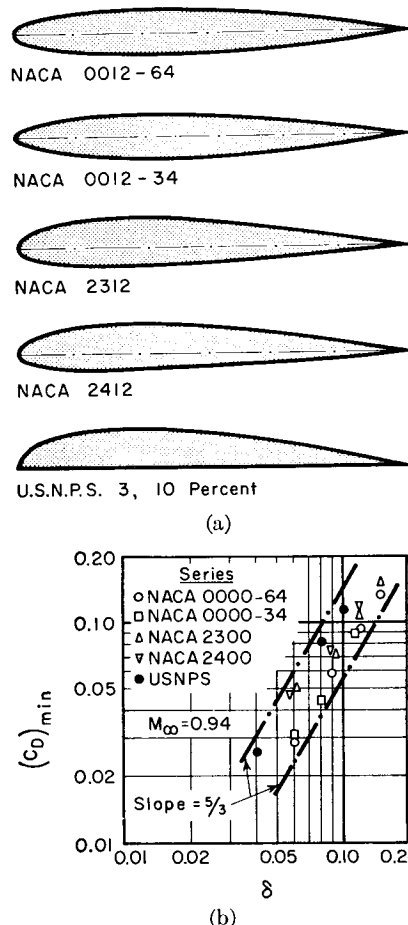


FIG. 22.3. Minimum drag of several families of affinely related profiles at  $M_\infty = 0.94$  (after Ferri).

- (a) Typical profiles of the five families.
- (b)  $C_D$  versus thickness ratio. Dashed lines indicate transonic similarity law for  $M_\infty = 1$ .

small perturbations somewhat questionable. The agreement with the theoretical curve of Fig. 21.29 is also seen to be fairly good.\*

**Effect of Thickness on Drag near Mach Number Unity.** <sup>(8)</sup> Fig. 22.3b shows the minimum drag coefficient as a function of thickness ratio for several families of affine profiles at  $M_\infty = 0.94$ , typical profiles in these families being shown in Fig. 22.3a. Presumably the minimum drag is principally pressure drag plus a certain amount of skin-friction drag.

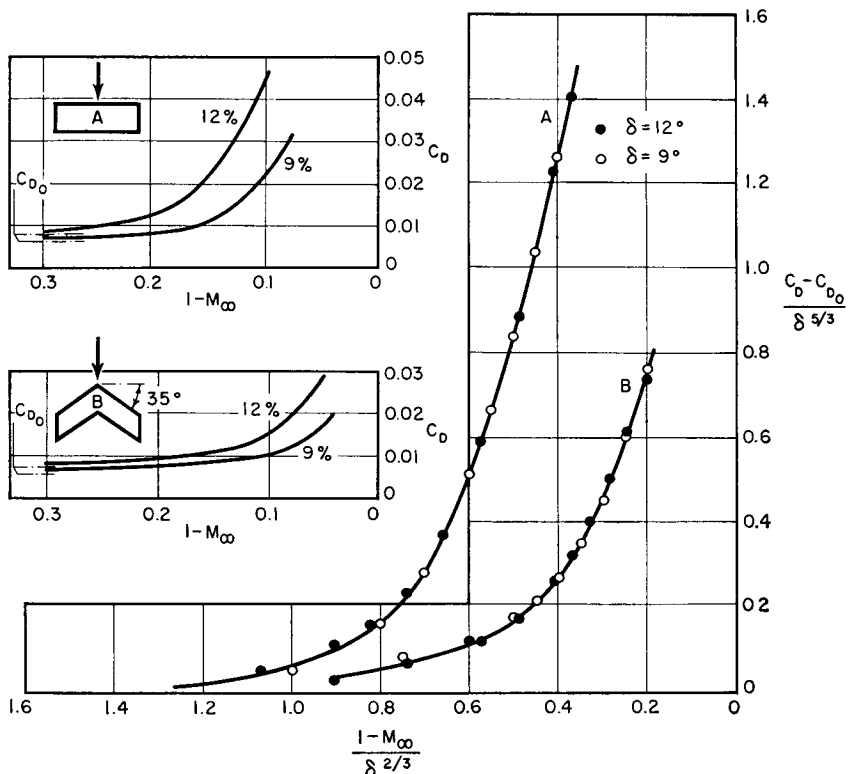


FIG. 22.4. Measured drag of rectangular and sweptback wings (aspect ratio = 3.25) having same profiles in streamwise direction. Insert charts show  $C_D$  versus  $(1 - M_\infty)$  for each planform and with profile thicknesses of 9 per cent and 12 per cent. (NACA 0-0009-1.1-30 and NACA 0-0012-1.1-30.) Large chart shows plots of same data (with skin-friction drag deducted from total drag) in transonic similarity form (after Ackeret, Degen, and Rott).

\*Note added in proof. As indicated in the footnote on page 809, the transonic similarity law is most successful if, in Eqs. 21.17 through 21.32, the term  $(k + 1)$  is replaced by  $(k + 1)M_\infty^2$ . When the experimental results of Fig. 22.2e are replotted with the modified variables  $[(k + 1)M_\infty^2]^{1/3}C_D/\delta^{5/3}$  and  $(M_\infty^2 - 1)/[(k + 1)M_\infty^2\delta]$ , it is found<sup>(31)</sup> that the data points do indeed lie much closer to a single curve, thus signifying that the modified variables provide a better correlation. Moreover, the theoretical curve of Fig. 21.29, when the coordinate variables are replaced by the modified forms, is in nearly perfect agreement with the modified experimental results.

According to the transonic similarity law, at  $M_\infty = 1$  the pressure drag coefficient should, in the absence of boundary-layer separation, vary as  $\delta^{5/3}$ . It is seen from the chart that this rule fits the data quite well even at  $M_\infty = 0.94$  for the uncambered profiles. For the cambered profiles the agreement is not so good, possibly because boundary-layer separation due to shocks or adverse pressure gradients is more likely to occur with a cambered section in consequence of the higher local Mach Numbers reached for a given free-stream Mach Number.

**Pressure Drag of Wings at Zero Lift.** <sup>(28)</sup> Fig. 22.4 shows the results of drag measurements at high subsonic speeds on two wings having uncambered subsonic profiles. The insert charts show plainly that the onset of drag rise owing to compressibility effects may be delayed by using thin profiles or by employing the sweepback principle.

The same data (except with the skin-friction drag subtracted from the total drag) are plotted in the large chart in terms of the transonic similarity groups. For each planform the points for the two thickness ratios fall on a common curve and provide a striking confirmation of the transonic similarity principle. This is especially gratifying because the similarity law does not strictly apply to wings of fixed planform, but requires, rather, adjustments in aspect ratio as well as in thickness ratio.

### 22.3. Characteristics of Wing Profiles

We shall now discuss some typical experimental data which illustrate the behavior of wing sections in the transonic range.

**Flow Patterns.** <sup>(7)</sup> Fig. 22.5 shows typical flow patterns for an airfoil passing through the transonic range.

The diagram for  $M_\infty = 0.70$  represents a condition beyond the critical Mach Number  $M_{cr}$  at which the local Mach Number first reaches unity. There is a small zone of supersonic flow. If  $M_\infty$  is only slightly greater than  $M_{cr}$ , no shocks are observed. For values of  $M_\infty$  appreciably greater than  $M_{cr}$ , however, the supersonic zone is usually terminated by a lambda shock. Later we shall discuss whether the supersonic zone can be traversed smoothly without shocks.

As  $M_\infty$  increases, the lambda shock moves rearward and the local supersonic zone increases rapidly in much the same manner as near the throat of a nozzle. Ultimately the shock becomes so strong that, as a result of a shock-boundary layer interaction, boundary-layer separation occurs somewhat upstream of the main shock, as illustrated for  $M_\infty = 0.90$ . This gives rise to *shock stall*, evidenced by a rapid decrease in  $C_L$  with increasing  $M_\infty$ . Basically, both shock stall and the old-fashioned stall at low speeds (owing to excessively large angles of

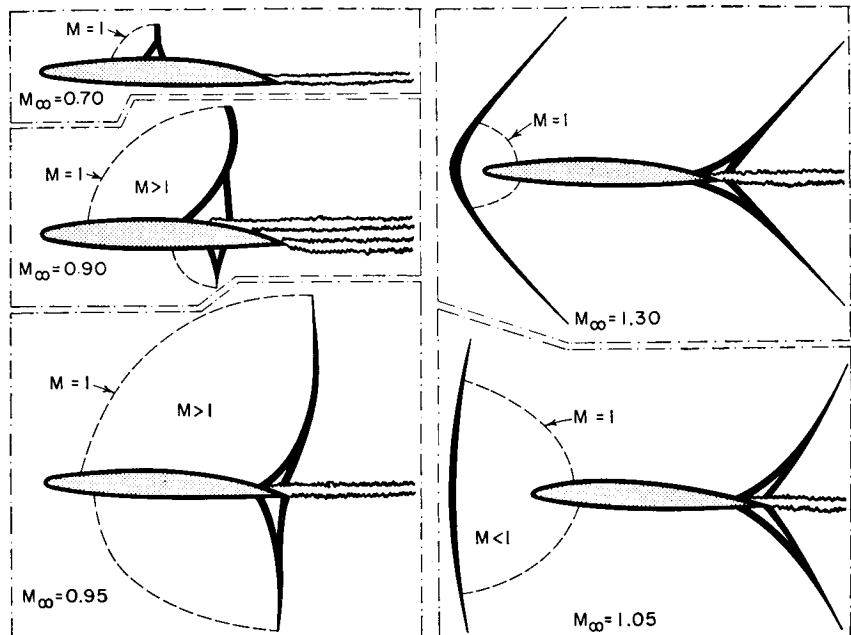


FIG. 22.5. Schematic representation of flow patterns for subsonic profiles in transonic range. Dashed lines represent boundary between subsonic and supersonic regions, heavy lines indicate shocks, and wavy lines indicate wakes and separated boundary layers (after Becker).

incidence) are due to the same physical phenomenon, namely, boundary-layer separation caused by excessive adverse pressure gradients.

Further increases in  $M_\infty$ , as illustrated in the sketch for  $M_\infty = 0.95$ , cause the shock to move to the rear of the profile and to become stronger. The flow over the surface is now predominantly supersonic, except near the nose. Since boundary-layer separation occurs so far aft, the lift coefficient increases again, but at the same time there is a further increase of drag.

When the flow is slightly supersonic, as illustrated for  $M_\infty = 1.05$ , the flow over the surface is again predominantly supersonic except for a small region near the nose. As discussed in the previous chapter, the flow near the profile for  $M_\infty = 1.05$  is substantially the same as for  $M_\infty = 0.95$  except for the detached shock well ahead of the profile in the former case.

The sketch for  $M_\infty = 1.30$  illustrates a typical pattern just prior to attachment of the leading-edge shock. Except for the fact that the shock is detached and that there is a small subsonic region near the nose, the flow pattern is similar to that for supersonic flow past sharp-edged profiles. The comparatively high pressures (corresponding to

subsonic flow) acting on the nose, as compared with the low pressures (corresponding to supersonic flow) acting on the rearward portion of the profile, lead to a significant pressure drag.

Some of these effects, together with similar effects for supersonic-type profiles, are shown in the schlieren photographs of Fig. 22.6.

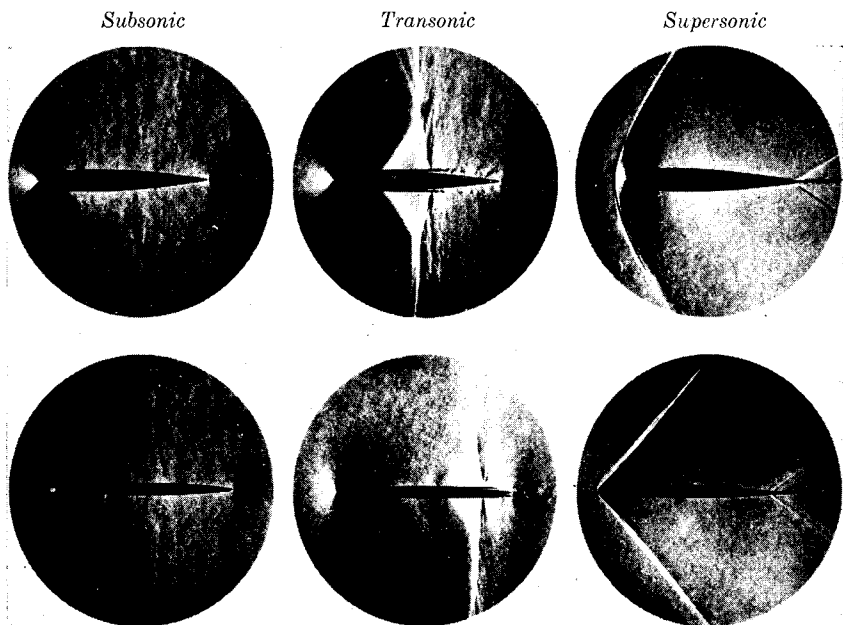


FIG. 22.6. Schlieren photographs of flows at subsonic, transonic, and supersonic speeds past a typical subsonic profile (rounded nose, moderate thickness) and a typical supersonic profile (sharp nose, small thickness). Table below summarizes main features (courtesy NACA).

	Subsonic	Transonic	Supersonic
Shocks	None	Lambda-type	Bow and trailing edge
Flow	Steady	Fluctuating	Steady
Boundary layer	Thin	Thick	Thin
Wake	Small	Large and violent	Small

**Pressure Distribution.**<sup>(7)</sup> The influence of Mach Number on pressure distribution in the transonic region is illustrated by Fig. 22.7, which indicates also the corresponding changes in  $C_L$  and  $C_D$ . It is instructive to compare these measurements with the patterns of Figs. 22.5 and 22.6.

For subcritical speeds, as illustrated by the curves for  $M_\infty = 0.29$  and  $M_\infty = 0.59$ , there is observed the usual increase in  $C_p$  with  $M_\infty$ , corresponding approximately to the Prandtl-Glauert and Kármán-Tsien rules.

The chart for  $M_\infty = 0.74$  shows, at about 45% chord on the upper surface, a sudden increase in  $C_p$  from a value corresponding to super-

sonic flow to a value corresponding to subsonic flow. This indicates that there is a sizable supersonic zone terminated by a strong shock. At this Mach Number there are seen to be no unduly large adverse effects on the lift and drag coefficients.

For  $M_\infty = 0.88$ , the pressure distribution shows that the flow over

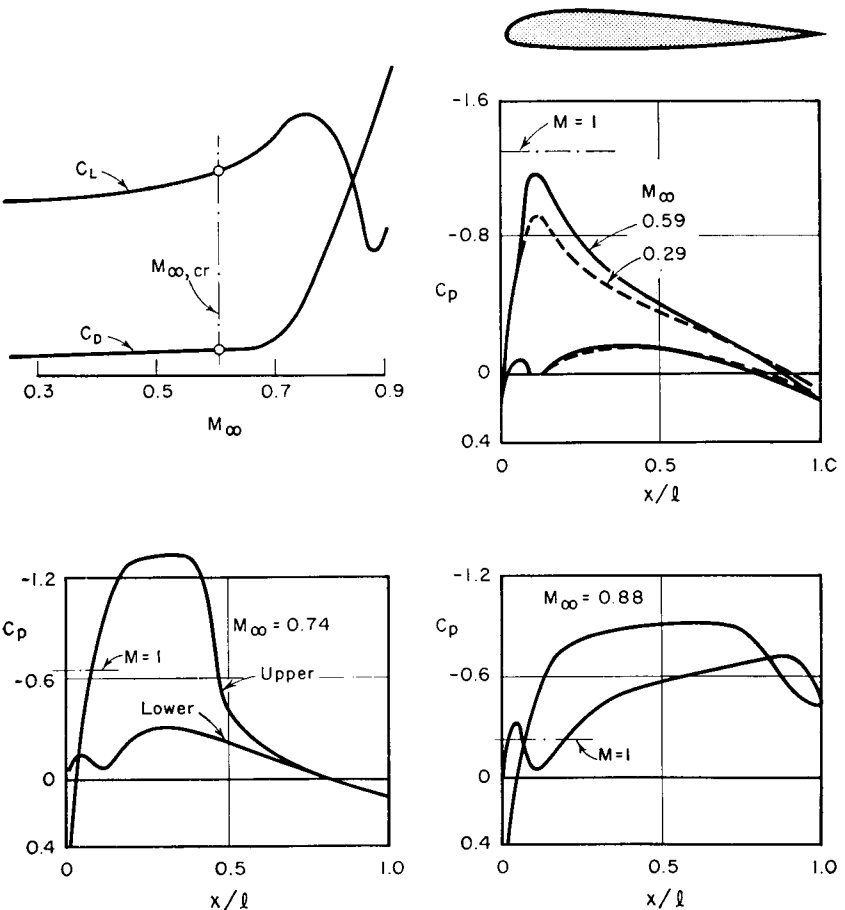


FIG. 22.7. Effect of  $M_\infty$  on pressure distribution and lift and drag coefficients of subsonic profile (NACA 23012 at  $1.6^\circ$  angle of attack).  $M_{\infty, cr}$  is the lower critical Mach Number (after Becker).

most of the profile is supersonic, with shocks near the trailing edge. Beyond the point where  $M = 1$  is reached on the surface, the pressure decreases in the direction of flow, which of course is typical of supersonic flow over a convex surface.

By comparing the pressure distributions for the several Mach Numbers, it is seen that beyond the lower critical Mach Number the pressures

on the forward portions of the profile are increased relative to the pressures over the rearward portions, thus explaining the large increase of  $C_D$  at Mach Numbers beyond  $M_{cr}$ . The area enclosed by the curves of  $C_p$  for the upper and lower surface increases as  $M_\infty$  increases from 0.59 to 0.74, and leads to a corresponding increase in  $C_L$ , whereas in going from  $M_\infty = 0.74$  to  $M_\infty = 0.88$  there is a marked decrease in the area, corresponding to a large loss in lift coefficient.

**Effects of Thickness Ratio.** <sup>(7)</sup> AFFINE PROFILES OPERATING WITH SAME  $C_L$ . Fig. 22.8 shows the aerodynamic characteristics with chang-

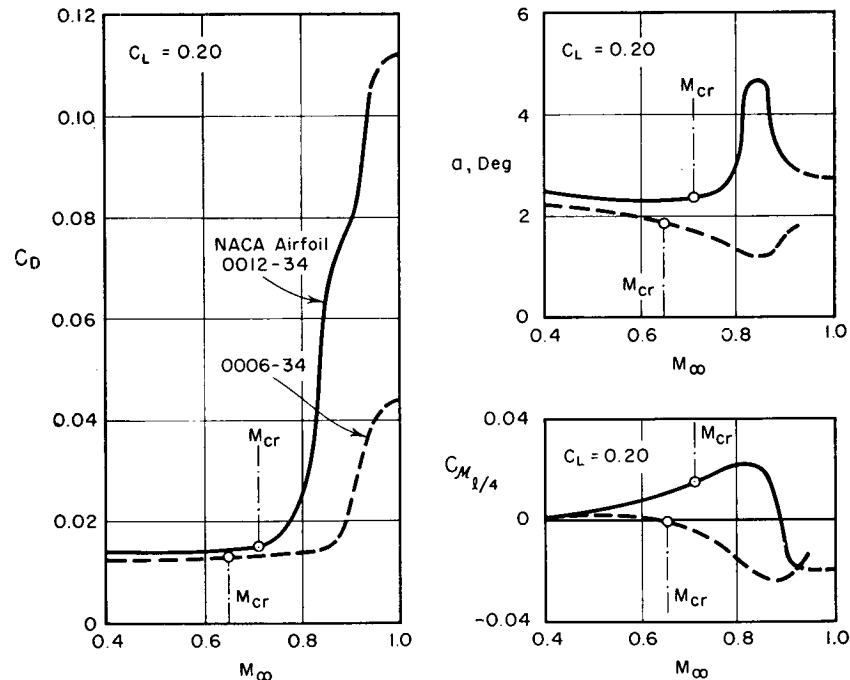


FIG. 22.8. Effect of thickness ratio on aerodynamic properties of affine profiles operating with same  $C_L$  (after Becker).

ing Mach Number of two affine profiles, having 6% and 12% thickness ratios, which operate with the same lift coefficients. Although the 6% profile has a smaller lower-critical Mach Number, it has a larger shock-stall Mach Number. Moreover, the thinner profile has smaller undesirable changes in force characteristics after shock stall. These results demonstrate that the critical Mach Number represents only the lower limit of where transonic effects might begin. It is otherwise unrelated to the "force-break" Mach Number and to airfoil behavior beyond the shock stall. The drag coefficient of the 6% profile at

$M_\infty = 1$  is about three times as large as at  $M_\infty \approx 0$ ; for the 12% profile the corresponding drag ratio is about eight.

**MINIMUM DRAG OF AFFINE PROFILES.** Typical curves of minimum drag coefficient versus thickness ratio (Fig. 22.9) show that at low Mach

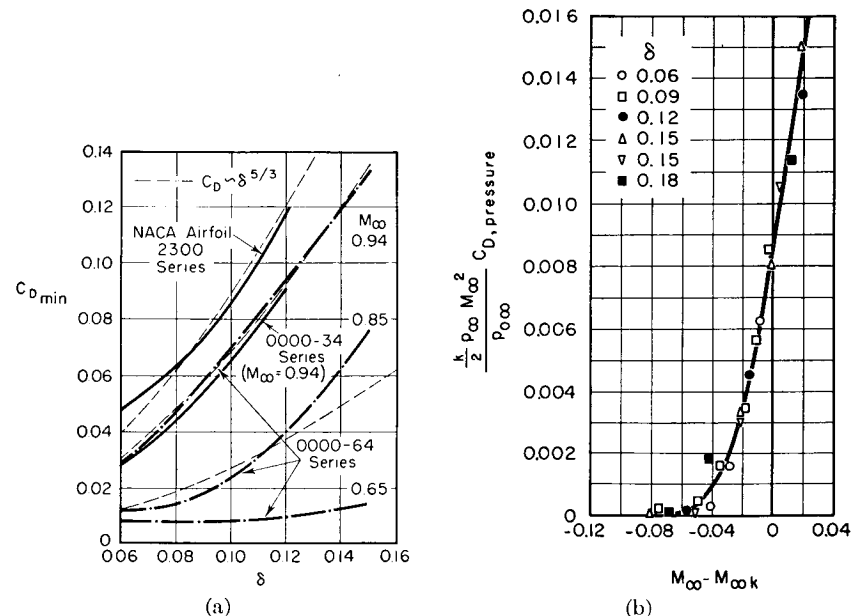


FIG. 22.9. (a) Effect of thickness ratio on minimum drag coefficient of affine profiles (after Becker).

(b) Semi-empirical correlation of pressure drag of NACA 4-digit series uncambered profiles (after Nitzberg and Crandall).

Numbers the minimum drag is insensitive to thickness ratio. At high Mach Numbers, however, beginning at about the shock-stall Mach Number, the effect of thickness ratio becomes pronounced. Near  $M_\infty$  equal to unity, indeed, both the transonic similarity rule and the experimental data show a very strong influence of the form  $C_{D \min} \sim \delta^{5/3}$ . For purely supersonic flow, it will be recalled that  $C_{D \min} \sim \delta^2$ , and therefore a smooth transition in the effect of thickness ratio from transonic speeds to supersonic speeds may be expected.

**SEMI-EMPIRICAL CORRELATION OF PRESSURE DRAG.** Nitzberg and Crandall <sup>(30)</sup> have shown that the pressure drag of families of profiles may be correlated by plotting the ratio of pressure drag to free-stream stagnation pressure ( $p_{0\infty}$ ) against an empirically determined free-stream Mach Number ( $M_{\infty k}$ ). Such a correlation is shown in Fig. 22.9b, for which the value of  $M_{\infty k}$  was taken to be the value of  $M_\infty$  at which the

modified drag coefficient had a value of 0.008. The pressure drags plotted in this chart were found by subtracting the skin-friction drag from the measured total drag.

Correlations approximately as good as that of Fig. 22.9b were obtained for the same family of profiles at various angles of attack and also for several families of cambered profiles.

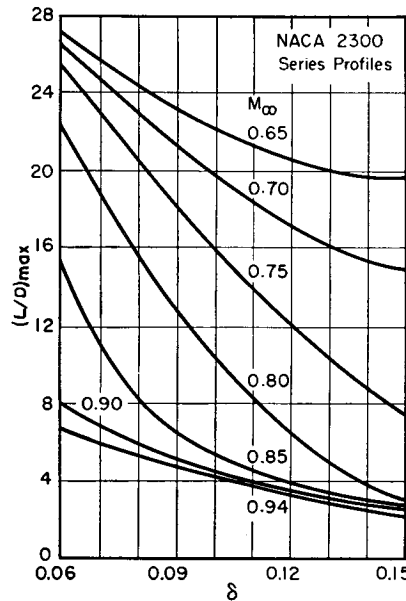


FIG. 22.10. Effect of thickness ratio on maximum lift-drag ratio of affinely related profiles (after Ferri).

It is obvious that, to have reasonable values of  $(L/D)_{\max}$  in the transonic range, thin profiles must be employed.

**Effects of Camber.** <sup>(7)</sup> Fig. 22.11 shows the aerodynamic characteristics with changing Mach Number of two profiles which are alike except for camber, and which operate with the same lift coefficients. The symmetrical profile has a somewhat higher force-break Mach Number. More important, however, the uncambered section has much smaller undesirable changes in incidence and moment coefficient after shock stall.

These results are further illuminated by the data in Fig. 22.12. For the same lift coefficient, the symmetrical section must operate with a higher incidence, and thus, as shown in Fig. 22.12a, the symmetrical section has a high suction peak near the nose, while the cambered section has a relatively flat pressure distribution. With this particular pair of profiles, the symmetrical section has the lower critical Mach Number. Nevertheless, as shown in Fig. 22.12b, it has a higher shock-stall Mach Number.

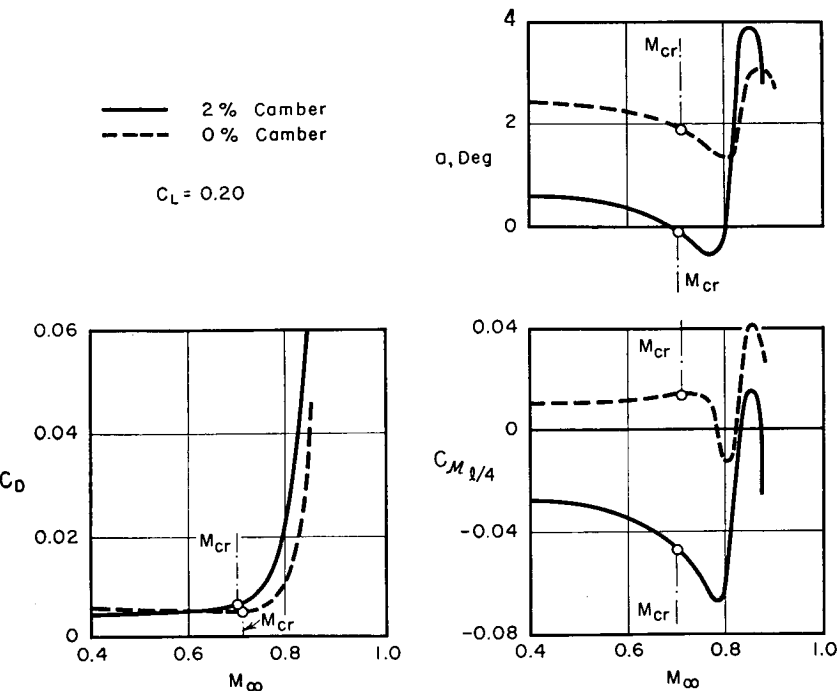


FIG. 22.11. Effect of camber on aerodynamic properties of two profiles with same thickness distribution (after Becker).

The mechanism underlying these observations is explained by Fig. 22.12c, which is sketched from a schlieren photograph. It is seen that the uncambered profile develops sonic regions and shocks near the nose at low  $M_{\infty}$ . Thin boundary layers do not separate easily, however, and thus there are no significant adverse effects until  $M_{\infty}$  is exceeded by a considerable amount. The flow pattern for the cambered profile (Fig. 22.12d), on the other hand, indicates considerable boundary-layer separation because shocks first occur over the rearward portions of the profile where the boundary layer is relatively thick and hence easily susceptible to separation. Thus, with the cambered profile, the Mach Number of shock stall is only slightly greater than  $M_{cr}$ .

**Low-Drag Profiles.** This description of the flow also explains the behavior of high-critical-speed and low-drag types of airfoils when operating over a wide range of  $C_L$  (Fig. 22.13). For operation near the design  $C_L$ , the force-breaks occur shortly after  $M_{cr}$  is exceeded. For operation with  $C_L$  considerably different from the design value, high suction peaks appear near the nose, the flow pattern is as illustrated in Fig. 22.12c, and shock stall does not occur until  $M_{\infty}$  is very much larger than  $M_{cr}$ .

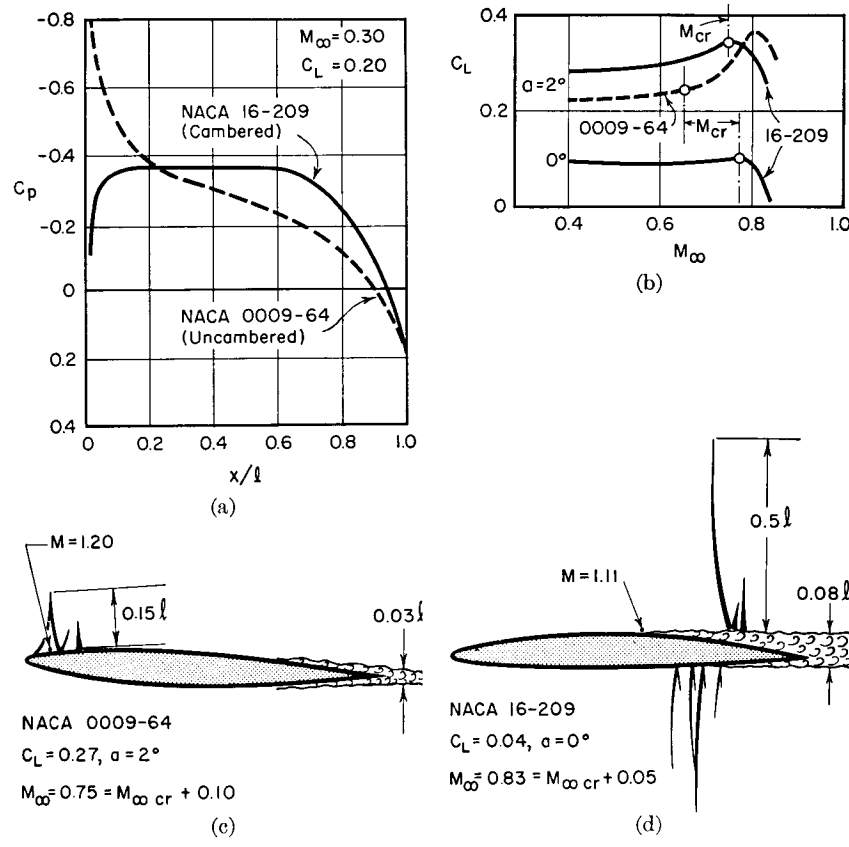


FIG. 22.12. Comparison of cambered with uncambered profiles (after Becker).

- (a) Pressure distributions for  $C_L = 0.20$  and  $M_\infty = 0.30$ .
- (b)  $C_L$  versus  $M_\infty$  at constant incidence.
- (c) Flow pattern for uncambered profile.
- (d) Flow pattern for cambered profile.

**EMPIRICAL RULE FOR MACH NUMBER OF DRAG DIVERGENCE.** The same mechanism also explains in a less precise way the empirical observation<sup>(9)</sup> that the Mach Number of drag divergence is substantially the same as the Mach Number at which sonic speed is reached on the airfoil "crest"; the latter being defined as the chordwise station where the airfoil surface is tangent to the free-stream direction. Since the value of  $M_\infty$  for which sonic velocity is reached on the airfoil crest can be approximated by using the Prandtl-Glauert rule in conjunction with the low-speed pressure distribution, this correlation affords a simple means of estimating the drag-divergence Mach Number. For moderately thick profiles, the method as so outlined predicts with fairly good accuracy the drag-divergence Mach Number of profiles having diverse shapes and a wide range of thickness ratios.

**EMPIRICAL CORRELATION FOR SHOCK STALL.** Still another empirical result which is partly explainable by the same mechanism is the remarkable correlation<sup>(11)</sup> shown in Fig. 22.14 between the Mach Number of shock stall and the angle  $\epsilon$  between the flight direction and a line passing through the trailing edge and the 70% station on the upper surface. This correlation is based both on flight tests and wind tunnel tests, and includes profiles of varying camber and thickness ratio. In connection with flight tests, transonic separation appears to have associated with it unsteady effects which may limit the speed to which the pilot dare take an aircraft. These unsteady effects are felt in the form of shaking of the airframe and severe buffeting of the control surfaces.

**EFFECT OF CAMBER ON MAXIMUM LIFT-DRAG RATIO.** The effects of camber on the maximum lift-drag ratio obtainable with a family of profiles of variable camber but constant thickness are illustrated by Fig. 22.15. For low Mach Numbers, the percentage camber for  $(L/D)_{\max}$  varies approximately linearly with the required  $C_L$ . As  $M_\infty$  increases, the optimum camber rapidly decreases, especially for large  $C_L$ . Above  $M_{cr}$  the optimum camber drops rapidly to zero and remains

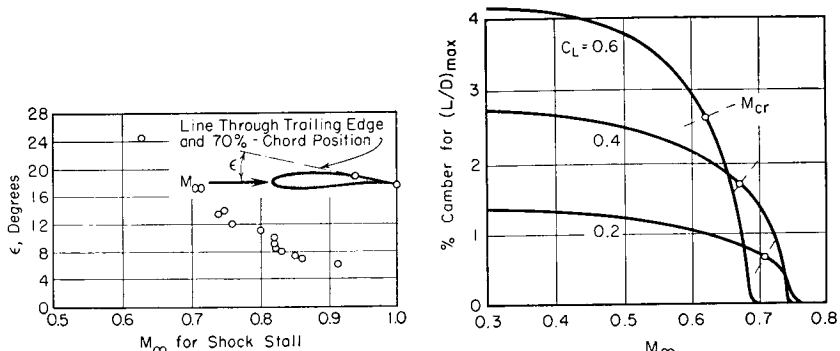


FIG. 22.14. Empirical correlation for Mach Number of shock stall (after Outman and Lambert).

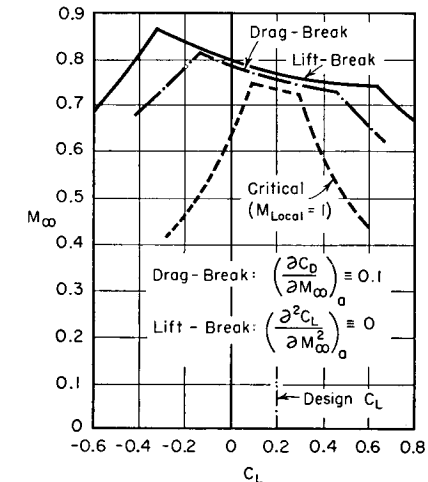


FIG. 22.13. Critical, drag-break, and lift-break Mach Numbers for typical low-drag profile (design  $C_L = 0.20$ ) operating with various values of  $C_L$  (after Becker).

there, whence it is concluded that transonic profiles should have virtually zero camber.

**Optimum Profiles for Transonic Speeds.** Becker,<sup>(7)</sup> on the basis of the type of data discussed above, suggests that the optimum profile for the high subsonic range should have the following properties:

- (i) No camber
- (ii) Maximum thickness near 50% chord
- (iii) Thickness ratio and trailing-edge included angle as small as strength considerations permit
- (iv) Small but finite leading-edge radius

With the exception of the leading-edge radius, these specifications are also suitable for purely supersonic flow. With regard to the low supersonic range, there is no reason to believe that a sharp leading edge offers any advantage over the rounded leading edge as long as there are detached shocks, and so it is likely that the specifications outlined above are also suitable for the supersonic portion of the transonic range.

The following symmetrical profiles, or thinner profiles with the same thickness distribution, are suggested by Becker as approximating the foregoing specifications:

NACA 0009-44

NACA 65-009

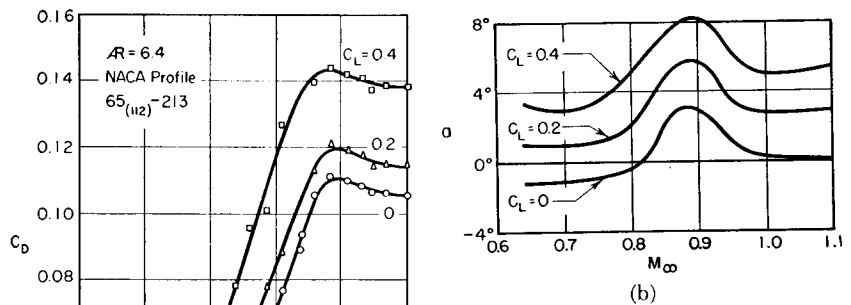
NACA 65A-009

## 22.4. Characteristics of Wings

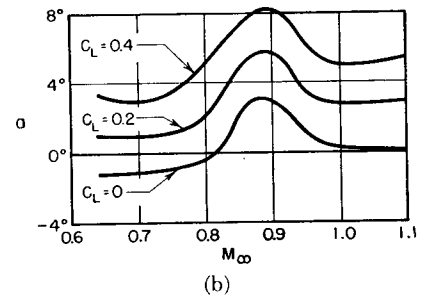
**Effect of Mach Number.**<sup>(12)</sup> Typical performance characteristics in transonic flow are shown in Fig. 22.16 for a wing of aspect ratio 6.4. The major changes in force coefficients are seen to occur between  $M_\infty \approx 0.8$  and  $M_\infty \approx 1$ . Beyond the latter value the boundary-layer separation effects which appear in transonic flow are no longer present (see Fig. 22.5), and the performance begins to take on a typically supersonic character.

For  $C_L = 0$ , the maximum drag coefficient is about 9 times the low-speed drag coefficient; for  $C_L = 0.4$ , on the other hand, the corresponding ratio is only about 6.

Between  $M_{cr}$  and  $M_\infty \approx 0.9$ , the lift coefficient for a given incidence decreases with increasing Mach Number. Above  $M_\infty \approx 0.9$ , however, and probably as the result of increasing boundary-layer reattachment, the lift coefficient increases for a short time with increasing Mach



(a)

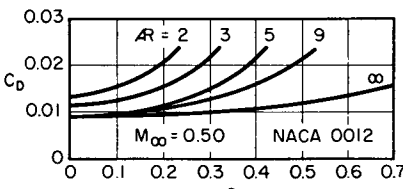


(b)

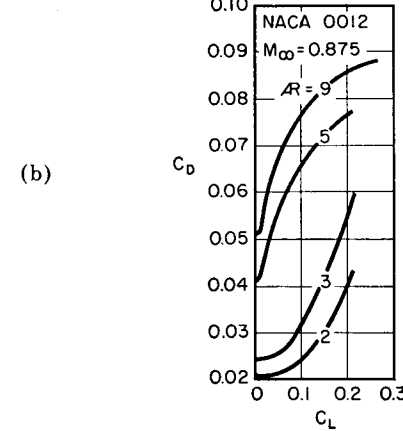
FIG. 22.16. Performance data for wing of aspect ratio 6.4 (after Weaver).

(a)  $C_D$  versus  $M_\infty$  for fixed values of  $C_L$ .

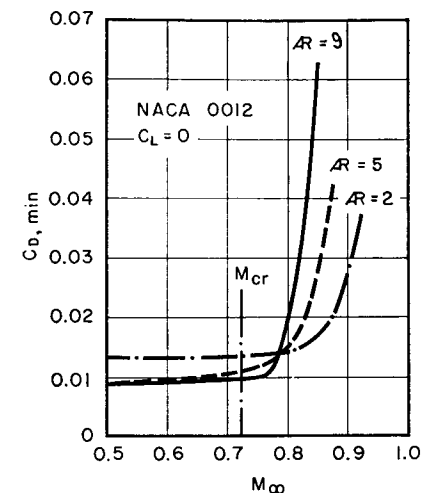
(b) Angle of incidence versus  $M_\infty$  for fixed values of  $C_L$ .



(a)



(b)



M\_cr

FIG. 22.17. Effect of aspect ratio on lift-drag polar (after Stack and Lindsey).

(a) Low subsonic Mach Number.

(b) High subsonic Mach Number.

FIG. 22.18. Effect of aspect ratio on minimum drag coefficient at low and high Mach Numbers (after Stack and Lindsey).

Number. Beyond  $M_\infty \approx 1.0$ ,  $C_L$  again begins to decrease with increasing Mach Number, which is typical of supersonic flow.

**Effect of Aspect Ratio.** <sup>(13)</sup> As a result of the induced drag associated with the trailing vortices of a finite wing, wings of large aspect ratio are desirable for superior aerodynamic performance at moderate subsonic speeds (Fig. 22.17a).

These trailing vortices are associated with the freedom of the air to flow spanwise. This freedom constitutes a three-dimensional "relieving" effect in the sense that the wing produces smaller disturbances in the flow. With high values of  $M_\infty$ , therefore, the local Mach Numbers on the wing are not so high as for a wing of infinite aspect ratio. Thus, as illustrated by Fig. 22.17b, there is a reversal in trend beyond the critical Mach Number, and, for high values of  $M_\infty$ , wings of small aspect ratio have a more desirable lift-drag polar.

For minimum drag at low Mach Numbers, wings of large aspect ratio should be used. At high Mach Numbers, however, Fig. 22.18 shows that wings of low aspect ratio have decidedly less drag. Moreover, the drag-break Mach Number is seen to be significantly higher for wings of low aspect ratio.

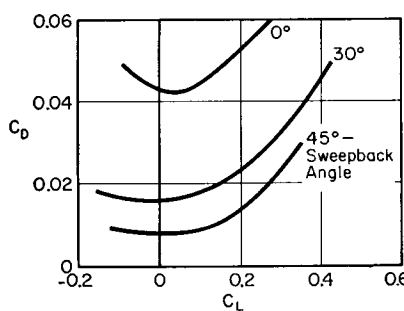


FIG. 22.19. Effect of sweepback on lift-drag polar of wings of fixed aspect ratio, all operating at  $M_\infty = 0.925$ , and all having NACA 65-110 profile in planes normal to leading edge (after Adler).

**Effect of Sweepback.** In Chapter 13 it was shown that the flow past a sweptback wing might be thought of as the sum of (i) a spanwise flow along the wing, which does not affect the pressure distribution but does influence the boundary layer; and (ii) a flow normal to the

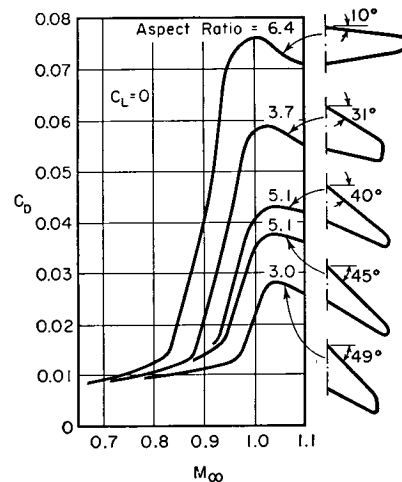


FIG. 22.20. Effects of sweepback and aspect ratio on zero-lift drag coefficient of wings (after Weaver).

wing, which, apart from viscous effects, controls the pressure distribution. Thus, neglecting viscosity, the effective Mach Number of the flow is based on the normal component of velocity and is therefore less than  $M_\infty$ . Hence it is to be expected that compressibility effects will be delayed by sweeping back the wing. The data of Fig. 22.19 <sup>(14)</sup> confirm this conclusion, and show that significant improvements in the lift-drag polar may be obtained at transonic speeds by means of a moderate amount of sweepback.

Still another striking demonstration of the reductions in transonic drag attainable through either sweepback or a decrease in aspect ratio is shown by Fig. 22.20, <sup>(12)</sup> which shows curves of zero-lift drag coefficient versus  $M_\infty$  for several wings of different sweepback and different aspect ratio. A decrease in maximum zero-lift drag coefficient is seen to go hand in hand with an increase in the Mach Number of drag-break and with an increase in the Mach Number at which the maximum zero-lift drag coefficient occurs. During the experiments it was also observed that the transonic flow over the wings became steadier as the sweepback angle was increased, thus implying a lesser amount of boundary-layer separation.

## 22.5. Transonic Drag of Bodies of Revolution

**High-Speed Aircraft.** The drag coefficient of a typical aircraft fuselage designed for high-speed flight is seen from Fig. 22.21 <sup>(12)</sup> to remain almost unaffected by Mach Number until about  $M_\infty \approx 0.95$ , after which the drag rises sharply and reaches a maximum at  $M_\infty \approx 1.05$ . The maximum drag coefficient is about three times the low-speed drag coefficient. That the Mach Number of drag rise is so high compared with wing sections is explained (Chapter 13) by the fact that three-dimensional objects allow the air flow to flow past the body with less disturbance, thus tending to reduce the peak local Mach Number for a given free-stream Mach Number.

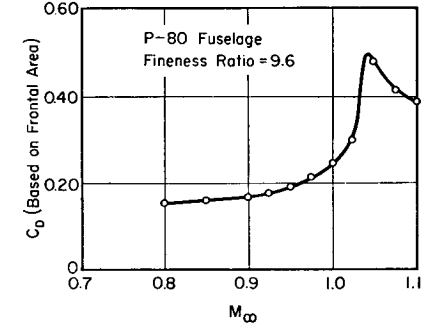


FIG. 22.21. Drag of P-80 fuselage (after Weaver).

**Projectiles.** The drag curves for several projectiles (Fig. 22.22) indicate that fineness ratio and bluntness of the nose are the important factors at supersonic speeds and through the transonic range. The bluntness of the base is known to be the controlling factor at low sub-

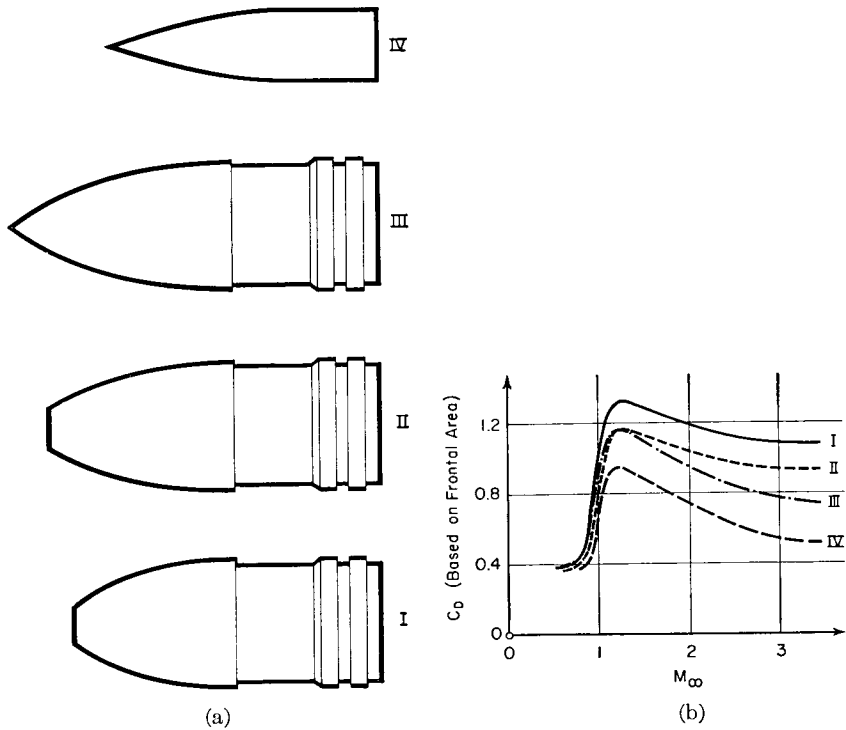
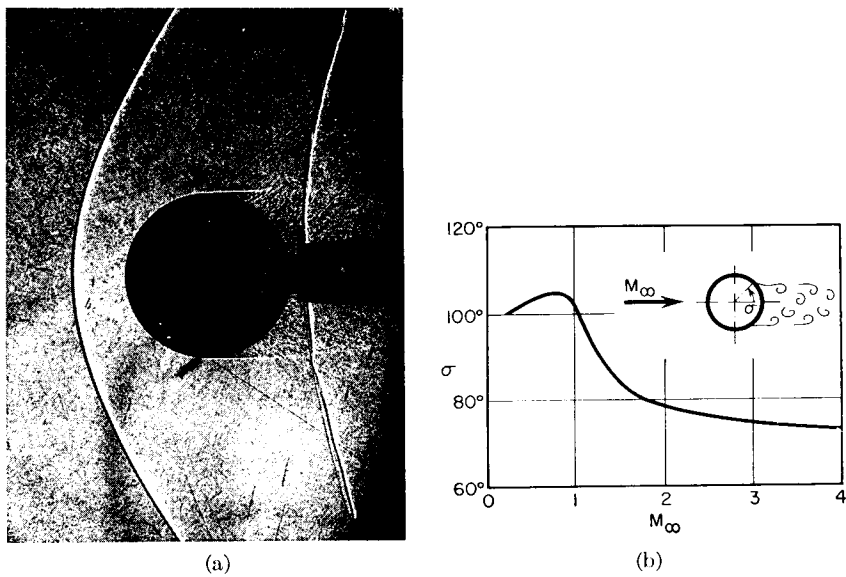


FIG. 22.22. Drag of projectiles (after Cranz).



(a) Schlieren photograph (Applied Physics Lab.).  
 (b) Separation point versus Mach Number (after Charters).

sonic speeds. For the bluntest projectile shown, the maximum drag coefficient is about 3.5 times the low-speed value, whereas for the least blunt projectile the corresponding ratio is only 2.5. All the projectiles show peak drag coefficients at  $M_\infty \cong 1.2$ .

**Spheres.** The drag coefficient of spheres at high speeds <sup>(15)</sup> is seen from Fig. 13.12 to begin a sharp rise at  $M_\infty \cong 0.6$ , and reaches its peak at the comparatively high value of  $M_\infty \cong 1.75$ , after which there is only a slight reduction in  $C_D$  in the supersonic range. The peak value of drag coefficient is about twice the low-speed value, while the value at  $M_\infty = 1$  is about 70 per cent greater than the low-speed value.

A detached bow wave (Fig. 22.23a) stands ahead of the sphere when  $M_\infty > 1$ . Near the point of maximum thickness the boundary layer separates from the body and a large turbulent wake is formed. Fig. 22.23b shows that through the transonic range the point of boundary-layer separation shifts from the forward half of the sphere to the aft half. This is doubtless a result of the change in pressure distribution, near the point of maximum thickness, from a typically subsonic distribution to a typically supersonic distribution.

## 22.6. Detached Shocks

Mixed flow patterns are always encountered when detached bow waves stand ahead of a body. The resulting flow patterns are therefore extremely complex and difficult to study analytically.

**Transition from Flow with Attached Shock to Flow with Detached Shock.** In a supersonic flow past a body having a given nose angle, there may be an attached shock if the Mach Number is sufficiently high, but, for sufficiently low Mach Numbers, there is always a detached bow wave. It is pertinent to ask, therefore, whether the transition from one type of flow to the other is continuous, or whether for an infinitesimal change of Mach Number there is a finite change in flow pattern. This question has been answered by Guderley, <sup>(5)</sup> and by Busemann, <sup>(17)</sup> who have shown that the transition is indeed continuous.

Typical wave patterns for the flow at various Mach Numbers past a wedge attached to a straight-sided profile are shown in Fig. 22.24a, and the corresponding shock polar diagrams are shown in Fig. 22.24b. In sketch 1, the free-stream Mach Number is sufficiently high so that there is a solution at  $1'$  on the shock polar. The flow downstream of the shock is uniform and supersonic, and the oblique shock remains straight up to the point where it is intersected by the first Mach wave of the Prandtl-Meyer flow originating at the shoulder.

With a lower Mach Number (sketch 2), the flow behind the shock near the tip is subsonic. Now it is known that in incompressible flow

the velocity at the convex corner of the shoulder is infinite. If a subsonic compressible flow approaches the corner, on the other hand, the velocity at the corner must be at least sonic. But the only length dimension in the flow is the distance from the nose to the shoulder, and the distance of the shock forward of the nose must depend on this dimension. Since the shoulder could not influence the flow upstream of the sonic line if the latter stood in front of the shoulder, it is a plausible conclusion that the sonic line for sketch 2 must begin at the shoulder. The flow behind the shock accelerates as it approaches the sonic line. Hence the shock must change in strength and be curved in such a way that the flow behind the shock is exactly sonic where the shock meets the sonic line (point 2'').

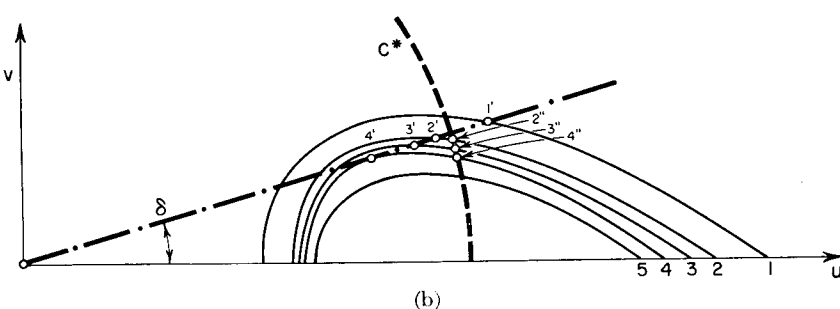
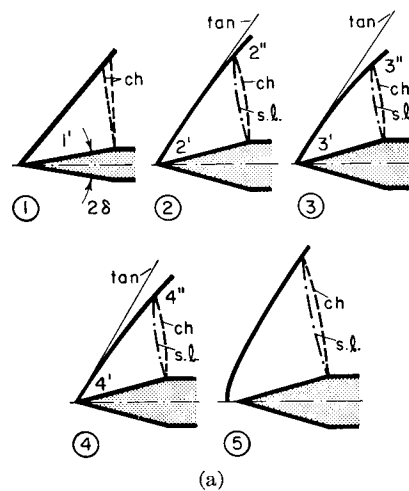


FIG. 22.24. Process of shock detachment from nose of wedge (after Guderley and Busemann).

- (a) Successive stages as  $M_\infty$  decreases ( $ch$  denotes Mach line,  $s.l.$  denotes sonic line, and  $tan$  denotes tangent to shock at nose).
- (b) Hodograph diagrams corresponding to various stages of (a).

In sketch 2 the shock is perfectly straight near the tip and the shock curvature increases with distance from the tip up to the point where the shock meets the sonic line.

With further decreases in Mach Number the main change is that (sketch 3) the shock wave has curvature over the entire length between the tip and sonic line. When the limiting Mach Number for shock attachment is reached (sketch 4), the curvature of the wave at the tip becomes infinite.

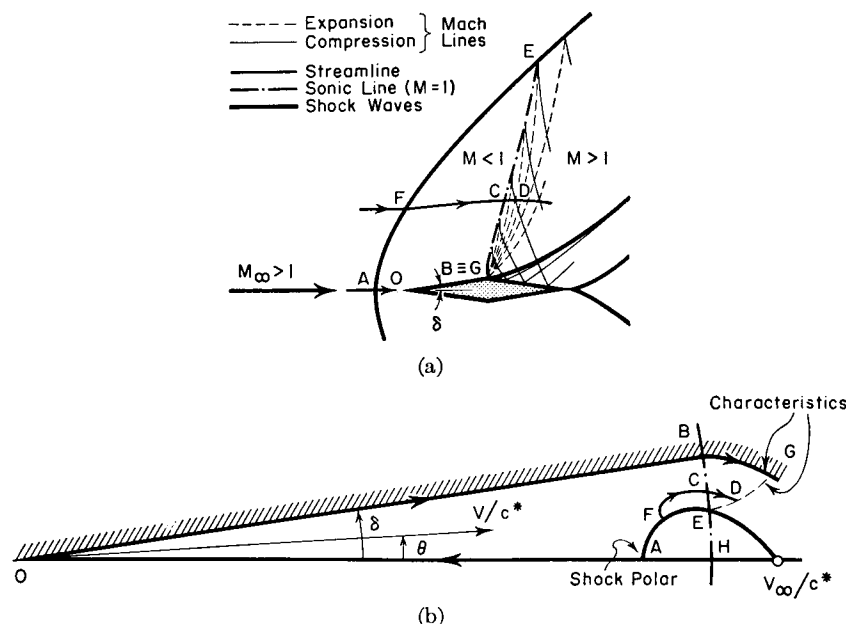


FIG. 22.25. Supersonic flow past double-wedge profile with detached shock (after Vincenti and Wagoner).

- (a) Physical plane.
- (b) Hodograph plane.

Thus, even before detachment occurs (sketch 5), the point of maximum curvature on the shock wave has shifted to the tip, and the transition to the detached shock occurs quite naturally and without discontinuities.

The hodograph and physical diagrams for the flow past a double-wedge profile with a detached shock wave are illustrated in Fig. 22.25.

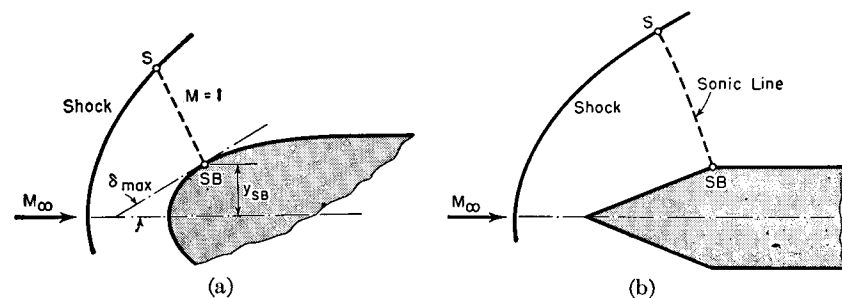


FIG. 22.26. Location of sonic point on body.

- (a) Body with gradual curvature.
- (b) Body with sharp shoulders.

**Approximate Method of Locating Detached Shock Waves.** The exact determination of the shape and location of detached shock waves is most laborious, and it is doubtful whether exact methods can ever lead to simple formulas showing the effect of Mach Number and body shape. Moeckel<sup>(18)</sup> has devised an approximate method which has the desirable property of yielding a single relation between free-stream Mach Number and distance of the shock wave from the sonic point on the body.

One of the assumptions of the method is that the sonic line may be approximated as a straight line. For bodies with sharp shoulders, the sonic line must begin at the shoulder (Fig. 22.26b). For gradually curved bodies (Fig. 22.26a), it has been shown<sup>(17, 18)</sup> that the sonic point (SB) on the body is approximately at the point where, depending on whether the flow is two-dimensional or axi-symmetric, the contour is

inclined, respectively, at the maximum wedge angle or the maximum cone angle for a shock at the given free-stream Mach Number.

Detached shock waves are normal to the free-stream direction on the axis of symmetry, and are asymptotic to the free-stream Mach lines at great distances from the axis of symmetry. Hence it seems plausible that the shape of the wave may be approximated by

FIG. 22.27. Nomenclature for approximate analysis of shock location.

a hyperbola (Fig. 22.27). We therefore postulate that the equation of the shock is

$$\beta y = \sqrt{x^2 - x_0^2} \quad (22.1)$$

where  $\beta \equiv \sqrt{M_\infty^2 - 1}$  and  $x_0$  is the location of the vertex of the wave.

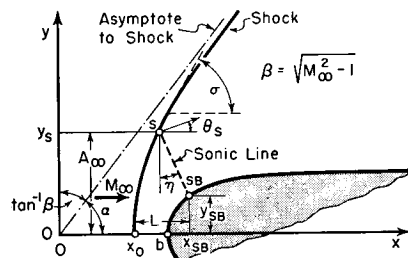
With this shape of wave, the shock angle is given by

$$\left( \frac{dy}{dx} \right)_{\text{shock}} = \tan \sigma = \frac{x}{\beta \sqrt{x^2 - x_0^2}} = \frac{\sqrt{x_0^2 + \beta^2 y^2}}{\beta^2 y} \quad (22.2)$$

Using subscript  $S$  to denote conditions at the intersection of the wave with the sonic line, the coordinates of  $S$  are found from this relation and Eq. 22.1 to be given by

$$y_S = \frac{x_0 \cot \sigma_S}{\beta \sqrt{\beta^2 - \cot^2 \sigma_S}} \quad (22.3a)$$

$$x_S = \frac{\beta x_0}{\sqrt{\beta^2 - \cot^2 \sigma_S}} \quad (22.3b)$$



Using  $y_{SB}$  as a reference dimension, the dimensionless distance to point  $S$  is found from Eq. 22.3b as

$$\frac{x_S}{y_{SB}} = \frac{\beta}{\sqrt{\beta^2 - \cot^2 \sigma_S}} \frac{x_0}{y_{SB}} \quad (22.4)$$

Solving for  $x_0/y_{SB}$ , and eliminating  $x_S$  by means of Eq. 22.1, we find the dimensionless distance to the vertex of the wave to be

$$\frac{x_0}{y_{SB}} = \beta \frac{y_S}{y_{SB}} \sqrt{\beta^2 \tan^2 \sigma_S - 1} \quad (22.5)$$

The quantity we wish to establish is the distance from the wave vertex to the sonic point on the body, expressed in the dimensionless form  $L/y_{SB}$ . From Fig. 22.27, it is evident that

$$\frac{L}{y_{SB}} = \frac{x_{SB}}{y_{SB}} - \frac{x_0}{y_{SB}}$$

and

$$\frac{x_{SB}}{y_{SB}} = \frac{x_S}{y_{SB}} + \left( \frac{y_S}{y_{SB}} - 1 \right) \tan \eta$$

Now, combining these with Eqs. 22.4 and 22.5, we get

$$\frac{L}{y_{SB}} = \frac{y_S}{y_{SB}} [\beta^2 \tan \sigma_S - \beta \sqrt{\beta^2 \tan^2 \sigma_S - 1} + \tan \eta] - \tan \eta \quad (22.6)$$

As  $\sigma_S$  is the shock angle for which the flow downstream of the wave is exactly sonic, the right-hand side of Eq. 22.6 depends, apart from  $M_\infty$ , only on  $\eta$  and  $y_S/y_{SB}$ . To determine the latter quantities we apply the continuity equation to the fluid that crosses the sonic line, using the approximation that the average stagnation pressure for this flow is that existing along the streamline representing the mass centroid of the flow crossing the sonic line. Using subscript  $c$  to denote the centroid streamline, it follows that, for plane flow,  $y_c = y_S/2$ , whereas, for axi-symmetric flow,  $y_c = 2y_S/3$ . The shock angle  $\sigma_c$  corresponding to the centroid streamline may then be found by combining Eqs. 22.2 and 22.3a and inserting the appropriate value of  $y_c/y_S$ :

$$\tan \sigma_c = \sqrt{\frac{1}{\cot^2 \sigma_S} \left( \frac{y_S}{y_c} \right)^2 - \frac{1}{\beta^2} \left[ \left( \frac{y_S}{y_c} \right)^2 - 1 \right]} \quad (22.7)$$

Having  $\sigma_c$  and  $M_\infty$ , the stagnation pressure ratio  $p_{oc}/p_{\infty}$  may be found from the oblique shock tables, where  $p_{oc}$  is the isentropic stagnation pressure on the centroid streamline downstream of the shock. Then, signifying by  $A_S$  the cross-sectional area offered by the sonic line, the continuity equation may be written approximately as

$$\frac{A_\infty}{A_S} = \frac{\rho_S V_S}{\rho_\infty V_\infty} = \frac{\rho^* V^*}{\rho_\infty V_\infty} \frac{\rho_S V_S}{\rho^* V^*} = \left( \frac{A}{A^*} \right)_{\text{isen}} \frac{p_{oc}}{p_\infty} \quad (22.8)$$

where  $(A/A^*)_{isen}$  is the area ratio for isentropic flow at the Mach Number  $M_\infty$ .

Employing the approximations that the sonic line is straight, and that it is normal to the local flow direction, Eq. 22.8 may, for plane flow, be put into the form

$$\frac{y_s}{y_{SB}} = \left[ 1 - \frac{p_{0\infty}}{p_{0c}} \left( \frac{A^*}{A} \right)_{isen} \cos \eta \right]^{-1} \quad (22.9a)$$

The corresponding result for axi-symmetric flow is

$$\frac{y_s}{y_{SB}} = \left[ 1 - \frac{p_{0\infty}}{p_{0c}} \left( \frac{A^*}{A} \right)_{isen} \cos \eta \right]^{-1/2} \quad (22.9b)$$

To determine  $\eta$ , we use the assumption that the sonic line is normal to the mean inclination of the velocity vector. At point  $S$ , the flow direction is  $\theta_s$ , the turning angle for a shock whose downstream condition is exactly sonic. At point  $SB$ , by assumption, the flow direction is  $\delta_{max}$ , the maximum possible turning angle for the given  $M_\infty$ . Therefore, on the average,

$$\eta \cong \frac{1}{2}(\theta_s + \delta_{max}) \quad (22.10)$$

The calculation procedure is as follows, assuming a given  $M_\infty$  and a given body shape:

(i)  $\beta$ ,  $\theta_s$ ,  $\delta_{max}$ ,  $(A^*/A)_{isen}$ ,  $\sigma_s$  are found for the given  $M_\infty$ ; (ii)  $y_{SB}$  is determined from the body shape and  $\delta_{max}$ ; (iii)  $\sigma_c$  is determined from Eq. 22.7, and then, from the oblique-shock relations,  $p_{0c}/p_{0\infty}$  is determined; (iv)  $\eta$  is determined from Eq. 22.10; (v)  $y_s/y_{SB}$  is computed from Eq. 22.9; (vi)  $L/y_{SB}$  is finally computed from Eq. 22.6. In addition, the shock wave shape may be plotted from Eq. 22.1, and the sonic line may be drawn at the angle  $\eta$ .

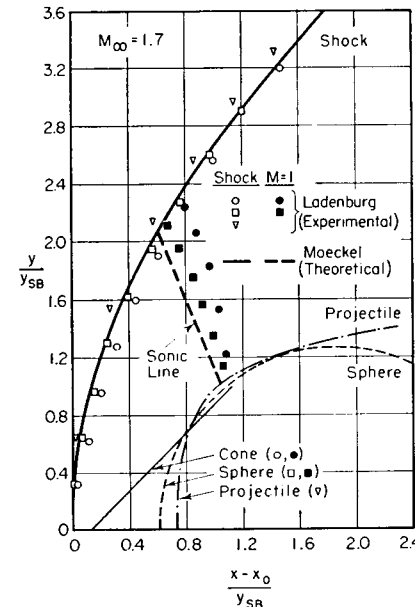


FIG. 22.28. Shape of shock line and sonic line for flow past cone, sphere, and projectile. Comparison between theory and experiment. Each body is in such a position that the vertex of the shock is at the origin of coordinates (after Moeckel).

An interesting feature of the method is that it indicates the shape of the nose upstream of the sonic point to be relatively unimportant in determining the shock shape and location.

**Experiments on Detached Shocks.** The shapes of the shock and sonic line for  $M_\infty = 1.7$  as determined by this method are shown in Fig. 22.28, together with corresponding experimental data for a cone, a sphere, and a projectile at the same  $M_\infty$ . To make comparisons easy, the vertex of the wave is placed at the origin in each case. Considering the nature of the approximations in the theory, the agreement with experiment is, by and large, satisfactory, and indicates at least that the method predicts accurately the main features of the flow.

Further comparisons of the approximate theory with experimental results are shown in Fig. 22.29 in terms of the distance of the vertex of the wave from the body, for a variety of body shapes. From Fig. 22.29a

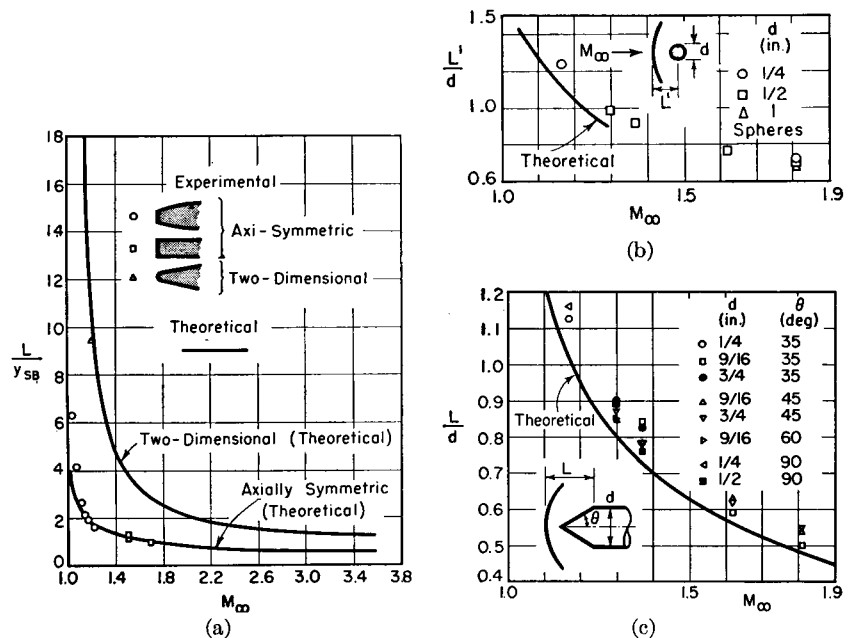


FIG. 22.29. Shock detachment distance versus Mach Number. Solid curves represent Moeckel's approximate theory.

- (a) Various two-dimensional and three-dimensional shapes (after Moeckel).  
 (b) Spheres (after Heberle, Wood, and Gooderum).  
 (c) Cones (after Heberle, Wood, and Gooderum).

it is evident that shocks stand considerably farther ahead of two-dimensional profiles than they do ahead of bodies of revolution. The theory seems to fit plane flow and axi-symmetric flow equally well, but appears to lose accuracy in the transonic range. It is significant that the data for cones of widely different vertex angle fall on a single curve in Fig. 22.29c, for this bears out the contention that the shape of

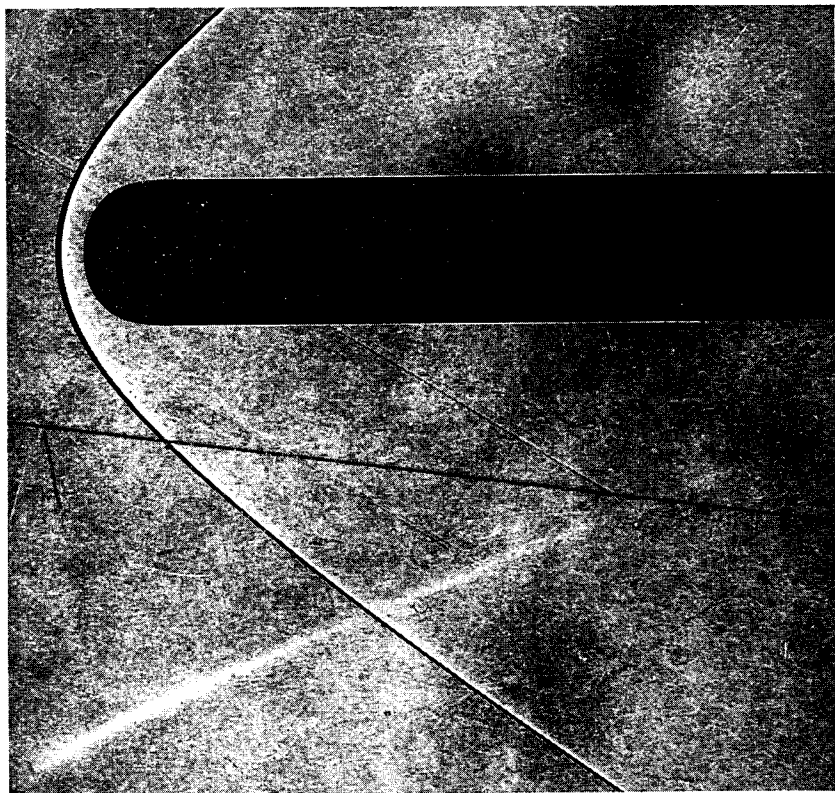


FIG. 22.30. Schlieren photograph of flow past a cylinder with a spherical nose (Applied Physics Lab.).

the body upstream of the sonic point plays a secondary role in determining the location of the shock wave.

A typical schlieren photograph of a detached shock is shown in Fig. 22.30 (see also Fig. 22.23).

## 22.7. Theoretical Consideration of Transonic Flow Without Shocks

We have already seen several theoretical examples of subsonic-transonic flows having local zones of supersonic flow for which, ignoring viscous effects, there is a smooth shock-free deceleration of the streamlines from the supersonic zone to the subsonic region aft of the body. As illustrations, refer to (i) the flow past a bump (Fig. 12.7), (ii) the flow at the throat of a nozzle (Fig. 21.10), and (iii) Ringleb's 180°-flow (Fig. 20.5).

In practice it is always observed that shocks appear on profiles

after a sizable local supersonic zone has appeared, with a consequent sharp rise in drag. It is of great practical importance, therefore, to ask why these shocks arise and whether it might not be possible to design profiles which could have local speeds greatly in excess of the sonic speed and yet be free of shocks. The answers to these questions are not fully known, but we shall discuss several points which seem relevant.

**Nature of Supersonic Zone.** Fig. 22.31a shows a typical supersonic zone, free of shocks, attached to a thin profile at high subsonic Mach Number. Employing the concept that the Mach lines are waves across which the fluid properties change, the left-running Mach lines are seen to be expansion waves, and the right-running Mach lines to be compression waves.

That the wave pattern must be of this nature may be proved by considering a very short segment of the sonic line (Fig. 22.31b), at one point of which wave *A* ends and wave *B* begins. Wave *B* may be regarded as the reflection of wave *A*. The pressure on the sonic line is constant because the velocity there is constant, and hence the reflection of wave *A* is as from a surface of constant pressure, i.e., it is in unlike sense. If wave *A* is a rarefaction, wave *B* must therefore be a compression; but if *A* is a compression, *B* must be a rarefaction. However, in crossing the sonic line from the supersonic side to the subsonic side, the velocity decreases and thus the pressure must increase, whence it follows that the pressure in region 2 must be less than the sonic pressure which exists in regions 1 and 3. This can be so only if wave *A* is a rarefaction and wave *B* a compression, as illustrated in the hodograph diagram (Fig. 22.31c).

Thus we conclude that *the waves incident on the sonic line must be expansions, and those reflected from the sonic line must be compressions*. This is true even when the supersonic zone is terminated by a shock, as in Fig. 22.31d. The conclusion is not necessarily true, however, for those left-running waves which end on the shock.

Another conclusion which is immediately evident from Figs. 22.31b and 22.31c is that *as one travels along the sonic line so that the supersonic zone lies to the right, the velocity vector turns monotonically in the clockwise direction*.

A more important practical result follows from the consideration that the left-running expansion waves originate at the profile and may be thought of as the reflections at the solid surface of the right-running compression waves which begin at the sonic line. Now a compression wave is reflected from a straight solid boundary as a compression wave, and is reflected as a rarefaction wave only if the boundary is *sufficiently convex*. We conclude, therefore, that if the downstream-running charac-

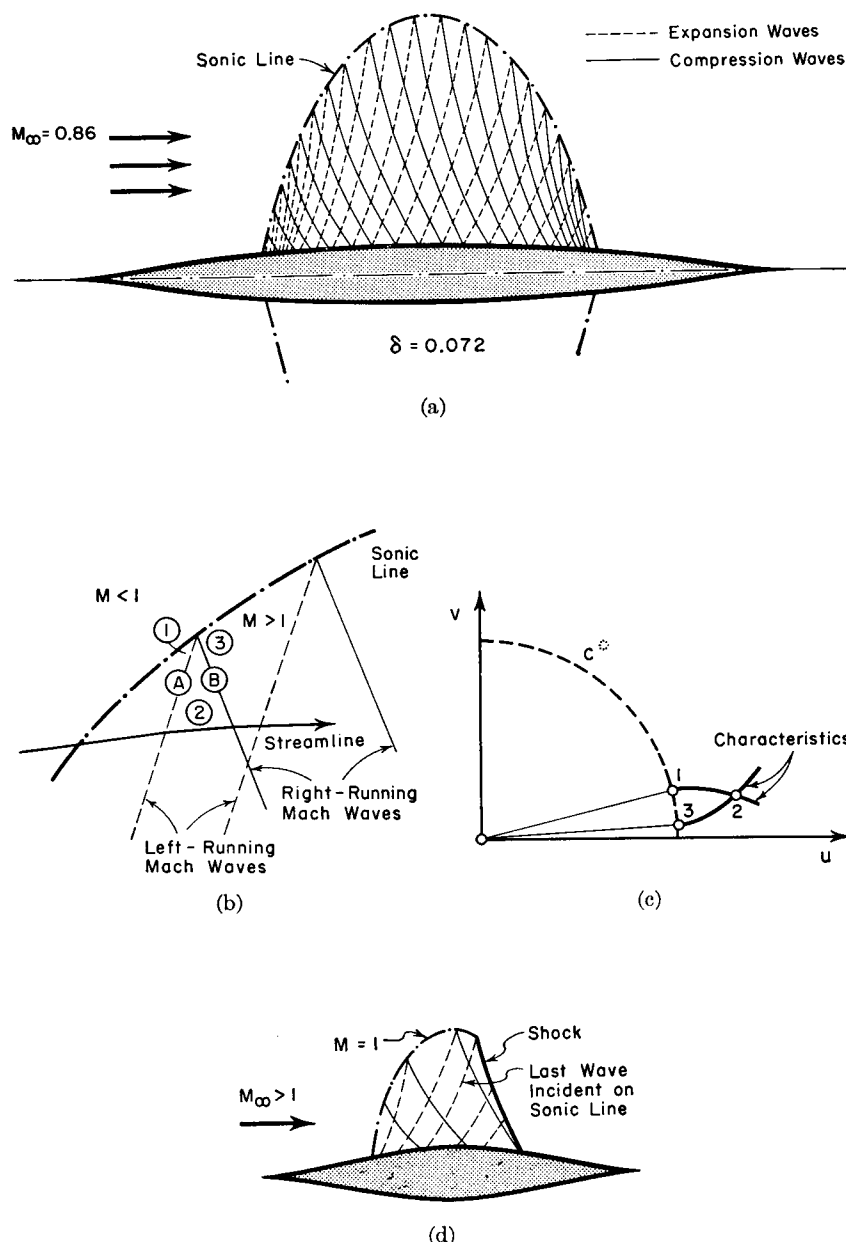


FIG. 22.31. Flow with embedded supersonic zone.

- (a) Typical flow pattern.
- (b) Conditions at a point on the sonic line.
- (c) Hodograph diagram for (b).
- (d) Termination of supersonic zone by shock.

teristics originating from a portion of the profile end on the sonic line rather than on a shock, then that portion of the profile must be convex. And if the supersonic zone is not terminated by a shock, the entire portion of the profile adjacent to the supersonic zone must be convex. By the same argument, if even a short segment of the profile adjacent to the supersonic zone is straight-sided or concave, a shock will be formed as the result of the coalescence of the compression waves reflected from or generated by this segment.

By putting these arguments into analytical form, it has been shown<sup>(20)</sup> that the criterion for the supersonic zone to be terminated smoothly without shocks is that

$$\frac{dM_s^*}{d\theta_s} \leq M_s^* \tan \alpha_s$$

where subscript  $s$  denotes conditions at the surface of the profile adjacent to the supersonic zone,  $\theta_s$  is the stream direction,  $M_s^* = V_s/c^*$ , and  $\alpha_s$  is the Mach angle.

This criterion has been applied to the flow past a Kaplan bump and to the flow past a wavy wall, and it has been found that the conditions under which irrotational flow for these two examples becomes impossible do indeed agree with the criterion stated above.

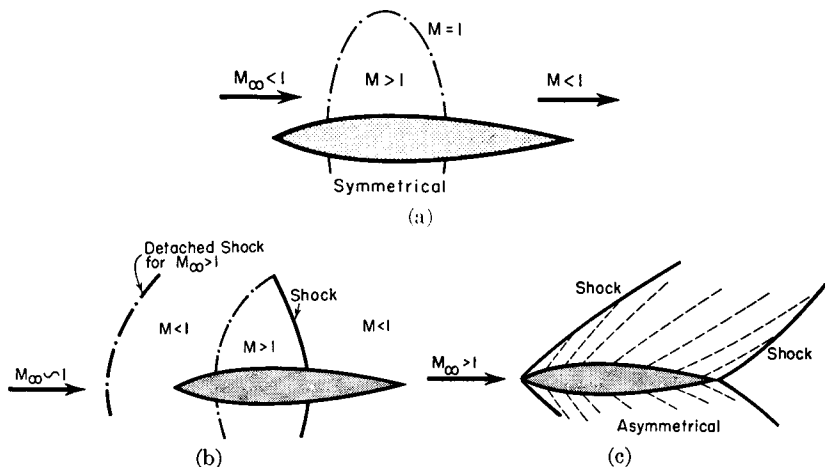


FIG. 22.32. Transition from symmetrical flow without pressure drag to asymmetric flow with pressure drag.

**Change from Symmetric Flow to Asymmetric Flow.** Consider a profile symmetrical about both the  $x$ - and  $y$ -axes and having sharp leading and trailing edges (Fig. 22.32). At high subsonic speeds, there is a local supersonic zone (Fig. 22.32a), the details of which are as shown in Fig. 22.3a, but the flow pattern is completely symmetrical, and there

is no pressure drag. At sufficiently high supersonic speeds (Fig. 22.32c), the entire flow is supersonic, there are oblique shocks carrying momentum to infinity, the flow pattern is definitely asymmetric, and there is a finite pressure drag even for a fluid without viscosity. For  $M_\infty$  near unity, whether slightly below or slightly above, the flow pattern near the profile (apart from boundary-layer effects) is as shown in Fig. 22.32b, representing an intermediate phase between the symmetric and asymmetric flows. This transition from a symmetric to an asymmetric flow should be compared with the similar transition which occurs at a nozzle throat (Art. 21.4).

Assuming now that  $M_\infty < 1$ , it is of great practical interest to determine why and how the symmetric flow without drag passes over into the flow with drag in which there is a supersonic zone terminated by a shock. For, if this were known, it might be possible to design profiles for which pressure drag could be avoided up to a Mach Number of unity.

When the symmetrical solution of Fig. 22.31a is extended to slightly higher free-stream Mach Numbers, it is found that the rarefaction waves at the forward end tend to form an envelope, as do the compression waves at the aft end of the supersonic zone. Such an envelope constitutes a limit line and indicates that a discontinuity must be formed. Now a stationary rarefaction discontinuity is impossible, since it is well known that a rarefaction shock, if formed momentarily, cannot persist in a steady way, but rather, with the passage of time, decays into a continuous wave. This thought suggests that, as  $M_\infty$  increases, the steady symmetric flow becomes impossible because shocks are formed through the coalition of compression waves and because unsteady effects are introduced through the tendency of rarefaction waves to spread out.

There is in fact considerable experimental evidence to the effect that flows like that of Fig. 22.32b are unsteady. A series of schlieren pictures of what is ostensibly the same flow often show, near the profile, a number of shock and expansion waves whose positions are different from picture to picture. These possibly are waves traveling with and against the general direction of flow. It is also observed that the shock which terminates a supersonic zone extends *upstream* from the profile, thus supporting the supposition that the shock is formed by the coalition of compression waves originating at the sonic line.

Sears<sup>(21)</sup> has pointed out that three effects have at various times been advanced to explain the discrepancy between the observed Mach Numbers at which shocks appear on profiles and the relatively higher Mach Numbers at which it would appear from potential theory that shock-free flow is possible. These effects are (i) the effects of viscosity, (ii) the possible nonexistence of neighboring flows, and (iii) the possible

nonexistence of steady flow or the possible instability of steady flows. These will now be discussed.

**Viscous Effects.** One of the effects of viscosity is to increase the displacement thickness of the boundary layer, thus altering the effective contour of the profile. An increasing displacement thickness in a supersonic zone changes the slope of the profile in a manner the effect of which is to generate incremental compression waves (or to weaken

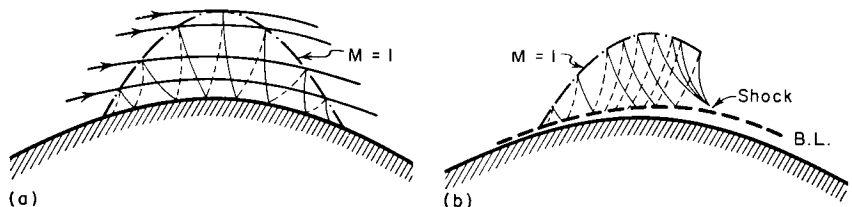


FIG. 22.33. Effect of boundary layer on transonic potential flow. Dashed lines are expansion waves; solid lines compression waves (after Busemann).

(a) Without boundary layer.

(b) With boundary layer (B.L.) of increasing displacement thickness.

the rarefaction waves) at the contour. As illustrated by Fig. 22.33, this may lead to the coalescence of compression waves into a shock which destroys the potential nature of the flow.

If this were the only effect of viscosity, it would appear that the shock-free character of the flow could be readily re-established merely by changing the shape of the profile to take account of the boundary-layer displacement thickness.

However, as pointed out by Liepmann<sup>(1)</sup> and others, there may be, in supersonic boundary layers, a kind of instability which is illustrated by the flat-plate flow of Fig. 22.34a. Suppose that normally the displacement thickness is substantially constant and that the flow outside the boundary layer is at uniform pressure and Mach Number. Then

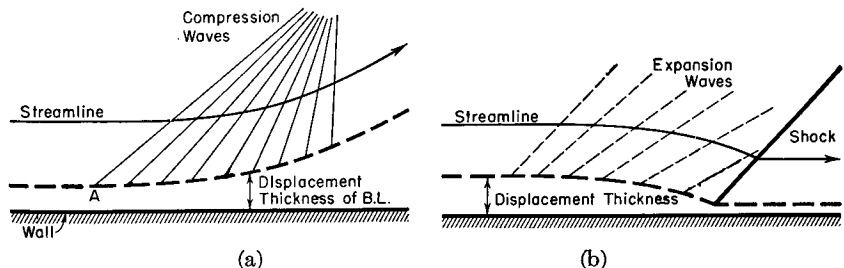


FIG. 22.34. Possible instability of boundary layer in supersonic flow (after Liepmann).

(a) Catastrophic thickening with creation of detached shock.

(b) Catastrophic thinning followed by terminal shock.

imagine that at some point, say *A*, the thickness accidentally increases owing to a disturbance. A compression wave is generated there owing to the resulting convexity of the effective contour. This wave produces a pressure rise in the direction of flow, which in turn produces a further thickening of the boundary layer. Thus there may exist a self-exciting chain of events which leads to a catastrophic thickening of the boundary layer and to a shock wave. A similar argument would indicate also the possibility of a catastrophic thinning of the boundary layer, terminated ultimately by a shock (Fig. 22.34b).

It is an experimental fact, however, that neither of the instabilities mentioned above are observed on flat plates. Very likely the reason is that a slight bump in the boundary layer generates, in addition to the compression wave on the upstream side, a compensating rarefaction wave on the downstream side. It would appear, however, that the type of instability illustrated by Fig. 22.34a might be much more probable over the aft portion of the supersonic zone of Fig. 22.32a because of the adverse pressure gradient which already exists in this region. As  $M_\infty$  increases, the adverse pressure gradient associated with the potential flow solution increases very rapidly, which is a different way of saying that the compression waves originating at the sonic line tend to become very closely spaced. Now, with sufficiently adverse pressure gradients, a reverse flow occurs near the wall inside the boundary layer, and the ensuing separation aggravates the type of instability of Fig. 22.34a. Thus it is conceivable that, at Mach Numbers for which potential flow is still possible, an accidental thickening of the boundary layer in the region of adverse pressure gradient might produce a catastrophic change to a flow with shock waves. The latter flow would appear to be more stable than the original flow, because the intense pressure gradient produced by the shock wave creates an upstream thickening of the boundary layer which "feeds" the shock wave and which could not easily be altered by a small disturbance. An essential feature of this line of thought is the interaction between the boundary layer, the shock wave, and the main flow, which we shall discuss more fully in Art. 22.8.

**Uniqueness of Profile for Flow Without Shocks.** It seems possible that there may be certain unique profiles which allow of steady potential flow at very high subsonic Mach Numbers, and that there are no neighboring solutions to the flow in the sense that the slightest alteration of the original unique shape immediately leads to a flow with shocks. If this were true, it would mean that shock-free flow at very high subsonic Mach Numbers is in practice impossible, for no amount of manufacturing precision could possibly avoid deviations from a mathematically unique contour.

Such a situation may indeed arise in channel flow, as can be seen by considering the flow on one side of the line of symmetry of a reversed Laval nozzle (Fig. 22.35) which smoothly decelerates a parallel, supersonic flow through the sonic velocity. Suppose that the contour is

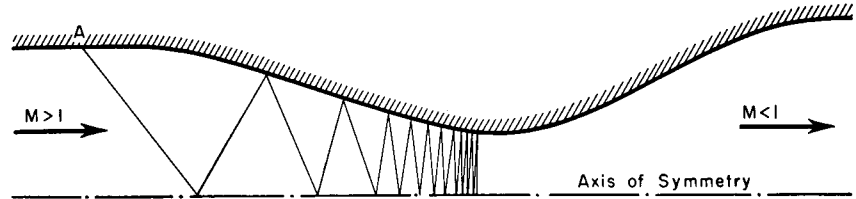


FIG. 22.35. Two-dimensional diffuser designed for shock-free deceleration. Infinitesimal compression wave produced inadvertently at *A* propagates along original Mach lines and forms finite shock near throat (after Busemann).

correctly designed by the method of characteristics to decelerate the initially parallel flow smoothly without shocks; this is the reverse of designing a nozzle for uniform, parallel, supersonic flow. Now imagine that at point *A* there is a very small error in the actual contour employed for the passage. The effects of such a perturbation can be superposed on the original design, and thus the actual flow may be thought of as the design flow pattern plus the incremental flow pattern produced by the disturbance at *A*. Since we are dealing with a small perturbation, the effects of the disturbance will be propagated as pressure waves along the Mach lines of the original flow, as illustrated by the sketch. From the small-perturbation theory for two-dimensional supersonic flow (Chapter 14),

$$\delta p = \pm \frac{kpM^2}{\sqrt{M^2 - 1}} \delta\theta$$

where  $\delta p$  and  $\delta\theta$  are the changes in pressure and flow direction across a wave, and  $M$  is the local Mach Number. Assuming that the wave originating at *A* is a compression wave, it will each time be reflected as a compression, the value of  $|\delta\theta|$  being the same for every wave of the system. Since the waves are inclined at the local Mach angle to the flow, it is clear that they become infinitely numerous near the throat. Furthermore, the pressure rise across the wave becomes larger as  $M \rightarrow 1$ . From these considerations, it follows that a finite shock forms near the throat. Thus, although there are many contours which could decelerate the flow past the sonic line without shocks, such contours are unique in that the slightest alteration at a typical point *A* leads to cumulative and violent changes further downstream. Mathematically, the solutions for potential flow do not have neighboring solutions.

In passing, it is of interest to note that similar considerations when

applied to an accelerating supersonic passage indicate no such difficulties, but show rather that the effects of accidental alterations in contour decay as they pass downstream. Measurements on supersonic nozzles verify closely the computed potential flow pattern, the minor deviations being explained entirely by the difficulties in estimating exactly the boundary-layer growth. However, reversed nozzles (diffusers) have never been observed to operate without shocks.

These arguments have been extended to transonic flow over a profile by Busemann.<sup>(22)</sup> Suppose that there exists a symmetrical supersonic

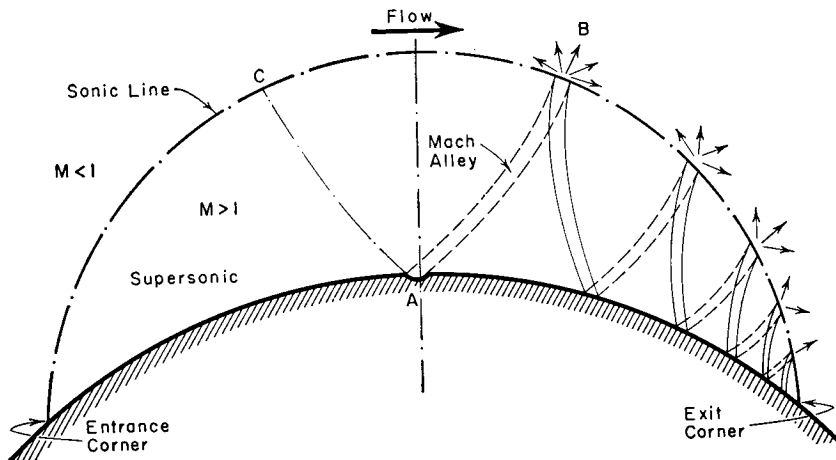


FIG. 22.36. Accumulation of disturbances near exit corner of supersonic zone (after Busemann).

zone without shocks past a certain profile (Fig. 22.36) and that at point *A* a small alteration is made in the contour. This change is propagated along a Mach "alley" which leads downstream to the sonic line, from which it is reflected down another Mach "alley," and so on, until the exit corner is reached. But, because the local Mach Number approaches unity, the perturbation waves become infinitely crowded near the exit corner. Moreover, the pressure increment across the disturbance wave becomes larger as the latter zigzags downstream. Thus there is a tendency for a shock to occur near the exit corner, and for the potential flow to be destroyed. Here again, profiles for smooth transonic flow, if they exist, are unique and without neighboring solutions, inasmuch as the slightest alteration in contour leads to large changes in flow pattern.

There is one questionable feature, however, of this line of reasoning. The flow upstream of point *A* is in fact affected by the disturbance at *A*, because the disturbance reaches the sonic line at points such as *B*, and, once in the subsonic region, the disturbance may work its way

upstream and make itself felt throughout the entire field of flow. Thus there exists the possibility, improbable as it may appear to be, that the signals escaping from the sonic line at a typical point *B* re-enter the supersonic region at points such as *C* and act to cancel the original disturbance to an extent sufficient to avoid irregularities at the exit corner.

**Stability of Flows with Imbedded Supersonic Zones.** Kuo<sup>(25)</sup> has investigated analytically the dynamic stability of shock-free, steady, transonic flow by the usual method of inquiring as to the time history of disturbances which may accidentally appear in the originally steady flow. If the original steady motion is stable, the disturbances will die out; but, if it is unstable, the disturbances will amplify and eventually become shock waves, with a consequent production of drag.

Without going into the details of calculation, the conclusions reached by Kuo are as follows:

(i) Downstream-moving pressure pulses propagate with unchanged strength, irrespective of the curvature of the surface or of whether the

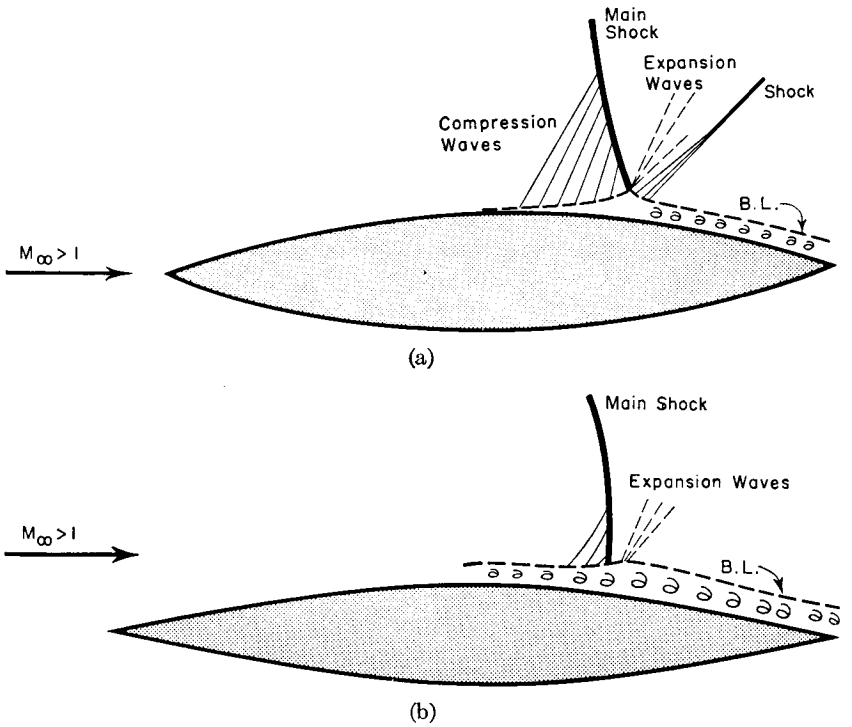


FIG. 22.37. Interaction between shock wave and boundary layer in transonic flow.

- (a) Laminar boundary layer.
- (b) Turbulent boundary layer.

steady flow is accelerating or decelerating. If they are initially weak, they remain weak. Thus they cannot lead to instability.

(ii) In *decelerating* transonic flow over a *convex* surface, an upstream-propagating *compression* pulse grows continuously by consuming the kinetic energy of the steady flow, ultimately becoming so strong as to change drastically the nature of the flow pattern. Upstream-propagating *expansion* pulses in *decelerating* transonic flow over a *convex* surface, however, decay and are ultimately dissipated.

(iii) In *accelerating* transonic flow over any shape of surface, both compression and expansion pulses propagating upstream decay as time progresses and thus cannot lead to instability.

Since imbedded supersonic zones without shocks can exist only adjacent to convex surfaces, it follows from point (ii) that such flows are unstable.

Whether these conclusions are entirely correct for real flows is not yet known, as it is an established experimental fact that finite supersonic zones without appreciable shocks do exist over convex profiles. The discrepancy noted here is perhaps explainable in terms of whether the maximum amplitude of pulse which is formed can be measured, or in terms of the behavior of the boundary layer under the action of a pressure pulse.

## 22.8. Interaction Between Boundary Layer and Shock Wave

The discussion of transonic flow could hardly be complete without mention of the interaction between boundary layers and shock waves. Regardless of the exact mechanism by which shocks are first formed in a transonic flow, it is firmly established by experiment that, once such shocks do appear, their interaction with the boundary layer exerts a considerable magnifying influence on changes in flow pattern, particularly when the boundary layer is laminar and thick.

Typical transonic flows with shocks are sketched in Figs. 22.37 and schlieren photographs are shown in Fig. 22.39. Additional schlieren photographs are presented in Chapter 28.

The main shock seen in Fig. 22.37 is generated through the coalescence of right-running compression waves which originate at the sonic line. As this shock enters the boundary layer near the profile, it tends to produce extraordinary adverse pressure gradients, but these are considerably softened by upstream and downstream propagation in the boundary layer.

**Laminar Boundary Layer.** Within a laminar boundary layer (Figs. 22.37a, 22.39a, and 22.39c), the influence of the shock extends far upstream. The rising pressure in the boundary layer causes the latter to thicken, and this thickening in turn generates compression waves which

propagate along the Mach lines into the main stream. The thickened boundary layer, which often is separated for sufficiently strong shocks, cannot have within itself large longitudinal pressure gradients. It may be thought of as a comparatively stagnant air mass which cushions the surface from the main flow and thus "softens" the shock. When the main shock is incident on this comparatively stagnant layer, the shock reflects approximately as from a constant-pressure surface, that is, it reflects as a Prandtl-Meyer expansion wave. The latter usually turns the stream too far toward the solid surface, and the subsequent turning of the stream to the direction of the surface initiates compression waves which coalesce into a weak shock.

**Turbulent Boundary Layer.** With a turbulent boundary layer (Figs. 22.37b, 22.39b and 22.39d), somewhat similar effects are observed except that the influence of the shock on the pressure distribution and the reflected wave pattern is very much less, for two reasons: (i) the thickness of the subsonic layer is very much less for a turbulent boundary layer than for a laminar layer of the same displacement thickness, and thus the effects of the adverse pressure gradient are propagated upstream to a correspondingly lesser extent; (ii) the ability of a turbulent boundary layer to transmit momentum from the main stream into the slow-moving layers near the wall makes the turbulent layer much less sensitive than the laminar boundary layer to adverse pressure gradients.

The schlieren photographs show in striking fashion that, for a given Mach Number, the character of the potential flow depends strongly on whether the boundary layer is laminar or turbulent. It is of interest to speculate on the appearance of the potential flow if viscous effects were altogether absent. Presumably the flow would then be more like that with a turbulent layer than with a laminar layer because the former is considerably less sensitive to pressure gradients.

### Effect on Pressure Distribution.

The difference in surface Mach Number which results from the two different types of interaction is illustrated in Fig. 22.38. <sup>(1)</sup> In the particular test shown, the influence of the shock begins to be felt at about 50% chord in the case of the laminar boundary layer. With a turbulent boundary layer the influence of the shock does not begin until about 65% chord. As a result of the difference in pressure distributions for the two curves of

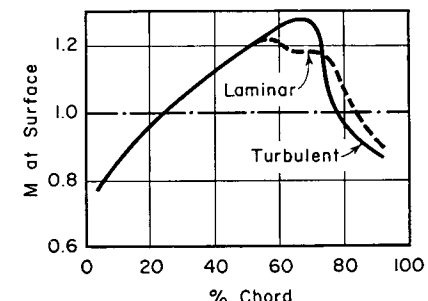
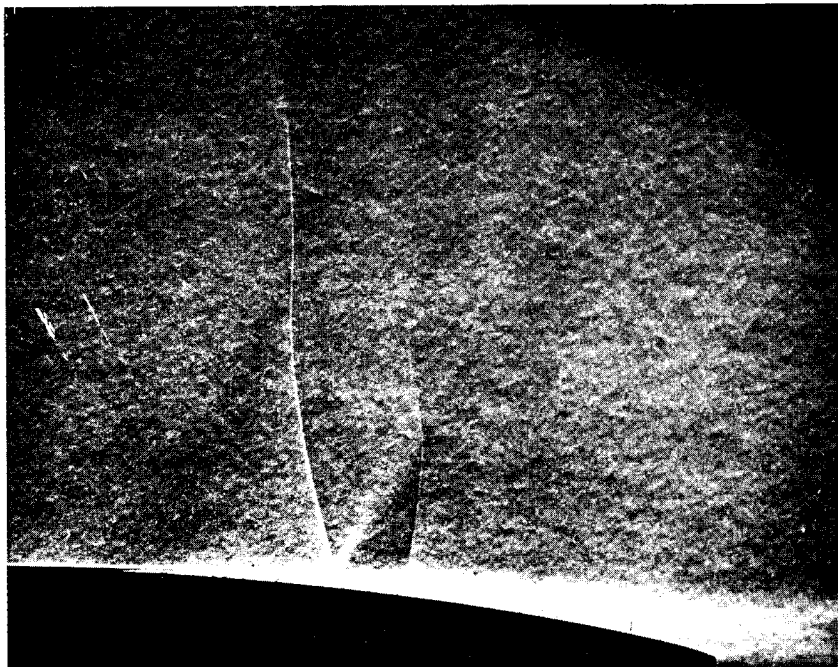
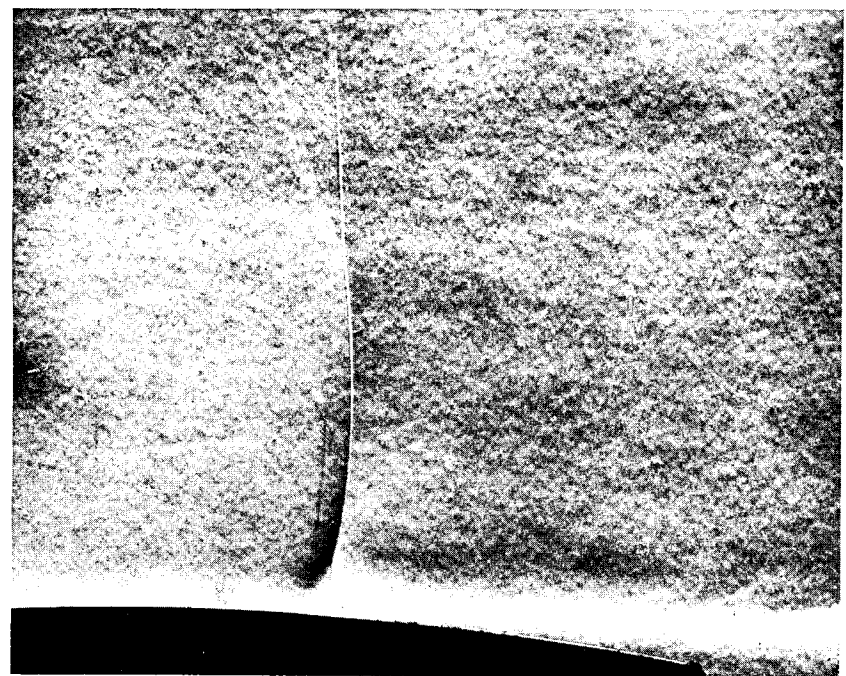


Fig. 22.38. Surface Mach Number distribution on 12% thick biconvex, circular-arc profile at  $M_{\infty} = 0.889$  (after Liepmann, Ashkenas, and Cole).

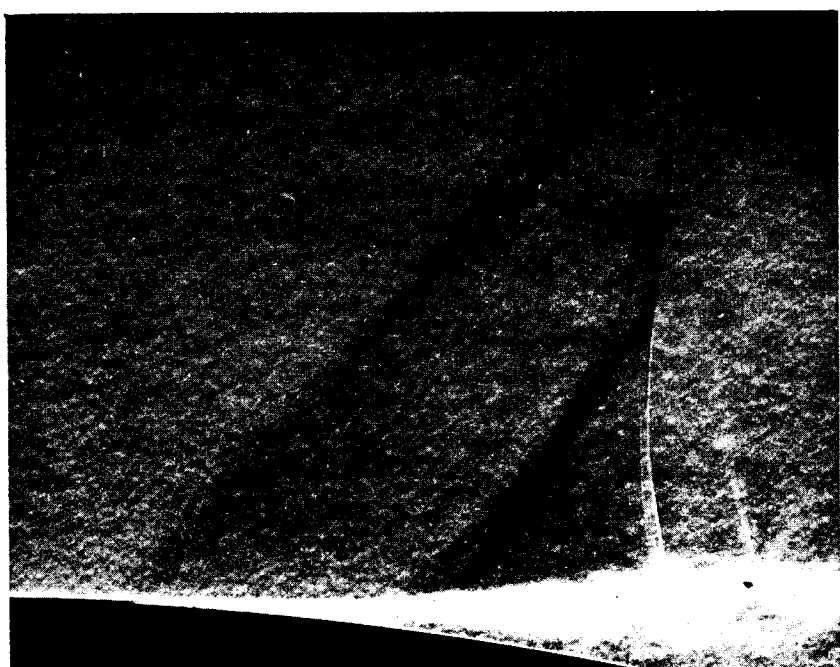


(a)

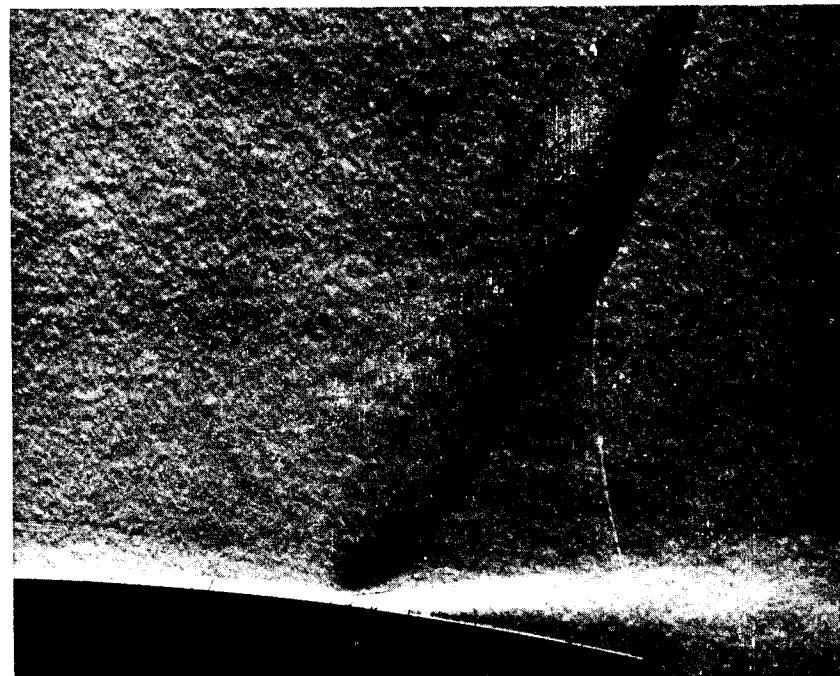


(b)

FIG. 22.39. Schlieren photographs of shock-boundary layer interaction in transonic flow. Region shown in photographs is near trailing edge of 12% biconvex, circular-arc profile. Flow is from left to right. Schlieren knife-edge is parallel to flow direction (after H. W. Liepmann). (Continued on following page).



(c)



(d)

(a) Laminar boundary layer,  $M_\infty = 0.84$ .  
(b) Turbulent boundary layer,  $M_\infty = 0.84$ .  
(c) Laminar boundary layer,  $M_\infty = 0.90$ .  
(d) Turbulent boundary layer,  $M_\infty = 0.90$ .

Fig. 22.38, the pressure drag is less for the flow with turbulent boundary layer.

### REFERENCES AND SELECTED BIBLIOGRAPHY

1. LIEPMANN, H. W., ASHKENAS, H., and COLE, J. D. Experiments in Transonic Flow, *U.S. Air Force Technical Report*, No. 5667 (1948).
2. LIEPMANN, H. W., and BRYSON, A. E., JR. Transonic Flow Past Wedge Sections, *Jour. Aero. Sci.*, Vol. 17, No. 12 (1950), p. 745.
3. GUDERLEY, G. Considerations of the Structure of Mixed Subsonic and Supersonic Flow Patterns, *AMC Wright Field Technical Report*, No. F-TR-2168-ND (1947).
4. VINCENTI, W. G., and WAGONER, C. B. Transonic Flow Past a Wedge Profile with Detached Bow Wave—General Analytical Method and Final Calculated Results, *NACA Tech. Note*, No. 2339 (1951).
5. GUDERLEY, G., and YOSHIHARA, H. The Flow Over a Wedge Profile at Mach Number One, *U.S. Air Force Technical Report*, No. 5783 (1949).
6. COLE, J. D. Drag of a Finite Wedge at High Subsonic Speeds, *Jour. Math. and Phys.*, Vol. 30, No. 2 (1951), p. 79.
7. BECKER, J. V. Characteristics of Wing Sections at Transonic Speeds, *NACA—University Conference on Aerodynamics* (1948).
8. FERRI, A. Completed Tabulation in the United States of Tests of 24 Airfoils at High Mach Numbers, *NACA Wartime Report*, L-143 (1945).
9. NITZBERG, G. E., and CRANDALL, S. A Study of Flow Changes Associated with Airfoil Drag Rise at Supercritical Speeds, *NACA Tech. Note*, No. 1813 (1949).
10. LINDSEY, W. F., DALEY, B. N., and HUMPHREYS, M. D. The Flow and Force Characteristics of Supersonic Airfoils at High Subsonic Speeds, *NACA Tech. Note*, No. 1211 (1947).
11. OUTMAN, V., and LAMBERT, A. A. Transonic Separation, *Jour. Aero. Sci.*, Vol. 15, No. 11 (1948), p. 671.
12. WEAVER, J. H. A Method of Wind-Tunnel Testing Through the Transonic Range, *Jour. Aero. Sci.*, Vol. 15, No. 1 (1948), p. 28.
13. STACK, J., and LINDSEY, W. F. Characteristics of Low-Aspect-Ratio Wings at Supercritical Mach Numbers, *NACA Tech. Note*, No. 1665 (1948).
14. ADLER, A. A. Effects of Combinations of Aspect Ratio and Sweepback at High Subsonic Mach Numbers, *NACA RM*, No. L7C24 (1947).
15. CHARTERS, A. C., and THOMAS, R. N. The Aerodynamic Performance of Small Spheres from Subsonic to High Supersonic Velocities, *Jour. Aero. Sci.*, Vol. 12, No. 4 (1945), p. 468.
16. PRANDTL, L., POSCHL, T., and EWALD, P. P. *The Physics of Solids and Fluids*. 2d ed. London: Blackie & Son, 1936.
17. BUSEMANN, A. A Review of Analytical Methods for the Treatment of Flows with Detached Shocks, *NACA Tech. Note*, No. 1858 (1949).
18. MOECKEL, W. E. Approximate Method for Predicting Form and Location of Detached Shock Waves Ahead of Plane or Axially Symmetric Bodies, *NACA Tech. Note*, No. 1921 (1949).
19. HEBERLE, J. W., WOOD, G. P., and GOODERUM, P. B. Data on Shape and Location of Detached Shock Waves on Cones and Spheres, *NACA Tech. Note*, No. 2000 (1950).
20. NIKOLSKII, A. A., and TAGENOV, G. I. Gas Motion in a Local Supersonic Region and Conditions of Potential-Flow Breakdown, *NACA Tech. Memo*, No. 1213 (1949).
21. SEARS, W. R. Transonic Potential Flow of a Compressible Fluid, *Jour. App. Phys.*, Vol. 21 (1950), p. 771.
22. BUSEMANN, A. The Drag Problem at High Subsonic Speeds, *Jour. Aero. Sci.*, Vol. 16, No. 6 (1949), p. 337.
23. GUDERLEY, G. New Aspects of Transonic Flow Theory, *Technical Data Digest, Air Materiel Command*, Vol. 12, No. 9 (1947).
24. FRANKL, F. I. On the Formation of Shock Waves in Subsonic Flows with Local Supersonic Velocities, *NACA Tech. Memo.*, No. 1215 (1950).
25. KUO, Y. H. On the Stability of Two-Dimensional Smooth Transonic Flows, *Jour. Aero. Sci.*, Vol. 18, No. 1 (1951), p. 1.
26. ACKERET, J., FELDMANN, F., and ROTR, N. Investigations of Compression Shocks and Boundary Layers in Gases Moving at High Speed, *NACA Tech. Memo.*, No. 1113 (1947).
27. BRYSON, A. E., JR. An Experimental Investigation of Transonic Flow Past Two-Dimensional Wedge and Circular-Arc Sections Using a Mach-Zehnder Interferometer, *NACA Tech. Note*, No. 2560 (1951).
28. ACKERET, J., DEGEN, M., and ROTR, N. Investigations on Wings With and Without Sweepback at High Subsonic Speeds, *NACA Tech. Memo.*, No. 1320 (1951).
29. JOHNSTON, G. W. An Investigation of the Flow About Cones and Wedges at and Beyond the Critical Angle, *UTIA Report*, No. 24 (1952), Univ. of Toronto.
30. NITZBERG, G. E., and CRANDALL, S. M. Comparative Examination of Some Measurements of Airfoil Section Lift and Drag at Supercritical Speeds, *NACA Tech. Note*, No. 2825 (1952).
31. SPREITER, J. R. On Alternative Forms for the Basic Equations of Transonic Flow Theory, *Jour. Aero. Sci.*, Vol. 21, No. 1 (1954), p. 70.

### REFERENCES AND SELECTED BIBLIOGRAPHY

PART VII  
UNSTEADY MOTION IN ONE DIMENSION

## Chapter 23

### UNSTEADY WAVE MOTION OF SMALL AMPLITUDE

#### 23.1. Introductory Remarks

In most engineering problems the flow pattern may be considered steady, or at least quasi-steady, yet there are many instances where the unsteady features of the fluid motion play a dominant role.

Perhaps the best-known example of unsteady gas motion is the field of acoustics, the propagation of sound in the form of very small pressure disturbances through a gas. The analytical methods of acoustics are highly developed, but are applicable only to disturbances of small amplitude. In this and succeeding chapters we shall concern ourselves with problems of unsteady, one-dimensional motion with waves of large amplitude. Chapters 23 and 24 are devoted to continuous motions while Chapter 25 deals with motions in which shock discontinuities are present.

The consideration of unsteady flow enters into all transient processes, as, for example, the behavior of a gas turbine plant under a suddenly changing load. In certain kinds of power plants, such as the high-speed reciprocating engine or the Holzwarth explosion turbine, the unsteady motions in the ducts of the machine are an integral part of the power cycle. It is also well known that by "tuning" the inlet and exhaust ducts of high-speed piston engines, it is often possible to improve the volumetric efficiency and mean effective pressure. Finally, we may mention certain "wave engines" whose very functioning depends on unsteady flow processes, namely, (i) the Comprex, and (ii) the intermittent-jet engine of the V-1 "buzz-bomb."

In this chapter we shall set down the physical equations describing problems of this nature, and we shall introduce some of the important concepts and methods of representation with the help of a simplified linear theory.

To avoid mathematical difficulties, it will be necessary to make a number of simplifying assumptions. First of all, it will be assumed that the flow is geometrically one-dimensional, implying that all fluid properties are uniform over each cross section of the passage, and that changes in cross-sectional area take place very slowly.

The viscosity and thermal conductivity of the gas will be neglected. This means that all parts of the gas are related through the isentropic

relations unless shocks of changing strength (*curved shocks* in time-distance coordinates) appear.

When normal shocks of constant strength are present, the methods we shall develop are valid on either side of the shock. When the shocks are of varying strength they produce unequal changes of entropy for different fluid particles. Often the entropy variations on either side of such a curved shock are negligible, but on occasion it is necessary to employ more complex methods to take account of these entropy variations. Such methods are described in Chapter 24; in the present chapter we shall assume the flow to be isentropic.

As in the analysis of steady-flow problems, we shall assume that the equation of state is that of a perfect gas, that gravity effects are negligible and that the fluid may be treated as a continuum.

### NOMENCLATURE

$A$	area	$V$	velocity
$c$	speed of sound	$x$	Cartesian coordinate
$k$	ratio of specific heats	$\rho$	density
$L$	length	$\varphi$	perturbation velocity potential
$M$	Mach Number	$\Phi$	velocity potential
$p$	pressure	$\tilde{\Phi}$	auxiliary velocity potential
$R$	gas constant		
$s$	entropy per unit mass		
$t$	time	$(\bar{\ })$	signifies mean properties
$T$	absolute temperature	$(\delta)$	signifies a perturbation from a time-mean property
$u$	velocity in $x$ -direction		

### 23.2. Equations of Motion

Consider the one-dimensional, unsteady, shock-free flow through the control surface of Fig. 23.1. The physical properties tabulated refer to a given instant of time.

**Conservation of Mass.** The continuity equation states that the net mass rate of flow *out* of the control surface is equal to the rate of *decrease* of mass within the control surface. At a given instant, the mass flow into the left-hand side of the control volume is  $\rho A u$ , and the mass within the control volume is  $\rho A dx$ . Hence we write

$$\frac{\partial(\rho A u)}{\partial x} dx = -\frac{\partial}{\partial t}(\rho A dx) \quad (23.1)$$

Expanding this, and noting that the cross-sectional area  $A$  depends only on the space coordinate  $x$ , we get

$$\frac{\partial \rho}{\partial t} + u \frac{\partial \rho}{\partial x} + \rho \frac{\partial u}{\partial x} + \rho u \frac{dA/dx}{A} = 0 \quad (23.2)$$

**Dynamic Equation.** The momentum theorem as applied to a control surface states that the net force acting on the fluid within the control surface is equal to the time rate of change of momentum within the control surface plus the excess of the outgoing momentum flux over the incoming momentum flux. This may be written

$$\begin{aligned} pA + p dA - \left( A + \frac{dA}{dx} dx \right) \left( p + \frac{\partial p}{\partial x} dx \right) \\ = \frac{\partial}{\partial t} (\rho A dx u) + \frac{\partial}{\partial x} (\rho A u^2) dx \end{aligned}$$

or, after simplification,

$$-\frac{\partial p}{\partial x} = \frac{\partial}{\partial t} (\rho u) + u \frac{\partial}{\partial x} (\rho u) + \frac{\rho u}{A} \frac{\partial}{\partial x} (A u)$$

Expanding the right-hand side, and subtracting from it Eq. 23.2, we get

$$-\frac{1}{\rho} \frac{\partial p}{\partial x} = \frac{\partial u}{\partial t} + u \frac{\partial u}{\partial x} \quad (23.3)$$

This is Euler's equation for unsteady motion. The right-hand side is the substantial derivative of velocity with respect to time, that is, the acceleration of a fluid particle of fixed identity.

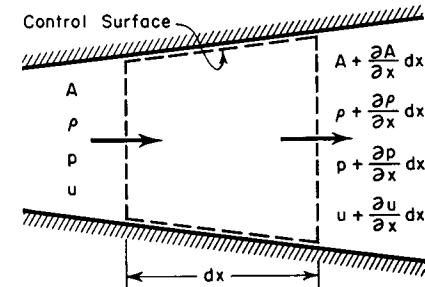


FIG. 23.1. Flow through control surface.

**Isentropic Pressure-Density Relation.** Since all fluid states have the same entropy, we may write

$$(\partial p / \partial \rho)_s = dp / d\rho = c^2 \quad (23.4a)$$

so that

$$\frac{1}{\rho} \frac{\partial p}{\partial x} = \frac{1}{\rho} \frac{dp}{d\rho} \frac{\partial \rho}{\partial x} = \frac{c^2}{\rho} \frac{\partial p}{\partial x} \quad (23.4b)$$

**Velocity Potential.** We now define a *velocity potential*  $\Phi(x, t)$  through the relation

$$u = \partial \Phi / \partial x = \Phi_x \quad (23.5)$$

It should be noted that we are entirely free to do this—no restrictions such as the irrotationality condition of two-dimensional and three-dimensional flow are applicable here. The main reason for introducing  $\Phi$  is that the resulting equations then bear a formal resemblance to those of steady two-dimensional and axi-symmetric motion, and useful parallels may be drawn.

Substituting Eqs. 23.4b and 23.5 into Eq. 23.3, we get

$$\Phi_{xt} + \Phi_x \Phi_{xx} + \frac{c^2}{\rho} \frac{\partial \rho}{\partial x} = 0$$

Multiplying each term by  $dx$  and integrating with respect to  $x$  at constant time (note that the constant of integration will be a function of  $t$ ), we find

$$\Phi_t + \frac{\Phi_x^2}{2} + \int_{\rho_0}^{\rho} \frac{c^2}{\rho} d\rho = f(t) \quad (23.6)$$

where  $\rho_0$  is a reference density.

**Thermodynamic Properties.** The isentropic relation, the equation of state, and the expression for the sound velocity, are, respectively,

$$p/\rho^k = \text{constant}; \quad p/\rho T = \text{constant}; \quad c = \sqrt{kRT}$$

These may be expressed in the convenient differential forms

$$\frac{dp}{\rho} = \frac{1}{k} \frac{dp}{p} = \frac{1}{k-1} \frac{dT}{T} = \frac{2}{k-1} \frac{dc}{c} \quad (23.7)$$

We may now evaluate the integral in Eq. 23.6 as

$$\int_{\rho_0}^{\rho} \frac{c^2}{\rho} d\rho = \frac{2}{k-1} \int_{c_0}^c c \, dc = \frac{c^2 - c_0^2}{k-1}$$

and Eq. 23.6 accordingly becomes

$$\Phi_t + \frac{\Phi_x^2}{2} + \frac{c^2 - c_0^2}{k-1} = f(t) \quad (23.8)$$

To eliminate the density terms in Eq. 23.2, we differentiate Eq. 23.6 with respect to  $x$  and then again with respect to  $t$ . Thus we get

$$\Phi_{xt} + \Phi_x \Phi_{xx} + \frac{c^2}{\rho} \frac{\partial \rho}{\partial x} = 0$$

$$\Phi_{tt} + \Phi_x \Phi_{xt} + \frac{c^2}{\rho} \frac{\partial \rho}{\partial t} = f'(t)$$

Solving for  $\partial \rho / \partial x$  and  $\partial \rho / \partial t$  and inserting these into Eq. 23.2, we obtain

$$(c^2 - \Phi_x^2) \Phi_{xx} - 2\Phi_x \Phi_{xt} - \Phi_{tt} + c^2 \frac{dA/dx}{A} \Phi_x = -f'(t) \quad (23.9)$$

We may now eliminate the function  $f(t)$  by defining the auxiliary velocity potential

$$\tilde{\Phi} \equiv \Phi - \int f(t) \, dt$$

from which

$$u = \Phi_x = \tilde{\Phi}_x; \quad \Phi_{xx} = \tilde{\Phi}_{xx}; \quad \Phi_{xt} = \tilde{\Phi}_{xt}$$

$$\Phi_t = \tilde{\Phi}_t + f(t); \quad \Phi_{tt} = \tilde{\Phi}_{tt} + f'(t)$$

By inserting these into Eqs. 23.5, 23.6, and 23.9, we obtain identical equations in terms of the derivatives of  $\tilde{\Phi}$  except that neither the function  $f(t)$  nor its derivatives appear in the governing Eqs. 23.5, 23.6, and 23.9 when these are written in terms of  $\tilde{\Phi}$ . From this we conclude that  $f(t)$  was immaterial to the problem to begin with, and may arbitrarily be set equal to zero.

**Governing Differential Equations.** Setting  $f(t) = 0$ , we obtain the following set of governing differential equations:

$$u = \partial \Phi / \partial x = \Phi_x \quad (23.5)$$

$$c^2 = c_0^2 - \frac{k-1}{2} \Phi_x^2 - (k-1)\Phi_t = c_0^2 - \frac{k-1}{2} u^2 - (k-1)\Phi_t \quad (23.8)$$

$$(c^2 - \Phi_x^2) \Phi_{xx} - 2\Phi_x \Phi_{xt} - \Phi_{tt} + c^2 \frac{dA/dx}{A} \Phi_x = 0 \quad (23.9)$$

Eq. 23.9 (with  $c^2$  expressed by Eq. 23.8) is strongly nonlinear and always hyperbolic in form. For the latter reason we may expect that the solutions will be mathematically similar to those of steady, two-dimensional (either plane or axi-symmetric), supersonic flow. In the discussions which follow notice should be taken of the similarities between steady, two-dimensional, supersonic flow, and unsteady, one-dimensional motion.

### 23.3. Waves of Small Amplitude

Many qualitative features of nonlinear, unsteady motion, as well as the method of calculation, may most easily be appreciated by restricting the discussion at first to the case where there are only small perturbations from a condition of steady flow. Also, to simplify the approach, we shall consider a tube of constant cross-sectional area ( $dA/dx = 0$ ). Then the flow pattern may be thought of as a steady flow, having properties  $\bar{u}$ ,  $\bar{\rho}$ ,  $\bar{c}$ , and  $\bar{p}$  which are independent of  $x$  and  $t$ , on which is superposed a perturbation motion with incremental properties  $\delta u$ ,  $\delta \rho$ ,  $\delta c$ , and  $\delta p$ .

**Perturbation Properties.** According to the assumption of small perturbations we may write

$$u \equiv \bar{u} + \delta u; \quad \rho \equiv \bar{\rho} + \delta \rho; \quad c \equiv \bar{c} + \delta c; \quad p \equiv \bar{p} + \delta p \quad (23.10)$$

The velocity potential is likewise written as the sum of the potential due to the steady motion plus the perturbation potential  $\varphi$ ,

$$\Phi = \bar{u}x + \varphi$$

The derivatives of  $\Phi$  are then given by

$$\begin{aligned}\Phi_x &= \bar{u} + \varphi_x; & \Phi_{xt} &= \varphi_{xt}; & \Phi_t &= \varphi_t \\ \Phi_{xx} &= \varphi_{xx}; & \Phi_{tt} &= \varphi_{tt}\end{aligned}$$

The expression for  $\Phi_x$  indicates that

$$\delta u = \partial \varphi / \partial x = \varphi_x \quad (23.11a)$$

Substituting  $c$  and  $u$  from Eq. 23.10 into Eq. 23.8, and then subtracting from the resulting expression the steady-flow version of Eq. 23.8, we get

$$2\bar{c} \delta c = -(k-1)\bar{u} \delta u - (k-1)\varphi_t \quad (23.11b)$$

**Linearized Equation.** Substituting the foregoing into Eq. 23.9 (with  $dA/dx = 0$ ), and assuming that the squares and products of perturbation terms are negligible and that  $\bar{u}$  is not close to  $\bar{c}$ , we obtain the differential equation for small perturbations,

$$(\bar{c}^2 - \bar{u}^2)\varphi_{xx} - 2\bar{u}\varphi_{xt} - \varphi_{tt} = 0 \quad (23.12)$$

**General Solution.** Since the coefficients of Eq. 23.12 are constant, the equation is linear, and particular solutions may be linearly superposed to give new solutions.

The equation is of the form of the *wave equation*, and has the general solution

$$\varphi = f_1[x - (\bar{u} + \bar{c})t] + f_2[x - (\bar{u} - \bar{c})t] \quad (23.13)$$

where  $f_1$  and  $f_2$  are arbitrary functions of their respective arguments. That Eq. 23.13 is indeed the general solution may be verified by taking derivatives and finding that Eq. 23.12 is identically satisfied by the arbitrary functions  $f_1$  and  $f_2$ .

The arbitrariness and superposability of the functions  $f_1$  and  $f_2$  produce (as in the case of steady, supersonic flow) a great simplification, for flow patterns may be constructed by choosing the forms of these functions at will. In acoustics it is customary to express the solution as the sum of Fourier series in the arguments of  $f_1$  and  $f_2$ , the coefficients of the series being determined by the initial conditions and the boundary conditions. However, as we shall see presently, it is often more convenient to synthesize solutions in terms of the "waves" which propagate along the lines of constant  $f_1$  and  $f_2$ .

**Path Lines and Physical Characteristics.** By analogy with steady, two-dimensional motion, we shall call the  $x, t$ -plane the *physical plane*.

Referring to Fig. 23.2, the various events which occur at different times at a fixed location in the duct are found by following a vertical line; the variations of fluid properties in the duct at a given instant of time are found by following a horizontal line.

The *path line*, or the time-space trajectory of a fluid particle of fixed identity, is defined by the relation

$$\left( \frac{dx}{dt} \right)_{\text{path line}} = u$$

Fig. 23.2 shows the path lines corresponding to the main velocity  $\bar{u}$ . The path lines are analogous to the streamlines of a steady flow.

Lines of constant  $f_1$  and  $f_2$  are represented in the  $x, t$ -diagram by two families of parallel straight lines designated respectively, by the symbols  $I$  and  $II$ , according to the relations

$$\left( \frac{dx}{dt} \right)_{I, II} = \bar{u} \pm \bar{c} \quad (23.14)$$

the upper sign referring to the symbol  $I$  and the lower to the symbol  $II$ . We shall see presently that the perturbation properties are propagated along these lines and that they are analogous to the Mach waves (characteristic curves) of steady, two-dimensional flow.

**Simple Wave.** The linearity of Eq. 23.13 allows us to superpose elementary solutions. Let us consider, therefore, an elementary solution for which the function  $f_2$  is constant *throughout* the  $x, t$ -plane. The resultant flow is called a *simple wave*.

From Eqs. 23.11 and 23.13 we obtain, for the perturbation velocity in such a simple wave,

$$\delta u = \varphi_x = f_1'$$

where the prime designates differentiation with respect to the argument of  $f_1$ . Differentiating Eq. 23.13 with respect to  $t$ , and using the expression above, we obtain

$$\varphi_t = -(\bar{u} + \bar{c})f_1' = -(\bar{u} + \bar{c})\delta u \quad (23.15)$$

Eliminating  $\varphi_t$  by means of Eq. 23.11b, we obtain

$$\left( \frac{\delta c}{\delta u} \right)_I = \frac{k-1}{2} \quad (23.16a)$$

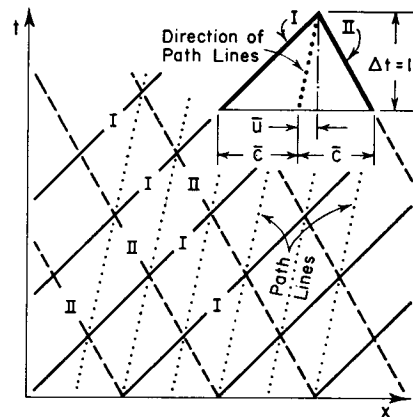


FIG. 23.2. Physical plane, showing path lines and Mach lines.

the subscript *II* indicating (by convention) that we are considering changes of state for a process in which the function  $f_2$  is everywhere constant.

For a simple wave with  $f_1$  set equal to a constant we would obtain, similarly,

$$\left(\frac{\delta c}{\delta u}\right)_I = -\frac{k-1}{2} \quad (23.16b)$$

From these results we see that in a simple wave for which  $f_2$  is everywhere constant, the perturbation velocity and sound velocity associated with a certain function  $f_1$  (and, from Eq. 23.7, all stream properties) are constant along lines on which the argument of  $f_1$  is constant. Thus the lines on which the arguments of  $f_1$  and  $f_2$  are constant may be thought of as the lines along which disturbances are propagated. These lines are therefore commonly spoken of as *waves*.

Referring to Eq. 23.14, the propagation speed of these waves,  $(dx/dt)_{I,II}$ , is seen to be the speed of sound *relative* to the moving fluid. Waves of family *I* travel *rightward* relative to the fluid, and waves of family *II* travel *leftward* relative to the fluid.

Using Eqs. 23.7 and 23.16, the pressure perturbation produced by a wave is found to be given by

$$\left(\frac{\delta p}{\bar{p}}\right)_{I,II} = \mp \frac{k}{\bar{c}} (\delta u)_{I,II} \quad (23.17)$$

where it is to be noted again that the subscript *I* in Eqs. 23.16 and 23.17 corresponds to a wave with subscript *II* in Eq. 23.14, and vice versa. The justification for this seemingly irrational procedure is given later but for the present it suffices to point out that the choice of subscripts is merely a convention and is therefore arbitrary.

**Calculation Procedure.** Usually it is not possible to work out practical problems in terms of analytic forms of the functions  $f_1$  and  $f_2$ . Instead, an approximate stepwise procedure is employed, in which the  $x,t$ -plane is imagined to be covered by a finite number of *I* and *II* lines. The approximation involves a replacement of the continuous variation of  $\delta u$ ,  $\delta c$  and  $\delta p$  in the  $x,t$ -plane by a pattern in which these perturbation properties are assumed to be constant in each of the quadrilaterals, or fields, formed by the net of *I* and *II* lines. Changes in fluid properties are then assumed to occur only across the lines bounding the fields. That is, a fluid particle is assumed to undergo changes in  $\delta u$ ,  $\delta c$ , and  $\delta p$  only when it is crossed by either a left-moving or right-moving pressure wave. Fig. 23.3 illustrates how a continuous wave may be represented approximately in such a way as to make it amenable to this type of stepwise procedure.

We may now dispense with the velocity potential as a device for actual calculations, retaining only the result (Eqs. 23.13 and 23.14) that the equation of the velocity potential may be satisfied by constructing a net of left-running and right-running pressure pulses which respectively propagate leftward and rightward with the speed  $\bar{c}$  relative to the fluid. Since each pressure pulse may be thought of as a special type of simple wave across which a small discontinuity occurs, Eqs. 23.16 and 23.17 may be used for determining the changes of  $\delta c$  and  $\delta p$  corresponding to the particular difference of  $\delta u$  between adjacent fields.

#### FOUR BASIC PRESSURE PULSES.

Flow patterns may be synthesized in terms of four elementary types of pressure pulses, depending on whether they are of family *I* (*right-running*) or of family *II* (*left-running*), and on whether they are *compressions* or *rarefactions*. In a rarefaction (expansion) wave, the fluid over which the wave passes undergoes a reduction in pressure; the opposite is true for a compression (condensation) wave.

The four elementary types of waves are illustrated in Fig. 23.4. In Figs. 23.4a, b, c, d are shown the physical planes together with typical wave forms at a given instant of time.

The corresponding changes in fluid properties are represented in the  $u,c$ -state plane of Fig. 23.4e. It may be noted that on the  $u,c$ -plane the states on the two sides of a left-running pressure pulse lie on a straight line of slope  $-(k-1)/2$ ; the states on the two sides of a right-running pulse lie on a straight line of slope  $(k-1)/2$ . According to Eq. 23.17 a similar representation may be made on a  $p,u$ -plane, the slopes of the lines of state change then being equal to  $\mp k\bar{p}/\bar{c}$ .

**SUMMARY OF RULES OF CALCULATION.** The *I*, *II*-system of identification for the two families of waves has been adopted so as to conform to the usual practice in the theory of characteristic curves (Art. 23.5). The seeming inconsistency of the notation is explained by the fact that Eq. 23.14 applies *along* a wave of a given family, whereas Eqs. 23.16 and 23.17 apply *across* the wave of the given family (and therefore along a wave of the opposite family). The rules of calculation may, without reference to the *I*, *II*-system of subscripts, be summarized in the following way:

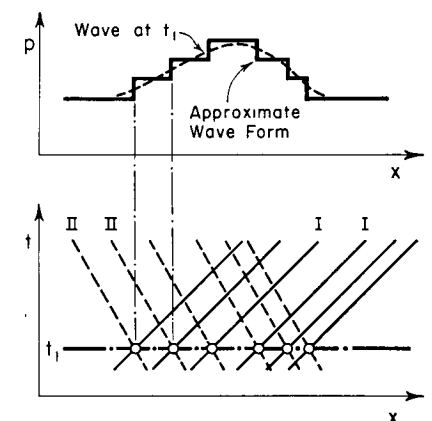


FIG. 23.3. Replacement of continuous wave by stepwise wave.

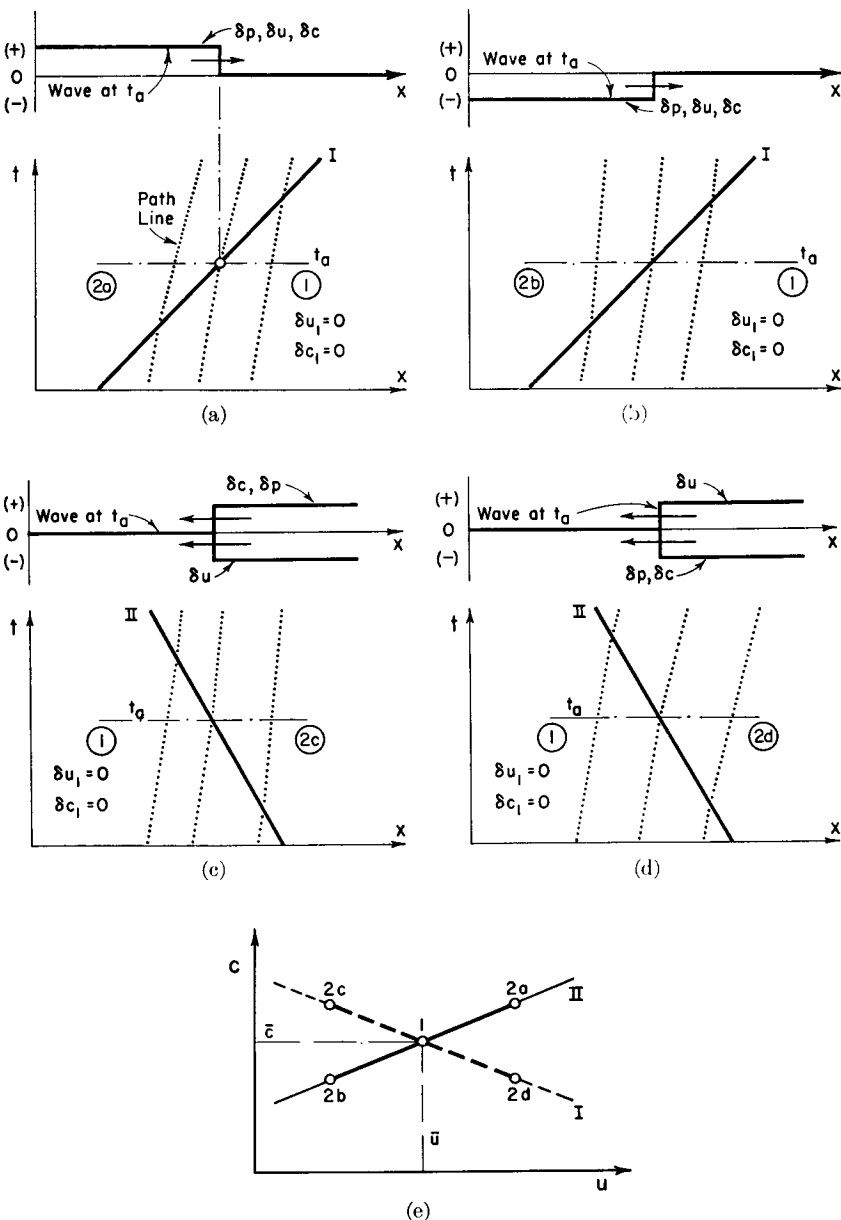


FIG. 23.4. Four elementary pressure pulses.

- (a) Right-running compression.
- (b) Right-running rarefaction.
- (c) Left-running compression.
- (d) Left-running rarefaction.
- (e) Representation of changes in state on  $u, c$ -plane.

*Right-Running Waves.*

$$\frac{dx}{dt} = \bar{u} + \bar{c} \quad \text{along the wave}$$

$$\delta c = \frac{k-1}{2} \delta u \quad \text{across the wave}$$

*Left-Running Waves.*

$$\frac{dx}{dt} = \bar{u} - \bar{c} \quad \text{along the wave}$$

$$\delta c = -\frac{k-1}{2} \delta u \quad \text{across the wave}$$

The values of  $\delta p$ ,  $\delta \rho$ , and  $\delta T$  may be computed from the corresponding value of  $\delta c$  by means of Eq. 23.7.

**Bending of Path Lines.** Examination of the path lines for the four elementary waves of Fig. 23.4 yields the rules that (i) in a rarefaction the path lines bend *away* from the wave front, and (ii) in a compression the path lines bend *toward* the wave front.

### 23.4. Simplified Physical Analysis of Pressure Pulse

The results of the preceding article may be found, in a manner which emphasizes physical rather than mathematical considerations, by considering the effects produced by a pressure pulse propagating through a constant-area duct.

Referring to Fig. 23.5a, suppose that the fluid is generally moving

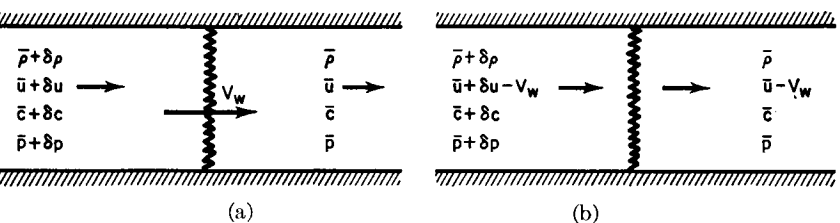


FIG. 23.5. Moving pressure pulse.

- (a) Actual flow.
- (b) Coordinate system in which pulse appears stationary.

at the speed  $\bar{u}$ , with properties  $\bar{p}$ ,  $\bar{\rho}$ , and  $\bar{c}$ . A pressure pulse of amplitude  $\delta p$  is generated somewhere upstream and moves down the tube with the velocity  $V_w$ . By imposing on the entire flow pattern a uniform velocity  $V_w$  to the left, the wave front becomes stationary and the steady-flow relations may be applied to the flow pattern of Fig. 23.5b.

**Conservation of Mass.** The continuity equation is

$$(\bar{\rho} + \delta\rho)(\bar{u} + \delta u - V_w) = \bar{\rho}(\bar{u} - V_w)$$

or,

$$\bar{\rho} \delta u + (\bar{u} - V_w) \delta \rho = 0$$

**Dynamic Equation.** The Euler equation may be written for the steady flow of Fig. 23.5b as

$$\delta p = -\bar{\rho}(u - V_w) \delta u$$

**Working Formulas.** Eliminating  $\delta u$  from this pair of equations, we obtain

$$V_w = \bar{u} \pm \sqrt{\delta p / \delta \rho} = \bar{u} \pm \bar{c}$$

This result shows that the pressure wave moves with the sound velocity *relative* to the fluid, either with or against the direction of principal flow.

The Euler equation may now be written as

$$\frac{\delta p}{\delta u} = -\bar{\rho}(\bar{u} - V_w) = \pm \bar{\rho}\bar{c} = \pm \frac{k\bar{p}}{\bar{c}}$$

Then, with the help of the isentropic (Eq. 23.7), we get

$$\delta c = \pm \frac{k-1}{2} \delta u$$

These results are equivalent to those obtained previously in the form of Eqs. 23.14, 23.16, and 23.17. The upper sign in each case refers to a right-running wave and the lower to a left-running wave.

### 23.5. Characteristic Curves

Let us now investigate Eq. 23.12 in the light of the theory of characteristics (Appendix A). Comparing Eq. A.11 with Eq. 23.12 (see also Art. 24.3), we obtain for the coefficients of Eq. A.11 (with  $t$  taken as  $y$ ),

$$A = \bar{c}^2 - \bar{u}^2; \quad B = -\bar{u}; \quad C = -1; \quad D = 0$$

Since  $B^2 - AC$  equals  $\bar{c}^2$ , and the latter is always positive, it follows that the equations of unsteady motion are always hyperbolic in type.

**Physical Characteristics.** Equation A.17 gives, for the characteristic curves in the physical plane,

$$\left( \frac{dt}{dx} \right)_{I,II} = \frac{-\bar{u} \pm \sqrt{\bar{u}^2 + \bar{c}^2 - \bar{u}^2}}{\bar{c}^2 - \bar{u}^2} = \frac{-\bar{u} \pm \bar{c}}{(\bar{c} + \bar{u})(\bar{c} - \bar{u})} = \frac{1}{(\bar{u} \pm \bar{c})}$$

Thus the *physical characteristics* are identical with the lines on which the arguments of  $f_1$  and  $f_2$  are constant. They are "propagated" through the duct with the speed  $\pm \bar{c}$  *relative* to the fluid, and thus the characteristics are identified as the lines along which pressure waves are propagated.

**Hodograph Characteristics.** From Eq. A.18 we get, for the *hodograph*  $(\varphi_t, \varphi_i)$  *characteristics*,

$$\left( \frac{d\varphi_t}{d\varphi_x} \right)_{I,II} = \left( \frac{d\varphi_t}{d\delta u} \right)_{I,II} = -(\bar{u} \pm \bar{c})$$

Comparison with the expression for the physical characteristics shows that the hodograph characteristics form two families of parallel lines which are mutually orthogonal to the respective physical characteristics of the opposite family. Integrating this expression, and setting equal to zero the immaterial constant of integration, we obtain

$$(\varphi_t / \delta u)_{I,II} = -(\bar{u} \pm \bar{c})$$

**State Characteristics.** To find the characteristics in the  $u, c$ -state plane, we first find from Eq. 23.11b that

$$\frac{\delta c}{\delta u} = \frac{k-1}{2\bar{c}} \left( \bar{u} + \frac{\varphi_t}{\delta u} \right)$$

Inserting this into the previous expression for  $(\varphi_t / \delta u)_{I,II}$ , and simplifying, we get

$$\left( \frac{\delta c}{\delta u} \right)_{I,II} = \mp \frac{k-1}{2}$$

which is identical with Eq. 23.16, and indicates that in the state plane the characteristics for a gas with  $k = 1.4$  are two families of straight lines with slopes  $\mp 0.2$  (Fig. 23.4e).

### 23.6. Application of Theory

If only waves of small amplitudes were of interest, the characteristics method described here, requiring stepwise numerical calculations, would not be of great value because analytical methods (Fourier analysis) are available from the theory of sound. However, our ultimate aim is to make calculations for waves of finite amplitude, for which analytical methods are usually not available. It is therefore worth while to pursue further the application of the method of characteristics to the linearized theory because the method illustrates the concepts and techniques we shall later use, and also because it is a useful preliminary for obtaining quick estimates of what to expect from a more exact solution for waves of large amplitude.

**Example.** Let us consider the problem illustrated by Fig. 23.6. A tube, open at one end and closed at the other, is divided by a partition across which a small pressure difference exists initially. The partition is suddenly broken, and we wish to determine how the velocity, pressure, density, etc., subsequently vary with time for each location in the tube.

Since the gas is initially at rest, we may set  $\bar{u} = 0$ . For simplicity, let us suppose that there is an initial temperature difference of such a magnitude that the entropy is the same on both sides of the membrane. Then we may locate, at  $t = 0$ , points 1 and 2 in the  $u, c$ -diagram to

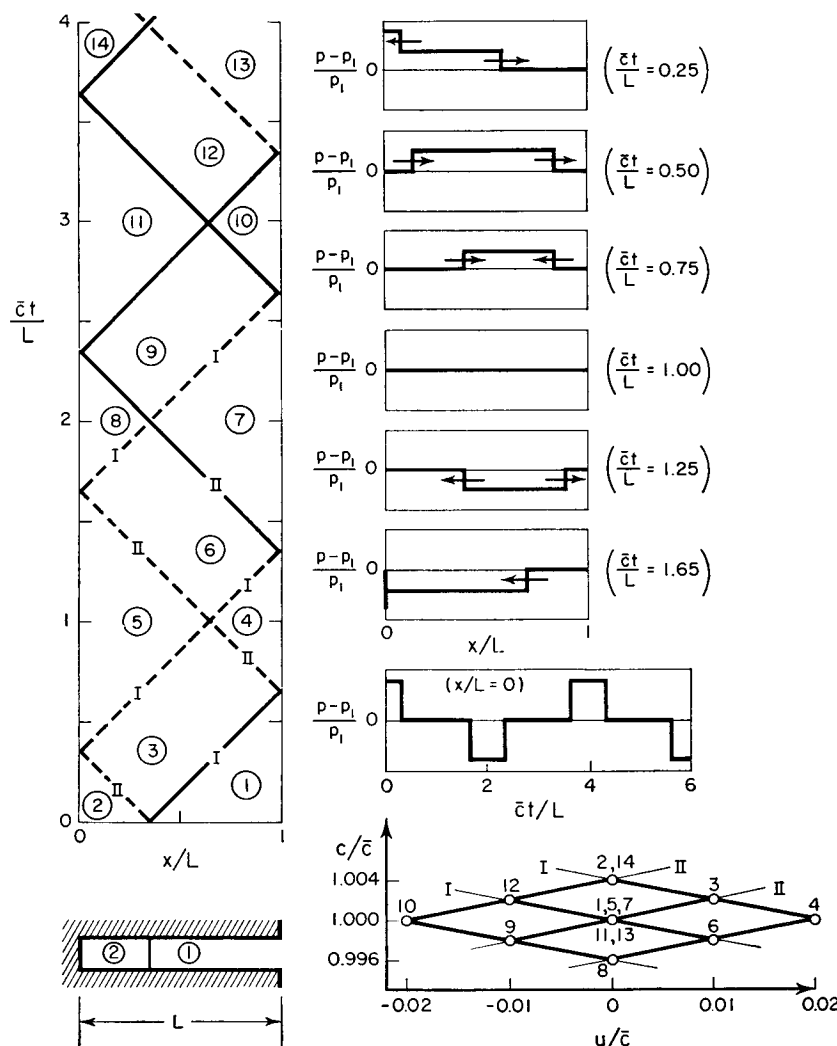


FIG. 23.6. Solution for the problem of the bursting of a diaphragm which separates region 1 (high pressure) from region 2 (low pressure).

represent the states in gas regions 1 and 2. For convenience, we denote the gas properties in region 1, corresponding to atmospheric pressure, by  $\bar{p}$ ,  $\bar{c}$ , etc.

**NUMERICAL SOLUTION.** When the partition is broken, there is a discontinuity of pressure which cannot persist, and pressure waves are accordingly propagated from the discontinuity in both directions. Part of the gas in zone 3, between the two waves, is compressed by the right-moving compression wave of family I, and another part is rarefied by the left-moving rarefaction wave of family II. But, since all the gas in zone 3 is at uniform pressure and velocity, we find from Eq. 23.17 that

$$(p_3 - p_1)/\bar{p} = k(u_3 - u_1)/\bar{c}$$

$$(p_3 - p_2)/\bar{p} = -k(u_3 - u_2)/\bar{c}$$

Adding and then subtracting this pair of equations, and noting that  $u_2 = u_1 = 0$ , we may solve for  $p_3$  and  $u_3$  in the forms

$$p_3/\bar{p} = \frac{1}{2} (p_1/\bar{p} + p_2/\bar{p})$$

$$u_3/\bar{c} = \frac{1}{2k} (p_2/\bar{p} - p_1/\bar{p})$$

From Eq. 23.16, we find similarly that

$$\frac{c_3}{\bar{c}} - 1 = \frac{k-1}{2} \frac{u_3}{\bar{c}}; \quad \frac{c_3}{\bar{c}} - \frac{c_2}{\bar{c}} = -\frac{k-1}{2} \frac{u_3}{\bar{c}}$$

To make the problem more specific, let us suppose that  $u_3/\bar{c} = 0.01$ . Then the initial pressure difference required to impart this velocity is, for  $k = 1.4$ ,

$$\frac{p_2 - p_1}{\bar{p}} = 2k \frac{u_3}{\bar{c}} = 0.028; \quad \frac{p_2}{\bar{p}} = 1.028$$

Furthermore

$$p_3/\bar{p} = 0.5(1.000 + 1.028) = 1.014$$

and

$$c_3/\bar{c} = 1.002; \quad c_2/\bar{c} = 1.004$$

**GRAPHICAL SOLUTION.** These same results might be found graphically by using the simple geometrical properties of the  $u, c$ -diagram as given by Eq. 23.16 and illustrated in Fig. 23.4e. On this diagram the characteristics are straight lines with slopes  $\mp 0.2$ . Regions 1 and 3 lie on the same II-characteristic, and regions 2 and 3 lie on the same I-characteristic. The intersection defines the location of point 3 in

the state plane. Given  $u_3/\bar{c} = 0.01$ , the values of  $c_3/\bar{c}$  and  $c_2/\bar{c}$  may be read graphically, and the corresponding pressures found from the isentropic relation, Eq. 23.7.

**Reflection of Wave from Solid Surface.** When the left-running wave which separates region 2 from region 3 strikes the solid end of the tube, it must be reflected, for otherwise the gas would lose contact with the wall. If the reflected wave leaves the gas in a state denoted by 5, then this state is defined, first, by the fact that  $u_5 = 0$  (since the gas is in contact with a stationary wall), and secondly, by the fact that states 3 and 5 lie on the same  $II$ -characteristic. Thus, point 5 may be located on the diagram, and from the latter we read

$$c_5/\bar{c} = 1.000; \quad u_5/\bar{c} = 0$$

The same result might be found of course from Eq. 23.16a,

$$\frac{c_5 - c_3}{\bar{c}} = \frac{k-1}{2} \frac{u_5 - u_3}{\bar{c}} = -\frac{k-1}{2} \frac{u_3}{\bar{c}} = -0.002; \quad c_5/\bar{c} = 1.000$$

while from Eq. 23.17,

$$\frac{p_5 - p_3}{\bar{p}} = k \frac{u_5 - u_3}{\bar{c}} = -1.4(0.01) = -0.014$$

$$p_5/\bar{p} = 1.014 - 0.014 = 1.000$$

The reflected wave, like the incident wave, is a rarefaction. We therefore draw the general conclusion that *waves are reflected from stationary end walls in like sense*. Furthermore, for waves of small amplitude, *the reflected and incident waves are of equal strength*.

**Reflection of Wave from Open End.** For the present we shall make the simplifying assumption that dynamic effects near the tube opening may be ignored and that the pressure at the open end is always atmospheric. Then the right-traveling wave between regions 1 and 3 must be reflected at the open end in order to preserve atmospheric pressure at this end. From the condition that states 3 and 4 lie on a  $I$ -characteristic, and that  $p_4 = p_1$ , or  $c_4 = c_1$ , point 4 may be located in the  $u, c$ -diagram, and we find graphically that

$$u_4/\bar{c} = 0.02; \quad c_4/\bar{c} = 1.000; \quad p_4/\bar{p} = 1.000$$

As in the previous calculations, the same results might also have been obtained from Eqs. 23.16 and 23.17.

In this case the incident wave is a compression and the reflected wave is a rarefaction. Hence we conclude that *waves are reflected from a constant-pressure end in unlike sense*. For waves of small amplitude, *the incident and reflected waves are of equal strength*.

**Intersection of Waves.** We next investigate the crossing of waves, that is, we calculate conditions in region 6. States 6 and 5 lie on the same  $I$ -characteristic, and states 6 and 4 lie on the same  $II$ -characteristic. Point 6 may therefore be located in the  $u, c$ -diagram, and we read directly that

$$u_6/\bar{c} = 0.01; \quad c_6/\bar{c} = 0.998; \quad p_6/\bar{p} = 0.986$$

The general rule for the intersection of two waves may be found by applying Eq. 23.16. Thus

$$c_6 - c_5 = -\frac{k-1}{2} (u_6 - u_5)$$

$$c_6 - c_4 = \frac{k-1}{2} (u_6 - u_4)$$

Adding and then subtracting, we get, after simplification, the desired results in the forms

$$c_6 = \frac{c_5 + c_4}{2} + \frac{k-1}{2} \frac{u_5 - u_4}{2}$$

$$u_6 = \frac{u_5 + u_4}{2} + \frac{2}{k-1} \frac{c_5 - c_4}{2}$$

By comparing the fluid states in regions 3, 4, 5, and 6, we may conclude that *intersecting waves of small amplitude do not influence each other*. For example, the differences in pressure and velocity between regions 3 and 4 on the one hand, and between 5 and 6 on the other hand, are alike. Thus, to each wave may be assigned a certain strength as to pressure and velocity changes, and this strength is not altered when the wave crosses a wave of opposite family.

**Complete Solution.** By repeated application of the reasoning described in the previous paragraphs, the course of the process may be completely analyzed in terms of the pressure waves. Fig. 23.6 shows the locus of positions of the various waves on the physical diagram, rarefaction waves being denoted by dashed lines and compression waves by solid lines. It will be noted that, at  $\bar{c}t/L = 4$ , the states in the tube are the same as at the beginning of the process, and the entire process begins again. Thus the period, or the time for a complete cycle of events to occur, is  $4L/\bar{c}$ .

If it is desired to know the pressure distribution, say, at various times, this may easily be found by drawing horizontal lines in the  $x, t$ -diagram and consulting the  $u, c$ -diagram for the fluid properties in each region of the tube. Fig. 23.6 shows the pressure distribution along the tube at several values of  $\bar{c}t/L$ . It is of interest that the process

"overshoots," that is, at  $\bar{c}t/L = 2$  the pressure on the closed end is below atmospheric by the amount by which it was originally above atmospheric. This is similar to the so-called "Kadenacy effect" which may be used for improving the performance of high-speed piston engines by "tuning" the inlet and exhaust ducts.

The variation of pressure at a fixed location may be found by following a vertical line on the  $x, t$ -diagram and referring to the  $u, c$ -diagram for the fluid properties at each instant of time. Fig. 23.6 shows the pressure variation at the left-hand end of the tube as a function of time.

In this example the *field method* was used. That is, the  $x, t$ -diagram was divided into several fields separated by characteristics, with all fluid properties uniform in each field, and changes in properties occurring only across the characteristics. Sometimes it is more convenient to employ the *lattice-point method*, in which the fluid properties are found at the lattice points of the characteristics mesh in the  $x, t$ -plane.

### 23.7. Development of Wave Forms

The term *wave form*, or *wave shape*, refers to the instantaneous curve of some fluid property, usually the pressure, as a function of longitudinal distance.

A wave of any shape may be thought of as a succession of pulses which, taken together, form the complete wave. If the entire wave is of small amplitude, then, according to Eq. 23.14, all parts of a wave

traveling in only one direction travel at the same speed. Therefore, since each part of such a simple wave can neither overtake nor be overtaken by other parts of the same wave, the wave form must remain unchanged with the passage of time. This rule is illustrated by Fig. 23.7 for the times  $t_1$  and  $t_2$  for both right-traveling and left-traveling simple waves. As was shown in Art. 5.6, and as we shall see later, when the amplitudes are not vanishingly small the nonlinearities in the motion require (i) that compression waves become steeper and ultimately form shocks, and (ii) that rarefaction waves become less steep.

compression waves become steeper and ultimately form shocks, and (ii) that rarefaction waves become less steep.

Since, for small amplitudes, crossing waves do not influence each other, the pressure disturbances due to two waves traveling in opposite

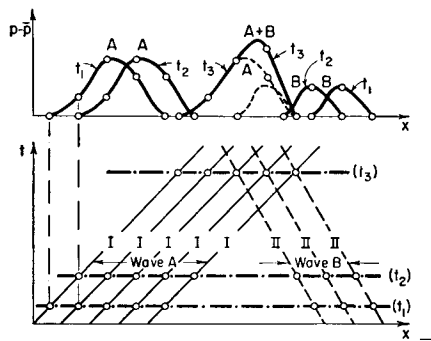


FIG. 23.7. Development of wave form. Wave A is originally a right-traveling simple wave. Wave B is originally a left-traveling simple wave.

directions may be added linearly. This rule is also illustrated in Fig. 23.7 for the time  $t_3$ .

### 23.8. Effects of Gradual Changes in Area

Some of the effects due to changes in cross-sectional area may be seen by considering the case where there are small perturbations in fluid properties  $u'$ ,  $c'$ ,  $\rho'$ , etc., superposed on the steady-state conditions  $\bar{u}$ ,  $\bar{c}$ ,  $\bar{\rho}$ , etc., and where the rate of change of cross-sectional area,  $d(\ln A)/dx$ , is also of perturbation magnitude.

**Analytical Formulation.** The main stream conditions  $\bar{u}$ ,  $\bar{c}$ ,  $\bar{\rho}$  are now assumed to be functions of  $x$  but not of  $t$ . Writing

$u \equiv \bar{u} + u'$ ;  $c \equiv \bar{c} + c'$ ;  $\rho \equiv \bar{\rho} + \rho'$ ;  $p \equiv \bar{p} + p'$ ;  $\Phi \equiv \bar{\Phi} + \varphi$   
and substituting these into Eq. 23.9, it may be shown that

$$(\bar{c}^2 - \bar{u}^2)\varphi_{xx} - 2\bar{u}\varphi_{xu} - \varphi_{uu} = 0 \quad (23.18)$$

where this simplified form is obtained by

- (i) Omitting squares and products of perturbation terms
- (ii) Using the steady-state relation,  $d\bar{u}/\bar{u} = -(1/1 - \bar{M}^2) dA/A$
- (iii) Writing Eq. 23.9 in terms of the steady-state quantities  $\bar{c}$ ,  $\bar{u}$ ,  $\bar{\varphi}$ , etc., with all time derivatives set equal to zero

Carrying out similar operations for Eq. 23.8, it may be shown that

$$c' = -\frac{k-1}{2} \left[ \frac{\bar{u}}{\bar{c}} u' + \frac{\varphi_t}{\bar{c}} \right]$$

from which, by differentiation, we may obtain

$$\frac{dc'}{du'} = -\frac{k-1}{2} \left( \frac{\bar{u}}{\bar{c}} + \frac{1}{\bar{c}} \frac{d\varphi_t}{du'} \right) \quad (23.19)$$

**Characteristic Curves.** Applying the characteristics theory of Appendix A to Eqs. 23.18 and 23.19, it may be shown that

$$\left( \frac{dt}{dx} \right)_{I,II} = -\frac{1}{\bar{u} \pm \bar{c}} \quad (23.20)$$

$$\left( \frac{d\varphi_t}{du'} \right)_{I,II} = -(\bar{u} \pm \bar{c}) \quad (23.21)$$

$$\left( \frac{dc'}{du'} \right)_{I,II} = \mp \frac{k-1}{2} \quad (23.22)$$

Introducing the critical sound velocity of the steady flow,  $\bar{c}^*$ , and using the adiabatic steady-state relation of Chapter 4 between  $\bar{c}/\bar{c}^*$  and  $\bar{M}$ , we get, for the physical characteristics,

$$\bar{c}^* \left( \frac{dt}{dx} \right)_{I,II} = \sqrt{\frac{2}{k+1} \left( 1 + \frac{k-1}{2} \bar{M}^2 \right)} \frac{1}{\bar{M} \pm 1} \quad (23.20a)$$

The slope of the path line is found in dimensionless terms as

$$c^* \left( \frac{dt}{dx} \right)_{\text{path}} = \frac{\bar{c}^*}{\bar{u}} = \frac{\bar{c}^* \bar{c}}{\bar{c} \bar{u}} = \sqrt{\frac{2}{k+1} \left( 1 + \frac{k-1}{2} \bar{M}^2 \right)} \frac{1}{\bar{M}} \quad (23.23)$$

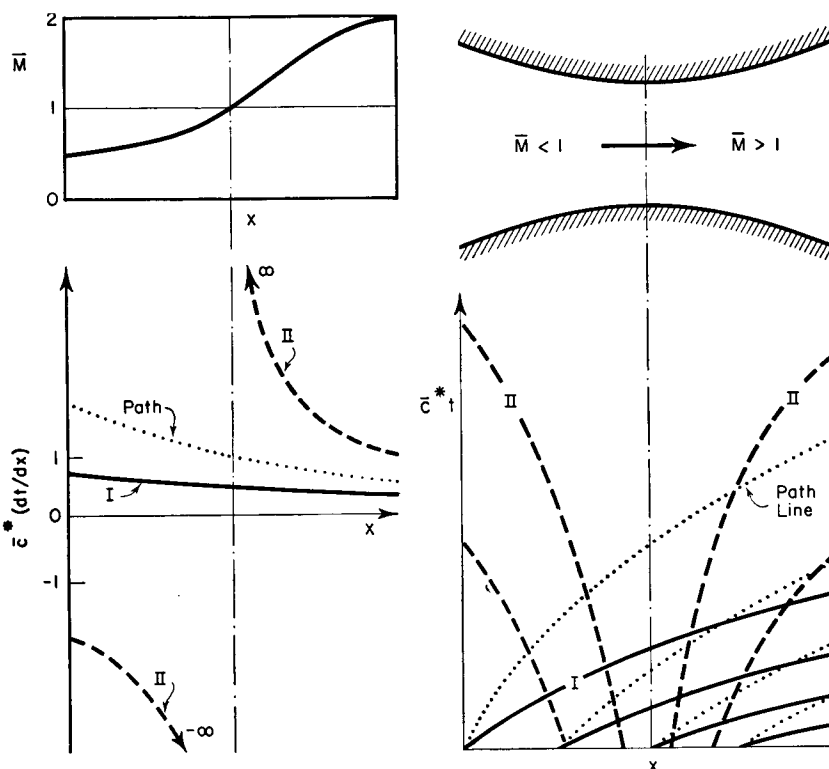


FIG. 23.8. Path lines and pressure waves in a duct of slowly changing cross section.

**Accelerating Flow.** In Fig. 23.8 the physical characteristics and path lines, as calculated by these equations, are shown for an accelerating flow. Considering only simple waves, and examining the change of spacing with respect to time between characteristics of a single family,

we conclude that, in an accelerating flow, (i) waves which move downstream relative to the fluid (family *I*) become less steep, and (ii) waves which move upstream relative to the fluid (family *II*) also become less steep. The amplitude of a simple wave appears to be constant according to this analysis; if the rate of area change is not vanishingly small, however, a more exact analysis indicates that a simple wave of small amplitude decreases in amplitude if the wave broadens, and increases in amplitude if the wave steepens.

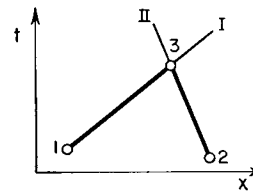
**Decelerating Flow.** By considering in a similar manner a gradually decelerating flow, it is concluded that simple waves in a decelerating flow, whether moving upstream or downstream relative to the fluid, tend to steepen.

**Conclusions.** In Chapter 5, it was shown that in a constant-area duct finite compression waves steepen and finite expansion waves broaden at a time rate proportional to the square of the wave slope. Combining this effect with the effect due to area change, we conclude that

- Compression waves always steepen in a decelerating flow and tend toward shocks.
- Rarefaction waves always become less steep in an accelerating flow.
- Compression waves in an accelerating flow, and expansion waves in a decelerating flow, may either steepen or broaden, depending upon the relative magnitudes of the wave slope and of the acceleration (or deceleration).

### PROBLEMS

**23.1.** In using the lattice-point method for solving problems, the basic operation is to solve for the location and fluid properties of a point 3, given data as to



PROB. 23.1.

the location and fluid properties at two other points 1 and 2, assuming that points 1 and 3 lie on a common *I*-characteristic and that 2 and 3 lie on a common *II*-characteristic.

Show that this basic operation for constant-area ducts with small perturbations may be carried out with the following formulas:

$$x_3 = \frac{\bar{u}^2 - \bar{c}^2}{2\bar{c}} (t_1 - t_2) + \frac{\bar{u} + \bar{c}}{2\bar{c}} x_2 - \frac{\bar{u} - \bar{c}}{2\bar{c}} x_1$$

$$t_3 = \frac{1}{2\bar{c}} (x_2 - x_1) - \frac{\bar{u} - \bar{c}}{2\bar{c}} t_2 + \frac{\bar{u} + \bar{c}}{2\bar{c}} t_1$$

$$c_3 = \frac{c_1 + c_2}{2} + \frac{k - 1}{2} \frac{u_1 - u_2}{2}$$

$$u_3 = \frac{u_1 + u_2}{2} + \frac{2}{k - 1} \frac{c_1 - c_2}{2}$$

Derive a similar formula for  $p_3$ .

Illustrate the relations for  $c_3$  and  $u_3$  geometrically on the  $u, c$ -diagram.

**23.2.** A constant-area tube 10 ft in length is closed at the left-hand end and is separated from the atmosphere at the right-hand end by a paper diaphragm. Initially the pressure and temperature in the tube are 15 psia and 70°F. The atmosphere is at 12.7 psia.

The diaphragm is suddenly broken.

- Show the pressure at the left-hand as a function of time.
- What is the "period" for the process?
- What is the maximum velocity attained by a fluid particle?

**23.3.** A tube 10 ft in length is closed by pistons at both ends and contains air at 100 psia and 70°F. The left-hand piston is sinusoidally pushed inward 0.1 ft during a time of 0.01 second, is then sinusoidally pulled outward the same distance in an equal time, and finally remains at rest.

(a) Assuming that the right-hand piston is stationary, plot the pressures on the two pistons as a function of time for one complete period.

(b) Describe the motion which the right-hand piston must possess if there are to be no reflections of the pressure waves originating at the left-hand piston.

(c) Describe the motion of the right-hand piston if the pressure on the latter remains constant. For this case plot the pressures and velocities at the two piston faces for one complete period.

**23.4.** A tube 10 ft long is closed at both ends and contains air at a mean temperature of 70°F and a mean pressure of 100 psia.

At one instant of time the pressure and temperature are uniform throughout the tube; at the same instant the fluid velocity at the center of the tube is 20 ft/sec, and varies linearly to zero at the two ends.

Find the variation with time of pressure and velocity at the two ends and at the middle of the tube for a complete cycle.

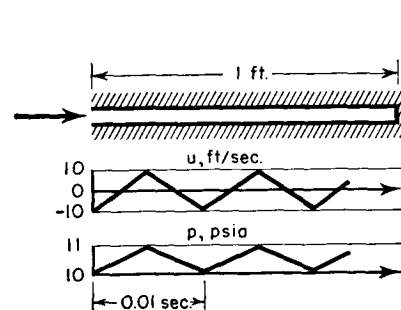
**23.5.** A tube 10 ft long is closed at both ends and contains air which at a given instant of time is completely at rest. At the same instant the pressure varies linearly from 100 psia at the left-hand end to 110 psia at the right-hand;

the temperature at the center of the tube is 70°F at this instant and varies isentropically with the pressure.

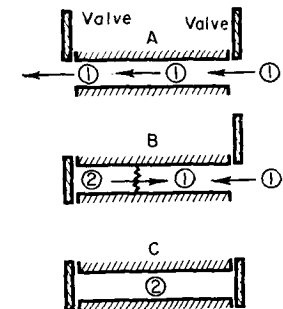
Find the variation with time of the pressure and velocity at the two ends and at the center of the tube for a complete cycle.

**23.6.** Suppose that a pitot tube is idealized in the form shown by the sketch, and that when placed in a pulsating flow the pressure and velocity at the open end vary with time as shown in the graph. The mean temperature in the tube is 70°F.

Estimate the time-average pressure on the right-hand end of the tube.



PROB. 23.6.



PROB. 23.7.

**23.7.** The three sketches show in a highly idealized fashion the charging process in a positive displacement machine.

In sketch A the air is flowing through the constant-area passage in steady flow.

In sketch B the left-hand valve has been abruptly closed, and a pressure wave is traveling toward the open end.

In sketch C the right-hand valve has been closed just as the pressure wave reaches the open end.

(a) Assuming that  $V_1 = 200$  ft/sec,  $T_1 = 70^\circ\text{F}$ , and  $p_1 = 14.0$  psia, find  $p_2$  in the most accurate way, and compare your answer with the results of the linear theory.

(b) Assuming that  $V_1$  is very small compared with  $c_1$  find a simple approximate formula for  $p_2/p_{01}$  in terms of  $V_1/c_1$ , where  $p_{01}$  is the isentropic stagnation density corresponding to the steady flow entering the cylinder. Note that when  $p_2$  is greater than  $p_{01}$ , the cylinder is "supercharged" in the sense that it contains a larger mass of air than would be contained in a like volume of air at the inlet stagnation conditions.

**23.8.** A gas with  $k = 1.4$  flows steadily in a pipe at a Mach Number of 0.10. The end of the pipe is instantaneously closed by a valve, and a compression wave therefore propagates back into the gas. Calculate, by means of the linear theory, the percentage changes in pressure, temperature, and density produced by the wave. Compare these approximate answers with the exact answers obtained by treating the wave as a normal shock.

## Chapter 24

## UNSTEADY, ONE-DIMENSIONAL, CONTINUOUS FLOW

## 24.1. Introductory Remarks

In the introduction to the preceding chapter the practical reasons for studying unsteady motion were outlined, and the implications of the assumptions of isentropic, frictionless, and one-dimensional flow were discussed. Some of the features of unsteady flow were then discussed from the standpoint of a linearized theory based on the assumption of small perturbations.

For many problems the assumption of small perturbations leads to excessively large errors, and, moreover, fails to predict certain important qualitative features, such as the tendency for compression waves to steepen into shock waves. The intermittent pulse jet, the Comprex, internal ballistics, and the inlet and exhaust manifolds of high-speed reciprocating machinery are examples of practical applications where the nonlinearities of large-amplitude waves are important.

In this chapter we shall therefore consider unsteady flow without the restriction of small perturbations. At first we shall restrict the study to constant-area ducts and shall suppose the flow to be one-dimensional in a geometric sense. Also, all fluid particles will be assumed to have the same entropy, friction will be ignored, the fluid will be taken as a perfect gas, and the implications of a fluid continuum will be accepted.

Later in the chapter, we shall discuss the effects of area change, friction, and entropy variations.

Finally, some specific examples and comparisons of experiment with theory are presented.

## NOMENCLATURE

$A$	area	$s$	entropy per unit mass
$c$	velocity of sound	$t$	time
$c_v$	specific heat at constant volume	$T$	absolute temperature
$c_p$	specific heat at constant pressure	$u$	velocity in $x$ -direction
$D$	diameter	$x$	Cartesian coordinate
$f$	friction coefficient	$\rho$	mass density
$F$	wall friction term (Eq. 24.43)	$\tau_w$	wall shearing stress
$k$	ratio of specific heats	$\Phi$	velocity potential
$K_I, K_{II}$	constants of integration (Eqs. 24.10)	$I, II$	characteristic coordinates (Eq. 24.17)
$M$	Mach Number	$(\bar{\ })$	signifies the average value of a property in two adjoining fields
$p$	pressure	$(\ )_0$	signifies an arbitrary reference state
$q$	rate of heat transfer per unit mass of fluid and per unit time	$(\ )^*$	signifies state where $M = 1$
$R$	gas constant		

**Summary of Governing Equations for Constant-Area, Isentropic Motion.** Under these conditions, the motion is governed by Eqs. 23.5, 23.8, and 23.9 (with  $dA/dx$  set equal to zero), which we write here for easy reference:

$$(c^2 - \Phi_x^2)\Phi_{xx} - 2\Phi_x\Phi_{xt} - \Phi_{tt} = 0 \quad (24.1)$$

$$c^2 = c_0^2 - \frac{k-1}{2} \Phi_x^2 - (k-1)\Phi_t = c_0^2 - \frac{k-1}{2} u^2 - (k-1)\Phi_t \quad (24.2)$$

$$u = \partial\Phi/\partial x = \Phi_x \quad (24.3)$$

where  $\Phi$  is the velocity potential, the space derivative of which gives the velocity of fluid particles, and  $c_0$  is the value of the sound velocity at the conditions  $u = 0$  and  $\Phi_t = 0$ . The value of  $\Phi_t$  (as shown in Chapter 23) may arbitrarily be set equal to zero at any desired condition, i.e., for any specific combination of  $u$  and  $c$ .

We work with the *dependent state variables*  $u$  and  $c$  as functions of the *independent space variables*  $x$  and  $t$ . Such fluid properties as pressure and density are then related to the sound velocity through the isentropic relations, namely,

$$\frac{c}{c_0} = \sqrt{\frac{T}{T_0}} = \left(\frac{p}{p_0}\right)^{\frac{k-1}{2k}} = \left(\frac{\rho}{\rho_0}\right)^{\frac{k-1}{2}} \quad (24.4)$$

## 24.2. Extension of Linearized Theory

Let us introduce the methods of treating nonlinear motion by means of an extension of the physical concepts underlying the theory of propagation of small pressure pulses in a moving stream, as outlined previously in Art. 23.4. There we saw that if there are small pressure pulses propagating downstream and upstream in an otherwise uniform stream characterized by the fluid properties  $\bar{u}$  and  $\bar{c}$ , the pulses propagate at the speed

$$\left(\frac{dx}{dt}\right)_{\text{wave}} = \bar{u} \pm \bar{c} \quad (24.5)$$

and the changes in fluid properties across the pulse are given by

$$\delta c = \pm \frac{k-1}{2} \delta u \quad (24.6)$$

where the upper and lower signs refer respectively to waves traveling rightward and leftward relative to the fluid.

Now let us drop the assumption of small perturbations, and let us suppose instead that there are large variations of  $u$  and  $c$  in space and time. For such flows we may think of pressure waves of large amplitude being propagated in both directions along the duct. However, these large pressure waves may also be thought of as a succession of small pressure pulses which, when superposed on each other, form the complete wave of large amplitude. The justification for this procedure lies in the hyperbolic nature of the governing equations, thereby permitting discontinuities in the derivatives of  $u$ ,  $c$ , and  $p$  on the characteristic curves. Thus regions which are analytically different may be joined along the characteristics. Or, from a different viewpoint, the arbitrariness of the functions  $f_1$  and  $f_2$  in Eq. 23.13 means that the velocity potential may undergo arbitrary jumps across the lines on which  $f_1$  and  $f_2$  are constant, these lines being recognized as the lines in the  $x,t$ -plane along which small pressure pulses are propagated.

Across one of the small pulses forming a large wave there are only small changes in  $u$  and  $c$  compared with the values of  $u$  and  $c$  themselves in the small regions or *fields* in each of which  $u$  and  $c$  are assumed to be constant. The changes in  $u$  and  $c$  from field to field are assumed to occur across the small pressure pulses which divide the fields from each other.

Our task then is to construct the wave pattern in the  $x,t$ -plane and to determine the values of  $u$  and  $c$  (and thus of all fluid properties) in each field, given suitable initial data for each problem. The waves are constructed with the slope given by Eq. 24.5, where the symbols  $\bar{u}$  and  $\bar{c}$  are now taken to represent the average values of  $u$  and  $c$  in the

two regions which the pressure pulse (or wave) separates, the appropriate sign to be used depending upon whether the wave is right-traveling or left-traveling. Likewise, the changes in  $u$  and  $c$  which occur from field to field across each wave are found from Eq. 24.6, the appropriate sign again being chosen according to the direction of the wave. Thus, the wave pattern may be constructed step by step from the initial data and boundary conditions for each problem.

Since the values of  $u$  and  $c$  vary throughout the  $x,t$ -plane, the lines representing the waves (that is, the *characteristics*, or *Mach lines*) will, according to Eq. 24.5, be curved and in general not parallel. This is in contrast to the small-amplitude waves of the preceding chapter, which were represented in the  $x,t$ -plane by two families of parallel straight lines.

With regard to the fluid properties, Eq. 24.6 indicates that the changes in fluid properties may conveniently be traced on a  $u,c$ -diagram on which the two families of parallel straight lines represented by

$$c \mp \frac{k-1}{2} u = \text{constant}$$

are drawn. The *nodal points* of this mesh represent the fluid properties in each of the  $x,t$ -fields, and the changes in  $u$  and  $c$  between fields are found by passing from one nodal point to another along one of the straight lines of the mesh.

A detailed example illustrating this *field method* of solution is given in Art. 24.5.

## 24.3. Method of Characteristics

The results of the preceding article may be obtained more rigorously through the application of the *theory of characteristics*, as outlined in Appendix A. There it is shown that if a differential equation has the form

$$A\Phi_{xx} + 2B\Phi_{xt} + C\Phi_{tt} = 0$$

where  $A$ ,  $B$ , and  $C$  are functions of  $x$ ,  $t$ ,  $\Phi_x$ , and  $\Phi_t$ , then the characteristic curves are defined by the ordinary differential equations

$$\left(\frac{dt}{dx}\right)_{I,II} = \frac{B \pm \sqrt{B^2 - AC}}{A}, \quad \left(\frac{d\Phi_t}{d\Phi_x}\right)_{I,II} = -\frac{B \pm \sqrt{B^2 - AC}}{C}$$

**Characteristic Curves.** Referring to Eq. 24.1, we see that in the present case the coefficients are

$$A = c^2 - u^2; \quad B = -u; \quad C = -1$$

The characteristic curves are therefore defined by

$$\left(\frac{dt}{dx}\right)_I = \frac{1}{u+c}; \quad \left(\frac{dt}{dx}\right)_{II} = \frac{1}{u-c} \quad (24.7)$$

$$\left(\frac{d\Phi_t}{du}\right)_I = -(u-c); \quad \left(\frac{d\Phi_t}{du}\right)_{II} = -(u+c) \quad (24.8)$$

We note that the characteristics are real for all problems of isentropic, non-steady motion in straight ducts of constant area. Remembering that the characteristics are lines of possible discontinuities in the derivatives of  $u$  and of  $c$ , we see from Eq. 24.7 that the propagation speed,  $dx/dt$ , of such discontinuities is given by  $u \pm c$ . This means that the velocity of propagation *relative* to the fluid itself is the local sound velocity,  $c$ . Interpreting the discontinuity lines as *waves*, the plus sign indicates a wave traveling to the right, and the minus sign a wave traveling to the left, each with respect to a fluid particle (assuming that  $x$  is positive toward the right). Thus, the waves of family  $I$  are *right-running* waves and those of family  $II$  are *left-running* waves. By analogy with two-dimensional, steady, supersonic flow, these waves are sometimes spoken of as *Mach waves*.

Also by analogy, the  $x, t$ -plane for brevity will be referred to as the *physical plane*, and the  $u, \Phi_t$ -plane will be referred to as the *hodograph plane*. The  $u, c$ -plane, which we shall find even more useful than the hodograph plane, will be called the *state plane*.

Inspection of Eqs. 24.7 and 24.8 shows that the physical characteristics are mutually orthogonal to the hodograph characteristics of the opposite family, a fact which permits a simple geometrical construction. Furthermore, since  $c$  depends only on  $u$  and  $\Phi_t$ , the equations of the hodograph characteristics may be found in a fixed form for all problems by integration of Eq. 24.8 after  $c$  has been eliminated with the help of Eq. 24.2.

**State Characteristics.** The determination of the hodograph characteristics is simpler if we first find the characteristics in the state plane.

Differentiating Eq. 24.2 with respect to  $u$ , we get

$$\frac{dc}{du} = -\frac{k-1}{2c} \left( u + \frac{d\Phi_t}{du} \right)$$

Then, eliminating  $d\Phi_t/du$  with the help of Eq. 24.8, we obtain for the state characteristics,

$$\left(\frac{dc}{du}\right)_I = -\frac{k-1}{2}; \quad \left(\frac{dc}{du}\right)_{II} = +\frac{k-1}{2} \quad (24.9)$$

We therefore have the remarkably simple result that the characteristics in the state plane are two families of parallel straight lines with

slopes  $\mp(k-1)/2$ . These lines, moreover, are uniquely determined in the sense that they are independent of the particular example under consideration. The physical characteristics, on the other hand, form a different network for each example.

Upon integration of Eq. 24.9, and dividing by  $c_0$  to get dimensionless ratios, we obtain the equations of the state characteristics in the form

$$\frac{u}{c_0} = -\frac{2}{k-1} \left( \frac{c}{c_0} - \frac{K_I}{c_0} \right); \quad \frac{u}{c_0} = \frac{2}{k-1} \left( \frac{c}{c_0} - \frac{K_{II}}{c_0} \right) \quad (24.10)$$

where  $K_I$  and  $K_{II}$  are the respective constants of integration. The  $u, c$ -characteristics are shown in Fig. 24.1, on which the indexes  $I$  and  $II$  are related to the constants  $K_I$  and  $K_{II}$  by Eq. 24.17.

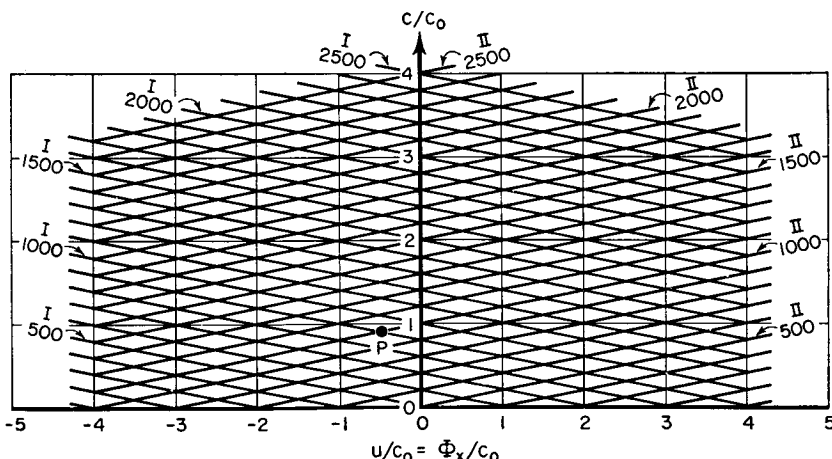


FIG. 24.1. State characteristics for  $k = 1.4$ .

**Hodograph Characteristics.** The hodograph characteristics are now found by eliminating  $c$  from Eq. 24.10 with the help of Eq. 24.2.

After rearrangement, we obtain the dimensionless form

$$\frac{\Phi_t}{c_0^2} - \frac{k+1-2\left(\frac{K_{I,II}}{c_0}\right)^2}{(k+1)(k-1)} = -\frac{k+1}{4} \left[ \frac{u}{c_0} \mp \frac{2}{k+1} \left( \frac{K_{I,II}}{c_0} \right) \right]^2 \quad (24.11)$$

From the form of this equation it may be seen that the  $u, \Phi_t$ -characteristics are congruent parabolas with their axes parallel to the  $\Phi_t$ -axis (Fig. 24.2). Thus, both families of parabolas may be constructed rapidly with the help of a single template.

VERTEXES OF HODOGRAPH CHARACTERISTICS. The vertexes of the parabolas, according to Eq. 24.11, are at the coordinates

$$\left(\frac{\Phi_t}{c_0^2}\right)_{\text{vert}} = \frac{k+1-2\left(\frac{K_{I,II}}{c_0}\right)^2}{(k+1)(k-1)}; \quad \left(\frac{u}{c_0}\right)_{\text{vert}} = \pm \frac{2}{k+1} \left(\frac{K_{I,II}}{c_0}\right) \quad (24.12)$$

Eliminating  $K_{I,II}$  from this pair of equations, the locus of vertexes becomes

$$\left(\frac{\Phi_t}{c_0^2}\right)_{\text{vert}} = \frac{1}{k-1} - \frac{k+1}{2(k-1)} \left[\left(\frac{u}{c_0}\right)_{\text{vert}}\right]^2 \quad (24.13)$$

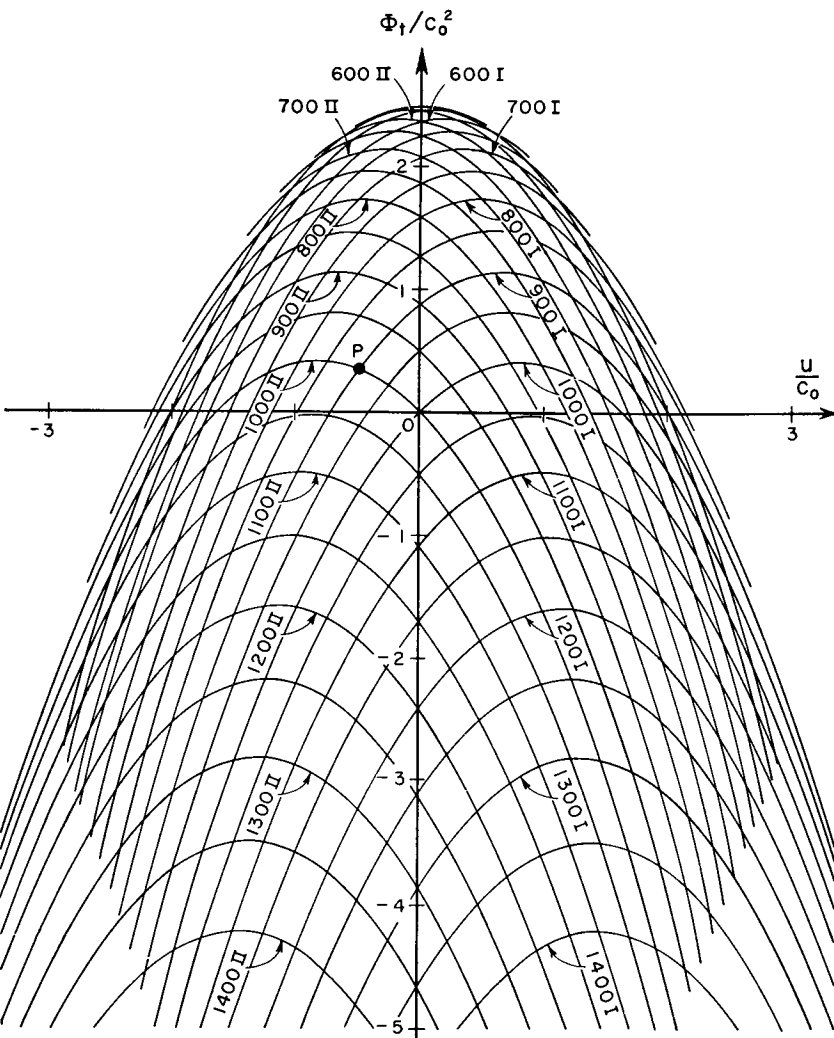


FIG. 24.2. Hodograph characteristics for  $k = 1.4$ .

which shows that the line of vertexes is itself a parabola with its axis lying along the  $\Phi_t$ -axis. Now, by eliminating  $\Phi_t/c_0^2$  from Eq. 24.13 with the help of Eq. 24.2, we find that

$$\left(\frac{c}{c_0}\right)_{\text{vert}} = \pm \left(\frac{u}{c_0}\right)_{\text{vert}} \quad (24.14)$$

which shows that at the vertexes of the hodograph characteristic parabolas the speed of the fluid and the local speed of sound are identical. In the  $u, c$ -plane this condition is represented by  $\pm 45^\circ$ -lines drawn through the origin.

ENVELOPE OF HODOGRAPH CHARACTERISTICS. The system of  $u, \Phi_t$ -characteristic parabolas given by Eq. 24.11 has an envelope which is found by taking the partial derivatives (in Eq. 24.11) of  $\Phi_t$  with respect to  $K_I$  and  $K_{II}$  and setting these equal to zero. Thus, on the envelope,

$$\pm \frac{u}{c_0^2} - \frac{2}{k-1} \frac{K_{I,II}}{c_0^2} = 0 \quad (24.15a)$$

Using this relation to eliminate  $K_{I,II}$  from Eq. 24.11, we obtain, for the equation of the envelope,

$$\left(\frac{\Phi_t}{c_0^2}\right)_{\text{env}} - \frac{1}{k-1} = -\frac{1}{2} \left(\frac{u}{c_0}\right)_{\text{env}}^2 \quad (24.15b)$$

Thus, the envelope, like the line of vertexes, is a parabola with its axis along the  $\Phi_t$ -axis. Its vertex is located at  $\Phi_t/c_0^2 = 1/(k-1) = 2.5$  for air. In the next paragraph it is shown that along the envelope the temperature and pressure of the gas are zero.

LINES OF CONSTANT THERMODYNAMIC PROPERTIES. The lines of constant sound velocity are, through the isentropic relations, also lines of constant temperature and pressure. To find the equations of these lines, we rearrange Eq. 24.2 in the form

$$\frac{\Phi_t}{c_0^2} - \frac{1 - (c/c_0)^2}{k-1} = -\frac{1}{2} \left(\frac{u}{c_0}\right)^2 \quad (24.16)$$

Lines of constant  $c/c_0$ , and hence of constant  $T/T_0$  and  $p/p_0$ , are therefore congruent parabolas in the  $u, \Phi_t$ -plane, with their axes lying along the  $\Phi_t$ -axis, and with their vertexes lying at  $\Phi_t/c_0^2 = [1 - (c/c_0)^2]/(k-1)$ . By comparing Eq. 24.16 with Eq. 24.15, we see that the envelope of characteristic parabolas is the line of zero sound velocity, zero temperature, and zero pressure. Thus, although the hodograph characteristics extend beyond the point of tangency to the envelope, the portions lying beyond the point of tangency refer to negative gas temperatures on the absolute scale and are, consequently, physically

unrealizable. Only the parts of the characteristic parabolas extending from each vertex to the envelope are of physical significance.

In the  $u, c$ -plane, states of constant sound velocity, temperature, and pressure lie on horizontal lines. Since the absolute temperature is zero at the line  $c/c_0 = 0$ , the parts of the characteristics lying below this line are physically meaningless.

**Characteristic Coordinates.** The constants  $K_I$  and  $K_{II}$  may be considered as characteristic coordinates, since each of them defines a particular characteristic curve. To obtain numbers of convenient size, however, we define a new set of characteristic coordinates  $I$  and  $II$  in terms of  $K_I$  and  $K_{II}$ , respectively, by the following relations:

$$I = 500 \left( 1 + \frac{K_I}{c_0} \right); \quad II = 500 \left( 1 + \frac{K_{II}}{c_0} \right) \quad (24.17)$$

Using these to eliminate  $K_I$  and  $K_{II}$  from Eq. 24.10, we obtain the equations of the state characteristics in the form

$$I = 500 \left( 1 + \frac{c}{c_0} + \frac{k-1}{2} \frac{u}{c_0} \right); \quad II = 500 \left( 1 + \frac{c}{c_0} - \frac{k-1}{2} \frac{u}{c_0} \right) \quad (24.18)$$

By first adding and then subtracting this pair of equations, we get the useful relations

$$\frac{c}{c_0} = \frac{I + II}{1000} - 1; \quad \frac{u}{c_0} = \frac{2}{k-1} \frac{I - II}{1000} \quad (24.19)$$

from which the speed of sound and fluid velocity may be calculated from values of the characteristic coordinates  $I$  and  $II$ .

The hodograph equations of the characteristics, line of vertexes, envelope curve, and curves of constant thermodynamic properties may easily be found in terms of the characteristic coordinates  $I$  and  $II$  by using Eq. 24.17 in conjunction with Eqs. 24.11, 24.12, 24.15, and 24.16.

Fig. 24.1 shows the characteristic curves in the state plane as found from Eq. 24.18. In the case of air, for which  $k = 1.4$ , these curves are straight lines with slopes  $\mp 0.2$ . Fig. 24.2 is a working chart of hodograph characteristics for  $k = 1.4$ .

**Geometrical Constructions.** Some useful geometrical relationships are illustrated in Fig. 24.3, in which the characteristic curves in the neighborhood of a point  $P$  are shown in the physical, hodograph, and state planes. The same point  $P$  is also shown in Figs. 24.1 and 24.2.

**RELATIONS BETWEEN PHYSICAL AND HODOGRAPH PLANES.** Between the physical and hodograph planes there exist the reciprocal orthogonality relationships (Eqs. 24.7 and 24.8) which require that the physical characteristics be normal to the hodograph characteristics

of the opposite family. For example, Fig. 24.3 shows how the  $x, t$ -characteristic of family  $I$  is constructed normal to the  $u, \Phi_t$ -characteristic of family  $II$ , and how the physical  $II$ -characteristic is constructed normal to the hodograph  $I$ -characteristic.

In addition, Fig. 24.3 shows how the direction of the path line, i.e., the direction of motion of the fluid particle at point  $P$ , is found by

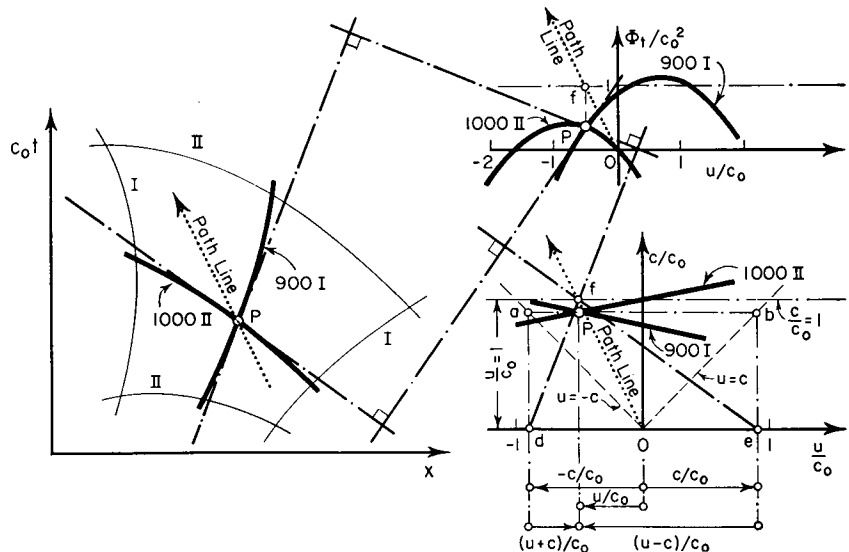


FIG. 24.3. Determination of the slope of the path line and of the characteristics at a point in the physical plane by means of graphical constructions at the image point in the hodograph and state planes.

constructing in the hodograph plane a line from the origin to point  $f$ . Point  $f$  lies vertically above  $P$  and lies above the horizontal axis by a distance corresponding to unit magnitude of  $u/c_0$ . The reader may verify that this construction satisfies the equation of a particle following the path line, namely,

$$\frac{dx}{dt} = u; \quad \frac{d(c_0 t)}{dx} = \frac{1}{u/c_0}$$

**RELATIONS BETWEEN PHYSICAL AND STATE PLANES.** The physical characteristics may also be constructed geometrically with the help of the fixed state characteristics of Fig. 24.1. Referring to the  $u, c$ -characteristics diagram of Fig. 24.3, there are first drawn the straight lines  $u = c$  and  $u = -c$ . Then, from the point  $P$ , horizontal lines are struck to give points  $a$  and  $b$ . Next, vertical lines are dropped from  $a$  and  $b$  to the horizontal axis, thus giving points  $d$  and  $e$ . Point  $f$  is found (as above) by projecting  $P$  vertically on the horizontal line lying above

the horizontal axis by an amount equal to unity on the scale of  $u/c_0$ .

The line  $d-f$  gives the slope of the  $I$ -characteristic in the  $x, t$ -diagram; and the line  $e-f$  gives the direction of the  $II$ -characteristic in the  $x, t$ -diagram. It may be verified that the construction described here satisfies Eq. 24.7.

The line from the origin through point  $f$  in the  $u, c$ -diagram gives the direction of the path line in the physical plane, as was shown previously.

The constructions given here are of course valid only when the scales of the  $x, t$ -diagram are laid out so that a unit increment in  $x$  corresponds in length to a unit increment in  $t$ . If this is not so, the construction must be suitably adjusted.

In comparing the two graphical constructions described above, we note that fewer steps are required when using the hodograph diagram, although this method is likely to be less accurate because of the difficulty of drawing tangents accurately. The state diagram has the great advantage that any portion of it may be quickly and accurately drawn to any desired scale, whereas the hodograph diagram is troublesome to construct accurately. On the whole, the hodograph characteristics are advantageous for illustrative purposes, and the state characteristics are preferable for accurate graphical constructions.

#### 24.4. Simple Waves

Proceeding from the elementary to the complex, we may distinguish three classes of flow patterns:

(i) *Steady-state flows*, in which there are no pressure waves, and in which  $u$  and  $c$  have constant values throughout the entire physical plane. This case, which is in a sense trivial for our present purposes, is *doubly degenerate*, since any arbitrary area of the physical plane is mapped as a single point in the state plane.

(ii) *Simple-wave flows*, in which either right-traveling or left-traveling pressure waves, but not both, are present. This case, for which the physically significant physical characteristics are straight lines on which all properties are constant, is *singly degenerate*, since an area of the physical plane is mapped as a single line in the state plane (these features are proved below).

(iii) *Double-wave flows*, in which there are both right-traveling and left-traveling waves, and in which an area of the physical plane maps as an area in the state plane.

**Generation of Simple Wave.** The manner in which a simple wave may be physically originated is illustrated by Fig. 24.4c. With the gas to the right of the piston originally at rest, the piston gradually acceler-

ates leftward. We may imagine the motion of the piston as being approximated by a series of sudden changes in velocity with a constant-velocity interval between each pair of impulsive accelerations; this is equivalent to replacing the continuous  $x, t$  "piston curve" by a series of

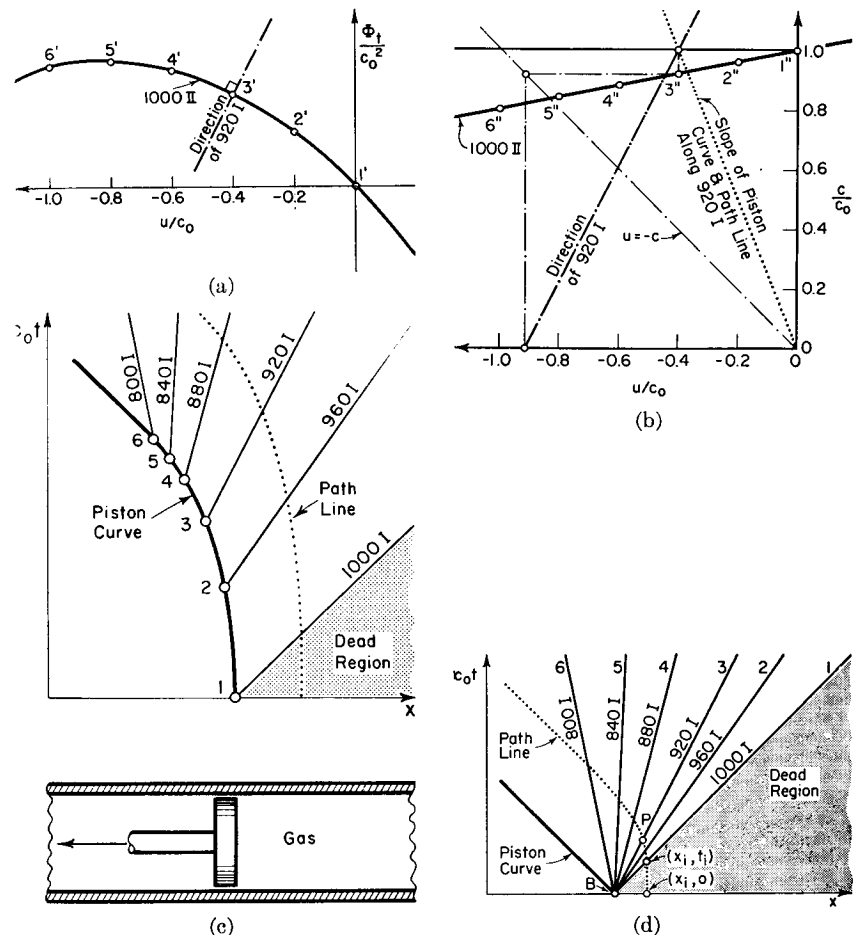


FIG. 24.4. Left-traveling simple rarefaction wave.

(a) Hodograph diagram.  
(b) State diagram.

(c) Physical plane.  
(d) Centered wave.

straight-line chords. Using the physical concept of pressure pulses, a rarefaction wave will propagate rightward into the gas each time the piston changes velocity. These pressure pulses are represented as physical  $I$ -characteristics. Since the fluid undergoes changes in  $u$  and  $c$  only as it is influenced by the successive pressure waves, the fluid properties must be constant along  $I$ -characteristics and hence, according

to Eq. 24.7, the physical *I*-characteristics must be straight lines which are represented as single points in the state and hodograph planes. Furthermore, the fluid properties change only across the *I*-characteristics, that is, while following a *II*-characteristic. Therefore, all states are mapped in the hodograph and state planes on a single *II*-characteristic.

**Definition of Simple Wave by Method of Characteristics.** From a more rigorous analytical point of view, we shall define a zone of simple waves as one in which the fluid properties  $u$  and  $c$  are not independent but are, rather, functions of each other. From Eq. 24.2, therefore, it follows that  $\Phi_x$  and  $\Phi_t$  are uniquely related. With this condition we may write

$$\frac{d\Phi_x}{dx} = \frac{\partial\Phi_t}{\partial x} \frac{d\Phi_x}{d\Phi_t}, \quad \frac{\partial\Phi_t}{\partial t} = \frac{\partial\Phi_x}{\partial t} \frac{d\Phi_t}{d\Phi_x} = \frac{\partial\Phi_t}{\partial x} \frac{d\Phi_t}{d\Phi_x}$$

where the last equation is found by employing the mathematical identity that  $\Phi_{tx} \equiv \Phi_{xt}$ .

Inserting these expressions for  $\Phi_{xx}$  and  $\Phi_{tt}$  into Eq. 24.1, we find that the term  $\Phi_{xt}$  vanishes, and thus we obtain

$$(c^2 - \Phi_x^2) \frac{d\Phi_x}{d\Phi_t} - 2\Phi_x - \frac{d\Phi_t}{d\Phi_x} = 0$$

Solving this quadratic for  $d\Phi_t/d\Phi_x$ , and simplifying, we get

$$\frac{d\Phi_t}{d\Phi_x} = -(\Phi_x \mp c) = -(u \mp c)$$

Now this expression is identical with the equation of the hodograph characteristic (Eq. 24.8), and therefore we conclude without further calculation that the series of states in a zone of simple waves is mapped on *one* of the *hodograph* characteristic parabolas of Fig. 24.2. It is to be noted that only the plus or minus sign in the above expression, but not both, is applicable in a region of simple waves, since otherwise  $u$  and  $c$  would not be uniquely related.

Because of the relation between  $c$ ,  $\Phi_t$ , and  $\Phi_x$  given by Eq. 24.2, and the fact that the states in a region of simple waves are mapped on *one*  $\Phi_x, \Phi_t$ -characteristic, it follows that the states in such a region are mapped also on *one* of the state characteristics of Fig. 24.1.

We now investigate the nature of the motion in the physical plane for a region of simple waves. Making use of the mathematical identity  $\Phi_{xt} \equiv \Phi_{tx}$ , we write

$$\frac{d\Phi_t}{d\Phi_x} = \frac{\frac{\partial\Phi_t}{\partial x} \frac{d\Phi_t}{d\Phi_x}}{\frac{\partial\Phi_t}{\partial x}} = \frac{\frac{\partial\Phi_x}{\partial t} \frac{d\Phi_t}{d\Phi_x}}{\frac{\partial\Phi_x}{\partial x}} = \frac{\frac{\partial\Phi_x}{\partial t} \frac{d\Phi_x}{d\Phi_x}}{\frac{\partial\Phi_x}{\partial x}} = \frac{\frac{\partial\Phi_x}{\partial t}}{\frac{\partial\Phi_x}{\partial x}}$$

Then, since  $\Phi_x$  is a function only of  $\Phi_t$  in a region of simple waves, we put this in the form

$$\frac{\frac{d\Phi_t}{d\Phi_x} \frac{d\Phi_x}{d\Phi_t} \frac{d\Phi_t}{d\Phi_x}}{\frac{d\Phi_t}{d\Phi_x}} = \frac{\frac{\partial\Phi_t}{\partial\Phi_x} \frac{\partial\Phi_x}{\partial\Phi_t}}{\frac{\partial\Phi_t}{\partial x}} = \frac{\partial\Phi_t/\partial t}{\partial\Phi_t/\partial x}$$

But, since

$$d\Phi_t = (\partial\Phi_t/\partial x) dx + (\partial\Phi_t/\partial t) dt$$

the slope of a line of constant  $\Phi_t$  in the physical plane is given by

$$\left(\frac{dt}{dx}\right)_{\text{const. } \Phi_t} = -\frac{\partial\Phi_t/\partial x}{\partial\Phi_t/\partial t}$$

and thus we see that in a region of simple waves

$$\left(\frac{dt}{dx}\right)_{\text{const. } \Phi_t} = -\frac{1}{d\Phi_t/d\Phi_x} = \frac{1}{u \mp c}$$

This shows that a line of constant  $u$  (since  $u$  is a function only of  $\Phi_t$ ) in the physical plane is normal to the characteristic of one family in the hodograph plane. From this orthogonality relation, and also by comparing the above expression with Eq. 24.7, we see that lines of constant  $\Phi_t$ ,  $u$ , and  $c$  are characteristics of one family in the physical plane. Moreover, since the slope of the physical characteristic depends only on  $u$  and  $c$ , the appropriate family of physical characteristics in a region of simple waves are straight lines. An examination of the signs of  $d\Phi_t/d\Phi_x$  and of  $(dt/dx)_{\text{const. } \Phi_t}$  in a region of simple waves shows that if all states are mapped on a hodograph or state characteristic of family *I*, then the fluid properties are constant on straight-line physical characteristics of family *II*, and vice versa.

**Summary of Simple Wave.** To sum up, in a region of simple waves, the fluid properties  $u$  and  $c$  lie on a single state characteristic, and the lines of constant fluid properties in the physical plane are straight lines which coincide with the physical characteristics of the opposite family.

By pursuing this type of reasoning, two important rules may be proved:

- (i) If along some portion of a physical characteristic the values of  $u$  and  $c$  are constant, then the regions adjacent to this section must be either steady-flow or simple-wave in type.
- (ii) If in some physical region the flow is steady, then in the adjacent regions the flow must be of the simple-wave variety.

**Example.** Returning now to the example of Fig. 24.4, we note that the first rarefaction wave produced by the piston's motion is propagated to the right with the speed of sound,  $c_0$ , of the "dead" or undisturbed gas. Since the dead region is one of steady flow, we conclude from rule (ii) of the preceding paragraph that the flow in the disturbed region is of the simple-wave type. Or we might reach the same conclusion by arguing that there is no physical agency for initiating left-traveling waves. As the initial condition of the gas is described by the properties

$$u/c_0 = 0; \quad c/c_0 = 1$$

it follows from Eq. 24.18 that at state 1 the characteristic coordinates are

$$I_1 = 1000; \quad II_1 = 1000$$

Since the piston motion produces rarefactions, and since the gas at the face of the piston travels with the piston speed (which is negative), inspection of Figs. 24.1 and 24.2 shows that all states must lie on the characteristic  $1000II$ . This might have been deduced also by noting that the rarefaction waves can proceed only to the right, and, since these waves are the physical  $I$ -characteristics, they are all normal to *one* of the hodograph  $II$ -characteristics, in this case the characteristic  $1000II$ . Assuming that the piston curve of Fig. 24.4c is given, several points along it are selected, and, from the corresponding slopes, the image points of the gas adjacent to the piston are located in Figs. 24.4a and 24.4b. The construction of Fig. 24.3 may be used for this purpose. From each of the points 1 to 6 the corresponding  $I$ -characteristic is drawn, again by using either of the constructions shown in Fig. 24.3. Along each of these characteristics, which might be considered as rarefaction lines or as elements of a continuous rarefaction wave, the fluid properties  $u$  and  $c$  are constant and may be found from the piston speed together with either Fig. 24.4b or Eq. 24.18b. Thus the entire flow pattern is established, since the temperature and pressure depend only on  $c$ . Along any rarefaction line the gas speed is the same as the piston speed. Hence the path lines of fluid particles are transformations of the piston curve, and are found by transferring the slopes of the piston curve out along the physical  $I$ -characteristics, and by drawing integral curves tangent to these slopes.

As an example of the method, the slope at point 3 of the piston curve shows that the piston speed there (and hence the speed of the gas next to the piston) is

$$\frac{dx}{d(c_0 t)} = \left(\frac{u}{c_0}\right)_3 = \frac{u_3}{c_1} = -0.4$$

From Eq. 24.18b, with  $II_3 = 1000$  and  $k = 1.4$ , we find that

$$\left(\frac{c}{c_0}\right)_3 = \frac{c_3}{c_1} = 0.92$$

and, therefore, from the isentropic relations,

$$\begin{aligned} p_3/p_1 &= (c_3/c_1)^{\frac{2k}{k-1}} = 0.56 \\ T_3/T_1 &= (c_3/c_1)^2 = 0.846 \end{aligned}$$

Next, using Eq. 24.18a, we find that  $I_3 = 920$ . Also, Eq. 24.16 yields  $(\Phi_1/c_0^2)_3 = 0.304$ . The slope of the rarefaction wave emanating from point 3 is found from Eq. 24.7a to be

$$\left[ \frac{d(c_0 t)}{dx} \right]_{I_3} = \frac{1}{\left(\frac{u}{c_0}\right)_3 + \left(\frac{c}{c_0}\right)_3} = 1.92$$

The straight line  $920I$  in Fig. 24.4c may be laid off with this slope, or either of the graphical constructions shown in Fig. 24.3 may be employed.

In Fig. 24.4c the region covered by the characteristics emanating from points 1 to 6 is one of simple waves and is singly degenerate, since points lying on straight lines in this region all have the same fluid properties. The dead region below  $1000I$  and the region of steady flow to the left of  $800I$  are also zones of simple waves, but are doubly degenerate, for in each of these areas the fluid properties  $u$  and  $c$  are constant. The preceding statements illustrate the role of the characteristics as lines of possible discontinuities in the derivatives of  $u$  and  $c$  along which different types of motions may be patched. In this case the characteristic  $1000I$  joins a region of simple rarefaction waves to a region where the gas is at rest; and the characteristic  $800I$  joins a region of simple rarefaction waves to a region in which there exists a state of uniform motion and pressure.

**Centered Simple Wave.** The waves in Fig. 24.4c are noncentered. Corresponding to the Prandtl-Meyer corner flow in a steady, two-dimensional motion, we may conceive of a *centered simple-wave* motion in which the piston velocity is altered instantaneously. The flow pattern, which is shown in Fig. 24.4d, is found in the same way as that of Fig. 24.4c except that the piston curve 1-6 has shrunk to a point. The pattern of Fig. 24.4d is one of centered simple waves. Although this particular case is not practical because the piston has infinite acceleration, a motion of the piston along one of the path lines of Fig. 24.4d would involve finite accelerations and at the same time would produce a motion with centered simple waves.

**Formulas for Simple Wave.** Certain analytical relations which apply to simple waves will now be derived. Using Eq. 24.9, we find by integration that the relation between  $u$  and  $c$  in a simple wave is

$$\frac{c}{c_1} = 1 \pm \frac{k-1}{2} \left( \frac{u}{c_1} - \frac{u_1}{c_1} \right) \quad (24.20)$$

where the upper and lower signs refer respectively to right-traveling and left-traveling simple waves, and where the subscript 1 refers to conditions at the beginning of the wave. From Eq. 24.4, the temperature and pressure are then given by

$$\frac{T}{T_1} = \left( \frac{c}{c_1} \right)^2 = \left[ 1 \pm \frac{k-1}{2} \left( \frac{u}{c_1} - \frac{u_1}{c_1} \right) \right]^2 \quad (24.21)$$

$$\frac{p}{p_1} = \left( \frac{c}{c_1} \right)^{\frac{2k}{k-1}} = \left[ 1 \pm \frac{k-1}{2} \left( \frac{u}{c_1} - \frac{u_1}{c_1} \right) \right]^{\frac{2k}{k-1}} \quad (24.22)$$

If, as in many cases, the wave starts in a gas which is at rest, we would have  $u_1 = 0$ . Then the foregoing relations reduce to

$$\frac{c}{c_1} = 1 \pm \frac{k-1}{2} \frac{u}{c_1} \quad (24.23)$$

$$\frac{T}{T_1} = \left( 1 \pm \frac{k-1}{2} \frac{u}{c_1} \right)^2 \quad (24.24)$$

$$\frac{p}{p_1} = \left( 1 \pm \frac{k-1}{2} \frac{u}{c_1} \right)^{\frac{2k}{k-1}} \quad (24.25)$$

In the last expression the exponent is equal to 7 for  $k = 1.4$ , which implies that relatively small piston speeds produce relatively large pressure changes.

**ESCAPE SPEED.** It is evident from Eqs. 24.20 and 24.23 that in a simple rarefaction wave the absolute magnitude of  $u/c_0$  cannot exceed a certain value, for otherwise the sound velocity would become negative, which is physically meaningless. For simple waves starting from rest,

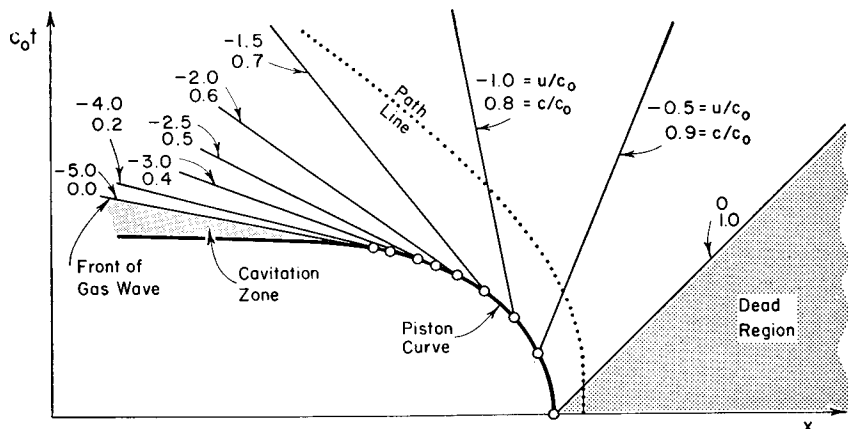


FIG. 24.5. Complete simple rarefaction wave starting with stagnant gas and ending at escape speed.

Eq. 24.23 with  $c/c_1 = 0$  shows that the maximum absolute value of  $u/c_0$ , corresponding to zero pressure and temperature, is given by

$$| (u/c_0)_{\max} | = 2/(k-1) \quad (24.26)$$

Thus, for  $k = 1.4$ , the maximum gas speed, or the *escape speed*, is five times the sound velocity in the initially undisturbed gas. If the piston in Figs. 24.4c and 24.4d were to attain a velocity greater than this, the gas would be unable to follow the piston. The gas nearest the piston would travel at the escape speed, and there would be a cavitation region near the piston in which there would be no gas whatsoever. According to Eq. 24.7, the rarefaction wave in the region where the gas travels at the escape speed would also propagate at the escape speed and thus the path line would coincide with the rarefaction line. Fig. 24.5 illustrates the type of motion which arises when the piston speed exceeds the escape speed of the gas.

The above considerations are of course based on the treatment of the gas as a continuum, and they are accordingly not valid at very low pressures, for then the continuum treatment would have to be replaced by a kinetic theory treatment.

#### Path Lines in a Simple Wave.

As pointed out previously, the path line of a particle, in the case of simple waves, may be found graphically by transforming the piston curve in such a way that the path line and the piston curve have equal slopes at the points of intersection with a given rarefaction line. Although the equation of the path line may be found analytically for an arbitrary piston curve given in analytical form, the development is complex and will therefore not be given here. However, for centered simple waves, the equation of the path line may be found rather simply and is derived in the following paragraphs.

Referring to Fig. 24.4d, point  $B$ , with coordinates  $x_B$  and  $t_B$ , is the center of the wave system. Point  $P$  is the location of a particle on a given path line at the time  $t$  and distance  $x$ . Since the line connecting  $P$  and  $B$  is a  $I$ -characteristic, we find from Eq. 24.7 that

$$\left( \frac{dt}{dx} \right)_I = \frac{t - t_B}{x - x_B} = \frac{1}{u + c}$$

or, using the relation between  $u/c_0$  and  $c/c_0$  given by Eq. 24.23, we get

$$c_0 \frac{t - t_B}{x - x_B} = \frac{1}{\frac{u}{c_0} + \frac{c}{c_0}} = \frac{1}{1 + \frac{k+1}{2} \frac{u}{c_0}} \quad (24.27)$$

The path line is defined through the equation  $u = dx/dt$ . Introducing this, we find that

$$c_0 \frac{t - t_B}{x - x_B} = \frac{1}{1 + \frac{k+1}{2c_0} \frac{dx}{dt}} \quad (24.27)$$

or, rearranging,

$$\frac{dx}{dt} = \frac{2}{k+1} \left[ \frac{(x - x_B) - c_0(t - t_B)}{t - t_B} \right] \quad (24.28)$$

To facilitate the integration of Eq. 24.28, we define the auxiliary variable

$$\xi = (x - x_B) - \frac{2c_0}{k-1} (t - t_B)$$

from which

$$\frac{d\xi}{dt} = \frac{dx}{dt} - \frac{2c_0}{k-1}$$

Replacing terms in  $x$  in Eq. 24.28 by terms in  $\xi$ , we get after rearrangement,

$$\frac{d\xi}{\xi} = \frac{2}{k+1} \frac{dt}{t - t_B}$$

Integrating, and reverting to  $x$  as a variable, we find that

$$x - x_B = (t - t_B) \left[ K(t - t_B)^{-\frac{k-1}{k+1}} - \frac{2c_0}{k-1} \right] \quad (24.29)$$

where  $K$  is a constant of integration which is now evaluated by noting that, at the beginning of the motion of the particle now at  $P$ , Eq. 24.27 may be written as

$$\frac{t_i - t_B}{x_i - x_B} = 1$$

where  $x_i$  and  $t_i$  give the coordinates of the fluid particle when it is influenced by the first rarefaction wave. Inserting this relation into Eq. 24.29, the constant  $K$  may be evaluated, and we finally obtain the equation of the path line as

$$x - x_B = \frac{2c_0}{k-1} (t - t_B) \left\{ \frac{k+1}{2} \left[ \frac{x_i - x_B}{c_0(t - t_B)} \right]^{\frac{k-1}{k+1}} - 1 \right\} \quad (24.30)$$

This is valid, of course, only in the region between rarefaction lines 1 and 6 in Fig. 24.4d.

For centered rarefactions proceeding to very low pressures, the term  $c_0(t - t_B)$  becomes very large compared with  $(x_i - x_B)$ , in which case the motion of the gas in the low-pressure region may be described approximately by

$$x - x_B \cong -\frac{2c_0}{k-1} (t - t_B) \quad (24.31)$$

Expressions similar to Eqs. 24.30 and 24.31 may be obtained for left-traveling simple waves, such as would be generated in a gas region to the left of the piston.

**Four Classes of Simple Waves.** We may distinguish four types of simple waves, depending on whether they are right-traveling or left-

traveling, and on whether they are rarefactions or compressions. The four types are illustrated in Fig. 24.6. Note that *in compressions the path line bends toward the wave line; in rarefactions, away from the wave line.*

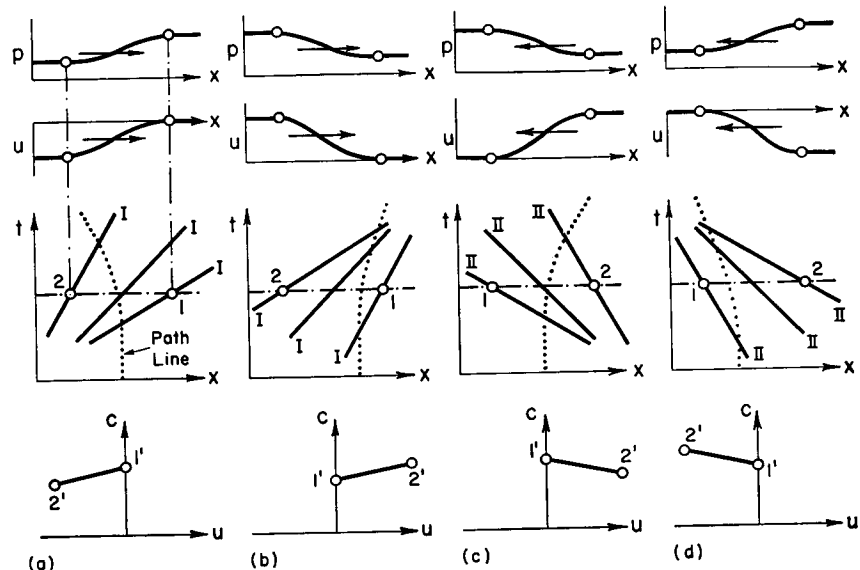


FIG. 24.6. Four classes of simple waves.

(a) Right-traveling rarefaction.  
(b) Right-traveling compression.

(c) Left-traveling rarefaction.  
(d) Left-traveling compression.

**Change in Form of a Simple Wave.** The *wave form* at a given instant is defined as the curve of some fluid property (usually  $p$  or  $u$ ) against  $x$ , and is therefore found by tracing the course of pressure, say, on a horizontal line of the  $x, t$ -diagram. With simple waves, fluid properties are constant on each physical characteristic. Reference to Fig. 24.6 shows that in simple rarefactions the characteristics diverge as time progresses, while with simple compressions the characteristics converge. Thus, the rarefaction part of a simple wave always broadens, while the compression part always steepens, as illustrated by Fig. 24.8 for a right-traveling wave. The compression part of the wave ultimately forms a vertical tangent. In the  $x, t$ -plane this condition corresponds to the intersection of the characteristics and to the formation of an envelope of characteristics, as illustrated by Fig. 24.7. Clearly this type of flow is no longer possible after the characteristics intersect, because at given values of  $t$  and  $x$  there would be several possible values of  $u$  and  $c$ . The difficulty is resolved by the appearance of a discontinuous compression shock, the entropy increase across which invalidates one of the assumptions of the simple-wave theory. It is interesting to

note that the envelope of physical characteristics is a *limit line* such as is found also for steady, plane, supersonic flow.

Changes in wave form such as those described here are observed in gravity waves near an ocean beach. However, surface "compression"

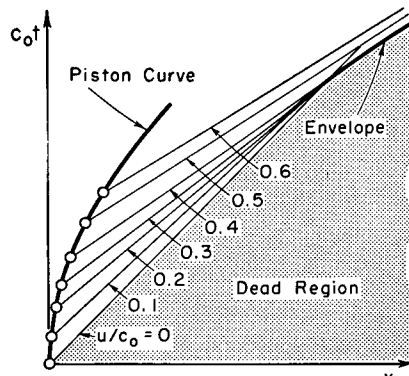


FIG. 24.7. Formation of a limit-line envelope by the coalescence of compression waves.

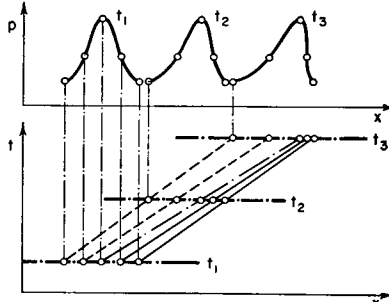


FIG. 24.8. Development of wave form for right-traveling simple wave. Upper diagram shows wave form at three successive times. Compression portion of wave steepens; rarefaction portion broadens.

waves cannot only steepen to a vertical tangent, but can "break," thus forming a surf.

A simple physical explanation of the change in wave form may be given with the help of the concept of pressure pulses. Referring to Fig. 24.7, suppose that the motion is produced by a right-traveling piston which initiates pressure pulses each time it undergoes an increase in velocity. Now each pressure pulse travels with the local speed of sound relative to the fluid in which it is moving. But the fluid nearest the piston has the largest velocity and also the highest temperature. Hence the pressure pulses nearer the piston travel most rapidly, and, therefore overtake the pressure pulses farthest from the piston. Thus the wave becomes progressively steeper. Similar arguments apply to the broadening of a rarefaction wave. (See also Art. 5.6.)

By carrying through the same reasoning mathematically, we obtain further information of value. Let us consider the instantaneous slope of the velocity curve at a given point,  $\partial u / \partial x$ , to be a measure of the wave form. Then we wish to investigate how the slope  $\partial u / \partial x$  changes with respect to time for the given point on the wave, that is, while following the wave. In other words, we wish to calculate  $[(d/dt)(\partial u / \partial x)]_{\text{wave}}$ .

Since  $\partial u / \partial x$  depends on both  $x$  and  $t$ , we may write

or,

$$\left( \frac{d}{dt} \frac{\partial u}{\partial x} \right)_{\text{wave}} = \frac{\partial}{\partial t} \left( \frac{\partial u}{\partial x} \right) + \left( \frac{dx}{dt} \right)_{\text{wave}} \frac{\partial^2 u}{\partial x^2} \quad (24.32)$$

We may also write the mathematical identity

$$(\partial / \partial t)(\partial u / \partial x) = (\partial / \partial x)(\partial u / \partial t)$$

In addition, the dynamic equation, Eq. 23.3, yields

$$\frac{\partial u}{\partial t} = -u \frac{\partial u}{\partial x} - \frac{1}{\rho} \frac{\partial p}{\partial x}$$

However, since the flow is isentropic, we find, with the help of Eq. 23.7, that

$$\frac{1}{\rho} \frac{\partial p}{\partial x} = \frac{1}{\rho} \frac{dp}{d\rho} \frac{\partial \rho}{\partial x} = \frac{c^2}{\rho} \frac{\partial \rho}{\partial x} = \frac{2}{k-1} c \frac{\partial c}{\partial x}$$

Also, since we are considering a simple wave, in which  $c$  is a function of  $u$ , we obtain, with the help of Eq. 24.9,

$$\frac{\partial c}{\partial x} = \frac{dc}{du} \frac{\partial u}{\partial x} = \pm \frac{k-1}{2} \frac{\partial u}{\partial x}$$

and, therefore,

$$\frac{\partial u}{\partial t} = -u \frac{\partial u}{\partial x} \mp c \frac{\partial u}{\partial x} = -(u \pm c) \frac{\partial u}{\partial x}$$

Differentiating this with respect to  $x$  and using the previous relation for  $\partial c / \partial x$ , we get

$$\begin{aligned} \frac{\partial}{\partial x} \left( \frac{\partial u}{\partial t} \right) &= -(u \pm c) \frac{\partial^2 u}{\partial x^2} - \frac{\partial u}{\partial x} \left( \frac{\partial u}{\partial x} \pm \frac{\partial c}{\partial x} \right) \\ &= -(u \pm c) \frac{\partial^2 u}{\partial x^2} - \frac{k+1}{2} \left( \frac{\partial u}{\partial x} \right)^2 \end{aligned}$$

Finally, inserting this expression for  $(\partial / \partial x)(\partial u / \partial t)$  and Eq. 24.7 for  $(dx/dt)_{\text{wave}}$  into Eq. 24.32, we obtain the simple result that

$$\left( \frac{d}{dt} \frac{\partial u}{\partial x} \right)_{\text{wave}} = -\frac{k+1}{2} \left( \frac{\partial u}{\partial x} \right)^2 \quad (24.33)$$

Reference to Fig. 24.6 shows that in simple rarefactions  $\partial u / \partial x$  is always positive, while in simple compressions  $\partial u / \partial x$  is always negative. Since, according to the form of Eq. 24.33, the slope always *decreases algebraically* as time progresses, it follows that the *absolute magnitude* of the slope decreases for a simple rarefaction and increases for a simple compression wave. Therefore, rarefaction waves progressively broaden whereas compression waves progressively steepen and thus tend to form compression shocks.

The time history of the wave slope may be found by separating variables in Eq. 24.33 and integrating. Thus we get, after rearrangement,

$$\frac{\partial u}{\partial x} = 1 / \left[ \frac{1}{(\partial u / \partial x)_0} + \frac{k+1}{2} t \right] \quad (24.34)$$

where  $(\partial u / \partial x)_0$  is the slope of a given part of the wave at zero time. The varia-

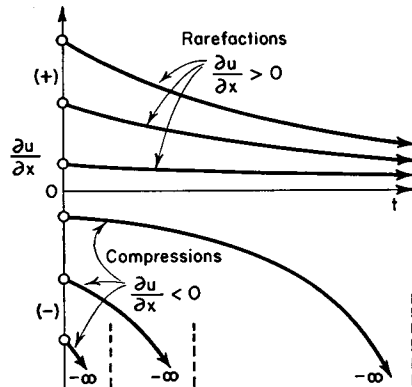


FIG. 24.9. Slope of simple wave versus time.

tion with time of the wave slope  $\partial u / \partial x$  is shown in Fig. 24.9 for various initial values of the slope.

To find the time required for the wave to approach a condition of incipient shock, we set  $\partial u / \partial x$  equal to infinity in Eq. 24.34. Thus we obtain

$$(t)_{\partial u / \partial x \rightarrow \infty} = - \frac{2}{(k+1)(\partial u / \partial x)_0} \quad (24.35)$$

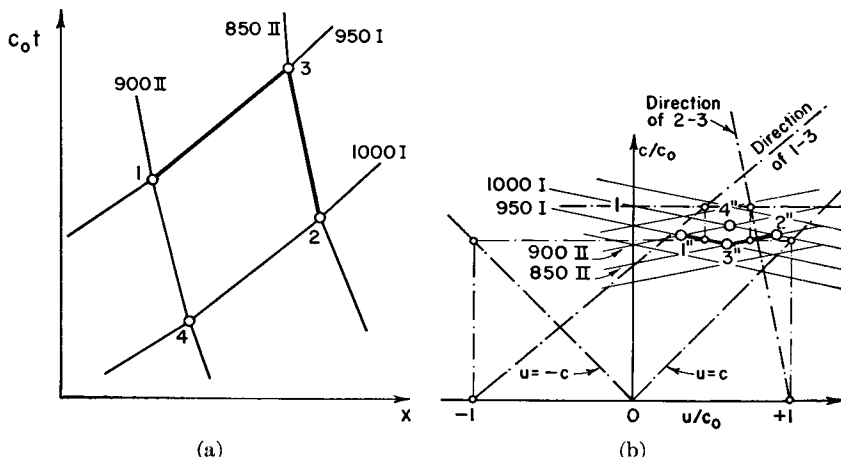
## 24.5. Waves of Both Families

In general, pressure waves of both families are present in a flow pattern. Such problems may be solved by noting that the characteristic curves are not only lines of possible discontinuities in the derivatives of the fluid properties, but also satisfy the equations of motion. Therefore, by constructing the characteristics nets for given initial conditions, we find a solution in the sense that at each physical point  $x, t$  all the fluid properties  $u, c, p$ , etc., are known. Since, for the isentropic, constant-area case, the hodograph and state characteristics are already known for all problems, we need construct for each problem only the physical characteristics net. Because of the simple geometrical relationships between the physical, hodograph, and state characteristics, this construction may be carried out in a purely graphical way. Or, as will be discussed later, purely numerical methods may be used in the interest of accuracy.

A stepwise solution is employed. For this purpose the curvilinear characteristics net is replaced by a net of straight-line chords. Therefore the characteristic curves which are used for calculation must be spaced closely enough so that linear interpolation is tolerable.

**Basic Step in Construction of Characteristics Net.** In general, the fundamental operation of the method of characteristics is to find the location of a third point from given data at two other points. Repeated application of this step yields the complete characteristics net.

For example, suppose that (Fig. 24.10a) all properties  $(u, c, x, t)$  are



(a)

Direction of 2-3  
Direction of 1-3

$c/c_0$   
 $u=c$   
 $u/c_0$

(b)

$u=-c$

(c)

$\varphi_t / c_0^2$

Direction of 2-3  
Direction of 1-3

$850 \text{ II}$   
 $900 \text{ II}$   
 $875$   
 $3'$   
 $1'$   
 $4'$   
 $2'$   
 $950 \text{ I}$   
 $975$   
 $1000 \text{ I}$

$u/c_0$

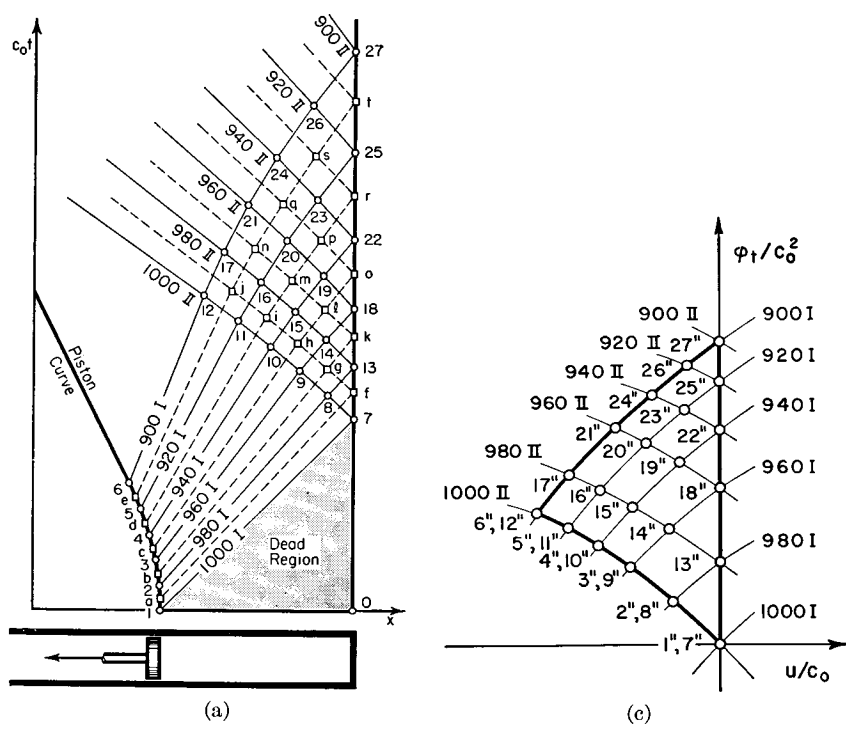
(d)

FIG. 24.10. Determination of location and properties at point 3 from known location and properties at points 1 and 2 on the characteristics passing through 1 and 2.

(a) Physical plane.

(b) State plane.

(c) Hodograph plane.



(c)

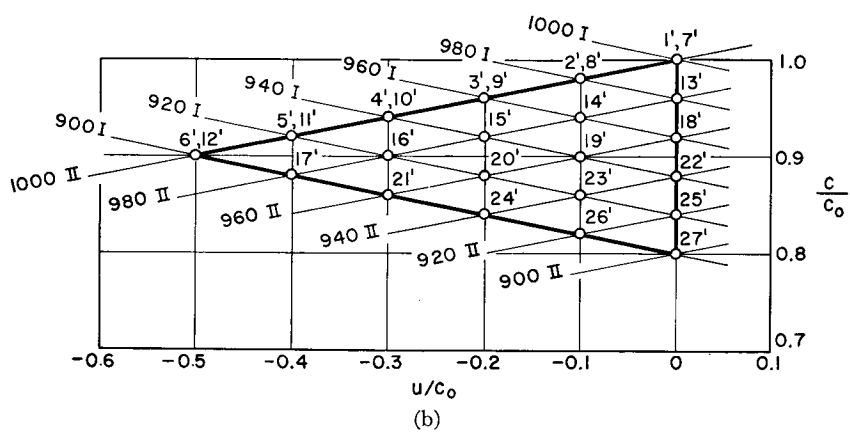


FIG. 24.11. Example showing construction of characteristics nets.

- (a) Physical plane.
- (b) State plane.
- (c) Hodograph plane.

known at a pair of typical points (1 and 2) of the physical characteristics net. Since  $u$  and  $c$  are known, the image points (1', 2', 1'', 2'') may be located in the hodograph and state planes. Point 3 lies on the characteristic of family *I* passing through point 1, and also lies on the characteristic of family *II* passing through point 2; hence points 3' and 3'' may be located in Figs. 24.10b and 24.10c. The direction of the physical characteristic 950*I* between points 1 and 3 may be found by either of the graphical methods shown in Fig. 24.3. It is important to note, however, that the direction of 950*I* is taken to correspond to the mean of the fluid properties between points 1 and 3, thus improving the accuracy of the stepwise method. Similar considerations apply to the direction of the physical characteristics 850*II* between points 2 and 3. Having constructed the direction of 950*I* through point 1 and of 850*II* through point 2, the location of point 3 in the physical plane is then uniquely determined at the intersection of 950*I* and 850*II*. By carrying out similar constructions, the complete flow pattern may be determined in step-by-step fashion.

EXAMPLE. An example will best show how this unit operation is used in repeated fashion to solve practical problems. Let us consider the motion of gas within a cylinder which is closed at one end and which has a movable piston at the other end. (Fig. 24.11a). The gas and the piston are initially at rest. The piston then moves to the left with uniform acceleration until the value of  $u/c_0$  for the piston is  $-0.5$ , after which the piston moves with constant speed. These specifications define the piston curve of Fig. 24.11a.

Fig. 24.11 shows two methods of solution: (i) the lattice-point method, and (ii) the field method. For the present we shall consider only the lattice-point method, in which case the solid characteristics net and the numbered circles of Fig. 24.11a are applicable. The dashed characteristics and the lettered squares pertain to the field method and will be discussed later.

*Lattice-Point Method.* In keeping with the stepwise nature of the solution, points 1 to 6 are located on the piston curve, corresponding to increments of piston speed of  $0.1c_0$ . Since the gas is initially at rest, the motion of the piston generates first of all a simple wave of the type previously discussed in connection with Fig. 24.4. The image points 1' to 6' are located in the state plane of Fig. 24.11b, and the directions of the characteristics of family *I* emanating from points 1 to 6 are found in the manner shown in Fig. 24.4.

Point 7 is located at the intersection of 1000*I* with the end of the cylinder, and indicates the time at which the motion of the piston is first felt at the fixed wall.

To locate point 8, we draw the characteristic 1000*II* through point 7 with a direction corresponding to the mean fluid property between points 7 and 8 (note that the properties at 8 are the same as those at 2), using the construction of Fig. 24.10. Points 9, 10, 11, and 12, and the connecting segments of 1000*II*, are found in similar fashion. The direction of 1000*II* beyond point 12 is drawn to correspond to the fluid properties at point 12, since the region beyond the line 12-27 is one of simple waves.

Point 13 lies on the characteristic  $980I$  passing through point 8. Moreover, the fluid at 13 is in contact with a stationary wall and is therefore at rest. These facts permit 13' to be located in the state plane. The physical characteristic  $980I$  between 8 and 13 is drawn to correspond to the mean fluid properties between 8 and 13.

Point 14 lies on the characteristic  $960I$  passing through 9 and on the characteristic  $980II$  passing through 13. Thus point 14' may be located in the  $u, c$ -plane. Next, the direction of the physical characteristic  $960I$  is drawn through point 9 on the basis of the mean fluid properties between 9 and 14, and the direction of the physical characteristic  $980II$  is drawn through 13 on the basis of the mean fluid properties between 9 and 13. The intersection of these two physical characteristics gives the location of point 14. The same procedure is used for locating point 15 from data at 10 and 14; point 16 from data at 11 and 15; and point 17 from data at 12 and 16.

We note that conditions at points 13 to 17 have been found from data at points 7 to 12, together with the physical conditions that the gas speed is zero at the stationary wall. In the same way the conditions at points 18 to 21 may be obtained from the newly found data at points 13 to 17. Then, again in the same way, the conditions at points 22 to 24 may be obtained from the newly found data at points 18 to 21. By following this process, the fluid motion is determined completely in the characteristic semiquadrilateral 7-12-27.

The region to the left of the characteristic line 12-27 is one of simple waves, since in this region all the states are mapped on the hodograph characteristic  $900I$ . In this region the physical characteristics of family  $II$  appear as straight lines, and all fluid properties are constant along each of these lines.

We may summarize the general nature of the flow pattern as follows:

- (i) The dead region 1-7-0 is a doubly degenerate region of steady flow.
- (ii) The region 1-6-12-7 is a singly degenerate region of simple waves.
- (iii) The region 7-12-27 is one with waves of both families.
- (iv) The region to the left of 6-12 is a doubly degenerate region of steady flow.
- (v) The region to the left of 12-27 is a singly degenerate region of simple waves.
- (vi) The simple expansion wave emanating from the piston along 1-6 is reflected at the end of the cylinder, and the reflected waves, which are of family  $II$ , interact with the incident waves, which are of family  $I$ , before the former pass into the region to the left of 12-27. The expansion waves are reflected from the stationary solid boundary in like sense, i.e., as expansion waves.

Using Figs. 24.11a and 24.11b conjointly, together with the isentropic relations between  $c$ ,  $p$ , and  $T$ , the speed, temperature, and pressure of a fluid particle at any value of  $x$  and  $t$  may be determined. Furthermore, since the particle speed determines the direction of the path line in the  $x, t$ -plane, the path line of any fluid particle may be constructed in the physical plane. The temperature or pressure distribution in the cylinder at a given time may be found by drawing in Fig. 24.11a a horizontal line corresponding to the selected time. Or, if the

history of the temperature or pressure at a certain location is desired, a vertical line is drawn at the specified location.

*Field Method of Solution.* To illustrate the field method of solution, let us again consider the example of Fig. 24.11a. A dashed characteristics net has been interpolated midway between the solid characteristics net of the lattice-point solution. In the field method we imagine that a region of continuously varying fluid properties in the physical plane is, for purposes of stepwise calculation, broken into a large number of small regions in each of which the fluid properties are assumed constant. For example, we consider the characteristic quadrilateral  $n-q-p-m$  surrounding lattice point 20 to be a field of constant fluid properties, and denote it field 20. This is done throughout the entire physical plane, with the result that the physical plane is divided into a large number of dashed characteristic quadrilaterals, in each of which the fluid properties are constant, so that each physical field maps as a single point in the state and hodograph planes. A fluid particle in the cylinder undergoes changes in velocity and pressure only when it goes from one field to another, i.e., only when it crosses a characteristic, or, in physical terms, only when it is crossed by a pressure wave.

To carry out the solution by the field method, we begin by replacing the piston curve by several straight-line segments along each of which the piston speed is taken to be constant. In this case the segments are 1- $a$ ,  $a-b$ ,  $b-c$ , and so on. The mean conditions for the segment  $a-b$  are represented by point 2, and so forth. Each time the piston changes its speed, a small wave is propagated into the gas. Thus, from 1 to  $a$  the piston is stationary, and there are no effects. At point  $a$  the piston speed changes to the value corresponding to point 2, and an expansion wave emanates from  $a$ . This wave divides field 1 from field 2, and its direction is therefore taken at the mean of the fluid properties between fields 1 and 2. Thus the wave  $a-f$ , corresponding to the characteristic  $990I$ , may be drawn. The waves  $970I$ ,  $950I$ ,  $930I$ , and  $910I$  are drawn on the basis of similar considerations.

A particle near the end of the cylinder acquires a velocity to the left when the wave  $a-f$  reaches the particle. From continuity considerations, however, a particle at the dead end of the cylinder must remain motionless. Hence, there must be a reflected wave at point  $f$  which reduces the particle velocity to zero. The reflected wave travels to the left relative to the gas and is consequently of family  $II$ . To obtain the direction of the reflected wave  $f-g$ , we first note that field 13 may be reached from field 8 (or 2) along a characteristic of family  $I$ , and also that the particle velocity is zero in field 13. Thus, point 13' is located in Fig. 24.11b, and the wave  $f-g$ , which is also the characteristic  $990II$ , is drawn with a direction corresponding to the mean of the fluid properties of fields 8 and 13. The intersection of the direction lines  $b-g$  and  $f-g$  establishes point  $g$ .

Next, we note that field 14 may be reached from field 13 along a characteristic of family  $II$ , and from field 9 (or 3) along a characteristic of family  $I$ . This allows us to locate point 14' in the  $u, c$ -plane. Then drawing the direction lines  $c-h$  and  $g-h$  by one of the methods previously described, point  $h$  is located. Following the same procedure, we locate points  $i$  and  $j$ , after which the next row of points,  $k$ ,  $l$ ,  $m$ ,  $n$  is determined, and so on, until the entire physical plane is covered by a characteristics net. We note that the field method involves

determining, point by point, the corners of the fields, and that the loci of these corners form the dashed characteristics net.

As in the case of two-dimensional, steady, supersonic flow, the lattice-point method illustrates the role of the characteristics as solution curves of the differential equation, while the field method illustrates the role of the characteristics as possible lines of discontinuity in the derivatives of fluid properties.

## 24.6. Unit Operations and Boundary Conditions

It has already been seen that problems in unsteady motion may be solved by constructing the characteristics nets in the physical and state planes. The construction of a complete net usually requires the repeated application of certain typical steps in the interior of the duct and of certain typical steps representing the boundary conditions at the ends of the duct. We shall now classify these various unit processes out of which complex solutions are synthesized, and shall show how they are applied.

The *field method* will be employed. That is, we shall imagine the  $x, t$ -plane to be divided into small fields in each of which all fluid properties are constant, and changes in fluid properties will be assumed to take place only across the waves or characteristics separating the various fields.

**Intersection of Waves.** The most common unit process in the interior of the duct is the intersection of two waves traveling in opposite directions. Referring to Fig. 24.12, suppose that the fluid properties (i.e.,

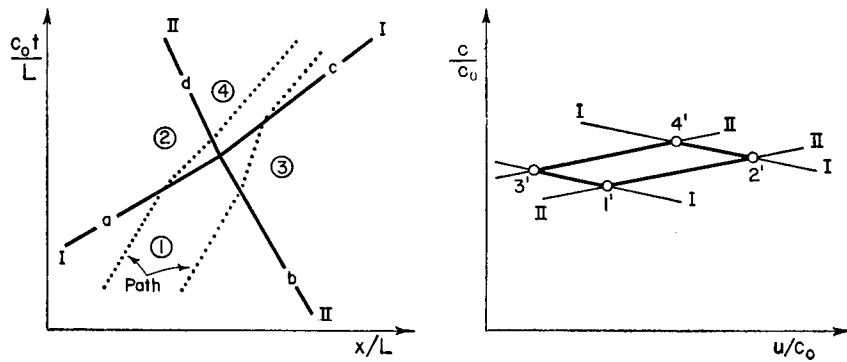


FIG. 24.12. Intersection of waves.

$u$  and  $c$ ) are known in field 1, and that waves  $a$  and  $b$  advance into this region. Assuming that the strength of wave  $a$  in terms of the ratio  $c_2/c_1$  is known, point  $2'$  may be located on the state diagram, since fields 1 and 2 lie on a common  $II$ -characteristic. Also, the direction of

wave  $a$  may be drawn corresponding to the mean properties between  $1'$  and  $2'$ . Likewise, if the strength of wave  $b$  is known, point  $3'$  may be located, and the direction of wave  $b$  determined.

Fields 3 and 4 lie on a common  $II$ -characteristic, and fields 2 and 4 lie on a common  $I$ -characteristic. Hence point  $4'$  may be located in the  $u, c$ -plane, and the fluid properties in field 4 are thus determined. The direction of wave  $d$  is determined from the mean of the properties at  $2'$  and  $4'$ ; and that of wave  $c$  from the mean of the properties at  $3'$  and  $4'$ .

In passing through each other, the waves are curved, or refracted. Therefore, the characteristics usually form a curvilinear net. The sense of a wave, that is, whether compression or rarefaction, is not altered as it passes through a wave of the opposite family.

The repeated application of this unit process has already been illustrated in Fig. 24.11.

**Reflection of Wave from Stationary Wall.** In many problems we have a tube closed at one end, and we must apply the boundary condition that at all times  $u = 0$  at the closed end.

Referring to Fig. 24.13, suppose that wave  $a$ , of known strength, advances into region 1 near the wall. From the assumed known conditions in region 1 and the strength of wave  $a$ , points  $1'$  and  $2'$  may be located in the state plane. As the velocity in field 2 is not zero, there must be a reflected wave  $b$  to preserve the condition of zero speed at the wall.

Since fields 2 and 3 lie on a common  $I$ -characteristic, and since  $u_3 = 0$ , point  $3'$  may be located in the  $u, c$ -diagram, thus defining completely the fluid properties in field 3. Wave  $b$  is drawn with the direction corresponding to the mean properties between  $2'$  and  $3'$ .

In this example both waves  $a$  and  $b$  are compressions. If wave  $a$  had been a rarefaction, wave  $b$  would likewise have been a rarefaction. Therefore we conclude that *waves are reflected from a stationary wall in like sense*.

This unit process has previously been illustrated in Fig. 24.11.

**Reflection from Moving Piston.** Sometimes, as in the cylinder of a reciprocating machine, or as in the bore of a rifle, waves are reflected

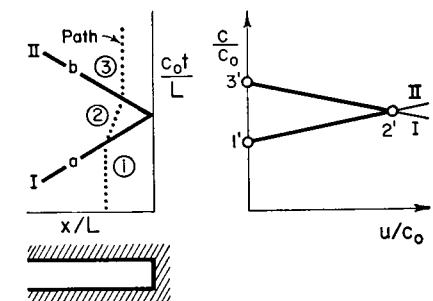


FIG. 24.13. Reflection of wave from closed end.

from a moving piston. Here we apply the boundary condition that the fluid at the face of the piston must have the same speed as the piston.

Referring to Fig. 24.14a, suppose that the piston curve is given, and that wave  $a$  of known strength is incident on the piston. Assuming

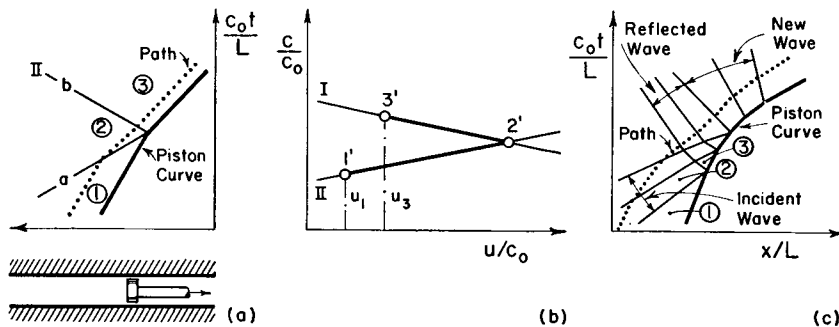


FIG. 24.14. Reflection of wave from moving boundary.

that the state in field 1 is known, points 1' and 2' may be located in the state plane (Fig. 24.14b).

In accordance with the stepwise nature of the characteristics method, the continuous piston curve is replaced by a series of straight-line chords. Usually it is convenient to place the break in the stepwise piston curve at the point where the incident wave  $a$  strikes the piston, as shown in Fig. 24.14a.

Since the velocity in field 3 must be identical with the known piston speed at the boundary of field 3, and also since fields 3 and 2 lie on a common  $I$ -characteristic, we may locate point 3' in the state plane and thus determine all fluid properties in field 3. Wave  $b$  is drawn with the direction corresponding to the mean properties between 2' and 3'.

The reflected wave  $b$  may be either a rarefaction, a compression, or of zero strength, depending on whether the piston speed bounding field 3 is respectively greater than, less than, or equal to the fluid velocity in field 2.

If the stepwise piston curve undergoes a change in slope at a point where there is no incident wave, the boundary conditions require that a new wave be propagated into the gas from the point where the piston changes in velocity.

Fig. 24.14c illustrates the reflection of a simple wave and the initiation of a new wave from a moving piston.

**Outflow Through Open End of Duct.** In such applications as the inlet and exhaust ducts of reciprocating machines and the exhaust pipe of the intermittent-jet engine, one end of the duct is open to a large exhaust region, and there may be either outflow or inflow at the

open end. An exact analysis of this process must take account of the unsteady motions in the exhaust region, but this is so difficult that it is common instead to employ plausible approximations for the boundary conditions at the open end. It will be convenient to discuss separately outflow and inflow at the open end.

**SUBSONIC OUTFLOW.** With outflow through the open end, we shall assume that the pressure at the end is equal to  $p_e$ , the pressure in the exhaust region, provided that the flow at the end is subsonic. According to a theory of Helmholtz, the inertia of the fluid outside the duct exit may be taken account of approximately by adding to the duct an equivalent length  $\pi d/8$ , where  $d$  is the duct diameter.

Referring to Fig. 24.15, suppose that the state is known for field 1 near the duct end and that wave  $a$  of known strength approaches the open end. Points 1' and 2' may accordingly be located in the state diagram.

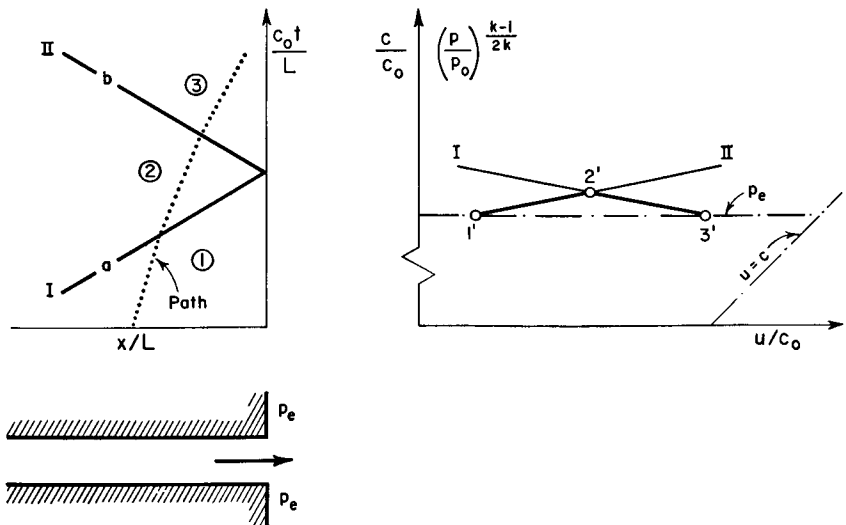


FIG. 24.15. Reflection of wave from open end when Mach Number in exit plane is less than unity.

In field 1 the pressure is  $p_e$ . In order to preserve this pressure at the open end, wave  $b$  must be reflected and must be of such strength that the pressure in field 3 is also  $p_e$ . From the isentropic relation between  $p$  and  $c$ , it follows that  $c_3 = c_1$ . Also, since fields 2 and 3 lie on a common  $I$ -characteristic, point 3' may be located in the state diagram, and thus all fluid properties in field 3 are determined. Wave  $b$  has a direction corresponding to the mean properties between 2' and 3'.

Since wave  $a$  is a compression and wave  $b$  is a rarefaction, we conclude that *a wave is reflected from a constant-pressure end in unlike sense*.

**SONIC OUTFLOW.** If, with the assumption that the exit pressure is  $p_e$ , it is found that  $u > c$  at the open end, the construction would fail because wave  $b$  would then be propagated outside the duct, and the assumption of a one-dimensional geometry would have to be abandoned. In order to make the one-dimensional approach workable, we assume that at the open end the fluid velocity cannot exceed the sonic speed. How large an error this entails for typical cases is not known.

The boundary conditions for outflow at an open end are then: (i) the pressure at the open end is  $p_e$ , provided that  $u \leq c$ ; (ii) if assumption (i) gives  $u > c$ , we replace it by the assumption that  $u = c$  at the open end.

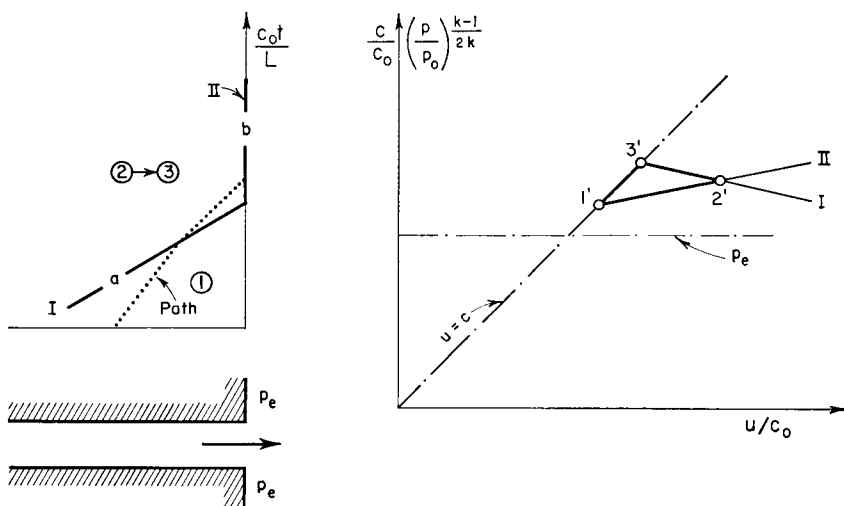


FIG. 24.16. Reflection of wave from open end when pressure in exit plane is greater than pressure in exhaust space.

To illustrate the case of reflection from an open end with outflow and with  $u = c$ , Fig. 24.16 shows compression wave  $a$  of given strength advancing into field 1 where all fluid properties are given and where, in addition,  $u_1 = c_1$  and  $p_1 > p_e$ . Points  $1'$  and  $2'$  may, from the given data, be located in the  $u, c$ -diagram. Wave  $b$  must be reflected and must be of proper strength to insure that  $u = c$  at the open end. From the latter condition, and from the condition that fields 2 and 3 lie on a common  $I$ -characteristic, point  $3'$  is located in the state diagram. Now, in the limit where an infinitely fine characteristics net is employed, points  $2'$  and  $3'$  must, by assumption, coincide. Hence, in practical applications we suppose that the properties in field 2 are those of state  $3'$ , and from this it follows that wave  $b$  is propagated directly upward in the physical plane.

**Inflow Through Open End of Duct.** When there is flow into the open end of the duct from a large and relatively stagnant atmosphere, a workable approximation is to assume that the flow from the atmosphere into the duct may be treated as though it were quasi-steady at each instant of time. This is equivalent to assuming that, when the rate of change of cross-sectional area is very large, the term  $\partial u / \partial t$  is negligible compared with the term  $u \partial u / \partial x$  in the Euler equation, and that similar approximations are applicable in the continuity equation.

**STEADY-STATE ELLIPSE.** With the assumption of quasi-steady flow from the reservoir to the duct inlet plane, we may write the energy equation of steady flow as

$$T_r = T_i + u_i^2 / 2c_p$$

where subscript  $r$  denotes stagnation conditions in the reservoir, and subscript  $i$  denotes the duct inlet plane. Eliminating  $T$  in favor of  $c$  through the relation  $c = \sqrt{kRT}$ , and dividing by  $c_0$  to obtain dimensionless ratios, we obtain the equation of the *steady-state ellipse*,

$$\left(\frac{c_i}{c_0}\right)^2 + \frac{k-1}{2} \left(\frac{u_i}{c_0}\right)^2 = \left(\frac{c_r}{c_0}\right)^2 \quad (24.36)$$

For a fixed value of  $c_0$  corresponding to the unsteady flow in the duct, and for a fixed value of  $c_r$  corresponding to stagnation conditions in the reservoir, Eq. 24.36 defines an ellipse on which must lie all states at the duct inlet.

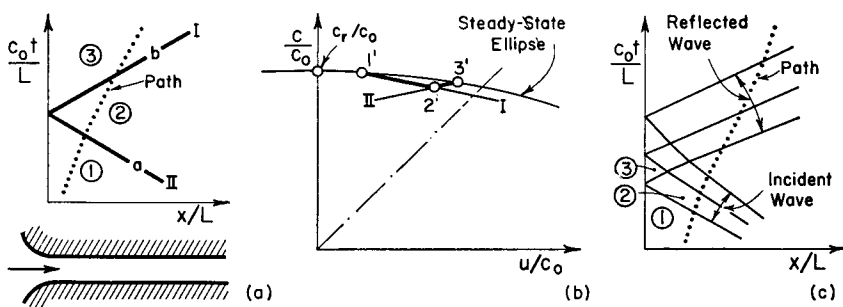


FIG. 24.17. Reflection of wave from open end at which there is an inflow.

**EXAMPLE.** Fig. 24.17 shows inflow to state 1 at the open end of a duct, with rarefaction wave  $a$  approaching the open end. Point  $1'$  lies on the particular steady-state ellipse defined by  $c_r/c_0$ , and point  $2'$  may be located from the given strength of wave  $a$ .

Wave  $b$  must be reflected in order to preserve the condition that all inflow states at the duct inlet must lie on the ellipse. Using this boundary condition, together with the further condition that fields 2 and 3 lie on a common  $II$ -characteristic, point  $3'$  may be located in the state plane, and thus all fluid properties in field 3 may be determined. The direction of wave  $b$  is determined from the mean properties between  $2'$  and  $3'$ .

Considering the slope of the steady-state ellipse, it may be shown that the reflection is in unlike sense, provided that the flow is subsonic at the inlet.

As in the preceding example, the procedure described here is limited by the condition that the inflow velocity at the open end shall not exceed the sonic velocity, unless there is a converging-diverging nozzle at the inflow end.

**Outflow Through Nozzle at Open End.** Occasionally (as in the inlet duct of reciprocating machines), the open end of the duct is terminated by a nozzle or its equivalent.

When there is outflow through the nozzle, we apply boundary conditions similar to those used for outflow through an open end discharging into a large atmosphere at the pressure  $p_e$ , namely: (i) the pressure at the nozzle exit is  $p_e$ , provided that  $u \leq c$  at the exit; (ii) if assumption (i) leads to  $u > c$ , we use instead the boundary condition that  $u = c$  at the nozzle exit.

The nozzle is assumed to be so short that (for the flow through the nozzle) (i) the term  $\partial u / \partial t$  is negligible compared with  $u \partial u / \partial x$  in the Euler equation, and (ii) similar assumptions apply to the derivatives in the continuity equation. Then we may treat the flow in the nozzle as quasi-steady. That is, the steady-state equations may be written for each instant of time.

Referring to Fig. 24.18a, we write the energy equation of steady flow as a generalization of Eq. 24.36,

$$\left(\frac{c_s}{c_0}\right)^2 = \left(\frac{c_y}{c_0}\right)^2 + \frac{k-1}{2} \left(\frac{u_y}{c_0}\right)^2 = \left(\frac{c_z}{c_0}\right)^2 + \frac{k-1}{2} \left(\frac{u_z}{c_0}\right)^2 \quad (24.37)$$

where the subscript  $s$  refers to the instantaneous quasi-steady-state adiabatic stagnation condition in the nozzle. At any one instant of time, both states  $y$  and  $z$  lie on the particular ellipse defined by Eq. 24.37.

**CONSTRUCTION OF AUXILIARY AREA-RATIO CURVES.** According to the boundary conditions previously mentioned, point  $z'$  in the state plane lies either on the horizontal line  $p_z = p_e$  or on the  $45^\circ$  line  $u_z = c_z$ . To illustrate, suppose that state  $z$  lies at the known point  $z_1'$  (Fig. 24.18). The corresponding location of  $y_1'$  on the steady-state ellipse passing through  $z_1'$  is found by writing the continuity equation between sections  $y$  and  $z$  and by using the isentropic relation (Eq. 24.4),

$$\frac{A_z}{A_y} = \frac{\rho_y u_y}{\rho_z u_z} = \left(\frac{c_y}{c_z}\right)^{\frac{2}{k-1}} \frac{u_y}{u_z} \quad (24.38)$$

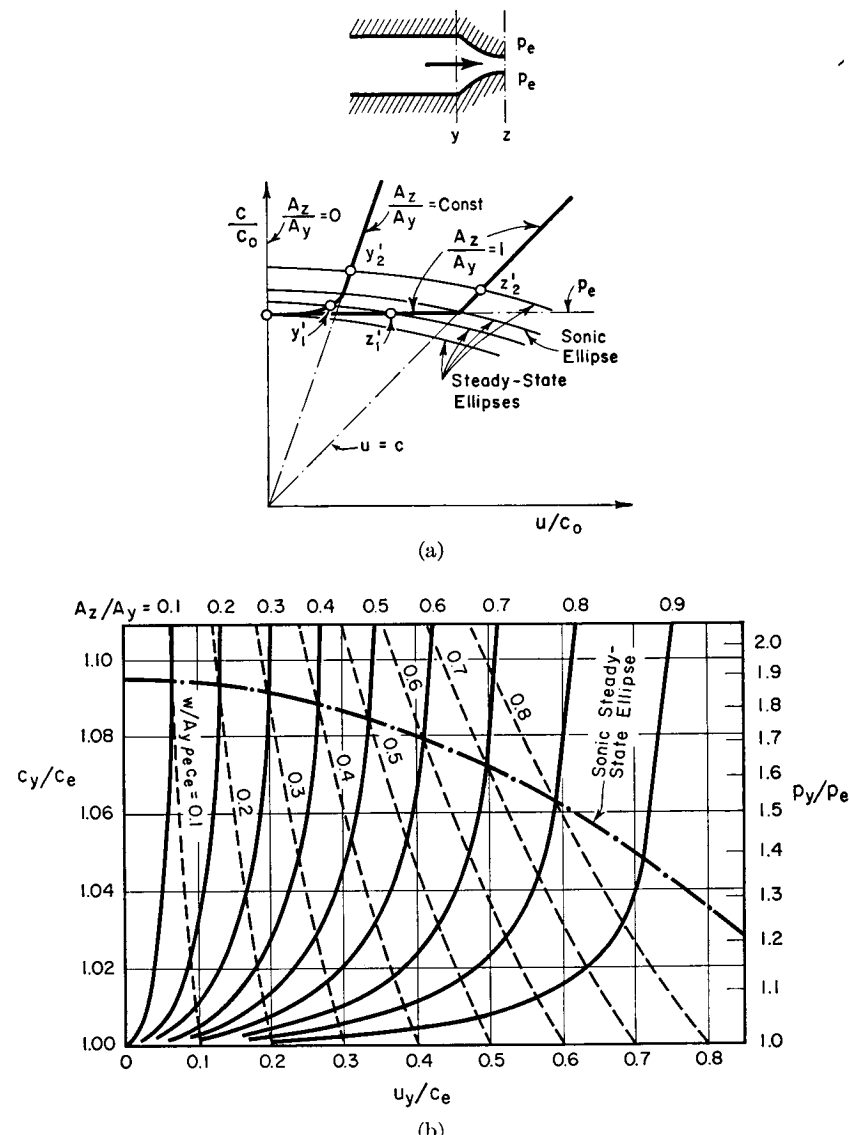


FIG. 24.18. Boundary conditions for outflow through a nozzle.

- (a) States  $y_1'$  and  $z_1'$  correspond to subsonic flow in exit plane. States  $y_2'$  and  $z_2'$  correspond to sonic flow in exit plane.  
 (b) Universal chart of auxiliary area-ratio curves ( $\rho_e$  and  $c_e$  are, respectively, the density and speed of sound at the pressure  $p_e$  and at the entropy of state  $y$ ). The portion below the sonic steady-state ellipse is for subsonic outflow, with  $u_z < c_z$  and  $p_z = p_e$ ; the portion above is for sonic outflow, with  $u_z = c_z$  and  $p_z > p_e$  (after Jenny).

Since  $A_z/A_y$  is known from the geometry of the nozzle, and since  $u_{z_1}$  and  $c_{z_1}$  are assumed to be known, Eqs. 24.37 and 24.38 may be solved simultaneously for  $u_{y_1}$  and  $c_{y_1}$ .

It is convenient to carry out these calculations with the methods of Chapter 4, which may be outlined as follows: (i) Given  $u_z$  and  $c_z$ , calculate  $M_z = u_z/c_z$ . (ii) From the isentropic tables at this  $M_z$ , find  $A_z/A^*$ ,  $u_z/u^*$ , and  $c_z/c_s$ . (iii) Knowing  $A_z/A_y$ , calculate  $A_y/A^*$ . (iv) With this  $A_y/A^*$ , from the isentropic tables find  $M_y$  and the corresponding values of  $u_y/u^*$  and  $c_y/c_s$ . (v) Finally, calculate  $u_y$  and  $c_y$ . When this is done for a number of points  $z'$  lying on the assumed boundary-condition curve, the corresponding points  $y'$  define a curve corresponding to the particular area ratio  $A_z/A_y$ . Having constructed this curve beforehand, point  $y_1'$  is found at the intersection of this curve with the steady-state ellipse passing through  $z_1'$ .

It should be noted that for each value of  $p_e$  there is a family of such curves, each corresponding to a particular value of  $A_z/A_y$ . By working with dimensionless ratios, however, one universal family of area-ratio curves on the  $u, c$ -plane may be constructed, each curve of the family being applicable to a particular value of  $A_z/A_y$ . If extensive calculations are to be made, it is well to prepare such a set of universal curves beforehand. Fig. 24.18b shows convenient forms of these curves for  $k = 1.4$ .<sup>(5,6)</sup> These are derived by writing (as in Chapter 4) the steady-state equations of energy and continuity together with the isentropic relations between sections  $y$  and  $z$ , thus giving (for subsonic outflow)

$$\left(\frac{u_y}{c_y}\right)^2 = \frac{2}{k-1} \left[ \left( \frac{p_y}{p_e} \right)^{\frac{k-1}{k}} - 1 \right] \left( \frac{A_z}{A_y} \right)^2$$

For sonic outflow, the back pressure  $p_e$  has no effect on the flow, and the steady-flow equations then show that, for a given area ratio,  $u_y$  and  $c_y$  are proportional to each other. Accordingly, above the sonic steady-state ellipse the curves of constant  $A_z/A_y$  are straight lines passing through the origin.

**EXAMPLE.** To illustrate these ideas, suppose that in Figs. 24.19a and 24.19b compression wave  $a$  of known strength advances into field 1 of known state, and that there is subsonic flow at the nozzle exit. Points  $1'$  and  $2'$  may, from the given data, be located in the state plane. Point  $1z'$ , representing the state at the nozzle outlet corresponding to state  $1'$  at the nozzle inlet, lies at the intersection of the horizontal line  $p_e$  with the steady-state ellipse through point  $1'$ .

For the given area ratio of the nozzle and the given values of  $c_y$  and  $p_e$ , the curve marked  $A_z/A_y = \text{const}$  may be constructed with the help of Fig. 24.18b.

To satisfy the boundary conditions, it will usually be necessary for wave  $b$  to be reflected at section  $y$ . Point  $3'$  lies on the curve  $A_z/A_y = \text{const}$ , and, furthermore, points  $2'$  and  $3'$  lie on a common  $I$ -characteristic. Hence point  $3'$  may be located in the state plane, and all fluid properties in field 3 may be determined. Point

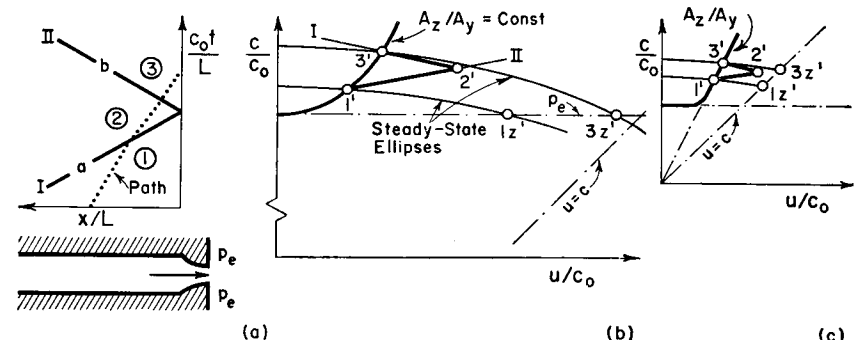


FIG. 24.19. Reflection of wave from an end at which there is outflow through a nozzle.

(a) Physical plane.

(b) State plane for condition of subsonic flow in exit plane.

(c) State plane for condition of sonic flow in exit plane.

$3'$ , representing the state at the nozzle exit, lies at the intersection of the steady-state ellipse through point  $3'$  with the line  $p_e$ .

The corresponding construction for sonic flow at the exit is illustrated in Fig. 24.19c.

The nozzle may be considered as either a partially open or partially closed end, the limiting cases being (i) closed end for  $A_z/A_y = 0$ ; (ii) open end for  $A_z/A_y = 1$ . The incident wave  $a$  may consequently be reflected in like sense, or in unlike sense, or may be canceled entirely, depending upon the area ratio and on the state in field 1. These various possibilities can easily be illustrated by reference to the  $u, c$ -diagram of Fig. 24.18.

**Inflow Through Nozzles.** When there is inflow to the nozzle of Fig. 24.19, methods similar to those outlined above are applicable, the nozzle (or diffuser) being treated as a part of the quasi-steady-state flow from the atmosphere (or reservoir) to the duct. Universal area-ratio curves representing the boundary conditions for waves incident on section  $y$  are shown in Fig. 24.20.<sup>(5,6)</sup>

**Change in Cross-Sectional Area.** In some problems two tubes of different cross-sectional area may be joined together by a short transition piece. The flow in the transition may then, as an approximation, be treated as quasi-steady in character and we may replace the actual flow by a model in which there is a sudden change in cross section. The analysis of this process may also be used for studying unsteady motion in ducts of varying size if the actual duct is, for computation purposes,

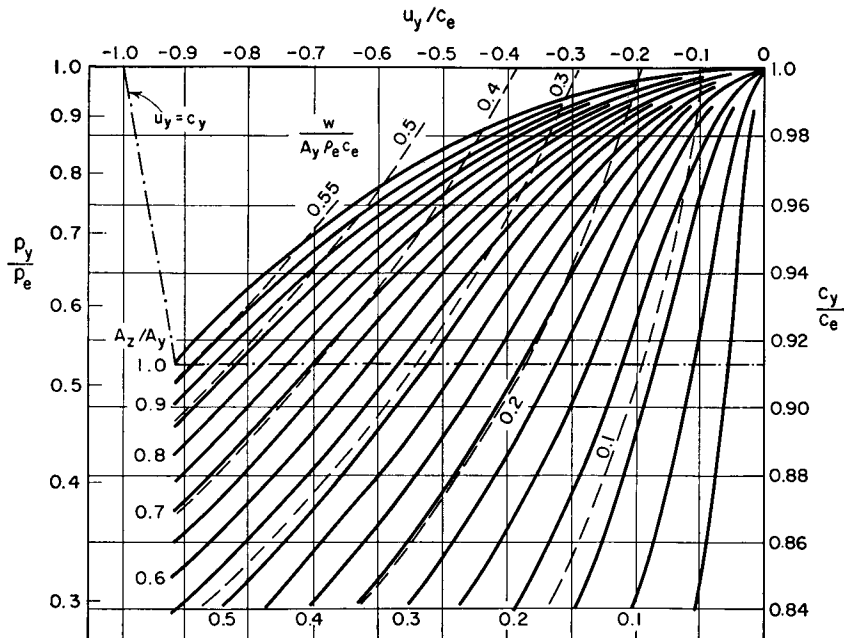


Fig. 24.20. Universal chart ( $k = 1.4$ ) of auxiliary area-ratio curves for determining boundary conditions at section  $y$  in the case of inflow to the nozzle of Fig. 24.18a (after Jenny).

replaced by an approximately equivalent duct composed of sections of constant-area duct joined by discontinuities in area.

**EXAMPLE OF SUBSONIC FLOW.** Referring to the subsonic flow of Fig. 24.21a, suppose that compression wave  $a$  is incident on a cross section where there is a sudden decrease of area. Given the state in

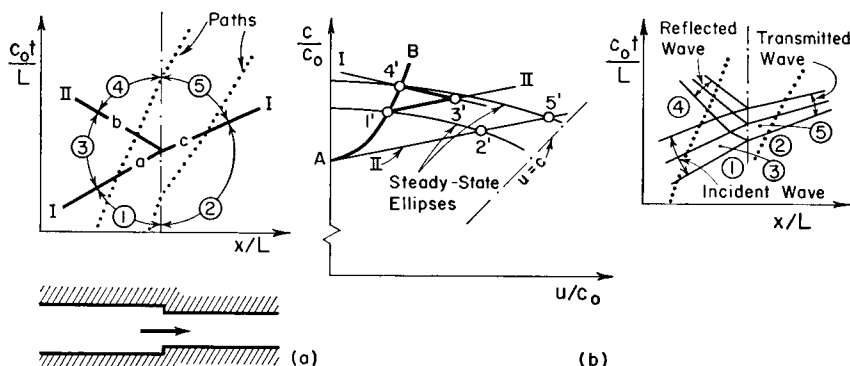


Fig. 24.21. Reflection and transmittal of wave at change in cross section (subsonic flow).

field 1 and the area ratio across the area discontinuity, the state in field 2 may be found with the help of the steady-flow isentropic tables. Thus, points 1' and 2', which lie on a common steady-state ellipse, may be located in the state plane (Fig. 24.21b). From the strength of wave  $a$ , point 3' may also be located in the state plane.

To satisfy the quasi-steady conditions at the discontinuity, there must in general be a reflected wave  $b$  and a transmitted wave  $c$ . State 5' lies somewhere on the  $II$ -characteristic passing through 2'. For each point on this characteristic we may determine from the steady-flow isentropic tables a corresponding point which refers to the left-hand side of the area discontinuity, and in this way curve  $A-B$  may be constructed. Point 4' lies on the curve  $A-B$ , and, in addition, lies on the  $I$ -characteristic passing through 3'. Hence, point 4' may be located in the state plane. Then point 5' is located at the intersection of the steady-state ellipse passing through 4' with the  $II$ -characteristic passing through 2'.

Fig. 24.21c illustrates how a simple compression wave is in part transmitted and in part reflected at an area discontinuity.

**EXAMPLE OF SUPERSONIC FLOW.** When the flow is supersonic, the situation is different because the reflected wave then travels in the

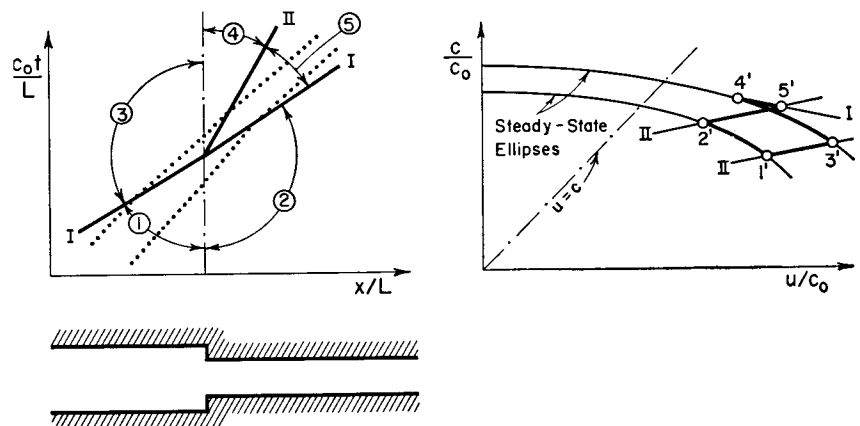


Fig. 24.22. Transmission and reflection of wave at change in cross section (supersonic flow).

downstream direction, and it is not necessary to construct the line  $A-B$ . The construction for this case is illustrated in Fig. 24.22.

**Temperature Discontinuity.** In many problems of practical importance waves are incident on the interface between two slugs of gas which are at different temperature.

For example, either low- or high-temperature gases may be drawn

in at the open end of a duct. Or, as in the V-1 buzz-bomb, a slug of combustible gas adjacent to another slug of incombustible gas suddenly explodes, producing a temperature discontinuity at the interface. Or, when a shock interacts with a continuous wave, the shock strength changes continuously and produces different entropy augmentations for different fluid particles; the resulting continuous entropy variation may as an approximation be replaced in stepwise fashion by regions of constant entropy joined by entropy discontinuities. In all these cases, the fluid pressure and velocity must be respectively equal on the two sides of a gas discontinuity in a constant-area duct. Therefore, whether the adjacent slugs of gas are unlike at the interface because of combustion, or because of entropy variations, or because one of the slugs has been taken from the atmosphere, the nature of the discontinuity is the same: it is a temperature discontinuity.

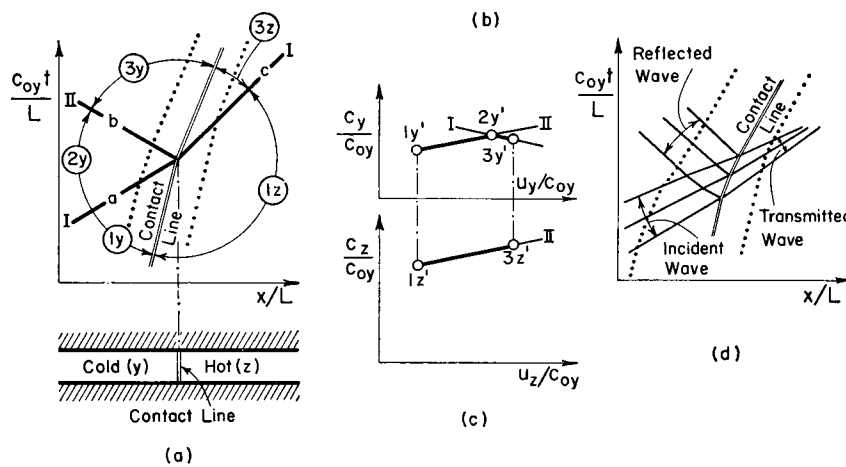


FIG. 24.23. Transmission and reflection of a wave at a contact discontinuity.

Fig. 24.23a shows compression wave  $a$  approaching a temperature discontinuity. The cold gas is denoted by subscript  $y$  and the hot gas by  $z$ . The temperature discontinuity, which we shall call a *contact line*, moves with the interface of the two fluids and is therefore a path line. It is convenient to represent the states on the two sides of the discontinuity on separate state diagrams, but with the same normalizing factor,  $c_{0y}$ , for obtaining dimensionless ratios. If the abscissa and ordinate of the dimensionless physical plane are taken as  $x/L$  and  $c_{0y}t/L$ , the graphical constructions of Fig. 24.3 remain valid provided that they are carried out with the respective state planes (Figs. 24.23b and c) corresponding to gases  $y$  and  $z$ .

Fields  $1y$  and  $1z$  have the same pressure and speed, but different

values of  $c$ . Assuming that the states are known in these fields, we may locate the state points  $1y'$  and  $1z'$ . Also, if the strength of wave  $a$  is given, point  $2y'$  may be located in the state plane.

To satisfy the boundary conditions across a contact line, it is generally necessary to have both a reflected wave  $b$  and a transmitted wave  $c$ . These must be of such strength as to satisfy the contact conditions at the discontinuity, namely:

$$\text{and} \quad \frac{u_{3y}}{c_{0y}} = \frac{u_{3z}}{c_{0y}} \quad (24.39)$$

$$\frac{p_{3y}}{p_{1y}} = \frac{p_{3z}}{p_{1z}}$$

But, since the isentropic relation is valid on each side of the contact line, the latter condition may be written

$$(c_{3y}/c_{1y})^{\frac{2k_y}{k_y-1}} = (c_{3z}/c_{1z})^{\frac{2k_z}{k_z-1}} \quad (24.40a)$$

or, if the specific-heat ratios are alike,

$$c_{3y}/c_{1y} = c_{3z}/c_{1z} \quad (24.40b)$$

Eqs. 24.39 and 24.40, together with the additional facts that  $2y'$  and  $3y'$  lie on a common  $I$ -characteristic, and  $1z'$  and  $3z'$  lie on a common  $II$ -characteristic, serve to locate points  $3y'$  and  $3z'$  in the state plane.

**ALGEBRAIC SOLUTION.** To solve this problem algebraically, we write the characteristics equations as

$$u_{3y} - u_{2y} = -\frac{2}{k-1} (c_{3y} - c_{2y})$$

$$u_{1z} - u_{3z} = \frac{2}{k-1} (c_{1z} - c_{3z})$$

Combining these with Eqs. 24.39 and 24.40b, we get

$$c_{3y} = \left[ (c_{1z} + c_{2y}) - \frac{k-1}{2} (u_{1z} - u_{2y}) \right] / \left( 1 + \frac{c_{1z}}{c_{1y}} \right)$$

$$c_{3z} = \left[ (c_{1z} + c_{2y}) - \frac{k-1}{2} (u_{1z} - u_{2y}) \right] / \left( 1 + \frac{c_{1y}}{c_{1z}} \right)$$

$$u_{3y} = u_{3z} = u_{2y} + \frac{u_{1z} - u_{2y}}{1 + \frac{c_{1z}}{c_{1y}}} + \frac{2}{k-1} \left[ c_{2y} - \frac{c_{1z} + c_{2y}}{1 + \frac{c_{1z}}{c_{1y}}} \right]$$

These give the fluid properties in field  $3y$  and  $3z$  in terms of the known properties in fields  $1z$  and  $2y$ .

Fig. 24.23d illustrates the transmission and partial reflection of a simple compression wave at a contact discontinuity.

### 24.7. Unsteady, One-Dimensional Flow with Area Change, Friction, and Heat Transfer or Combustion

We shall now develop a calculation procedure based on the method of characteristics and suitable for solving problems of unsteady motion in a duct of slowly varying area when wall friction and changes in temperature owing to heat transfer or combustion must be taken into account.<sup>(5,6)</sup>

**Governing Equations.** The governing physical laws may be written for the flow through the control surface of Fig. 24.24. The flow is

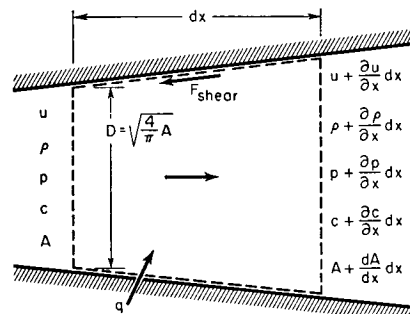


FIG. 24.24. Control surface.

assumed to be one-dimensional at each value of  $x$ . This requires that  $d(\ln A)/dx$  be small compared with unity, i.e., the cross-sectional area must change only gradually with distance. The effects of wall friction and of heat conduction from the walls are in essence not one-dimensional, but a one-dimensional model (using the appropriate mean quantities) is employed in order to simplify the analysis.

**CONTINUITY.** The principle of conservation of mass may be expressed by

$$\frac{\partial}{\partial x} (\rho u A) dx = - \frac{\partial}{\partial t} (\rho A dx)$$

or, after simplification, by

$$\frac{\partial \rho}{\partial t} + \rho \frac{\partial u}{\partial x} + u \frac{\partial \rho}{\partial x} + \frac{\rho u}{A} \frac{dA}{dx} = 0 \quad (24.41)$$

**MOMENTUM.** We shall assume that the effects of friction are expressed in terms of the conventional pipe friction coefficient  $f$  defined by

$$f \equiv \frac{\tau_w}{\frac{1}{2} \rho u^2}$$

where  $\tau_w$  is the wall shearing stress.

The momentum theorem may then be written as

$$-\frac{\partial}{\partial x} (pA) dx + p \frac{dA}{dx} dx - f \frac{\rho u^2}{2} \pi D dx = \frac{\partial}{\partial t} (\rho A u dx) + \frac{\partial}{\partial x} (\rho A u^2) dx$$

Expanding this equation, and subtracting from it Eq. 24.41, we obtain

$$\frac{\partial u}{\partial t} + u \frac{\partial u}{\partial x} + \frac{1}{\rho} \frac{\partial p}{\partial x} + F = 0 \quad (24.42)$$

where  $F$  is a wall-friction term defined by

$$F \equiv \frac{4f}{D} \frac{u^2}{2} \frac{u}{|u|} \quad (24.43)$$

The factor  $u/|u|$  being introduced in order to guarantee that the frictional force shall always act opposite to the direction of motion.

**ENERGY.** We shall let  $q$  represent the rate of heat transfer per unit time and per unit mass of fluid. The heat transfer may either be through the walls or be the result of longitudinal heat conduction. In the event of combustion, we replace the actual process of chemical reaction by an approximately equivalent process in which there is no chemical reaction but, rather, a heat transfer equal in magnitude to the constant-volume heat of combustion of the actual process.

The First Law of Thermodynamics may accordingly be written

$$q \rho A dx = \frac{\partial}{\partial t} \left[ (\rho A dx) \left( c_v T + \frac{u^2}{2} \right) \right] + \frac{\partial}{\partial x} \left[ (\rho u A) \left( c_v T + \frac{p}{\rho} + \frac{u^2}{2} \right) \right]$$

where the internal energy per unit mass is written as  $c_v T$  for a perfect gas with constant specific heats. Expanding this relation, and subtracting from it the continuity equation, we get

$$\frac{d}{dt} \left( c_v T + \frac{u^2}{2} \right) = q - \frac{u}{\rho} \frac{\partial p}{\partial x} - \frac{p}{\rho A} \frac{\partial}{\partial x} (Au)$$

where  $D/dt \equiv (\partial/\partial t) + (u)(\partial/\partial x)$  represents the substantial (or material) derivative.

The term  $\partial p/\partial x$  may be eliminated from the foregoing expression by means of Eq. 24.42, thus leaving

$$q + uF = \frac{D(c_v T)}{dt} + \frac{p}{\rho A} \frac{\partial}{\partial x} (Au) \quad (24.44)$$

Now, from the perfect-gas laws,

$$c_v T = c_v \frac{p}{\rho R} = \frac{1}{k-1} \frac{p}{\rho}$$

and therefore, after differentiation by parts, we obtain

$$\frac{D(c_v T)}{dt} = \frac{1}{(k-1)\rho} \left[ \left( \frac{\partial p}{\partial t} + u \frac{\partial p}{\partial x} \right) - \frac{p}{\rho} \left( \frac{\partial \rho}{\partial t} + u \frac{\partial \rho}{\partial x} \right) \right]$$

The term  $\partial(Au)/\partial x$  may be evaluated with the help of the continuity equation as

$$\frac{\partial(Au)}{\partial x} = - \frac{A}{\rho} \left( \frac{\partial \rho}{\partial t} + u \frac{\partial \rho}{\partial x} \right)$$

Substituting this relation and the one preceding it into Eq. 24.44 and simplifying, we obtain the energy equation in the form

$$(k-1)\rho(q + uF) = \frac{\partial p}{\partial t} + u \frac{\partial p}{\partial x} - c^2 \left( \frac{\partial \rho}{\partial t} + u \frac{\partial \rho}{\partial x} \right) \quad (24.45)$$

**ENTROPY.** The entropy change may be evaluated from the thermodynamic relation

$$T ds = d(c_v T) + pd\left(\frac{1}{\rho}\right) = \frac{1}{k-1} d\left(\frac{p}{\rho}\right) + pd\left(\frac{1}{\rho}\right)$$

or

$$\frac{p}{\rho R} ds = \frac{1}{k-1} \frac{dp}{\rho} - \frac{k}{k-1} \frac{p}{\rho^2} d\rho$$

Since  $p$  and  $\rho$  are to be evaluated while following a particle of fixed identity (for which  $u dt = dx$ ), we may replace  $dp$  and  $d\rho$  by

$$dp = \frac{\partial p}{\partial x} dx + \frac{\partial p}{\partial t} dt = \left(u \frac{\partial p}{\partial x} + \frac{\partial p}{\partial t}\right) dt$$

$$d\rho = \frac{\partial \rho}{\partial x} dx + \frac{\partial \rho}{\partial t} dt = \left(u \frac{\partial \rho}{\partial x} + \frac{\partial \rho}{\partial t}\right) dt$$

Substituting these into the relation for  $ds$ , and combining the resulting expression with Eq. 24.45, we obtain

$$(ds)_{\text{path}} = \frac{uF + q}{T} (dt)_{\text{path}} \quad (24.46)$$

which applies while following a fluid particle.

At this point it is convenient to derive a special relation for later use. The pressure may be thought of as a function of the sound speed and entropy, and thus we may write

$$dp = \left(\frac{\partial p}{\partial c}\right)_s dc + \left(\frac{\partial p}{\partial s}\right)_c ds$$

From the isentropic relation (Eq. 24.4) between  $p$  and  $c$  we find that

$$\left(\frac{\partial p}{\partial c}\right)_s = \frac{2k}{k-1} \frac{p}{c}$$

From the thermodynamic relation  $T ds = c_v dT - dp/\rho$ , we get, upon noting that  $c$  depends only on  $T$ ,

$$\left(\frac{\partial p}{\partial s}\right)_c = -\rho T$$

Combining these with Eq. 24.46, we obtain

$$(dp)_{\text{path}} = \frac{2k}{k-1} \frac{p}{c} (dc)_{\text{path}} - \rho(uF + q)(dt)_{\text{path}} \quad (24.47)$$

**Characteristic Curves.** The *characteristic curves* are defined as curves on which the *derivatives* of the fluid properties are indeterminate and may, therefore, undergo arbitrary discontinuities. The derivatives in question are, in the present case,  $\partial u/\partial x$ ,  $\partial u/\partial t$ ,  $\partial p/\partial x$ ,  $\partial p/\partial t$ ,  $\partial \rho/\partial x$ ,

and  $\partial \rho/\partial t$ . In order to find under what conditions these derivatives may be discontinuous, we set down the following array of six simultaneous equations. The first three of these equations express mathematically the conditions that the properties themselves (i.e.,  $u$ ,  $p$ , and  $\rho$ ) vary continuously with  $x$  and  $t$ ; the last three equations are, respectively, those of continuity (Eq. 24.41), momentum (Eq. 24.42), and energy (Eq. 24.45).

$$\begin{aligned} +dx \frac{\partial u}{\partial x} + dt \frac{\partial u}{\partial t} &= du \\ +dx \frac{\partial p}{\partial x} + dt \frac{\partial p}{\partial t} &= dp \\ +dx \frac{\partial \rho}{\partial x} + dt \frac{\partial \rho}{\partial t} &= d\rho \\ +\rho \frac{\partial u}{\partial x} &+ u \frac{\partial \rho}{\partial x} + \frac{\partial \rho}{\partial t} = -\frac{\rho u}{A} \frac{dA}{dx} \\ +u \frac{\partial u}{\partial x} + \frac{\partial u}{\partial t} + \frac{1}{\rho} \frac{\partial p}{\partial x} &= -F \\ +u \frac{\partial p}{\partial x} + \frac{\partial p}{\partial t} - uc^2 \frac{\partial \rho}{\partial x} - c^2 \frac{\partial \rho}{\partial t} &= (k-1)\rho(uF + q) \end{aligned}$$

These may be regarded as six simultaneous equations with the six derivatives as unknowns. Solving for one of the derivatives, say  $\partial u/\partial x$ , we obtain, in determinant notation,

$$\frac{\partial u}{\partial x} = \frac{\begin{vmatrix} du & dt & 0 & 0 & 0 & 0 \\ dp & 0 & dx & dt & 0 & 0 \\ d\rho & 0 & 0 & 0 & dx & dt \\ -\frac{\rho u}{A} \frac{dA}{dx} & 0 & 0 & 0 & u & 1 \\ -F & 1 & 1/\rho & 0 & 0 & 0 \\ (k-1)\rho(uF + q) & 0 & u & 1 & -uc^2 & -c^2 \end{vmatrix}}{\begin{vmatrix} dx & dt & 0 & 0 & 0 & 0 \\ 0 & 0 & dx & dt & 0 & 0 \\ 0 & 0 & 0 & 0 & dx & dt \\ \rho & 0 & 0 & 0 & u & 1 \\ u & 1 & 1/\rho & 0 & 0 & 0 \\ 0 & 0 & u & 1 & -uc^2 & -c^2 \end{vmatrix}} \quad (24.48)$$

**PHYSICAL CHARACTERISTICS.** The condition that  $\partial u/\partial x$  be indeterminate is that the denominator of Eq. 24.48 be equal to zero. Since  $\partial u/\partial x$  is in general finite, it is necessary that the numerator also be equal to zero. By setting the two determinants of Eq. 24.48 equal to zero we therefore obtain the differential equations of the characteristic curves. It should be noted that to obtain these, it is sufficient to follow this procedure for any one of the six derivatives in the system of simultaneous equations.

Setting the denominator equal to zero, and simplifying, we get the roots

$$\left(\frac{dx}{dt}\right)_{I,II} = u \pm c \quad (\text{Mach Lines}) \quad (24.49)$$

$$\frac{dx}{dt} = u \quad (\text{Path Lines}) \quad (24.50)$$

Equation 24.49 is already familiar, and signifies that discontinuities in the derivatives may occur on lines which travel either rightward or leftward with the local speed of sound relative to the fluid. This is the same as saying that disturbances are propagated on such lines. Note that area change, friction, and heat transfer have no influence on this result.

Eq. 24.50 did not previously appear when we considered isentropic motions. For the more general type of unsteady motion we are considering here, Eq. 24.50 indicates that the trajectories of the fluid particles themselves may be the loci of discontinuities. Physically, this means that frictional and heat transfer effects act on individual fluid particles, and, since these effects may be varied arbitrarily, the path lines are characteristic curves on which the entropy or temperature gradients may have discontinuities.

**STATE CHARACTERISTICS.** Setting the numerator of Eq. 24.48 equal to zero, expanding the determinant, and eliminating  $dx$  by means of Eqs. 24.49, we obtain the following expression for the differential equations of the Mach lines in terms of the state coordinates  $p$  and  $u$ :

$$(du)_{I,II} = \mp \frac{(dp)_{I,II}}{\rho c} \mp \frac{cu}{A} \frac{dA}{dx} (dt)_{I,II} \\ \pm (k-1) \frac{q}{c} (dt)_{I,II} - F \left[ 1 \mp (k-1) \frac{u}{c} \right] (dt)_{I,II} \quad (24.51)$$

It has been found more convenient to work with the  $c, u$ -characteristics. To this end we form

$$\begin{aligned} \left(\frac{dp}{dt}\right)_{I,II} &= \frac{\partial p}{\partial t} + \left(\frac{dx}{dt}\right)_{I,II} \frac{\partial p}{\partial x} = \frac{\partial p}{\partial t} + (u \pm c) \frac{\partial p}{\partial x} \\ &= \frac{\partial p}{\partial t} + u \frac{\partial p}{\partial x} \pm c \frac{\partial p}{\partial x} = \frac{\partial p}{\partial t} + \left(\frac{dx}{dt}\right)_{\text{path}} \frac{\partial p}{\partial x} \pm c \frac{\partial p}{\partial x} \\ &= \left(\frac{dp}{dt}\right)_{\text{path}} \pm c \frac{\partial p}{\partial x} \end{aligned}$$

In similar manner it may be shown that

$$\left(\frac{dc}{dt}\right)_{I,II} = \left(\frac{dc}{dt}\right)_{\text{path}} \pm c \frac{\partial c}{\partial x}$$

By combining these relations with Eq. 24.47 we may obtain

$$\left(\frac{dp}{dt}\right)_{I,II} = \frac{2k}{k-1} \frac{p}{c} \left(\frac{dc}{dt}\right)_{I,II} \mp pc \frac{\partial}{\partial x} \left( \ln \frac{c^{\frac{2k}{k-1}}}{p} \right) - \rho(uF + q)$$

Insertion of this into Eq. 24.51 yields, after simplification, the state characteristics in the form

$$(du)_{I,II} = \mp \frac{2}{k-1} (dc)_{I,II} \\ + \left[ \mp \frac{cu}{A} \frac{dA}{dx} \pm k \frac{q}{c} - F \left( 1 \mp \frac{u}{c} \right) + \frac{c^2}{k} \frac{\partial}{\partial x} \left( \ln \frac{c^{\frac{2k}{k-1}}}{p} \right) \right] (dt)_{I,II} \quad (24.52)$$

The last term of this expression is related to the lengthwise distribution of entropy, as may be seen by noting that for a perfect gas,

$$\frac{ds}{R} = \ln \frac{c^{\frac{2k}{k-1}}}{p}$$

For isentropic motion in the absence of area change, friction, and heat transfer, Eq. 24.52 becomes identical with Eq. 24.9.

**Numerical Solutions.** Eq. 24.52 contains terms which depend upon  $t$  and  $x$  as well as upon  $c$  and  $u$ . Consequently it is not possible (as it was for isentropic motions) to integrate the state characteristics in a universal form applicable to all problems. Instead, the net of state characteristics is different for each physical problem, and it must be constructed *simultaneously* with the physical Mach net by means of a stepwise iterative procedure. At the same time that the state and physical characteristics nets are under construction, it is necessary to integrate Eq. 24.47 stepwise along the path lines. This not only provides useful information concerning the pressure at each value of  $x$  and  $t$  but also leads to the determination of the last term in Eq. 24.52.

Iterative stepwise procedures of the type necessary here have already

been outlined in connection with similar problems in Chapters 15 and 17 and are also discussed in Appendix A.

**Graphical Method of Solution.** <sup>(5,6)</sup> The iterative procedure described above may be carried out more rapidly with the help of a semi-graphical method. For this purpose we write Eq. 24.52 in the finite-difference form

$$(\Delta u)_{I,II} = \mp \frac{2}{k-1} (\Delta c)_{I,II} + (\Delta u_A)_{I,II} + (\Delta u_a)_{I,II} + (\Delta u_F)_{I,II} + (\Delta u_s)_{I,II}$$

where  $\Delta u_A$ ,  $\Delta u_a$ , etc., represent respectively the terms in Eq. 24.52 connected with the effects of (i) area change; (ii) heat transfer or combustion; (iii) wall friction; and (iv) longitudinal entropy gradients owing to heat transfer or combustion, to wall friction, to nonuniform starting conditions, to the introduction of hot or cold gas, or to the passage of variable-strength shocks through the gas. For example,

$$(\Delta u_A)_{I,II} \equiv \mp \frac{cu}{A} \frac{dA}{dx} (\Delta t)_{I,II}$$

where the coefficient of  $(\Delta t)_{I,II}$  is evaluated at its mean value over the interval.

The basic step in the construction of the characteristics nets is this: Given data  $(u, c, x, t)$  at two points 1 and 2, it is necessary to find similar data at the intersection point 3 of the two characteristics passing through points 1 and 2. Repeated application of this step, given suitable initial data, leads to the construction of the complete nets in the two planes.

Fig. 24.25 illustrates the procedure. It is assumed that  $A$  is known as a function of  $x$  and that  $(1/A)(dA/dx)$  is accordingly known at each value of  $x$ . It is further assumed that the values of  $F$  and  $q$  are known

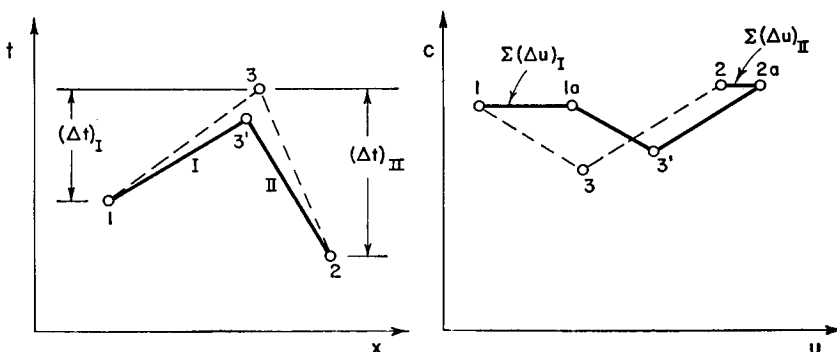


FIG. 24.25. Semi-graphical method of constructing characteristics nets.

in the neighborhood of the particular locations  $(x, t)$  and states  $(u, p, c)$  under consideration. It is also assumed that Eq. 24.47 has been integrated on several path lines as far as the current stage of the calculations permits, and that the  $x$ -derivative in the expression for  $\Delta u$ , is therefore known in the neighborhoods of points 1 and 2. The method may be outlined as follows:

(i) A crude first approximation to point 3 in the state plane is found by ignoring the terms  $\Delta u_A$ ,  $\Delta u_a$ ,  $\Delta u_F$ , and  $\Delta u_s$ . It is then only necessary to find the intersections of the lines passing through points 1 and 2 with the slopes  $\mp(k-1)/2$ , respectively.

(ii) Using the mean values of  $\bar{u}_{1-3}$  and  $\bar{c}_{1-3}$  between 1 and 3, the physical  $I$ -characteristic is drawn through point 1 with the slope  $\bar{u}_{1-3} + \bar{c}_{1-3}$ . Similarly, the physical  $II$ -characteristic is drawn through point 2 with the slope  $\bar{u}_{1-2} - \bar{c}_{1-2}$ . The intersection of these two lines establishes a first approximation to point 3 in the physical plane, and yields tentative values of  $(\Delta t)_{I,II}$ .

(iii) The values of  $(\Delta u_A)_I$ ,  $(\Delta u_a)_I$ ,  $(\Delta u_F)_I$ , and  $(\Delta u_s)_I$  are calculated from Eq. 24.52 and the given data, the coefficient of  $(dt)_I$  in each case being taken at the mean conditions between points 1 and 3. The sum of these values,  $\Sigma(\Delta u)_I$ , is then laid off horizontally (and algebraically) from point 1, thus yielding point 1a. Similarly,  $\Sigma(\Delta u)_{II}$  is calculated and laid off horizontally from point 2, thus giving point 2a. Straight lines with slopes  $\mp(k-1)/2$  are then drawn through points 1a and 2a, respectively. Their intersection at point 3' gives a second, and better, approximation to the desired point. The construction outlined here satisfies Eq. 24.52.

(iv) Using the mean values of  $u$  and  $c$  between 1 and 3', and between 2 and 3', point 3' is established in the physical plane as an improvement over point 3.

(v) Steps (iii) and (iv) are repeated with the values at 1, 2, and 3', and lead to the establishment of point 3'' (a still better approximation) in the state and physical planes. This iterative procedure is continued until satisfactory convergence is obtained.

#### 24.8. Remarks on Details of Working Out the Method of Characteristics

**Graphical Versus Numerical Procedures.** For the actual working out of problems, three procedures are possible, namely: (i) purely graphical, (ii) purely numerical, and (iii) a combination of graphical and numerical methods. The choice of these will depend on the type of problem, on the accuracy desired, on the importance of speed, on the number of problems of a given type to be worked out, and on the skills of the computer.

**GRAPHICAL METHOD.** The purely graphical procedure derives from the geometric properties illustrated by Fig. 24.4. Such problems as those shown in Figs. 24.5 and 24.11 may be worked out rapidly on the drafting board without making any numerical calculations whatsoever, using either the lattice-point or the field method.

As a guide to the essential physical features of a process, and for illustrative purposes, the graphical representations are indispensable even where numerical methods are made the basis for the design calculations. Where great accuracy is essential, however, the inherent limitations in this respect of graphical techniques leaves the numerical approach as the only acceptable alternative for design purposes.

**NUMERICAL METHOD.** The purely numerical procedure is based on a stepwise integration of the differential equations of the characteristics by the method of finite differences.

It will be recalled that the unit operation in working out the characteristics nets, using either the lattice-point or field approach, is the calculation of data  $(u, c, t, x)$  at a point 3 from similar data, previously found or initially given, at points 1 and 2 which lie on the two characteristics passing through the point 3. We shall outline the numerical procedure for the case of constant-area, isentropic flow.

Referring to Fig. 24.10a, and assuming that at points 1 and 2 we know the values of  $u$ ,  $c$ ,  $x$ , and  $t$ , we find from an integration of Eq. 24.9 that

$$\frac{c_3}{c_0} - \frac{c_1}{c_0} = -\frac{k-1}{2} \left( \frac{u_3}{c_0} - \frac{u_1}{c_0} \right)$$

$$\frac{c_3}{c_0} - \frac{c_2}{c_0} = \frac{k-1}{2} \left( \frac{u_3}{c_0} - \frac{u_2}{c_0} \right)$$

These may be regarded as a pair of simultaneous equations in the variables  $c_3/c_0$  and  $u_3/c_0$ . Solving for these, we obtain

$$\frac{c_3}{c_0} = \frac{1}{2} \left( \frac{c_1}{c_0} + \frac{c_2}{c_0} \right) + \frac{k-1}{4} \left( \frac{u_1}{c_0} - \frac{u_2}{c_0} \right) \quad (24.53)$$

$$\frac{u_3}{c_0} = \frac{1}{k-1} \left( \frac{c_1}{c_0} - \frac{c_2}{c_0} \right) + \frac{1}{2} \left( \frac{u_2}{c_0} + \frac{u_1}{c_0} \right) \quad (24.54)$$

Since, by supposition, the right-hand sides of these equations are known, we may solve for the values of  $u$  and  $c$  at point 3. It remains to find the values of  $x$  and  $t$  at point 3. This is done by integrating Eqs. 24.7 approximately, making the assumption that over a short interval the values of  $u$  and  $c$  may be taken to be constant at their respective mean values. Thus we obtain

$$x_3 - x_1 = \left( \frac{\bar{u}_{1-3}}{c_0} + \frac{\bar{c}_{1-3}}{c_0} \right) (c_0 t_3 - c_0 t_1)$$

$$x_3 - x_2 = \left( \frac{\bar{u}_{2-3}}{c_0} - \frac{\bar{c}_{2-3}}{c_0} \right) (c_0 t_3 - c_0 t_2)$$

where  $\bar{u}_{1-3}$  is the average value of  $u$  between points 1 and 3, and similarly for  $\bar{c}_{1-3}$ . The values of  $\bar{c}_{1-3}$  and  $\bar{u}_{1-3}$  may be computed after Eqs. 24.53 and 24.54 have been solved for  $u_3$  and  $c_3$ .

Regarding the relations above as a pair of simultaneous equations in  $x_3$  and  $c_0 t_3$ , and solving for these variables, we finally get

$$x_3 = \frac{\left( \frac{\bar{u}_{1-3}}{c_0} + \frac{\bar{c}_{1-3}}{c_0} \right) \left[ x_2 - \left( \frac{\bar{u}_{2-3}}{c_0} - \frac{\bar{c}_{2-3}}{c_0} \right) c_0 t_2 \right] - \left( \frac{\bar{u}_{2-3}}{c_0} - \frac{\bar{c}_{2-3}}{c_0} \right) \left[ x_1 - \left( \frac{\bar{u}_{1-3}}{c_0} + \frac{\bar{c}_{1-3}}{c_0} \right) c_0 t_1 \right]}{\left( \frac{\bar{u}_{1-3}}{c_0} + \frac{\bar{c}_{1-3}}{c_0} \right) - \left( \frac{\bar{u}_{2-3}}{c_0} - \frac{\bar{c}_{2-3}}{c_0} \right)} \quad (24.55)$$

$$c_0 t_3 = \frac{\left[ x_2 - \left( \frac{\bar{u}_{2-3}}{c_0} - \frac{\bar{c}_{2-3}}{c_0} \right) c_0 t_2 \right] - \left[ x_1 - \left( \frac{\bar{u}_{1-3}}{c_0} + \frac{\bar{c}_{1-3}}{c_0} \right) c_0 t_1 \right]}{\left( \frac{\bar{u}_{1-3}}{c_0} + \frac{\bar{c}_{1-3}}{c_0} \right) - \left( \frac{\bar{u}_{2-3}}{c_0} - \frac{\bar{c}_{2-3}}{c_0} \right)} \quad (24.56)$$

The values of  $x_3$  and  $c_0 t_3$  may now be calculated from Eqs. 24.55 and 24.56, and therefore all the required data at point 3 are known.

Referring to Fig. 24.11a, it will be noted that the numerical procedure is directly applicable to determining a point such as 20 from data at 16 and 19; or to determining a point such as  $n$  from data at  $j$  and  $m$ . In certain cases, however, a point is determined not at the intersection of two characteristics, but rather at the intersection of a characteristic with one of the boundaries of the problem. The numerical procedure is then modified accordingly and is completely analogous to the graphical solution. For example, point 13 is found by analytical geometry at the intersection of 980 $I$  passing through point 8 and the line representing the dead end of the cylinder passing through point 7. Similar techniques may be worked out for the various unit operations outlined in Art. 24.6.

**ORGANIZATION OF CALCULATIONS.** The accuracy of the final results depends not only on the accuracy of the individual steps in constructing the characteristics, but also on the fineness of the characteristics net. Here again no general rules may be laid down which apply to all situations. As in similar finite-difference procedures, however, the final criterion of whether the net is sufficiently detailed to yield a certain accuracy is to rework the problem with ever finer nets until it is clear that further refinement is not necessary. Naturally, after a number of

examples have been worked, the judgment of the computer is a good guide in this respect.

From these remarks and the nature of the characteristics method it is clear that much can be gained in the way of accuracy and time by considering in advance the best procedures for each problem and by laying out an organization form for the various steps. Through ingenious planning, the actual calculations may be reduced to a few simple, repetitive operations which allow final results to be obtained quite rapidly. In Chapter 15, for example, there are shown computation forms and work sheets which expedite the application of the method of characteristics to problems of two-dimensional, supersonic flow. Similar computation forms and work sheets may be devised for the types of problems under discussion here.

It has been found convenient to work with dimensionless forms of the equations. For this purpose,  $x$  may be normalized with respect to some length parameter  $L$  of the problem,  $u$  and  $c$  may be normalized with respect to some reference value  $c_0$  of the speed of sound,  $t$  may be normalized with respect to  $L/c_0$ ,  $A$  may be normalized with respect to  $L^2$  and so on. The advantages of employing dimensionless ratios are that (i) the numerical values have convenient sizes, and (ii) each solution in dimensionless form may quickly be converted into many other solutions in dimensional form.

**Analogy Between One-Dimensional, Unsteady Motion and Two-Dimensional, Steady, Supersonic Flow.** <sup>(3)</sup> We have already noted several similarities between the type of problem discussed in this chapter and the supersonic, steady flow problems of Chapters 15 and 17. The analogies may be conveniently summarized by means of a table:

#### Unsteady One-Dimensional

Physical coordinates:  $x$  and  $t$   
Hodograph coordinates:  $u$  and  $\Phi$ ,  
State coordinates:  $u$  and  $c$   
Supersonic and subsonic speeds  
Flow through cylindrical pipes  
Flow through pipe of changing area  
Infinitesimal pressure pulses  
Path lines  
Isentropic flow  
Nonisentropic flow

#### Steady Two-Dimensional

Physical coordinates:  $x$  and  $y$   
Hodograph coordinates:  $u$  and  $v$   
State coordinates:  $u$  and  $c$   
Exclusively supersonic speeds  
Plane flow  
Axi-symmetric flow  
Mach waves  
Streamlines  
Irrational isentropic flow  
Flow with rotation

**Initial-Value Theorems.** In Appendix A and in Chapters 14 and 15 there are discussions of the *initial-value theorem* and its corollaries for quasi-linear, second order, partial differential equations of hyperbolic type with two independent variables. Without going into details, it will be remarked that these discussions are entirely applicable to problems of unsteady, one-dimensional motion. Of particular interest

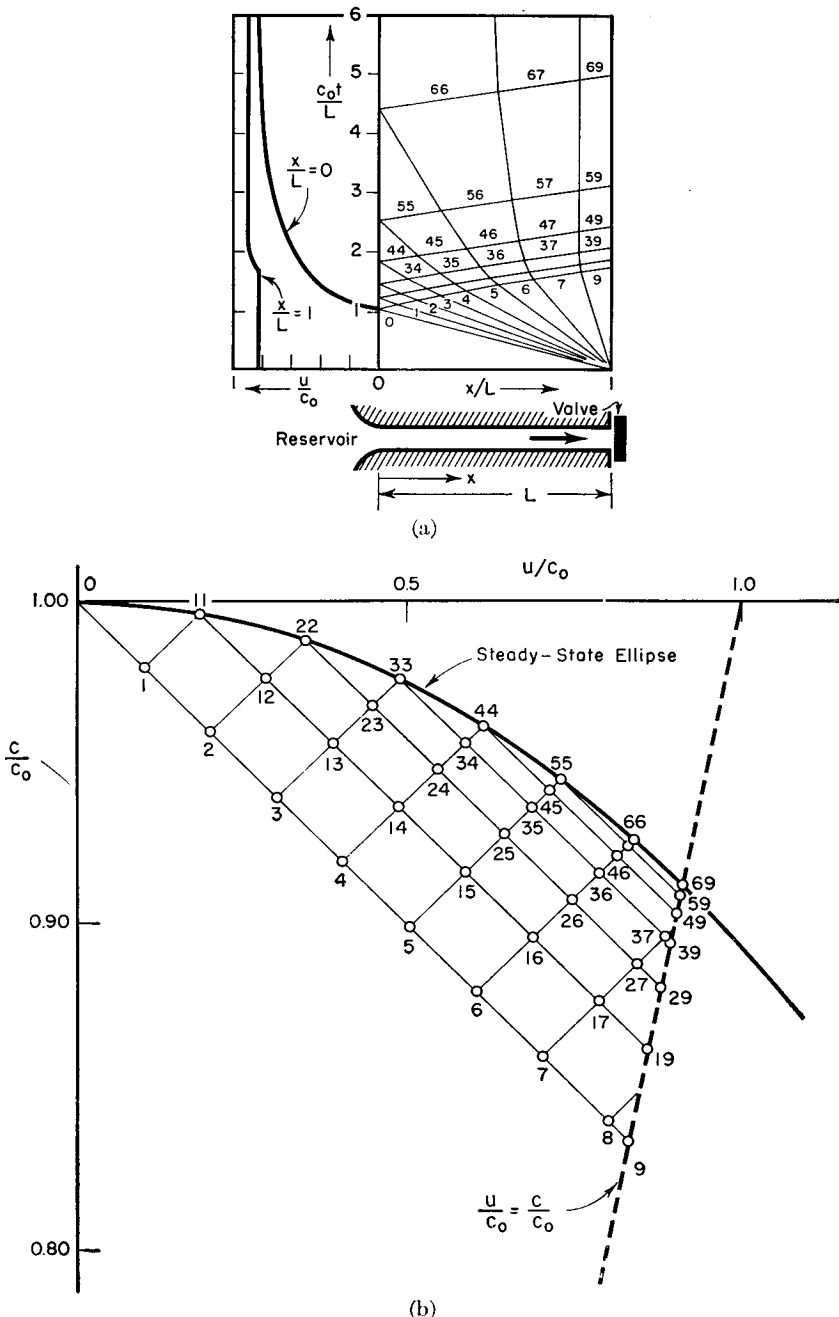
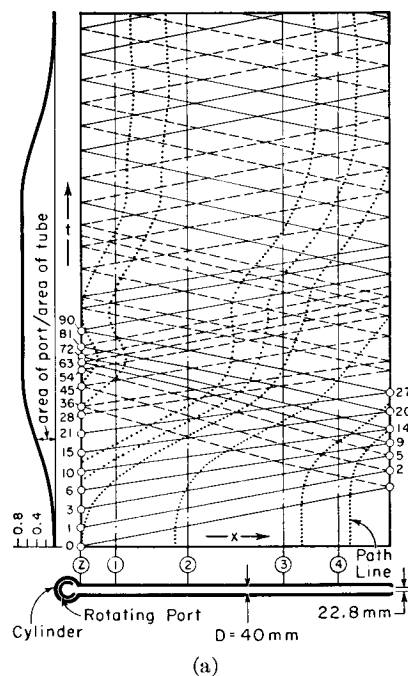


FIG. 24.26. Calculated results for starting of flow from reservoir (after de Haller).

- (a) Physical plane. Diagram at left shows variation of velocity with time at left-hand and right-hand ends of pipe.
- (b) State diagram. Note that  $c/c_0$  scale is 5 times as large as  $u/c_0$  scale, so that (for  $k = 1.4$ ) state characteristics are  $\pm 45^\circ$  lines.  $c_0$  is the speed of sound in the initially stagnant gas.

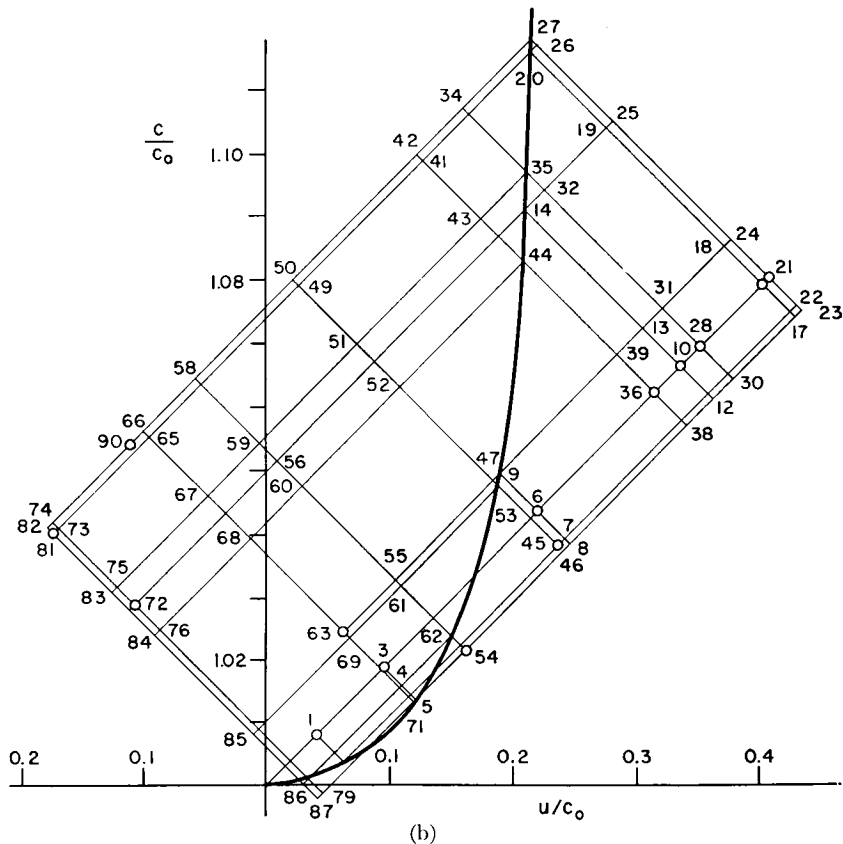


(a)

FIG. 24.27. Theoretical and experimental results for model of duct at discharge of a four-stroke reciprocating engine. Valve rotates at 225 rpm (after Jenny).

- (a) Calculated characteristics and path lines in  $x, t$ -plane (ignoring friction). The ordinate ( $t$ ) is expressed in degrees of rotation of the port. Compression waves are shown by solid lines; rarefaction waves by dashed lines. Path lines are shown by short dashed lines. The upper left-hand diagram shows the port area as a function of time. At  $t = 0$ , the air in the tube is stagnant, with the pressure  $p_0$ , and the pressure in the cylinder is  $4.4p_0$ .
- (b) State diagram corresponding to (a), again ignoring friction.
- (c) Comparison of calculated and measured pressure-time history at five stations. The calculated curves are based on charts similar to those of (a) and (b) except that friction is taken into account. Parts (a) and (b) are shown without the effects of friction for the sake of clarity in the diagrams. The agreement of theory with experiment when friction is ignored is only slightly less good than shown here.

(See opposite page.)



(b)

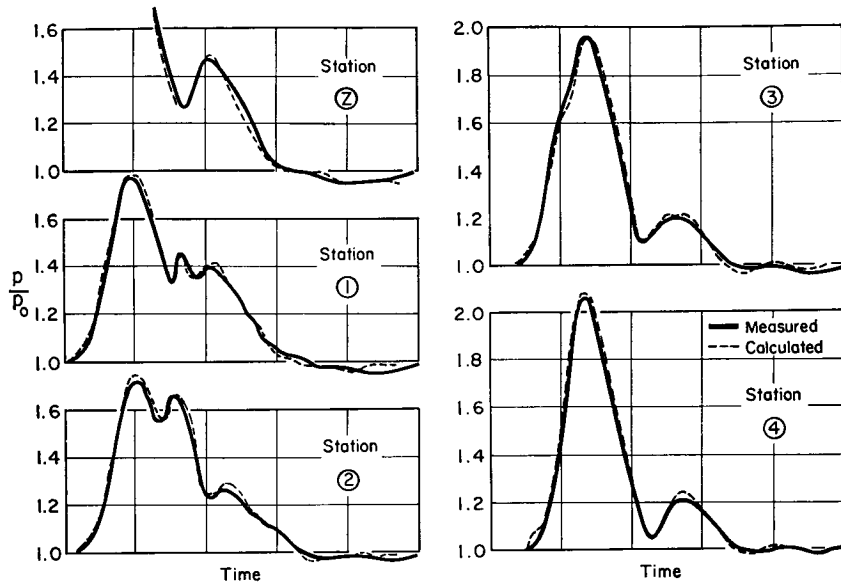


FIG. 24.27. (Continued)

are the results concerning (i) the regions where, for given types of *initial data*, the characteristics nets may be constructed; (ii) the concept of *regions of influence*; (iii) the concept of *domains of dependence*; and (iv) the *propagation of disturbances* in the solution along the physical characteristics.

### 24.9. Some Examples

**Development of Discharge from Reservoir.** Fig. 24.26<sup>(2)</sup> shows the results of applying the method of characteristics to the calculation of the way in which a high-pressure gas begins to discharge through a tube from a reservoir. The left-hand end of the tube is open to a reservoir of constant pressure. Initially, the right-hand end is closed by a valve and the gas in the system is stagnant. At  $t = 0$  the valve is suddenly opened, thus exposing the right-hand end to a region of very low pressure.

When the valve is opened, a simple rarefaction wave travels leftward into the duct. The front of the wave is at the state  $u = 0, c = c_0$ ; the rear is at the sonic condition,  $u/c_0 = c/c_0 = 2/(k + 1) = 0.833$ . When the left-running rarefaction waves reach the left-hand end they are reflected as compressions, the boundary condition at  $x/L = 0$  lying on the steady-state ellipse. Since the pressure in exhaust region is assumed to be very low, the boundary condition at  $x/L = 1$  always lies on the sonic line,  $u/c_0 = c/c_0$ .

From the steady-state solution it is known that at  $t = \infty$  the flow in the pipe is uniform, with  $u^*/c_0 = c^*/c_0 = \sqrt{2/(k + 1)} = 0.905$ . It may be seen from Fig. 24.26 that this condition is approximated with a value of  $c_0 t/L$  of about 5. At the right-hand end the steady-state sonic speed is attained with a value of  $c_0 t/L$  of only about 2 (this corresponds to the time required for a sound wave to travel the distance  $2L$  at the speed  $c_0$ ).

**Discharge Duct of Four-Stroke Engine.** Fig. 24.27<sup>(5,6)</sup> shows the calculated and measured time history of the events in the discharge duct of a four-stroke reciprocating engine. At the left-hand end is a rotating valve simulating the discharge port of the engine. At the right-hand end is a nozzle to simulate the nozzles of a blow-down turbine attached to the exhaust of the engine.

The agreement of the calculated with the measured pressure variations at several points in the duct (Fig. 24.27c) is seen to be remarkably good.

### REFERENCES AND SELECTED BIBLIOGRAPHY

1. COURANT, R., and FRIEDRICH, K. O. *Supersonic Flow and Shock Waves*. New York: Interscience Publishers, Inc., 1948.

2. DE HALLER, P. The Application of a Graphic Method to some Dynamics Problems in Gases, *Sulzer Technical Review*, No. 1 (1945), p. 6.
3. ROBERTS, R. C., and LIN, C. C. The Method of Characteristics in Compressible Flow, Part II (Unsteady Flow), *Air Materiel Command Report*, No. F-TR-1173D-ND (1947).
4. SAUER, R. Theory of the Nonstationary Gas Flow, Part I, Laminar Steady Gas Waves, *Air Materiel Command Translation*, No. F-TS-763-RE (1946).
5. JENNY, E. *Berechnungen und Modellversuche über Druckwellen Grosser Amplituden in Auspuff-Leitungen*, Doctoral dissertation, E.T.H., Zurich, Amabu-Druck, Basel, 1949.
6. JENNY, E. Unidimensional Transient Flow with Consideration of Friction, Heat Transfer, and Change of Section, *The Brown Boveri Review*, Vol. 37, No. 11 (1950), p. 447.
7. GUDERLEY, G. Nonstationary Gas Flow in Thin Pipes of Variable Cross-Section, *NACA Tech. Memo.*, No. 1196 (1948).
8. HESS, R. V. Study of Unsteady Flow Disturbances of Large and Small Amplitudes Moving Through Supersonic or Subsonic Steady Flows, *NACA Tech. Note*, No. 1878 (1949).

### PROBLEMS

- 24.1.** Draw to scale on a dimensionless physical plane ( $c_0 t/L$  versus  $x/L$ ) the characteristics lines and the path lines for the twelve possible cases corresponding to  $c/c_0 = 0.5, 1.0, 2.0$ , and  $u/c_0 = 0, 0.5, 1.0, 2.0$ .

For each of these cases illustrate on the physical plane and on the  $u, c$ -diagram the changes in fluid velocity and in slopes of the characteristics and path lines for (a) right-traveling compression waves, (b) left-traveling compression waves.

- 24.2.** Consider simple right-traveling waves in which properties at the forward end are denoted by subscript 1 and properties at the rear are denoted by subscript 2.

Demonstrate by means of binomial expansions the following approximate formulas which are useful for calculating simple waves of moderate amplitude:

$$c_2 = c_1 + \frac{k-1}{2} (u_2 - u_1)$$

$$p_2 = p_1 \left[ 1 + k \left( \frac{u_2 - u_1}{c_1} \right) + \frac{k(k+1)}{4} \left( \frac{u_2 - u_1}{c_1} \right)^2 + \dots \right]$$

$$\rho_2 = \rho_1 \left[ 1 + \frac{u_2 - u_1}{c_1} + \frac{3-k}{4} \left( \frac{u_2 - u_1}{c_1} \right)^2 + \dots \right]$$

Derive similar formulas for simple left-traveling waves.

- 24.3.** Consider a simple wave, the front end of which propagates into stagnant gas.

Show that the ratios of fluid properties at the front end to those at the rear end of the wave may be expressed in terms of the Mach Number at the rear end through the formulas

$$\frac{c}{c_1} = \left( \frac{T}{T_1} \right)^{\frac{1}{2}} = \left( \frac{p}{p_1} \right)^{\frac{k-1}{2k}} = \frac{1}{1 \mp \frac{k-1}{2} \frac{u}{c}}$$

where the upper sign refers to right-traveling waves, and subscript 1 denotes conditions in the stagnant gas.

**24.4.** Consider a simple rarefaction wave at the front end of which is stagnant air and the back end of which is moving at Mach Number unity. Find the ratio of the pressure at the back end to the pressure at the front end.

**24.5.** It is desired to investigate the importance of the nonlinearities of sound waves in the audible range of frequencies.

As one approach to this problem, suppose that a note of 5000 cycles per second is generated by a vibrating diaphragm at one end of a long tube. Assuming that the generated wave is sinusoidal in form, and neglecting reflections from the other end of the tube, plot versus sound intensity (decibels) the distance from the diaphragm at which the wave form becomes saw-toothed, that is, the distance at which shock waves are formed. Carry out the calculations over a range from 60 decibels to 160 decibels.

What conclusions do you reach from the results?

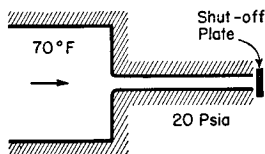
**24.6.** A tube 10 ft long containing air is closed at one end and is open to the atmosphere (14.7 psia) at the other end. At one instant of time the pressure and temperature are uniform throughout the tube, with respective values of 14.7 psia and 70°F. At the same instant the fluid velocity varies linearly from zero at the closed end to 500 ft/sec at the open end.

Find the variation with time of pressure and velocity at the center and ends of the tube for a total duration of 0.05 sec. Determine whether the states in the tube are cyclically repetitive or whether compression shocks are formed.

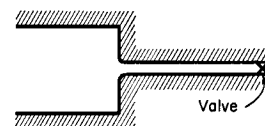
**24.7.** It is desired to estimate the time required for steady-state conditions to be reached after starting the flow in a long tube supplied from a constant-pressure reservoir.

Referring to the sketch, assume that initially the end of the tube is closed and that the air is at rest through the system. The end of the tube is suddenly opened to an atmosphere at 20 psia. Estimate the time required for the pressure and velocity at all sections of the tube to arrive within one per cent of their respective steady-state values, for initial pressures of (a) 100 psia, and (b) 25 psia.

Assume that the pressure in the reservoir does not change during the process, and that friction may be neglected. The tube is 10 ft long.



PROB. 24.7.



PROB. 24.8.

**24.8.** It is desired to investigate the time history of the shutting down of an initially steady flow.

Assume that initially air flows from the reservoir ( $p = 20$  psia,  $t = 100^\circ\text{F}$ )

through a tube 10 ft long without friction, and that it exhausts through a completely open valve to an atmosphere at 15 psia.

The valve is shut in a time of 0.01 sec. During this period, treat the valve as a nozzle whose cross-sectional area decreases linearly with time.

Estimate the time required for the velocity at all points in the tube to be reduced to one per cent of its initial value.

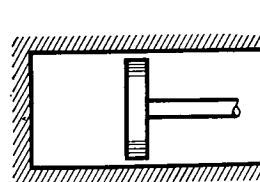
**24.9.** To investigate the importance of unsteady gas motions in the cylinder of a high-speed reciprocating engine, consider the simple model of a piston traveling in simple harmonic motion in a closed cylinder.

Suppose that initially the piston is at its outermost position and that there is stagnant air in the cylinder at 20 psia and 100°F. The piston then commences its simple harmonic motion.

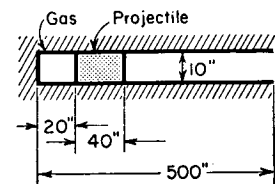
Assume that the ratio of maximum to minimum cylinder volumes is 10:1, that the average piston speed is 100 ft/sec (an unusually high value), and that the air processes are isentropic.

Plot the pressure on the cylinder head as a function of time, taking account of the unsteady gas motions.

Compare these results with the result obtained from the common assumption that the air is static and that the pressure and volume in the cylinder vary isentropically.



PROB. 24.9.



PROB. 24.10.

**24.10.** The sketch shows a simplified model of an artillery rifle at the moment after the powder charge is assumed to explode instantaneously and to be converted into gas at 40,000 psi and 6000°F.

To simplify the calculations, assume that at the instant shown by the sketch everything is stationary and that the gas has the properties of air. The projectile has a density of 400 lbm/ft<sup>3</sup>. During the acceleration of the projectile, ignore the pressure waves on the right-hand side of the projectile.

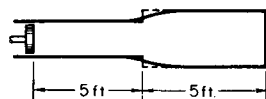
Estimate the muzzle velocity of the projectile, taking account of the unsteady motion of the burned gas.

Compare your result with the muzzle velocity calculated on the basis that the burned gas is stationary and uniform in properties during the process and that the gas pressure varies isentropically with its volume.

**24.11.** The sketch shows a piston in a tube of varying cross section with a closed end. For purposes of calculation the tube is replaced by two constant-area sections joined by a discontinuity in area. The larger tube is 10 per cent greater in cross-sectional area than the smaller.

Initially the piston is at rest, and the enclosed air is also at rest, with a pressure

of 100 psia and temperature of 100°F. The piston accelerates to the left at the rate of 100 ft/sec<sup>2</sup> for a time of 0.001 sec and then decelerates at the same rate until it is stationary again, after which it remains stationary.

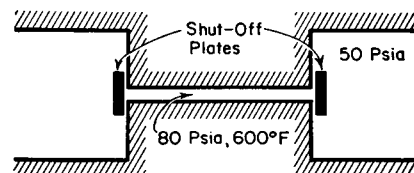


PROB. 24.11.

Plot versus time, for a duration of 0.05 sec, the pressure and velocity at the piston face, at the closed end, and at the center of the tube.

**24.12.** One of the processes of the Comprex is illustrated schematically in the sketch.

Air is initially at rest at uniform conditions of 80 psia, 600°F, in a tube 3 ft long. The right-hand shut-off plate is instantaneously opened.

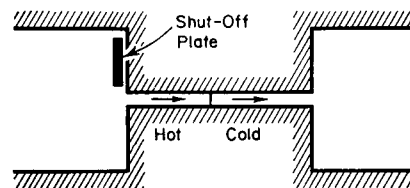


PROB. 24.12.

Find the pressure and velocity distribution in the tube (a) when the first part of the rarefaction wave reaches the left-hand shut-off plate, and (b) when the last part of the rarefaction wave reaches the left-hand shut-off plate.

**24.13.** One of the processes of the Comprex is illustrated schematically in the sketch.

Air flows in a tube (say, 3 ft long) between two reservoirs at 100 psia. At one instant of time there are two slugs of air in the tube, one at 70°F and the other at 600°F, but the entire mass of air moves with a uniform speed of 500 ft/sec.

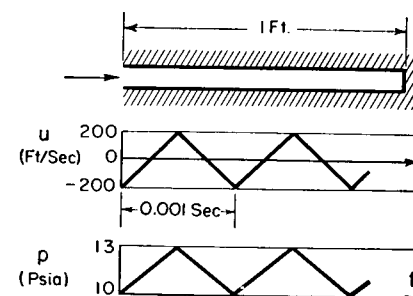


PROB. 24.13.

When the interface is one ft from the left-hand end, the left-hand end is instantaneously closed by the shut-off plate.

Find the velocity and pressure distribution when the interface reaches the right-hand end.

**24.14.** Suppose that a pitot tube is idealized in the form shown by the sketch, and that when placed in a pulsating flow the pressure and velocity at the open end vary with time as shown by the graph.



PROB. 24.14.

Estimate the time-average pressure on the right-hand end of the tube, assuming a mean air temperature in the tube of 70°F.

**24.15.** "Earnshaw's Paradox" states that a simple plane pressure wave of finite amplitude can propagate with unchanged form only in the case of a fluid with a special pressure-density relation.

Determine the necessary form of the pressure-density relation of the gas in order that the wave may propagate with unchanged form.

*Hint:* The motion appears steady to an observer moving with the wave.

**24.16.** Suppose that the pressure-volume isentrope of a perfect gas is approximated by a straight line which is tangent to the actual isentrope at some point in the range of states corresponding to a particular problem. The equation of the isentrope would then be

$$p = A + \frac{B}{\rho}$$

where  $A$  and  $B$  are constants.

- Find the equations of the physical, hodograph, and state characteristics.
- Show that simple waves propagate with unchanged form.

**24.17.** Investigate the nature of unsteady, constant-area, isentropic motions in a gas for which  $k = 1$ .

## Chapter 25

## UNSTEADY, ONE-DIMENSIONAL, SHOCK WAVES

## 25.1. Introductory Remarks

In the preceding chapter it was found that continuous compression waves continuously steepen and that ultimately a vertical tangent forms at some point of the wave, after which the type of flow postulated is no longer physically possible. When this occurs, it can mean only that one or more of the underlying assumptions break down.

The type of flow referred to is based on (i) the continuity equation, (ii) the dynamic equation, and (iii) the assumption that each fluid particle undergoes only isentropic changes in state. Of these three premises, the only one which can reasonably be abandoned is the last. In other words, when the *limit line*, or *envelope of the physical characteristics*, is first reached, we must seek solutions in which entropy increases may occur. How such entropy changes come about is explained below.

As the wave steepens toward a vertical tangent, the longitudinal velocity and temperature gradients approach infinity. Hence, no matter how small the coefficients of viscosity and thermal conductivity, longitudinal viscous stresses and longitudinal heat conduction, which have hitherto been assumed negligible, must ultimately become of the same order of magnitude as the other terms in the dynamic and energy equations. Accordingly, the type of flow originally assumed is severely modified. The vertical tangent to the wave is never formed in fact, because of the "spreading" or "smoothing-out" effects of viscosity and heat conduction. Instead, a zone of rapidly changing fluid properties is formed, within which viscous stresses and heat conduction play controlling roles. As time progresses, more and more of the compression wave merges into this zone, thus increasing the amplitude of the pressure change within the zone. Ultimately the entire compression wave is coalesced into a zone so thin that viscosity and heat conduction are significant for the complete wave and the wave subsequently propagates with unchanged form. The part of the wave with a nearly vertical tangent is called a *shock wave*, *compression shock*, or *shock front*. It is plain that the existence of viscous stresses and heat transfer within the zone of the shock wave leads in general to nonisentropic changes of state for a fluid particle.

Within the shock wave all fluid properties change continuously. A complete analysis should recognize this state of affairs and the viscous and heat conduction effects which go with it. Only under greatly simplifying assumptions, however, and only with considerable mathematical complexity, can the conditions within the shock wave be solved for.

From a practical point of view, on the other hand, it is almost never necessary to take account of conditions within the shock wave. Theoretical analyses <sup>(8)</sup> (Chapter 5) indicate that the shock-wave thickness is of the order of only a few mean free molecular path lengths. Experiments with x-ray reflection confirm the theory, and spark photographs show the shock waves as lines so thin that their widths cannot be measured. As a result of this happy circumstance we may assume for purposes of calculation that the shock wave is so thin that it may be replaced by a simple model in which all fluid properties change discontinuously across a mathematical line. This line will henceforth be called the shock wave.

In making calculations according to this model of the shock, we need consider only conditions fore and aft of the shock wave. Although viscous stresses and heat transfer are significant within the wave, and in fact determine the form of the wave, the change from the initial to the final conditions of the discontinuity may be treated as occurring without external friction and heat transfer, because the shock zone is so thin that heat transfer and friction from bodies external to the gas stream (such as the walls of a duct) are negligibly small.

In this chapter we shall consider one-dimensional shock discontinuities which, in general, are not stationary. After discussing the general relations governing moving shocks we shall see how many of the calculations may be simplified when we are dealing with weak shocks. The reflections of shock waves from the ends of a duct will be investigated, as will the interactions of shocks with each other and with continuous waves. The passage of shocks through regions of changing cross-sectional area and through zones of varying entropy will also be discussed.

Additional material relevant to the subject matter of this chapter may be found in Chapters 3, 5, 23, and 24.

## NOMENCLATURE

$c$	speed of sound	$W$	speed of shock relative to gas into which it propagates
$c^*$	critical speed of sound for steady, adiabatic flow	$x$	longitudinal coordinate
$c_p$	specific heat at constant pressure	$\rho$	mass density
$c_v$	specific heat at constant volume	( $)_x$	signifies conditions upstream of stationary shock
$h$	enthalpy per unit mass	( $)_y$	signifies conditions downstream of stationary shock
$k$	ratio of specific heats	( $)_1$	signifies conditions on front side of moving shock
$M$	Mach Number	( $)_2$	signifies conditions on back side of moving shock
$M^*$	$V/c^*$	[ $O$ ]	signifies "terms of the order of"
$p$	pressure		
$R$	gas constant		
$T$	temperature		
$t$	time		
$u$	speed in $x$ -direction		
$V$	speed		

## 25.2. Analysis in Terms of Stationary Shock Formulas

In the special case where a shock of constant strength (i.e., constant pressure rise) travels into a region of constant fluid properties, the shock will travel with constant speed and all fluid properties aft of the shock will be constant. Therefore, by imagining that the observer travels with the uniform linear speed of the shock, the phenomenon may be reduced to one of steady flow. The one-dimensional shock relations of Chapter 5 may accordingly be applied directly in the new system of coordinates.

In the more general case where the shock is of variable strength and is traveling into a region of variable fluid properties, the shock will travel with variable speed and the fluid properties aft of the shock will also be variable from instant to instant. At first sight it might appear, therefore, that the phenomenon could not be reduced to one of steady flow. However, we recall that the shock zone may with good accuracy be treated as a discontinuity. Hence, if the observer moves with the shock, and if the continuity, momentum, and energy equations are written for a control surface which encloses only the shock, the unsteady-flow terms pertaining to the time rates of change of mass, momentum, and internal plus kinetic energy within the control volume are equal to zero. From this it follows that the steady-flow relations are applicable to the states on the two sides of the variable shock.

We conclude, therefore, that the flow through a shock discontinuity may be considered as quasi-steady (i.e., it may be treated as though it were steady at each instant of time) in terms of the properties seen by an observer to whom the shock is stationary. The steady-flow normal

shock relations of Chapter 5 may therefore be applied in terms of a coordinate system which moves with the shock.

**Stationary Shock Formulas.** For the coordinate system moving with the shock let us (as in Chapter 5) denote the state of the gas moving *toward* the shock by subscript  $x$ , and the state of the gas moving *away* from the shock by subscript  $y$ . The important formulas of Chapter 5, relating the fluid properties on the two sides of a stationary shock, are summarized below for convenient reference.

$$M_y^2 = \frac{M_x^2 + \frac{2}{k-1}}{\frac{2k}{k-1} M_x^2 - 1} \quad (25.1)$$

$$V_x V_y = c^{*2} \quad (25.2)$$

$$\frac{V_y}{V_x} = \frac{1}{M_x^{*2}} = \frac{1 + \frac{k-1}{2} M_x^2}{\frac{k+1}{2} M_x^2} \quad (25.3)$$

$$\frac{p_y}{p_x} = \frac{2k}{k+1} M_x^2 - \frac{k-1}{k+1} \quad (25.4)$$

$$\left(\frac{c_y}{c_x}\right)^2 = \frac{T_y}{T_x} = \frac{\left(1 + \frac{k-1}{2} M_x^2\right) \left(\frac{2k}{k-1} M_x^2 - 1\right)}{\frac{(k+1)^2}{2(k-1)} M_x^2} \quad (25.5)$$

The graphs or tables (Appendix B) representing these formulas, with  $M_x$  as the independent argument, may conveniently be employed for numerical calculations.

It will be recalled that, as a consequence of the second law of thermodynamics, the gas enters the shock with a speed which is supersonic relative to the shock, and that it leaves with a speed which is subsonic relative to the shock. As the gas crosses the shock, the speed relative to the shock decreases in absolute magnitude, and the pressure, temperature, density, and sound velocity all increase.

**Moving Shocks.** Now let us consider the moving shock. The *front side* of the shock is defined as the side into which a gas particle enters, and the *back side* as that from which a gas particle leaves. Let us denote by subscript 1 conditions on the front side, and by subscript 2 conditions on the back side. Then state 1 of the moving shock corresponds to state  $x$  of the stationary shock and, likewise, states 2 and  $y$  correspond. As in the case of continuous waves, there are two families of shocks: (i) *right-traveling shocks*, which travel rightward *relative to*

the gas, and (ii) *left-traveling shocks*, which travel leftward *relative to the gas*. By our previous definitions, therefore, the front of a right-traveling shock is always on the right-hand side of the shock line, and the front of a left-traveling shock is always on the left-hand side of the shock line.

Let us denote the velocity of the shock *relative to the gas* into which it moves (i.e., the gas in state 1) by  $\pm W$ , where  $W$  is always a positive number. The upper sign represents right-traveling waves and the lower sign left-traveling waves.

**RIGHT-TRAVELING SHOCK.** A right-traveling shock is shown in Fig. 25.1a. According to our convention the gas on the front side of the

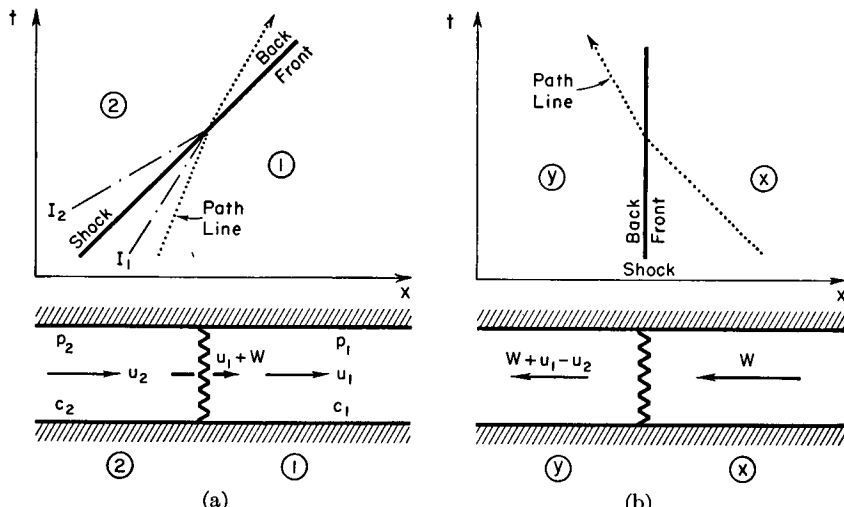


FIG. 25.1. Right-traveling shock.

- (a) Moving shock in stationary coordinate system.  
(b) Stationary shock in moving coordinate system.

shock, into which the shock moves, is denoted by state 1; and the gas on the back side, over which the shock has passed, by state 2. The velocity of the moving shock is then  $(u_1 + W)$ , and, since  $W$  is always positive, it is clear that the shock overtakes the gas in region 1. Now we imagine that the observer moves with the shock. This is equivalent to adding the velocity  $(-u_1 - W)$  to all the velocities in Fig. 25.1a, and leads to the flow pattern of Fig. 25.1b, with the shock stationary.

**LEFT-TRAVELING SHOCK.** In Fig. 25.2 a similar coordinate transformation is shown for a left-traveling shock. Here the gas into which the shock travels is on the left of the shock, and the speed of the shock is  $(u_1 - W)$ . Since  $W$  is always positive, this result is in accord with the convention that the gas in state 1 travels into the shock.

**TRANSFORMATION OF STATIONARY SHOCK FORMULAS.** Such thermodynamic properties as the pressure, temperature, density, and sound velocity are not influenced by the motion of the observer. Hence,

$$p_1 = p_x; \quad p_2 = p_y \quad (25.6)$$

$$T_1 = T_x; \quad T_2 = T_y \quad (25.7)$$

$$\rho_1 = \rho_x; \quad \rho_2 = \rho_y \quad (25.8)$$

$$c_1 = c_x; \quad c_2 = c_y \quad (25.9)$$

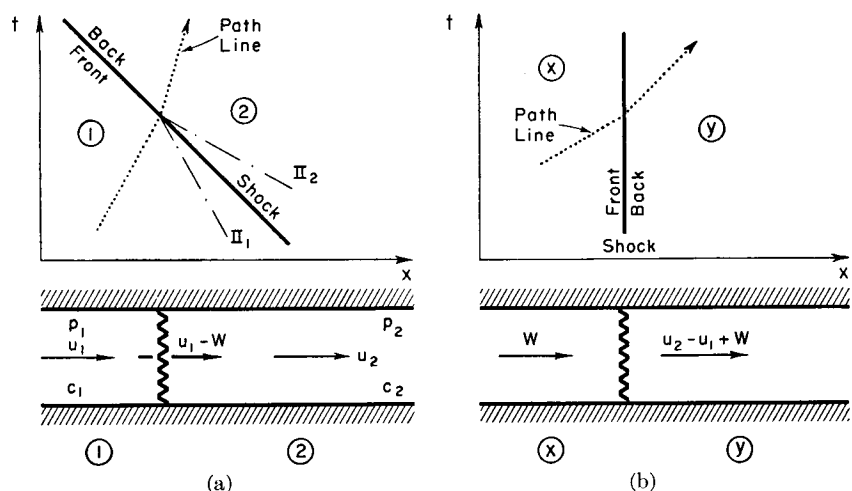


FIG. 25.2. Left-traveling shock.

- (a) Moving shock in stationary coordinate system.  
(b) Stationary shock in moving coordinate system.

Letting  $V$  represent the gas speed for the steady-flow picture, reference to Figs. 25.1b and 25.2b leads to the following transformation formulas in respect to velocities:

$$V_x = W \quad (25.10a)$$

$$V_y = W \pm (u_1 - u_2) \quad (25.10b)$$

where the upper sign refers to right-traveling waves. Then the steady-flow Mach Numbers may be expressed in terms of the moving-shock variables by the relations

$$M_x = \frac{V_x}{c_x} = \frac{W}{c_1} \quad (25.11a)$$

$$M_y = \frac{V_y}{c_y} = \frac{W \pm (u_1 - u_2)}{c_2} \quad (25.11b)$$

Using the transformation formulas of Eqs. 25.6 to 25.11, numerical calculations for moving shocks may now easily be carried out with the help of the one-dimensional, normal shock tables.

**EXAMPLE.** As an illustration, suppose that we are given the fluid properties in state 1 as

$$u_1 = 200 \text{ ft/sec}; \quad c_1 = 1000 \text{ ft/sec}; \quad p_1 = 10 \text{ psia}$$

and that a right-traveling shock with a speed of 2200 ft/sec travels into region 1. What are the corresponding fluid properties in state 2?

Since we are given  $u_1 + W = 2200$ , it follows that  $W = 2000$ . Hence,  $M_x = W/c_1 = 2000/1000 = 2$ . Now, from Table B.3, with  $k = 1.4$  and  $M_x = 2.0$ , we find

$$M_y = 0.577; \quad p_y/p_x = 4.500; \quad V_x/V_y = 2.667; \quad T_y/T_x = 1.688$$

Then

$$c_2 = c_1 \frac{c_2}{c_1} = c_1 \sqrt{\frac{T_y}{T_x}} = 1000 \sqrt{1.688} = 1300 \text{ ft/sec}$$

$$p_2 = 10(4.50) = 45.0 \text{ psia}$$

$$\frac{V_x}{V_y} = 2.667 = \frac{W}{W + u_1 - u_2}; \quad \therefore u_2 = 1450 \text{ ft/sec}$$

As a check, using Eq. 25.11b,

$$M_y = \frac{2000 + 200 - 1450}{1300} = 0.577$$

Another situation that often arises in practical problems is that the conditions in state 1 and the pressure ratio across the shock are given. For the given pressure ratio, there may be found from the tables the values of  $M_x$ ,  $M_y$ ,  $p_y/p_x$ ,  $T_y/T_x$ , etc. Then  $W$  may be found from Eq. 25.11a, and  $u_2$  from Eq. 25.10b. The remaining fluid properties may be found as in the preceding example.

**Shock Configurations.** It should be noted that  $u_1$  and  $u_2$  are to be treated as algebraic quantities which may be either positive or negative, but that  $W$  is always a positive number. Keeping this in mind, it is possible to show that there are seven different configurations for either right-traveling or left-traveling shocks.

Considering for the present only right-traveling shocks, Fig. 25.1 shows two configurations. The remaining configurations are easily found by following the rule that during a coordinate transformation the shock path and particle paths all rotate in the same direction, although not by the same amount; they are illustrated in Fig. 25.3.

In Fig. 25.3a the gas in front of the shock is at rest, and the gas behind the shock follows the shock. This situation would obtain if a piston were suddenly accelerated rightward into a stagnant gas.

In Fig. 25.3b the gas in front of the shock is traveling to the left, and the gas behind the shock is stationary. This situation would obtain if a gas traveling leftward were suddenly brought to rest at a closed end.

In Fig. 25.3c the gas particles on the two sides of the shock discontinuity travel in opposite directions.

In Fig. 25.3d the gas moves leftward on both sides of the shock, but the shock moves rightward.

In Fig. 25.3e the gas moves leftward on both sides of the shock and the latter, too, moves leftward. In other words, the shock moves to the left in absolute coordinates, although according to our definition it is a right-traveling shock relative to the gas.

Similar considerations apply to left-traveling shocks.

**Interaction of Shocks with Continuous Waves.** Let us now see how the shock speed compares with the speed of propagation of small pressure waves in the gas before and after the shock. First considering right-traveling shocks, we recall that  $u_1 + W$  is the shock speed,  $u_1 + c_1$  is the propagation speed of small disturbances in the gas before the shock, and  $u_2 + c_2$  is the propagation speed of small disturbances in the gas behind the shock. Now, since  $M_x$  is always greater than unity, it follows from Eq. 25.11a that

$$W > c_1$$

or, adding  $u_1$  to both sides, that

$$u_1 + W > u_1 + c_1 \quad (25.12)$$

Furthermore,  $M_y$  is always less than unity, and hence, from Eq. 25.11b,

$$W + u_1 - u_2 < c_2$$

or,

$$u_1 + W < u_2 + c_2 \quad (25.13)$$

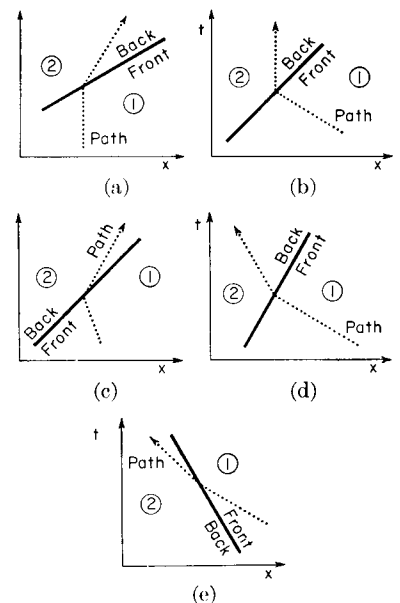


FIG. 25.3. Some flow configurations for right-traveling shocks.

What do these equations mean? Eq. 25.12 shows that the shock travels faster than small pressure waves in the gas ahead of the shock, and Eq. 25.13 shows that the shock travels slower than small pressure waves in the gas behind the shock. By pursuing similar arguments, the same conclusions would be obtained for left-traveling shocks. Thus we reach the general rule that *shock waves always overtake continuous waves of the same family in the region ahead of the shock, and are always overtaken by continuous waves of the same family in the region behind the shock.*

These results are illustrated in Figs. 25.1 and 25.2, which show the relative directions of the physical characteristics (corresponding to the paths of propagation of small pressure waves) in the regions ahead of and behind the shock.

If the shock overtakes a continuous compression wave of the same family, the continuous wave is gradually absorbed into the shock wave and the latter grows stronger. On the other hand, if the shock overtakes a continuous rarefaction wave of the same family the two tend to cancel each other, the rarefaction wave gradually disappearing and the shock wave gradually weakening.

If the shock is overtaken by a continuous compression wave of the same family, the two coalesce, the continuous wave gradually disappearing as the shock wave grows stronger. On the other hand, if the shock is overtaken by a continuous rarefaction wave of the same family, the two tend to cancel each other, the rarefaction wave gradually disappearing and the shock wave gradually weakening.

### 25.3. Analysis of Moving Shocks

In the preceding article it was shown how the changes across moving shocks may be calculated with the familiar formulas, tables, and graphs for one-dimensional, steady, normal shocks. Often it is desirable to have relations which apply directly to moving shocks, especially where graphical methods are being employed. Let us, therefore, derive such relations and see what graphical methods may be developed. The ratio  $W/c_1$ , that is,  $\mathbf{M}_x$ , will be used as the independent variable.

**Derivation of Formulas.** We begin by writing the governing physical equations in terms of the notation of Figs. 25.1 and 25.2.

$$\text{Continuity: } \rho_1 W = \rho_2 [W \pm (u_1 - u_2)] \quad (25.14)$$

$$\text{Momentum: } p_1 + \rho_1 W^2 = p_2 + \rho_2 [W \pm (u_1 - u_2)]^2 \quad (25.15)$$

$$\text{Energy: } h_1 + \frac{W^2}{2} = h_2 + \frac{[W \pm (u_1 - u_2)]^2}{2} \quad (25.16)$$

$$\text{Perfect Gas: } h_2 - h_1 = c_p(T_2 - T_1) \quad (25.17a)$$

$$c_p - c_v = R; \quad c_p/c_v = k \quad (25.17b)$$

$$c^2 = kRT \quad (25.17c)$$

$$p = \rho RT = \rho c^2/k \quad (25.17d)$$

As in our previous analyses, the upper sign always refers to right-traveling waves and the lower sign to left-traveling waves.

From Eqs. 25.17a, 25.17b, and 25.17c, we get

$$h_2 - h_1 = \frac{1}{k-1} (c_2^2 - c_1^2)$$

Substituting this relation into Eq. 25.16 and simplifying, we obtain

$$c_2^2 - c_1^2 = -\frac{k-1}{2} (u_1 - u_2)[(u_1 - u_2) \pm 2W] \quad (25.18)$$

Elimination of  $\rho_2$  from Eq. 25.15 with the value found from Eq. 25.14 yields, after rearrangement,

$$p_1 - p_2 = \pm \rho_1 W (u_1 - u_2) \quad (25.19)$$

Writing  $p$  in terms of  $\rho$  and  $c$  according to Eq. 25.17d, and eliminating  $\rho_2$  with the help of Eq. 25.14, Eq. 25.19 may be reduced to

$$\frac{c_1^2}{W \pm (u_1 - u_2)} c_2^2 = \pm kW(u_1 - u_2)$$

Solving for  $c_2^2$ , and substituting the resulting expression into Eq. 25.18, we obtain an expression for the velocity change in the form

$$\frac{u_2 - u_1}{c_1} = \pm \frac{2}{k+1} \left( \frac{W}{c_1} - \frac{c_1}{W} \right) = \pm \frac{2}{k+1} \left( \mathbf{M}_x - \frac{1}{\mathbf{M}_x} \right) \quad (25.20)$$

Substituting this value for  $u_2 - u_1$  into Eq. 25.18 and simplifying, we get

$$\begin{aligned} \left( \frac{c_2}{c_1} \right)^2 &= 1 + \frac{2(k-1)}{(k+1)^2} \left[ k \left( \frac{W}{c_1} \right)^2 - \left( \frac{c_1}{W} \right)^2 - (k-1) \right] \\ &= 1 + \frac{2(k-1)}{(k+1)^2} \left[ k \mathbf{M}_x^2 - \frac{1}{\mathbf{M}_x^2} - (k-1) \right] \end{aligned} \quad (25.21)$$

Eliminating  $u_2 - u_1$  from Eqs. 25.20 and Eq. 25.14, we obtain for the density ratio

$$\frac{\rho_2}{\rho_1} = \frac{1}{1 - \frac{2}{k+1} \left[ 1 - \left( \frac{c_1}{W} \right)^2 \right]} = \frac{1}{1 - \frac{2}{k+1} \left( 1 - \frac{1}{\mathbf{M}_x^2} \right)} \quad (25.22)$$

Setting Eq. 25.20 into Eq. 25.19, and making use of Eq. 25.17d, we find the pressure ratio to be given by

$$\frac{p_2}{p_1} = 1 + \frac{2k}{k+1} \left[ \left( \frac{W}{c_1} \right)^2 - 1 \right] = 1 + \frac{2k}{k+1} (\mathbf{M}_x^2 - 1) \quad (25.23)$$

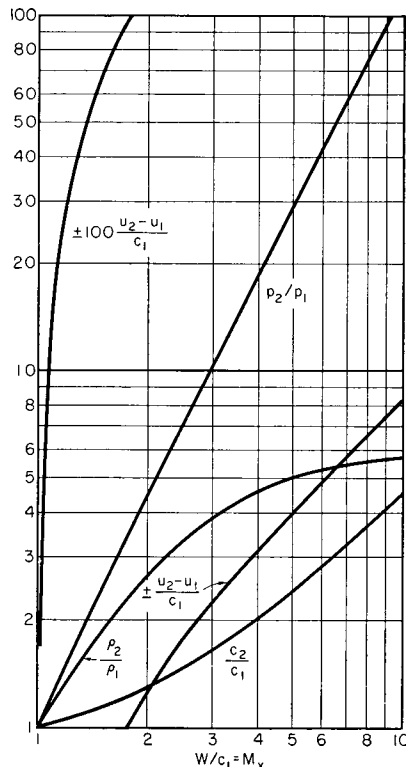


FIG. 25.4. Working chart for moving shocks ( $k = 1.4$ ).

$$\frac{u_2 - u_1}{c_1} \cong \pm \frac{2}{k+1} \frac{W}{c_1} \quad (25.24)$$

$$\left( \frac{c_2}{c_1} \right)^2 \cong \frac{2k(k-1)}{(k+1)^2} \left( \frac{W}{c_1} \right)^2 \quad (25.25)$$

$$\frac{p_2}{p_1} \cong \frac{k+1}{k-1} \quad (\cong 6 \text{ for air}) \quad (25.26)$$

$$\frac{p_2}{p_1} \cong \frac{2k}{k+1} \left( \frac{W}{c_1} \right)^2 \quad (25.27)$$

Thus, for strong shocks the pressure ratio varies in proportion to the square of the Mach Number  $W/c_1$ , the velocity change increases

in direct proportion to  $W/c_1$ , the density ratio remains approximately constant with a value of about 6, and the ratio of sonic speeds is directly proportional to  $W/c_1$ .

As a practical example, consider a strong shock wave advancing into stationary air, in which case the absolute wave speed is  $W$ . Then Eqs. 25.24 and 25.27 show that the gas behind the wave travels approximately with the speed of the wave and that the wave speed is larger than the speed of sound in the stationary gas by a factor equal approximately to the square root of the pressure ratio. In a detonation wave with a pressure ratio of, say, 100, the wave speed and the gas speed behind the wave would be of the order of ten times the speed of sound in the undisturbed gas.

**Very Weak Shocks.** Turning now to the case of very weak shocks, Eq. 25.23 shows that the criterion in this respect is that  $\mathbf{M}_x$  be near unity, or, mathematically, that  $(\mathbf{M}_x - 1) \ll 1$ . Making this assumption, Eqs. 25.20 to 25.23 take the following approximate forms:

$$\frac{u_2 - u_1}{c_1} \cong \pm \frac{4}{k+1} (\mathbf{M}_x - 1) \quad (25.28a)$$

$$\left( \frac{c_2}{c_1} \right)^2 \cong 1 + \frac{4(k-1)}{k+1} (\mathbf{M}_x - 1) \quad (25.29a)$$

$$\frac{p_2}{p_1} \cong 1 + \frac{4k}{k+1} (\mathbf{M}_x - 1) \quad (25.30a)$$

$$\frac{\rho_2}{\rho_1} \cong 1 + \frac{4}{k+1} (\mathbf{M}_x - 1) \quad (25.31a)$$

Now, employing the notation that

$$\frac{c_2}{c_1} = \frac{c_1 + \Delta c}{c_1} = 1 + \frac{\Delta c}{c_1}, \quad \text{etc.}$$

these may be put in the form

$$\Delta u/c_1 \cong \frac{4}{k+1} (\mathbf{M}_x - 1) \quad (25.28b)$$

$$\Delta c/c_1 \cong \frac{2(k-1)}{k+1} (\mathbf{M}_x - 1) \quad (25.29b)$$

$$\Delta p/p_1 \cong \frac{4k}{k+1} (\mathbf{M}_x - 1) \quad (25.30b)$$

$$\Delta \rho/\rho_1 \cong \frac{4}{k+1} (\mathbf{M}_x - 1) \quad (25.31b)$$

From the last set of equations we obtain

$$\frac{\Delta c}{\Delta u} \cong \pm \frac{k-1}{2}; \quad \frac{\Delta p}{\Delta u} \cong \pm k \frac{p_1}{c_1} = \pm \rho_1 c_1; \quad \frac{\Delta p}{\Delta \rho} = c_1^2$$

By comparison of these with the results of the linearized analysis of Chapter 23 and with the characteristics analysis of Chapter 24, we draw the conclusion that *very weak shock waves are approximately equivalent to continuous, isentropic compression waves*.

As a practical example, consider a weak shock wave advancing into stationary air, in which case the absolute wave speed is  $W$ . Then Eqs. 25.28b and 25.30b may be put in the form

$$\frac{\Delta p}{p} \cong \frac{4k}{k+1} \frac{W - c_1}{c_1}; \quad u_2 \cong \pm \frac{4}{k+1} (W - c_1)$$

These indicate (i) that the percentage by which the wave speed exceeds the sound speed is approximately half the percentage pressure rise through the wave, and (ii) that the gas speed behind the wave is approximately twice as large as the excess of wave speed over sound speed. A shock wave with a 10 per cent pressure rise travels about 4 per cent faster than a sound wave; with a sound speed of, say, 1000 ft/sec, the gas behind such a shock would have a speed of about 70 ft/sec.

**Graphical Shock Polars.** For simple waves we found it convenient to map the series of states through the wave on the  $u, c$ -state diagram, and we learned that all states in a simple wave map on a single state characteristic. Let us represent in a similar manner the states fore and aft of a moving shock on the  $u, c$ -diagram. By analogy with the hodograph shock-polar representation of two-dimensional, steady, oblique shocks, the  $u, c$ -chart for moving shocks is called the  $u, c$ -shock polar.

**FORM OF SHOCK POLARS.** The relations defining the  $u, c$ -shock polars are Eqs. 25.20 and 25.21, where  $M_x$  appears as a parameter. For arbitrarily selected values of  $M_x$  there may be calculated the corresponding values of  $(u_2/c_1) - (u_1/c_1)$  and of  $c_2/c_1$ . The resulting curve (Fig. 25.5), on which the values of  $M_x$  are marked, is a dimensionless and generalized form of the shock polar.

In any specific case, with given values of  $u_1$  and  $c_1$  before the shock, the general curve of Fig. 25.5 may be replotted (by appropriate changes in the horizontal and vertical scales) in terms of  $u_2$  and  $c_2$ , as in Fig. 25.6. The intersection of the two branches of the curve represents the conditions before the shock, defined by  $u_1$  and  $c_1$ . The right-hand branch represents all states (in terms of  $u_2$  and  $c_2$ ) which may be reached from state 1 through a right-traveling shock, and the value of  $M_x$  at each such state 2 represents the dimensionless relative shock speed,  $W/c_1$ . Similarly, the left-hand branch represents states which may be reached from state 1 across a left-traveling shock.

**CONSTRUCTION OF FAMILIES OF SHOCK POLARS.** For graphical purposes it is desirable to have a chart like Fig. 25.6 with a great many shock polars on it. Since each shock polar is defined by given values of  $u_1$  and  $c_1$ , it is evident that the number of shock polars is doubly

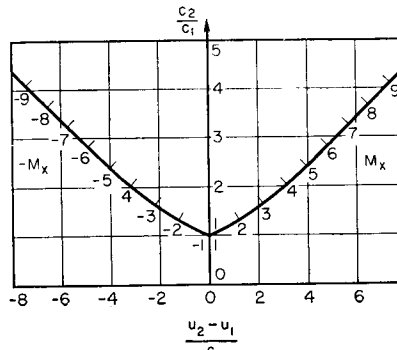


FIG. 25.5. Generalized  $u, c$ -shock polar ( $k = 1.4$ ).

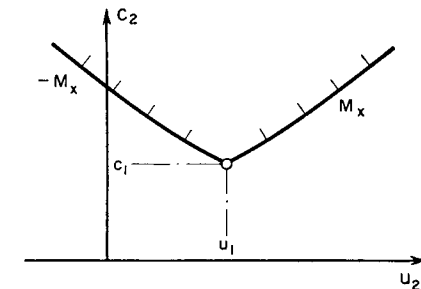


FIG. 25.6. Shock polar for specific values of  $u_1$  and  $c_1$ .

infinite. However, Eqs. 25.20 and 25.21 show that if we consider shock polars having the same value of  $c_1$ , a change in  $u_1$  produces an equal change in  $u_2$ . Hence all shock polars for a given  $c_1$  may be generated by horizontally sliding the shock polar for  $u_1 = 0$  until the apex of the shock polar is at the proper value of  $u_1$ . Therefore, if the shock polars for  $u_1 = 0$  and different values of  $c_1$  are drawn on a single sheet, the shock polars for other values of  $u_1$  may easily be found by sliding this master sheet under a sheet of tracing paper.

With regard to the effect of  $c_1$  on the individual shock polars, Eq. 25.21 shows that for a given value of  $M_x$ ,  $c_2$  is proportional to  $c_1$ . For the same value of  $M_x$ , furthermore,  $u_2$  (with  $u_1 = 0$ ) is also proportional to  $c_1$ . Therefore the ratio of  $c_2$  to  $u_2$  (with  $u_1 = 0$ ) depends only on  $M_x$ . Lines of constant  $M_x$  are therefore radial lines passing through the origin. With these rules it is easy to draw the family of shock polars with  $u_1 = 0$ , provided that there has first been drawn a single shock polar for a specific value of  $c_1$ .

The rules outlined above permit all shock polars to be drawn from a single master shock polar.

**PROPERTIES OF SHOCK POLARS.** Since the individual shock polars which cover the  $u, c$ -plane are transformations of the generalized shock polar of Fig. 25.5, we may use the latter curve for studying the properties of all shock polars.

First of all, we note that the branches of the curves extending below the point of intersection of the two branches correspond to values of  $M_x$  less than unity, and therefore are physically not real. To find the

slope of the curves at their intersection, that is, at  $M_x = 1$ , we differentiate Eqs. 25.20 and 25.21 with respect to  $M_x$ , and thus we obtain

$$\left[ \frac{d(c_2/c_1)}{dM_x} \right] \left/ \left[ \frac{d(u_2 - u_1)}{dM_x} \right] \right|_{M_x=1} \rightarrow \pm \frac{k-1}{2}$$

This shows that for  $M_x$  equal to unity, corresponding to very weak shocks, the shock polar has the same slope as the  $u, c$ -characteristic (Arts. 24.2 and 24.3). By differentiating further, we find that

$$\left( \frac{d^2c}{du^2} \right)_{M_x=1} \rightarrow 0; \quad \left( \frac{d^3c}{du^3} \right)_{M_x=1} \neq 0$$

from which we conclude that the shock polar is identical with the characteristic curve (see Fig. 25.11) up to terms of second order in  $(u_2 - u_1)$ . In other words, weak shocks may, for calculation purposes, be treated as continuous, simple, compression waves.

For very strong shocks differentiation of Eqs. 25.20 and 25.21, with  $M_x \rightarrow \infty$ , yields

$$\left[ \frac{d(c_2/c_1)}{d\left( \frac{u_2 - u_1}{c_1} \right)} \right]_{M_x \rightarrow \infty} \rightarrow \pm \sqrt{\frac{k(k-1)}{2}} \quad (= 0.53 \text{ for air})$$

Therefore the dimensionless shock polar is asymptotic to a line with slope  $\pm 0.53$  for  $k = 1.4$ .

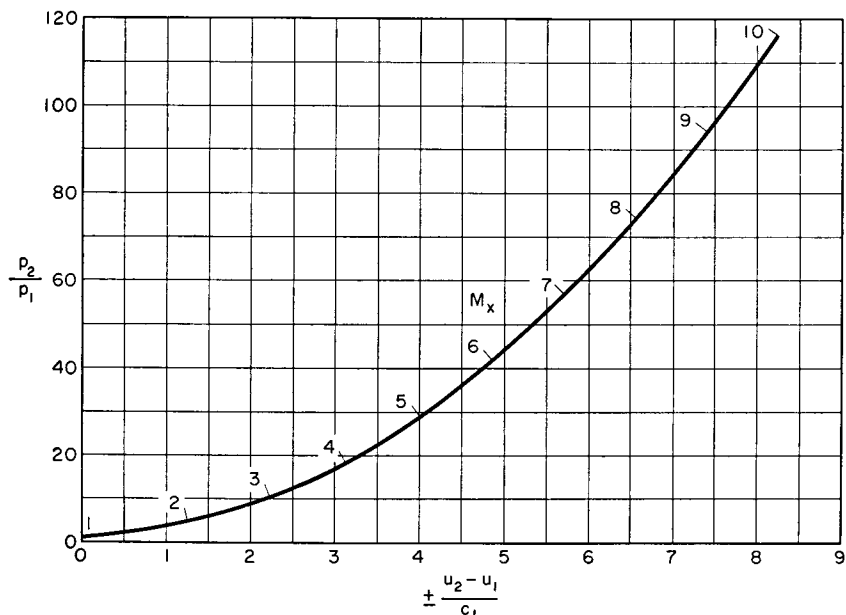


FIG. 25.7. Generalized  $p, u$ -shock polar ( $k = 1.4$ ).

THE  $u, p$ -SHOCK POLARS. Whenever shocks are involved, entropy increases occur, and there is a possibility of forming contact surfaces between adjacent slugs of gas having different temperatures, as previously mentioned in Chapter 24. The masses of gas adjacent to each other at the contact line have equal velocities and pressures. For this reason, it is often convenient for graphical purposes to employ the  $u, p$ -shock polars rather than the  $u, c$ -shock polars described above.

The generalized  $u, p$ -shock polar is defined parametrically by Eqs. 25.20 and 25.23, and is plotted in Fig. 25.7. Individual shock polars, corresponding to specific values of  $u_1$  and  $p_1$ , may be generated from a master shock polar in the same way as was described for the  $u, c$ -shock polars.

#### 25.4. The Shock Tube—Riemann's Problem

As an example of the foregoing discussions, let us consider one of the problems which stimulated the researches of the great mathematician, Riemann, into the properties of nonlinear partial differential equations.

A long tube (Fig. 25.8) is initially divided into two parts by a diaphragm, on the left-hand side of which there is high-pressure stagnant gas, and on the right-hand side of which there is low-pressure stagnant gas. The temperatures, and hence the sound velocities, are alike for states 1 and 3. When the diaphragm is broken, a right-traveling shock propagates into gas 1, and a left-traveling rarefaction wave travels into gas 3. Denoting the state after the shock by 2, and the state after the rarefaction wave by 4, it is evident that  $p_2 = p_4$  and  $u_2 = u_4$ . However, since there is no entropy change between 3 and 4, and since there is an entropy increase across the shock from 1 to 2, the temperatures in zones 2 and 4 are not alike. A contact discontinuity therefore separates the two adjacent slugs of gas which have been respectively accelerated by the shock wave and rarefaction wave.

It will be noted that this problem is the extension to large amplitudes of the first part of the linearized example of Art. 23.6.

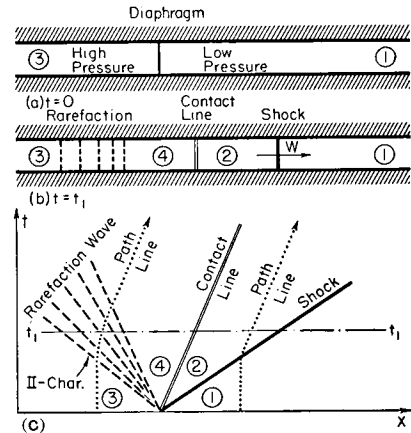


FIG. 25.8. The shock tube.

- (a) Flow pattern at  $t = 0$ .
- (b) Flow pattern at  $t = t_1$ .
- (c) Physical plane, showing shock wave, rarefaction wave, contact discontinuity, and path lines.

The process described here is one around which simple experiments may be devised for making measurements on shock waves and rarefaction waves.<sup>(7,11,12)</sup> The experimental apparatus is usually called a shock tube. It may also be used as a simple wind tunnel because there are locations where the flow is uniform and supersonic for finite periods of time. Additional subjects accessible to study by the shock tube include the structure of shock fronts, wave interactions, wave diffraction and refraction, shock loading of structures, measurement of speed of sound, relaxation phenomena, flame propagation, chemical reaction kinetics, and atomic physics of nonequilibrium states.

We shall show how numerical results may be obtained by three methods: (i) by using the steady, normal shock tables; (ii) by employing analytical shock relations; and (iii) by employing the  $u, p$ -shock polar. The problem is to find  $p_1/p_2$ ,  $u_2/c_1$ , and  $W/c_1$  as functions of  $p_1/p_3$ .

**Solution with Normal Shock Tables.** Select an arbitrary value of  $M_x = W/c_1$ . From the shock tables, find  $p_y/p_x = p_2/p_1$ ;  $T_y/T_x = T_2/T_1$ ; and  $M_y = (W - u_2)/c_2$ . Then, since  $T_2/T_1 = (c_2/c_1)^2$ , calculate  $u_2/c_1$ . But  $u_2/c_1 = u_4/c_3$ . Therefore, from the simple-wave relation, Eq. 24.25, calculate  $p_4/p_3 = p_2/p_3$ . Finally, compute  $p_1/p_3 = (p_1/p_2)(p_2/p_3)$ . By repeating these calculations for several values of  $M_x$ , the problem is solved.

**Analytical Solution.** From Eqs. 25.20 and 25.23 for a right-traveling shock, with  $u_1 = 0$ , we have

$$\frac{u_2}{c_1} = \frac{2}{k+1} \frac{W}{c_1} \left[ 1 - \left( \frac{c_1}{W} \right)^2 \right] \quad (25.32a)$$

$$\frac{p_2}{p_1} = 1 + \frac{2k}{k+1} \left[ \left( \frac{W}{c_1} \right)^2 - 1 \right] \quad (25.32b)$$

Eliminating  $W/c_1$  from this pair of equations, we obtain

$$\frac{u_2}{c_1} = \frac{\frac{p_2}{p_1} - 1}{k \sqrt{1 + \frac{k+1}{2k} \left( \frac{p_2}{p_1} - 1 \right)}} \quad (25.32c)$$

Now, for the simple left-traveling rarefaction wave with  $u_3 = 0$ , Eq. 24.23 yields

$$\frac{u_4}{c_3} = \frac{2}{k-1} \left( 1 - \frac{c_4}{c_3} \right) \quad (25.32d)$$

Introducing the isentropic relation between  $c$  and  $p$ , this becomes

$$\frac{u_4}{c_3} = \frac{2}{k-1} \left[ 1 - \left( \frac{p_4}{p_3} \right)^{\frac{k-1}{2k}} \right]$$

However, since  $u_4 = u_2$ ,  $c_3 = c_1$ , and  $p_4 = p_2$ , we may rearrange this in the form

$$\frac{u_2}{c_1} = \frac{2}{k-1} \left[ 1 - \left( \frac{p_2}{p_1} \right)^{\frac{k-1}{2k}} \left( \frac{p_1}{p_3} \right)^{\frac{k-1}{2k}} \right] \quad (25.32e)$$

Equating the expressions for  $u_2/c_1$  in Eqs. 25.32c and 25.32e, and solving for  $p_1/p_3$ , we get

$$\frac{p_1}{p_3} = \frac{p_1}{p_2} \left[ 1 - \frac{k-1}{2k} \frac{\frac{p_2}{p_1} - 1}{\sqrt{1 + \frac{k+1}{2k} \left( \frac{p_2}{p_1} - 1 \right)}} \right]^{\frac{2k}{k-1}} \quad (25.32f)$$

From this we may find  $p_1/p_2$  for any value of  $p_1/p_3$ . Then, using Eq. 25.32c,  $u_2/c_1$  may be found; and, from Eq. 25.32b,  $W/c_1$  may be found.

**SMALL PRESSURE DIFFERENCE.** This analysis lends itself to exploring the two possible extreme conditions. At one extreme,  $p_1/p_3$  is almost unity, and the waves are of small amplitude. Then, by expanding Eq. 25.32f by the binomial theorem, with the assumption that  $[(p_2 - p_1)/p_1] \ll 1$ , it may be shown that

$$\frac{p_1}{p_2} \cong \frac{p_2}{p_3} \quad \text{and} \quad p_3 - p_2 \cong p_2 - p_1$$

The latter result is seen to agree with the linearized theory (Art. 23.6).

**LARGE PRESSURE DIFFERENCE.** At the other extreme, suppose that  $p_1/p_3$  approaches zero. Now  $p_2/p_1$  may become very large, but  $p_2/p_3$  can never become less than zero. Since Eq. 25.32f may also be written as

$$\frac{p_2}{p_3} = \left[ 1 - \frac{k-1}{2k} \frac{\frac{p_2}{p_1} - 1}{\sqrt{1 + \frac{k+1}{2k} \left( \frac{p_2}{p_1} - 1 \right)}} \right]^{\frac{2k}{k-1}}$$

it is evident that as  $p_3/p_1$  approaches infinity,  $p_2/p_1$  approaches a finite maximum value found by setting  $p_2/p_3$  equal to zero in this expression. Thus we find that

$$\left( \frac{p_2}{p_1} - 1 \right)_{\max} = \frac{k(k+1)}{(k-1)^2} + \frac{k}{k-1} \sqrt{\left( \frac{k+1}{k-1} \right)^2 + 4}$$

Inserting this into Eq. 25.32b, we obtain

$$\left( \frac{W}{c_1} \right)_{\max} = \frac{1}{2} \frac{k+1}{k-1} + \frac{1}{2} \sqrt{\left( \frac{k+1}{k-1} \right)^2 + 4}$$

For  $k = 1.4$ , the numerical values are

$$(p_2/p_1)_{\max} = 44.1; (W/c_1)_{\max} = 6.16$$

Since  $p_1/p_3 = 0$  and  $p_2/p_1$  is finite, it follows that  $p_4/p_3 = 0$ . In addition, Eq. 25.32e yields

$$(u_2/c_1)_{\max} = (u_4/c_1)_{\max} = \frac{2}{k-1} = 5.00$$

and we conclude that when the pressure ratio across the diaphragm is infinite, the shock wave is of finite strength, and the rarefaction wave accelerates the gas to the escape speed.

**Graphical Solution with  $u,p$ -Shock Polar.** Corresponding to given conditions at state 1, we may draw the shock polar for a right-traveling wave (Fig. 25.9).

In Chapter 24 we discussed the  $u,c$ -state characteristics. Since  $u$  and  $p$  are uniquely related in isentropic flow, it is clear that we may equally well work with the characteristics in the  $u,p$ -plane. The  $u,p$   $I$ -characteristic passing through state 3 may therefore be drawn.

States 2 and 1 lie on a common right-traveling shock polar, states

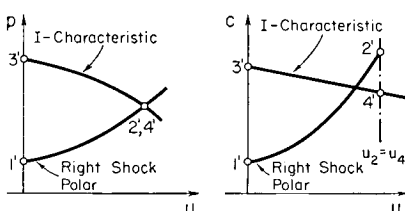


Fig. 25.9. Representation of shock-tube process on  $u,p$ - and  $u,c$ -diagrams.

3 and 4 lie on a common  $I$ -characteristic, and states 2 and 4 have equal values of  $u$  and  $p$ . Hence, the intersection of the two curves on the  $u,p$ -diagram yields the solution to our problem.

**Working Charts for Shock Tube.** Fig. 25.10 shows in convenient form the theoretical results to the shock-tube problem, as found by any of the three methods described above.

The curve of  $(u_4 - c_4)/c_1$ , representing the absolute propagation speed of the rear part of the rarefaction wave, shows that, when  $p_1/p_3 > 0.097$ , the rear part of the wave travels to the left. When  $p_1/p_3 < 0.097$ , however, it travels to the right (relative to the tube).

For  $p_1/p_3 = 0.097$ , the rear part of the wave remains at a fixed cross section of the tube.

## 25.5. Weak Shock Waves

We shall now discuss weak shocks in more detail, and show how the calculation procedure for weak shocks may be greatly simplified.

In Chapter 5 it was proved that the entropy increase across a normal shock is of the third order in shock strength, thus indicating that little error is involved in employing the isentropic relations for the changes in state across weak shocks.

Essentially the same results were obtained in a different way in Art. 25.3, where it was shown that the relations between  $\Delta c$ ,  $\Delta u$ ,  $\Delta p$ , and  $\Delta \rho$  in a weak shock are identical with those for isentropic waves of small amplitude. It was also shown that the  $u, c$ -shock polar and  $u, c$ -characteristic have equal first and second derivatives, and differ only in the third derivative  $d^3c/du^3$ , thus indicating that the shock relations and simple-wave relations are identical up to terms of second order in the shock strength.

**Polynomial Expansions of Shock Relations in Terms of Shock Strength.** It is useful to carry this approach further and to compare directly the shock-wave relations and simple-wave relations in terms of the wave strength. We recall that the strength of a wave may be expressed in any of several ways—for example, in terms of the pressure ratio across the wave, the density ratio across the wave, or the change in gas speed across the wave. For the present purpose, it is convenient to employ the last-named measure of wave strength.

We return to Eqs. 25.20, 25.21, and 25.23, therefore, and expand the shock relations in terms of  $(u_2 - u_1)$ . Omitting the detailed calculations, the main results may be summarized as

$$c_2 - c_1 = \pm \frac{k-1}{2} (u_2 - u_1) + \dots [O](u_2 - u_1)^3 \quad (25.33a)$$

$$\left( u_2 \mp \frac{2}{k-1} c_2 \right) = \left( u_1 \mp \frac{2}{k-1} c_1 \right) + \dots [O](u_2 - u_1)^3 \quad (25.33b)$$

$$\begin{aligned} \frac{p_2}{p_1} = 1 + k \frac{u_2 - u_1}{c_1} + \frac{k(k+1)}{4} \left( \frac{u_2 - u_1}{c_1} \right)^2 \\ + \dots [O] \left( \frac{u_2 - u_1}{c_1} \right)^3 \end{aligned} \quad (25.33c)$$

$$u_1 \pm W = \frac{(u_1 \pm c_1) + (u_2 \pm c_2)}{2} + \dots [O](u_2 - u_1)^2 \quad (25.33d)$$

where  $[O]$  signifies “terms of the order of.”

**Polynomial Expansions for Simple Waves.** By expanding Eqs. 24.9 and 24.4 we may obtain the following analogous relations for simple waves (see Problem 24.2):

$$c_2 - c_1 = \pm \frac{k-1}{2} (u_2 - u_1) \quad (25.34a)$$

$$u_2 \mp \frac{2}{k-1} c_2 = u_1 \mp \frac{2}{k-1} c_1 \quad (25.34b)$$

$$\begin{aligned} \frac{p_2}{p_1} = 1 + k \frac{u_2 - u_1}{c_1} + \frac{k(k+1)}{4} \left( \frac{u_2 - u_1}{c_1} \right)^2 \\ + \dots [O] \left( \frac{u_2 - u_1}{c_1} \right)^3 \end{aligned} \quad (25.34c)$$

**Comparison of Shock with Simple Wave.** By comparing Eq. 25.34a with Eq. 25.33a, and Eq. 25.34c with Eq. 25.33c, we observe that the velocity and pressure changes across shocks and across simple waves are identical up to (and including) terms in the second order of shock strength.

Eqs. 25.33b and 25.34b show, furthermore, that if terms in the third order of shock strength are ignored, then the magnitude of the appropriate characteristic coordinate (i.e., the coordinate *I* or *II*) is unchanged in a shock wave.

From Eq. 25.33d we see that, if terms in the second order of shock strength are negligible, the speed of the shock is the arithmetic mean between the propagation speeds of infinitesimal waves before and after the shock.

From all this we conclude that, for calculation purposes, weak shocks may be treated as though they were continuous compression waves. The accuracy of this approximation is especially good in respect to the velocity and pressure changes, and somewhat less good in respect to the wave propagation speed.

**NUMERICAL EXAMPLE.** Let us test the approximate method of calculation against the example which was worked out by the exact method in Art. 25.2. The initial data are

$$u_1 = 200 \text{ ft/sec}; \quad c_1 = 1000 \text{ ft/sec}; \quad u_1 + W = 2200 \text{ ft/sec}$$

$$\text{From Eq. 25.33d,} \quad u_2 + c_2 = 3200$$

$$\text{From Eq. 25.33a,} \quad c_2 - 1000 = 0.2(u_2 - 200)$$

Solving this pair of equations simultaneously, we get

$$u_2 = 1867 \text{ ft/sec}; \quad c_2 = 1333 \text{ ft/sec}$$

The isentropic relation yields

$$p_2/p_1 = (c_2/c_1)^{2k/(k-1)} = (1.333)^7 = 7.5$$

The exact solution gave, in comparison,

$$u_2 = 1450; \quad c_2 = 1300; \quad p_2/p_1 = 4.5$$

Thus, there is an error of 67 per cent in pressure ratio, an error of 33 per cent in  $(u_2 - u_1)$ , and an error of 11 per cent in  $(c_2 - c_1)$ .

**A SECOND EXAMPLE.** The foregoing is rather an extreme example, since a shock with a pressure ratio of 4.5 could scarcely be called a weak shock. Let us try a second example with the following initial data:

$$u_1 = 200; \quad c_1 = 1000; \quad u_1 + W = 1700; \quad W/c_1 = 1.50$$

The results of the calculations are shown in the following table:

	Approximate	Exact	Percentage Error
$u_2$	1033	895	
$c_2$	1167	1150	
$p_2/p_1$	2.94	2.46	20
$u_2 - u_1$	833	695	20
$c_2 - c_1$	167	150	11

For still weaker shocks the errors shown here would decrease very rapidly. For example, by reducing  $W/c_1$  to about 1.2, all the errors would be one per cent or less. It should also be noticed that we are comparing shocks and simple compressions on the basis of Eq. 25.33d, which is valid only up to terms in first order of wave strength. If we were to compare on the basis of equal pressure ratio, say, the agreement would be considerably better in both examples.

#### Graphical Comparison of Shock Wave with Simple Compression Wave.

The approximate method of calculation may be compared with the exact method in a different way by plotting on the same diagram the  $u, c$ -shock polar and  $u, c$ -characteristic curve. This has been done in Fig. 25.11, on which the values of the pressure ratio across the wave have been marked for both the shock polar and the characteristic curve.

Comparing a shock wave and a simple compression wave of equal pressure ratio, Fig. 25.11 shows that both the change in gas velocity and in sound velocity are greater for the shock than for the simple compression. For pressure ratios of the order of 2, however, there is scarcely any difference between the two curves.

The type of comparison described above is summarized by Fig. 25.12, in which the relative wave speed and the changes in gas velocity and sound velocity are compared for shock waves and simple compression waves having equal pressure ratios. Note that  $W$  for the simple wave is defined as  $(c_1 + c_2)/2$ .

From this chart we see that, if the allowable error incurred by using

the simple-wave relations rather than the exact shock relations is one per cent, then (i) the maximum pressure ratio for computing the change in gas speed is about 2.5, (ii) the maximum pressure ratio for computing the change in sound velocity is about 1.4, and (iii) the maximum pres-

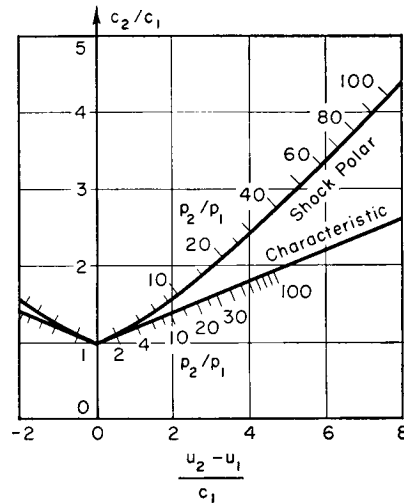


FIG. 25.11. Comparison of shock polar and characteristic curve ( $k = 1.4$ ).

sure ratio for computing the relative wave speed is about 1.45. These figures are a guide for deciding whether the approximate method of calculation is satisfactory in a particular problem.

## 25.6. Modified Calculation Procedure for Weak Shocks

The results obtained in the preceding article suggest a greatly simplified procedure when dealing with weak shocks. We simply ignore the entropy increase across the weak shock as being negligible. Then we may use the simple-wave relations for the shock, with the absolute shock speed computed as the arithmetic mean of the absolute wave speeds before and after the shock. Since the flow is considered as isentropic, all the methods and unit processes of Chapter 24 may be used if we regard the shock wave as an isentropic pressure wave. No contact discontinuities are produced by traveling weak shocks of varying strength, because entropy changes are ignored completely.

By this means the treatment of weak shocks may be made an integral part of the treatment of continuous waves outlined in Chapter 24. There is one essential difference, however, which is worth mentioning. If the stepwise methods for calculating continuous waves are re-examined,

it will be seen that, for purposes of computation, we lumped a continuous wave into a number of isentropic discontinuities, and assumed that the discontinuity (or wave) traveled at the mean of the absolute wave speeds in the regions ahead of and behind the discontinuity. This is exactly what we propose to do with a weak shock wave. However, the process may be made as exact as we wish in the case of continuous waves, merely by increasing the number and decreasing the strength of the imaginary discontinuities. The weak shock, on the other hand, is a true discontinuity, and the error in treating it with the isentropic relations can be eliminated only by using instead the exact shock-wave relations. A weak shock may not be divided into several weaker discontinuities, for the essence of the shock is that it is a discontinuity of fixed strength.

When dealing with weak shocks by the isentropic methods of Chapter 24, the field method is usually more convenient than the lattice-point method.

**Formation of Shock Wave.** As an example of the approximate treatment of weak shocks, consider the formation of a shock wave by a piston traveling into a mass of gas initially at rest (Fig. 25.13).

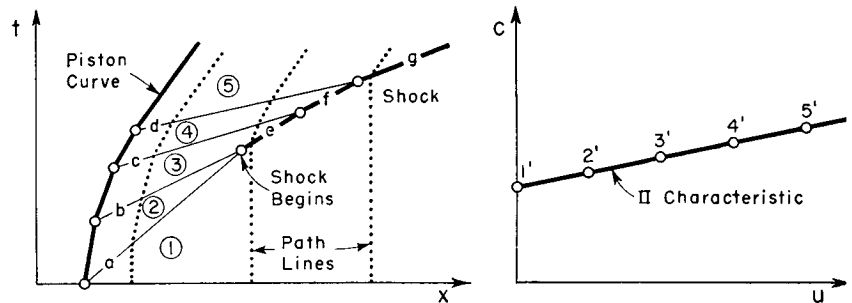


FIG. 25.13. Coalescence of a continuous compression wave into a shock.

Using the field method, we replace the piston curve by a series of straight chords, and we suppose that a compression wavelet is originated each time the piston undergoes a change in speed. Then the states in fields 1, 2, 3, 4, and 5 may be identified through their image points on the  $u, c$  I-characteristic, and the slopes of the waves  $a$ ,  $b$ ,  $c$ , and  $d$  may be drawn, all according to the methods of Chapter 24.

When wavelets  $a$  and  $b$  merge, they form a small compression shock, shown as line  $e$ , across which the state changes from 1 to 3. The slope of wave  $e$  is drawn with the value of  $(u + c)$  corresponding to the mean conditions between points 1' and 3'. If the points in the  $u, c$ -plane are equally spaced, wave  $e$  propagates at the speed  $u_2 + c_2$ .

Next, when wavelet  $c$  merges with shock  $e$ , the two combine to form

wave  $f$ , which is stronger than shock  $e$ . Wave  $f$  propagates at a speed corresponding to the mean value of  $(u + c)$  for states  $1'$  and  $4'$ .

As successive wavelets merge with the shock, the latter becomes stronger (in terms of pressure rise) and propagates at an increasingly higher speed. Naturally, the accuracy of the procedure suggested here decreases as the shock strength increases.

**Shock Interacting with Continuous Waves Traveling in Same Direction.** In Art. 25.2 it was shown that shock waves always tend to interact with continuous waves of the same family. In the examples which follow, compression wavelets are shown as thin solid lines, expansion wavelets as dashed lines, and shock waves as heavy solid lines.

**SHOCK OVERTAKING EXPANSION.** Fig. 25.14a shows a shock wave overtaking an expansion wave. The shock and the expansion gradually

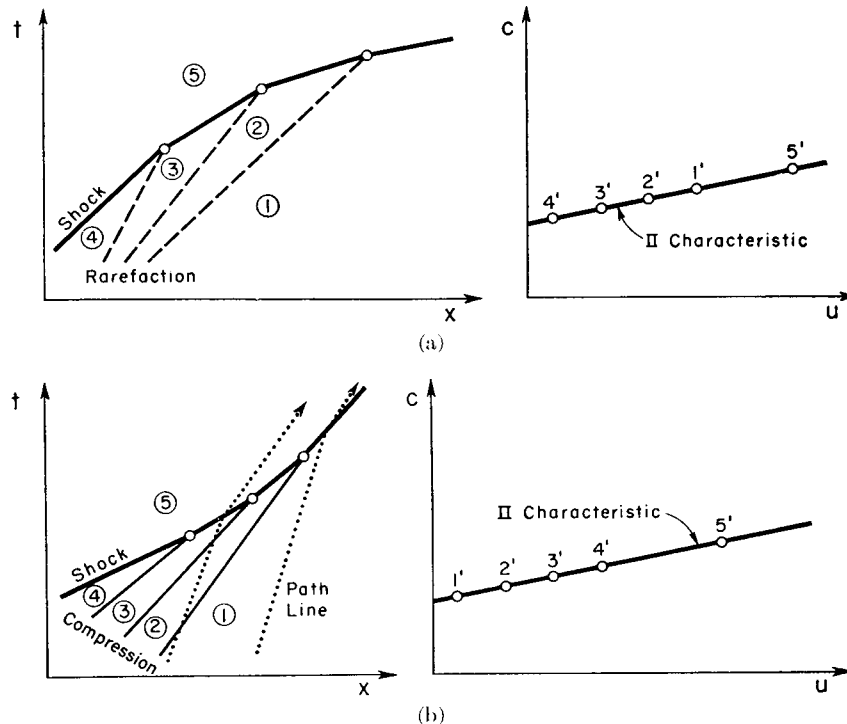


FIG. 25.14. (a) Shock overtaking continuous rarefaction wave.  
(b) Shock overtaking continuous compression wave.

cancel each other, and each grows weaker. In this example the shock was assumed to be stronger than the rarefaction. After sufficient time, therefore, the rarefaction disappears completely, and there remains a shock which is weaker than the original shock.

**SHOCK OVERTAKING COMPRESSION.** Fig. 25.14b shows a shock overtaking a continuous compression wave. The continuous wave is absorbed into the shock, and the latter gradually grows stronger. Ultimately the continuous wave disappears and there remains only a shock which is stronger than the original shock.

**RAREFACTION OVERTAKING SHOCK.** Fig. 25.15a shows a shock being overtaken by a continuous rarefaction. The two gradually cancel each

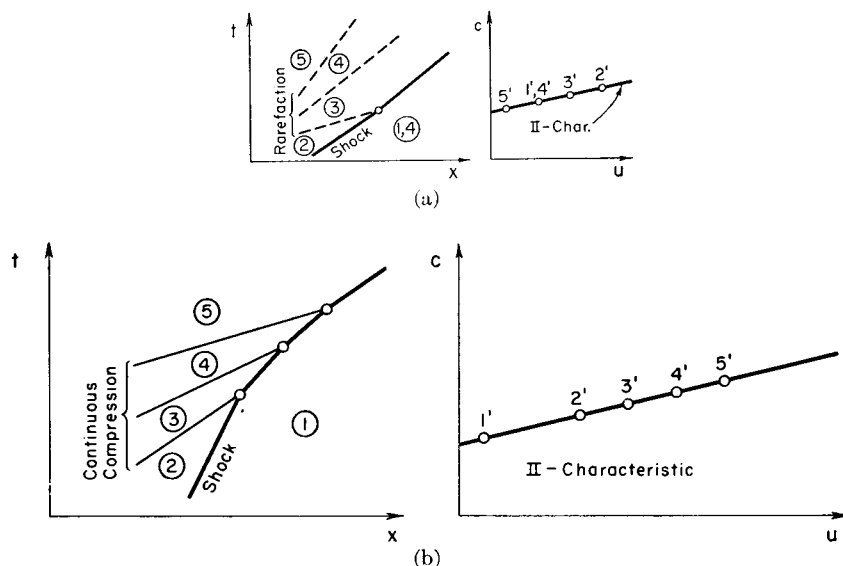


FIG. 25.15. (a) Shock being overtaken by continuous rarefaction wave.  
(b) Shock being overtaken by continuous compression wave.

other and the shock becomes weaker. In this example the rarefaction is stronger than the shock. If the limiting solution where the rarefaction wave is broken up into an infinite number of steps is considered, it will be seen that ultimately the shock completely disappears, and only a portion of the original rarefaction wave remains.

**COMPRESSION OVERTAKING SHOCK.** Fig. 25.15b shows a shock being overtaken by a continuous compression wave. The compression wavelets gradually merge into and strengthen the shock wave, until finally only the shock remains.

**Shock Interacting with Continuous Waves Traveling in Opposite Direction.** As a further example of the approximate method, Fig. 25.16a shows a right-traveling shock interacting with a left-traveling rarefaction wave. The graphical solution to this problem shows that the shock is refracted in a continuous way as it crosses the rarefaction,

and that the rarefaction is refracted suddenly as it crosses the shock. Speaking in terms of pressure ratios, the shock wave is strengthened and the rarefaction wave is weakened as a result of the interaction.

Fig. 25.16b shows a right-traveling shock interacting with a left-

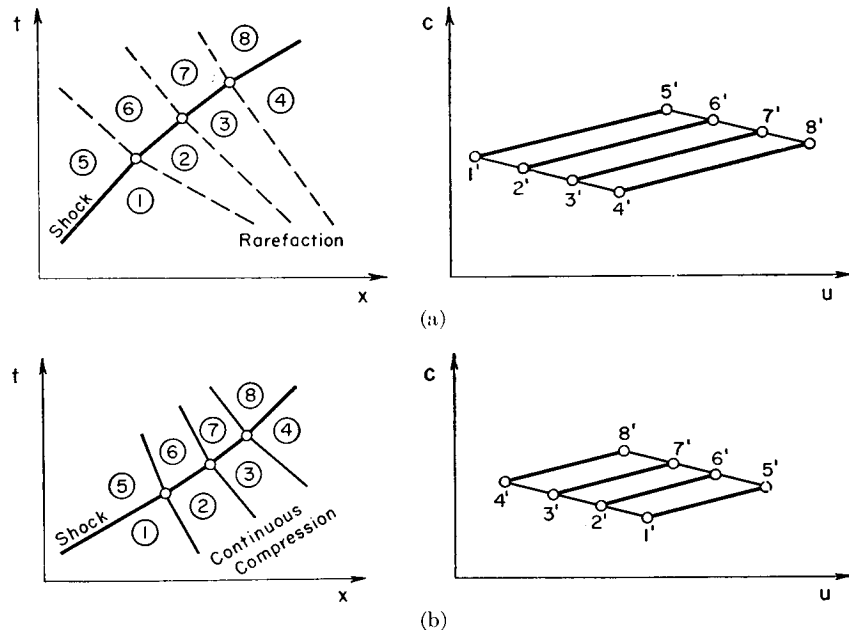


FIG. 25.16. (a) Interaction of right-traveling shock with left-traveling simple-wave rarefaction. (b) Interaction of right-traveling shock with left-traveling simple-wave compression.

traveling continuous compression wave. The refraction effects are similar to those of Fig. 25.16a. In this example, however, both the shock and the continuous compression are weakened as a result of the interaction.

### 25.7. End Conditions and Interaction Effects for Strong Shocks

When strong shocks occur, the substantial entropy changes that go with them make the approximate method of the preceding article inaccurate. It is then necessary to carry out computations based on the exact shock relations. Several methods of calculation based on these exact relations for the instantaneous changes across a single shock were outlined in Arts. 25.2 and 25.3.

We shall now discuss the extension of these methods to such unit processes as (i) the reflections of shocks from the ends of a pipe, and (ii) the interaction of shocks with other shocks, with continuous waves,

with contact discontinuities, and with area discontinuities. The general line of attack in handling these various unit processes will be seen to be similar to the methods of Chapter 24, except that now we are dealing with finite discontinuities whereas previously small discontinuities were introduced fictitiously as part of the calculation procedure. The field method will be employed throughout. Although the methods of procedure will be illustrated graphically, it is to be understood that equivalent algebraic methods are often more desirable.

**Reflection of Shock from Closed End.** Referring to Fig. 25.17, suppose that a right-traveling shock is incident on the closed end of a tube.

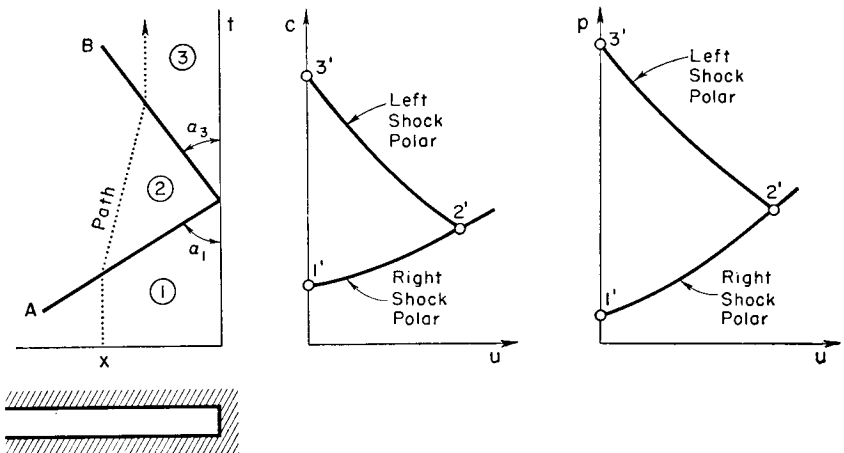


FIG. 25.17. Reflection of shock from closed end.

When shock  $A$  reaches the closed end, shock  $B$  must be reflected in order to preserve the condition that the gas adjacent to the wall is at rest.

**GRAPHICAL SOLUTION.** Assuming that the strength of shock  $A$  is known, that is, that  $p_1$ ,  $p_2$ ,  $c_1$ ,  $c_2$ , and  $u_2$  are known, the conditions in region 3 may be worked out by several methods. Graphically, we first draw the shock polar connecting states  $1'$  and  $2'$  (Fig. 25.17). Next we draw the left-traveling shock polar for shock  $B$  with its apex starting at point  $2'$ . Where shock polar  $B$  crosses the  $c$ -axis determines the location of state  $3'$ .

**NUMERICAL SOLUTION.** To illustrate the numerical method of computation, let us assume the following initial data:

$$u_1 = 0; c_1 = 1000; W_A = 2000; u_1 + W_A = 2000; p_1 = 100$$

Then  $M_{x_A} = W_A/c_1 = 2.0$ . From Eqs. 25.20, 25.21, and 25.23 we may find

$$u_2 = 1250, c_2 = 1299, p_2 = 450$$

Next, writing Eq. 25.20 for the left-traveling shock  $B$ , with  $u_3 = 0$ , we get  $M_{x_B} = 1.71$ . Then  $W_B = M_{x_B} c_2 = 2220$ . The absolute propagation speed of wave  $B$  is then

$$u_2 - W_B = 1299 - 2220 = -920$$

as compared with the absolute propagation speed of wave  $A$  of 2000. This shows that the angle of reflection,  $\alpha_3$ , is less than the angle of incidence,  $\alpha_1$ . Substituting the value of  $M_{x_B}$  into Eq. 25.23, we obtain  $p_3 = 1460$ .

From the point of view of pressure ratio, this example shows that the incident wave is stronger than the reflected wave, the pressure ratios being 4.50 and 3.24, respectively. From another point of view, however, the reflected wave  $B$  is stronger insofar as the pressure rise across  $B$  is 1010 as compared with 350 for the pressure rise across  $A$ .

**ANALYSIS OF RELATIVE STRENGTHS OF INCIDENT AND REFLECTED WAVES.** These results for the pressure relations across the shock system may be worked out analytically. Writing Eq. 25.20 for the incident and reflected shocks, and noting that  $(u_2 - u_1) = -(u_3 - u_2)$ , we get

$$M_{x_B} - \frac{1}{M_{x_B}} = \frac{c_1}{c_2} \left( M_{x_A} - \frac{1}{M_{x_A}} \right)$$

But Eq. 25.21 gives  $c_1/c_2$  in terms of  $M_{x_A}$ . Hence  $M_{x_B}$  may be found in terms of  $M_{x_A}$ . Using Eq. 25.23, we write

$$\frac{p_2}{p_1} = 1 + \frac{2k}{k+1} (M_{x_A}^2 - 1); \quad \frac{p_3}{p_2} = 1 + \frac{2k}{k+1} (M_{x_B}^2 - 1)$$

Since  $M_{x_B}$  is in terms of  $M_{x_A}$ , it follows that  $p_3/p_2$  may be found also in terms of  $M_{x_A}$ . But  $M_{x_A}$  depends only on  $p_2/p_1$ , and hence  $p_3/p_2$  may be expressed directly in terms of  $p_2/p_1$ .

Omitting the detailed calculations outlined above, it may be shown that

$$\frac{p_3}{p_2} = \frac{\left(1 + 2 \frac{k-1}{k+1} \frac{p_2}{p_1} - \frac{k-1}{k+1}\right)}{\frac{k-1}{k+1} \frac{p_2}{p_1} + 1} \quad (25.35)$$

For very strong incident shocks,  $p_2/p_1$  goes to infinity. The pressure ratio across the reflected shock reaches a limiting value, however, given by

$$\left( \frac{p_3}{p_2} \right)_{\max} = \frac{3k-1}{k-1} \quad (= 8 \text{ for } k = 1.4)$$

To compare the pressure rises across the incident and reflected shocks, we form the expression

$$\frac{p_3 - p_2}{p_2 - p_1} = \frac{\frac{p_3}{p_2} - 1}{\frac{p_2}{p_1} - 1} = \frac{\frac{p_3}{p_2} - 1}{\frac{p_2}{p_1} - 1} = \frac{\frac{p_2}{p_1} \left( \frac{p_3}{p_2} - 1 \right)}{\frac{p_2}{p_1} - 1}$$

Substituting for  $p_3/p_2$  with the help of Eq. 25.35, and simplifying, we get

$$\frac{p_3 - p_2}{p_2 - p_1} = \frac{\frac{2k}{k+1}}{\frac{p_1}{p_2} + \frac{k-1}{k+1}} \quad (25.36)$$

As the pressure ratio of the incident shock becomes very large, the above expression approaches the limit

$$\left( \frac{p_3 - p_2}{p_2 - p_1} \right)_{\max} \rightarrow \frac{2k}{k-1} \quad (= 7 \text{ for } k = 1.4)$$

from which it follows that for strong shock systems, the pressure rise across the reflected shock is very much larger than that across the incident shock.

For very weak incident shocks,  $p_1/p_2$  approaches unity, and

$$\frac{p_3 - p_2}{p_2 - p_1} \rightarrow 1$$

thus showing that for weak shock systems the incident and reflected shocks have equal pressure rises. This agrees, of course, with the results of the linearized theory for waves of small amplitude.

**Reflection of Shock from Open End at Constant Pressure.** In Fig. 25.18, right-traveling shock  $A$  is incident on the open end of the pipe,

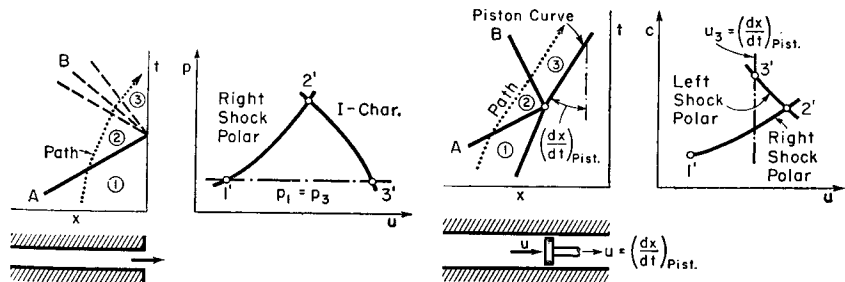


FIG. 25.18. Reflection of shock from constant-pressure end.

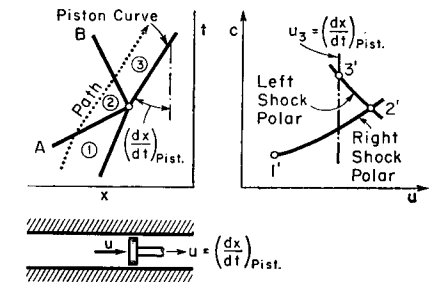


FIG. 25.19. Reflection of shock from moving piston.

at which point the pressure is assumed to be constant. Assuming that the state before the shock and the strength of the shock are known, points 1' and 2' may be located in the  $u, p$ -diagram.

To satisfy the condition of constant pressure at the open end, an expansion wave must be reflected at the open end at the instant when wave  $A$  is incident. This expansion wave must be continuous, and therefore isentropic, since a discontinuous expansion is barred out by the second law of thermodynamics. Furthermore, the rarefaction wave must be centered, for it is only in this way that the pressure rise across shock  $A$  can be instantaneously canceled by a corresponding pressure drop across expansion wave  $B$ . Noting that states  $2'$  and  $3'$  lie on a common  $I$ -characteristic, and that  $p_2 = p_3$ , state  $3'$  may be located. Thus all properties of the reflected wave may be calculated.

**Reflection of Shock from Moving Piston.** Certain problems contain a unit process which involves the incidence of a shock wave on a moving piston or its equivalent. Fig. 25.19 shows, for example, shock  $A$  incident on an accelerating piston. The piston curve is represented by a series of chords, and, with the field method, it is convenient to locate the points of sudden change in piston speed at the points where the waves are incident.

Given states  $1'$  and  $2'$ , and the piston motion, the reflected wave is determined by the condition that the gas speed in field  $3$  must be equal to the piston speed adjacent to field  $3$ . If this piston speed is less than  $u_2$ , the reflected wave must be a compression shock, and states  $2'$  and  $3'$  must lie on a left-traveling shock polar originating at  $2'$  and terminating at  $u_3 = (dx/dt)_{\text{piston}}$ ; this situation is illustrated in Fig. 25.19. On the other hand, if the piston speed adjacent to zone  $3$  were greater than  $u_2$ , the reflected wave would be a centered rarefaction, and states  $3'$  and  $2'$  would lie on a common  $I$ -characteristic.

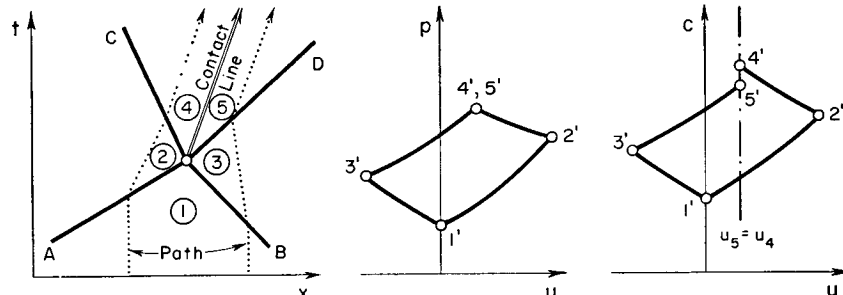


FIG. 25.20. Intersection of shocks of opposite families.

**Crossing of Shocks.** Fig. 25.20 shows right-traveling shock  $A$  meeting left-traveling shock  $B$ , with both shocks traveling into field 1 where, for this example, the gas is assumed to be stagnant. Assuming that the respective strengths of shocks  $A$  and  $B$  are given, states  $1'$ ,  $2'$ , and  $3'$  may be located in the  $u,p$ - and  $u,c$ -diagrams with the help of the shock polar curves.

The strengths of the two refracted shocks,  $C$  and  $D$ , are determined by the simultaneous conditions that  $p_4 = p_5$  and  $u_4 = u_5$ . The  $u,p$ -shock polar diagram is most convenient for this calculation. In general, the entropy change of a gas particle passing through shocks  $A$  and  $C$  will be different from the entropy change of a gas particle passing through shocks  $B$  and  $D$ . Since fields 4 and 5 have the same pressure but different entropies, they will have different temperatures, as illustrated by the  $u,c$ -diagram. A contact line, therefore, separates fields 4 and 5.

For the special case where shocks  $A$  and  $B$  are of equal strength, complete symmetry exists, the contact line vanishes, and the problem is equivalent to the reflections of a shock from a solid boundary (see Fig. 25.17).

**Shock Overtaking Shock.** We have previously seen (Art. 25.2) that an infinitesimal wave always overtakes a shock moving in the same direction. Furthermore, a shock wave always travels faster than an infinitesimal wave passing through the same medium into which the shock propagates. From these two facts it follows that when two shocks travel in the same direction, the rearward shock always overtakes the forward shock. We may also reach the same conclusion by noting that a shock travels at *subsonic speed relative to the gas behind it, and at supersonic speed relative to the gas ahead of it*.

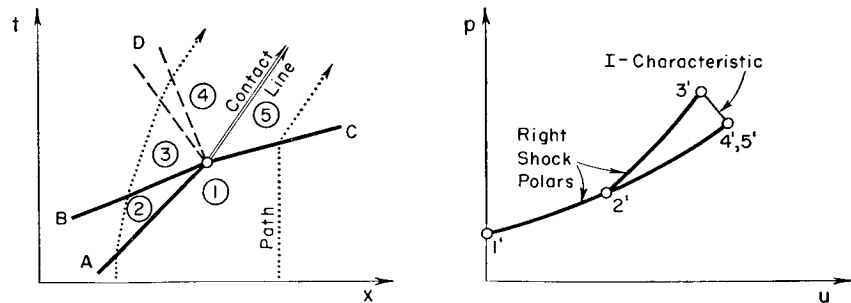


FIG. 25.21. Intersection of shocks of same family.

Fig. 25.21 shows, for example, shock  $B$  overtaking shock  $A$ . Assuming that the gas in field 1 is at rest, and that the strengths of shocks  $A$  and  $B$  are given, states  $1'$ ,  $2'$ , and  $3'$  may be located in the  $u,p$ -diagram with the help of the appropriate shock polars.

The events which occur after the two shocks meet are determined by the condition that gas particles passing respectively to the left and right of the junction point must ultimately have the same pressure and speed. For this condition to prevail it is necessary that there be, in general, a transmitted shock  $C$  and a reflected, centered rarefaction wave  $D$ .<sup>(1)</sup> Because of the different entropy changes for gas particles

passing respectively to the left and to the right of the junction point, a contact line separates fields 4 and 5. The solution to the problem is most easily carried out graphically with the help of the  $u, p$ -shock polars and  $u, p$ -characteristics. A trial-and-error procedure is necessary if numerical solutions are desired.

**Shock Wave Incident on Contact Discontinuity.** We have seen in this chapter and in the preceding one that there are numerous ways in which contact surfaces, separating slugs of gas with different temperatures but equal speeds and pressures, may arise.

To illustrate the calculation procedure for a shock wave incident on such a contact surface, Fig. 25.22 shows shock wave A propagating

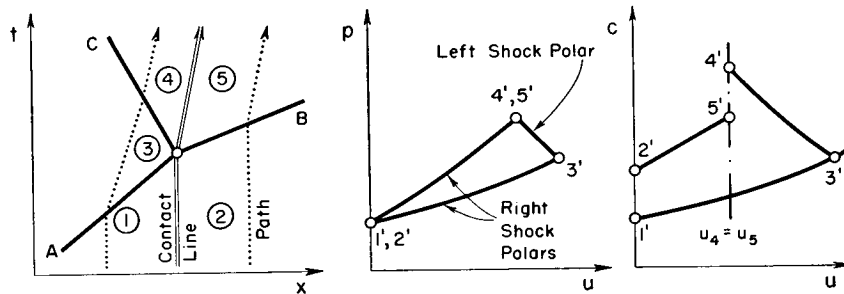


FIG. 25.22. Shock incident on contact discontinuity.

into field 1 where the gas is at rest. Adjacent to gas 1 is gas 2, also at rest, but with a different temperature and sound speed. The interaction of the incident shock with the contact line results, in general, in a transmitted wave and a reflected wave. The nature and strength of these waves will depend on whether the sound speed in field 2 is greater or less than that in field 1, and on the strength of the incident shock.<sup>(1)</sup> The solution to the problem is determined by the conditions that  $p_4 = p_5$  and  $u_4 = u_5$ . Here again the  $u, p$ -shock polars and  $u, p$ -characteristics provide the most rapid means of solution.

Fig. 25.22 illustrates the process when  $c_2 > c_1$ . In this case both the transmitted wave B and reflected wave C are shock waves.

For the case where  $c_2 < c_1$ , two possibilities exist: (i) the transmitted wave is a shock, and the reflected wave is a centered rarefaction, and (ii) the transmitted wave is a centered rarefaction, and the reflected wave is a shock. Although there are no simple rules for predicting which of these alternatives will occur, it appears that possibility (i) is generally associated with relatively weak incident shocks and relatively small values of  $c_2/c_1$ , and that possibility (ii) is generally associated with relatively strong incident shocks and with the condition that  $c_2/c_1 > 2/(k+1)$ .

**Development of Strong Shock from Continuous Compression Wave.** We have noted previously the tendency for continuous compression waves to develop into shock waves. To investigate the outcome of such a development, let us consider (Fig. 25.23) a right-traveling

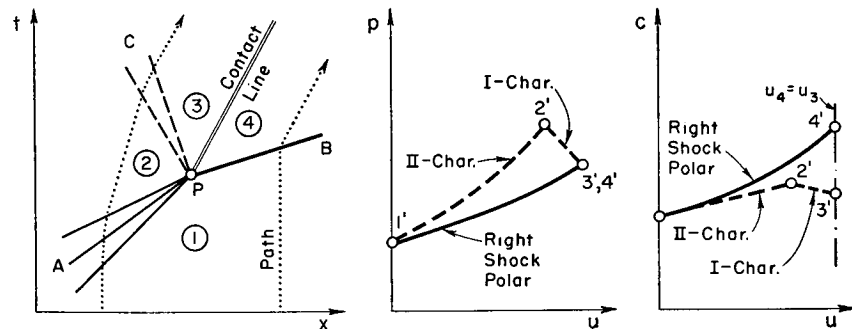


FIG. 25.23. Development of strong shock from continuous compression wave.

compression wave A which, for simplicity, is assumed to be centered at point P. It is evident that a solution with compression shock B alone emanating from point P is physically impossible, for such a solution would mean that two neighboring gas particles passing on opposite sides of P, one of which was accelerated by wave A and the other of which was accelerated to the same speed by shock B, would arrive at different pressures.

Reference to Fig. 25.11 shows that, for the same initial state, the  $u, p$ -shock polar lies lower than the  $u, p$ -characteristic. With this in mind, a consideration of various wave configurations centered at point P indicates that centered rarefaction wave C, of opposite family to the original compression wave A, must be reflected at point P. This is the only solution which gives equal speeds and pressures in fields 3 and 4. Because of the entropy increase through the shock, the temperature in field 4 must be greater than that in field 3, and a contact surface is accordingly generated. The pressure rise across shock B may be shown to be less than that across compression wave A.

To generalize the foregoing argument, suppose now that the original compression wave A were noncentered. By extending our analysis to this case, we may show that the shock wave is formed in a continuous manner and that reflected rarefaction waves are also generated as the shock gathers strength. No distinct contact surfaces appear, but instead the region behind the shock is one of constantly varying entropy. By imagining this region to be approximated by strips of constant entropy, with the entropy changes lumped along the contact lines dividing the strips, we may show further that the region behind the shock must have continuous waves of both families because the reflected

rarefactions originating at the curved shock are in turn partly reflected at the contact lines.

**Interaction of Shocks with Continuous Waves.** In Art. 25.6 we discussed approximate but simple methods for studying the interaction of continuous waves with weak compression shocks. We shall now see how very much more complex is the interaction of a continuous wave with a strong compression shock.

Six possible configurations may occur. A shock may overtake either a continuous compression wave or a continuous rarefaction wave traveling in the same direction; it may be overtaken either by a continuous compression or a continuous rarefaction traveling in the same direction; or it may cross a continuous compression or rarefaction wave traveling in the opposite direction. Let us, by way of illustrating the line of attack for such problems, examine the case of a shock being overtaken by a continuous rarefaction wave.

Referring to Fig. 25.24, suppose that right-traveling, strong shock *A* is overtaken by right-traveling, rarefaction wave *B*. The interaction begins at point 1. Following the type of reasoning employed previously, we may show that the shock is propagated from point 1 to point 2 with diminished strength, that the first portion of the rarefaction is partially reflected to point 3, and that a contact surface originates at point 1. A similar process occurs when the second portion of the rarefaction wave meets the partially weakened shock wave at point 2. The remaining parts of the wave diagram

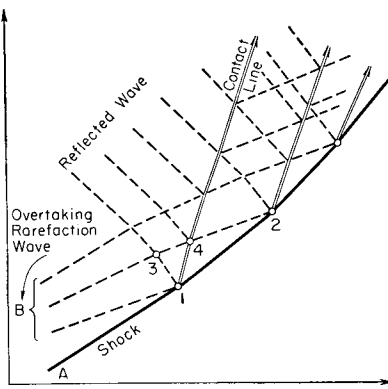


FIG. 25.24. Strong shock overtaken by continuous rarefaction wave.

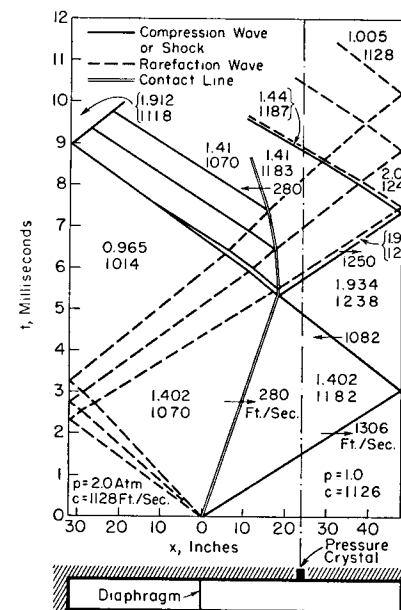
are constructed by using the unit processes of (i) interaction of continuous waves (as at point 3) and (ii) interaction of a continuous wave with a contact line (as at point 4).

The reflected wave system is usually much weaker than the original shock and original rarefaction. Furthermore, the waves originating at the contact lines are usually much weaker than the main reflected waves.

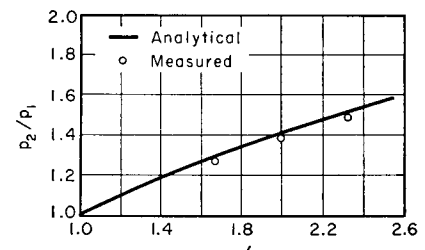
**Interaction of a Shock Wave with an Area Discontinuity.** In Art. 24.6 we discussed the concept of quasi-steady flow through a short section of duct of rapidly changing area, that is, a flow where  $\partial u / \partial x$  could be ignored compared to  $u \partial u / \partial x$  and where  $\partial \rho / \partial t$  could be ignored compared to  $u \partial \rho / \partial x$ , thus rendering the steady-state equations valid for

each instant of time. Also, we have seen how the analysis of flow at an area discontinuity could be employed for stepwise calculations in the case of a duct of gradually varying area.

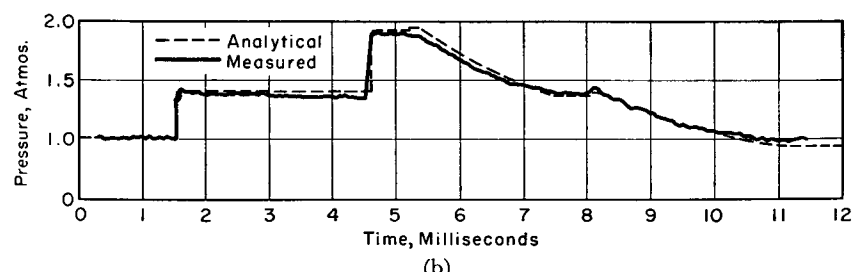
The analysis of a shock wave incident on an area discontinuity is very similar to the analysis in Art. 24.6 of a continuous wave incident on an area discontinuity. The main points of difference are that (i) the  $u, c$ -shock polars and  $u, c$ -characteristics are used in combination, rather than the  $u, c$ -characteristics alone, and (ii) a contact surface is formed at the area discontinuity. The incident shock is transmitted in modified form, and either a shock wave or a centered rarefaction is reflected from the area discontinuity.



(a)



(b)



(c)

FIG. 25.25. Results of shock-tube experiment (after Huber, Fitton, and Delpino).

## 25.8. Comparison Between Experimental and Theoretical Results

As an illustration of the synthesis of many of the unit processes already discussed, Fig. 25.25 shows analytical and experimental results for a shock tube experiment.<sup>(7)</sup>

Fig. 25.25a is the theoretical wave pattern for an initial pressure ratio of 2.0. By means of a piezo-crystal 24 in. to the right of the diaphragm, the static pressure at that location was measured as a function of time. How the measured pressure variation compares with the theoretical is shown in Fig. 25.25b. The pressure ratio across the shock, as a function of the original pressure ratio across the diaphragm, was also inferred from the measurements, and is compared with the theoretical solution in Fig. 25.25c (see Fig. 25.8 for nomenclature).

The agreement between theory and experiment is seen to be adequate for most engineering calculations.

Experimental studies of many shock tube phenomena are described by Glass *et al.*<sup>(12)</sup>

## REFERENCES AND SELECTED BIBLIOGRAPHY

1. COURANT, R., and FRIEDRICH, K. O. *Supersonic Flow and Shock Waves*. New York: Interscience Publishers, Inc., 1948.
2. SAUER, R. Theory of Nonstationary Gas Flow, Part II, Plane Gas Waves with Compression Shocks, *Air Materiel Command Translation*, No. F-TS-758-RE (1946).
3. ROBERTS, R. C., and LIN, C. C. The Method of Characteristics in Compressible Flow, Part II (Unsteady Flow), *Air Materiel Command Report*, No. F-TR-1173-ND (1947).
4. KANTROWITZ, A. The Formation and Stability of Normal Shock Waves in Channel Flows, *NACA Tech. Note*, No. 1225 (1947).
5. SHULTZ-GRUNOW, F. Gas-Dynamic Investigations of the Pulse-Jet Tube, Parts I and II, *NACA Tech. Memo.*, No. 1131 (1947).
6. HESS, R. V. Study of Unsteady Flow Disturbances of Large and Small Amplitudes Moving Through Supersonic or Subsonic Steady Flows, *NACA Tech. Note*, No. 1878 (May 1949).
7. HUBER, P. W., FIRRON, C. E., JR., and DELPINO, F. Experimental Investigation of Moving Pressure Disturbances and Shock Waves and Correlation with One-Dimensional Unsteady-Flow Theory, *NACA Tech. Note*, No. 1903 (1949).
8. TAYLOR, G. I., and MACCOLL, J. W. The Mechanics of Compressible Fluids, Division H, Vol. 3, of *Aerodynamic Theory*, edited by W. F. Durand. Berlin: Julius Springer, 1934.
9. SAUER, R. Theory of the Nonstationary Gas Flow, Part IV, Plane Gas Flow with Friction, Heat Transfer, and Temperature Differences, *Air Materiel Command Translation*, No. F-TS-949-RE (1947).
10. DONALDSON, C. DUP., and SULLIVAN, R. D. The Effect of Wall Friction on the Strength of Shock Waves in Tubes and Hydraulic Jumps in Channels, *NACA Tech. Note*, No. 1942 (1949).
11. RESLER, E. L., LIN, S. C., and KANTROWITZ, A. The Production of High Temperature Gases in Shock Tubes. *Jour. App. Phys.*, Vol. 23, No. 12 (1952), p. 1390.
12. GLASS, I. I., MARTIN, W., and PATTERSON, G. N. A Theoretical and Experimental Study of the Shock Tube. UTIA Report No. 2, Institute of Aerophysics, Univ. of Toronto, 1953.

## PROBLEMS

25.1. A right-traveling shock with a pressure ratio of 4.50 travels into a region where  $c_1 = 1000$  ft/sec. For values of  $u_1$  of  $+1000, 0, -500, -1250, -1500, -2000$ , and  $-3000$  ft/sec, calculate the shock speed, the speed of the gas at the back of the shock, and the speeds of propagation of small right-traveling pressure pulses in front of and behind the shock. Plot to scale the lines representing these various speeds on a chart of  $c_1 t$  versus  $x$ .

25.2. A shock wave is formed in a tube of initially stagnant air (state 1) by the sudden acceleration of a piston to the speed  $u_P$ .

Find an algebraic relation between the dimensionless shock speed,  $W/c_1$ , and the dimensionless piston speed,  $u_P/c_1$ . Determine the limiting forms of this relation as  $u_P/c_1$  goes to infinity and as  $u_P/c_1$  goes to zero. Plot  $W/c_1$  against  $u_P/c_1$  on log-log paper for values of the latter between 0.1 and 100.

25.3. Consider the reflection of a strong shock from an open end at constant pressure. Find analytically the relation between the velocity change across the incident shock and the velocity change across the reflected rarefaction.

25.4. A right-traveling shock of pressure ratio 2.0 crosses a left-traveling shock of pressure ratio 4.0. Both shocks propagate into stagnant air at 70°F and 10 psia. Calculate the pressure, temperature, gas speed, and wave speed for all the zones around the point of interaction, using (a) the approximate treatment for weak shocks, and (b) the exact method for strong shocks.

25.5. A right-traveling shock of pressure ratio 2.0 is overtaken by a second right-traveling shock of pressure ratio 2.0. The first shock propagates into stagnant air at 70°F and 10 psia. Calculate the pressure, temperature, gas speed, and wave speed for all the zones around the point of interaction, using (a) the approximate treatment for weak shocks, and (b) the exact method for strong shocks.

25.6. Air is initially stagnant in a long tube at 70°F and one atm. A piston is instantaneously accelerated rightward to a speed of 200 ft/sec, and continues at that speed for a distance of one ft. It is then instantaneously decelerated to zero speed, and subsequently remains motionless. Work out the wave pattern in the  $x, t$ -diagram, showing gas pressures, gas temperatures, gas speeds, and wave speeds, up to the point where the pressure ratio across the shock wave has been reduced to 25 per cent of its original value, using (a) the approximate treatment for weak shocks, and (b) the exact treatment for strong shocks.

25.7. Consider a variation of Riemann's shock-tube problem, in which the high pressure on one side of the diaphragm is produced by the uniform explosion of a combustible mixture.

(a) Referring to Fig. 25.8, and letting  $T_3$  and  $p_3$  represent, respectively, the temperature and pressure in the completely burned gas at the instant the diaphragm ruptures, find  $p_2/p_1$  as a function of  $p_3/p_1$  and  $T_3/T_1$ , assuming that  $k_1 = k_3$ .

(b) Find the special form of the above relation when the initial pressures and temperatures are connected through the isentropic relation  $T_3/T_1 = (p_3/p_1)^{(k-1)/k}$ .

**25.8.** A very long tube is closed at one end. Between the closed end and a diaphragm one ft away is a combustible mixture. On the other side of the diaphragm is air at 70°F and one atm. The combustible mixture is exploded. When combustion is complete the gas is at 3000°F and 5 atm. At this instant the diaphragm shatters. Assuming that the burned gas has the same gas constants as air, plot the pressure distribution on the closed end for a period of 0.01 sec.

**25.9.** A shock tube 10 ft long is closed at both ends and has a diaphragm midway between the two ends. Initially the air on both sides is at 70°F. The pressures are initially 1.0 atm and 3.0 atm. The diaphragm is then broken.

Work out the wave pattern in the  $x, t$ -plane up to the time when the original shock wave has been reflected once from each end. Show in each zone the pressure, temperature, and gas speed, and show the absolute speed of each wave.

## PART VIII

### FLOW OF REAL GASES WITH VISCOSITY AND HEAT CONDUCTIVITY

Chapter 26  
THE LAMINAR BOUNDARY LAYER

**26.1. Introductory Remarks**

Most of the analytical discussions in this book have been based on the hypothesis of a *perfect fluid* without viscosity and without heat conductivity. The usefulness of this hypothesis proceeds from the premise implied in the term *boundary layer*, namely, that the viscous terms in the momentum and energy equations and the heat-conduction terms in the energy equation are, respectively, negligible compared with the remaining terms in those equations, except for the narrow regions near solid boundaries where the velocity and temperature gradients are of necessity so large as not to be negligible. In brief, for practical purposes, and assuming that the Reynolds Number of the flow is large compared with unity, viscous and heat conduction effects may be thought of as being confined to thin boundary layers near solid surfaces (or at the interface between streams of different speeds), and may be ignored elsewhere.

This point of view has been of the greatest practical utility, for it permits the field of flow for a given problem to be treated in two parts: (i) the potential flow outside the boundary layer, where viscous stresses are negligible compared with inertia stresses; and (ii) the thin boundary layer, where viscous stresses are of the same order of magnitude as inertia stresses, but the flow geometry is comparatively simple. For purely subsonic flows, the presence of a boundary layer on a body influences the potential flow only in a secondary way (unless reverse flow and separation occur) through an alteration in the effective boundaries of the potential flow by the amount of the boundary-layer displacement thickness. The potential flow, on the other hand, establishes the longitudinal pressure distribution for the boundary layer, and thereby plays a controlling role in the behavior and formation of the boundary layer.

When shocks appear in the field of flow, they may produce such large changes in boundary-layer flow as to have a first-order effect on the potential flow. This effect in turn influences the boundary layer, and thus there may be a considerable interaction between the potential flow, the shock wave, and the boundary layer.

The purpose of this chapter and of the two chapters which follow is

to round out the understanding of high-speed flows by investigating the most important features of compressible boundary layers. In this chapter we shall introduce some fundamental concepts and shall give primary attention to the laminar boundary layer.

### NOMENCLATURE

$c_p$	specific heat at constant pressure	$U_\infty$	velocity outside boundary layer
$C_f$	local skin-friction coefficient	$x$	curvilinear coordinate along surface
$C_D$	integrated skin-friction coefficient	$y$	curvilinear coordinate normal to surface
$C_H$	local Stanton Number	$\delta$	boundary-layer thickness
$h$	enthalpy per unit mass	$\delta_r$	thickness of thermal boundary layer
$\beta C$	film coefficient of heat transfer	$\delta_u$	thickness of velocity boundary layer
$k$	ratio of specific heats	$\zeta$	(See Eq. 26.28)
$L$	a characteristic length dimension	$\lambda$	coefficient of thermal conductivity
$M$	Mach Number	$\mu$	coefficient of viscosity
$n$	exponent in $\mu \sim T^n$	$\rho$	mass density
$\text{Nu}$	Nusselt Number	$\tau$	shear stress
$p$	pressure	$\psi$	stream function
$\text{Pr}$	Prandtl Number	$(\cdot)_\infty$	signifies conditions at edge of boundary layer
$q$	heat transfer per unit time and per unit area	$(\cdot)_w$	signifies conditions at wall
$r$	radius in cylindrical coordinates	$(\cdot)$	signifies dimensionless variable (see Eq. 26.22)
$R$	radius of curvature	$[O]$	signifies "of the order of magnitude of"
$\text{Rey}$	Reynolds Number		
$\mathcal{R}$	recovery factor		
$T$	absolute temperature		
$T_{aw}$	adiabatic wall temperature		
$T_0$	stagnation temperature		
$u, v$	velocity components in $x$ - and $y$ -directions, respectively		

**Simultaneous Action of Friction and Heat Transfer.** The frictional behavior of a boundary layer, even when it flows over a completely insulated wall, is always, to a greater or lesser extent, affected by heat transfer between fluid layers within the boundary layer. Viscous stresses within the boundary layer do shearing work on fluid particles. This shearing work tends to alter the temperatures of the fluid particles, and such variations in temperature not only lead to heat conduction but also produce changes in viscosity and density. Since the velocity distribution in the boundary layer depends on the density and viscosity distributions, as well as on the shear stress distribution, it follows that the skin-friction coefficient is in part controlled by heat transfer within the boundary layer.

For the flow of most liquids and of gases at low Mach Numbers

past an insulated body, such heat transfers are relatively unimportant, inasmuch as the internal heat transfers within the boundary layer are then of the same order as the viscous shearing work, and the latter is not large except at high Mach Numbers. In the case of liquids having coefficients of viscosity very sensitive to temperature, however, or in the case of gases at high speed, the effect is quite marked, and the analysis of the boundary layer must proceed not only from momentum considerations but from energy considerations as well.

To illustrate this train of thought, consider the high-speed boundary-layer flow next to a flat wall insulated against heat transfer. The outer layers of fluid do viscous shearing work on the inner layers, and, consequently, the internal energy and temperature of the fluid in the inner layers tend to rise. If there were no heat conduction whatsoever, the inner layers and the wall would become progressively hotter. On the other hand, the temperature gradients created by the viscous shearing work lead to a conduction of heat away from the wall which ultimately counterbalances the effects of the shearing work. The resulting steady-

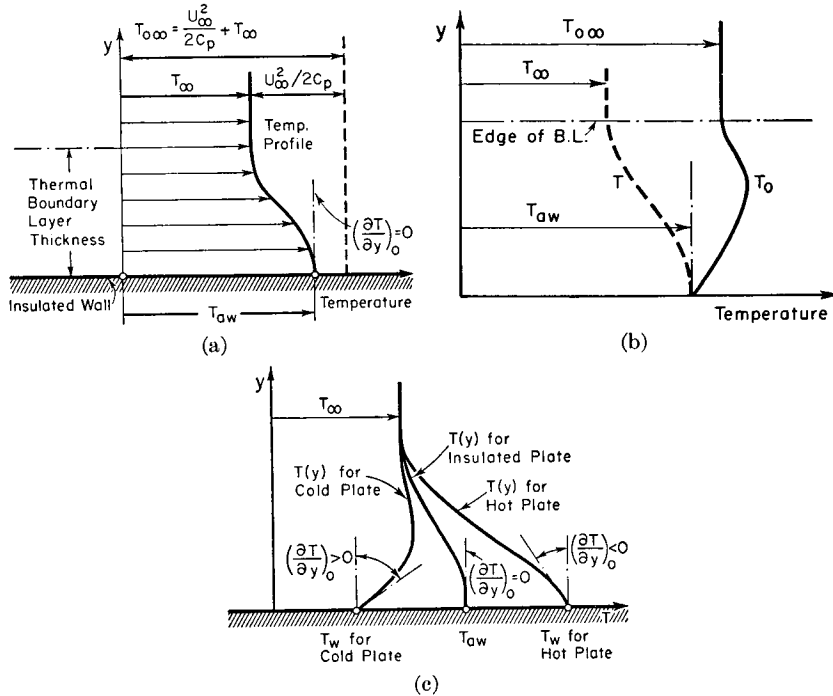


FIG. 26.1. Thermal boundary layer.

- Temperature distribution near insulated wall.
- Distribution of temperature and stagnation temperature near insulated wall.
- Effect of heating and cooling on temperature distribution.

state temperature distribution is illustrated in Fig. 26.1a. The *adiabatic wall temperature*  $T_{aw}$  is greater than the free-stream temperature  $T_\infty$ . Moreover, the temperature gradient at the wall is zero, in accordance with the Fourier equation of heat conduction in the  $y$ -direction together with the assumption of zero heat flux at the wall,

$$q = -\lambda \frac{\partial T}{\partial y} \quad (26.1)$$

where  $\lambda$  denotes the coefficient of thermal conductivity.

In gases the adiabatic wall temperature is always less than the free-stream stagnation temperature  $T_{0\infty}$ . For practical computations it is convenient to define a quantity known as the *recovery factor* which is a measure of the fraction of the local free-stream dynamic-temperature rise,  $U_\infty^2/2c_p$ , recovered at the wall:

$$\mathcal{R} = \frac{T_{aw} - T_\infty}{U_\infty^2/2c_p} = \frac{T_{aw} - T_\infty}{T_{0\infty} - T_\infty} = \frac{2}{(k - 1)\mathbf{M}_\infty^2} \left( \frac{T_{aw}}{T_\infty} - 1 \right) \quad (26.2)$$

If the entire plate is adiabatic, energy considerations dictate that the mean stagnation temperature with respect to mass flow must be equal to  $T_{0\infty}$ . Since the wall temperature is less than  $T_{0\infty}$ , it follows that the distribution of stagnation temperature within the boundary layer must be of the form shown in Fig. 26.1b, with some portion of the boundary layer having a stagnation temperature greater than  $T_{0\infty}$ .

When the wall is uninsulated, the temperature distributions in the boundary layer for heating and cooling of the stream are as shown schematically in Fig. 26.1c, the slopes of the curves at the wall being established by Eq. 26.1.

The important conclusion from these preliminary considerations is that the analysis of the high-speed compressible boundary layer must take into account the viscous shearing work and heat conduction effects within the boundary layer.

In gases the density varies inversely with the temperature, and the coefficients of viscosity and thermal conductivity vary approximately in proportion to the three-fourths power of the temperature. This observation leads to the conclusion that at high speeds the consideration of the variation of  $\mu$  and  $\lambda$  with temperature is of the same order of importance as the consideration of compressibility effects.

## 26.2. Differential Equations of the Laminar Boundary Layer

The most fundamental and the surest way of arriving at the differential equations of the compressible laminar boundary layer is to derive first the exact differential equations representing (i) the continuity equation, (ii) the momentum (Navier-Stokes) equation, and (iii) the energy

equation, and then to simplify these equations by bringing in the order-of-magnitude assumptions which are collectively known as the "boundary-layer approximations." This procedure (see Reference 1, for example) is too lengthy for our present purposes, and we shall proceed instead by first making the boundary-layer approximations and then deriving the simplified differential equations with the aid of these approximations.

**Boundary-Layer Assumptions.** Referring to the curved wall of Fig. 26.2, and using  $x$  and  $y$  to denote curvilinear coordinates along and normal to the wall, with corresponding velocity components  $u$  and  $v$ , the basic boundary-layer approximations may be listed as follows:

(i) The effects of viscosity are confined to a narrow region close to the wall, and thus the boundary-layer thickness  $\delta$  is very small compared with the distance from the stagnation point  $x$ . Considering only orders of magnitude, it follows from a consideration of the streamline slope that

$$v/u = [O]\delta/x$$

where  $[O]$  signifies "of the order of magnitude of." By assumption,  $\delta/x \ll 1$ , and thus it follows that the component of velocity normal to the plate is very small compared with the component along the plate, and that the boundary-layer flow is almost parallel to the wall.

(ii) The inertia forces and viscous forces within the boundary layer are of comparable magnitudes. Thus, considering again only orders of magnitude,

$$\rho u \frac{\partial u}{\partial x} = [O] \frac{\partial}{\partial y} \left( \mu \frac{\partial u}{\partial y} \right)$$

or

$$\frac{\rho U_\infty^2}{x} = [O] \frac{U_\infty}{\delta^2} \mu$$

giving

$$\frac{\delta}{x} = [O] \sqrt{\frac{\mu}{\rho U_\infty x}} = [O] \frac{1}{\sqrt{\text{Rey}}}$$

It follows from this that  $\delta$  is proportional to  $\sqrt{x}$ , and thus it is seen that assumption (i) cannot be satisfied near the stagnation point, since the boundary layer thickens in parabolic fashion. More strictly, to make assumption (i) valid, we assume further that we limit our analysis to

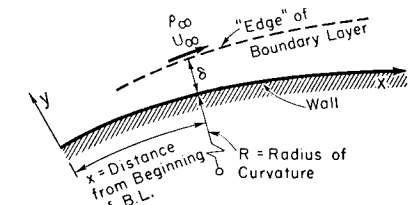


FIG. 26.2. Nomenclature. Note that  $\rho_\infty$  and  $U_\infty$  are the local properties outside the boundary layer, and are in general functions of  $x$ .

regions where the Reynolds Number ( $\rho U_\infty x / \mu$ ) is large compared with unity.

(iii) The radius of curvature of the wall,  $R$ , is at least of the same order of magnitude as  $x$ . The significance of this is seen by writing the leading terms in the momentum equation for the  $y$ -direction as

$$\frac{\partial p}{\partial y} = [O] \rho \frac{V^2}{R}$$

or

$$(\Delta p)_{\text{boundary layer}} = [O] \rho U_\infty^2 \frac{\delta}{R} = [O] \rho U_\infty^2 \frac{\delta}{x} \cdot \frac{x}{R}$$

Now if  $x/R$  is of order of magnitude unity or less, it follows that  $(\Delta p)_{\text{b.l.}}/\rho U_\infty^2$  is not greater in order of magnitude than  $\delta/x$ . In that case the pressure within the boundary layer at any value of  $x$  scarcely differs from the pressure at the edge of the boundary layer at the same value of  $x$ , and we are justified for practical purposes in assuming that the pressure within the boundary layer varies only in the  $x$ -direction. This leads to two important conclusions: (i) the pressure within the boundary layer is established by the potential flow outside the boundary layer, and (ii) the approximate momentum equation in the  $y$ -direction takes the trivial form  $\partial p/\partial y = 0$ . The latter conclusion would not be correct, however, in the vicinity of a sharp concave corner, or near an extremely slender body of revolution.

(iv) The velocity and temperature gradients in the  $x$ -direction are much smaller than in the  $y$ -direction. From this it follows that the viscous shear stresses associated with the term  $\partial u/\partial x$  and the heat conduction associated with the term  $\partial T/\partial x$  may be respectively ignored

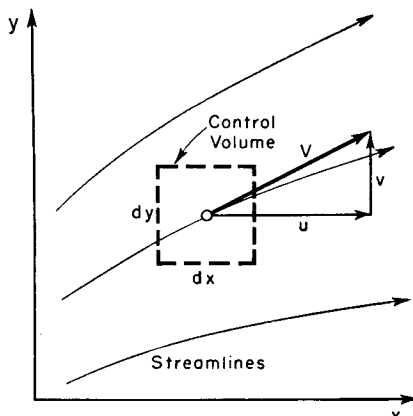


FIG. 26.3. Control volume for analysis of boundary layer.

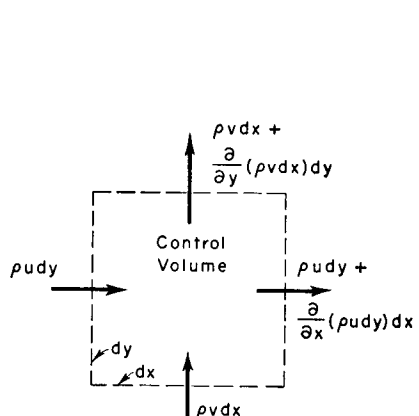


FIG. 26.4. Mass flows through control surface.

compared with the corresponding effects embodied in the terms  $\partial u/\partial y$  and  $\partial T/\partial y$ .

We shall now derive the laminar boundary-layer equations for a two-dimensional steady flow in rectangular Cartesian coordinates, making use of the stated approximations. Within these approximations, however, the equations are also valid for the curvilinear coordinates of Fig. 26.2. In deriving the three governing physical equations, we shall consider the flow through the infinitesimal control volume of Fig. 26.3, with unit width normal to the paper.

**Continuity Equation.** The mass flows entering and leaving the control volume are indicated in Fig. 26.4, from which the condition that the *net* mass efflux is zero becomes

$$\frac{\partial}{\partial x} (\rho u) + \frac{\partial}{\partial y} (\rho v) = 0 \quad (26.3)$$

There are no simplifications possible from the boundary-layer approximations.

**Momentum Equation.** As stated above, the momentum equation in the  $y$ -direction, within the boundary-layer approximations, may be written as

$$\frac{\partial p}{\partial y} = 0 \quad (26.4)$$

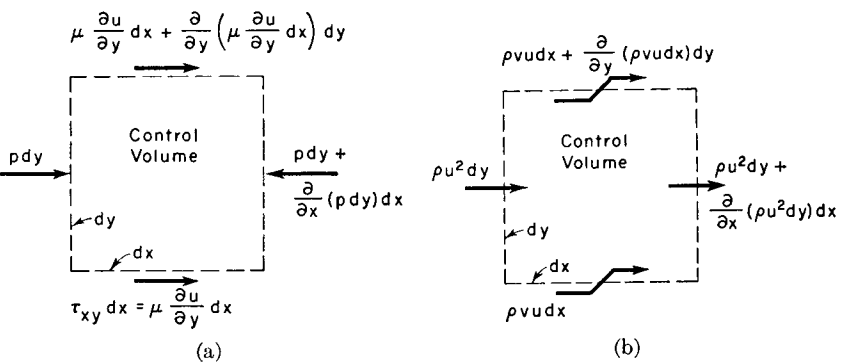


FIG. 26.5. Illustrates momentum equation.

(a) Forces acting on fluid within control volume.  
(b) Momentum fluxes in  $x$ -direction through control surface.

Fig. 26.5a shows the forces acting instantaneously in the  $x$ -direction on the fluid within the control volume (body forces are assumed negligible). The  $x$ -components of momentum fluxes entering and leaving the control volume are shown in Fig. 26.5b. We now set the net force

acting on the control volume in the  $x$ -direction equal to the net increase of momentum flux in the  $x$ -direction. Thus we obtain

$$\begin{aligned}-\frac{\partial p}{\partial x} + \frac{\partial}{\partial y} \left( \mu \frac{\partial u}{\partial y} \right) &= \frac{\partial}{\partial x} (\rho u^2) + \frac{\partial}{\partial y} (\rho v u) \\ &= u \left[ \frac{\partial}{\partial x} (\rho u) + \frac{\partial}{\partial y} (\rho v) \right] + \rho u \frac{\partial u}{\partial x} + \rho v \frac{\partial u}{\partial y}\end{aligned}$$

From the continuity equation, Eq. 26.3, the term in brackets on the right-hand side is exactly zero, and so we get the dynamic equation in the form

$$\rho u \frac{\partial u}{\partial x} + \rho v \frac{\partial u}{\partial y} = -\frac{\partial p}{\partial x} + \frac{\partial}{\partial y} \left( \mu \frac{\partial u}{\partial y} \right) \quad (26.5)$$

**Energy Equation.** The energy equation for steady flow through a control volume states that the net efflux of enthalpy plus kinetic energy

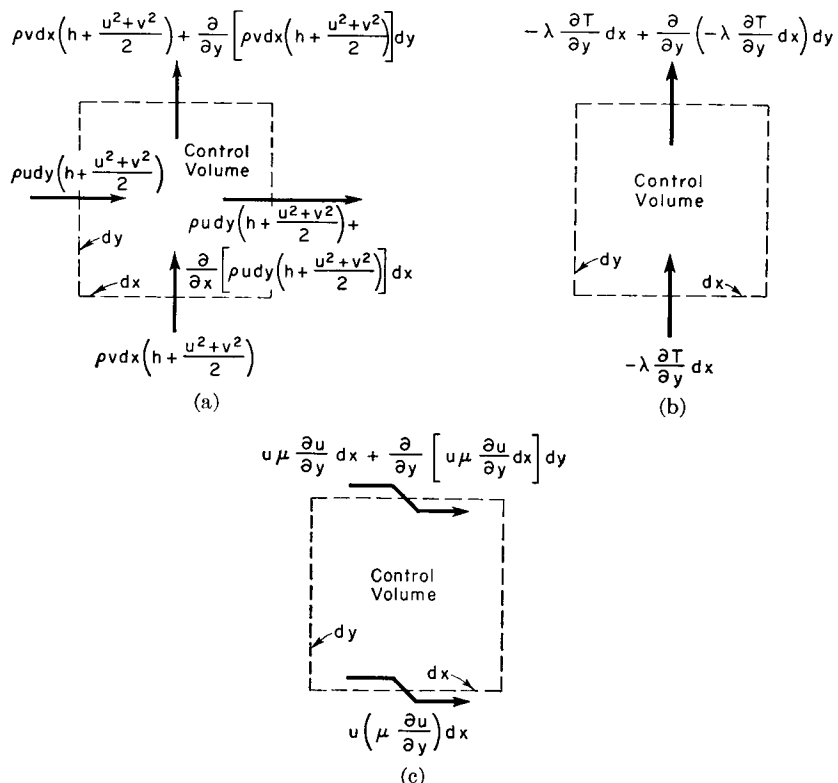


FIG. 26.6. Illustrates energy equation.

- (a) Fluxes of enthalpy and kinetic energy through control surface.
- (b) Heat conduction through control surface.
- (c) Rates of shearing work.

is equal to the net rate of heat transfer into the control volume plus the net rate of shear work into the control volume.

Fig. 26.6a shows the fluxes of enthalpy plus kinetic energy into and out of the control volume. The rates of heat conduction across the control surface are shown in Fig. 26.6b, the conduction in the  $x$ -direction being omitted because  $\partial T/\partial x$  is assumed small compared with  $\partial T/\partial y$ .

The term "shaft work" which is referred to in thermodynamics texts in connection with the steady-flow energy equation comprises work done by shearing forces at the control surface when the material at the control surface is in motion in the direction of these forces. At the lower surface of the control volume the fluid within the control volume exerts on the fluid outside the control volume a force  $\mu(\partial u/\partial y)dx$  in the  $x$ -direction, and the fluid on which this force is exerted moves with the speed  $u$  in the  $x$ -direction. At this boundary the fluid within the control volume therefore delivers shear work to the surroundings at the rate  $u\mu(\partial u/\partial y)dx$ . Similarly, the fluid within the control volume receives shear work from the surroundings at the upper boundary at the rate indicated in the sketch.

The net outgoing flux of enthalpy and kinetic energy per unit area  $dx dy$  is seen to be

$$\frac{\partial}{\partial x} (\rho u) \left( h + \frac{u^2 + v^2}{2} \right) + \frac{\partial}{\partial y} (\rho v) \left( h + \frac{u^2 + v^2}{2} \right)$$

Expansion of these terms yields

$$\begin{aligned}\left( h + \frac{u^2 + v^2}{2} \right) \left[ \frac{\partial}{\partial x} (\rho u) + \frac{\partial}{\partial y} (\rho v) \right] \\ + \rho u \frac{\partial}{\partial x} \left( h + \frac{u^2 + v^2}{2} \right) + \rho v \frac{\partial}{\partial y} \left( h + \frac{u^2 + v^2}{2} \right)\end{aligned}$$

and comparison with the continuity equation then shows that the term in square brackets is exactly zero.

We shall suppose that the enthalpy is a function only of temperature. This assumption, together with the perfect gas law  $p = \rho RT$ , leads to the thermodynamic relation

$$dh = c_p dT; \quad \partial h/\partial x = c_p(\partial T/\partial x); \quad \text{etc.}$$

Using the foregoing results, the energy equation may now be written in the form

$$\begin{aligned}\rho u \left[ c_p \frac{\partial T}{\partial x} + \frac{\partial}{\partial x} \left( \frac{u^2 + v^2}{2} \right) \right] + \rho v \left[ c_p \frac{\partial T}{\partial y} + \frac{\partial}{\partial y} \left( \frac{u^2 + v^2}{2} \right) \right] \\ = \frac{\partial}{\partial y} \left( \lambda \frac{\partial T}{\partial y} \right) + \frac{\partial}{\partial y} \left( \mu u \frac{\partial u}{\partial y} \right) \quad (26.6)\end{aligned}$$

ENERGY EQUATION FOR CONSTANT  $c_p$ . A form of the energy equation which is illuminating is found by assuming that  $c_p$  is constant, i.e., independent of  $T$ . Using the approximation that  $v/u \ll 1$ , we set

$$T_0 = T + \frac{u^2 + v^2}{2c_p} \cong T + \frac{u^2}{2c_p}$$

and from this we obtain

$$u \frac{\partial u}{\partial y} = \frac{\partial}{\partial y} \frac{u^2}{2} = c_p \left( \frac{\partial T_0}{\partial y} - \frac{\partial T}{\partial y} \right)$$

Eq. 26.6, after division by  $c_p$ , then takes the form,

$$\rho u \frac{\partial T_0}{\partial x} + \rho v \frac{\partial T_0}{\partial y} = \frac{\partial}{\partial y} \left( \mu \frac{\partial T_0}{\partial y} \right) + \frac{\partial}{\partial y} \left[ \left( \frac{1}{\text{Pr}} - 1 \right) \mu \frac{\partial T}{\partial y} \right] \quad (26.7)$$

where  $\text{Pr} \equiv c_p \mu / \lambda$  is the Prandtl Number. This form of the energy equation refers primarily to the variation in stagnation temperature, and indicates besides that the Prandtl Number must be reproduced in order to obtain similarity between model and prototype experiments.

ENERGY EQUATION FOR VARIABLE  $c_p$ . A third form of the energy equation is obtained by combining it with the momentum equation. Multiplying Eq. 26.5 by  $u$ , and rearranging, we obtain

$$\begin{aligned} \rho u \frac{\partial}{\partial x} \frac{u^2}{2} + \rho v \frac{\partial}{\partial y} \frac{u^2}{2} &= -u \frac{\partial p}{\partial x} + u \frac{\partial}{\partial y} \left( \mu \frac{\partial u}{\partial y} \right) \\ &= -u \frac{\partial p}{\partial x} + \frac{\partial}{\partial y} \left( \mu u \frac{\partial u}{\partial y} \right) - \mu \left( \frac{\partial u}{\partial y} \right)^2 \end{aligned}$$

Subtracting this expression from Eq. 26.6, and noting that the terms

$$u \frac{\partial v^2}{\partial x} \frac{1}{2} \quad \text{and} \quad v \frac{\partial v^2}{\partial y} \frac{1}{2}$$

may both be dropped in accordance with the boundary-layer assumptions, we get

$$\rho u c_p \frac{\partial T}{\partial x} + \rho v c_p \frac{\partial T}{\partial y} = u \frac{\partial p}{\partial x} + \frac{\partial}{\partial y} \left( \lambda \frac{\partial T}{\partial y} \right) + \mu \left( \frac{\partial u}{\partial y} \right)^2 \quad (26.8)$$

This equation, which is valid for variable  $c_p$ ,  $\lambda$ , and  $\mu$ , is the most commonly used form of the energy equation for the laminar boundary layer.

Mathematically, the problem of the laminar boundary layer may now be summarized as that of finding the simultaneous solution to Eqs. 26.3, 26.4, 26.5, and 26.8 for given wall conditions, for a given longitudinal pressure distribution  $p(x)$ , and for a gas with specified thermodynamic properties.

### 26.3. Flow with Prandtl Number Unity

Because of the large temperature variations which may exist within a high-speed boundary layer, consideration must be given to the variations with  $y$  and  $x$  of  $c_p$ ,  $\mu$ ,  $\lambda$  and  $\text{Pr}$ . For gases, the variation with pressure of these fluid properties is so small as not to be important for our present purpose. The variations of  $c_p$  and  $\text{Pr}$  with temperature are known to be small, and are therefore not usually taken into account in boundary-layer calculations except at very high Mach Numbers. However,  $\mu$  and  $\lambda$ , which are proportional to each other for constant  $c_p$  and  $\text{Pr}$ , are strong functions of temperature, and this dependency has a correspondingly significant influence on boundary-layer behavior.

**Simplified Energy Equation.** The Prandtl Number for gases is always less than unity, and is in the general neighborhood of 0.75. Examination of Eq. 26.7 shows that the energy equation is considerably simplified when the Prandtl Number is unity. Since this value does in fact agree approximately with the actual Prandtl Numbers for gases, we shall in this article assume that  $\text{Pr} = 1$ . Thus we may easily obtain some important practical results.

The special form of the energy equation we shall now consider is

$$\rho u \frac{\partial T_0}{\partial x} + \rho v \frac{\partial T_0}{\partial y} = \frac{\partial}{\partial y} \left( \mu \frac{\partial T_0}{\partial y} \right) \quad (26.9)$$

**Adiabatic Flow.** Obviously Eq. 26.9 is satisfied when  $T_0$  is everywhere constant, and therefore a particular solution is

$$T_0 = T + \frac{u^2}{2c_p} = \text{constant}$$

The value of the constant is found by noting that the stagnation temperature at the edge of the boundary layer is that of the adiabatic potential flow. Hence

$$T_0 = T + \frac{u^2}{2c_p} = T_{0\infty} \quad (26.10)$$

Since  $u = 0$  at the wall, it follows from Eq. 26.10 that the wall temperature is constant and equal to the free-stream stagnation temperature. Furthermore, the heat flux through the boundary layer in the  $y$ -direction is found from the Fourier equation and Eq. 26.10 to be given by

$$q = -\lambda \frac{\partial T}{\partial y} = \frac{u}{c_p} \frac{\partial u}{\partial y}$$

from which we reach the conclusion that at the wall, where  $u = 0$ , the heat flux is also zero. Elsewhere, however, heat flows from the wall toward the edge of the boundary layer.

**CONCLUSIONS.** To summarize, we have found that when a gas with Prandtl Number unity flows past an insulated wall, either with or without a longitudinal pressure gradient, the stagnation temperature is constant throughout the boundary layer. The adiabatic wall temperature  $T_{aw}$  is then equal to the free-stream stagnation temperature  $T_{0\infty}$ . According to Eq. 26.2, moreover, the recovery factor is unity.

**PHYSICAL INTERPRETATION.** A physical interpretation of this result may be reached from energy considerations by noting that the stagnation temperature can be constant throughout the boundary layer only when the rate of heat transfer crossing a surface in the fluid is exactly balanced by the rate of shear work crossing the same surface in the opposite direction. Referring to Fig. 26.6, this requirement may be stated as

$$-\lambda \frac{\partial T}{\partial y} = \mu u \frac{\partial u}{\partial y} = \mu \frac{\partial}{\partial y} \left( \frac{u^2}{2} \right)$$

Rearranging, and assuming  $c_p$  and  $\text{Pr}$  to be constant, we may restate this as

$$\frac{\partial}{\partial y} \left[ T + (\text{Pr}) \frac{u^2}{2c_p} \right] = 0$$

which yields a constant stagnation temperature only when  $\text{Pr} = 1$ .

Thus we may say in a crude way that (i) the Prandtl Number partially controls the ratio of viscous shear work to thermal heat conduction; and (ii) when the Prandtl Number is unity and the plate is insulated, this ratio is unity, and so the stagnation temperature is constant everywhere. A parallel argument would also lead us to the conclusion that, for a Prandtl Number of less than unity, the recovery factor is likewise less than unity, a conclusion which will shortly be verified.

The results obtained above indicate that the temperature reached by an insulated body in a high-speed gas stream is much closer to the free-stream stagnation temperature than to the free-stream static temperature. This conclusion has obvious and important practical implications in respect (i) to the surface temperatures of high-speed aircraft, rockets, and projectiles, (ii) to the problem of aircraft-cabin cooling at high speeds, (iii) to the surface temperatures of the blades and nozzle passages in steam and gas turbines, (iv) to the problem of thermometry at high Mach Numbers, and (v) to the temperature of the walls of high-speed wind tunnels. It explains also why the real obstacle to flight at extreme speeds is a "thermal barrier" rather than a "sonic barrier."

**Flow with Zero Pressure Gradient and Constant Wall Temperature.** Thus far we have not restricted the discussion to flows with zero pressure

gradients. To make further progress without introducing great analytical complexity, it is necessary to make this additional assumption. We shall therefore consider the flow along a flat plate which lies parallel to the gas stream. With the assumption that  $\partial p / \partial x = 0$ , Eq. 26.5 becomes

$$\rho u \frac{\partial u}{\partial x} + \rho v \frac{\partial u}{\partial y} = \frac{\partial}{\partial y} \left( \mu \frac{\partial u}{\partial y} \right) \quad (26.5a)$$

**PARTICULAR SOLUTION FOR CONSTANT WALL TEMPERATURE.** A comparison between Eqs. 26.5a and 26.9 now shows that they can be reduced to the same equation if

$$T_0 \equiv T + \frac{u^2}{2c_p} = au + b$$

where  $a$  and  $b$  are constants to be found from the boundary conditions. By using this special relation between temperature and velocity, the energy equation is automatically satisfied when the momentum equation is satisfied. The relation requires that the wall temperature be constant, inasmuch as  $u = 0$  at the wall.

The resulting physical situation is entirely plausible, since if we have uniform flow along a plate of constant temperature, there is no length dimension to the problem and one should expect similarity in the flow patterns at all values of  $x$ . One aspect of this anticipated similarity is that points in the boundary layer having the same velocity should also have the same temperature. This results, incidentally, in the viscous boundary layer and the thermal boundary layer having equal thicknesses.

These considerations indicate that we are considering a particular solution to the governing equations, a solution which corresponds to the flow past a flat plate (which may be either heated or cooled) having constant wall temperature.

**TEMPERATURE-VELOCITY RELATIONSHIP.** The constants  $a$  and  $b$  are evaluated by noting from the boundary conditions that

$$T_0 = T_{0\infty} \quad \text{when } u = U_\infty$$

$$T_0 = T_w \quad \text{when } u = 0$$

Thus we get, for the distribution of stagnation temperature,

$$\frac{T_0 - T_w}{T_{0\infty} - T_w} = \frac{u}{U_\infty} \quad (26.11)$$

Introducing the definition  $T_0 \equiv T + (u^2/2c_p)$  into Eq. 26.11, the distribution of temperature may be found as

$$\begin{aligned} T - T_w &= (T_{0\infty} - T_w) \frac{u}{U_\infty} - \frac{u^2}{2c_p} \\ &= (T_{0\infty} - T_w) \frac{u}{U_\infty} - \frac{k-1}{2} M_\infty^2 T_\infty \left( \frac{u}{U_\infty} \right)^2 \quad (26.12) \end{aligned}$$

**HEAT FLUX.** The heat flux in the  $y$ -direction (positive when away from the plate) may now be computed from Eqs. 26.1 and 26.12 as

$$q = \frac{\lambda}{U_\infty} \frac{\partial u}{\partial y} \left[ T_w - T_{0\infty} + (k-1) M_\infty^2 T_\infty \frac{u}{U_\infty} \right]$$

In the absence of separation the velocity always increases as  $y$  increases. Hence,  $\partial u / \partial y > 0$ , and the direction of heat transfer accordingly depends only on the sign of the quantity within the square brackets. When  $T_w$  exceeds  $T_{0\infty}$ , it is seen from the foregoing equation that the heat flux at all points within the boundary layer is away from the plate, corresponding to the curve marked "hot plate" in Fig. 26.1c. When  $T_w$  is less than  $T_{0\infty}$ , on the other hand, there may under certain circumstances be a heat flux away from the plate at some points in the boundary layer even though at the plate itself heat flows from the gas to the plate; this state of affairs corresponds to the curve marked "cold plate" in Fig. 26.1c.

We now eliminate  $\partial u / \partial y$  in the foregoing equation by employing the relation  $\tau = \mu(\partial u / \partial y)$ , and, furthermore, we make use of the assumption that  $\text{Pr} \equiv c_p \mu / \lambda = 1$ . Thus we get

$$q = \frac{c_p}{\text{Pr}} \frac{\tau}{U_\infty} \left[ T_w - T_{0\infty} + (k-1) M_\infty^2 T_\infty \frac{u}{U_\infty} \right]$$

for any point in the boundary layer. Of greatest importance is the heat flux at the wall ( $q_w$ ), which is found by setting  $u = 0$ , thus leading to

$$q_w = c_p \frac{\tau_w}{U_\infty} (T_w - T_{0\infty}) = c_p \frac{\tau_w}{U_\infty} (T_w - T_{aw}) \quad (26.13)$$

where on the right-hand side we have made use of the fact that  $T_{0\infty} = T_{aw}$  when  $\text{Pr} = 1$ .

**DEFINITION OF FILM COEFFICIENT OF HEAT TRANSFER.** The important conclusion to be drawn from Eq. 26.13 is that the direction of heat flow at the plate surface depends not on the difference between the wall temperature and the free-stream temperature ( $T_w - T_\infty$ ), but rather on the difference between the wall temperature and the adiabatic wall temperature. This suggests that in defining a film

coefficient of heat transfer,  $\mathfrak{C}$ , for compressible fluids, the appropriate temperature differential is  $(T_w - T_{aw})$ . Hence, we define

$$\mathfrak{C} \equiv \frac{q_w}{(T_w - T_{aw})} \quad (26.14)$$

**REYNOLDS ANALOGY BETWEEN FRICTION AND HEAT TRANSFER.** We introduce further the local skin-friction coefficient based on the local free-stream properties,

$$C_{f\infty} \equiv \frac{\tau_w}{\frac{1}{2} \rho_\infty U_\infty^2} \quad (26.15)$$

Eq. 26.13 may then be written as

$$C_{H\infty} \equiv \frac{\mathfrak{C}}{c_p \rho_\infty U_\infty} = \frac{C_{f\infty}}{2} \quad (26.16)$$

where  $C_H$  is the Stanton Number.

This result is recognized as being identical with the familiar Reynolds analogy between friction and heat transfer for incompressible flow. We therefore conclude that, at least for  $\text{Pr} = 1$ , the Reynolds analogy is valid also for compressible flow if  $\mathfrak{C}$  is defined as in Eq. 26.14.

By writing the identity

$$C_{H\infty} = \frac{\mathfrak{C}}{c_p \rho_\infty U_\infty} = \frac{\mathfrak{C} x}{\lambda_\infty} \cdot \frac{\lambda_\infty}{c_p \mu_\infty} \cdot \frac{\mu_\infty}{x \rho_\infty U_\infty} = \frac{\text{Nu}_\infty}{\text{Pr}_\infty \cdot \text{Rey}_\infty}$$

where  $\text{Nu}$  signifies the dimensionless Nusselt Number ( $\mathfrak{C} x / \lambda$ ), we get, upon noting again that  $\text{Pr} = 1$  for the present case,

$$\text{Nu}_\infty = \frac{C_{f\infty}}{2} \text{Rey}_\infty \quad (26.17)$$

as another form of the friction-heat transfer analogy.

**DIMENSIONLESS COEFFICIENTS BASED ON WALL PROPERTIES.** For some purposes it is more fundamental to base the several dimensionless coefficients on the fluid properties  $\rho$ ,  $\lambda$  and  $\mu$  taken at the local wall temperature, and denoted respectively by  $\rho_w$ ,  $\lambda_w$ , and  $\mu_w$ . Defining

$$C_{f_w} \equiv \frac{\tau_w}{\frac{1}{2} \rho_w U_\infty^2}; \quad \text{Nu}_w \equiv \frac{\mathfrak{C} x}{\lambda_w}; \quad \text{Rey}_w \equiv \frac{\rho_w x U_\infty}{\mu_w} \quad (26.18)$$

and beginning again with Eq. 26.13, we obtain

$$C_{Hw} \equiv \frac{\mathfrak{C}}{c_p \rho_w U_\infty} = \frac{C_{f_w}}{2}; \quad \text{Nu}_w = \frac{C_{f_w}}{2} \cdot \text{Rey}_w \quad (26.19)$$

The results obtained thus far, although of interest and practical importance, are based only on the connection between the temperature

and velocity profiles (Eq. 26.11). To arrive at the velocity and temperature distributions and at the skin-friction coefficient, it is now necessary to integrate Eqs. 26.5a and 26.3.<sup>(2,4)</sup>

**STREAM FUNCTION.** The latter equation, i.e., conservation of mass, is identically satisfied if we introduce a stream function  $\psi(x, y)$ , the derivatives of which yield

$$u = \frac{\rho_\infty}{\rho} \frac{\partial \psi}{\partial y}; \quad v = -\frac{\rho_\infty}{\rho} \frac{\partial \psi}{\partial x} \quad (26.20)$$

**TRANSFORMATION OF VON MISES.** We now transform from  $x$  and  $y$  as independent variables to  $x$  and  $\psi$ , a transformation first employed by von Mises for incompressible flow and one which leads to important simplifications in the momentum equation. The basic relations for this interchange of variables are

$$\left(\frac{d}{dy}\right)_x = \left(\frac{d\psi}{dy}\right)_x \left(\frac{\partial}{\partial \psi}\right)_x + \left(\frac{dx}{dy}\right)_x \left(\frac{\partial}{\partial x}\right)_\psi = \frac{\rho u}{\rho_\infty} \left(\frac{\partial}{\partial \psi}\right)_x$$

$$\left(\frac{d}{dx}\right)_y = \left(\frac{d\psi}{dx}\right)_y \left(\frac{\partial}{\partial \psi}\right)_x + \left(\frac{dx}{dx}\right)_y \left(\frac{\partial}{\partial x}\right)_\psi = -\frac{\rho v}{\rho_\infty} \left(\frac{\partial}{\partial \psi}\right)_x + \left(\frac{\partial}{\partial x}\right)_\psi$$

Applying these transformations to Eq. 26.5a, there results

$$\rho_\infty \frac{\partial u}{\partial x} = \frac{\partial}{\partial \psi} \left( \mu u \frac{\rho}{\rho_\infty} \frac{\partial u}{\partial \psi} \right) \quad (26.21)$$

where the partial derivatives are to be taken with  $x$  and  $\psi$  as independent variables.

**INTRODUCTION OF DIMENSIONLESS VARIABLES.** We now generalize the above equation by introducing the nondimensional variables

$$\begin{aligned} \tilde{u} &\equiv u/U_\infty & \tilde{T} &\equiv T/T_\infty \\ \tilde{x} &\equiv x/L & \tilde{\mu} &\equiv \mu/\mu_\infty \\ \tilde{\rho} &\equiv \rho/\rho_\infty & \tilde{\psi} &\equiv \psi/\sqrt{\mu_\infty L U_\infty / \rho_\infty} \\ \tilde{T}_{0\infty} &\equiv T_{0\infty}/T_\infty = 1 + \frac{k-1}{2} M_\infty^2 \end{aligned} \quad (26.22)$$

The temperature-velocity relation of Eq. 26.12 becomes, in terms of these dimensionless quantities,

$$\tilde{T} - \tilde{T}_w = (\tilde{T}_{0\infty} - \tilde{T}_w) \tilde{u} - \frac{k-1}{2} M_\infty^2 \tilde{u}^2 \quad (26.23)$$

Furthermore, since the pressure is constant through the boundary layer, it follows from the perfect gas law  $p = \rho RT$  that  $\tilde{\rho}\tilde{T} = 1$ .

**INTRODUCTION OF APPROXIMATE TEMPERATURE-VISCOSITY LAW.** We now assume that the viscosity-temperature relation for a gas may be written

$$\tilde{\mu} = \frac{\mu}{\mu_\infty} = \left(\frac{T}{T_\infty}\right)^n = \tilde{T}^n \quad (26.24)$$

The kinetic theory of gases predicts that  $n = 1/2$ , but experimental data for air indicate that  $n = 0.76$  is a better value.

Introducing the foregoing relations, Eq. 26.21 becomes

$$\frac{\partial \tilde{u}}{\partial \tilde{x}} = \frac{\partial}{\partial \tilde{\psi}} \left( \tilde{\mu} \tilde{T}^{n-1} \frac{\partial \tilde{u}}{\partial \tilde{\psi}} \right) \quad (26.25)$$

The shear stress may be written, with the help of the first transformation formula, as

$$\tau = \mu \left( \frac{\partial u}{\partial y} \right)_x = \mu \frac{\rho u}{\rho_\infty} \left( \frac{\partial u}{\partial \psi} \right)_x$$

We now form the dimensionless skin-friction coefficient, and we introduce the dimensionless variables of Eqs. 26.22 together with the relation  $\tilde{\rho}\tilde{T} = 1$ . Thus we obtain

$$C_{f\infty} = \frac{\tau_w}{\frac{1}{2} \rho_\infty U_\infty^2} = 2 \left[ \tilde{T}^{n-1} \tilde{\mu} \frac{\partial \tilde{u}}{\partial \tilde{\psi}} \right]_{\text{wall}} \sqrt{\frac{\mu_\infty}{\rho_\infty U_\infty L}} \quad (26.26)$$

**SPECIAL RESULTS WHEN VISCOSITY IS PROPORTIONAL TO TEMPERATURE.** Before going further with the solution for the velocity profile, we shall pause to reach a simple but important conclusion based on the assumption that the temperature-viscosity relation is approximately satisfied by setting  $n = 1$ . We then observe that Eq. 26.25 no longer depends in any way on the density. Therefore, the well-known solution of Blasius, in the form  $\tilde{u}(\tilde{x}, \tilde{\psi})$  for incompressible flow<sup>(1)</sup> must be equally valid for compressible flow. If this is true, then it follows from Eq. 26.26 that the magnitude of  $C_{f\infty} \sqrt{\text{Rey}_\infty}$  is independent of Mach Number, and that it must therefore be equal to the Blasius value, 0.664.

With  $n = 1$  (i.e.,  $\rho\mu = \text{constant}$ ), it is equally true that  $C_{f\infty} \sqrt{\text{Rey}_\infty} = 0.664$ . This is perhaps the preferable form, since we shall see presently that (when  $n \neq 1$ ) the influence of Mach Number is minimized if one bases the fluid properties on wall temperature rather than on free-stream temperature.

If  $\mu$  varied directly with  $T$ , the foregoing considerations show that the skin-friction coefficient would be independent of Mach Number, and, according to Eqs. 26.17 and 26.19, that the Nusselt Number would be likewise independent of Mach Number. Since  $\mu \propto T^{0.76}$  is a fairly accurate representation of the viscosity-temperature law, we would

expect that the skin-friction coefficient and Nusselt Number would depend on Mach Number, but only in a weak way. Later we shall see that this is true.

**REDUCTION TO ORDINARY DIFFERENTIAL EQUATION.** We now return to the problem of solving Eq. 26.25 for the velocity distribution. This is a partial differential equation, but since it is to be expected that there will be similarity of velocity profiles at different values of  $\tilde{x}$ , we seek a combined variable in  $\tilde{\psi}$  and  $\tilde{x}$  which will reduce the partial differential equation to an ordinary differential equation. Accordingly, we postulate that  $\tilde{u}$  is a function only of  $\xi$ , where the latter is defined arbitrarily by

$$\xi \equiv \tilde{\psi}^a \tilde{x}^b$$

where  $a$  and  $b$  are pure numbers to be determined in such manner that Eq. 26.25 may be expressed in terms of  $\xi$  as the single independent variable. Substituting into Eq. 26.25, we get

$$\frac{d\tilde{u}}{d\xi} \frac{\partial \xi}{\partial \tilde{x}} = \left( \frac{\partial \xi}{\partial \tilde{\psi}} \right) \frac{d}{d\xi} \left[ \tilde{u} \tilde{T}^{n-1} \frac{\partial \xi}{\partial \tilde{\psi}} \frac{d\tilde{u}}{d\xi} \right]$$

which gives

$$b\tilde{x}^{b-1} \tilde{\psi}^a \frac{d\tilde{u}}{d\xi} = a\tilde{\psi}^{a-1} \tilde{x}^b \frac{d}{d\xi} \left[ \tilde{u} \tilde{T}^{n-1} a\tilde{\psi}^{a-1} \tilde{x}^b \frac{d\tilde{u}}{d\xi} \right]$$

By setting  $a = 1$ , and noting that  $x$  and  $\xi$  are independent, this may be reduced to

$$b\tilde{x}^{-1} \xi \frac{d\tilde{u}}{d\xi} = \tilde{x}^{2b} \frac{d}{d\xi} \left( \tilde{u} \tilde{T}^{n-1} \frac{d\tilde{u}}{d\xi} \right)$$

Then, by setting  $b = -1/2$ , we succeed in eliminating  $x$  altogether, and thus we obtain an ordinary differential equation,

$$-\frac{\xi}{2} \frac{d\tilde{u}}{d\xi} = \frac{d}{d\xi} \left( \tilde{u} \tilde{T}^{n-1} \frac{d\tilde{u}}{d\xi} \right) \quad (26.27)$$

where the variable  $\xi$  is now given by

$$\xi \equiv \frac{\tilde{\psi}}{\sqrt{\tilde{x}}} = \frac{\psi}{\sqrt{U_\infty \mu_\infty x / \rho_\infty}} \quad (26.28)$$

**PROCEDURE FOR FINDING VELOCITY PROFILE.** The nonlinear equation Eq. 26.27 may be solved by successive approximations. The first approximation  $\tilde{u}(\xi)$  is conveniently assumed as the incompressible solution of Blasius. Then, since  $\tilde{T}(\xi)$  for the first approximation may be found from Eq. 26.23 for a given  $\tilde{T}_\infty$ , the term  $\tilde{u} \tilde{T}^{n-1}$  may be computed in first approximation. If we let

$$f(\xi) \equiv \tilde{u} \tilde{T}^{n-1}$$

Eq. 26.27 may be written

$$-\frac{\xi}{2} \frac{d\tilde{u}}{d\xi} = \frac{d}{d\xi} \left( f \frac{d\tilde{u}}{d\xi} \right)$$

By formally applying the standard methods for solving ordinary nonlinear differential equations, the solution of this is found to be (assuming the boundary condition that  $\xi = 0$  when  $\tilde{u} = 0$ ),

$$\tilde{u} = K \int_0^\xi \frac{F}{f} d\xi \quad (26.29a)$$

where

$$F \equiv \exp \left( - \int_0^\xi \frac{\xi}{f} d\xi \right) \quad (26.29b)$$

and  $K$  is a constant of integration to be determined from the boundary condition that

$$u = U_\infty \text{ when } y = \infty, \text{ i.e., when } \psi = \infty$$

which, in dimensionless variables, is

$$\tilde{u} = 1 \text{ when } \xi = \infty$$

Applying this boundary condition to Eq. 26.29a, we get

$$\frac{1}{K} = \int_0^\infty \frac{F}{f} d\xi \quad (26.29c)$$

Having found  $f(\xi)$  in first approximation,  $F(\xi)$  may be found from Eq. 26.29b by simple quadrature. The constant  $K$  may then be found from Eq. 26.29c by simple quadrature, and finally  $\tilde{u}(\xi)$  may be found from Eq. 26.29a by simple quadrature. Thus we obtain what may be regarded as the second approximation. By repeating the calculation procedure with the second approximation as a starting point, a third approximation may be computed, and so on, until the desired accuracy has been obtained (in Reference 2 the third or fourth approximation is stated to give satisfactory accuracy).

Having computed  $\tilde{u}(\xi)$  with acceptable accuracy,  $\tilde{T}(\xi)$  is computed from Eq. 26.23, and then the skin-friction coefficient is computed from

$$\sqrt{\frac{\rho_\infty U_\infty x}{\mu_\infty}} C_{f_\infty} = 2 \left( \tilde{T}^{n-1} \tilde{u} \frac{d\tilde{u}}{d\xi} \right)_{\text{wall}} \quad (26.30)$$

which is found by combining Eq. 26.26 with Eq. 26.28. The Nusselt Number may be found for a given Reynolds Number from Eq. 26.19.

It finally remains only to determine the  $y$ -coordinate corresponding to a given value of  $\tilde{u}$ . At constant  $x$ ,

$$d\psi = \left( \frac{\partial \psi}{\partial \xi} \right)_x d\xi = \left( \frac{\partial \psi}{\partial y} \right)_x dy$$

or, using Eqs. 26.28 and 26.20a,

$$\sqrt{\frac{U_\infty x \mu_\infty}{\rho_\infty}} d\xi = \frac{\rho u}{\rho_\infty} dy$$

This is now rearranged in dimensionless form and integrated between  $y = 0, \xi = 0$  and  $y = y, \xi = \xi$ , thus giving

$$y \sqrt{\frac{U_\infty \rho_\infty}{\mu_\infty x}} = \int_0^\xi \tilde{u} d\xi \quad (26.31)$$

where the integral is found by quadrature.

In reviewing the analysis, it is observed that (i)  $n$  is a parameter chosen to fit the experimental viscosity-temperature relationship, (ii)  $\tilde{T}_w \equiv T_w/T_\infty$  is an independent parameter which is constant for the entire plate, (iii)  $\text{Rey}_\infty \equiv \sqrt{\rho_\infty U_\infty x / \mu_\infty}$  is the dimensionless distance coordinate along the plate, and (iv) the  $y$ -coordinate is represented by the dimensionless similarity parameter  $y \sqrt{U_\infty \rho_\infty / \mu_\infty x} = (y/x) \sqrt{\text{Rey}_\infty}$ , all fluid properties being constant on parabolas for which  $y/\sqrt{x}$  is constant.

**THEORETICAL RESULTS.** Typical velocity and temperature profiles for an insulated plate<sup>(2)</sup> are shown in Fig. 26.7. The velocity profile

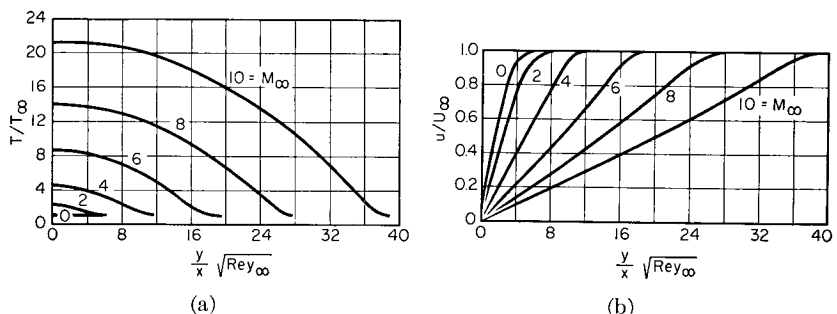


FIG. 26.7. Temperature and velocity profiles for flow past insulated plate, with  $\text{Pr} = 1$  and  $n = 0.76$  (after Kármán and Tsien).

becomes nearly linear at about  $M_\infty \approx 5$ , and at higher Mach Numbers develops a point of inflection. Evidently at high Mach Numbers the assumption of a linear velocity profile is fairly accurate. For a given free-stream Reynolds Number, the thickness of the boundary layer increases significantly with increasing  $M_\infty$ . At high free-stream Mach Numbers, the adiabatic wall temperature may reach serious proportions. For example, with  $T_\infty = 500^\circ\text{R}$  and  $M_\infty = 10$ , the adiabatic wall temperature reaches the staggering figure of  $10,500^\circ\text{R}$ .

Typical velocity and temperature profiles for a "cold plate," with  $T_w/T_\infty = 1/4$ , are shown in Fig. 26.8. The boundary-layer thickness

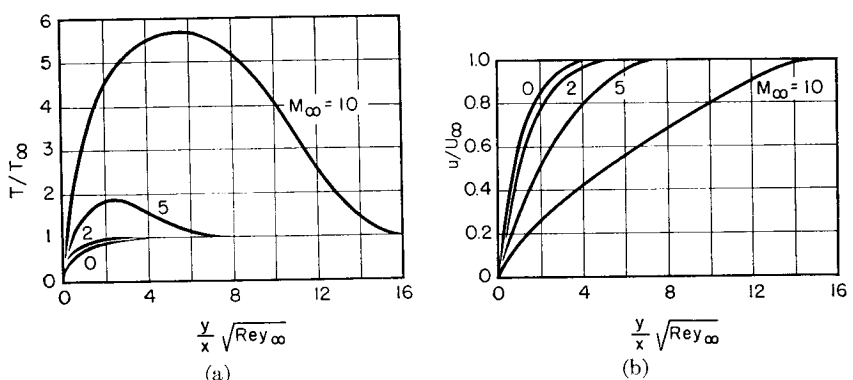


FIG. 26.8. Temperature and velocity profiles for flow past cold plate, with  $T_w/T_\infty = 1/4$ ,  $\text{Pr} = 1$ , and  $n = 0.76$  (after Kármán and Tsien).

is seen to be smaller than for the insulated plate, especially at high Mach Numbers. It is interesting to note that with  $M_\infty = 10$ , the maximum temperature in the boundary layer is almost six times as large as the free-stream temperature, even though the gas stream is being cooled by the wall.

The effects of compressibility and of cooling on the skin-friction coefficient and on the Nusselt Number are shown in Fig. 26.9. For the insulated wall, an increase in  $M_\infty$  from 0 (incompressible flow) to 10 changes the value of  $C_f \sqrt{\text{Rey}_\infty}$  from 0.664 to 0.487, which is a 30 per cent reduction. Thus it appears that the laminar skin-friction coefficient depends only weakly on  $M_\infty$ . In the range of subsonic speeds, the variation of  $C_f$  owing to  $M_\infty$  is negligible for most practical applications.

Fig. 26.9 shows that cooling of the stream tends to increase the skin-friction coefficient and the Nusselt Number, but this again is not a very large effect.

**THEORETICAL RESULTS IN TERMS OF PROPERTIES AT THE WALL TEMPERATURE.** Since the principal viscous and heat conduction effects occur immediately adjacent to the wall, it might be argued that it is more appropriate to base the fluid properties on the *wall* temperature rather than on the free-stream temperature.

As shown in Fig. 26.10 for the adiabatic wall, when the parameters

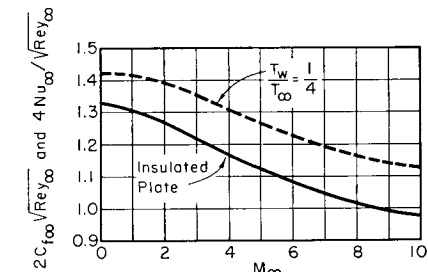


FIG. 26.9. Effect of  $M_\infty$  on local skin-friction coefficient and on local Nusselt Number for flow past flat plate, with  $\text{Pr} = 1$  and  $n = 0.76$  (after Kármán and Tsien).

are evaluated in this way the velocity profiles show but little dependence on Mach Number (compare with Fig. 26.7b). The profiles are practically independent of  $M_\infty$  in the inner half of the boundary layer, and only begin to deviate from each other in the outer half.

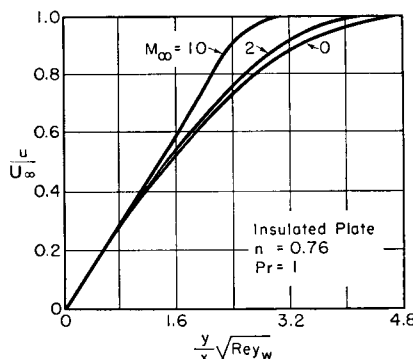


FIG. 26.10. Velocity profiles plotted in similarity form, with fluid properties based on wall temperature. Insulated flat plate, with  $\text{Pr} = 1$  and  $n = 0.76$  (after Hantsche and Wendt).

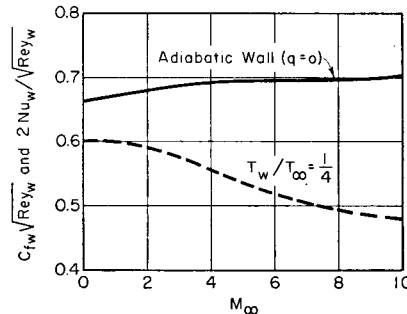


FIG. 26.11. Theoretical skin friction and heat transfer for flow past flat plate, with  $\text{Pr} = 1$  and  $n = 0.76$ . Fluid properties based on wall temperature.

A similar modification of Fig. 26.8b, for  $T_w/T_\infty = 1/4$ , produces the same result—the velocity profiles group together in a narrow band.

As to the skin-friction coefficient and Nusselt Number, use of the various definitions previously set forth yields

$$C_{f_w} \sqrt{Rey_w} = C_{f_\infty} \sqrt{Rey_\infty} \left( \frac{T_w}{T_\infty} \right)^{\frac{1-n}{2}}$$

and modification of Fig. 26.9 according to this formula then leads to Fig. 26.11. For adiabatic flow there is less than 6 per cent change in  $C_{f_w} \sqrt{Rey_w}$  over the range of  $M_\infty$  from 0 to 10.

These results, and other results cited later lead to the approximate rule that the velocity profile, skin-friction coefficient, and Nusselt Number are all approximately independent of Mach Number up to  $M_\infty \approx 5$  if all fluid properties in the dimensionless parameters are evaluated at the wall temperature. By empirical fitting of theoretical results, it has been found<sup>(14)</sup> that the curve of  $C_f' \sqrt{Rey'}$  is for all practical purposes independent of Mach Number up to very high values of  $M_\infty$  if the fluid properties  $\rho'$ ,  $\mu'$ , and  $\lambda'$  on which  $C_f'$  and  $\text{Rey}'$  are based are taken at a temperature  $T'$  defined by

$$\frac{T'}{T_\infty} = 1 + 0.032 M_\infty^2 + 0.58 \left( \frac{T_w}{T_\infty} - 1 \right)$$

INTEGRATED DRAG COEFFICIENT. It should be noted that the average drag coefficient for one side of the plate, from  $x = 0$  to  $x = x$ , is given by

$$C_D = \frac{\int_0^x \tau_w dx}{\frac{1}{2} \rho_\infty U_\infty^2 x} = \frac{1}{x} \int_0^x C_f dx$$

and, since  $C_f \sim 1/\sqrt{x}$ , it follows that

$$C_{D_\infty} \sqrt{Rey_\infty} = 2C_{f_\infty} \sqrt{Rey_\infty}$$

and

$$C_{D_w} \sqrt{Rey_w} = 2C_{f_w} \sqrt{Rey_w}$$

EFFECT OF VISCOSITY VARIATION. The effects of the variation of viscosity with temperature on the local skin-friction and heat transfer coefficients are shown in Fig. 26.12.<sup>(8)</sup> It is seen, as demonstrated earlier, that with  $\text{Pr} = 1$  and  $\mu \sim T$ , the coefficients are independent of  $M_\infty$ . However, with a viscosity-temperature relationship more akin to that of real gases, say  $n = 0.8$ , the coefficients decrease as the result of compressibility. On the other hand, if Fig. 26.12 is replotted in terms of  $C_{f_w} \sqrt{Rey_w}$  and  $\text{Nu}_w / \sqrt{Rey_w}$ , it is found that all the curves are very nearly horizontal, illustrating again the rule that the incompressible flow formulas are approximately correct for compressible flow if in the latter case the fluid properties are based on the temperature at the wall.

Effect of Pressure Gradient. Howarth<sup>(10)</sup> has investigated the effects of an adverse pressure gradient on the separation of a laminar boundary layer, based on the assumptions that (i)  $\text{Pr} = 1$ , (ii)  $\mu \sim T$ , and (iii) the

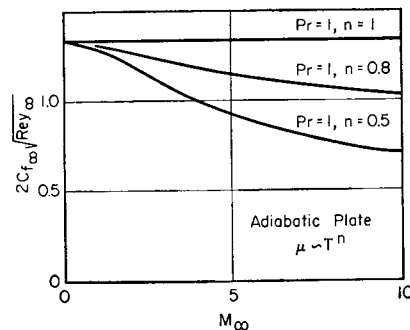


FIG. 26.12. Effect of viscosity-temperature law on theoretical skin friction for flow past flat plate (after Hantsche and Wendt).

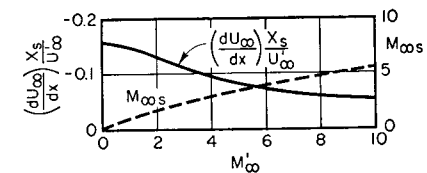


FIG. 26.13. Effect of Mach Number on point of separation of laminar boundary layer in adverse pressure gradient (after Howarth).

main-stream velocity  $U_\infty$  decreases linearly with distance from the leading edge, i.e.,

$$U_\infty = U_\infty' - (dU_\infty/dx)x$$

where  $(dU_\infty/dx)$  is a constant, and  $U_\infty'$  is the main-stream velocity at the beginning of the plate. The results are shown in Fig. 26.13, where  $x_s$  denotes the distance to the point of laminar separation and  $M_\infty$  denotes the local free-stream Mach Number where separation occurs.

At high Mach Numbers the boundary layer is not able to support so large a deceleration as at low Mach Numbers, according to Fig. 26.13.

#### 26.4. Flow with Arbitrary Prandtl Number

When the Prandtl Number is not unity, the governing physical relations, Eqs. 26.3, 26.4, 26.5, and 26.8, can be integrated only with

difficulty, and then only by iterative methods, by numerical integration, or with the help of a differential analyzer. The details of such calculations are too lengthy to be set out here, but we shall summarize the most important results.

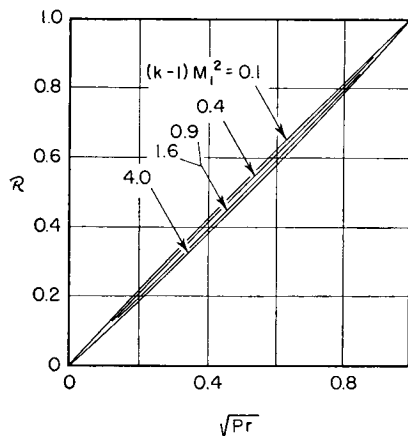


FIG. 26.14. Recovery factor for flow past flat plate (after Emmons and Brainerd).

square root of the Prandtl Number and is almost independent of Mach Number, and hence for thin laminar layers we may assume for practical purposes that

$$\mathcal{R} \cong \sqrt{\text{Pr}} \quad (26.32)$$

In Reference 9 it is confirmed that this rule is also accurate when account is taken of the viscosity variation through the boundary layer.

**VELOCITY AND TEMPERATURE PROFILES.** Fig. 26.15<sup>(6)</sup> shows that as the Prandtl Number increases the velocity boundary layer increases in thickness but the thermal boundary-layer thickness decreases. With  $\text{Pr} = 1$ , the two thicknesses are alike. In the range of  $\text{Pr}$  from 0.5 to 1.0,

within which all gases lie, the velocity profiles are substantially independent of Prandtl Number. Within the same range the temperature profiles are also substantially identical when normalized with respect to the wall temperature, but of course the latter increases with  $\text{Pr}$  according to the rule that  $\mathcal{R} \cong \sqrt{\text{Pr}}$ .

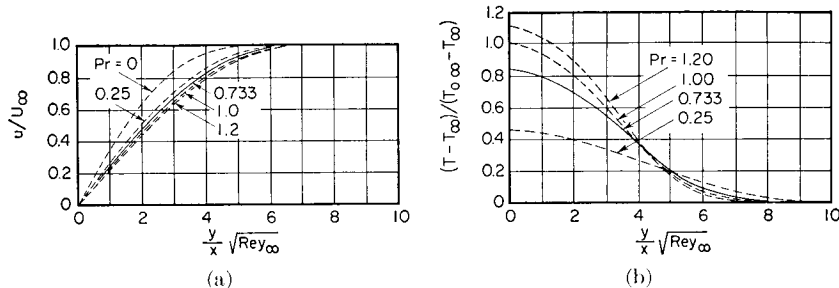


FIG. 26.15. Effect of Prandtl Number on shape of velocity and temperature profiles. Insulated plate, with  $(k-1)M_\infty^2 = 10$  and constant viscosity (after Emmons and Brainerd).

When the velocity profiles are plotted as in Fig. 26.16 with kinematic viscosity based on the wall temperature,<sup>(8)</sup> the effects of variations in  $\text{Pr}$  and  $M_\infty$  are insignificant near the plate and make themselves felt only in the outer half of the boundary layer. With this method of correlation the difference between the profiles for  $M_\infty = 0$  and  $M_\infty = \infty$  is surprisingly small and would be negligible up to  $M_\infty \cong 3$ . At low Mach Numbers the velocity profile is approximately parabolic, whereas at supersonic Mach Numbers it is approximately linear. The effect of  $\text{Pr}$  is small at high Mach Numbers.

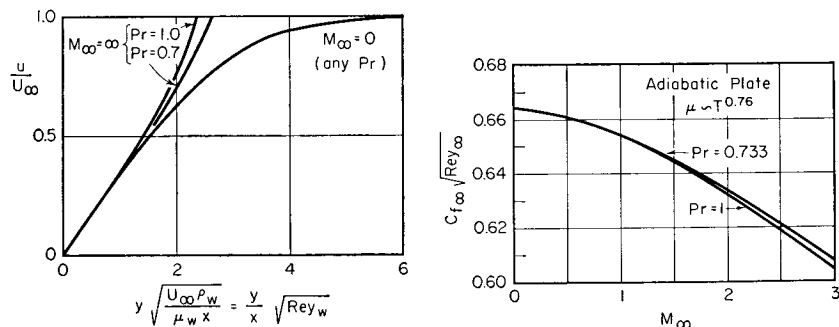


FIG. 26.16. Effect of Prandtl Number on velocity profiles when represented in similarity form, with properties based on wall temperature. Insulated plate with  $n = 1$  (after Hantzsch and Wendt).

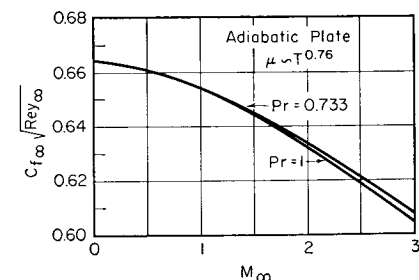


FIG. 26.17. Effect of Prandtl Number on skin-friction coefficient. Flat plate with  $n = 0.76$  (after Emmons and Brainerd).

**SKIN-FRICTION COEFFICIENT.** The effect of Prandtl Number on the skin-friction coefficient <sup>(7)</sup> is seen from Fig. 26.17 to be almost negligible. The curve for  $\text{Pr} = 0.733$  may be closely represented by

$$2C_{f\infty} \sqrt{\text{Rey}_\infty} = 1.328 - 0.0217 M_\infty^{3/2}$$

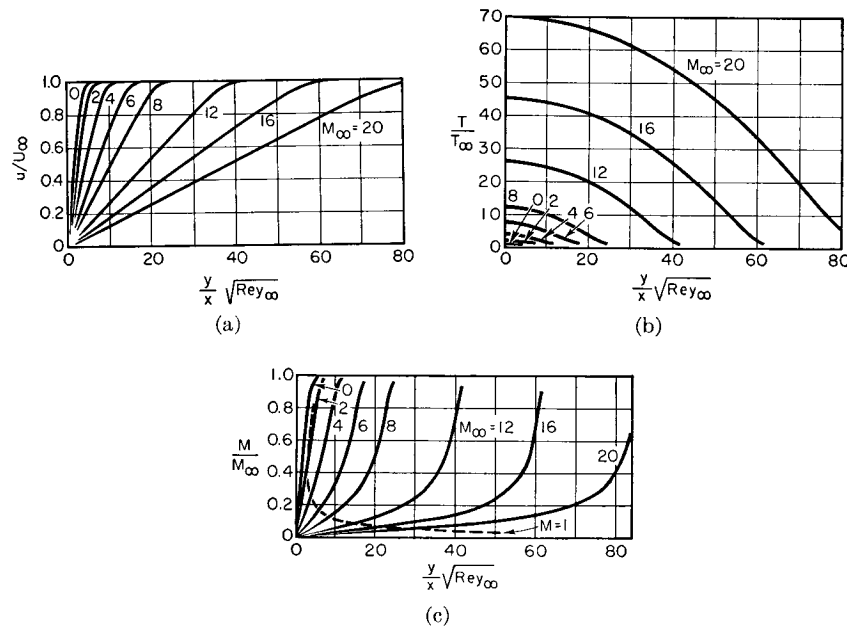


FIG. 26.18. Insulated plate, with  $\text{Pr} = 0.75$  and Sutherland law of viscosity ( $S/T_\infty = 0.505$ ) (after van Driest).

- (a) Velocity profiles.
- (b) Temperature profiles.
- (c) Mach Number profiles.

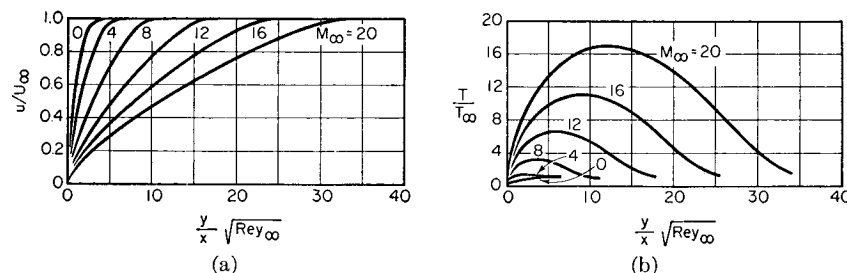


FIG. 26.19. Cold flat plate, with  $T_w/T_\infty = 0.25$ ,  $\text{Pr} = 0.75$  and Sutherland law of viscosity ( $S/T_\infty = 0.505$ ) (after van Driest).

- (a) Velocity profiles.
- (b) Temperature profiles.

**Flow Past Heated or Cooled Flat Plate.** The viscosity-temperature relation which best fits experimental data over the range between  $-250^\circ\text{F}$  and  $3250^\circ\text{F}$  is the Sutherland law,

$$\frac{\mu}{\mu_\infty} = \left(\frac{T}{T_\infty}\right)^{3/2} \frac{T_\infty + S}{T + S} = \left(\frac{T}{T_\infty}\right)^{1/2} \frac{1 + \frac{S}{T_\infty}}{1 + \frac{S/T_\infty}{T/T_\infty}}$$

where the ratio  $S/T_\infty$  is empirically taken as 0.505. Using this law, van Driest <sup>(9)</sup> has worked out by a method due to Crocco an extensive

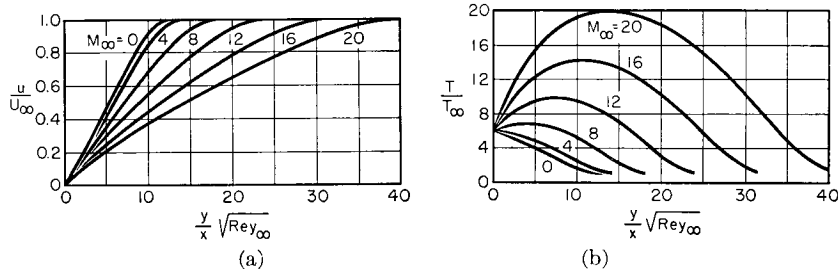


FIG. 26.20. Hot flat plate, with  $T_w/T_\infty = 6$ ,  $\text{Pr} = 0.75$  and Sutherland law of viscosity ( $S/T_\infty = 0.505$ ) (after van Driest).

- (a) Velocity profiles.
- (b) Temperature profiles.

set of solutions for the laminar boundary-layer flow over a flat plate, based on  $\text{Pr} = 0.75$ . Some typical results are summarized here.

The velocity, temperature, and Mach Number profiles are shown in Fig. 26.18 for the insulated plate over the range of free-stream Mach Numbers from 0 to 20. There is a remarkable difference between the velocity distributions and the Mach Number distributions.

When the stream is cooled by the plate at such a rate that  $T_w/T_\infty = 1/4$ , the velocity and temperature profiles are as shown in

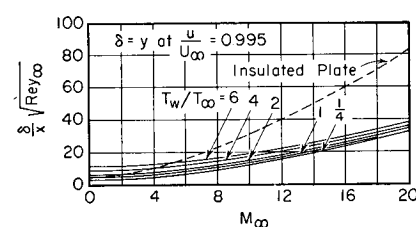


FIG. 26.21. Thickness of laminar boundary layer on flat plate, based on  $\text{Pr} = 0.75$  and Sutherland viscosity law ( $S/T_\infty = 0.505$ ) (after van Driest).

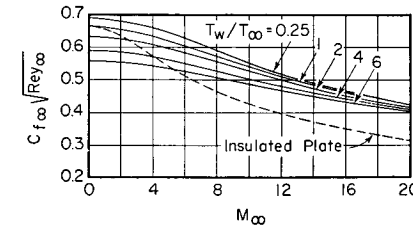


FIG. 26.22. Skin friction on flat plate, based on  $\text{Pr} = 0.75$  and Sutherland viscosity law ( $S/T_\infty = 0.505$ ) (after van Driest).

Fig. 26.19. On comparing this figure with Fig. 26.18, it is seen that the chief effect of reducing  $T_w$  is on the temperature distribution.

When the stream is heated (or cooled) by the plate at such a rate that  $T_w/T_\infty = 6.0$ , the velocity and temperature profiles are as given in Fig. 26.20. When  $M_\infty$  is less than about 5.5, the stream is heated, whereas when  $M_\infty$  is greater than about 5.5, the stream is cooled.

According to Fig. 26.21, the boundary-layer thickness on an insulated plate increases quite rapidly with Mach Number. In addition, heating of the stream can cause marked increases in thickness whereas cooling can cause significant decreases in thickness. In terms of the parameter  $(\delta/x)\sqrt{\text{Rey}_\infty}$ , based on kinematic viscosity at the wall, however, the changes in boundary-layer thickness owing to variations in  $M_\infty$  and cooling rate are very much smaller than those shown in Fig. 26.21.

The local skin-friction coefficient is shown as a function of Mach Number in Fig. 26.22 for the adiabatic plate and for various ratios  $T_w/T_\infty$ . Here again, although  $C_{f\infty}\sqrt{\text{Rey}_\infty}$  depends considerably on both  $T_w/T_\infty$  and  $M_\infty$ , a similar plot of  $C_{f\infty}\sqrt{\text{Rey}_\infty}$  shows only minor dependency.

Finally, the local heat transfer coefficient is shown in Fig. 26.23 as a function of  $M_\infty$  and  $T_w/T_\infty$ .

The curves of this chart are very similar to those of Fig. 26.22, and indeed the theoretical results follow closely the empirical rule that

$$\frac{Nu_\infty}{Pr\sqrt{\text{Rey}_\infty}} \approx \frac{1}{Pr^{2/3}} \frac{C_{f\infty}\sqrt{\text{Rey}_\infty}}{2} \quad (26.33)$$

Except at high Mach Numbers, the results given in Reference 9 and summarized here agree well with the simpler results based on the law  $\mu \sim T^{0.76}$  with  $Pr = 1$ .

## 26.5. Integral Equations of the Laminar Boundary Layer

As in the case of incompressible flow, the most powerful method for solving practical boundary-layer problems, especially when pressure gradients are present, is the so-called *integral method*.

In obtaining exact solutions to the boundary-layer equations, we begin with the differential equations representing the governing physical laws, and therefore the resulting solutions satisfy these physical laws in the small, i.e., at every point of the flow field.

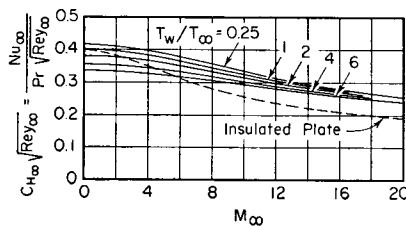


Fig. 26.23. Heat transfer for flat plate, based on  $Pr = 0.75$  and Sutherland viscosity law ( $S/T_\infty = 0.505$ ) (after van Driest).

With integral methods, however, we do not attempt to satisfy the physical laws in the small, but only in the large. That is, we require only that the physical laws be satisfied for the boundary-layer flow as a whole. Such an approach, of course, cannot be expected to give exact information concerning local temperatures, velocities, etc. Indeed, to apply the method it is necessary to make "plausible" assumptions, guided by the exact differential equations and boundary conditions, as to the shapes of the velocity and temperature profiles. On the other hand, the integral method does furnish fairly accurate information concerning such gross quantities as the skin-friction coefficient, heat transfer coefficient, and boundary-layer thickness.

Let  $\delta_u$  represent the thickness of the *velocity boundary layer*, defined as the distance from the solid boundary to the point where  $u = U_\infty$ . Note that  $U_\infty$  is taken as the local free-stream velocity outside the boundary layer, and that in general it may depend on  $x$ . Similarly, let  $\delta_r$  be the thickness of the *thermal boundary layer*. Now  $\delta_u$  and  $\delta_r$  will usually be different from each other, and we therefore denote the larger of the two by  $\delta$ , the latter representing the distance from the surface beyond which there are no further changes in both velocity and temperature.

**Integral Momentum Equation.** Referring to Fig. 26.24a,  $\delta$  represents the boundary-layer thickness at a local value of  $x$  in the sense stated immediately above, and the control volume has its upper boundary parallel to the wall and outside the edge of the boundary layer. The mass flows entering and leaving the control volume are shown in Fig. 26.24b, where the flow entering the part of the control surface outside the boundary layer is found from the condition that for steady flow the net mass efflux is zero. The forces acting on the fluid within the control volume are indicated in Fig. 26.24c, and the momentum fluxes entering and leaving are shown in Fig. 26.24d.

Equating the net force of Fig. 26.24c to the net outgoing momentum flux of Fig. 26.24d, we obtain

$$-\tau_w - \delta \frac{\partial p}{\partial x} = \frac{\partial}{\partial x} \int_0^\delta \rho u^2 dy - U_\infty \frac{\partial}{\partial x} \int_0^\delta \rho u dy \quad (26.34)$$

where the integrals are taken at constant  $x$ , and the upper limit of integration is a function of  $x$ .

Since the flow outside the boundary layer is without friction, Euler's equation expresses the pressure gradient as

$$\frac{\partial p}{\partial x} = -\rho_\infty U_\infty \frac{\partial U_\infty}{\partial x}$$

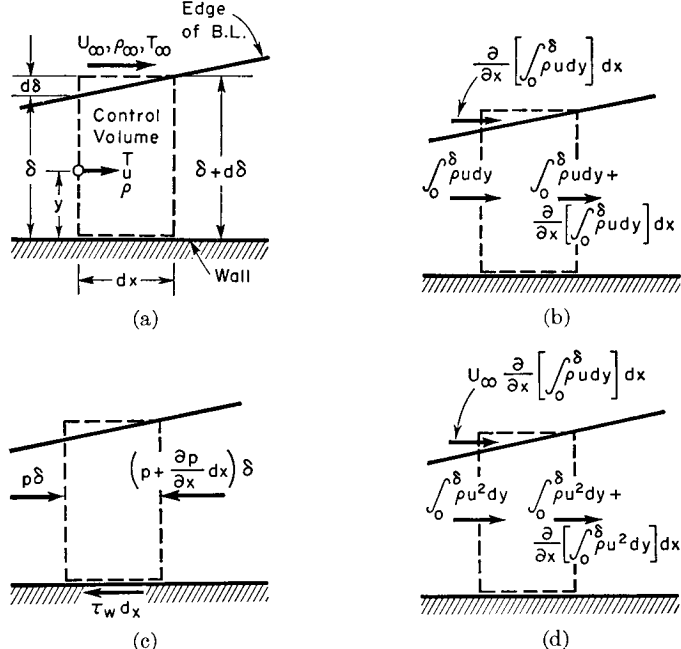


FIG. 26.24. Integral equations of boundary layer.

- (a) Definition of control volume.
- (b) Mass flows.
- (c) Forces.
- (d) Momentum fluxes.

Inserting this into Eq. 26.34, and carrying out several rearrangements to obtain the integral momentum equation in convenient working form, we obtain

$$\begin{aligned}
 \tau_w &= \delta \rho_\infty U_\infty \frac{\partial U_\infty}{\partial x} - \frac{\partial}{\partial x} \int_0^\delta \rho u^2 dy + U_\infty \frac{\partial}{\partial x} \int_0^\delta \rho u dy \\
 \tau_w &= \frac{\partial U_\infty}{\partial x} \int_0^\delta \rho_\infty U_\infty dy - \frac{\partial}{\partial x} \int_0^\delta \rho u^2 dy + U_\infty \frac{\partial}{\partial x} \int_0^\delta \rho u dy \\
 \tau_w &= \frac{\partial}{\partial x} U_\infty \int_0^\delta \rho_\infty U_\infty dy - U_\infty \frac{\partial}{\partial x} \int_0^\delta \rho_\infty U_\infty dy \\
 &\quad - \frac{\partial}{\partial x} \int_0^\delta \rho u^2 dy + U_\infty \frac{\partial}{\partial x} \int_0^\delta \rho u dy \\
 \tau_w &= \frac{\partial}{\partial x} \int_0^\delta (\rho_\infty U_\infty^2 - \rho u^2) dy - U_\infty \frac{\partial}{\partial x} \int_0^\delta (\rho_\infty U_\infty - \rho u) dy \quad (26.35)
 \end{aligned}$$

This may also be written in terms of the *displacement and momentum thicknesses* (see Eqs. 27.19, 27.20, and 27.21).

**Integral Energy Equation.** Fig. 26.25 shows the rate of heat transfer and fluxes of stagnation enthalpy crossing the control surface under consideration, the rate of shearing work being zero. Equating the net rate of heat transfer to the net outgoing flux of stagnation enthalpy, we get

$$q_w = \frac{\partial}{\partial x} \int_0^\delta \rho u c_p T_0 dy - c_p T_{0\infty} \frac{\partial}{\partial x} \int_0^\delta \rho u dy$$

This may be arranged in a form similar to that of the momentum equation:

$$q_w = \frac{\partial}{\partial x} \int_0^\delta c_p (\rho u T_0 - \rho_\infty U_\infty T_{0\infty}) dy - c_p T_{0\infty} \frac{\partial}{\partial x} (\rho u - \rho_\infty U_\infty) dy \quad (26.36)$$

where

$$T_0 = T + \frac{u^2}{2c_p} \quad (26.37a)$$

$$T_{0\infty} = T_\infty + \frac{U_\infty^2}{2c_p} \quad (26.37b)$$

An alternate form of the integral energy equation, in terms of the *stagnation-temperature thickness*, is given by Eqs. 27.23 and 27.24.

**Velocity and Temperature Profiles.** We now assume that the velocity distribution at any value of  $x$  is given by

$$u/U_\infty = f_u(y/\delta_u) \quad \text{for } 0 < y < \delta_u$$

$$u/U_\infty = 1 \quad \text{for } y > \delta_u$$

The choice of the function  $f_u(y/\delta_u)$  is partly arbitrary, but the actual shape of the velocity profile is restricted within rather narrow limits by making the function satisfy the following physical conditions derived from the boundary conditions and the differential equations of motion.

(i) At  $y = \delta_u$ , the velocity profile must merge smoothly with the inviscid main-stream flow. Thus, for  $y/\delta_u = 1$ ,

$$u = U_\infty$$

At the edge of the boundary layer, where  $y = \delta_u$ , the last term in Eq. 26.5 must vanish, because by definition the edge of the boundary layer is the location where viscous forces become negligible. Neglecting the variation of viscosity at this point, we get  $\partial u/\partial y = 0$ . By differ-

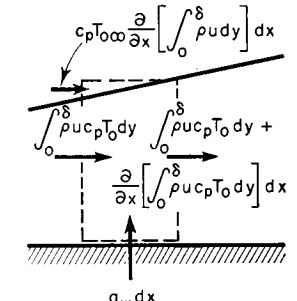


FIG. 26.25. Illustrates integral energy equation.

entiating Eq. 26.5 successively with respect to  $y$ , and applying the foregoing reasoning to each of the resulting equations, we get

$$\frac{\partial u}{\partial y} = \frac{\partial^2 u}{\partial y^2} = \frac{\partial^3 u}{\partial y^3} = \cdots = 0$$

(ii) At  $y = 0$ , the fluid is in contact with the wall, and therefore  $u = 0$ . Furthermore, since  $v = 0$  at  $y = 0$ , Eq. 26.5 gives

$$\left[ \frac{\partial}{\partial y} \left( \mu \frac{\partial u}{\partial y} \right) \right]_{y=0} = \frac{\partial p}{\partial x}$$

and further conditions may be obtained by successively differentiating Eq. 26.5 with respect to  $y$  and setting  $y = u = v = 0$ .

Similarly, the temperature distribution is taken as

$$\frac{T}{T_\infty} = f_r \left( \frac{y}{\delta_T} \right) \quad \text{for } 0 < y < \delta_T$$

$$\frac{T}{T_\infty} = 1 \quad \text{for } y > \delta_T$$

The function  $f_r$  is selected arbitrarily (usually as a polynomial) but is constrained to satisfy the following requirements based on the boundary conditions and on the energy equation (Eq. 26.8) in differential form:

(i) When  $y = \delta_T$ ,

$$T = T_\infty$$

$$\frac{\partial T}{\partial y} = \frac{\partial^2 T}{\partial y^2} = \cdots = 0$$

(ii) When  $y = 0$ ,

$$T = T_\infty$$

$$\left[ \frac{\partial}{\partial y} \left( \lambda \frac{\partial T}{\partial y} \right) \right]_{y=0} + \left[ \mu \left( \frac{\partial u}{\partial y} \right)^2 \right]_{y=0} = 0$$

The local density in the boundary layer depends only on the local pressure and temperature. Assuming that the potential flow outside of the boundary layer is known to begin with, it is clear that the local  $\rho$  depends on the functions  $f_u$  and  $f_r$  and on the supposedly known variation of free-stream properties.

**Method of Solution.** Having chosen the forms of the functions  $f_u$  and  $f_r$  involving the unknowns  $\delta_u$  and  $\delta_T$ , they are substituted into the right-hand sides of Eqs. 26.35 and 26.36. The left-hand sides of these equations are now expressed in terms of  $\delta_u$ ,  $\delta_T$ ,  $U_\infty$ , and  $T_\infty$  through the relations

$$\tau_w = \mu \left( \frac{\partial u}{\partial y} \right)_{y=0} \quad (26.38a)$$

$$q_w = -\lambda \left( \frac{\partial T}{\partial y} \right)_{y=0} \quad (26.38b)$$

Eqs. 26.35 and 26.36, after the definite integrals are evaluated, yield two first-order ordinary differential equations for  $\delta_u$  and  $\delta_T$ . These are then solved simultaneously to give  $\delta_u$  and  $\delta_T$  as functions of  $x$ . From this there follow the velocity and temperature profiles at each value of  $x$ . Eqs. 26.38 then yield  $\tau_w$  and  $q_w$  as functions of  $x$ , thus completing the solution to the problem.

The calculation procedure outlined above is similar to the well-known Pohlhausen method for incompressible flow, except that both the velocity and thermal boundary layers must be solved for, resulting in laborious computations. A great simplification may be obtained, however, by assuming that the temperature distribution is represented by Eq. 26.12. Such an assumption will not lead to large errors unless there are present large pressure gradients, or extremely high Mach Numbers, or very high rates of heat transfer.

The use of Eq. 26.12 in effect connects the temperature distribution with the velocity distribution, and makes the energy equation (Eq. 26.36) superfluous. Nor is  $\delta_T$  any longer a variable, since the thicknesses  $\delta_u$  and  $\delta_T$  are automatically alike. Consequently, only the momentum equation need be solved for  $\delta_u$ , and the procedure is then very similar to that of Pohlhausen.

Detailed elaborations of the integral method are given in References 3, 26, 36, 39, and 43 along the lines of Pohlhausen's procedure for incompressible flow, together with extensions of the integral method to flow past bodies of revolution and to turbulent flows. The work of Libby *et al.* <sup>(36)</sup> is especially illuminating and useful in showing the degree of accuracy obtainable by using different forms of polynomials for the velocity distribution.

As an illustration of the type of results to be expected by the integral method, Fig. 26.26 shows (i) the measured boundary-layer thickness at a fixed station on an airfoil profile as the approach velocity is increased, and (ii) the corresponding calculated values based on the

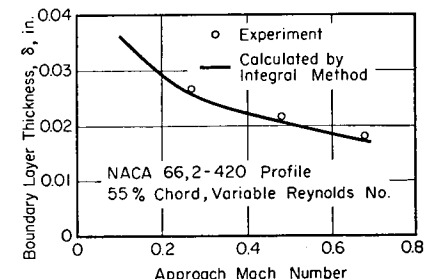


FIG. 26.26. Comparison of theoretical and experimental boundary-layer thickness at 55%-chord point of NACA 66, 2-420 profile. Tests were conducted so that Reynolds Number increased as Mach Number increased (after Allen and Nitzberg).

integral method and on the assumptions that  $\delta_u = \delta_r$  and that Eq. 26.12 is valid. The agreement is seen to be adequate for engineering purposes. It is to be noted that Fig. 26.26 does not indicate the effects of Mach Number alone, since the Reynolds Number was simultaneously varied.

For flat plates it is shown in Reference 36 that the skin-friction and heat transfer coefficients found by the integral method are in excellent accord with the results shown in Figs. 26.22 and 26.23.

The influence of pressure gradients is illustrated by the results of calculations<sup>(42)</sup> for the *mean* skin-friction coefficients of biconvex airfoils in supersonic flow. Over the range of approach Mach Numbers from 1.5 to 4.0 the increase in mean skin-friction coefficient over that for a flat plate varies approximately linearly with the thickness ratio. When the latter is 0.05, the increase is 30% at an approach Mach Number of 1.5; 24% at 2.0; 22% at 2.5, 3.0, and 3.5; and 23% at 4.0.

## 26.6. Laminar Boundary Layer for Axi-Symmetric Flow

Although, for thin boundary layers on the outside of bodies of revolution or on the inside of nozzles and ducts, the equations of motion and of energy are the same as for plane flow, the continuity equation takes a different form, and thus the results of boundary-layer calculations for plane flow cannot be directly transferred to axi-symmetric flow except for the special case where the radius of the wall is unchanging.

**Differential Equations.** Let us signify by  $r$  the radius in cylindrical coordinates, by  $x$  the curvilinear distance along the profile in a meridian plane, and by  $y$  the distance normal to the profile. Then  $r$  at the body surface is a function only of  $x$  for axi-symmetric flow. If we assume further that within the boundary layer  $r$  is small compared with  $x$ , and that the boundary-layer thickness is small compared with  $r$  (assumptions which may fail near the front and back of a body of revolution), then the dynamic and energy equations as expressed by Eqs. 26.4, 26.5, and 26.8 are valid for axi-symmetric flow. The continuity equation, however, assumes the form

$$\frac{\partial}{\partial x}(\rho u r) + \frac{\partial}{\partial y}(\rho v r) = 0 \quad (26.39)$$

We shall go no further with this approach except to point out that Mangler<sup>(12)</sup> has devised a set of transformations which reduces the equations of axi-symmetric boundary-layer flow to those of plane boundary-layer flow. Consequently there is no essential difference between obtaining solutions to the boundary-layer equations in the two cases, the chief difficulty being that of taking pressure gradients into account.

A special application of this is worth mentioning here. For supersonic flow past a cone with an attached shock, the surface pressure and velocity are constant along the cone. Thus this case bears a simple relation to the boundary layer on a flat plate. Based on free-stream properties just outside the boundary layer (not upstream of the conical shock), and for equal Reynolds Numbers in the same sense, the analysis yields for the local and average skin-friction coefficients, respectively,

$$(C_f)_{\text{cone}}/(C_f)_{\text{plate}} = \sqrt{3}$$

$$(C_D)_{\text{cone}}/(C_D)_{\text{plate}} = 2/\sqrt{3}$$

Eqs. 26.17 and 26.33 show that similar rules apply to the coefficient of heat transfer.

**Integral Equations.** Since pressure gradients are usually significant in axi-symmetric flow, the integral method of boundary-layer calculation is the most powerful for practical use.

By considering the fluxes of mass, momentum, and stagnation enthalpy into and out of a ring-shaped control volume the cross section of which has dimensions  $dx$  and  $\delta$ , the momentum and energy equations corresponding to Eqs. 26.35 and 26.36 become, respectively,

$$\begin{aligned} \tau_w r &= \frac{\partial}{\partial x} \int_0^\delta (\rho_\infty U_\infty^2 - \rho u^2) r dy - U_\infty \frac{\partial}{\partial x} \int_0^\delta (\rho_\infty U_\infty - \rho u) r dy \\ q_w r &= \frac{\partial}{\partial x} \int_0^\delta c_p (\rho u T_0 - \rho_\infty U_\infty T_{0\infty}) r dy - c_p T_{0\infty} \frac{\partial}{\partial x} \int_0^\delta (\rho u - \rho_\infty U_\infty) r dy \end{aligned} \quad (26.41)$$

where  $r$  here denotes the radius at the body surface.

The remarks in Art. 26.5 as to the choice of velocity and temperature profiles and of the method for reaching solutions are all applicable as well here.

Practical details of the calculation method are given in References 15 and 3.

## 26.7. Experimental Results for Laminar Boundary Layers

We shall now discuss some typical experimental results which illustrate the degree of validity of the theoretical analyses of the laminar boundary layer.

**Velocity Profiles.**<sup>(16)</sup> Fig. 26.27 shows a generally good agreement between the measured and theoretical velocity profiles on an insulated flat plate at  $M_\infty = 2.06$ . The significant discrepancies are that (i) the measured boundary-layer thickness is somewhat greater than the

theoretical, and (ii) the measured velocity gradient at the wall is appreciably greater than the theoretical. These discrepancies are perhaps partly explainable by the fact that in supersonic flow there are always interactions at the leading edge between the boundary layer and a leading-edge shock (see Fig. 26.28), thus giving rise to an initial distortion in the boundary layer not taken account of in the theory. (See also discussion of Fig. 26.29.)

The measured velocity profile of Fig. 26.27 was determined by means of interferograms like those of Fig. 26.28.

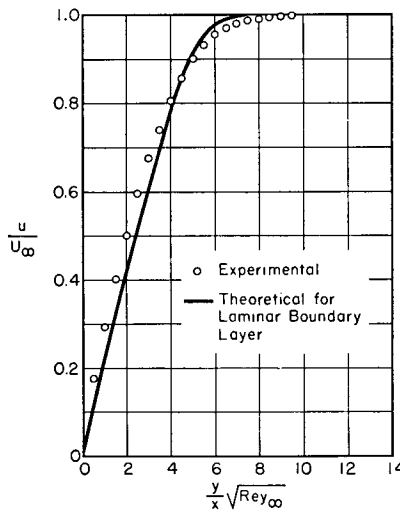


FIG. 26.27. Comparison of theoretical and experimental velocity profiles in laminar boundary layer on insulated flat plate, with  $M_\infty = 2.06$  and  $Rey_\infty = 0.39 \times 10^6$  (after Blue).

tube traverses, the integrated skin-friction coefficient between the leading edge and the measuring station may be computed approximately from the momentum theorem. Measurements of these types<sup>(16,38)</sup> at  $M_\infty = 2.0$  generally yield drag coefficients from 10 to 50 per cent greater than the theoretical values. For a number of reasons, however, these measurements are inherently less reliable than those found with the floating-element technique, and Fig. 26.29 may therefore be regarded as indicative of the accuracy of the theory. In particular, Blue and Low<sup>(37)</sup> have shown that the size of the impact tube influences the observed skin-friction coefficient. From a series of tests made with different sizes of impact tube it was possible to determine by extrapolation the skin-friction coefficient for a probe of vanishingly small size. The extrapolated skin-friction coefficients thus found are in substantially perfect agreement with the theoretical values of skin-friction coefficient.

Experimental skin-friction coefficients for a hot plate<sup>(21)</sup> at  $M_\infty = 2.40$  over a range of  $T_w/T_\infty$  from 2.0 to 2.8, based on measured velocity profiles, lie about 35 per cent above the theoretical values.

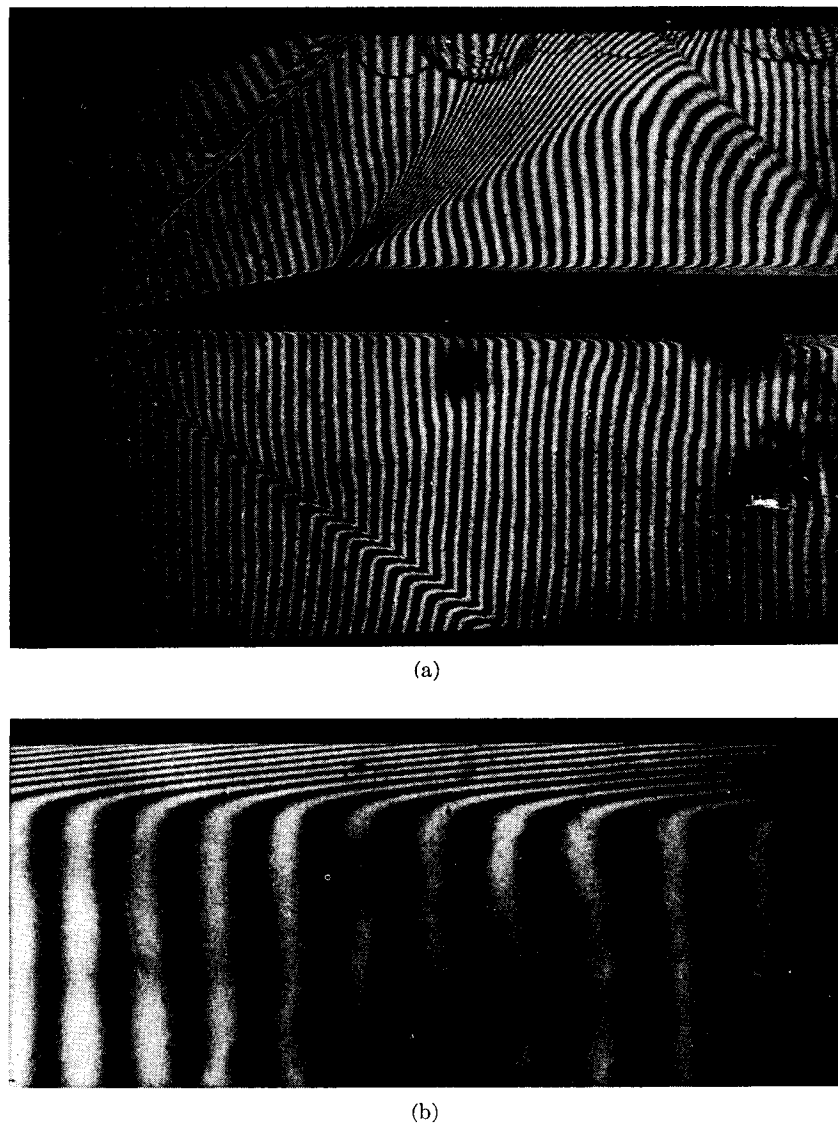


FIG. 26.28. Interferograms of laminar flow on flat plate at  $M_\infty = 1.78$ , flow left to right (courtesy NACA).

(a) Entire plate.

(b) Enlarged view of boundary layer.

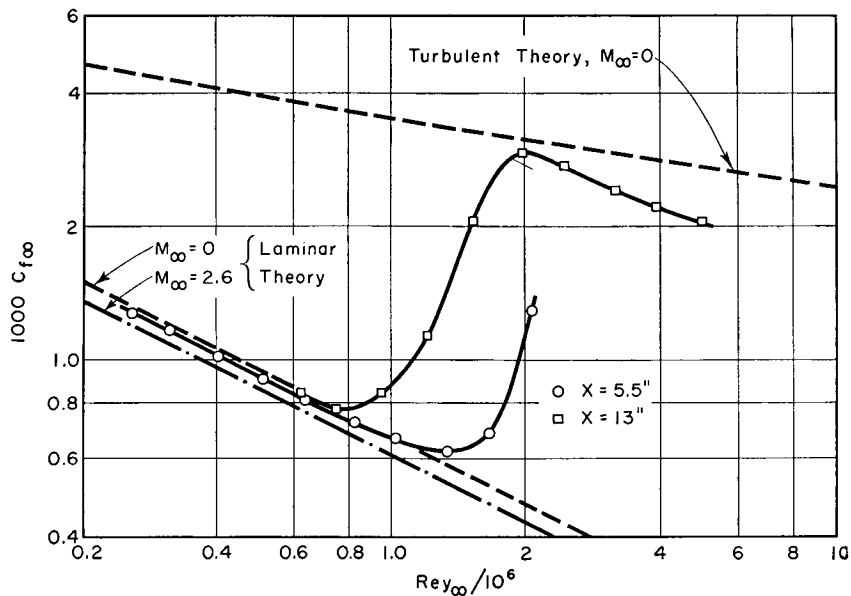


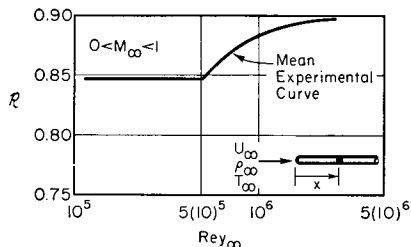
FIG. 26.29. Comparison of theoretical and experimental skin-friction coefficients on flat plate at  $M_{\infty} = 2.6$  (after Coles).

**Recovery Factor.** Air at normal temperatures has a Prandtl Number of 0.72. The laminar recovery factor is theoretically  $\sqrt{0.72}$ , or 0.85, and is substantially independent of  $M_{\infty}$ , except for very high values of  $M_{\infty}$ .

**SUBSONIC SPEEDS.** The recovery factor measured at subsonic speeds for axial flow along wires<sup>(17)</sup> shows excellent agreement with the theoretical value (Fig. 26.30) up to  $Re_{\infty} \leq 5 \times 10^5$ , at which point transition to turbulent flow would normally be expected to occur. In the turbulent range the recovery factor seems to approach a value of about 0.90.

FIG. 26.30. Measured recovery factor at subsonic speeds for flow parallel to long wires (after Eckert and Weise).

**SUPERSONIC SPEEDS.** At supersonic speeds, recovery factors on cones having an attached shock<sup>(28)</sup> are given in Fig. 26.31, based on local conditions at the surface of the cone. Within the scatter of the data, the results are substantially independent of Mach Number, of cone angle, and of Reynolds Number, and agree well with the expression  $\sqrt{Pr}$ .



A survey of additional data on laminar recovery factors (compiled in part by J. Kaye<sup>(45)</sup>) is given below.

DATA ON RECOVERY FACTOR FOR LAMINAR BOUNDARY LAYER

Author	Reference	Geometry	$10^6 Re_{\infty}$	$M_{\infty}$	$R$
Wimbrow	25, 32	Cone (20°)	0.7-5	2.0	$0.855 \pm .008$
		Cone (20°)	0.7-3	1.5	$0.845 \pm .008$
		Paraboloid	0.5-5	2.0	$0.855 \pm .008$
Stalder, Rubesin, and Tendeland*	18	Flat plate	0.2-1	2.4	$0.881 \pm .007$
Eber	28	Cones (10°-80°)	0.006-0.5	0.88-4.65	$0.845 \pm .008$
des Clers and Sternberg	33	Cone (10°)	0.1-1.3	1.4-3.4	$0.851 \pm .007$
Slack	34	Flat Plate	0.15-3	2.4	$0.884 \pm .006$
Stine and Scherrer	35	Cone	0.2-1.3	2.0-3.8	0.845
Ladenburg and Bershadier	38	Flat Plate	0.45	2.35	$0.860 \pm .005$
Mackay and Nagamatsu	44	Cone (20°)	0.02-0.5	4.9**	$0.844 \pm .008$

\*See Fig. 27.15.

\*\*  $\sqrt{Pr_w} = 0.837$ ;  $\sqrt{Pr_{\infty}} = 0.873$

For bodies of revolution (cones and paraboloid) the measured recovery factors are in close agreement with the theoretical value of  $\sqrt{Pr}$  when the latter is evaluated at the adiabatic wall temperature. The recovery factor for flat plates is some 3 to 4 per cent greater than the theoretical value, for reasons which are not clear.

There is no evidence of any dependence of the laminar recovery factor on Reynolds Number or on the Mach Number up to values of the latter of 4.

**CIRCULAR CYLINDERS AT SUBSONIC SPEEDS.** Fig. 26.32 shows the results of temperature-recovery measurements<sup>(17)</sup> on the surface of circular cylinders at subsonic speeds. The recovery factor based on the approach velocity and temperature to the cylinder and on the local adiabatic wall temperature, shown as a solid line in Fig. 26.32b, varies from unity at the leading edge to approximately zero at the trailing edge (the sharp break at  $\theta \cong 90^\circ$  is due to separation of the flow). The dashed line shows the local recovery factor in the sense we have

thus far been using, that is, based on the local  $T_{aw}$  and on the local value of  $U_{\infty}$  and  $T_{\infty}$  at the edge of the boundary layer. This recovery factor, denoted by  $\mathcal{R}$ , is remarkably independent of  $\theta$  up to the point of flow separation, and agrees with the theoretical value of  $\sqrt{Pr}$ . From this result we draw the important conclusion that negative pressure gradients have virtually no effect on the local recovery factor so long as the latter is based on the local conditions at the edge of the boundary layer. Fig. 26.32c, showing the recovery factor at a fixed station on the cylinder, shows  $\mathcal{R}$  to be substantially independent of the approach Mach Number

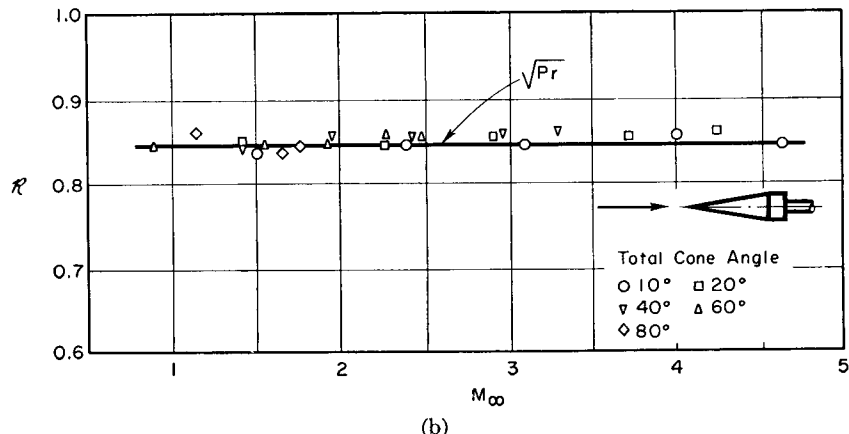
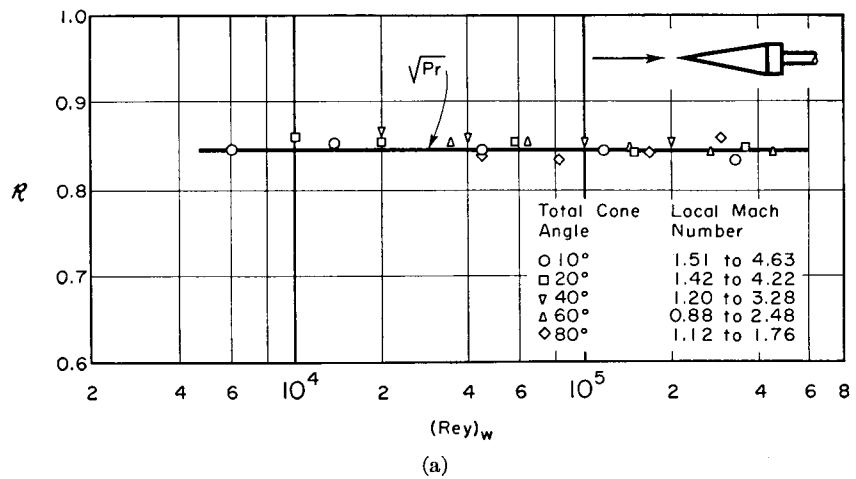


FIG. 26.31. Measured recovery factors on cones with attached shock. Note that  $M_{\infty}$  is the Mach Number at the surface of the cone for inviscid flow (after Eber).

- (a) Effect of Reynolds Number.
- (b) Effect of Mach Number.

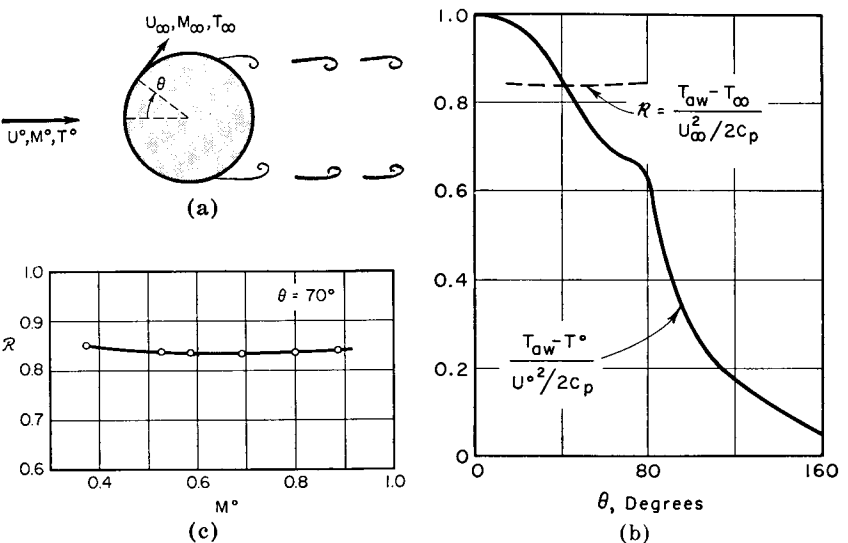


FIG. 26.32. Measured recovery factors at surface of circular cylinder for subsonic speeds (after Eckert and Weise).

- (a) Nomenclature.
- (b) Recovery factors based on approach conditions and on local conditions,  $M_{\infty} = 0.53$ .
- (c) Effect of approach Mach Number.

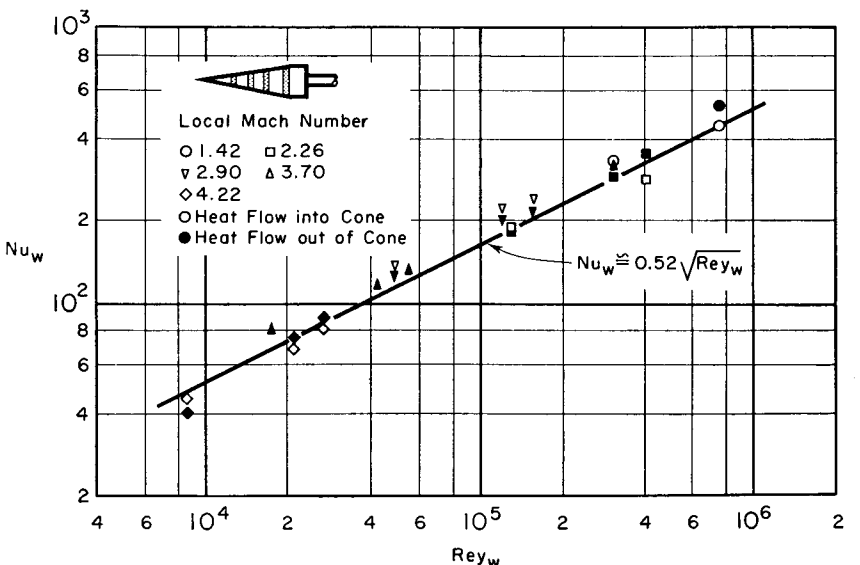


FIG. 26.33. Measured local heat transfer coefficient at surface of cones with attached shocks. Solid curve shows theoretical value (after Eber).

up to values of the latter near unity, corresponding to local Mach Numbers well in excess of unity.

**Heat-Transfer Coefficients.** The measured local heat-transfer coefficients for supersonic flow past cones with attached shocks are shown in Fig. 26.33 for a range of Reynolds and Mach Numbers. <sup>(28)</sup>

Based on the previously mentioned correction factor  $\sqrt{3}$  between supersonic cones and flat plates, using  $Pr = 0.72$  for air, and evaluating  $C_{f\infty} \sqrt{Rey_\infty}$  for flat plates from Fig. 26.22, it may be found from Eq. 26.33 that

$$Nu_w / \sqrt{Rey_w} \cong 0.52$$

This value is shown in Fig. 26.33 as a solid line and is seen to be in excellent agreement with the data.

Heat transfer measurements for supersonic flow with attached shocks past bodies of revolution having parabolic profiles in a meridian plane <sup>(20)</sup>

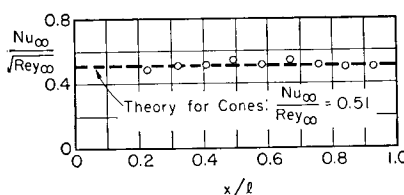
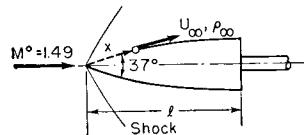


FIG. 26.34. Measured local heat transfer coefficient at surface of parabolic nose with attached shock (after Wimbrow and Scherrer).

line shows the theoretical value for a cone, and the remarkable agreement of this with the experimental data indicates that the effects mentioned above tend effectively to cancel each other. From this follows the rule of thumb that heat transfer over the fore portions of bodies of revolution at supersonic speeds may be predicted approximately by means of the cone formula,

$$\frac{Nu_\infty}{\sqrt{Rey_\infty}} = \sqrt{3} Pr_\infty^{1/3} \frac{C_{f\infty} \sqrt{Rey_\infty}}{2}$$

## 26.8. Stability of the Laminar Boundary Layer

It is well established, both experimentally and theoretically, that a laminar boundary layer may become turbulent at high Reynolds Numbers because the steady flow is dynamically unstable to small disturbances above a certain critical Reynolds Number. Accidental unsteady disturbances which appear in the flow (Tollmien-Schlichting waves) are self-excited, and these initially infinitesimal disturbances amplify to the point where the steady laminar motion is destroyed. A typical theoretical curve of neutral stability to infinitesimal disturbances is shown schematically in Fig. 26.35. This curve has been fully verified experimentally for low-speed flow over an insulated flat plate, and we now query as to the effects of compressibility and heat transfer on this type of instability.

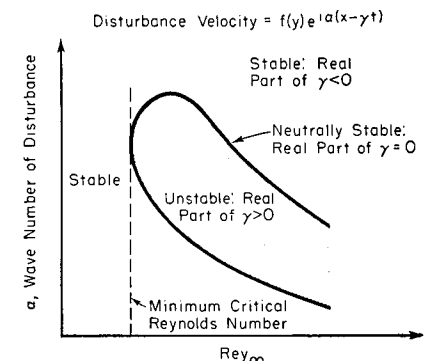


FIG. 26.35. Typical neutral stability curve.

**Effect of Mach Number.** Theoretical calculations of Lees <sup>(22)</sup> indicate that the laminar boundary layer becomes less stable as the free-stream Mach Number is increased (Fig. 26.36a). In this respect it is important to note that the minimum critical  $Rey_\infty$ , defined as in Fig. 26.35, merely marks the onset of possible amplification of infinitesimal disturbances in the boundary layer, and does not directly indicate the Reynolds Number of transition at which the disturbances have multiplied non-linearly to the point where the flow is turbulent. For flat plates, the Reynolds Number of transition is usually about an order of magnitude larger than the minimum critical Reynolds Number.

**Effect of Heat Transfer.** Lees found further (Fig. 26.36b) that cooling of the stream leads to substantial increases in stability, while heating of the stream has an opposite effect. If the wall is maintained below a certain temperature, indicated in Fig. 26.36c by  $(T_w/T_\infty)_{\text{stable}}$ , the boundary layer is stable at any Reynolds Number, and transition would presumably never occur if large-amplitude disturbances were initially absent.\*

\*Note added in proof: Recent unpublished work by C. C. Lin shows that the results of Fig. 26.36c apply only to two-dimensional disturbances, and that at high Mach Numbers the boundary layer is less stable to three-dimensional disturbances than to two-dimensional ones; at subsonic Mach Numbers the reverse is true.

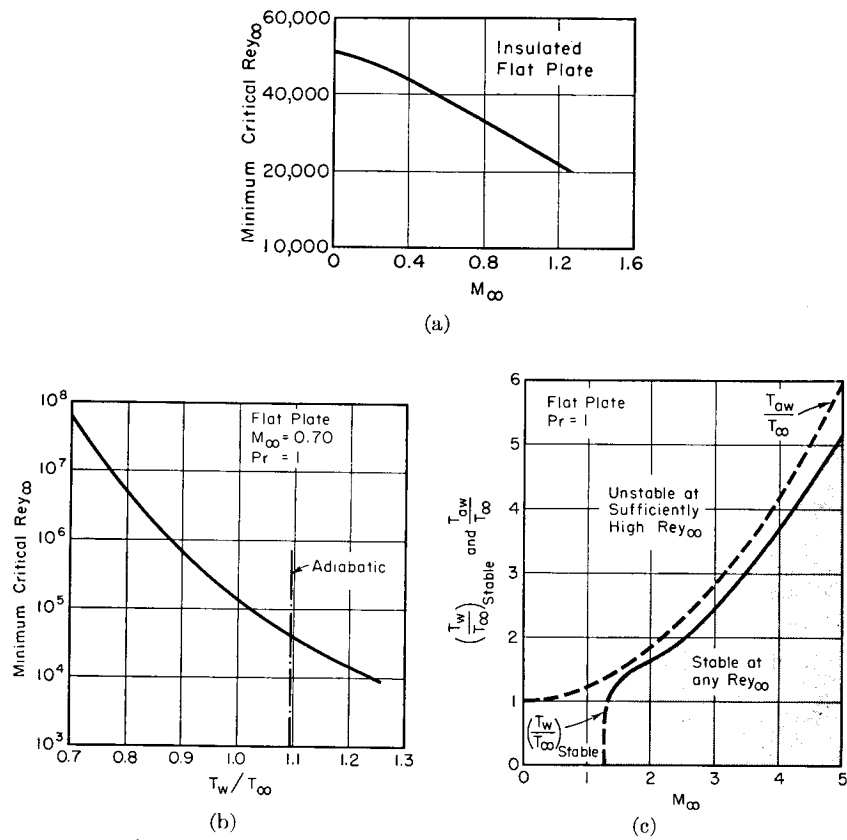


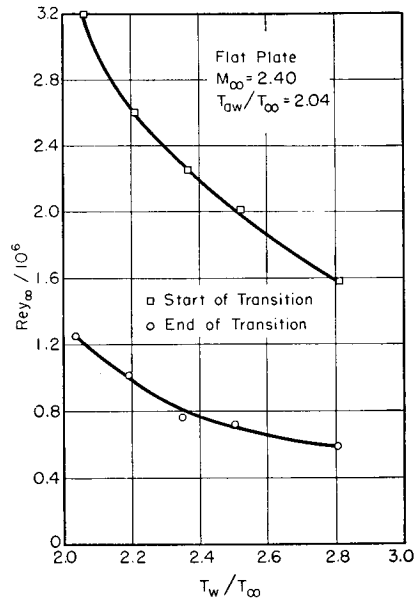
FIG. 26.36. Stability of flat-plate laminar flow for two-dimensional disturbances (after Lees).

- Effect of  $M_{\infty}$ .
- Effect of heat transfer.
- Region of stability at any Reynolds Number.

**Experimental Results.** The destabilizing effects of a hot surface and the stabilizing effects of a cold surface have been verified qualitatively<sup>(23,24)</sup> by experiments at supersonic speeds with cones. These experiments showed that transition to turbulence occurred earlier as the cone temperature was raised, and occurred later as the cone temperature was reduced.

For supersonic flow on a flat plate, the measured destabilizing effect of surface heating<sup>(21)</sup> is shown quantitatively in Fig. 26.37 and illustrates again the powerful influence of this factor. Additional experimental data are given in Art. 27.7.

FIG. 26.37. Effect of wall temperature on transition of laminar boundary layer (after Higgins and Pappas).



#### REFERENCES AND SELECTED BIBLIOGRAPHY

- GOLDSTEIN, S. *Modern Developments in Fluid Mechanics*. Vol. 2. London: Clarendon Press (Oxford), 1938, Chapters 14, 15.
- VON KÁRMÁN, T., and TSIEN, H. S. Boundary Layer in Compressible Fluids, *Jour. Aero. Sci.*, Vol. 5 (1938), p. 227.
- KALIKHMAN, L. E. Heat Transmission in the Boundary Layer, *NACA Tech. Memo.*, No. 1229 (1949).
- CHAPMAN, D. R. Laminar Mixing of a Compressible Fluid, *NACA Report*, No. 958 (1950).
- ECKERT, E., and DREWITZ, O. The Heat Transfer to a Plate in Flow at High Speed, *NACA Tech. Memo.*, No. 1045 (1943).
- EMMONS, H. W., and BRAINERD, J. G. Temperature Effects in a Laminar Compressible-Fluid Boundary Layer Along a Flat Plate, *Jour. App. Mech., Trans. A.S.M.E.*, Vol. 63 (1941), p. A-105.
- EMMONS, H. W., and BRAINERD, J. G. Effect of Variable Viscosity on Boundary Layers, with a Discussion of Drag Measurements, *Jour. App. Mech., Trans. A.S.M.E.*, Vol. 64 (1942), p. A-1.
- HANTZSCHE, W., and WENDT, H. Integration der laminaren Grenzschicht der ebenen Platte mit und ohne Wärmeübergang, *Luftfahrtforschung*, Bericht 139 (October, 1941).
- VAN DRIEST, E. R. Investigation of the Laminar Boundary Layer in Compressible Fluids Using the Crocco Method, *NACA Tech. Note*, No. 2597 (1952).
- HOWARTH, L. Concerning the Effects of Compressibility on Laminar Boundary Layers, *Proc. Roy. Soc. (A)*, Vol. 194 (1948), p. 16.
- ALLEN, H. J., and NITZBERG, G. E. The Effect of Compressibility on the Growth of the Laminar Boundary Layer on Low-Drag Wings and Bodies, *NACA Tech. Note*, No. 1255 (1947).
- MÄGLER, W. Zusammenhang zwischen ebenen und rotations symmetrischen Grenzschichten in kompressiblen Flüssigkeiten, *Z.a.M.M.*, Vol. 28 (1948), p. 7.
- HANTZSCHE, W., and WENDT, H. Die laminare Grenzschicht bei einem mit Überschallgeschwindigkeit angestromten nichtangestallten Kreiskegel, *Jahrbuch 1941 der deutschen Luftfahrtforschung*, Sect I (1941), p. 76.

14. JOHNSON, H. A., and RUBESIN, M. W. Aerodynamic Heating and Convective Heat Transfer—Summary of Literature Survey, *Trans. A.S.M.E.*, Vol. 71 (1949), p. 447.
15. SCHERRER, R. The Effects of Aerodynamic Heating and Heat Transfer on the Surface Temperature of a Body of Revolution in Steady Supersonic Flight, *NACA Tech. Note*, No. 1300 (1947).
16. BLUE, R. E. Interferometer Corrections and Measurements of Laminar Boundary Layers in Supersonic Stream, *NACA Tech. Note*, No. 2110 (1950).
17. ECKERT, E., and WEISE, W. Measurement of Temperature Distribution on the Surface of Unheated Bodies in High-Velocity Flow, *Forschung a. d. Geb. d. Ing.*, Vol. 13 (1942), p. 226.
18. STALDER, J. R., RUBESIN, M. W., and TENDELAND, T. A Determination of the Laminar-, Transitional-, and Turbulent-Boundary-Layer Temperature-Recovery Factors on a Flat Plate in Supersonic Flow, *NACA Tech. Note*, No. 2077 (1950).
19. SCHERRER, R., and GOWEN, F. E. Comparison of Theoretical and Experimental Heat Transfer on a Cooled 20°-Cone with a Laminar Boundary Layer at a Mach Number of 2.02, *NACA Tech. Note*, No. 2087 (1950).
20. WIMBROW, W. R., and SCHERRER, R. Laminar-Boundary-Layer Heat-Transfer Characteristics of a Body of Revolution with a Pressure Gradient at Supersonic Speeds, *NACA Tech. Note*, No. 2148 (1950).
21. HIGGINS, R. W., and PAPPAS, C. C. An Experimental Investigation of the Effect of Surface Heating on Boundary-Layer Transition on a Flat Plate in Supersonic Flow, *NACA Tech. Note*, No. 2351 (1951).
22. LEES, L. The Stability of the Laminar Boundary Layer in a Compressible Fluid, *NACA Tech. Note*, No. 1360 (1947).
23. SCHERRER, R., WIMBROW W. R., and GOWEN, F. E. Heat-Transfer and Boundary-Layer Transition on a Heated 20°-Cone at a Mach Number of 1.53, *NACA R.M.*, No. A8L28 (1949).
24. SCHERRER, R. Boundary-Layer Transition on a Cooled 20°-Cone at Mach Numbers of 1.5 and 2.0, *NACA Tech. Note*, No. 2131 (1950).
25. WIMBROW, W. R. Experimental Investigation of Temperature Recovery Factors on Bodies of Revolution at Supersonic Speeds, *NACA Tech. Note*, No. 1975 (1949).
26. LOW, G. M. Simplified Method for Calculation of Compressible Laminar Boundary Layer with Arbitrary Free-Stream Pressure Gradient, *NACA Tech. Note*, No. 2531 (1951).
27. KLUNKER, E. B., and McLEAN, F. E. Laminar Friction and Heat Transfer at Mach Numbers from 1 to 10, *NACA Tech. Note*, No. 2499 (1951).
28. EBER, G. R. Recent Investigation of Temperature Recovery and Heat Transmission on Cones and Cylinders in Axial Flow in the N.O.L. Aeroballistics Wind Tunnel, *Jour. Aero. Sci.*, Vol. 19, No. 1 (1952), p. 1.
29. YOUNG, G. B. W., and JANSEN, E. The Compressible Boundary Layer, *Jour. Aero. Sci.*, Vol. 19, No. 4 (1952), p. 229.
30. SCHLICHTING, H. *Grenzschicht-Theorie*. Karlsruhe: Verlag G. Braun, 1951.
31. COLES, D. Direct Measurement of Supersonic Skin Friction, *Jour. Aero. Sci.*, Vol. 17, No. 10 (1952), p. 717.
32. SCHERRER, R. Comparison of Theoretical and Experimental Heat-Transfer Characteristics of Bodies of Revolution at Supersonic Speeds, *NACA Tech. Rep.*, No. 1055 (1951).
33. DES CLERS, B., and STERNBERG, J. On Boundary-Layer Temperature Recovery Factors, *Jour. Aero. Sci.*, Vol. 19, No. 9 (1952), p. 645.
34. SLACK, E. G. Experimental Investigation of Heat Transfer Through Laminar and Turbulent Boundary Layers on a Cooled Flat Plate at a Mach Number of 2.4, *NACA Tech. Note*, No. 2686 (1952).
35. STINE, H. A., and SCHERRER, R. Experimental Investigation of the Turbulent-Boundary-Layer Temperature-Recovery Factor on Bodies of Revolution at Mach Numbers from 2.0 to 3.8, *NACA Tech. Note*, No. 2664 (1952).

36. LIBBY, P. A., MORDUCHOW, M., and BLOOM, M. Critical Study of Integral Methods in Compressible Laminar Boundary Layers, *NACA Tech. Note*, No. 2655 (1952).
37. BLUE, R. E., and LOW, G. M. Factors Affecting Laminar Boundary Layer Measurements in a Supersonic Stream, *NACA Tech. Note*, No. 2891 (1953).
38. LADENBURG, R., and BERSHADER, D. Optical Studies of Boundary Layer Phenomena on a Flat Plate at Mach Number 2.35, *Princeton University Report*, NR061-020 (December, 1952).
39. LIBBY, P. A., and MORDUCHOW, M. Method for Calculation of Compressible Laminar Boundary Layer with Axial Pressure Gradient and Heat Transfer, *NACA Tech. Note*, No. 3157 (1954).
40. SCHLICHTING, H. Zur Berechnung der laminaren Reibungsschicht bei Überschallgeschwindigkeit, *Braunschweigischen Wissenschaftlichen Gesellschaft*, Vol. 3 (1951), p. 239.
41. O'DONNELL, R. M. Experimental Investigation at a Mach Number of 2.41 of Average Skin-Friction Coefficients and Velocity Profiles for Laminar and Turbulent Boundary Layers and an Assessment of Probe Effects, *NACA Tech. Note*, No. 3122 (1954).
42. BOISON, J. C. Mean Skin-Friction Coefficients for Biconvex Airfoils in Supersonic Flow, *Jour. Aero. Sci.*, Vol. 20, No. 11 (1953), p. 787.
43. BECKWITH, I. E. Heat Transfer and Skin Friction by an Integral Method in the Compressible Laminar Boundary Layer with a Streamwise Pressure Gradient, *NACA Tech. Note*, No. 3005 (1953).
44. MACKAY, D. S., and NAGAMATSU, H. T. Laminar Boundary-Layer Temperature Recovery Factor on a Cone at Nominal Mach Number Six, *Jour. Aero. Sci.*, Vol. 21, No. 1 (1954), p. 65.
45. KAYE, J. Survey of Friction Coefficients, Recovery Factors, and Heat-Transfer Coefficients for Supersonic Flow, *Jour. Aero. Sci.*, Vol. 21, No. 2 (1954).

## Chapter 27

### THE TURBULENT BOUNDARY LAYER

#### 27.1. Introductory Remarks

In by far the greatest number of practical applications the boundary layer is turbulent rather than laminar. Or, more precisely, the bulk of the boundary layer is turbulent, with a thin *laminar sublayer* near the wall.

The essential difference between laminar and turbulent flows lies in the relative steadiness of the two types of flows. In a steady laminar flow, the macroscopic fluid properties and velocity at each and every point are truly constant with respect to time. Therefore the streamlines have constant shapes, and the fluid flows in "lamina," or in sheets which do not intermingle. Strictly, it is a contradiction in terms to speak of a "steady, turbulent flow," but the phrase is used to denote a turbulent flow which is steady in the mean. That is, at each point of such a flow the fluid properties and velocity may fluctuate wildly, but, when averaged over time periods comprising many cyclic fluctuations, the time-mean properties and velocity are constant with respect to time. In a steady laminar flow only the convective acceleration of the fluid (e.g.,  $u \frac{\partial u}{\partial x}$ ) is significant, whereas in a steady turbulent flow the time-varying acceleration  $\frac{\partial u}{\partial t}$  may be very much larger than the convective acceleration.

As a result of the rapid fluctuations in velocity at each point in a turbulent flow, the instantaneous streamlines have a highly irregular and jagged appearance. Moreover, the instantaneous streamlines change in form from instant to instant. This leads to a macroscopic intermingling, or transport, of fluid between different time-mean streamlines. Blobs of fluid when transported in this way tend to retain for a short period the time-mean velocity and temperature corresponding to the location from which they migrated. In the new location to which they are transported by turbulent fluctuations, there may be a very different time-mean velocity and temperature. Physically, then, turbulence acts to magnify enormously the local, instantaneous gradients of velocity and temperature, and thus it greatly augments the viscous stresses and rate of heat conduction acting in the fluid. The most important practical consequence of this is that the skin-friction and heat transfer coefficients for a turbulent boundary layer are several

#### NOMENCLATURE

$c_p$	specific heat at constant pressure	$x, y$	curvilinear coordinates along and normal to wall
$C_D$	integrated skin-friction coefficient	$y^+$	dimensionless friction length (Eq. 27.27b)
$C_f$	local skin-friction coefficient	$\Gamma$	stagnation-temperature thickness (Eq. 27.24)
$C_H$	Stanton Number (Eq. 27.17c)	$\delta$	boundary-layer thickness
$\mathfrak{C}$	film coefficient of heat transfer (Eq. 27.17b)	$\delta^*$	displacement thickness (Eq. 27.19a)
$K$	mixing-length constant (Eq. 27.60)	$\epsilon$	eddy viscosity
$l$	mixing length	$\theta$	momentum thickness (Eq. 27.19b)
$M$	Mach Number	$\kappa$	eddy heat conductivity
$N$	exponent for turbulent velocity profile (Eq. 27.25)	$\lambda$	coefficient of thermal conductivity
$\mathbf{Nu}$	Nusselt Number (Eq. 27.17c)	$\mu$	coefficient of viscosity
$p$	pressure	$\rho$	mass density
$Pr$	Prandtl Number	$\tau$	shear stress
$q$	rate of heat transfer per unit area	$\overline{(\ )}$	signifies time-mean of quantity
$Q$	See Eq. 27.54b.	$( )'$	signifies instantaneous deviation from time-mean
$\mathfrak{R}$	recovery factor	$( )_w$	signifies conditions at wall
$Rey$	Reynolds Number	$( )_\infty$	signifies conditions at edge of boundary layer
$t$	time	$( )_i$	signifies interface between laminar sublayer and turbulent layer
$T$	temperature	$( )_{am}$	signifies conditions at $(T_\infty + T_w)/2$
$T_0$	adiabatic stagnation temperature		
$u, v$	velocity components in $x$ - and $y$ -directions		
$u^+$	dimensionless friction velocity (Eq. 27.27a)		
$U_\infty$	velocity at edge of boundary layer		

orders of magnitude larger than the corresponding values for a laminar boundary layer at the same Reynolds Number.

Although turbulent flows are of greater practical significance than laminar flows, they are less well understood theoretically, and are less amenable to analytical prediction. This situation stems from the great unsteadiness of turbulent flows. The exceedingly complex character of such flows not only makes the mathematical description extremely awkward, but makes an exact analytical development almost hopeless. To make the analysis of turbulent flows manageable, it is usual to write the governing equations in terms of the time-mean fluid properties as though the flow were in fact steady, and then to add certain terms (such as the *Reynolds stress*) which represent, at least crudely, the influence of the unsteadiness on the time-mean flow field. It is usually necessary, in addition, to introduce a certain amount of empirical information (such as the measured shape of turbulent mean velocity profiles) in order to arrive at useful "theoretical" results.

In this chapter we shall first introduce some of the basic concepts useful for treating turbulent motions, after which we shall outline some of the principal analytical approaches to turbulent flows, and finally we shall summarize the most significant experimental information concerning turbulent flows at high Mach Numbers.

## 27.2. Differential Equations of the Turbulent Boundary Layer<sup>(1,2)</sup>

We shall now set down the differential equations for two-dimensional, turbulent flow. The derivation of these equations is substantially identical with the derivation in Art. 26.2 of the corresponding equations for laminar flow, except that it is essential to introduce the terms connected with the unsteady nature of the motion.

**Continuity Equation.** Taking account of the rate of change of mass within the control volume of Fig. 26.4, the principle of conservation of mass may be written as

$$\frac{\partial \rho}{\partial t} + \frac{\partial}{\partial x} (\rho u) + \frac{\partial}{\partial y} (\rho v) = 0 \quad (27.1)$$

**Definition of Time-Mean Properties and of Fluctuating Components.** The fluctuating nature of turbulent motion suggests that the instantaneous value of each fluid property may be considered as the sum of two parts: (i) a *mean value* which varies slowly with time, if at all; and

(ii) a *fluctuating component* which is a function of time. We therefore define

$$\begin{aligned} u &\equiv \bar{u} + u'; & \rho u &\equiv \bar{\rho} \bar{u} + (\rho u)' \\ v &\equiv \bar{v} + v'; & \rho v &\equiv \bar{\rho} \bar{v} + (\rho v)' \\ \rho &\equiv \bar{\rho} + \rho' \end{aligned} \quad (27.2)$$

where the bar over a symbol denotes the slowly varying *temporal mean value* of the quantity, and the prime denotes the instantaneous deviation from the mean value.

If  $t$  denotes time, then, by definition,

$$\bar{u} \equiv \frac{1}{t^*} \int_0^{t^*} u \, dt, \quad \text{etc.}$$

where  $t^*$  is large compared with the period of the fluctuations. From the latter relation and Eq. 27.2 it follows that the time average of any fluctuating component is zero, e.g.,  $\bar{u}' = 0$ . It may also be shown from the definition of a mean property that

$$\frac{\partial \bar{u}}{\partial x} = \frac{\partial}{\partial x} (\bar{u}) = \frac{\partial \bar{u}}{\partial x}, \quad \text{etc.}$$

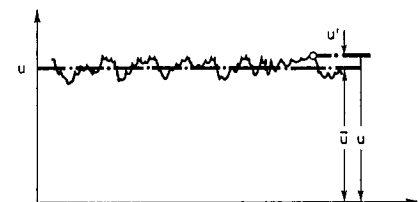


FIG. 27.1. Typical time variation of fluid property in a turbulent flow.

**CONTINUITY EQUATION IN TIME-MEAN FORM.** Substituting Eqs. 27.2 into Eq. 27.1, we obtain

$$\frac{\partial \bar{\rho}}{\partial t} + \frac{\partial \rho'}{\partial t} + \frac{\partial}{\partial x} (\bar{\rho} \bar{u}) + \frac{\partial}{\partial x} (\rho \bar{u})' + \frac{\partial}{\partial y} (\bar{\rho} \bar{v}) + \frac{\partial}{\partial y} (\rho \bar{v})' = 0$$

Now, taking the time mean of this equation, and noting that

$$\frac{\partial}{\partial t} (\rho') = \frac{\partial}{\partial t} (\bar{\rho}') = \frac{\partial}{\partial t} (0) = 0, \quad \text{etc.}$$

we obtain the continuity equation in the form

$$\frac{\partial \bar{\rho}}{\partial t} + \frac{\partial}{\partial x} (\bar{\rho} \bar{u}) + \frac{\partial}{\partial y} (\bar{\rho} \bar{v}) = 0 \quad (27.3)$$

By definition, however,

$$\begin{aligned}\bar{\rho}u &= \bar{(\rho + \rho')(\bar{u} + \bar{u}')} = \bar{\rho}\bar{u} + \bar{\rho}\bar{u}' + \bar{u}\bar{\rho}' + \bar{\rho}'\bar{u}' = \bar{\rho}\bar{u} + \bar{\rho}'\bar{u}' \\ \bar{\rho}v &= \bar{(\rho + \rho')(\bar{v} + \bar{v}')} = \bar{\rho}\bar{v} + \bar{\rho}\bar{v}' + \bar{v}\bar{\rho}' + \bar{\rho}'\bar{v}' = \bar{\rho}\bar{v} + \bar{\rho}'\bar{v}'\end{aligned}\quad (27.4)$$

and so the continuity equation may be written as

$$\frac{\partial \bar{\rho}}{\partial t} + \frac{\partial}{\partial x}(\bar{\rho}\bar{u}) + \frac{\partial}{\partial y}(\bar{\rho}\bar{v}) + \frac{\partial}{\partial x}(\bar{\rho}'\bar{u}') + \frac{\partial}{\partial y}(\bar{\rho}'\bar{v}') = 0 \quad (27.5)$$

The first three terms of Eq. 27.5 are recognized as the form which Eq. 27.1 would take if there were no turbulent fluctuations, and would be the form which one would write down for the continuity equation if one observed only the time-mean flow properties  $\bar{\rho}$ ,  $\bar{u}$ , etc., and took no account of the unsteadiness in the flow. The terms  $\bar{\rho}'\bar{u}'$  and  $\bar{\rho}'\bar{v}'$  represent, therefore, *apparent flows* in the  $x$ - and  $y$ -directions, respectively. These must be added to the time-mean flows  $\bar{\rho}\bar{u}$  and  $\bar{\rho}\bar{v}$  when one wishes to treat a turbulent flow in terms of time-mean properties.

**Momentum Equation.** Using the control volume of Fig. 26.5, denoting by  $\tau_{yx}$  the shear stress acting on a  $y$ -face in the  $x$ -direction, and taking account of the rate of change of momentum within the control volume, the momentum equation in the  $x$ -direction may be written as

$$\frac{\partial}{\partial t}(\rho u) + \frac{\partial}{\partial x}(\rho u^2) + \frac{\partial}{\partial y}(\rho uv) = -\frac{\partial p}{\partial x} + \frac{\partial \tau_{yx}}{\partial y}$$

In analogous fashion to Eqs. 27.2, we define

$$p \equiv \bar{p} + p'; \quad \tau_{yx} \equiv \bar{\tau}_{yx} + \tau_{yx}'$$

These, together with Eqs. 27.2, are now substituted into the momentum equation, and the time average of the latter is taken, thus yielding

$$\begin{aligned}\frac{\partial}{\partial t}(\bar{\rho}\bar{u} + \bar{\rho}'\bar{u}') + \frac{\partial}{\partial x}[\bar{\rho}\bar{u}\bar{u} + \bar{(\rho u)'}\bar{u}'] + \frac{\partial}{\partial y}[\bar{\rho}\bar{v}\bar{u} + \bar{(\rho v)'}\bar{u}'] \\ = -\frac{\partial \bar{p}}{\partial x} + \frac{\partial \bar{\tau}_{yx}}{\partial y}\end{aligned}\quad (27.6)$$

Differentiating by parts the product terms containing  $\bar{u}$  in this expression, three terms may be eliminated with the help of Eq. 27.3, and thus there is obtained

$$\begin{aligned}\bar{\rho}\frac{\partial \bar{u}}{\partial t} + \bar{\rho}\bar{u}\frac{\partial \bar{u}}{\partial x} + \bar{\rho}\bar{v}\frac{\partial \bar{u}}{\partial y} \\ = -\frac{\partial \bar{p}}{\partial x} + \frac{\partial \bar{\tau}_{yx}}{\partial y} - \frac{\partial}{\partial t}\bar{\rho}'\bar{u}' - \frac{\partial}{\partial x}\bar{(\rho u)'}\bar{u}' - \frac{\partial}{\partial y}\bar{(\rho v)'}\bar{u}'\end{aligned}\quad (27.7)$$

We now simplify this greatly by assuming that:

(i) The boundary layer is very thin, and hence

$$\frac{\partial}{\partial x}\bar{(\rho u)'}\bar{u}' \ll \frac{\partial}{\partial y}\bar{(\rho v)'}\bar{u}'$$

(ii) The flow is steady in the mean, and hence

$$\frac{\partial}{\partial t}\bar{\rho}'\bar{u}' = 0; \quad \frac{\partial \bar{u}}{\partial t} = 0$$

(iii) The time-mean viscous stress, which is shown by experience to be small compared with  $\bar{(\rho v)'}\bar{u}'$ , may be approximated by

$$\bar{\tau}_{yx} = \mu\left(\frac{\partial u}{\partial y} + \frac{\partial v}{\partial x}\right) = \bar{\mu}\left(\frac{\partial \bar{u}}{\partial y} + \frac{\partial \bar{v}}{\partial x}\right) + \mu'\frac{\partial \bar{u}}{\partial y} + \mu'\frac{\partial \bar{v}}{\partial x} \cong \bar{\mu}\frac{\partial \bar{u}}{\partial y}$$

With these assumptions, Eq. 27.7 reduces to

$$\bar{\rho}\bar{u}\frac{\partial \bar{u}}{\partial x} + \bar{\rho}\bar{v}\frac{\partial \bar{u}}{\partial y} = -\frac{\partial \bar{p}}{\partial x} + \frac{\partial}{\partial y}\left(\bar{\mu}\frac{\partial \bar{u}}{\partial y}\right) + \frac{\partial}{\partial y}[-\bar{(\rho v)'}\bar{u}'] \quad (27.8)$$

**REYNOLDS STRESS.** If we considered only the time-mean properties of the flow, and disregarded the turbulent fluctuations, we would write the momentum equation in the form of Eq. 26.5, except that all the symbols would be barred. But Eq. 27.8 shows that we would then be omitting the term containing  $[-\bar{(\rho v)'}\bar{u}']$ , a term which arises from the unsteadiness of the flow, and which has the same effect in the momentum equation as the mean viscous stress  $\bar{\mu}\partial\bar{u}/\partial y$ .

The term  $[-\bar{(\rho v)'}\bar{u}']$  is the generalization for compressible flow of the well-known *Reynolds stress*, or *turbulent stress*, for incompressible flow, and is analogous to the apparent mass flow in Eq. 27.5. It should be recognized that the Reynolds stress is not a stress at all, but is rather the time-mean of the  $x$ -momentum flux crossing a surface aligned normal to the  $y$ -direction. It is called an *apparent shear stress* only by analogy between Eq. 27.8 and Eq. 26.5. More precisely, however, it represents a momentum-exchange term which must be introduced to take account of the unsteadiness of the flow when the momentum equation is written in terms of the time-mean flow properties.

For thin, steady, turbulent boundary layers, the momentum equation in the  $y$ -direction reduces, as in laminar motion, to

$$\frac{\partial \bar{p}}{\partial y} = 0 \quad (27.9)$$

**Energy Equation.** The corresponding formulation for the energy equation is very lengthy in its details. Van Driest<sup>(2)</sup> has shown that,

based on assumptions analogous to those underlying Eq. 27.8, the time-mean energy equation may be written as

$$\begin{aligned} \overline{\rho u} c_p \frac{\partial \bar{T}}{\partial x} + \overline{\rho v} c_p \frac{\partial \bar{T}}{\partial y} &= \bar{u} \frac{\partial \bar{p}}{\partial x} + \frac{\partial}{\partial y} \left( \lambda \frac{\partial \bar{T}}{\partial y} \right) + \bar{\mu} \left( \frac{\partial \bar{u}}{\partial y} \right)^2 \\ &+ \frac{\partial}{\partial y} \left[ -c_p (\rho v)' \bar{T}' \right] - (\rho v)' \bar{u}' \frac{\partial \bar{u}}{\partial y} \end{aligned} \quad (27.10)$$

If we took no account of the unsteadiness of the flow, the energy equation would be written in terms of time-mean properties simply by copying Eq. 26.8 with bars over each symbol. It is evident from Eq. 27.10 that we would then be omitting the last two terms, both of which are connected with the unsteadiness of the flow, and both of which are in fact much larger than the two terms preceding them. By comparison of terms, it is evident that the term  $[c_p (\rho v)' \bar{T}']$  is in the nature of an *apparent heat flux* in the time-mean motion, and  $[-(\rho v)' \bar{u}']$ , as in Eq. 27.8, is an apparent shear stress in the time-mean motion.

**Turbulent Exchange Coefficients.** For convenience in practical computations, a *turbulent exchange coefficient for momentum*, or *eddy viscosity*,  $\epsilon$ , is often defined by

$$\bar{\tau}_{\text{turb}} \equiv -(\rho v)' \bar{u}' \equiv \epsilon \frac{\partial \bar{u}}{\partial y} \quad (27.11)$$

Although  $\epsilon$  is formally analogous to the coefficient of viscosity  $\mu$ , the two are essentially different in that the latter is a fluid property whereas the former depends on the dynamics of the flow. In a turbulent flow  $\epsilon/\mu$  is very large compared with unity, and therefore the viscous term is usually omitted from Eqs. 27.8 and 27.10.

Similarly, we define a *turbulent exchange coefficient for temperature*, or *eddy heat conductivity*,  $\kappa$ , by formal analogy with the Fourier equation,

$$-\bar{q}_{\text{turb}} \equiv -c_p (\rho v)' \bar{T}' \equiv \kappa \frac{\partial \bar{T}}{\partial y} \quad (27.12)$$

Here again, the molecular heat conductivity  $\lambda$  is a fluid property connected only with the thermodynamic state of the fluid, whereas the eddy conductivity  $\kappa$  is controlled primarily by the nature of the fluid motion. The ratio  $\kappa/\lambda$  is of the same order of magnitude as the ratio  $\epsilon/\mu$ , i.e., both are very much larger than unity, and therefore the heat conduction and viscous terms are usually dropped from Eq. 27.10.

**Prandtl Mixing Length.** The simplest formulation of the turbulent shear stress having any physical interpretation is that of Prandtl, who argued that the turbulent fluctuations  $u'$  and  $T'$  are chiefly the result of a lateral migration of a small fluid mass over some average

*mixing length*  $l$ , and that the fluid mass approximately retains its identity and properties during the migration. According to this concept the turbulent fluctuation at the new location is chiefly the result of the difference in time-mean properties between the old and the new locations.

Referring to Fig. 27.2, if a particle migrates from  $A$  to  $B$ , Prandtl's argument indicates that

$$u' \cong l \frac{\partial \bar{u}}{\partial y} \quad (27.13a)$$

and, similarly, that

$$T' \cong l \frac{\partial \bar{T}}{\partial y} \quad (27.13b)$$

The mixing length  $l$  is the same in both equations because it is usually assumed that the mechanisms for transport of velocity and temperature are identical.

Substituting Eqs. 27.13 into Eqs. 27.11 and 27.12, we get

$$-(\rho v)' l \frac{\partial \bar{u}}{\partial y} = \epsilon \frac{\partial \bar{u}}{\partial y}; \quad \text{whence} \quad \epsilon = -(\rho v)' l$$

$$-c_p (\rho v)' l \frac{\partial \bar{T}}{\partial y} = \kappa \frac{\partial \bar{T}}{\partial y}; \quad \text{whence} \quad \kappa = -c_p (\rho v)' l$$

From these it follows further that

$$c_p \epsilon / \kappa = 1 \quad (27.14)$$

**TURBULENT PRANDTL NUMBER.** By analogy with the ratio  $c_p \mu / \lambda$ , the ratio  $c_p \epsilon / \kappa$  is called the *turbulent Prandtl Number*. We see from Eq. 27.14 that the mixing-length theory of Prandtl predicts a turbulent Prandtl Number of unity.

The physical model on which this result is based is so oversimplified that the result can at best be regarded as indicating the order of magnitude, rather than the actual value, of the turbulent Prandtl Number. For one thing, temperature is a scalar quantity, but velocity is a vector. The temperature of a migrating fluid particle may be conserved if the migration is rapid, but its momentum is generally not conserved because there are usually pressure gradients in any non-steady flow.

An analysis of the results of many different types of experiments with turbulent flows has led to the remarkable conclusion <sup>(3)</sup> that the turbulent Prandtl Number is substantially independent of the value of the laminar Prandtl Number and is also substantially independent of

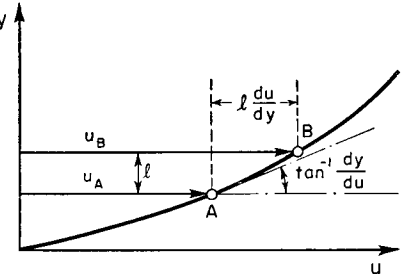


FIG. 27.2. Illustrates mixing-length hypothesis.

the type of experiment. These various experiments indicate that, within a margin of  $\pm 10$  per cent,

$$(\text{Pr})_{\text{turb}} \equiv c_p \epsilon / \kappa \cong 0.70 \quad (27.15)$$

For most practical purposes, therefore, the laminar and turbulent Prandtl Numbers for air may be assumed identical.

**Differential Equations with Exchange Coefficients.** When the definitions of  $\epsilon$  and  $\kappa$ , as given by Eqs. 27.11 and 27.12, are inserted into Eqs. 27.8 and 27.10, the time-mean equations of continuity, momentum, and energy for a thin, steady, turbulent boundary layer may be summarized as follows:

$$\frac{\partial}{\partial x} (\bar{\rho} \bar{u}) + \frac{\partial}{\partial y} (\bar{\rho} \bar{v}) = 0 \quad (27.16a)$$

$$\bar{\rho} \bar{u} \frac{\partial \bar{u}}{\partial x} + \bar{\rho} \bar{v} \frac{\partial \bar{u}}{\partial y} = - \frac{\partial \bar{p}}{\partial x} + \frac{\partial}{\partial y} \left[ (\epsilon + \bar{\mu}) \frac{\partial \bar{u}}{\partial y} \right] \quad (27.16b)$$

$$0 = \frac{\partial \bar{p}}{\partial y} \quad (27.16c)$$

$$\bar{\rho} \bar{u} c_p \frac{\partial \bar{T}}{\partial x} + \bar{\rho} \bar{v} c_p \frac{\partial \bar{T}}{\partial y} = \bar{u} \frac{\partial \bar{p}}{\partial x} + \frac{\partial}{\partial y} \left[ (\kappa + \bar{\lambda}) \frac{\partial \bar{T}}{\partial y} \right] + (\epsilon + \bar{\mu}) \left( \frac{\partial \bar{u}}{\partial y} \right)^2 \quad (27.16d)$$

These bear a formal resemblance to Eqs. 26.3, 26.5, 26.4, and 26.8, respectively, pertaining to steady laminar flow. Since  $\bar{\mu}$  and  $\bar{\lambda}$  are respectively so small compared with  $\epsilon$  and  $\kappa$  for turbulent flows, they are usually omitted from the equations.

**Flow with Prandtl Number Unity.** In gases both the laminar and turbulent Prandtl Numbers are in the vicinity of 0.7. This is sufficiently close to unity to make it of practical interest to investigate the special but simple case where both the turbulent boundary layer and laminar sublayer are assumed to have Prandtl Numbers of unity. The results of such an analysis are presumably good approximations except when there are large temperature differentials in the boundary layer.

Eqs. 27.16 are completely similar to the corresponding equations for steady, laminar flow. Moreover, the boundary conditions at the wall and at the edge of the boundary layer are the same as for laminar flow. Consequently all the results of Art. 26.3 (up through Eq. 26.19) for laminar flow with Prandtl Number unity are also applicable to the time-mean properties of a turbulent flow with Prandtl Number unity. The principal conclusions applicable to turbulent flows are summarized below.

**FLOW PAST INSULATED SURFACE.** If the wall is insulated, the stagnation temperature is constant throughout the boundary layer. This result is independent of the pressure gradient.

The adiabatic wall temperature is therefore equal to the free-stream stagnation temperature, and the recovery factor is unity.

**FLOW PAST FLAT PLATE AT CONSTANT TEMPERATURE.** If the wall is not insulated, but is instead at constant temperature, and if there are no longitudinal pressure gradients, then we may conclude that:

- (i) The time-mean temperature distribution in the boundary layer is uniquely determined by the time-mean velocity distribution, as given by Eq. 26.12.
- (ii) The film coefficient of heat transfer,  $\mathfrak{C}$ , is most appropriately defined in terms of the difference between the wall temperature and the adiabatic wall temperature, as in Eq. 26.14.
- (iii) Reynolds' analogy between friction and heat transfer, as given by Eqs. 26.16, 26.17, and 26.19, is valid.

The foregoing conclusion may be written as

$$\bar{T} - T_w = (T_{\infty} - T_w) \frac{\bar{u}}{U_{\infty}} - \frac{k - 1}{2} M_{\infty}^2 T_{\infty} \left( \frac{\bar{u}}{U_{\infty}} \right)^2 \quad (27.17a)$$

$$\mathfrak{C} \equiv \frac{q_w}{(T_w - T_{\infty})} \quad (27.17b)$$

$$C_{H\infty} \equiv \frac{\mathfrak{C}}{c_p \rho_{\infty} U_{\infty}} = \frac{C_{f\infty}}{2}; \quad \text{Nu}_{\infty} \equiv \frac{\mathfrak{C} x}{\lambda_{\infty}} = \frac{C_{f\infty}}{2} \text{Rey}_{\infty} \quad (27.17c)$$

$$C_{Hw} \equiv \frac{\mathfrak{C}}{c_p \rho_w U_{\infty}} = \frac{C_{f_w}}{2}; \quad \text{Nu}_w \equiv \frac{\mathfrak{C} x}{\lambda_w} = \frac{C_{f_w}}{2} \text{Rey}_w \quad (27.17d)$$

### 27.3. Integral Equations of the Turbulent Boundary Layer

Because the exact analysis of turbulent flows is so difficult, the integral methods of calculation play an even more important role than in the investigation of laminar flows. In what follows we shall consider only flows which are steady in the mean.

**Momentum Equation.** The analysis which leads to Eq. 26.34 is correct for turbulent flows (assuming that the symbols in that equation represent instantaneous values of the quantities) provided that we add to the right-hand side the term

$$\delta \frac{\partial}{\partial t} (\rho u)$$

representing the time-rate of change of  $x$ -momentum within the control volume of Fig. 26.24. However, we may write

$$\overline{\frac{\partial}{\partial t}(\rho u)} = \frac{\partial}{\partial t}(\overline{\rho u}) = \frac{\partial}{\partial t}(\bar{\rho} \bar{u}) + \frac{\partial}{\partial t}(\overline{\rho' u'})$$

and, since we have specified that the flow is steady in the mean, the time-mean of this term vanishes.

When we take the time-mean of the right-hand side of Eq. 26.34, there appear under the integrals such fluctuation terms as  $\overline{u'^2}$ ,  $\overline{\rho' u'}$ , and  $\overline{\rho' u'^2}$ . However, these double and triple correlations are to be integrated across the boundary layer, and it is a plausible assumption that, although these terms may be large locally, when integrated over a large surface they will tend to cancel themselves out. Employing this assumption, the time-mean momentum equation in integral form may be written

$$-\bar{\tau}_w - \delta \frac{\partial \bar{p}}{\partial x} = \frac{\partial}{\partial x} \int_0^\delta \bar{\rho} \bar{u}^2 dy - U_\infty \frac{\partial}{\partial x} \int_0^\delta \bar{\rho} \bar{u} dy \quad (27.18)$$

This may now be put into the form of Eq. 26.35, or, alternatively, we shall derive a somewhat different form which is often convenient for practical computations.

Since the pressure within the boundary layer is established by the free-stream pressure, the pressure gradient may be eliminated with the help of Euler's equation written for the inviscid flow at the edge of the boundary layer. Thus

$$\frac{\partial \bar{p}}{\partial x} = -\rho_\infty U_\infty \frac{\partial U_\infty}{\partial x}$$

where  $\rho_\infty$  and  $U_\infty$  are the local free-stream properties at the edge of the boundary layer. We now insert this into Eq. 27.18 and perform the algebraic rearrangements shown below:

$$\begin{aligned} \bar{\tau}_w &= \delta \rho_\infty U_\infty \frac{\partial U_\infty}{\partial x} - \frac{\partial}{\partial x} \int_0^\delta \bar{\rho} \bar{u}^2 dy + U_\infty \frac{\partial}{\partial x} \int_0^\delta \bar{\rho} \bar{u} dy \\ &= \frac{\partial U_\infty}{\partial x} \int_0^\delta \rho_\infty U_\infty dy + \frac{\partial}{\partial x} \int_0^\delta \bar{\rho} \bar{u} (U_\infty - u - U_\infty) dy \\ &\quad + \frac{\partial}{\partial x} U_\infty \int_0^\delta \bar{\rho} \bar{u} dy - \frac{\partial U_\infty}{\partial x} \int_0^\delta \bar{\rho} \bar{u} dy \\ &= \frac{\partial U_\infty}{\partial x} \rho_\infty U_\infty \int_0^\delta \left(1 - \frac{\bar{\rho} \bar{u}}{\rho_\infty U_\infty}\right) dy + \frac{\partial}{\partial x} \rho_\infty U_\infty^2 \int_0^\delta \frac{\bar{\rho} \bar{u}}{\rho_\infty U_\infty} \left(1 - \frac{\bar{u}}{U_\infty}\right) dy \end{aligned}$$

**DISPLACEMENT AND MOMENTUM THICKNESSES.** We now introduce the definitions of the *displacement thickness*  $\delta^*$  and the *momentum thickness*  $\theta$  as

$$\frac{\delta^*}{\delta} = \int_0^1 \left(1 - \frac{\bar{\rho} \bar{u}}{\rho_\infty U_\infty}\right) d\left(\frac{y}{\delta}\right) \quad (27.19a)$$

$$\frac{\theta}{\delta} = \int_0^1 \frac{\bar{\rho}}{\rho_\infty} \frac{\bar{u}}{U_\infty} \left(1 - \frac{\bar{u}}{U_\infty}\right) d\left(\frac{y}{\delta}\right) \quad (27.19b)$$

Physically, the *displacement thickness* is a measure of the deficiency in mass flow through the boundary layer as a result of the stream having been slowed down by friction. Since Eq. 27.19a may be put in the form

$$\int_0^\delta \bar{\rho} \bar{u} dy = \rho_\infty U_\infty (\delta - \delta^*)$$

it is evident from Fig. 27.3 that  $\delta^*$  represents the outward displacement of a streamline outside the boundary layer to make space for the rela-

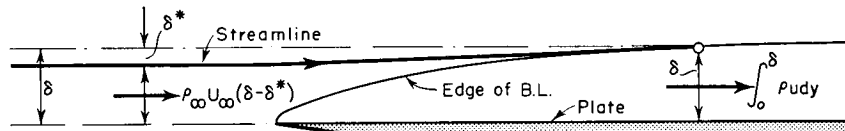


FIG. 27.3. Displacement thickness.

tively low-speed boundary-layer flow. From another point of view, the displacement thickness is the amount by which the walls should be displaced so that, by leaving sufficient room for the boundary-layer flow, the inviscid flow may not be affected by the thickening of the boundary layer.

The *momentum thickness* has an analogous significance. It represents the thickness of the free-stream flow necessary to make up the deficiency in momentum flux within the boundary layer.

With these definitions of  $\delta^*$  and  $\theta$ , the momentum equation may be written as

$$\frac{\bar{\tau}_w}{\rho_\infty U_\infty^2} = \frac{\delta^*}{U_\infty} \frac{\partial U_\infty}{\partial x} + \frac{1}{\rho_\infty U_\infty^2} \frac{\partial}{\partial x} (\rho_\infty U_\infty^2 \theta)$$

which, when expanded, may be rearranged to give

$$\frac{\bar{\tau}_w}{\rho_\infty U_\infty^2} = \frac{d\theta}{dx} + \left[ \frac{2 + \frac{\delta^*}{\theta}}{U_\infty} \frac{dU_\infty}{dx} + \frac{1}{\rho_\infty} \frac{d\rho_\infty}{dx} \right] \theta \quad (27.20)$$

By means of the isentropic relations,

$$\frac{dU_\infty}{U_\infty} = \frac{dM_\infty}{M_\infty \left(1 + \frac{k-1}{2} M_\infty^2\right)}; \quad \frac{d\rho_\infty}{\rho_\infty} = -\frac{M_\infty^2}{1 + \frac{k-1}{2} M_\infty^2} \frac{dM_\infty}{M_\infty}$$

Eq. 27.20 may be put in the form

$$\frac{\bar{\tau}_w}{\rho_\infty U_\infty^2} = \frac{d\theta}{dx} + \left[ \frac{(2 - M_\infty^2) + \frac{\delta^*}{\theta}}{M_\infty \left( 1 + \frac{k-1}{2} M_\infty^2 \right)} \frac{dM_\infty}{dx} \right] \theta \quad (27.21)$$

**Energy Equation.** By employing the same arguments which underlie the derivations of Eqs. 27.18, 27.20, and 27.21, a form of the energy equation analogous to Eq. 26.36 may be derived, namely,

$$\bar{q}_w = \frac{\partial}{\partial x} \int_0^\delta c_p (\bar{\rho} \bar{u} \bar{T}_0 - \rho_\infty U_\infty T_{0\infty}) dy - c_p T_{0\infty} \frac{\partial}{\partial x} \int_0^\delta (\bar{\rho} \bar{u} - \rho_\infty U_\infty) dy \quad (27.22)$$

**STAGNATION-TEMPERATURE THICKNESS.** Since  $T_{0\infty}$  is assumed to be independent of  $x$ , Eq. 27.22 may be rearranged in the form

$$\frac{\bar{q}_w}{c_p \rho_\infty U_\infty T_{0\infty}} = \frac{d\Gamma}{dx} + \frac{\Gamma}{M_\infty} \frac{1 - M_\infty^2}{1 + \frac{k-1}{2} M_\infty^2} \frac{dM_\infty}{dx} \quad (27.23)$$

where  $\Gamma$  is the *stagnation-temperature thickness*, defined, analogously to the momentum thickness, by

$$\frac{\Gamma}{\delta} \equiv \int_0^1 \frac{\bar{\rho} \bar{u}}{\rho_\infty U_\infty} \left( \frac{\bar{T}_0}{T_{0\infty}} - 1 \right) d\left(\frac{y}{\delta}\right) \quad (27.24)$$

The thickness  $\Gamma$  is a measure of the amount of free-stream flow required to account for the deficiency (or excess) of stagnation-temperature flux in the boundary layer.

As in the case of the laminar boundary layer, the  $\delta$  referred to in Eqs. 27.19 and 27.24 is the thickness of the velocity boundary layer or the thermal boundary layer, whichever is the greater.

If the turbulent and laminar Prandtl Numbers are assumed to be unity, and if it is also assumed that with small pressure gradients the connection between velocity and temperature distributions given by Eq. 27.17a remains valid, then the thicknesses of the velocity and thermal boundary layers will be alike. In that case there is no need for Eq. 27.24, inasmuch as a solution for the velocity boundary layer immediately yields (through Eq. 27.17a) a solution for the thermal boundary layer. Although this procedure is often used for the sake of simplicity in calculation, it should be recognized that it is likely to be of only mediocre accuracy for the pressure gradients which are present in practical problems.

**VELOCITY PROFILE IN TURBULENT BOUNDARY LAYER.** To apply the momentum integral analysis, it is necessary to choose a shape for the

velocity profile. Lacking extensive experimental data in compressible flows, the usual custom is to employ the empirically determined power law for incompressible flow,<sup>(4,5,6)</sup> namely,

$$\frac{\bar{u}}{U_\infty} = \left( \frac{y}{\delta} \right)^{1/N} \quad (27.25)$$

where  $N$  is a constant whose value depends primarily on the Reynolds Number of the flow. The value of  $N$  varies from  $N = 5$  ( $\text{Rey} \cong 10^5$ ) to about  $N = 10$  ( $\text{Rey} \cong 10^9$ ). Often a mean value of 7 is chosen for  $N$ .

Fortunately the values of  $\delta^*/\theta$  and  $\delta/\theta$  are insensitive to the exact shape of the velocity profile. The following table<sup>(37)</sup> shows the values of these ratios as a function of free-stream Mach Number, based on a value of  $N = 7$  in Eq. 27.25, and also based on the assumption that the stagnation enthalpy is constant throughout the boundary layer.

$M_\infty$	$\delta^*/\theta$	$\delta/\theta$	$M_\infty$	$\delta^*/\theta$	$\delta/\theta$	$M_\infty$	$\delta^*/\theta$	$\delta/\theta$
0	1.286	10.286	3.4	6.413	17.517	6.8	21.573	35.825
0.2	1.304	10.314	3.6	7.029	18.319	7.0	22.775	37.205
0.4	1.358	10.399	3.8	7.680	19.157	7.2	24.010	38.615
0.6	1.447	10.540	4.0	8.365	20.030	7.4	25.279	40.059
0.8	1.573	10.735	4.2	9.085	20.938	7.6	26.584	41.536
1.0	1.734	10.984	4.4	9.839	21.881	7.8	27.922	43.046
1.2	1.930	11.282	4.6	10.627	22.858	8.0	29.295	44.589
1.4	2.163	11.634	4.8	11.451	23.869	8.2	30.702	46.165
1.6	2.430	12.031	5.0	12.308	24.914	8.4	32.144	47.774
1.8	2.733	12.475	5.2	13.200	25.993	8.6	33.620	49.416
2.0	3.071	12.963	5.4	14.126	27.105	8.8	35.130	51.091
2.2	3.444	13.494	5.6	15.091	28.259	9.0	36.675	52.799
2.4	3.852	14.067	5.8	16.082	29.431	9.2	38.254	54.539
2.6	4.294	14.680	6.0	17.112	30.644	9.4	39.867	56.313
2.8	4.770	15.328	6.2	18.175	31.889	9.6	41.515	58.119
3.0	5.284	16.023	6.4	19.273	33.168	9.8	43.197	59.959
3.2	5.831	16.752	6.6	20.400	34.471	10.0	44.914	61.832

Wilson,<sup>(37)</sup> using Eq. 27.21 in conjunction with Eq. 27.68 and the table above, has given a simple method for determining boundary-layer growth under conditions of a favorable pressure gradient. Experiments on the boundary-layer growth in a supersonic wind-tunnel nozzle shows the method to be sufficiently accurate for most purposes.

**LAMINAR SUBLAYER.** The velocity profile of Eq. 27.25 is of course applicable only to the turbulent portion of the boundary layer. Since the laminar sublayer is very thin, it is a good approximation, at least for small pressure gradients, to assume a linear velocity profile in this region. Thus we write

$$\frac{\bar{u}}{\bar{u}_i} = \frac{y}{y'} \quad (27.26)$$

where the subscript  $i$  denotes the *interface* between the laminar sublayer and the turbulent layer.

The complete velocity profile corresponding to these assumptions is shown in Fig. 27.4. It is seen to have a discontinuity in slope at the interface.

**VELOCITY AT INTERFACE.** In order to complete the quantitative description of the velocity profile, it is necessary to know the velocity at the interface.

For incompressible flow, von Kármán<sup>(4,5)</sup> has reasoned from physical considerations that, in the laminar sublayer very close to the wall, the relation between the velocity distribution, the wall shear stress, and the fluid properties  $\rho$  and  $\mu$  should be nearly independent

FIG. 27.4. Velocity profile in turbulent boundary layer.

of conditions far from the wall. This postulate has been confirmed by experiment. It states that, near the wall,  $u = u(y, \tau_w, \rho_w, \mu_w)$ . Applying dimensional analysis to this relation, we conclude that a dimensionless *friction velocity*, defined by

$$u^+ \equiv \frac{u}{\sqrt{\tau_w / \rho_w}} = \frac{u}{U_\infty} \sqrt{\frac{2}{C_{f,w}}} \quad (27.27a)$$

should be a function only of a dimensionless *friction length*, defined by

$$y^+ \equiv \frac{y}{\sqrt{\rho_w \tau_w}} = \frac{y \rho_w U_\infty}{\mu_w} \sqrt{\frac{C_{f,w}}{2}} \quad (27.27b)$$

Having assumed a linear profile in the laminar sublayer, we may write the shear stress at the wall as

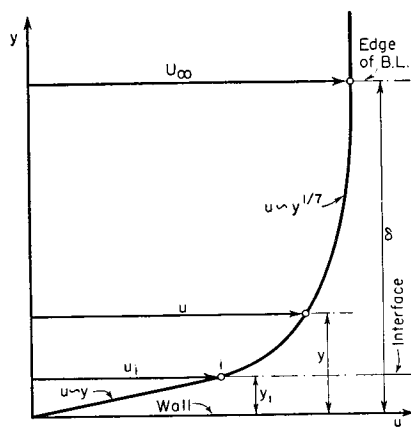
$$\tau_w = \mu \left( \frac{\partial u}{\partial y} \right)_0 = \mu \frac{u}{y} = \mu \frac{u_i}{y_i}$$

Combining this with Eqs. 27.27, we get the *universal velocity profile* of the laminar sublayer,

$$u^+ = y^+ \quad (27.28)$$

At the interface, experimental data for incompressible flow<sup>(5)</sup> show that

$$u_i^+ = y_i^+ \cong 11.5 \quad (27.29a)$$



and that the dimensionless slope on the turbulent side of the interface is

$$\left[ \left( \frac{du^+}{dy^+} \right)_i \right]_{turb} = 0.218 \quad (27.29b)$$

For incompressible flow,  $\rho$  and  $\mu$  are constant through the boundary layer. For compressible flow, on the other hand, they are not constant. However, since the laminar sublayer is confined to a narrow low-speed region near the wall, it seems reasonable to assume that the incompressible formulas of Eqs. 27.27, 27.28, and 27.29 will be applicable as well to compressible flow provided that  $\rho$  and  $\mu$  are evaluated at the wall temperature, or possibly at some mean temperature in the laminar sublayer.

**CALCULATED VELOCITY PROFILES IN TURBULENT LAYER.** Apart from assuming the empirical power-law velocity distribution of Eq. 27.25, it is possible to calculate the velocity profile in the turbulent zone by (i) employing either the empirical mixing-length expression of Prandtl (Eq. 27.49), or that of von Kármán (Eq. 27.51); and (ii) assuming the law of variation of  $\tau_{turb}$  through the turbulent boundary layer. This procedure will be discussed in Art. 27.4.

**Skin-Friction Law.** In applying the integral momentum method of Eq. 27.21, evaluation of the right-hand side depends of course on the velocity and temperature profiles and on the streamwise variation of free-stream Mach Number.

To evaluate the left-hand side, either (i) a set of empirical rules such as are embodied in Eqs. 27.27, 27.28, and 27.29 must be employed together with hypotheses concerning the variation of mixing length and Reynolds stress in the turbulent layer, or (ii) an empirical friction law for turbulent flow must be used.

Along the latter lines, Falkner<sup>(7)</sup> has given, for flat plates, the following low-speed law which is probably reliable also for favorable and for moderately adverse pressure gradients:

$$\frac{\tau_w}{\rho U_\infty^2} = \frac{0.0131}{Rey^{1/7}} \quad (27.30a)$$

In the case of compressible flow on insulated flat plates, Tucker<sup>(8)</sup> has shown by comparison with experiment that the same law applies at high speeds provided that  $\rho$  and  $\mu$  are evaluated at the arithmetic mean temperature between the wall and free stream,  $T_{am} = (T_w + T_\infty)/2$ . The law may then be written as

$$\frac{1}{2} C_{f,am} \equiv \frac{\tau_w}{\rho_{am} U_\infty^2} = \frac{0.0131}{(U_\infty x / \nu_{am})^{1/7}} = \frac{0.0131}{Rey_{am}^{1/7}} \quad (27.30b)$$

The various semi-empirical lines of attack for turbulent flow, all of which represent a judicious mixture of experiment, analysis, and physical intuition, are best explained through specific applications (Arts. 27.4 and 27.5).

#### 27.4. Analyses of Recovery Factor, Skin Friction, and Heat Transfer for Turbulent Flow Past a Flat Plate with Turbulent Prandtl Number of Unity

Because of the absence of pressure gradients, the flat plate aligned parallel to the flow is by far the simplest case to analyze. It is therefore the logical starting point for illustrating analytical methods.

Nearly all available analytical methods for the turbulent, compressible boundary layer are based on the assumption that the turbulent Prandtl Number is unity. This is partly because it was for many years thought that the mechanism of turbulent mixing demanded that the turbulent exchange coefficients for temperature and velocity be alike, although there are abundant data<sup>(3)</sup> that the turbulent Prandtl Number is about 0.7; and partly because the analysis is greatly simplified, indeed made manageable, through the assumption that  $(Pr)_{turb} = 1$ . In this article we shall proceed on the latter assumption.

**Velocity and Temperature Distributions in Laminar Sublayer.** <sup>(9)</sup> Since the laminar sublayer is very thin, Eq. 27.26 is used for the velocity distribution therein. The velocity distribution may then conveniently be expressed in terms of the wall shear stress as

$$\tau_w = \mu_w \left( \frac{\partial u}{\partial y} \right)_{y=0} = \mu_w \frac{u_i}{y_i} = \mu_w \frac{u}{y} \quad (27.31)$$

For the temperature distribution, we begin by writing the energy equation, Eq. 26.8,

$$\rho u c_p \frac{\partial T}{\partial x} + \rho v c_p \frac{\partial T}{\partial y} = \frac{\partial}{\partial y} \left( \lambda \frac{\partial T}{\partial y} \right) + \mu \left( \frac{\partial u}{\partial y} \right)^2$$

The left-hand side of this equation represents physically the time rate of enthalpy increase of a fluid particle. Compared with the terms on the right-hand side, which represent the net heat flux and net rate of delivery of shear work to the fluid particle, the left-hand side is very small for particles near the wall. By setting the left-hand side equal to zero, therefore, we are assuming in effect that the laminar sublayer is so thin that virtually all the heat transfer and shear work is transmitted across the layer, with only a negligible portion going to increase the enthalpy of the gas passing through the layer itself. Making this assumption, we have

$$\frac{\partial}{\partial y} \left( \lambda \frac{\partial T}{\partial y} \right) + \mu \left( \frac{\partial u}{\partial y} \right)^2 = 0$$

or, assuming  $\lambda$  and  $\mu$  constant through the thin sublayer, and employing Eq. 27.31, we get

$$\frac{\partial}{\partial y} \left( \lambda_w \frac{\partial T}{\partial y} \right) + \mu_w \left( \frac{\tau_w}{\mu_w} \right)^2 = 0$$

Multiplying by  $dy$  and integrating at constant  $x$ , between limits of  $y = 0$  and  $y = y$ , we obtain

$$\lambda_w \left[ \frac{\partial T}{\partial y} - \left( \frac{\partial T}{\partial y} \right)_{y=0} \right] + \frac{\tau_w^2}{\mu_w} y = 0$$

But, since the heat flux at the wall is given by

$$q_w = -\lambda_w \left( \frac{\partial T}{\partial y} \right)_{y=0}$$

the previous expression may be rearranged to give

$$\frac{\partial T}{\partial y} = -\frac{q_w}{\lambda_w} - \frac{\tau_w^2}{\mu_w \lambda_w} y$$

Integrating once again with respect to  $y$  at constant  $x$ , between the same limits as before, there is obtained a parabolic distribution of temperature in the laminar sublayer,

$$T - T_w = -\frac{q_w}{\lambda_w} y - \frac{\tau_w^2}{2\mu_w \lambda_w} y^2 \quad (27.32)$$

By taking the derivative of this expression, and evaluating the derivative at the interface  $i$ , we obtain, for later reference,

$$\left( \frac{\partial T}{\partial y} \right)_i = -\frac{q_w}{\lambda_w} - \frac{\tau_w^2}{\mu_w \lambda_w} y_i \quad (27.33)$$

Also for later reference, we express Eq. 27.32 in terms of conditions at the interface, and we replace  $y_i$  in favor of  $u_i$  by means of Eq. 27.31. Thus we obtain

$$T_i = T_w - \frac{q_w}{\tau_w c_p} \frac{\Pr}{c_p} u_i - \frac{\Pr}{c_p} \frac{u_i^2}{2} \quad (27.34)$$

where  $\Pr$  denotes the laminar Prandtl Number  $c_p \mu_w / \lambda_w$ .

**Velocity and Temperature Distribution in Turbulent Layer.** <sup>(9)</sup> Since the turbulent Prandtl Number is assumed as unity, Crocco's linear relation between the stagnation temperature and velocity, expressed

by the formula following Eq. 26.5a, is valid within the turbulent layer and at the two “edges” of the turbulent layer. Therefore we may write

$$c_p \bar{T}_0 = a\bar{u} + b$$

$$c_p T_{0\infty} = aU_\infty + b$$

$$c_p T_{0i} = au_i + b$$

Subtracting the third of these from the first, and the third from the second, and then dividing one of the resulting equations by the other, the constants  $a$  and  $b$  may be eliminated, thus leaving

$$\bar{T}_0 - T_{0i} = \frac{T_{0\infty} - T_{0i}}{U_\infty - u_i} (\bar{u} - u_i) \quad (27.35)$$

Taking the derivative of this expression, and evaluating the derivative at the interface, we get

$$\left( \frac{\partial \bar{T}_0}{\partial y} \right)_i = \frac{T_{0\infty} - T_{0i}}{U_\infty - u_i} \left( \frac{\partial \bar{u}}{\partial y} \right)_i \quad (27.36)$$

However, from the definition of stagnation temperature, we may obtain the relation

$$\left( \frac{\partial \bar{T}_0}{\partial y} \right)_i = \left( \frac{\partial \bar{T}}{\partial y} \right)_i + \left( \frac{\partial}{\partial y} \frac{\bar{u}^2}{2c_p} \right)_i = \left( \frac{\partial \bar{T}}{\partial y} \right)_i + \frac{u_i}{c_p} \left( \frac{\partial u}{\partial y} \right)_i \quad (27.37)$$

Elimination of  $(\partial \bar{T}_0 / \partial y)_i$  from Eqs. 27.36 and 27.37 now yields

$$\frac{T_{0\infty} - T_{0i}}{U_\infty - u_i} = \frac{u_i}{c_p} + \left[ \frac{(\partial \bar{T} / \partial y)_i}{(\partial \bar{u} / \partial y)_i} \right]_{\text{turb}} \quad (27.38)$$

where the subscript “turb” is used here to denote that the derivatives are evaluated on the turbulent side of the interface.

Although, for simplicity in calculation, we allow a discontinuity in the slopes of the velocity and temperature profiles at the interface (Fig. 27.4), there can be no discontinuity in the shear stress  $\tau_i$  and the heat flux  $q_i$ . We therefore equate the turbulent value of the stress  $\tau_i$  with the corresponding laminar value. Thus, using Eq. 27.31, we get

$$\tau_i = \epsilon_i \left[ \left( \frac{\partial \bar{u}}{\partial y} \right)_i \right]_{\text{turb}} = \mu_w \left[ \left( \frac{\partial u}{\partial y} \right)_i \right]_{\text{laminar}} = \mu_w \frac{u_i}{y_i} = \tau_w \quad (27.39a)$$

Similarly, we equate the turbulent heat flux  $q_i$  with the laminar heat flux  $q_i$ . With the aid of Eq. 27.33, we get

$$q_i = -\kappa_i \left[ \left( \frac{\partial \bar{T}}{\partial y} \right)_i \right]_{\text{turb}} = -\lambda_w \left[ \left( \frac{\partial T}{\partial y} \right)_i \right]_{\text{laminar}} = q_w + \frac{\tau_w^2}{\mu_w} y_i \quad (27.39b)$$

In order to evaluate the rightmost term of Eq. 27.38, we divide

Eq. 27.39b by Eq. 27.39a. Noting that  $(\text{Pr})_{\text{turb}} \equiv c_p \epsilon_i / \kappa_i = 1$ , and employing Eq. 27.31, we obtain, after simplification,

$$\left[ \frac{(\partial \bar{T} / \partial y)_i}{(\partial \bar{u} / \partial y)_i} \right]_{\text{turb}} = -\frac{q_w}{\tau_w c_p} - \frac{u_i}{c_p} \quad (27.40)$$

Substitution of Eq. 27.40 into Eq. 27.38 then yields an interesting relation between the wall heat flux and wall shear stress in terms of the temperatures and velocities at the edge of the turbulent layer,

$$-\frac{q_w}{\tau_w} = c_p \frac{T_{0\infty} - T_{0i}}{U_\infty - u_i} = \frac{c_p (T_\infty - T_i)}{U_\infty - u_i} + \frac{U_\infty^2 - u_i^2}{2(U_\infty - u_i)}$$

We may eliminate  $T_i$  from this expression with the help of Eq. 27.34. Thus we obtain after rearrangement and simplification,

$$\frac{q_w}{\tau_w} = \frac{c_p (T_w - T_\infty) - \frac{U_\infty^2 - (1 - \text{Pr}) u_i^2}{2}}{U_\infty - (1 - \text{Pr}) u_i} \quad (27.41)$$

**Recovery Factor.** <sup>(14)</sup> When the plate is insulated against heat transfer,  $q_w = 0$ , and the wall temperature becomes the adiabatic wall temperature,  $T_{aw}$ . Making these substitutions in Eq. 27.41, it is found after rearrangement that

$$\mathcal{R} \equiv \frac{T_{aw} - T_\infty}{U_\infty^2 / 2c_p} = 1 - (1 - \text{Pr}) \left( \frac{u_i}{U_\infty} \right)^2 \quad (27.42)$$

Now  $u_i / U_\infty$  is not accurately known for compressible flow, and is indeed not found unambiguously from experimental data in any case because the data do not obligingly follow exactly the simplified model of Fig. 27.4. However, we may set bounds upon  $\mathcal{R}$  by noting that  $u_i / U_\infty$  cannot be greater than one or less than zero, thus yielding respectively that  $\mathcal{R}$  may not be less than  $\text{Pr}$  or greater than unity.

A somewhat more revealing approach is to suppose that Eq. 27.29a is valid for compressible flow when the properties are evaluated at the wall temperature. Employing Eq. 27.27a, there is thus found

$$u_i^+ \equiv \frac{u_i}{U_\infty} \sqrt{\frac{2}{C_{fw}}} = 11.5$$

which, when inserted into Eq. 27.42, yields

$$\mathcal{R} = 1 - 66(1 - \text{Pr}) C_{fw} \quad (27.43)$$

This relation is plotted in Fig. 27.5 for air ( $\text{Pr} = 0.72$ ) over the range of  $C_{fw}$  associated with turbulent flow. In evaluating this result, it should be recalled that if the laminar Prandtl Number were also taken as unity,  $\mathcal{R}$  would be unity. Therefore, the departure of  $\mathcal{R}$  from unity

shown in Fig. 27.5 is associated with the laminar Prandtl Number of 0.72. For turbulent Prandtl Numbers less than unity, the theoretical values of  $\mathcal{R}$  would presumably be less than those shown in Fig. 27.5. This is in accord with experimental data, which show recovery factors

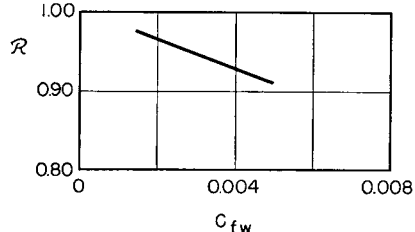


FIG. 27.5. Theoretical recovery factor for flow with  $(\text{Pr})_{\text{turb}} = 1$ .

**Reynolds' Analogy.** By substituting the value of  $u_i/U_\infty$  from Eq. 27.42 into Eq. 27.41, we get

$$\frac{q_w}{\tau_w} = \frac{c_p(T_w - T_\infty) - c_p(T_{aw} - T_\infty)}{U_\infty - (1 - \text{Pr})u_i} = \frac{c_p(T_w - T_{aw})}{U_\infty - (1 - \text{Pr})u_i} \quad (27.44)$$

This demonstrates clearly, as in the case of laminar flow, that the appropriate temperature differential for reckoning the heat transfer coefficient  $\mathcal{H}$  is the excess of the wall temperature over the adiabatic wall temperature. Hence we define

$$\mathcal{H} \equiv \frac{q_w}{T_w - T_{aw}} \quad (27.45)$$

Introducing the definitions of Stanton Number and of skin-friction coefficient, namely,

$$C_{H\infty} \equiv \frac{\mathcal{H}}{c_p \rho_\infty U_\infty}; \quad C_{Hw} \equiv \frac{\mathcal{H}}{c_p \rho_w U_\infty}$$

$$C_{f\infty} \equiv \frac{\tau_w}{\frac{1}{2} \rho_\infty U_\infty^2}; \quad C_{fw} \equiv \frac{\tau_w}{\frac{1}{2} \rho_w U_\infty^2}$$

we may put Eq. 27.44 into the dimensionless form

$$\frac{C_{H\infty}}{C_{f\infty}} = \frac{C_{Hw}}{C_{fw}} = \frac{0.5}{1 - (1 - \text{Pr}) \frac{u_i}{U_\infty}} \quad (27.46)$$

This may be recognized as being identical in form with the Reynolds' analogy for turbulent incompressible flow based on the same assumption that  $(\text{Pr})_{\text{turb}} = 1$ . It differs from the incompressible result, however, insofar as  $u_i/U_\infty$  may be a function of Mach Number. Employing Eq. 27.28 as an approximation for  $u_i/U_\infty$  in compressible flow, we get

$$\frac{C_{H\infty}}{C_{f\infty}} = \frac{C_{Hw}}{C_{fw}} = \frac{0.5}{1 - (1 - \text{Pr}) (11.5) \sqrt{C_{fw}}} \quad (27.47)$$

Taking  $\text{Pr} = 0.72$  for air, and using for illustrative purposes a typical value of  $C_{fw} \cong 0.003$  for turbulent flow, we obtain  $C_H \cong C_f/1.75$  as a representative result relating the friction and heat transfer coefficients according to the assumptions underlying the present theory.

**Turbulent Shear Stress According to Kármán's Hypothesis of Mechanical Similitude.** <sup>(1,5)</sup> In order to arrive at specific results concerning skin friction, heat transfer, and boundary-layer thickness, it is necessary to introduce one or more semi-empirical assumptions as to events within the turbulent layer. We shall set down here the basic concepts and definitions underlying the formulation of von Kármán, a formulation which has proved successful for incompressible flow.

**FURTHER DEVELOPMENT OF MIXING-LENGTH CONCEPT.** Expanding Eq. 27.11 for the turbulent shear stress, we have

$$\begin{aligned} \bar{\tau}_{\text{turb}} &= -(\bar{\rho}v)'u' = -[\bar{\rho}v - \bar{\rho}\bar{v}]u' \\ &= -[\bar{\rho}\bar{v} + \rho'\bar{v} + v'\bar{\rho} + \rho'v' - \bar{\rho}\bar{v}]u' \\ &= -\bar{v}\bar{\rho}'u' - \bar{\rho}\bar{v}'u' + \bar{\rho}'v'u' \end{aligned}$$

Now, in a thin boundary layer,  $\bar{v} \cong 0$ . If we further ignore the triple correlation, we get the same result as for incompressible flow, namely,

$$\bar{\tau}_{\text{turb}} = -\bar{\rho}\bar{u}'v' \quad (27.48)$$

The *correlation coefficient* between  $u'$  and  $v'$  is defined as

$$\xi \equiv \frac{\bar{u}'v'}{\sqrt{\bar{u}'^2} \sqrt{\bar{v}'^2}}$$

and hence, in terms of  $\xi$ , we have

$$\bar{\tau}_{\text{turb}} = -\xi\bar{\rho}\sqrt{\bar{u}'^2} \sqrt{\bar{v}'^2}$$

Eq. 27.13a, based on the mixing-length concept, may be written more precisely in the form

$$\sqrt{\bar{u}'^2} = l \frac{\partial \bar{u}}{\partial y}$$

where  $l$  is now constant with respect to time.

Considerations of continuity demand that  $\sqrt{\bar{v}'^2}$  be connected with  $\sqrt{\bar{u}'^2}$  because a turbulent fluctuation at some point giving rise to a certain  $v'$  must simultaneously have a comparable value of  $u'$ , for other-

wise mass would not be conserved. Assuming with Prandtl that  $\sqrt{v'^2}$  is proportional to  $\sqrt{u'^2}$ , and drawing both the factor of proportionality and the correlation coefficient  $\xi$  into the mixing length  $l$  (inasmuch as the latter must in any event be determined experimentally), we obtain

$$\bar{\tau}_{\text{turb}} = \bar{\rho} l^2 \left| \frac{\partial \bar{u}}{\partial y} \right| \left( \frac{\partial \bar{u}}{\partial y} \right) \quad (27.49)$$

where  $l^2$  is written rather than  $l$  in order to maintain dimensional homogeneity, and the equation is written in such a form as to preserve the correct relationship between the signs of  $\bar{\tau}_{\text{turb}}$  and  $\partial \bar{u} / \partial y$ .

KÁRMÁN'S HYPOTHESIS OF MECHANICAL SIMILITUDE. The mean velocity about any point  $y_i$  in the boundary layer may be expanded in a Taylor's series. Thus

$$\bar{u} - \bar{u}_i = \left( \frac{\partial \bar{u}}{\partial y} \right)_i (y - y_i) + \frac{\partial^2 \bar{u}}{\partial y^2} \frac{(y - y_i)^2}{2!} + \dots$$

Now the essential idea of Kármán's hypothesis of mechanical similitude is that there must be similarity between the large-scale turbulence (connected with the first derivative) and the small-scale turbulence (connected with the higher derivatives). Therefore the ratio of successive terms in this series must be independent of location, and hence

$$\frac{\left( \frac{\partial^2 \bar{u}}{\partial y^2} \right) (y - y_i)^2}{\left( \frac{\partial \bar{u}}{\partial y} \right) (y - y_i)} = \gamma$$

where  $\gamma$  is assumed to be a "universal" dimensionless constant. Representing  $(y - y_i)$  by the mixing length  $l$ , we get

$$l = \gamma \frac{\partial \bar{u} / \partial y}{\partial^2 \bar{u} / \partial y^2} \quad (27.50)$$

and Eq. 27.49 accordingly becomes

$$\bar{\tau}_{\text{turb}} = \bar{\rho} \gamma^2 \frac{(\partial \bar{u} / \partial y)^4}{(\partial^2 \bar{u} / \partial y^2)^2} \quad (27.51a)$$

Lacking better information, it is usually assumed that the turbulent shear stress is constant throughout the boundary layer, although it is very well known that it goes to zero at the outer edge. The practical justification for the assumption lies largely in the general agreement of theory with experiment. Apparently the error in the assumption is substantially canceled by opposite errors on account of the assumption that  $\gamma$  is a constant. Using the assumption of constant turbulent shear stress we may write

$$\bar{\tau}_{\text{turb}} = \tau_{\text{wall}} = \bar{\rho} \gamma^2 \frac{(\partial \bar{u} / \partial y)^4}{(\partial^2 \bar{u} / \partial y^2)^2} \quad (27.51b)$$

where  $\gamma$  for incompressible flow has been determined empirically to be about 0.40.

SKIN-FRICTION BASED ON THE KÁRMÁN HYPOTHESIS. Introducing the dimensionless velocity  $u^+$  and the dimensionless length  $y^+$  of Eqs. 27.27 into Eq. 27.51b, we get an ordinary differential equation between  $u^+$  and  $y^+$ ,

$$\frac{(\partial^2 u^+ / \partial y^+)^2}{(\partial u^+ / \partial y^+)^4} = \gamma^2 \frac{\bar{\rho}}{\rho_w} \quad (27.52)$$

The density ratio is equal to the inverse of the temperature ratio, inasmuch as the pressure is constant across the boundary layer. Hence,

$$\bar{\rho} / \rho_w = T_w / \bar{T}$$

Now, eliminating  $a$  and  $b$  from the three equations preceding Eq. 27.35, we may form

$$\bar{T}_0 - T_{0\infty} = \left( \frac{T_{0\infty} - T_{0i}}{U_\infty - u_i} \right) (\bar{u} - U_\infty)$$

Expanding the left-hand side of this expression by means of the definition of stagnation temperature, and eliminating the first bracket on the right-hand side through a combination of Eqs. 27.38 and 27.40, we get

$$\bar{T} - T_\infty + \frac{\bar{u}^2 - U_\infty^2}{2c_p} = - \frac{q_w}{c_p \tau_w} (\bar{u} - U_\infty)$$

We now insert the value of  $T_\infty$  given by this expression into Eq. 27.41, and thus we obtain a relation between the local velocity and local temperature in the turbulent boundary layer,

$$\frac{q_w}{\tau_w} = \frac{c_p (T_w - \bar{T}) - \frac{\bar{u}^2 - (1 - \text{Pr}) u_i^2}{2}}{\bar{u} - (1 - \text{Pr}) u_i} \quad (27.53)$$

At the outer edge of the layer, this is seen to agree with Eq. 27.41.

The ratio  $\bar{T} / T_w$  is now formed from Eq. 27.53. In terms of the dimensionless quantities already defined, and employing Eq. 27.27a for  $u_i^+$ , we get

$$\frac{\bar{T}}{T_w} = 1 - \mathcal{Q}[u^+ - 11.5(1 - \text{Pr})]$$

$$- \frac{C_{fw}}{2} \frac{T_{0\infty}}{T_w} \frac{\frac{k-1}{2} M_\infty^2}{1 + \frac{k-1}{2} M_\infty^2} [u^{+2} - 132.2(1 - \text{Pr})] \quad (27.54a)$$

where  $\mathcal{Q}$  is a dimensionless heat transfer quantity defined by

$$\mathcal{Q} \equiv \frac{q_w}{c_p T_w \sqrt{\rho_w \tau_w}} \quad (27.54b)$$

By employing the definitions of  $C_{f\infty}$  and  $C_{H\infty}$  together with the Reynolds' analogy in the form of Eq. 27.46, we may also express  $\mathcal{Q}$  as

$$\begin{aligned} \mathcal{Q} = & \left[ \frac{\sqrt{C_{f\infty}/2}}{1 - 11.5(1 - \text{Pr}) \sqrt{C_{f\infty}/2}} \right] \\ & \times \left[ 1 - \frac{T_{0\infty}}{T_w} + \frac{T_{0\infty}}{T_w} \frac{\frac{k-1}{2} \text{M}_\infty^2}{1 + \frac{k-1}{2} \text{M}_\infty^2} (132.2)(1 - \text{Pr}) \frac{C_{f\infty}}{2} \right] \quad (27.54c) \end{aligned}$$

When  $\bar{\rho}/\rho_w$  in Eq. 27.52 is replaced by  $T_w/\bar{T}$  as given by Eqs. 27.54, there is obtained an ordinary nonlinear differential equation of second order between  $u^+$  and  $y^+$ , with  $\text{M}_\infty$ ,  $\text{Pr}$ ,  $C_{f\infty}$ , and  $T_{0\infty}/T_w$  as constants or parameters. The two necessary boundary conditions for this equation are expressed by Eqs. 27.29. That is,

$$\text{when } y^+ = 11.5, \quad \begin{cases} u^+ = 11.5 \\ du^+/dy^+ = 0.218 \end{cases}$$

In principle, therefore, it is possible by integration to obtain solutions to the differential equation. The solutions are of the general form

$$u^+ = u^+(y^+, \text{M}_\infty, \text{Pr}, C_{f\infty}, T_{0\infty}/T_w) \quad (27.55)$$

In practice, the integration of Eq. 27.52 is quite awkward. It usually must be effected numerically, by series expansions, or by means of other approximate methods.<sup>(9,10,11,12)</sup>

Writing the definition of momentum thickness (Eq. 27.19b) in the form

$$\theta \equiv \int_0^\infty \frac{\bar{\rho}}{\rho_\infty} \frac{\bar{u}}{U_\infty} \left( 1 - \frac{\bar{u}}{U_\infty} \right) dy$$

and introducing into this expression the dimensionless variables of Eqs. 27.27 and 27.54, we may obtain a convenient expression for the displacement-thickness Reynolds Number,

$$\frac{\rho_w U_\infty \theta}{\mu_w} = \frac{T_{0\infty}}{T_w} \frac{1}{1 + \frac{k-1}{2} \text{M}_\infty^2} \int_0^\infty \frac{T_w}{\bar{T}} u^+ \left( 1 - u^+ \sqrt{\frac{C_{f\infty}}{2}} \right) dy^+ \quad (27.56)$$

Assuming that the relation of Eq. 27.55 has been found in one way or another, and noting again that  $T_w/\bar{T}$  is given by Eqs. 27.54, it follows

that Eq. 27.56 may be integrated (usually by quadrature). Thus we may obtain a result of the general form

$$\frac{\rho_w U_\infty \theta}{\mu_w} = \text{function}(\text{M}_\infty, \text{Pr}, C_{f\infty}, T_{0\infty}/T_w) \quad (27.57)$$

In carrying out the integration indicated in Eq. 27.56 it is customary to employ the relations which apply to the turbulent layer, and to carry the integration all the way to the wall ( $y = 0$ ). This introduces an error because incorrect relations are being used for the laminar sublayer. However, since the sublayer is so thin, the error is very small, and the approximation is justified through the simplification which it affords. One of the virtues of the integral method is that it does allow simplifications of this sort.

Next we note that, for a flat plate with zero pressure gradient, the momentum equation (Eq. 27.21) may be written as

$$\frac{\tau_w}{\rho_\infty U_\infty^2} = \frac{d\theta}{dx} = \frac{d\left(\frac{\rho_w U_\infty \theta}{\mu_w}\right)}{d\left(\frac{\rho_w U_\infty x}{\mu_w}\right)}$$

Now, using the definition of  $C_{f\infty}$  and the relation  $\rho_\infty/\rho_w = T_w/T_\infty$ , this may be rearranged and integrated to give

$$\begin{aligned} \int_0^{\rho_w U_\infty x / \mu_w} d\left(\frac{\rho_w U_\infty x}{\mu_w}\right) &= \frac{\rho_w U_\infty x}{\mu_w} \\ &= \frac{1 + \frac{k-1}{2} \text{M}_\infty^2}{2} \frac{T_w}{T_{0\infty}} \int_\infty^{C_{f\infty}} \frac{d\left(\frac{\rho_w U_\infty \theta}{\mu_w}\right)}{dC_{f\infty}} \frac{dC_{f\infty}}{C_{f\infty}} \quad (27.58) \end{aligned}$$

where the lower limit of integration is obtained by noting that, when  $x = 0$ , the boundary layer has zero thickness, and that the velocity gradient and skin-friction coefficient are accordingly infinite. The term

$$\frac{d\left(\frac{\rho_w U_\infty \theta}{\mu_w}\right)}{dC_{f\infty}} / dC_{f\infty}$$

on the right-hand side is found by differentiation of Eq. 27.57, keeping  $\text{M}_\infty$ ,  $\text{Pr}$ , and  $T_{0\infty}/T_w$  all constant. The right-hand side, upon integration, is a function only of  $\text{M}_\infty$ ,  $\text{Pr}$ ,  $C_{f\infty}$ , and  $T_{0\infty}/T_w$ . The left-hand side is the value of the length Reynolds Number (based on wall properties) corresponding to the value of  $C_{f\infty}$  on the right-hand side.

The integration of Eq. 27.58 therefore yields the desired relation between skin-friction coefficient and Reynolds Number, in the general form

$$C_{f\infty} = \text{function}\left(\frac{\rho_w U_\infty x}{\mu_w}, \text{M}_\infty, \text{Pr}, \frac{T_{0\infty}}{T_w}\right) \quad (27.59)$$

The corresponding heat-transfer coefficient may then easily be found from Eq. 27.47.

**Skin Friction Based on the Prandtl Mixing-Length Hypothesis.**<sup>(13)</sup> Beginning again with Eq. 27.49 for the turbulent shear stress, a somewhat different formulation for determining the skin friction is that based on Prandtl's hypothesis concerning the mixing length  $l$ . This length must be zero at the wall and must, at least initially, increase as  $y$  increases. The simplest possible variation of  $l$  with  $y$  satisfying this requirement is the linear relation

$$l = Ky \quad (27.60)$$

where  $K$  is a "universal" constant, which, for incompressible flow, has the experimentally determined value of about 0.4.

As in Eq. 27.51, we assume that  $\bar{\tau}_{\text{turb}}$  is constant across the boundary layer, with the value  $\tau_w$ . The chief justification, as before, is that for incompressible flow the results fit well with experiment. Then Eq. 27.49 becomes

$$\frac{d\bar{u}}{dy} = \frac{1}{K} \sqrt{\frac{\tau_w}{\bar{\rho}} y}$$

Introducing into this the definitions of  $u^+$  and  $y^+$  as given by Eqs. 27.27, and the definition of  $C_{f,w}$ , we get the differential equation of the velocity profile in dimensionless form, namely,

$$y^+ \frac{du^+}{dy^+} = \frac{1}{K} \sqrt{\frac{\rho_w}{\bar{\rho}}} \quad (27.61)$$

This ordinary differential equation, based on the Prandtl hypothesis, corresponds to Eq. 27.52, based on the Kármán hypothesis. However, Eq. 27.61 is of first order, and only one boundary condition may be used. In order to assure the correct value of  $\tau_w$ , we employ for the boundary condition the values at the interface:

$$\text{when } y^+ = 11.5, \text{ then } u^+ = 11.5 \quad (27.62)$$

The procedure for solving Eq. 27.61 is exactly parallel to that for solving Eq. 27.52, the same expression for  $\bar{\rho}/\rho_w$  being applicable to both cases. Carrying out the necessary quadratures, the results for skin-friction and heat transfer coefficients, based on the Prandtl formulation, will be of the general form indicated by Eqs. 27.59 and 27.47.

The calculation procedure outlined for obtaining Eq. 27.59 is of course exceedingly laborious for the formulations of both Kármán and Prandtl. For details the reader is referred to References 9 through 13. Some typical results of the theoretical calculations are given in the next article, together with a comparison with experimental results.

## 27.5. Theoretical and Experimental Results for Skin Friction on Flat Plates

**Incompressible Drag Coefficient.** For the purpose of later comparison, Fig. 27.6 shows the theoretical curves of drag coefficient versus Reynolds Number for adiabatic, incompressible flow, as determined by the mixing-length formulations of Kármán and of Prandtl. Experi-

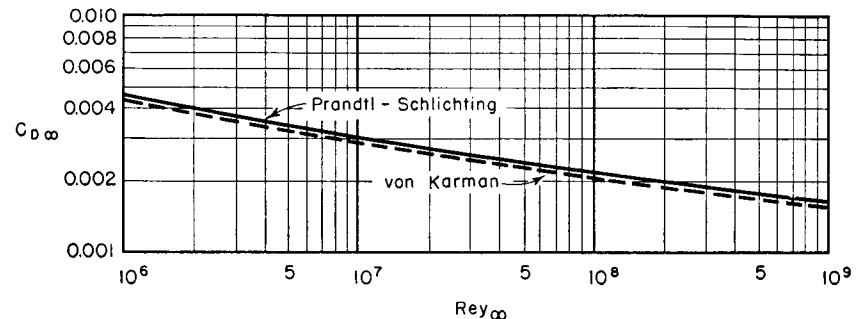


FIG. 27.6. Theoretical integrated drag coefficients for incompressible flow on flat plate ( $M_\infty = 0$ ,  $T_w/T_\infty = 1$ ), based on turbulent formulations of von Kármán (dashed curve) and of Prandtl (solid curve):

$$\text{Kármán: } \frac{0.242}{\sqrt{C_{D\infty}}} = \log_{10} (C_{D\infty} \text{ Rey}_\infty)$$

$$\text{Prandtl: } C_{D\infty} = \frac{0.472}{(\log_{10} \text{ Rey}_\infty)^{2.58}}$$

mental results for incompressible flow are in good agreement with both theoretical curves, which differ from each other only by about 4 per cent.

It is to be noted that the ordinate of Fig. 27.6 is the integrated drag coefficient,  $C_{D\infty}$ , based on the assumption that the flow is turbulent from  $x = 0$  to  $x = x$ , and referring to the total drag force acting on one surface of the plate. The relation between  $C_{D\infty}$  and  $C_{f\infty}$  is then

$$C_{D\infty} = \frac{\int_0^x \tau_w dx}{\frac{1}{2} \rho_\infty U_\infty^2 x} = \frac{1}{x} \int_0^x \frac{\tau_w}{\frac{1}{2} \rho_\infty U_\infty^2} dx = \frac{1}{x} \int_0^x C_{f\infty} dx \quad (27.63)$$

From this it follows that

$$C_{f\infty} = \frac{d(C_{D\infty}x)}{dx} = C_{D\infty} + x \frac{dC_{D\infty}}{dx} \quad (27.64a)$$

$$\begin{aligned} &= C_{D\infty} + \text{Rey}_\infty \frac{dC_{D\infty}}{d \text{Rey}_\infty} \\ &= C_{D\infty} \left[ 1 + \frac{d(\ln C_{D\infty})}{d(\ln \text{Rey}_\infty)} \right] \end{aligned} \quad (27.64b)$$

Hence, given a curve or formula of  $\ln C_{D\infty}$  versus  $\ln \text{Rey}_\infty$ , the variation of local skin-friction coefficient with  $\text{Rey}_\infty$  may be found by differentiation as indicated by Eq. 27.64b. The second term in the bracket of Eq. 27.64b is especially easy to evaluate from the slope of the curve of  $C_{D\infty}$  versus  $\text{Rey}_\infty$  when plotted on log-log paper. For example, the average slope in Fig. 27.6 is about  $-1/6$ ; therefore the value of  $C_{f\infty}$  is approximately  $5/6$  of the value of  $C_{D\infty}$ .

**Adiabatic Skin-Friction Coefficient Found by Applying Falkner's Incompressible Formula at Appropriate Reference Temperature.** For the laminar boundary layer it will be recalled that the relation between skin-friction coefficient and Reynolds Number is nearly independent of Mach Number when properties are evaluated at the wall temperature, i.e., when  $C_{fw}$  is related to  $\text{Rey}_w$ . This suggests that a similar correlation might be valid in turbulent flow, when the fluid properties are expressed at some *reference temperature*  $T_r$ . Then  $C_{fr}$ , denoting the skin-friction coefficient evaluated at the temperature  $T_r$ , is given by

$$C_{fr} \equiv \frac{\tau_w}{\frac{1}{2}\rho_r U_\infty^2} = \frac{\tau_w}{\frac{1}{2}\rho_\infty U_\infty^2} \cdot \frac{\rho_\infty}{\rho_r} = C_{f\infty} \frac{T_r}{T_\infty}$$

Now, assuming Eq. 27.30a as a reasonably good approximation for the low-speed skin-friction formula which has the additional virtue of simplicity of form, the assumption that the same formula applies at high speeds at the reference temperature  $T_r$ , may be expressed as

$$C_{fr} = 0.0262 \left( \frac{U_\infty x \rho_r}{\mu_r} \right)^{-1/7}$$

Combining the two equations, we get

$$C_{f\infty} (\text{Rey}_\infty)^{1/7} = 0.0262 \left( \frac{\mu_r}{\mu_\infty} \right)^{1/7} \left( \frac{T_\infty}{T_r} \right)^{6/7}$$

Since the viscosity ratio appears to the one-seventh power, almost any reasonable approximation relating  $\mu$  to  $T$  will be satisfactory, and so we assume the simple relation

$$\mu_r / \mu_\infty = T_r / T_\infty$$

which is in rough accord with experiment. Thus we obtain

$$C_{f\infty} (\text{Rey}_\infty)^{1/7} = 0.0262 \left( \frac{T_\infty}{T_r} \right)^{5/7} \quad (27.65a)$$

**REFERENCE TEMPERATURE ASSUMED EQUAL TO WALL TEMPERATURE.** If we take  $T_r$  to be the wall temperature,  $T_w$ , as suggested originally by von Kármán, and if we further assume a recovery factor of unity ( $T_w = T_{0\infty}$ ), then we get, for the insulated plate,

$$C_{f\infty} (\text{Rey}_\infty)^{1/7} = 0.0262 \left( \frac{1}{1 + \frac{k-1}{2} M_\infty^2} \right)^{5/7} \quad (27.65b)$$

This is plotted as the lowermost curve of Fig. 27.7. As we shall see later, the curve marked "Frankl and Voishel" is in best agreement

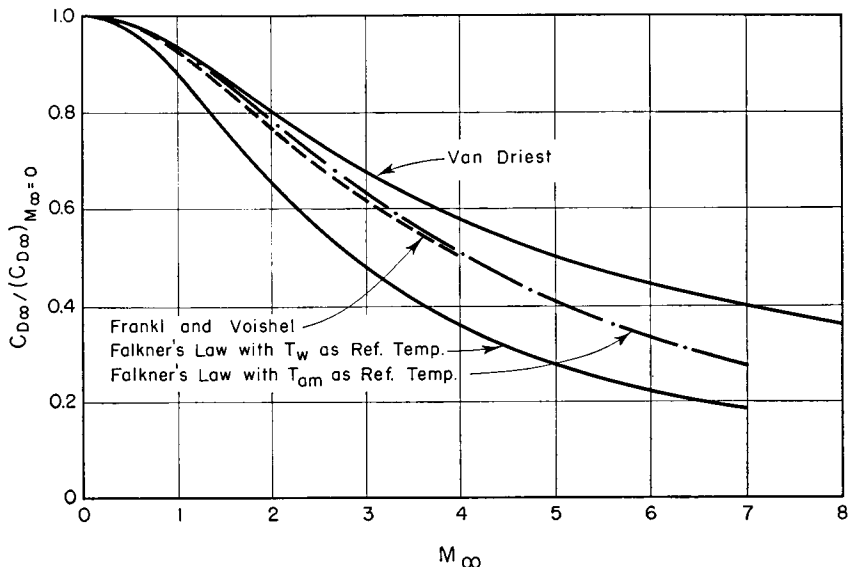


FIG. 27.7. Effect of Mach Number on drag coefficient of insulated flat plate at  $\text{Rey}_\infty = 7(10)^6$  (after Rubesin, Maydew, and Vargas).

with experiment. Fig. 27.7 therefore shows that, by using  $T_w$  as a reference temperature, the effects of compressibility on skin-friction coefficient are overestimated.

**REFERENCE TEMPERATURE ASSUMED AS MEAN OF  $T_w$  AND  $T_\infty$ .** A more successful approach<sup>(8)</sup> is to assume the reference temperature to be  $T_{am}$ , the arithmetic mean between  $T_w$  and  $T_\infty$ . Again assuming a recovery factor of unity, we may write

$$\frac{T_\infty}{T_r} = \frac{T_\infty}{T_{am}} = \frac{2T_\infty}{T_\infty + T_w} = \frac{2T_\infty}{T_\infty + T_{0\infty}} = \frac{2}{1 + \frac{T_{0\infty}}{T_\infty}} = \frac{2}{2 + \frac{k-1}{2} M_\infty^2}$$

and thus the effect of  $M_\infty$  on skin friction is indicated by

$$C_{f\infty} (\text{Rey}_\infty)^{1/7} = 0.0262 \left( \frac{2}{2 + \frac{k-1}{2} M_\infty^2} \right)^{5/7} \quad (27.65c)$$

This is plotted as one of the intermediate curves of Fig. 27.7, and is seen to be in almost perfect agreement with the curve marked "Frankl and Voishel" up to  $M_\infty = 4$ , beyond which the calculations for the latter curve have not been carried. Thus Eq. 27.65c is a convenient semi-empirical rule showing the effect of Mach Number on skin friction in turbulent, adiabatic flow.

#### Adiabatic Skin-Friction Coefficient Based on Kármán's Mixing-Length

**Formulation.** The curve marked "Frankl and Voishel" in Fig. 27.7 is based on the extension<sup>(10,12)</sup> of Kármán's mixing-length hypothesis to compressible flow. The results of the calculations, which have so far been carried out only for the insulated plate, are in numerical form, but are fitted with an accuracy of  $\pm 2$  per cent by the following formulas in the range  $0 < M_\infty < 4$ :

$$C_{D\infty} = \frac{0.472}{(\log_{10} \text{Rey}_\infty)^{2.58} \left(1 + \frac{k-1}{2} M_\infty^2\right)^{0.467}} \quad (27.66a)$$

$$C_{f\infty} = C_{D\infty} \left(1 - \frac{1.12}{\log_{10} \text{Rey}_\infty}\right) \quad (27.66b)$$

It is seen that the effects of  $\text{Rey}_\infty$  and  $M_\infty$  are entirely separate, at least in the range of applicability of this formula. That is, the influence of  $M_\infty$  does not depend on the Reynolds Number, and, conversely, the influence of  $\text{Rey}_\infty$  does not depend on the Mach Number.

**Skin-Friction Coefficient Based on Prandtl's Mixing-Length Formula.** Results of the form of Eq. 27.59, based on Eq. 27.61 as a starting point, have been computed by van Driest,<sup>(13)</sup> based on a Prandtl Number of unity, but covering the case of the cold plate as well as of the adiabatic plate. The results are in the form

$$\begin{aligned} \frac{0.242}{A \sqrt{C_{D\infty}} \sqrt{T_w/T_\infty}} & (\sin^{-1} \alpha + \sin^{-1} \beta) \\ & = \log_{10} (\text{Rey}_\infty C_{D\infty}) - \frac{1+2n}{2} \log_{10} \frac{T_w}{T_\infty} \quad (27.67a) \end{aligned}$$

$$C_{f\infty} = \frac{\frac{0.558}{A} (\sin^{-1} \alpha + \sin^{-1} \beta) C_{D\infty}}{\frac{0.558}{A} (\sin^{-1} \alpha + \sin^{-1} \beta) + 2 \sqrt{C_{D\infty}} \sqrt{T_w/T_\infty}} \quad (27.67b)$$

where

$$\left. \begin{aligned} A^2 & \equiv \frac{T_\infty}{T_w} \cdot \frac{k-1}{2} M_\infty^2 \\ B & \equiv \frac{T_\infty}{T_w} \left(1 + \frac{k-1}{2} M_\infty^2\right) - 1 \\ \alpha & \equiv \frac{2A^2 - B}{\sqrt{B^2 + 4A^2}} ; \quad \beta \equiv \frac{B}{\sqrt{B^2 + 4A^2}} \end{aligned} \right\} \quad (27.67c)$$

and  $n$  is the exponent in the temperature-viscosity relation  $\mu \sim T^n$ .

The uppermost curve of Fig. 27.7 shows the effect of  $M_\infty$  on drag coefficient as found by these formulas for the case of the adiabatic plate. By comparing with the "Frankl and Voishel" curve, it is seen that this calculation method tends to underestimate slightly the effects of compressibility on the frictional drag.

**Experimental Adiabatic Skin-Friction Coefficient at High Mach Numbers.** In comparing experimental data with the theoretical results, it is necessary to make corrections on account of the flow not being turbulent over the entire length of the plate. The experimental results given below have accordingly been corrected to a form where they apply to a hypothetical adiabatic plate having turbulent flow over its entire length. As these corrections are based on a number of assumptions which are difficult to verify, the results cannot be expected to have the accuracy of the initial data from which they are derived.

**TOTAL DRAG COEFFICIENT.** Fig. 27.8a<sup>(12)</sup> shows, for  $M_\infty = 2.5$ , a comparison between the measured curve of total drag coefficient versus Reynolds Number and the theoretical curve corresponding to the extension<sup>(12)</sup> of Frankl and Voishel's method<sup>(9)</sup> based on the Kármán similarity formulation. The agreement is seen to be generally excellent, except in the range of low  $\text{Rey}_\infty$ , where so much of the plate is covered by laminar flow that considerable errors are incurred when the results are corrected to the equivalent all-turbulent flow. The agreement between theory and experiment is confirmed by the data of O'Donnell.<sup>(40)</sup>

Fig. 27.8b<sup>(12)</sup> shows, in the range of high Reynolds Numbers, a comparison between the measured variation of  $C_{D\infty}$  with  $M_\infty$  (based on the data of References 11, 12, 35, and 36) and the corresponding variation based on the extension of the Frankl and Voishel theory mentioned previously. Here again the theory is seen to give satisfactory agreement with experiment up to the highest measured  $M_\infty$  of 3.6. The experiments of Chapman and Kester<sup>(35)</sup> demonstrated two additional facts: (i) Moderate variations in lengthwise pressure distribution, such as might be associated with thin airfoils or bodies of revolution, have no appreciable effect on the average skin friction. (ii) With cylindrical

bodies of revolution, the average skin-friction coefficient is substantially independent of nose shape and fineness ratio.

Wilson <sup>(11)</sup> has also extended Kármán's turbulent skin-friction formulation to compressible flow, using approximations for the numerical

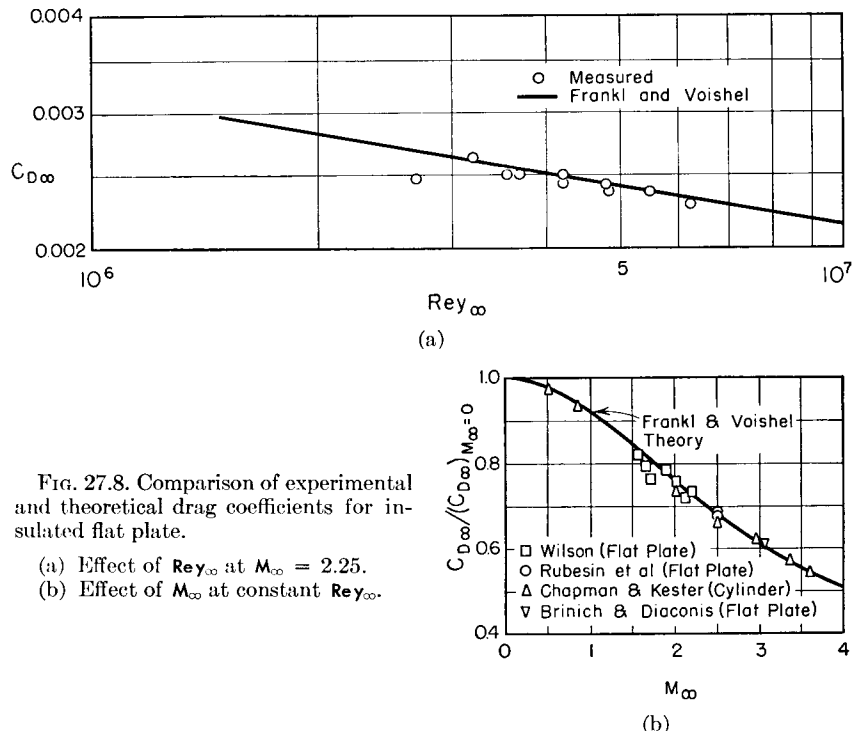


FIG. 27.8. Comparison of experimental and theoretical drag coefficients for insulated flat plate.

- (a) Effect of  $Re_\infty$  at  $M_\infty = 2.25$ .  
 (b) Effect of  $M_\infty$  at constant  $Re_\infty$ .

calculation somewhat different from those of References 9 and 12, and introducing the recovery factor in a semi-empirical fashion to bring the theory into closer agreement with experiment. The result of the calculations is given by

$$\frac{0.242 \sin^{-1} \sqrt{A}}{\sqrt{A \cdot B \cdot C_{D\infty}}} = \log_{10} \left[ \frac{A \cdot B}{(\sin^{-1} \sqrt{A})^2} C_{D\infty} \right] \left[ \frac{(\sin^{-1} \sqrt{A})^2}{A \cdot B^{1.768}} Re_\infty \right] \quad (27.68a)$$

where

$$A \equiv \frac{\frac{k-1}{2} M_\infty^2}{1 + \frac{k-1}{2} M_\infty^2}; \quad B \equiv 1 + \mathcal{R} \frac{k-1}{2} M_\infty^2 \quad (27.68b)$$

This formula, in which the effects of  $M_\infty$  and  $Re_\infty$  are intermixed, is plotted in Fig. 27.9 in terms of a modified  $C_{D\infty}$  and a modified  $Re_\infty$ ,

the modification factors being functions of  $M_\infty$  which respectively multiply  $C_{D\infty}$  and  $Re_\infty$ . On the same chart are plotted experimental data for  $M_\infty$  between 1.58 and 2.5. The theoretical curve is in accord with measurements within the experimental scatter of the data.

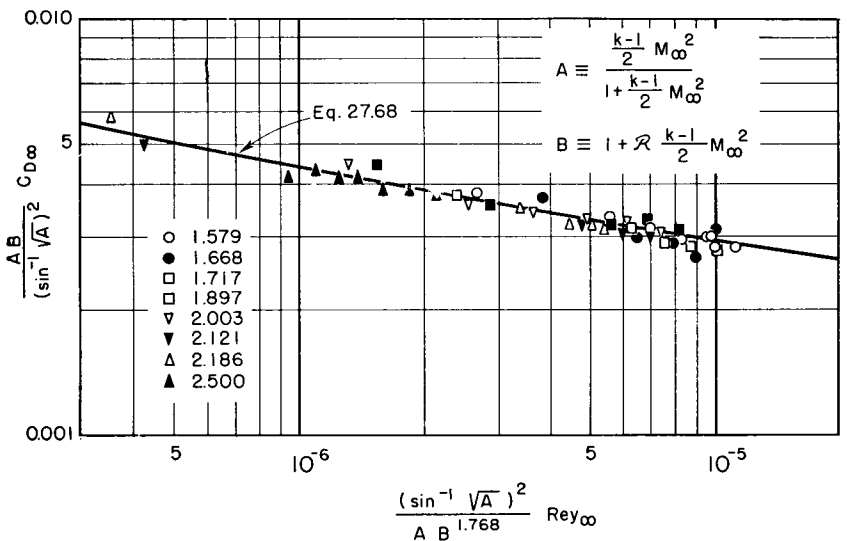


FIG. 27.9. Comparison of experimental data with Wilson's formula for turbulent flow on insulated flat plate. Numbers in legend show values of  $M_\infty$ . Theoretical curve is based on  $\mathcal{R} = 0.88$  (after Wilson).

Monaghan <sup>(33)</sup> has derived in a semi-empirical manner an interpolation formula for the integrated skin-friction coefficient. The interpolation formula, which is approximate but more convenient for numerical calculations, states that

$$C_{Dw} = 0.46 \frac{(\sin^{-1} \sqrt{A})^2}{A} \left\{ \log_{10} \left[ \frac{(\sin^{-1} \sqrt{A})^2}{A} Re_\infty \right] \right\}^{-2.6} \quad (27.68c)$$

where  $A$  is defined by Eq. 27.68b.

**LOCAL SKIN-FRICTION COEFFICIENT.** Fig. 27.10a shows the results of direct measurements of the local skin friction in the turbulent range by means of the floating-element dynamometer technique. <sup>(30)</sup> The data in the fully developed turbulent zone are in good agreement with the theoretical values of Eq. 27.66b. The effect of Mach Number on the local skin-friction coefficient is shown in Fig. 27.10b. According to Eqs. 27.66, the theoretical effect of  $M_\infty$  is the same for  $C_f$  and  $C_D$ . The close agreement of the mean curve of Fig. 27.10b with the curve of Fig. 27.8b is therefore additional confirmation of the extended Frankl and Voishel theory.

From Figs. 27.7 to 27.10 it may be concluded that the semi-empirical theories based on the mixing-length formulations of Kármán and of Prandtl, and that based on the extension of low-speed data through the use of the reference temperature  $T_{am}$ , all predict correctly the general

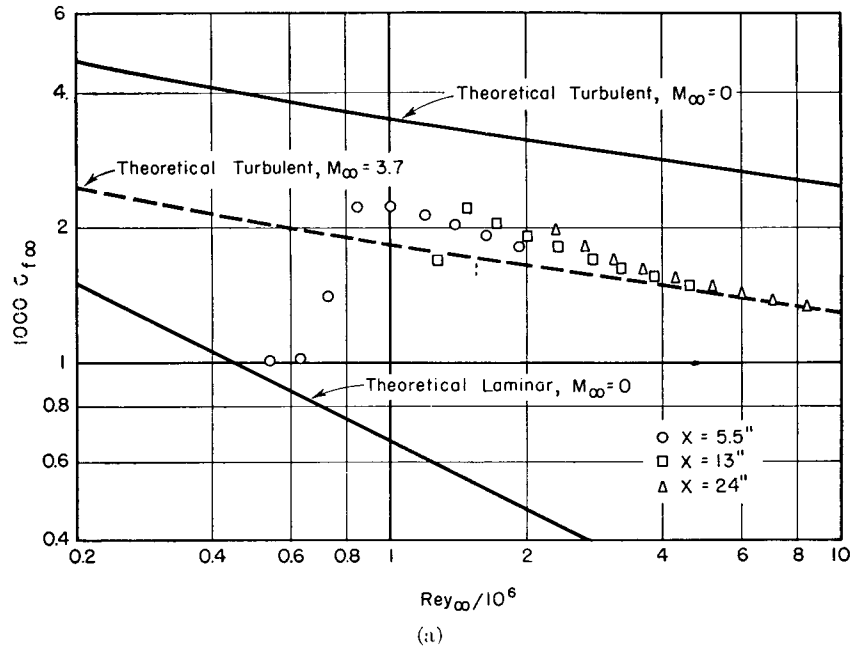


FIG. 27.10. Local skin-friction coefficient on flat plate (after Coles).

(a)  $C_f$  versus Reynolds Number for  $M_\infty = 3.7$ . Dashed curve represents Eqs. 27.66.

(b) Effect of Mach Number on local skin-friction coefficient, with  $Re_\infty = 8(10)^6$ .

variation of  $C_{f\infty}$  with  $M_\infty$ , and that the formulation of Kármán, as developed in References 9, 11, and 12, gives the best agreement with experiment up to  $M_\infty = 4$ .

A somewhat different approach to the problem of extending incom-

pressible friction data to compressible flows, formulated by Donaldson,<sup>(25)</sup> also agrees well with the data of Reference 11.

**Velocity and Stagnation-Temperature Profiles for Adiabatic Plate.** Fig. 27.11a shows a typical measured velocity profile<sup>(11)</sup> for supersonic flow at high Reynolds Numbers. Also shown is the theoretical velocity profile based on the integration<sup>(11)</sup> of Eq. 27.52. It is rather surprising

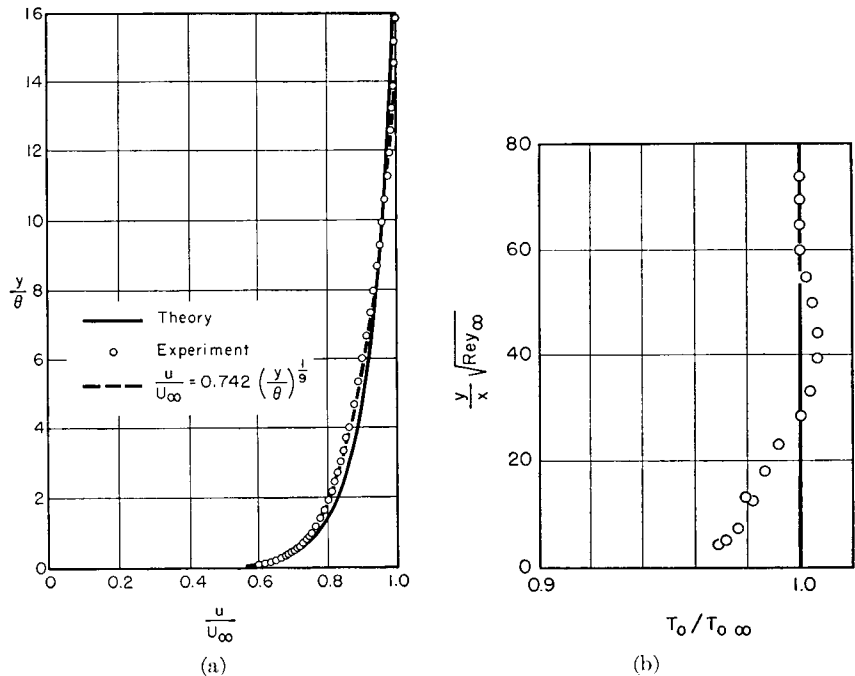


FIG. 27.11. (a) Theoretical and measured velocity profiles for turbulent flow on insulated flat plate, with  $M_\infty = 1.999$  and  $C_{f\infty} = 0.00264$  (after Wilson). (b) Stagnation-temperature profile on insulated flat plate with  $M_\infty = 2.28$  (after van Driest).

that the theory predicts the drag coefficient (Figs. 27.8, 27.9, and 27.10) so well when there is a substantial discrepancy between the measured and theoretical velocity profiles. This is strong evidence that there are mutually compensating errors in the theory.

Fig. 27.11a indicates additionally that at high Reynolds Numbers the compressible, turbulent velocity profile follows approximately a 1/9th power law. At Reynolds Numbers near  $10^6$ , a 1/7th power law fits the data.<sup>(40)</sup>

The measured stagnation-temperature profile for an insulated plate shown in Fig. 27.11b<sup>(12)</sup> is of interest inasmuch as it verifies the prediction that, even though there is no heat transfer to or from the plate,

the stagnation temperature in the boundary layer is at some points greater than both the wall temperature and the free-stream temperature.

**Skin Friction and Heat Transfer for the Nonadiabatic Plate.** The theoretical results of van Dreist,<sup>(13)</sup> based on the Prandtl mixing-length hypothesis (see Eqs. 27.67), are of special interest because they show how the skin-friction and heat transfer coefficients are affected by heat transfer from the free stream to the plate.

For example, referring to Fig. 27.12a, which shows the local coefficients  $C_{f\infty}$  and  $C_{H\infty}$  for  $M_\infty = 4$ , it is noted that the condition  $T_w/T_\infty = 4.2$  corresponds to the adiabatic plate. Extrapolating the curves to  $T_w/T_\infty = 0$ , corresponding to the maximum possible heat transfer to the plate, it is seen that when the plate receives heat at the maximum possible rate, the skin-friction and heat transfer coefficients are of the order of 40 to 50 per cent greater than for the insulated plate. Fig. 27.12b shows similar results for the integrated drag coefficient,  $C_{D\infty}$ .

Convenient nomographic charts<sup>(34)</sup> for rapidly solving Eqs. 27.67 are given in Figs. 27.12c and 27.12d.

Slack,<sup>(28)</sup> in tests on a flat plate at  $M_\infty = 2.4$ , measured values of  $C_{H\infty}$  in the turbulent zone which agree with van Dreist's theory within the accuracy of the experimental data.

## 27.6. Recovery Factor for Turbulent Flow

For the purpose of calculating drag and heat transfer it is possible to assume without excessive error that the Prandtl Number is unity, especially when the Mach Number is not very large and when the heat flux is not large. On the other hand, it is essential to take note of the deviation of  $\text{Pr}$  from unity when it is desired to reckon accurately the adiabatic wall temperature. This is obviously of great practical importance for estimating the adiabatic skin temperature at very high Mach Numbers, for high skin temperatures represent one of the trouble-

Fig. 27.12. Theoretical skin friction and heat transfer for flat plate at  $M_\infty = 4$ , based on  $\text{Pr} = 1$ . Curves for  $T_w/T_\infty = 4.2$  correspond to insulated plate (after van Dreist).

- Local skin-friction coefficient and Stanton Number.
- Integrated drag coefficient.
- and (d) Graphical solution of Eqs. 27.67 for local and integrated skin-friction coefficients (after Martin). Procedure for use of charts: (i) For given values of  $M_\infty$  and  $T_w/T_\infty$ , find auxiliary parameter  $\psi$  from Fig. 27.12c. (ii) In Fig. 27.12d, pass straight line through given value of  $T_w/T_\infty$  and given value of  $\text{Rey}_\infty$  (on the scale corresponding to  $C_{f\infty}$  or  $C_{D\infty}$ , as desired), and find intersection with "reference line." (iii) Pass straight line through point on reference line and value of  $\psi$ , and find value of  $C_{f\infty}$  or  $C_{D\infty}$  on "skin-friction coefficient" scale.

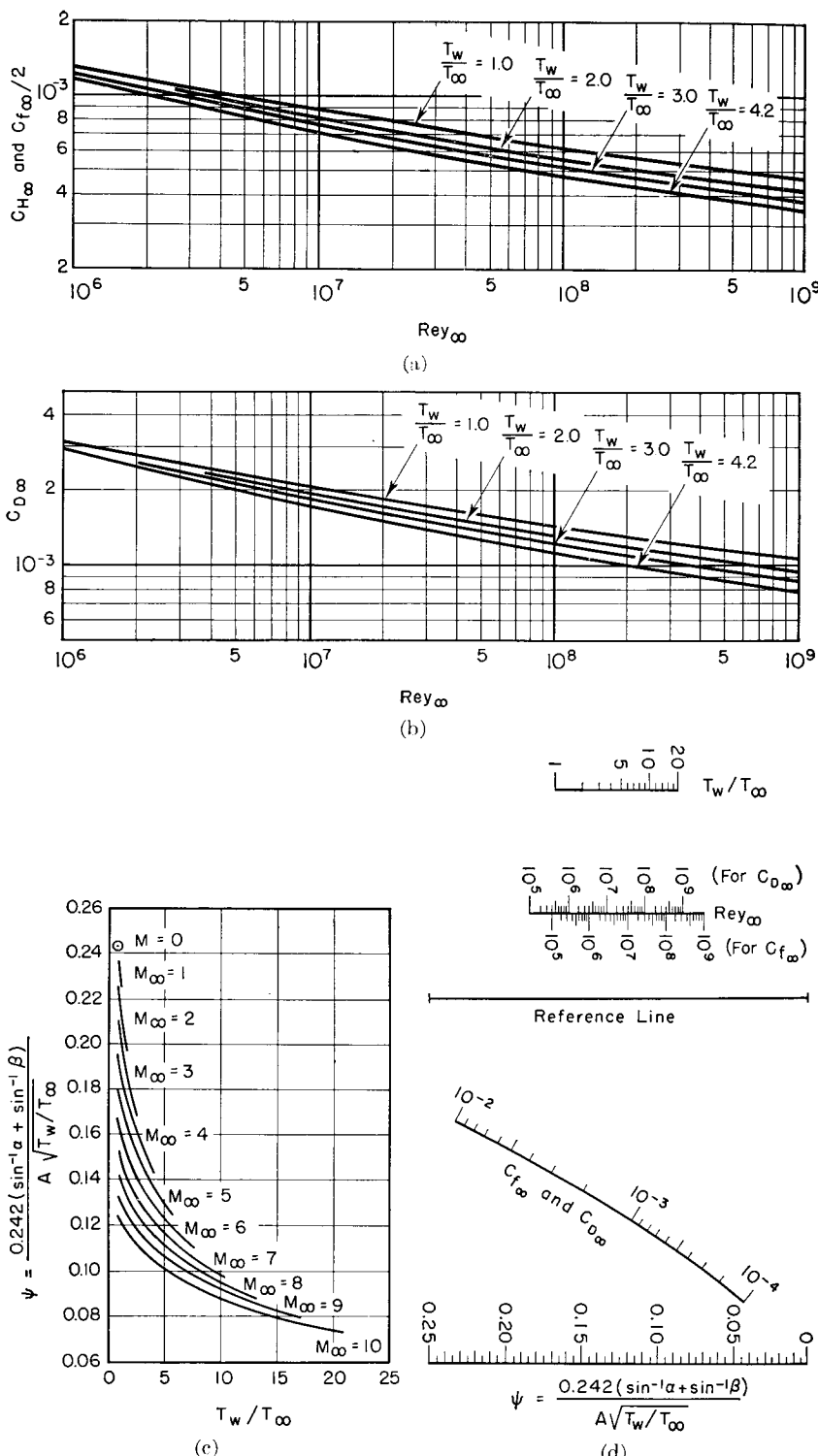


FIG. 27.12. (See page 1117.)

some practical problems in high-speed flight. Furthermore, accurate estimates of the recovery factor are necessary for calculations of heat transfer rates at high  $M_\infty$ , since the definition of the heat transfer coefficient involves the adiabatic wall temperature.

Experimental data at low speeds<sup>(3)</sup> show that, in a variety of different types of turbulent flow, the turbulent Prandtl Number is substantially constant and is in the vicinity of 0.7. This is fortunate, as many gases of practical interest have laminar Prandtl Numbers of the same order of magnitude, and so it is possible to simplify the analytical approach by assuming, with reasonable accuracy, that the Prandtl Number is uniform throughout the boundary layer.

**Analytical Estimate of Recovery Factor for Flat Plates.**<sup>(15)</sup> We shall calculate approximately the recovery factor for turbulent flow by introducing some arbitrary but physically plausible assumptions.

From the definition of recovery factor, Eq. 26.2, we have

$$\frac{T_{aw}}{T_\infty} = 1 + \mathfrak{R} \frac{k-1}{2} M_\infty^2$$

For flow with  $\text{Pr} = 1$ , whether laminar or turbulent, the recovery factor is unity, and the temperature ratio in the boundary layer is connected uniquely with the square of the velocity ratio, as given by Eq. 26.12 with  $T_w = T_{w\infty}$ . This equation may then be rewritten as

$$\frac{\bar{T}}{T_\infty} = 1 + \frac{k-1}{2} M_\infty^2 \left[ 1 - \left( \frac{\bar{u}}{U_\infty} \right)^2 \right] \quad (27.69)$$

**POSTULATED RELATION BETWEEN VELOCITY AND TEMPERATURE.** When the flow is turbulent and  $\text{Pr}$  is constant but less than unity, it is plausible to suppose that the temperature ratio will again be a function only of the square of the velocity ratio. However, a difficulty arises here because  $\delta_T$ , the thickness of the thermal boundary layer, is greater than  $\delta_u$ , the thickness of the velocity boundary layer. That is, although  $\bar{u}/U_\infty$  becomes unity when  $y = \delta_u$ ,  $T/T_\infty$  does not become unity until  $y = \delta_T$ . We may take care of this difficulty by supposing that if the velocity ratio is given by some function of  $y/\delta_u$ , say

$$\frac{\bar{u}}{U_\infty} = g\left(\frac{y}{\delta_u}\right) \quad (27.70)$$

then any dependence of the temperature ratio on  $y$  will be in terms of the square of the same function of  $y/\delta_T$ , i.e., in terms of

$$\left[ g\left(\frac{y}{\delta_T}\right) \right]^2$$

Now, when  $y = 0$ ,  $g = 0$ , and  $\bar{T} = T_{aw}$ . Furthermore, when  $y = \delta_T$ ,  $\bar{T} = T_\infty$ . Putting together these boundary conditions with the assumption regarding the connection between  $\bar{T}/T_\infty$  and  $(\bar{u}/U_\infty)^2$ , and keeping in mind that the definition of  $\mathfrak{R}$  must be satisfied when  $y = 0$ , we postulate by comparison with Eq. 27.69 the following relation for  $T/T_\infty$ :

$$\frac{\bar{T}}{T_\infty} = 1 + \mathfrak{R} \frac{k-1}{2} M_\infty^2 \left[ 1 - g^2\left(\frac{y}{\delta_T}\right) \right] \quad (27.71)$$

**RATIO OF VELOCITY THICKNESS TO THERMAL THICKNESS.** We next obtain a relation between  $\delta_u/\delta_T$ ,  $\text{Pr}$ , and  $\mathfrak{R}$  by using Eq. 27.71 together with the energy equation. Eq. 27.71 may be rearranged by multiplying through by  $T_\infty$ , giving

$$\bar{T} - T_\infty = \frac{\mathfrak{R} U_\infty^2}{2c_p} \left[ 1 - g^2\left(\frac{y}{\delta_T}\right) \right]$$

We next form, from the definition of stagnation temperature,

$$\begin{aligned} \bar{T}_0 - T_{0\infty} &= \bar{T} - T_\infty + \frac{\bar{u}^2 - U_\infty^2}{2c_p} \\ &= \frac{U_\infty^2}{2c_p} \left\{ \mathfrak{R} \left[ 1 - g^2\left(\frac{y}{\delta_T}\right) \right] - \left[ 1 - g^2\left(\frac{y}{\delta_u}\right) \right] \right\} \end{aligned} \quad (27.72a)$$

Differentiating this twice with respect to  $y$ , and evaluating the result at  $y = 0$  (at which point we note that  $g = 0$  inasmuch as  $u = 0$ ), we obtain after some calculation,

$$\left( \frac{\partial^2 \bar{T}_0}{\partial y^2} \right)_{y=0} = \frac{U_\infty^2}{c_p} \left[ -\frac{\mathfrak{R}}{\delta_T^2} + \frac{1}{\delta_u^2} \right] (g')_{y=0}^2$$

From Eq. 27.70, however,

$$(g')_{y=0} = \frac{\delta_u}{U_\infty} \left( \frac{\partial \bar{u}}{\partial y} \right)_{y=0}$$

and so the preceding equation becomes

$$\left( \frac{\partial^2 \bar{T}_0}{\partial y^2} \right)_{y=0} = \frac{1}{c_p} \left[ 1 - \mathfrak{R} \left( \frac{\delta_u}{\delta_T} \right)^2 \right] \left( \frac{\partial \bar{u}}{\partial y} \right)_{y=0}^2 \quad (27.72b)$$

Introducing the energy equation in the form of Eq. 26.7, but remembering that we are now dealing with a turbulent flow for which the "total viscosity" of the mean flow is  $\mu + \epsilon$ , we write (see also Eq. 27.16d)

$$\bar{\rho} \bar{u} \frac{\partial \bar{T}_0}{\partial x} + \bar{\rho} \bar{v} \frac{\partial \bar{T}_0}{\partial y} = \frac{\partial}{\partial y} (\mu + \epsilon) \frac{\partial \bar{T}_0}{\partial y} + \frac{\partial}{\partial y} \left[ \left( \frac{1}{\text{Pr}} - 1 \right) (\mu + \epsilon) \frac{\partial \bar{T}}{\partial y} \right]$$

We now evaluate this at the wall, where  $y = 0$ ,  $\bar{u} = 0$ ,  $\bar{v} = 0$ , and where, furthermore,  $\partial T/\partial y = 0$  (since the plate is insulated). The term  $\partial \bar{T}_0/\partial y$  is evaluated at the wall by noting that

$$\left(\frac{\partial \bar{T}_0}{\partial y}\right)_{y=0} = \left(\frac{\partial \bar{T}}{\partial y}\right)_{y=0} + \left[\frac{\partial}{\partial y} \left(\frac{\bar{u}^2}{2c_p}\right)_{y=0}\right] = \left(\frac{\partial \bar{T}}{\partial y}\right)_{y=0} + \left(\frac{\bar{u}}{c_p} \frac{\partial \bar{u}}{\partial y}\right)_{y=0} = 0$$

Substituting  $\bar{T} = \bar{T}_0 - (\bar{u}^2/2c_p)$  into the energy equation, carrying out the indicated differentiations, and employing the foregoing boundary conditions at the wall, we finally get the simple result

$$\left(\frac{\partial^2 \bar{T}_0}{\partial y^2}\right)_{y=0} = \frac{1 - \text{Pr}}{c_p} \left(\frac{\partial \bar{u}}{\partial y}\right)_{y=0}^2 \quad (27.73)$$

Comparison of this with Eq. 27.72b leads immediately to the desired relation, namely

$$\mathfrak{R} = \text{Pr} \left(\frac{\delta_r}{\delta_u}\right)^2; \quad \frac{\delta_u}{\delta_r} = \sqrt{\frac{\text{Pr}}{\mathfrak{R}}} \quad (27.74)$$

Note that for laminar flow, where  $\mathfrak{R} \cong \sqrt{\text{Pr}}$ , Eq. 27.74 yields  $\delta_u/\delta_r \cong (\text{Pr})^{1/4}$ .

#### INTEGRAL ENERGY EQUATION.

We now write the energy equation in integral form for the flows entering and leaving the control volume of Fig. 27.13. In terms of the stagnation temperature, we have

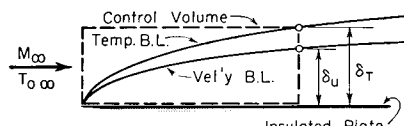


FIG. 27.13. Control volume for application of integral energy equation.

which, in the light of Eq. 27.74, may also be written as

$$\int_0^{\delta_r} \bar{\rho} \bar{u} c_p (\bar{T}_0 - T_{0\infty}) dy = 0 \quad (27.75)$$

Now  $\bar{\rho}/\rho_\infty = T_\infty/\bar{T}$ , and the latter is expressed by Eq. 27.71. Furthermore,  $\bar{u}/U_\infty$  is given by Eq. 27.70, and  $c_p(\bar{T}_0 - T_{0\infty})$  by Eq. 27.72a. Substituting these into Eq. 27.75, we get

$$\int_0^{\sqrt{\mathfrak{R}/\text{Pr}}} \frac{\bar{\rho}}{\rho_\infty} \frac{\bar{u}}{U_\infty} c_p (\bar{T}_0 - T_{0\infty}) d\left(\frac{y}{\delta_u}\right) = 0 \quad (27.76)$$

So far, nothing has been said concerning the form of the function  $g$ . However, as indicated by the experimental results of Figs. 27.10 and 27.11a, the assumption of the power-law variation of Eq. 27.25 is accurate as well as simple. We therefore assume that

#### Art. 27.6 RECOVERY FACTOR FOR TURBULENT FLOW

$$\frac{\bar{u}}{U_\infty} = \left(\frac{y}{\delta_u}\right)^{1/N} = g\left(\frac{y}{\delta_u}\right) \quad (27.77a)$$

and, taking note of Eq. 27.74, that

$$g\left(\frac{y}{\delta_r}\right) = \left(\frac{y}{\delta_r}\right)^{1/N} = \left(\frac{y}{\delta_u}\right)^{1/N} \left(\frac{\text{Pr}}{\mathfrak{R}}\right)^{1/2N} \quad (27.77b)$$

Substituting these into Eq. 27.76, there is finally obtained

$$\int_0^{\sqrt{\mathfrak{R}/\text{Pr}}} \frac{\mathfrak{R} \left[1 - \left(\frac{y}{\delta_u}\right)^{\frac{2}{N}} \left(\frac{\text{Pr}}{\mathfrak{R}}\right)^{\frac{1}{N}}\right] - \left[1 - \left(\frac{y}{\delta_u}\right)^{\frac{2}{N}}\right]}{1 + \mathfrak{R} \frac{k-1}{2} M_\infty^2 \left[1 - \left(\frac{y}{\delta_u}\right)^{\frac{2}{N}} \left(\frac{\text{Pr}}{\mathfrak{R}}\right)^{\frac{1}{N}}\right]} \left(\frac{y}{\delta_u}\right)^{\frac{1}{N}} d\left(\frac{y}{\delta_u}\right) = 0 \quad (27.78)$$

**APPROXIMATE FORMULA FOR RECOVERY FACTOR.** Evaluation of this definite integral at constant  $\mathfrak{R}$ ,  $\text{Pr}$  and  $N$  then yields the recovery factor as a function of the Prandtl Number and of the velocity-profile parameter  $N$ . The integral cannot be evaluated in closed form, but is found instead by iteration. For  $\text{Pr} = 0.7$ , the results of the calculations are represented by Fig. 27.14.

27.14.

The following formula<sup>(15)</sup> fits the results to within  $\pm 1$  per cent:

$$\mathfrak{R} \cong (\text{Pr})^{\frac{N+1+0.52\mathfrak{R} M_\infty^2}{3N+1+\mathfrak{R} M_\infty^2}} \quad (27.79)$$

For incompressible flow at very high Reynolds Numbers, for which  $N$  is very large compared with unity, Eq. 27.79 leads to the oft-quoted formula for turbulent flow,  $\mathfrak{R} \cong \sqrt[3]{\text{Pr}}$ . For smaller values of  $N$ , corresponding to smaller Reynolds Numbers, the theoretical recovery factor is also smaller.

It is seen from Fig. 27.14 that the turbulent recovery factor is higher than the laminar recovery factor at Mach Numbers less than 10, but that at higher Mach Numbers the turbulent recovery factor predicted by this theory decreases to a value less than the laminar recovery factor. For Mach Numbers between zero and two, the variation of  $\mathfrak{R}$  for turbulent flow is so small as to be almost negligible.

**Measured Recovery Factor for Flat Plates.** <sup>(16)</sup> Fig. 27.15 shows measured recovery factors for both laminar and turbulent flow at  $M_\infty = 2.4$ . In the laminar range, as observed in the previous chapter, the measured recovery factors are in excess of the theoretical value,

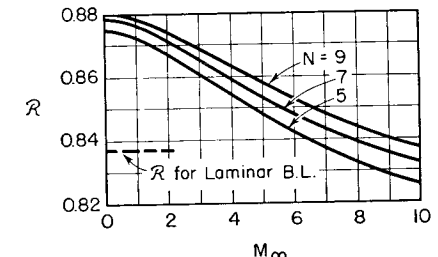


FIG. 27.14. Theoretical recovery factor for turbulent boundary layer with laminar and turbulent Prandtl Numbers of 0.70 (after Tucker and Mashin).

✓Pr. In the turbulent range, the comparison is difficult to make because of uncertainty as to the values of  $Pr$  and  $N$  to be inserted in the theoretical formula, but, using  $Pr = 0.72$  and values of  $N$  of both 5 and 7, which seem appropriate for the given range of  $Rey_\infty$ , the theory is in fairly good agreement with experiment.

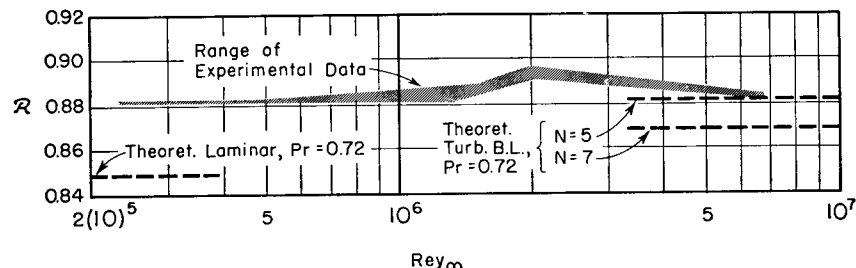


FIG. 27.15. Measured recovery factor for flat plate,  $M_\infty = 2.4$  (after Stalder, Rubesin, and Tendeland).

It is seen from Fig. 27.15 that the turbulent recovery factor decreases as the Reynolds Number increases. This indicates a defect in the theory, for, as  $Rey$  increases,  $N$  also increases, and Fig. 27.14 then predicts an increase in recovery factor.

It is of considerable practical consequence that the value of  $R$  in

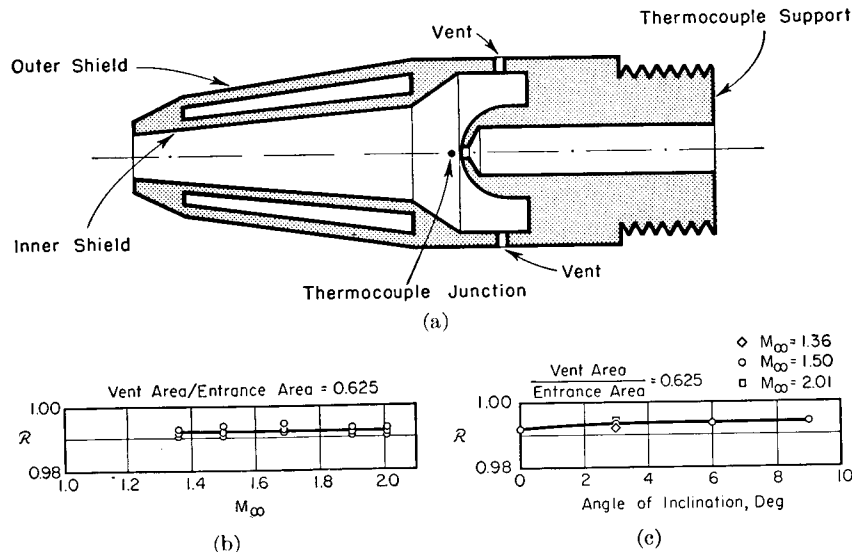


FIG. 27.16. Stagnation-temperature probe (after Goldstein and Scherrer).

- (a) Construction.
- (b) Effect of  $M_\infty$  at zero angle of attack, for optimum ratio of vent area to entrance area of 0.625.
- (c) Effect of angle of attack, with same dimensions as in (b).

the transition zone is greater than that for either laminar or turbulent flow.

**Measured Recovery Factors for Turbulent Flow for Miscellaneous Shapes.** We summarize here experimental results on recovery factors for a variety of shapes. The following table (based in part on a compilation by J. Kaye<sup>(39)</sup>) gives a concise comparison:

DATA ON RECOVERY FACTORS FOR TURBULENT BOUNDARY LAYER

Author	Reference	Geometry	$M_\infty$	$R$
Wimbrow	17, 26	Cone (20°)	2.0	$0.885 \pm .008$
		Paraboloid	1.5	$0.902 \pm .005$
		Paraboloid	2.0	$0.894 \pm .008$
Stalder, Rubesin, and Tendeland	16	Flat plate	2.4	$0.884 - .897$
Hilton	18	Ogive-cylinder	2.0	$0.880 \pm .004$
		Ogive-cylinder	1.73	$0.882 \pm .003$
des Clers and Sternberg	27	Cone (10°)	1.4-3.4	$0.882 \pm .007$
Slack	28	Flat plate	2.4	0.906
Stine and Scherrer	29	10° Cone	2.0-3.8	$0.882 \pm .008$
		40° Cone-cylinder	2.0-3.8	$0.885 \pm .011$
Eckert and Weise	19	Wire, axis normal to flow	0-1	0.84-0.87
Eber	20	Wire, axis normal to flow	1.2	0.83
			1.85	0.89
			2.5	0.91
			3.2	0.91
Eber	20	Stagnation point of disk normal to flow	1.5	0.96
			2.0	0.97
			2.5	0.98
			3.0	0.98
Ladenburg and Bershadier	32	Flat plate	2.35	$0.892 \pm .005$

Except for the wire and the disk, both of which are bluff bodies, all the recovery factors lie within the range 0.88 to 0.91. Curiously, the middle of this range is nearly exactly the cube root of the Prandtl Number.

**Stagnation-Temperature Probes.** Since it is almost impossible to measure static temperatures directly, it is more practical to measure

either a combination of (i) stagnation temperature and Mach Number, or (ii) adiabatic wall temperature and Mach Number. However, the latter method requires, for calculating the static temperature, an accurate knowledge of the recovery factor. Since the latter is seldom accurately known over a wide range of  $M_\infty$  and  $Rey$ , the scheme of measuring stagnation temperature is the most practical.

To measure the stagnation temperature, one must bring the gas to rest adiabatically, and must place the temperature probe in a low-velocity region. A typical method for doing this<sup>(21)</sup> is illustrated in Fig. 27.16a. The gas is first decelerated in a diverging duct and is then brought to rest on a sphere, the thermocouple being placed just in front of the stagnation point of the sphere. Heat transfer by radiation and conduction is minimized through the use of a double shield and by venting some gas continually through ports, the amount of vent area being a compromise between the desire to maintain low speeds within the probe and the desire to maintain good heat transfer rates within the probe.

Fig. 27.16b, which refers to a probe of this type with an optimum ratio of vent area to entrance area, indicates that, for supersonic free-stream velocities, the recovery factor is substantially independent of  $M_\infty$  and departs from unity by only about 0.8 per cent. It is seen further from Fig. 27.16c that the calibration of this probe is nearly independent of inclination to the flow direction up to values of inclination of 9°.

### 27.7. Turbulent Boundary Layer on Bodies of Revolution

The integral methods of calculation may be extended to boundary layers on bodies of revolution with little additional difficulty. In the case of flow past a cylinder, with the boundary-layer thickness small compared to the radius of the cylinder, the boundary-layer behavior and the relations governing the boundary layer may be expected to be substantially the same as for a plane boundary layer having the same pressure gradient. For bodies which are not cylindrical, or in cases where the boundary-layer thickness is not negligible compared with the radius of the body of revolution, the boundary-layer relations are different from those for plane flow because of the presence of terms containing  $r$  (radius in cylindrical coordinates) in the continuity and momentum equations.

**Cone with Attached Shock.** The effects of changes in the radius  $r$  can be most readily investigated by considering supersonic flow past a cone with an attached shock, for in this case there is no longitudinal pressure gradient at the surface of the cone.

**LAMINAR FLOW.** It may be recalled (Chapter 26) that the local values of  $C_{f,\infty}$  and of  $C_{H,\infty}$  for laminar flow may be found by merely multiplying by  $\sqrt{3}$  the corresponding values for a flat plate at the same value of  $Rey_\infty$ . Now the values of  $C_{f,\infty}$  and  $C_{H,\infty}$  for laminar flow vary in proportion to  $1/\sqrt{Rey_\infty}$ . Therefore the similarity rule may be stated in the alternative form that the cone values of  $C_{f,\infty}$  and  $C_{H,\infty}$  at a given  $Rey_\infty$  are respectively the same as the flat-plate values of  $C_{f,\infty}$  and  $C_{H,\infty}$  at a Reynolds Number one-third as large as the value of  $Rey_\infty$  for the cone.

**TURBULENT FLOW.** Van Driest,<sup>(23)</sup> by extending the momentum integral method to the case of a cone, and using Prandtl's formulation of the turbulent shear stress, has derived an analogous similarity rule for turbulent flow. He has shown that, for the same values of  $M_\infty$  (outside the boundary layer) and of  $T_w/T_\infty$ , the cone values of  $C_{f,\infty}$  and  $C_{H,\infty}$  at a given  $Rey_\infty$  are respectively the same as the flat-plate values of  $C_{f,\infty}$  and  $C_{H,\infty}$  at a Reynolds Number one-half as large as the value of  $Rey_\infty$  for the cone.

In turbulent flow Fig. 27.9 and Eq. 27.64b show that  $C_{f,\infty}$  and  $C_{H,\infty}$  vary approximately as  $Rey_\infty^{-0.2}$ . Accordingly the rule stated above

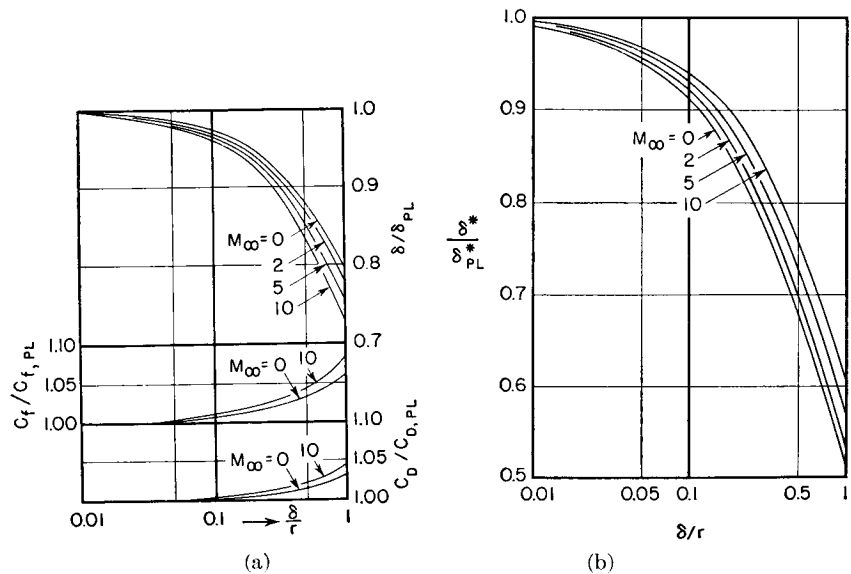


FIG. 27.17. Turbulent boundary layer on insulated circular cylinder with no pressure gradient. Notation:  $r$  denotes radius of cylinder;  $( )_{PL}$  signifies value of quantity for  $\delta/r \rightarrow 0$ , i. e., for flat plate (after Eckert).

- (a) Boundary-layer thickness, local skin-friction coefficient, and integrated skin-friction coefficient.
- (b) Displacement thickness.

may be stated approximately in the alternative form that, for the same values of  $M_\infty$ ,  $T_w/T_\infty$ , and  $Rey_\infty$ , the values of  $C_{f,\infty}$  and  $C_{H,\infty}$  for the cone are approximately 15 per cent larger than the corresponding values for the flat plate.

**Cylindrical Body of Revolution with Zero Pressure Gradient.** The effect of the lateral curvature of the boundary layer has been investigated with the help of the integral momentum method by Eckert<sup>(24)</sup> for the simple case of a circular cylinder aligned parallel to the flow, the longitudinal pressure gradient being zero.

Fig. 27.17 shows the results of the calculations in a form where the boundary-layer parameters are compared with the corresponding parameters for a flat plate at the same  $Rey_\infty$ . The results for  $\delta/r = 0$  are of course identical with those for the flat plate.

For values of  $\delta/r$  of the order of 0.01, there are virtually no deviations from the flat-plate values. Even when  $\delta$  is 10 per cent of  $r$  the deviations are negligible for most practical purposes. For very thick boundary layers, i.e., when  $\delta \cong r$ , the growth of the boundary layer is considerably less rapid than on a flat plate, but the skin-friction coefficients are nevertheless only a few per cent greater than for the flat plate.

**Experimental Results. RECOVERY FACTOR.** Des Clers and Sternberg<sup>(27)</sup> have made measurements of the surface temperature of  $10^\circ$ -cones at supersonic speeds in the laminar, transitional, and turbulent

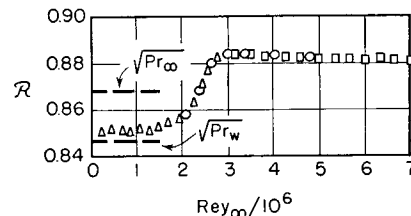


FIG. 27.18. Recovery factor for  $10^\circ$ -cone at  $M_\infty = 2.18$  (at surface). The Reynolds Number is measured along the surface from the tip of the cone (after des Clers and Sternberg).

ranges. Fig. 27.18 shows that the recovery factor rises smoothly from the laminar value to a value slightly greater than the fully developed turbulent value, then settles down to the turbulent value, which in the case shown was 0.881.

**HEAT TRANSFER.** Fig. 27.19 shows the results of Eber<sup>(22)</sup> for the local heat transfer coefficients on cones in the turbulent and transition ranges of Reynolds Numbers. The solid lines indicate the theoretical turbulent and laminar curves, based on the analyses of this and the preceding chapters for the case where  $T_w \cong T_{aw}$ .

Apart from the effect of the direction of heat transfer on the Reynolds Number of transition, there is an effect of  $T_w/T_\infty$  on the relation between  $Nu$ ,  $Rey$ , and  $Pr$ . This effect is unfortunately in the direction opposite to that predicted by Fig. 27.12. The general orders of magnitude of the data are seen, however, to be in agreement with the theoretical curves.

**TRANSITION.** As already mentioned, the direction of heat transfer produces substantial changes in the Reynolds Number of transition. This effect is shown even more strikingly by Fig. 27.20. These data

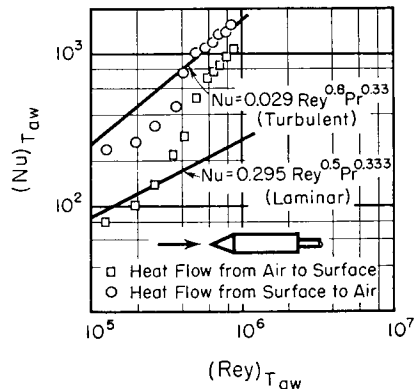


FIG. 27.19. Heat transfer for cone-cylinder at  $M_\infty = 2.87$ . The subscript  $(\ )_{Taw}$  signifies that the fluid properties are evaluated at the adiabatic wall temperature (after Eber).

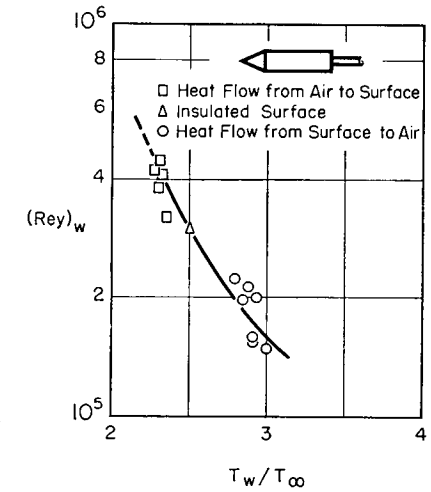


FIG. 27.20. Effect of heating and cooling on Reynolds Number of transition at  $M_\infty = 2.87$  (after Eber).

tend to confirm the results of the calculations of Lees concerning the stability of the laminar boundary layer—namely, that heat flux to the wall is stabilizing and heat flux away from the wall is destabilizing.

The influence of heat transfer increases as the initial turbulence level decreases, i.e., as the transition becomes more and more due to Tollmien-Schlichting waves.<sup>(38)</sup> For example, in tests at  $M_\infty = 1.61$  with a parabolic body of revolution having an adiabatic Reynolds Number of transition of  $11(10)^6$ , an increase to  $26(10)^6$  was achieved with  $(T_w - T_{aw})/T_{0\infty} = -0.1$ , and a decrease to  $3(10)^6$  with  $(T_w - T_{aw})/T_{0\infty} = 0.3$ . In free-flight tests of a cone on a missile, a value of  $90(10)^6$  was achieved.

## REFERENCES AND SELECTED BIBLIOGRAPHY

1. GOLDSTEIN, S. (ed.). *Modern Developments in Fluid Dynamics*. London: Clarendon Press (Oxford), 1938.
2. VAN DRIEST, E. R. Turbulent Boundary Layer in Compressible Fluids, *Jour. Aero. Sci.*, Vol. 18, No. 3 (1951), p. 145.
3. FORSTALL, W., JR., and SHAPIRO, A. H. Momentum and Mass Transfer in Coaxial Gas Jets, *Jour. App. Mech.*, Vol. 17, No. 4 (1950), p. 399.
4. VON KÁRMÁN, T. Turbulence and Skin Friction, *Jour. Aero. Sci.*, Vol. 1, No. 1 (1934), p. 1.
5. VON KÁRMÁN, T. Mechanical Similitude and Turbulence, *NACA Tech. Memo.*, No. 611 (1931).
6. PRANDTL, L., and TIETJENS, O. G. *Applied Hydro- and Aeromechanics*. New York: McGraw-Hill Book Co., Inc., 1934.
7. FALKNER, V. N. A New Law for Calculating Drag, *Aircraft Engineering*, Vol. 15, No. 169 (1943), p. 65.
8. TUCKER, M. Approximate Calculation of Turbulent Boundary-Layer Development in Compressible Flow, *NACA Tech. Note.*, No. 2337 (1951).
9. FRANKL, F. Heat Transfer in the Turbulent Boundary Layer of a Compressible Gas at High Speeds, and FRANKL, F., and VOISHEL, V. Friction in the Turbulent Boundary Layer of a Compressible Gas at High Speeds, *NACA Tech. Memo.*, No. 1032 (1942).
10. FRANKL, F., and VOISHEL, V. Turbulent Friction in the Boundary Layer of a Flat Plate in a Two-Dimensional Compressible Flow at High Speeds, *NACA Tech. Memo.*, No. 1053 (1943).
11. WILSON, R. E. Turbulent Boundary-Layer Characteristics at Supersonic Speeds—Theory and Experiment, *Jour. Aero. Sci.*, Vol. 17, No. 9 (1950), p. 585.
12. RUBESIN, M. W., MAYDEW, R. C., and VARGA, S. A. An Analytical and Experimental Investigation of the Skin Friction of the Turbulent Boundary Layer on a Flat Plate at Supersonic Speeds, *NACA Tech. Note.*, No. 2305 (1951).
13. VAN DRIEST, E. R. Turbulent Boundary Layer in Compressible Fluids, *Jour. Aero. Sci.*, Vol. 18, No. 3 (1951), p. 145.
14. DONALDSON, C. DUP. Some Considerations of Aerodynamic Heating, *NACA—University Conference on Aerodynamics*, NACA (1948).
15. TUCKER, M., and MASLIN, S. H. Turbulent Boundary-Layer Temperature Recovery Factors in Two-Dimensional Supersonic Flow, *NACA Tech. Note.*, No. 2296 (1951).
16. STALDER, J. R., RUBESIN, M. W., and TENDELAND, T. A Determination of the Laminar-, Transitional-, and Turbulent-Boundary-Layer Temperature-Recovery Factors on a Flat Plate in Supersonic Flow, *NACA Tech. Note.*, No. 2077 (1950).
17. WIMBROW, W. R. Experimental Investigation of Temperature Recovery Factors on Bodies of Revolution at Supersonic Speeds, *NACA Tech. Note.*, No. 1975 (1949).
18. HILTON, W. F. Wind-Tunnel Tests for Temperature Recovery Factors at Supersonic Velocities, *Jour. Aero. Sci.*, Vol. 18, No. 2 (1951), p. 97.
19. ECKERT, E., and WEISE, W. The Temperature of Unheated Bodies in a High-Speed Gas Stream, *NACA Tech. Memo.*, No. 1000 (1941).
20. JOHNSON, H. A., and RUBESIN, M. W. Aerodynamic Heating and Convective Heat Transfer—Summary of Literature Survey, *Trans. A.S.M.E.*, Vol. 71, No. 5 (1949), p. 447.
21. GOLDSTEIN, D. L., and SCHERRER, R. Design and Calibration of a Total-Temperature Probe for Use at Supersonic Speeds, *NACA Tech. Note.*, No. 1885 (1949).
22. EBER, G. R. Recent Investigation of Temperature Recovery and Heat Transmission on Cones and Cylinders in Axial Flow in the N.O.L. Aeroballistics Wind Tunnel, *Jour. Aero. Sci.*, Vol. 19, No. 1 (1952), p. 1.
23. VAN DRIEST, E. R. Turbulent Boundary Layer on a Cone in a Supersonic Flow at Zero Angle of Attack, *Jour. Aero. Sci.*, Vol. 19, No. 1 (1952), p. 55.

24. ECKERT, H. V. Simplified Treatment of the Turbulent Boundary Layer Along a Cylinder in Compressible Flow, *Jour. Aero. Sci.*, Vol. 19, No. 1 (1952), p. 23.
25. DONALDSON, C. DUP. On the Form of the Turbulent Skin-Friction Law and Its Extension to Compressible Flows, *NACA Tech. Note.*, No. 2692 (1952).
26. SCHERRER, R. Comparison of Theoretical and Experimental Heat-Transfer Characteristics of Bodies of Revolution at Supersonic Speeds, *NACA Tech. Rep.*, No. 1055 (1951).
27. DES CLERS, B., and STERNBERG, J. On Boundary-Layer Temperature Recovery Factors, *Jour. Aero. Sci.*, Vol. 19, No. 9 (1952), p. 645.
28. SLACK, E. G. Experimental Investigation of Heat Transfer Through Laminar and Turbulent Boundary Layers on a Cooled Flat Plate at a Mach Number of 2.4, *NACA Tech. Note.*, No. 2686 (1952).
29. STINE, H. A., and SCHERRER, R. Experimental Investigation of the Turbulent-Boundary-Layer Temperature-Recovery Factor on Bodies of Revolution at Mach Numbers from 2.0 to 3.8, *NACA Tech. Note.*, No. 2664 (1952).
30. COLES, D. Direct Measurement of Supersonic Skin Friction, *Jour. Aero. Sci.*, Vol. 19, No. 10 (1952), p. 717.
31. MONAGHAN, R. J. A Review and Assessment of Various Formulae for Turbulent Skin Friction in Compressible Flow, *Royal Aircraft Establishment Tech. Note Aero.*, No. 2182 (1952).
32. LADENBURG, R., and BERSHADER, D. Optical Studies of Boundary Layer Phenomena on a Flat Plate at Mach Number 2.35, *Princeton University Report*, NR061-020 (1952).
33. MONAGHAN, R. J. Further Comments on "Turbulent Boundary-Layer Characteristics at Supersonic Speeds," *Jour. Aero. Sci.*, Vol. 20, No. 2 (1953), p. 142.
34. MARTIN, J. J. Graphical Solution for "Turbulent Boundary Layer in Compressible Fluids," *Jour. Aero. Sci.*, Vol. 20, No. 2 (1953), p. 147.
35. CHAPMAN, D. R., and KESTER, R. H. Measurements of Turbulent Skin Friction on Cylinders in Axial Flow at Subsonic and Supersonic Velocities, *Jour. Aero. Sci.*, Vol. 20, No. 7 (1953), p. 142.
36. BRINICH, P. F., and DIACONIS, N. S. Boundary-Layer Development and Skin Friction at Mach Number 3.05, *NACA Tech. Note.*, No. 2742 (1952).
37. WILSON, R. E. Turbulent Boundary Layer Growth with Favorable Static Pressure Gradient at Supersonic Speeds, *Proceedings of the Second Midwestern Conference on Fluid Mechanics*, The Ohio State University (1952).
38. CZARNECKI, K. R., and SINCLAIR, R. Factors Affecting Transition at Supersonic Speeds, *NACA Research Memo.*, No. RM L53I18a (1953).
39. KAYE, J. Survey of Friction Coefficients, Recovery Factors, and Heat-Transfer Coefficients for Supersonic Flow, *Jour. Aero. Sci.*, Vol. 21, No. 2 (1954), p. 117.
40. O'DONNELL, R. M. Experimental Investigation at a Mach Number of 2.41 of Average Skin-Friction Coefficients and Velocity Profiles for Laminar and Turbulent Boundary Layers and an Assessment of Probe Effects, *NACA Tech. Note.*, No. 3122 (1954).

## Chapter 28

### BOUNDARY LAYERS IN TUBES AND IN THE PRESENCE OF SHOCK WAVES

#### 28.1. Introductory Remarks

In this chapter we shall round out the discussion of boundary layers in high-speed flow by considering two separate but important aspects of the subject: (i) flow in tubes, and (ii) the interaction between boundary layers and shock waves.

The subject of flow in tubes with friction and heat transfer was treated in Chapters 6, 7, and 8 from the one-dimensional point of view, in terms of certain average fluid properties ( $V$ ,  $T$ ,  $\rho$ , etc.) at each cross section. Friction and heat transfer are governed, however, by phenomena which are in essence *not* one-dimensional. A better understanding can be acquired, and the friction and heat transfer coefficients can be predicted analytically, only by considering the details of the boundary layer near the tube walls. It is appropriate, therefore, to reconsider the subject of internal flow after having studied, in the previous two chapters, the principal features of boundary layers in high-speed flow.

Some of the peculiar phenomena which appear near regions where both shock waves and boundary layers are present have already been mentioned briefly at several points in this book. In this chapter we shall discuss this important practical subject, the shock-boundary layer interaction, from a more unified point of view.

#### 28.2. Flow in Tubes

Although the mechanism of friction and heat transfer in tubes is associated with the radial variation of properties, it is convenient for practical calculations to express all results, both experimental and theoretical, in terms of the one-dimensional average properties  $V$ ,  $T$ ,  $p$ ,  $\rho$ ,  $p_0$ ,  $T_0$ , etc., as defined in Chapters 4 through 8. Thus, in what follows,  $V$  represents the "average velocity,"  $T$  the "average temperature," etc., at a given section of the pipe, and so on, the averages being found by treating the flow as completely one-dimensional. The pipe friction coefficient  $f$  is defined in Chapter 6.

**Friction Coefficient for Adiabatic, Subsonic, Turbulent Flow.** By applying the Kármán mixing-length hypothesis (Eqs. 27.50 and 27.51) to the case of turbulent compressible flow in a pipe, with the boundary layer filling the pipe, Deissler<sup>(2)</sup> has shown theoretically that the effects of compressibility, up to  $M = 1$ , are almost negligible with regard to the relationship between friction factor and Reynolds Number. At a pipe Reynolds Number of 6000, the theoretical effect is imperceptible up to  $M \leq 1$ , whereas at a pipe Reynolds Number of about 300,000 the pipe friction factor at  $M \leq 1.7$  is only about 5 per cent less than at  $M = 0$ .

These theoretical results have been fully confirmed by experiments for subsonic flow up to  $M = 1$ , the principal conclusion being that the incompressible friction formulas are applicable up to  $M = 1$ .<sup>(1,2,4)</sup> For example, Fig. 28.1,<sup>(1)</sup> based on measurements in long tubes at Mach Numbers up to unity, shows the measured friction coefficient to agree with the well-known Kármán-Nikuradse formula for incompressible flow, within the accuracy of the experiments.

**Friction Coefficient for Adiabatic, Supersonic Flow.** In supersonic flow the maximum  $L/D$  of pipe allowable before choking occurs is so small that in practice the flow never really approaches the fully developed condition. This difficulty is enhanced at supersonic speeds because the rates of change of all fluid properties are so large that, even with a boundary layer filling the pipe, the model of a fully developed flow would be inaccurate. For these reasons, the pipe friction factor computed from experimental tests by means of the one-dimensional formulas is called an *apparent friction coefficient*, inasmuch as it includes not only the effects of shearing stress at the wall, but also changes in momentum flux owing to alterations in shape of the velocity profile.

**LAMINAR FLOW NEAR INLET.** The boundary-layer flow near the inlet of a tube, where the boundary-layer thickness is small compared with the pipe radius, is more like the flow over a flat plate than like the flow in a pipe. Therefore, assuming that the flow enters the tube

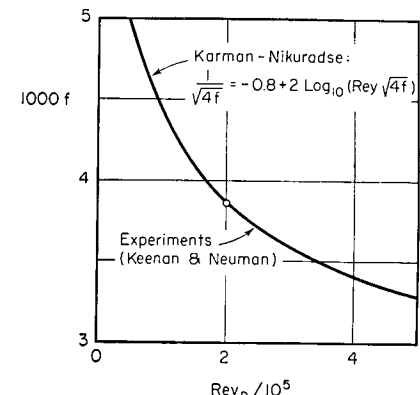


FIG. 28.1. Average apparent friction coefficient for subsonic flow in long tubes. The Mach Number in the tube varied from 0.3 near the inlet to 1.0 near the exit. The Reynolds Number is based on the average one-dimensional properties (after Keenan and Neumann).

smoothly and with little turbulence, the boundary layer may be expected to be laminar, irrespective of the value of  $Rey_D$  (diameter Reynolds Number), up to values of  $Rey_x$  (length Reynolds Number) of about  $10^6$ , the latter figure representing the Reynolds Number of transition for a flat plate.

Dimensional reasoning shows that both  $Rey_x$  and  $Rey_D$  are significant parameters near the tube entrance. When the boundary layer is thin and laminar, however, it may be further shown that the only parameter governing the flow, apart of course from  $M_1$ , is the combination

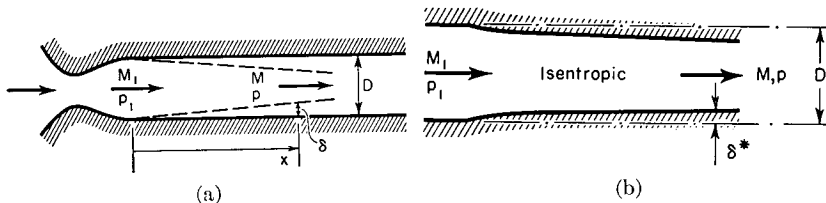


FIG. 28.2. Thin laminar boundary layer at tube inlet.

(a) Actual flow.  
(b) Approximate model.

$Rey_x/Rey_D^2$ . Referring to Fig. 28.2a, the flow near the inlet may be thought of as the combination of a viscous boundary layer and an isentropic core. The growth of the boundary layer reduces the cross-sectional area available for the core flow. In subsonic flow this reduction in area causes the Mach Number to increase and the pressure to fall; in supersonic flow the effects are just opposite. If we regard the pressure gradients as arising because of the reduction in the cross-sectional area of a stream-tube in the isentropic core, then the main physical effects may be explained in terms of the roughly analogous flow of Fig. 28.2b. Here there is isentropic flow in a tube of decreasing area, the diameter reduction being proportional to the displacement thickness  $\delta^*$  of the boundary-layer flow of Fig. 28.2a. Since the flow of Fig. 28.2b is governed by pressure forces and inertia forces, together with compressibility effects, we may write the physical equation

$$(p_1 - p) = \varphi(D, \delta^*, \rho_1, V_1, c_1)$$

By the principles of dimensional analysis, this physical equation may be expressed in the simpler form

$$\frac{p_1 - p}{\frac{1}{2} \rho_1 V_1^2} = \varphi(M_1, \delta^*/D)$$

But, in a laminar boundary layer on a flat plate,

$$\frac{\delta^*}{x} \sim \frac{1}{\sqrt{Rey_x}}$$

and hence

$$\frac{\delta^*}{D} = \frac{\delta^*}{x} \cdot \frac{x}{D} \sim \frac{1}{\sqrt{Rey_x}} \cdot \frac{Rey_x}{Rey_D} \sim \frac{\sqrt{Rey_x}}{Rey_D}$$

Therefore

$$\frac{p_1 - p}{\frac{1}{2} \rho_1 V_1^2} = \varphi(M_1, \frac{\sqrt{Rey_x}}{Rey_D})$$

which was to be proved.

Toong <sup>(11)</sup> has carried out lengthy theoretical calculations for the type of flow under consideration, starting with the differential equations of motion, and using methods similar to those of Chapter 26. The

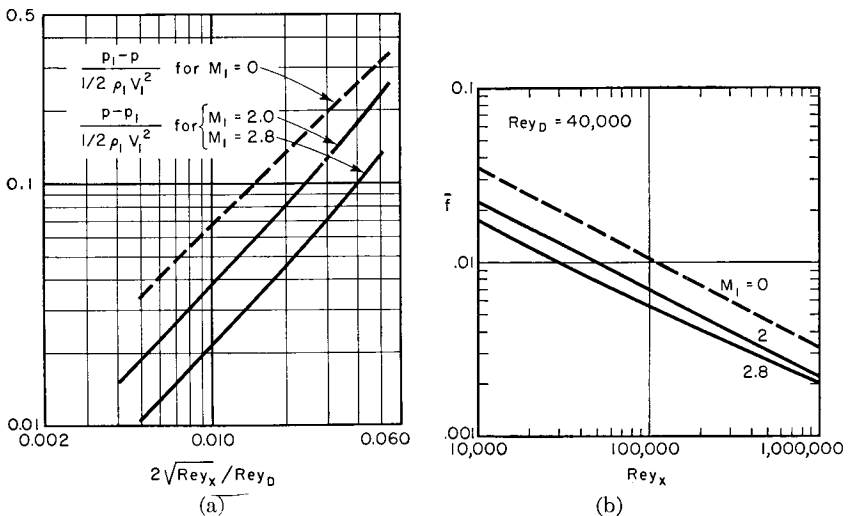


FIG. 28.3. Theoretical effects of thin laminar boundary layer near inlet of insulated tube. Reynolds Number is based on properties at section 1 (after Toong).

(a) Pressure changes.  
(b) Mean integrated apparent friction coefficient.

results are shown in Fig. 28.3. In Fig. 28.3a the results are in the form suggested by the foregoing physical equation. To make these results applicable to the one-dimensional analyses of Chapter 6 they may be converted to the form of Fig. 28.3b, which is for the specific  $Rey_D$  of 40,000. The ordinate is the mean integrated apparent friction coefficient between  $x = 0$  and  $x = x$ , defined by

$$\bar{f} \equiv \frac{1}{x} \int_0^x f \, dx$$

where  $f$  is the local apparent friction coefficient. On the basis of other analyses it may be expected that the curve of  $\bar{f}$  is nearly independent

of  $M_1$  for values of the latter between 0 and 1. It may be seen from Fig. 28.3b, therefore, that the values of  $\bar{f}$  for supersonic flow are of the order of half those for subsonic flow. This difference may be in part explained by the difference in the sign of the pressure gradient for subsonic flow and for supersonic flow; and in part by the fact that at supersonic speeds there is a considerable difference in temperature between the wall (where viscosity is most important) and at section 1 (the fluid properties of which are employed in the Reynolds Number).

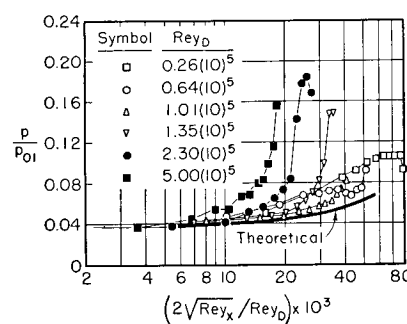


FIG. 28.4. Comparison of measured pressure distributions with theoretical results of Fig. 28.3a for laminar boundary layer,  $M_1 = 2.8$  (after Toong).

and seemingly chaotic variations in the pressure gradients. Some reasons for this behavior are discussed below.

**FLOW DOWNSTREAM OF TRANSITION POINT.** Theoretical calculations show that near the inlet of a tube the apparent friction coefficient is dependent on the rate of development of the velocity profile to as great a degree as it is on the rate of change of true skin-friction coefficient. During the transition of the boundary layer from a laminar flow to a turbulent flow, the rapid change from one velocity profile to another profile which is distinctly different in shape may therefore be expected to have radical effects on the apparent friction coefficient.

After the boundary layer has become completely turbulent some degree of order is probably restored to the variation of  $f$  with  $Rey_x$ , but it may be expected that both  $Rey_x$  and  $Rey_D$  are individually important.

The foregoing considerations indicate that in general there is no way of correlating frictional effects on the basis of a one-dimensional approach. Unfortunately, any other approach is too cumbersome for everyday calculations.

**EXPERIMENTAL RESULTS.** Typical experimental results<sup>(3)</sup> are summarized in Fig. 28.5 for tests in which  $M$  varied from about 2.5 at the tube inlet to about unity at the exit ( $x/D \cong 30$ ). Each shaded zone shows the range of experimental data, found with several tubes and

nozzles, for a given  $Rey_D$ . There is evidently a zone of laminar flow and a zone of turbulent flow, the dividing line being, approximately,  $Rey_x \cong 10^6$ . The negative apparent friction coefficients are most likely associated with a transition from a laminar to a turbulent boundary layer.

The general order of magnitude of the apparent friction factor is

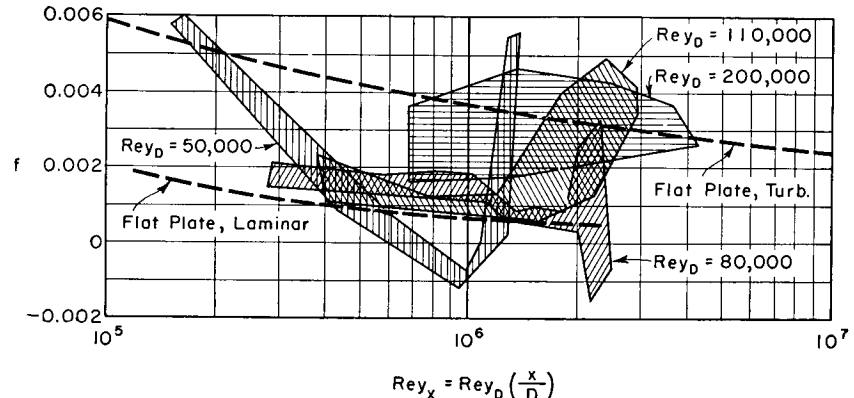


FIG. 28.5. Ranges of local apparent friction coefficients measured for flow in insulated tubes with  $M_1 = 2.5$  (after Kaye, Keenan, and Shoulberg).

comparable with that of subsonic flow, but the spread of data, for reasons given previously, is very wide.

The integrated apparent friction coefficients, representing the average value over a length of tube extending to about 30 or 40 diameters, of course shows much less spread.<sup>(1)</sup> For approximate calculations, an average value of the integrated coefficient of about 0.0025 may be used for reasonably long tubes.

**Recovery Factor for Subsonic Flow.**<sup>(5)</sup> Measurements near the end of a long insulated tube, with Mach Numbers ranging from about 0.3

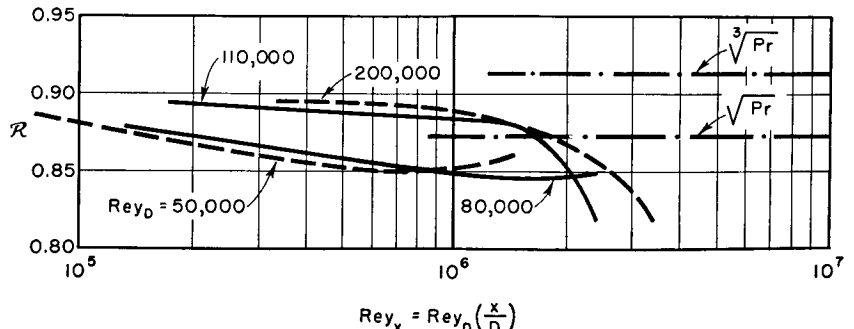


FIG. 28.6. Measured recovery factors for tests in which  $M$  varied from 2.5 at tube inlet to 1.0 at tube exit (after Kaye, Keenan, and Shoulberg).

to 1.0, and Reynolds Numbers in the range 25,000 to 35,000, indicate recovery factors (reckoned in terms of the difference between adiabatic wall temperature and one-dimensional average stream temperature) in the range between 0.87 and 0.91. This is generally in agreement with measurements of turbulent recovery factors on flat plates.

**Recovery Factor for Supersonic Flow.**<sup>(3)</sup> Fig. 28.6 shows the variation with distance along the tube of the measured recovery factor for four different Reynolds Numbers, with the Mach Number varying from 2.5 to 1.0 along the length of the tube. These recovery factors are, as before, defined in terms of the one-dimensional model,

$$\mathfrak{R} \equiv \frac{T_{aw} - T}{V^2/2c_p}$$

The lack of correlation of the experimental data, and the relatively wide variation in  $\mathfrak{R}$ , are indications that the one-dimensional model is too simple to draw together a variety of experimental data in meaningful relation to each other.

**Selection of Appropriate Temperature Differential for Definition of Heat Transfer Coefficients.** It will be recalled that the definition of the heat transfer coefficient  $\mathfrak{C}$  for compressible flow is arbitrary insofar as the choice of temperature differential is concerned. There are three simple possibilities in the choice of this differential for pipe flow:

- $T_w - T_0$ , the excess of the wall temperature over the one-dimensional stagnation temperature.
- $T_w - T_{aw}$ , the excess of the wall temperature over the adiabatic wall temperature.
- $T_w - T$ , the excess of the wall temperature over the one-dimensional static temperature.

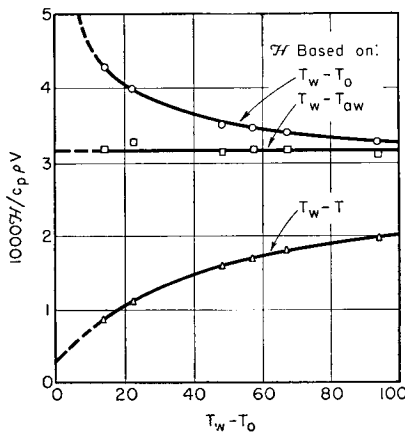


FIG. 28.7. Effect of choice of reference temperature difference on variation of Stanton Number with rate of heat transfer.  $Re_{D} = 24,500$  (after McAdams, Nicolai, and Keenan).

The theoretical arguments of Chapters 26 and 27 indicated that the second of these is the most appropriate inasmuch as it should lead to the simplest correlations. This is confirmed by the measurements<sup>(5)</sup>

on heat transfer rates for subsonic flow (from  $M = 0.5$  to  $M = 1$ ) in a long tube. As shown by Fig. 28.7, corresponding to tests at a fixed Reynolds Number, the dimensionless Stanton Number ( $\mathfrak{C}/c_p \rho V$ ) is independent of the rate of heat transfer only when  $\mathfrak{C}$  is based on the difference between  $T_w$  and  $T_{aw}$ . Therefore the most convenient definition of  $\mathfrak{C}$  is given by

$$\mathfrak{C} \equiv \frac{q}{T_w - T_{aw}}$$

**Heat Transfer in Subsonic Flow.**<sup>(4)</sup> Experiments involving simultaneous heat transfer and friction, with the Mach Number varying

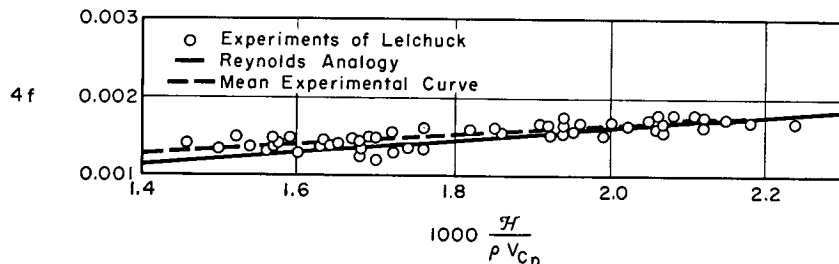


FIG. 28.8. Results of experiments involving combined friction and heat transfer at subsonic speeds, with  $M$  varying between 0 and 1 (after Lelchuk).

along the length of the tube, are shown by Fig. 28.8 to be in good agreement with Reynolds' analogy, thus indicating that the latter does not depend strongly on compressibility or on the rate of heat flux.

The experimental heat transfer data are shown separately in Fig. 28.9. Also shown on this chart is the predicted relation between the Nusselt Number and the product of  $Rey$  and  $Pr$ , found by employing the Reynolds' analogy. For Reynolds Numbers up to 100,000, the

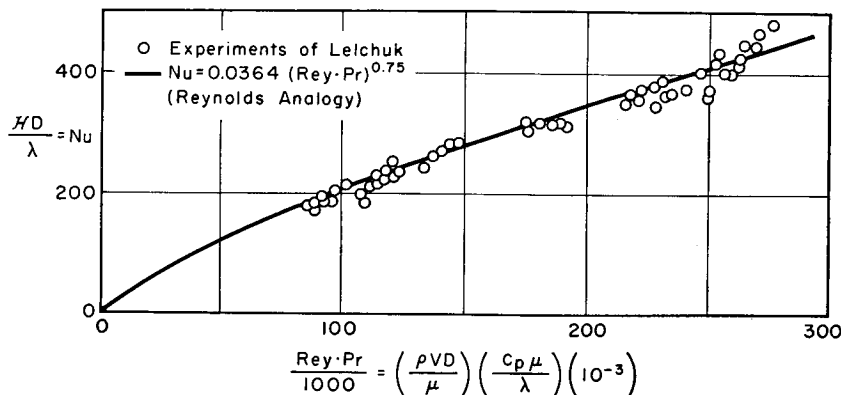


FIG. 28.9. Measurements of heat transfer in pipes with Mach Numbers varying between 0 and 1 (after Lelchuk).

pipe friction coefficient for incompressible flow may be accurately represented by

$$f \cong 0.079 \text{ Rey}^{-0.25}$$

The Reynolds' analogy yields

$$\frac{\xi c}{\rho V c_p} = \frac{f}{2} = 0.0395 \text{ Rey}^{-0.25}$$

which may be rearranged in the form

$$\frac{\xi c}{\rho V c_p} = \frac{\xi c D}{\lambda} \cdot \frac{\mu}{\rho V D} \cdot \frac{\lambda}{c_p \mu} = \frac{\text{Nu}}{\text{Rey} \cdot \text{Pr}} = \frac{0.0395}{\text{Rey}^{0.25}}$$

This may also be written as

$$\text{Nu} = 0.0395(\text{Rey} \cdot \text{Pr})^{0.75}(\text{Pr})^{0.25}$$

or, using  $\text{Pr} \cong 0.72$  for air, as

$$\text{Nu} = 0.0364(\text{Rey} \cdot \text{Pr})^{0.75}$$

This formula, which is plotted in Fig. 28.9, is seen to be in excellent agreement with the experimental results.

### 28.3. Shock-Boundary Layer Interactions in Supersonic Flow

In many problems of fluid dynamics it is possible to ignore viscous effects everywhere except in a thin layer adjacent to solid boundaries. Because the fluid is brought to rest at the boundary, however, the viscous stresses in the equation of motion are inevitably of the same order as the inertia stresses. Hence, they cannot be neglected in the aforementioned thin layer. This concept leads to a model of the flow past solid boundaries, invented by Prandtl, in which the pressure distribution is initially calculated as though the fluid were without viscosity and heat conduction, and subsequently the viscous effects at the wall are computed by boundary-layer theory.

Unless separation occurs, or unless there are extraordinary pressure gradients, the potential flow external to the boundary layer is substantially independent of the boundary-layer flow, except insofar as the potential flow streamlines are displaced outward from the wall owing to the displacement thickness of the boundary layer. This effect, however, is often negligible. The boundary-layer flow, on the other hand, depends strongly on the longitudinal pressure distribution established by the potential flow.

Shock waves, like boundary layers, are semi-discontinuities in which viscosity and heat conduction play a controlling role, the major difference being that the shock wave is considerably thinner than an ordinary

boundary layer, and therefore it creates prodigious pressure gradients.

When shock waves appear in the neighborhood of solid boundaries, they tend to impose such large pressure gradients on the boundary layer that the latter is necessarily distorted to a considerable extent. These effects on the boundary layer are, moreover, propagated both upstream and downstream through the subsonic portion of the boundary layer. The consequent changes in the boundary layer flow simultaneously act in such a manner as to propagate compression and expansion waves into the external flow. These in turn tend to change the original shock pattern. Thus there is likely to be a mutual interaction of considerable extent between the boundary layer flow and the external flow.

We shall consider in this article three examples of such interactions: (i) the reflection of oblique shocks from a boundary layer on a flat plate, (ii) the generation of shocks in a concave corner, and (iii) the generation of shocks at the leading edge of a wedge.

**Reflection of Oblique Shock from Flat Plate.** To best appreciate the effect of a boundary layer on the shock reflection, it is well first to review the types of reflection which occur in the total absence of boundary layers. If the turning angle through the shock is not too large, or if the initial Mach Number is not too small, regular reflection

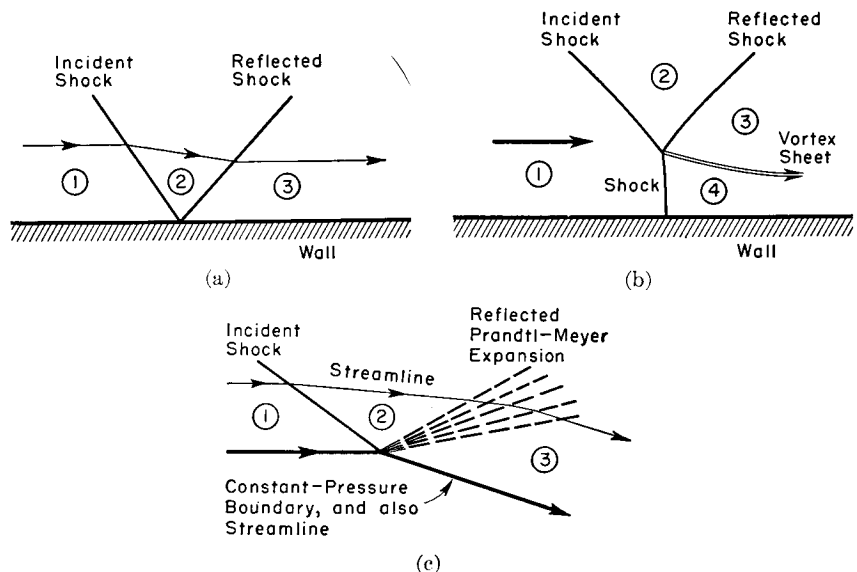


FIG. 28.10. Shock reflection in the absence of boundary layer.

- (a) Regular reflection from plane wall.
- (b) Mach reflection from plane wall.
- (c) Reflection from constant-pressure boundary.

(Fig. 28.10a) occurs when a shock is incident on a plane wall; the reflected wave is an oblique shock having the same turning angle as the incident shock. For either excessively large turning angles or excessively small initial Mach Numbers, regular reflection is impossible (for reasons given in Chapter 16), and "Mach reflection" occurs, as illustrated by Fig. 28.10b. In this case there is a triple-shock intersection, with a surface of discontinuity proceeding from the triple point, and the lower leg is necessarily normal at the wall. When a shock is incident on a free boundary at constant pressure (Fig. 28.10c) it reflects in unlike sense. That is, the reflected wave is a Prandtl-Meyer expansion,

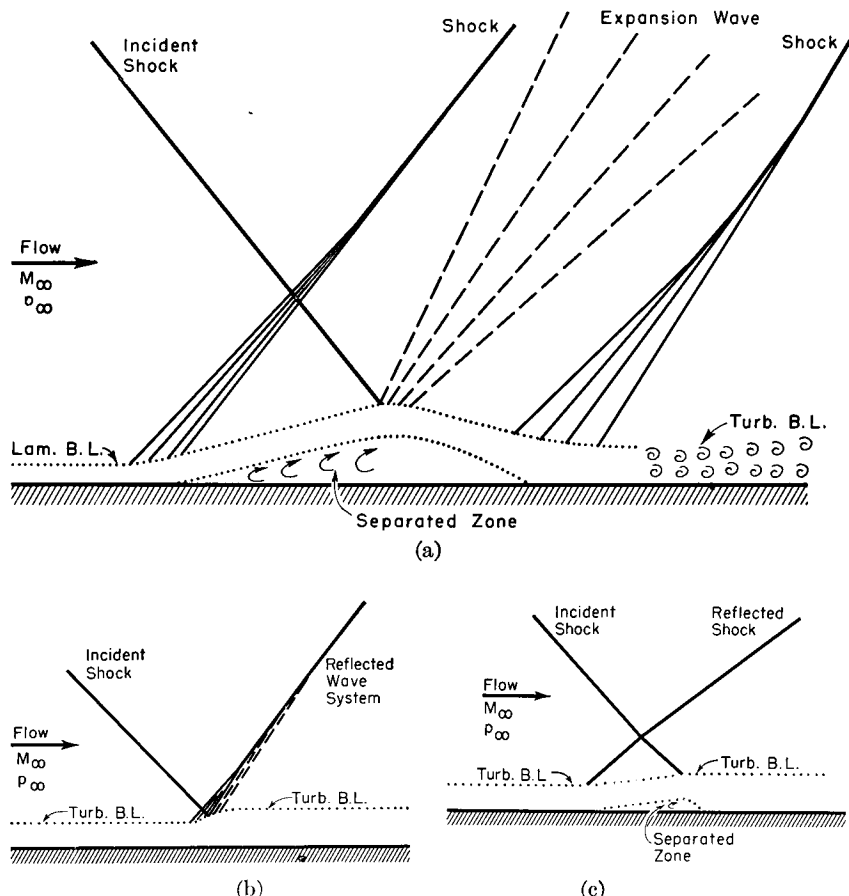


FIG. 28.11. Typical features observed in reflection of shock from walls with boundary layers.

- (a) Laminar boundary layer.
- (b) Turbulent boundary layer.
- (c) Turbulent boundary layer with separated zone.

the pressure change across the expansion being equal and opposite to the pressure change across the incident shock.

**LAMINAR BOUNDARY LAYER.** Several typical features observed in experiments where an oblique shock is incident on a laminar boundary layer are illustrated schematically in Fig. 28.11a. The regular reflection of Fig. 28.10a would impose on the boundary-layer flow pressure gradients which the latter could not negotiate. Therefore, a completely different pattern is established in which the pressure begins to rise in the boundary layer considerably upstream of the point of incidence of the shock. This pressure rise in turn leads to a thickening of the boundary layer, and the resulting streamline curvature generates compression wavelets which merge into a "reflected shock" whose apparent origin is upstream of the original point of incidence. If the adverse pressure gradient upstream of the point of incidence is sufficiently large, the boundary layer may even separate, thus augmenting the strength of the first reflected shock. The latter has the additional effect of modifying the incident shock at the point of intersection of the two. Since the motions in the separated zone are relatively small, it may be regarded approximately as a region of constant pressure. Consequently, the incident shock, as in Fig. 28.10c, reflects from this zone as a Prandtl-Meyer expansion. The latter turns the flow toward the plate again, producing reattachment of the boundary layer. Often the turning angle through the expansion wave is so large that the flow tends to go into the plate, and the subsequent adjustment of flow direction to the direction of the plate generates a second "reflected shock" whose apparent origin is well downstream of the original point of incidence. The boundary layer often becomes turbulent immediately downstream of this second reflected shock.

**TURBULENT BOUNDARY LAYER.** For our present purpose, the most significant difference between a laminar and a turbulent boundary layer is that, as a result of momentum being transferred into the layer by turbulent exchange, the turbulent layer is much better able to negotiate adverse pressure gradients. The interaction between the shock and boundary layer (Fig. 28.11b) is consequently much smaller than in the case of the laminar boundary layer. There is a moderate thickening of the boundary layer, with some wavelets generated upstream of and some downstream of the point of incidence. However, the extent of upstream and downstream influence is relatively small, and so the reflection of a shock from a turbulent layer may be regarded as corresponding closely to the regular reflection of Fig. 28.10a.

Fig. 28.11c shows another form of reflection sometimes observed with a turbulent boundary layer, especially when there is a slight separation of the boundary-layer flow. The separation gives rise to a "reflected"

shock which originates upstream of the point of incidence, and the shock pattern then takes on a bifurcated form immediately adjacent to the boundary layer.

EXPERIMENTAL RESULTS. Fig. 28.12<sup>(8)</sup> shows typical pressure distributions at the wall for shocks reflecting from laminar and turbulent layers.

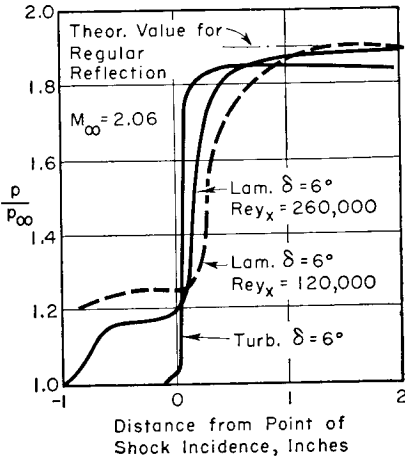


FIG. 28.12. Measured pressure distributions on a plane wall near the point of incidence of an oblique shock with turning angle  $\delta$  and Mach Number 2.06 (after Barry, Shapiro, and Neumann).

thickness is increased; that is, the extent of disturbance increases as the Reynolds Number for a given position on the flat plate is decreased.

PHOTOGRAPHS OF FLOW PATTERNS. Schlieren photographs of the reflection from a laminar layer are shown in Fig. 28.13. It may be seen that the entire flow pattern is quite sensitive to the thickness of the boundary layer.

The reflection from a turbulent layer (Fig. 28.14a), on the other hand, occurs with scarcely any disturbance of the boundary layer. Fig. 28.14b shows a number of interesting effects which are described in the caption to the figure.

Fig. 28.15 shows the results of an interferometric study of the reflection from a laminar layer. This figure should be compared with Figs. 28.11a and 28.13.

An example of Mach reflection from a turbulent boundary layer is shown in Fig. 28.16.

**Generation of Shock in Concave Corner.** Since the flow in the neighborhood of a concave corner is composed of a layer of subsonic flow on

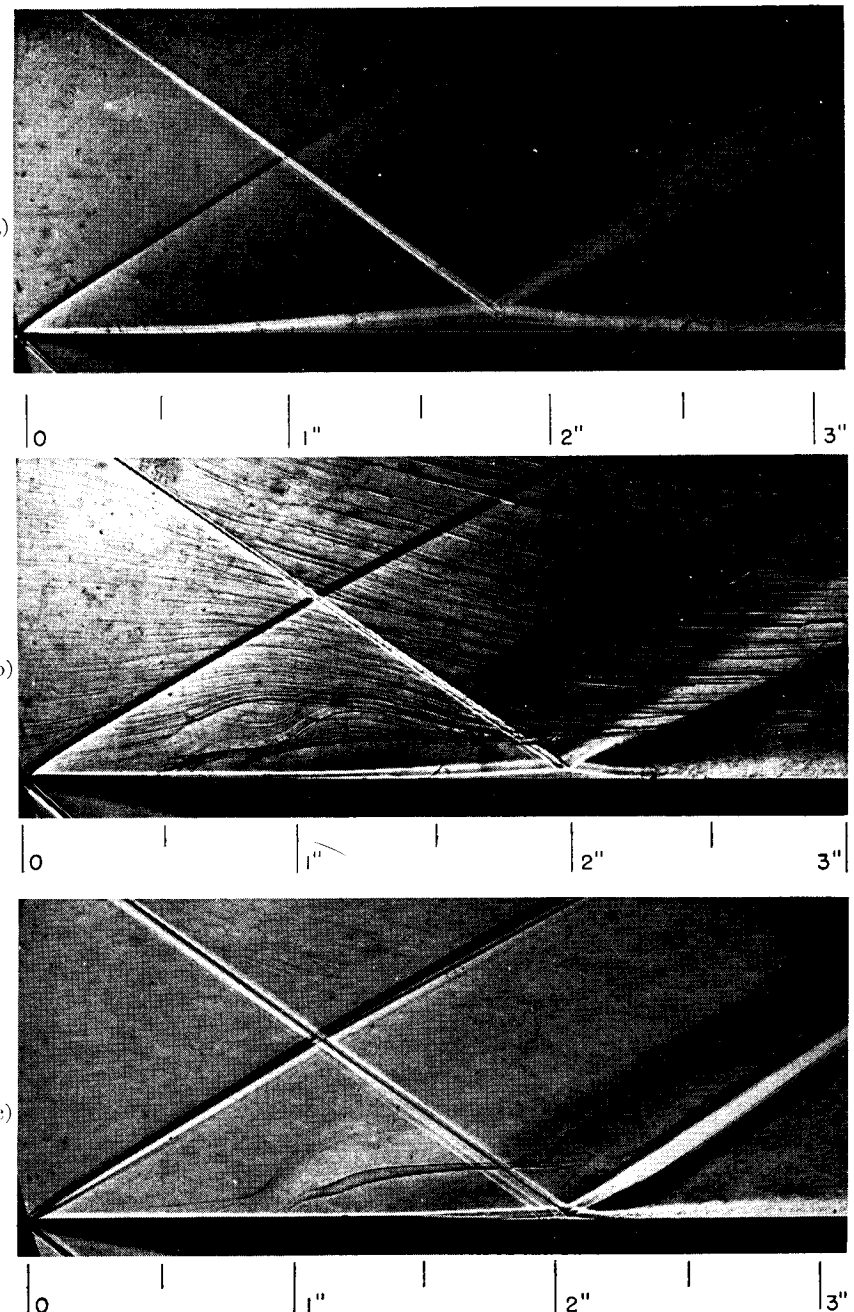


FIG. 28.13. Schlieren photographs of oblique shock (6° turning angle) incident on flat plate with laminar boundary layer,  $M_\infty = 2.06$ . Numbers below photographs indicate distance from leading edge, in inches (after Barry, Shapiro, and Neumann).

- (a)  $Re_x = 120,000$  at point of incidence.
- (b)  $Re_x = 260,000$  at point of incidence.
- (c)  $Re_x = 630,000$  at point of incidence.

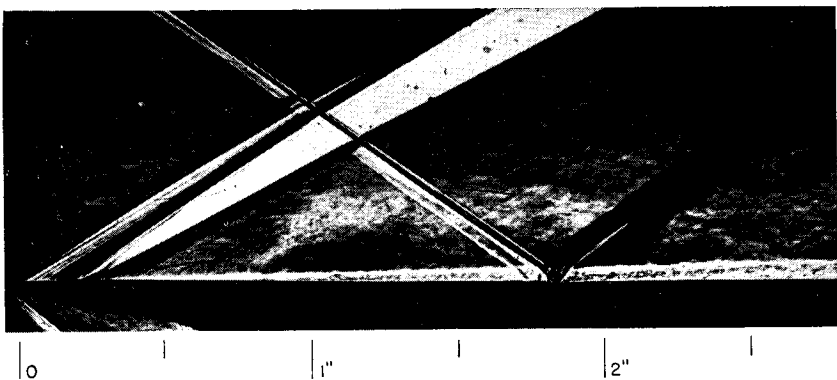


FIG. 28.14a. Schlieren photograph of oblique shock ( $6^\circ$  turning angle) incident on flat plate with turbulent boundary layer,  $M_\infty = 2.06$ . Boundary layer made turbulent by means of wire trip near leading edge of plate (after Barry, Shapiro, and Neumann).

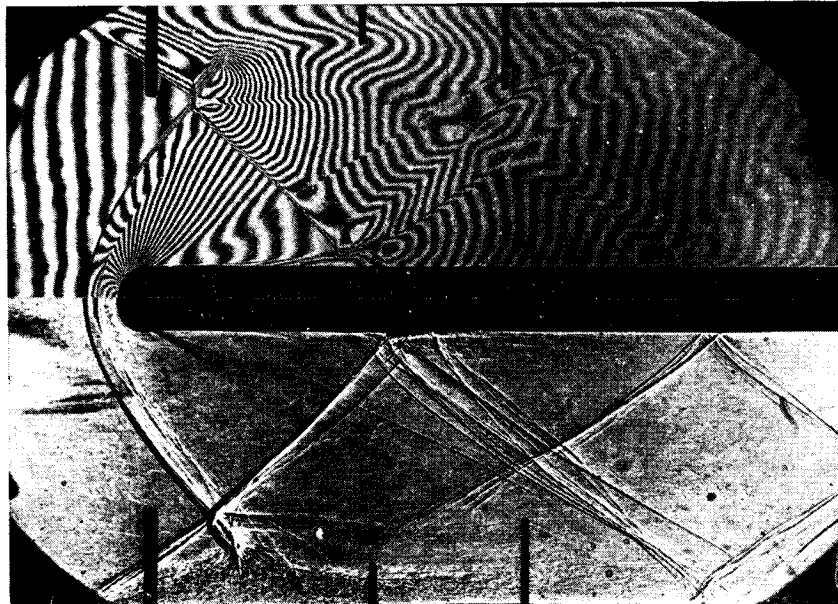


FIG. 28.14b. Composite schlieren and interferometer photograph of flow past two-dimensional flat plate with semi-circular nose. Easily seen are the detached bow wave, the boundary-layer separation and its subsequent reattachment near the nose, and the shock-turbulent boundary layer interactions on the plate and tunnel walls. The oblique shocks originating from the tunnel walls upstream of the plate are generated by the boundary-layer separation where the detached bow wave is incident on the tunnel walls. Note the vortex sheet generated at the intersection of the bow shock with the oblique shock generated at the wall (after Ladenburg and Bershad).

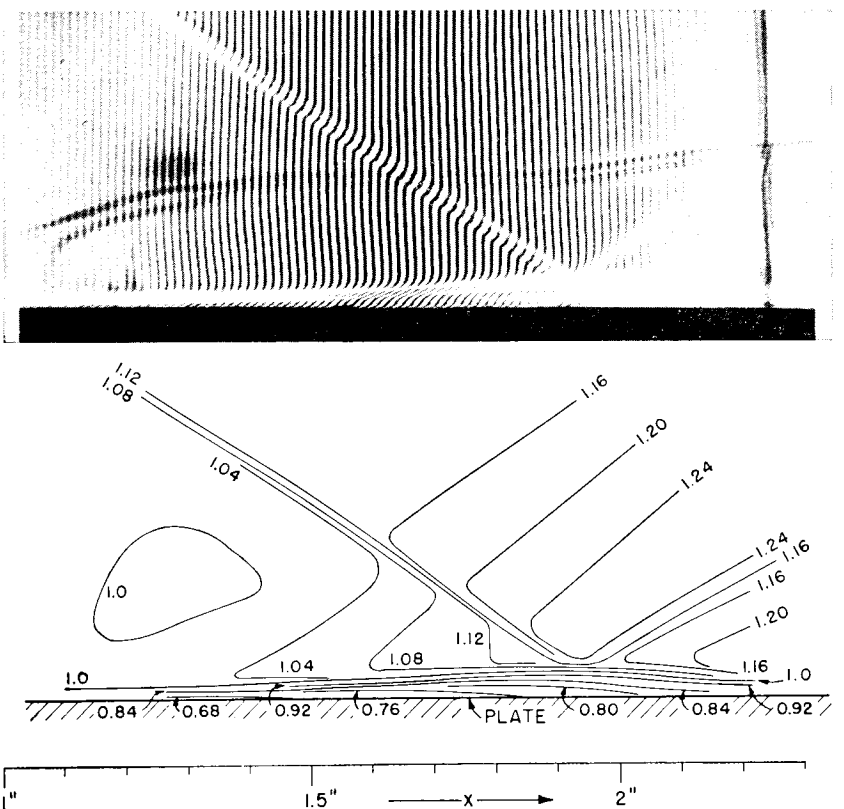
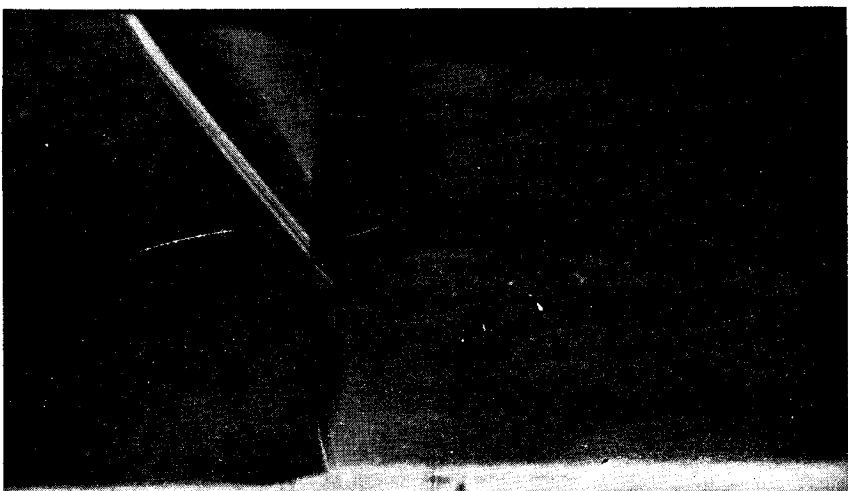


FIG. 28.15. Interferometric study of oblique shock ( $3^\circ$  turning angle) incident on flat plate with laminar boundary layer,  $M_\infty = 2.06$ . Upper part of figure shows interferogram. Lower part shows contours of constant density found from analysis of interferogram, the numbers on the curves representing the ratio of the local density to the free-stream density upstream of the incident shock (after Barry, Shapiro, and Neumann).

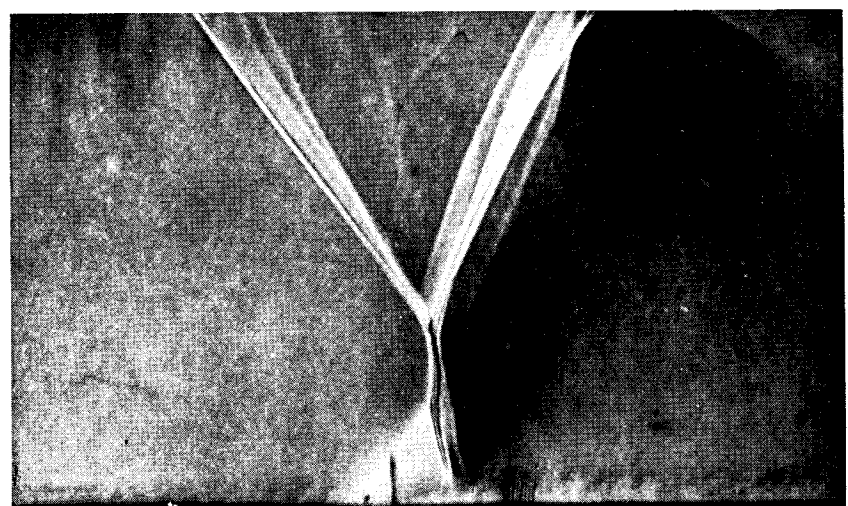
top of which is a layer of supersonic flow, it is well to begin by considering the individual features of the two types of flow. For simplicity, we shall at first ignore viscous effects. With a purely supersonic flow, all streamlines undergo equal turning angles across an oblique shock originating at the corner (Fig. 28.17a). With a purely subsonic inviscid flow, on the other hand, the corner is a stagnation point, and the streamlines are approximately hyperbolas which approach the two wall directions asymptotically (Fig. 28.17b).

The actual generation of a shock at a corner must have some aspects of both patterns discussed above, together with additional effects owing to viscosity in the boundary layer.

Typical wave patterns for laminar and turbulent layers are shown in Fig. 28.18, and the corresponding wall-pressure distributions are shown



(a)



(b)

FIG. 28.16. Schlieren photographs of Mach reflection from turbulent layer, flow left to right (after Liepmann, Roshko, and Dhawan).

- (a) Knife edge parallel to flow.
- (b) Knife edge normal to flow.

in Fig. 28.19.<sup>(12)</sup> For both types of layers the apparent origin of the shock is upstream of the corner itself, the shock is formed from the coalescence of compression wavelets generated in a region of pressure rise and consequent boundary-layer thickening, and there is a net increase in boundary-layer thickness. The flattening of the pressure-distribution curve for the laminar layer just before the curve rises sharply upward is an indication of a separated region near the wall where the pressure is nearly uniform.

Schlieren photographs<sup>(12)</sup> corresponding to the pressure distributions of Fig. 28.19 are shown in Figs. 28.20a and 28.20b. Fig. 28.20b shows evidence of a small separated region and indicates also that the boundary layer becomes turbulent a short distance downstream of the corner.

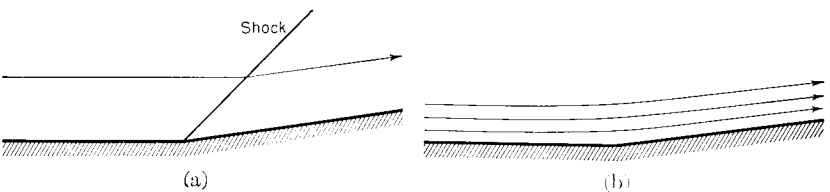
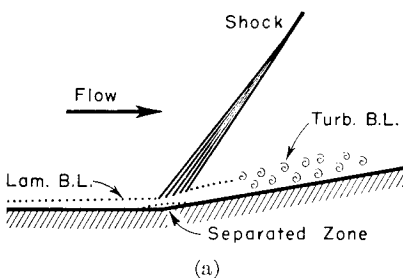
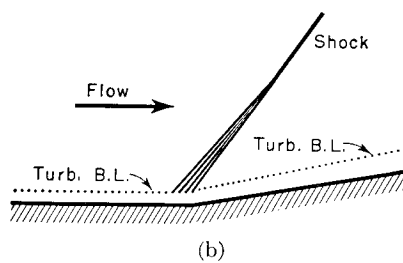


FIG. 28.17. Effect of concave corner in inviscid flow.

- (a) Supersonic.
- (b) Subsonic.



(a)



(b)

FIG. 28.18. Typical features observed in generation of shock in concave corner.

- (a) Laminar.
- (b) Turbulent.

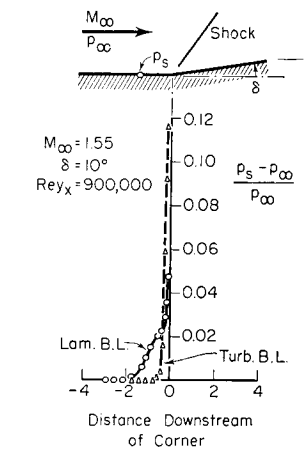


FIG. 28.19. Measured surface pressure distributions in neighborhood of concave corner (after Liepmann, Roshko, and Dhawan).

The thickening of the laminar layer (Fig. 28.20b) is seen to be markedly greater than that of the turbulent layer.

With a large turning angle in the corner,<sup>(14)</sup> the separation point moves well upstream of the corner and there is a large separated zone. The total turning of the stream occurs in two phases: (i) a turning produced by the shock generated at the point of separation, and (ii) a subsequent turning produced by the corner itself. The distance at which the separation point is located upstream of the corner is determined by the requirement that the maximum pressure rise supportable

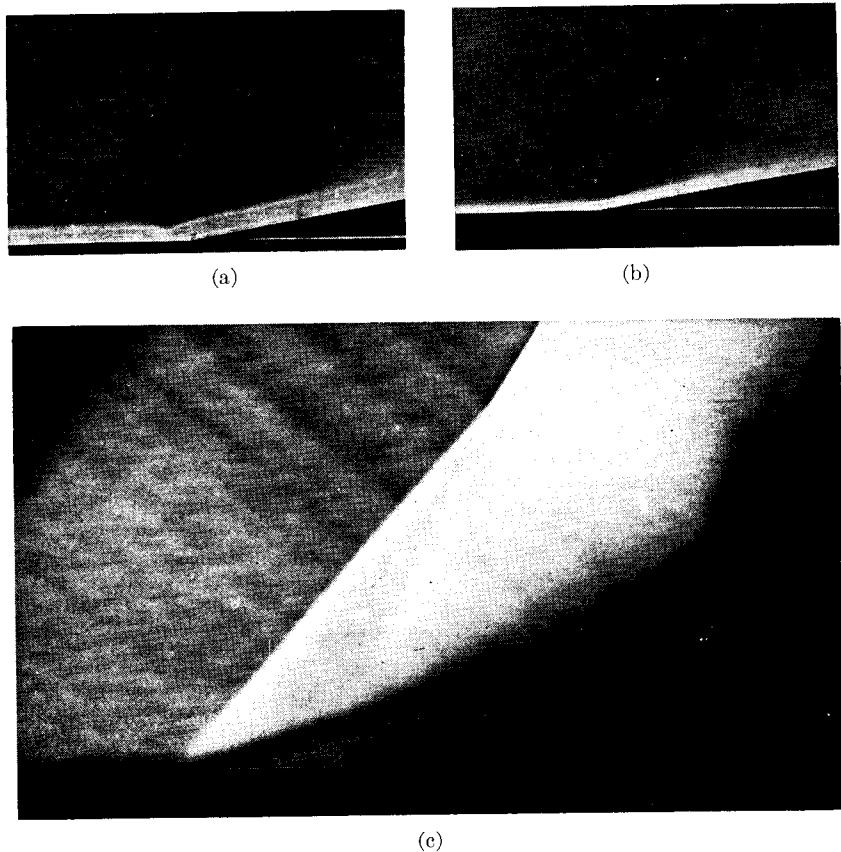


FIG. 28.20. Schlieren photographs of generation of shock in concave corner. Flow left to right.

- (a) Turbulent layer,  $M_\infty = 1.55$ , for experiment of Fig. 28.19 (after Liepmann, Roshko, and Dharwan).
- (b) Laminar layer,  $M_\infty = 1.55$ , for experiment of Fig. 28.19 (after Liepmann, Roshko, and Dharwan).
- (c) Turbulent layer,  $M_\infty = 1.56$ , with large turning angle (Institute of Aerophysics, University of Toronto).

by the boundary layer must be equal to the pressure rise produced by the shock which is generated as a result of the separation of the layer.

**Generation of Shock by Wedge.** The wedge is usually thought of as a shape giving a "clean" flow pattern with a single shock (Fig. 28.21a),

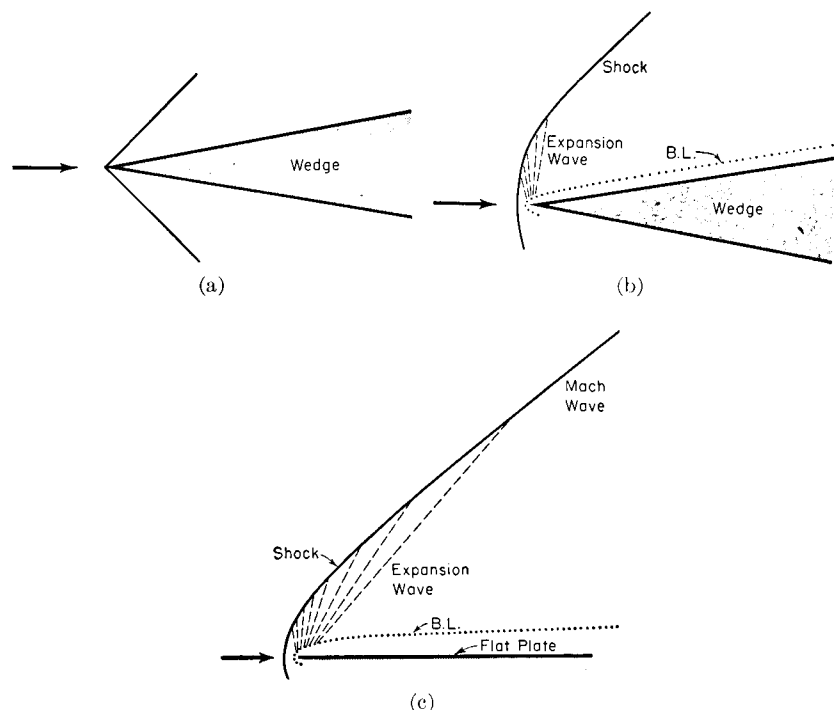


FIG. 28.21. Effect of boundary layer near leading edge of wedge.

- (a) Flow without viscosity.
- (b) Flow with viscosity.
- (c) Flow with viscosity near leading edge of flat plate.

and surface pressures on the wedge are often used for measuring stream direction and Mach Number.

However, there is a boundary layer on the wedge which also extends slightly ahead of the apex, and this boundary layer produces strong streamline curvatures near the apex. Consequently, the flow pattern and pressure distribution immediately adjacent to the apex are anything but simple. Fig. 28.21b shows features sometimes observed in such flows. The shock tends to be strongly curved near the apex, and is asymptotically weakened to the theoretical shock strength corresponding to Fig. 28.21a by means of expansion wavelets generated by the streamline curvature associated with formation of a viscous layer. In using

the wedge for making measurements, therefore, it is important not to place pressure taps too near the apex.

For similar reasons, the leading edge of a flat plate aligned with the flow generates a curved shock which is weakened by expansion wavelets until only a Mach wave remains (Fig. 28.21c).

#### 28.4. Shock-Boundary Layer Interactions in Transonic Flow

In Chapter 22 we discussed the question of whether the appearance of shocks in transonic flow over a curved surface was initiated by viscous effects in the boundary layer, or whether the shocks would appear even in an inviscid fluid. Whatever the reason for their appearance, it is now well established by experiment that, when the shocks do appear, the entire flow pattern is sensitive to viscous effects as the result of an interaction between the shock waves and the boundary layer.

**Laminar Boundary Layer.** Fig. 28.22 shows a typical flow pattern for slightly supersonic flow over a curved surface. There is considerable

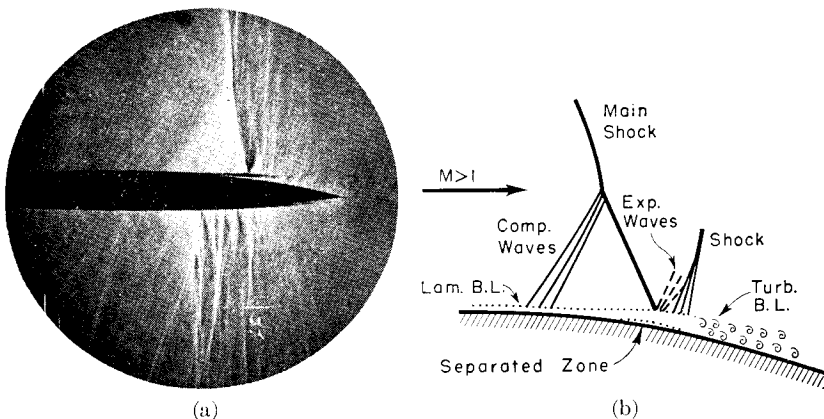


FIG. 28.22. Interaction of shock and laminar boundary layer on profile in transonic flow (after Becker, NACA).

- (a) Schlieren photograph.
- (b) Schematic flow pattern.

resemblance between this pattern and the corresponding pattern for a shock incident on a flat plate, except that in the present case the shock is of undetermined origin and strength. The main incident shock is right running; i.e., it seems to originate at the sonic line, and it is nearly normal. Thickening of the boundary layer upstream of the point of incidence of the main shock generates compression wavelets which end on the main shock, giving a typical *lambda* pattern. As a result of

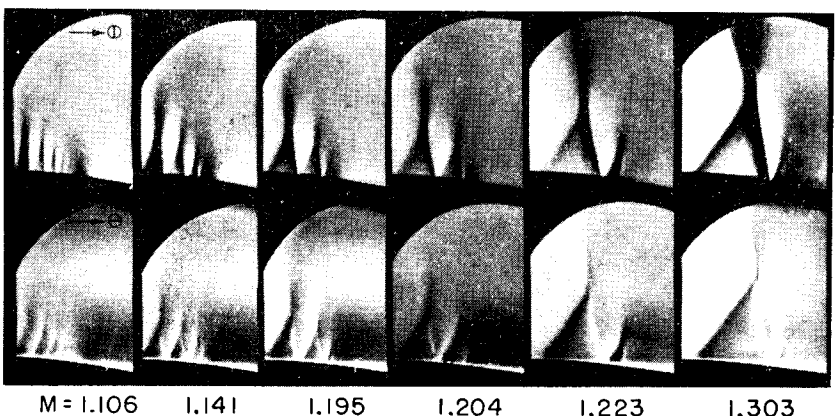


FIG. 28.23. Schlieren photographs showing effect of Mach Number on shock-laminar boundary layer interaction near curved profile in transonic flow. Reynolds Number at shock  $\cong 1.3(10^6)$ . Mach Number for each flow pattern refers to a point on profile just upstream of first shock. Flow left to right. In upper series of photographs the knife edge is normal to flow; in lower series it is parallel to flow (after Ackeret, Feldmann, and Rott).

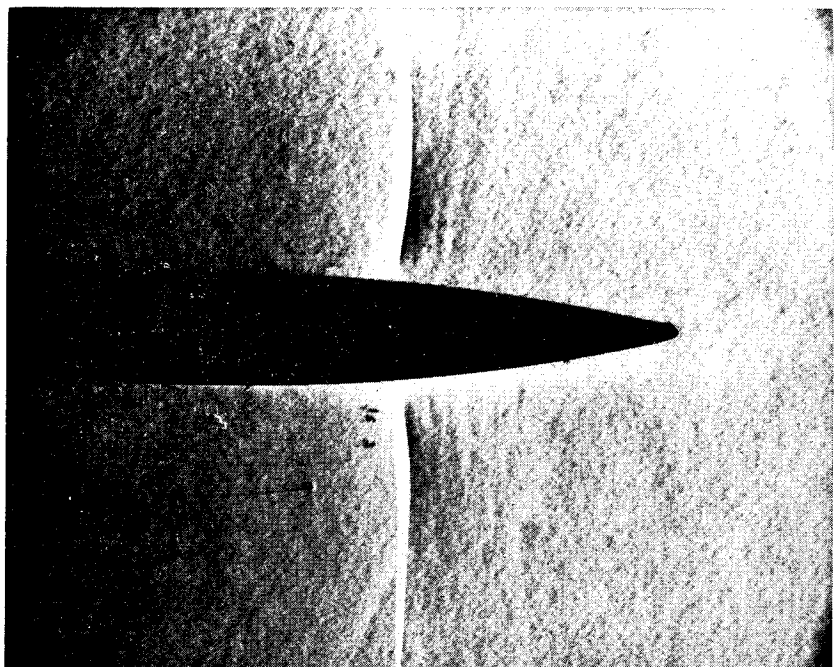


FIG. 28.24. Schlieren photograph showing interaction of shock and turbulent boundary layer near trailing edge of profile in transonic flow. Flow left to right (after Liepmann).

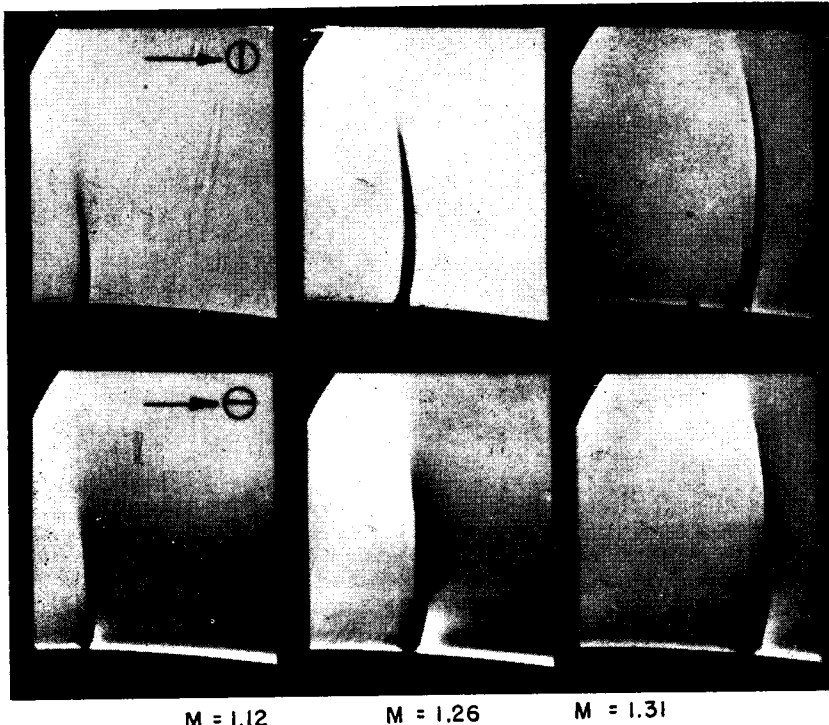


FIG. 28.25. Schlieren photographs showing effect of Mach Number on interaction between shock and turbulent boundary layer on profile in transonic flow. Reynolds Number at shock =  $2.7(10)^6$ . Mach Number for each flow pattern refers to a point on profile just upstream of shock. Flow left to right. In upper series of photographs the knife edge is normal to the flow; in lower series it is parallel (after Ackeret, Feldmann, and Rott).

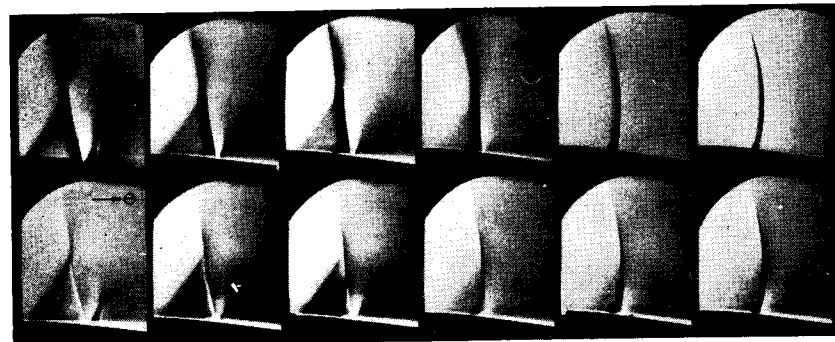


FIG. 28.26. Schlieren photographs showing effect of Reynolds Number on flow pattern in transonic flow. Mach Number for each flow pattern refers to a point on profile just upstream of first shock. Flow left to right. In upper series of photographs the knife edge is normal to the flow; in lower series it is parallel (after Ackeret, Feldmann, and Rott).

separation of the boundary layer, a "deadwater" zone is formed, and the main shock reflects from this region as a Prandtl-Meyer expansion. In the subsequent adjustment of the stream to the direction of the surface, compression wavelets are generated. There is a considerable net thickening of the boundary layer as the result of the interaction.

The effects on the pattern of variations in Mach Number, while the Reynolds Number is held constant, are illustrated in Fig. 28.23.<sup>(6)</sup> For very low supersonic Mach Numbers, there is a series of shocks followed by rarefactions. As the Mach Number increases, the number of such shocks is reduced until finally only one remains. A further increase in Mach Number tends to make all the waves stronger and of greater extent.

**Turbulent Boundary Layer.** Fig. 28.24 shows a typical interaction of a shock with a turbulent boundary layer. The shock is seen to be nearly normal, and the effect on the boundary layer to be not large.

As the Mach Number is increased, with Reynolds Number held constant, Fig. 28.25<sup>(6)</sup> shows that there is no change in the nature of the flow pattern, but rather a strengthening and lengthening of the shock. The latter effects are due most likely to the nature of the external flow rather than to viscous effects.

**Effect of Reynolds Number.** Fig. 28.26 gives striking confirmation of the importance of viscous effects in transonic flow. The series of photographs was taken at substantially constant Mach Number, and over a range of Reynolds Numbers for which the boundary layer changed from laminar to turbulent. The flow pattern is seen to change slowly from that corresponding to a laminar layer to that corresponding to a turbulent layer. Since turbulent layers are less susceptible than laminar layers to modification by adverse pressure gradients, it is plausible to suppose that the flow pattern with the turbulent layer resembles the more closely of the two the pattern which would be obtained with an inviscid fluid.

## 28.5. Normal Shocks in Ducts

Normal shocks produce pressure gradients considerably greater than those produced by oblique shocks, and so the shock-boundary layer interaction is understandably intensified when normal shocks are present.

When a "normal" shock is introduced into a duct by controlling the back pressure, it is found to assume one of several possible configurations. If the boundary layer is quite thin, there exists a single nearly normal shock over most of the duct, with bifurcated ends as the result of boundary layer separation, illustrated by Fig. 28.27a. With a thicker boundary layer (Fig. 28.27b), there is a series of such bifurcated normal

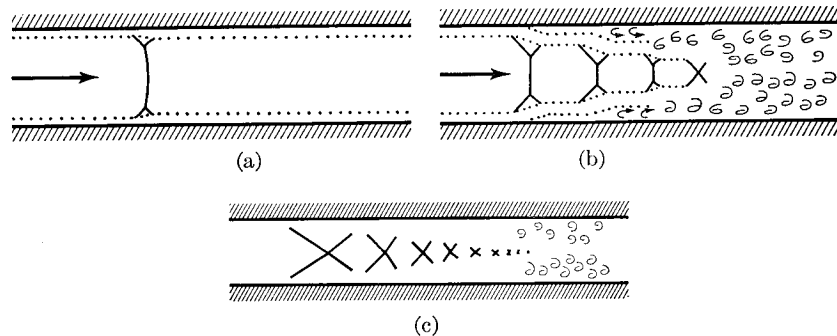


FIG. 28.27. Normal shocks in tubes.

(a) Thin boundary layer.  
(b), (c) Thick boundary layers.

shocks, with the normal segment growing progressively shorter, until finally the stream is entirely subsonic and the duct cross section is ultimately refilled by the stream as the result of turbulent mixing. For still thicker boundary layers (Fig. 28.27c), the normal parts of the multiple shocks disappear altogether because of the great boundary-layer separation, and the "normal" shock extends over a great distance.

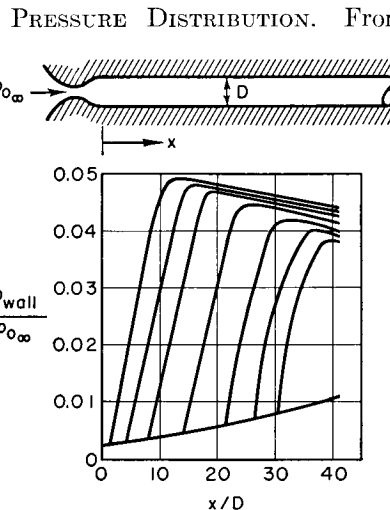
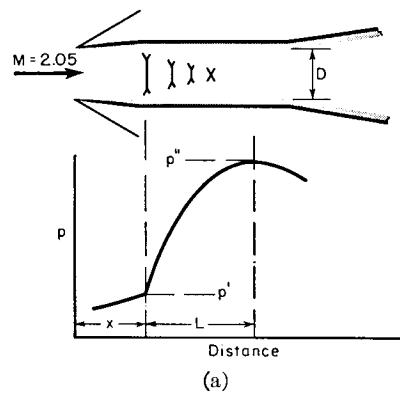
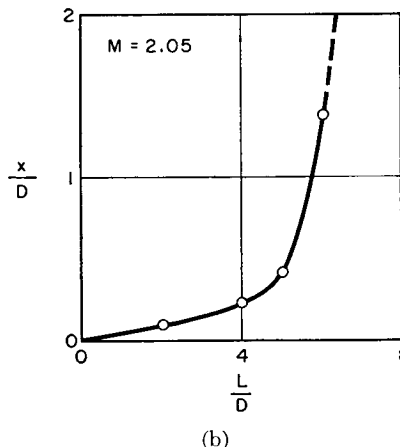


FIG. 28.28. Surface pressure distribution caused by normal shock in duct (after Neumann and Lustwerk).

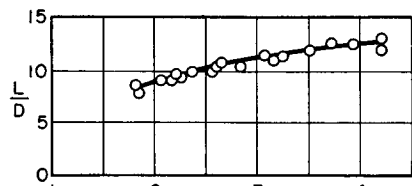
asymptotically a distance of about eight duct diameters as the boundary-layer thickness becomes very large. Additional data<sup>(9)</sup> for ducts with very thick boundary layers are shown in Fig. 28.29c. These data show



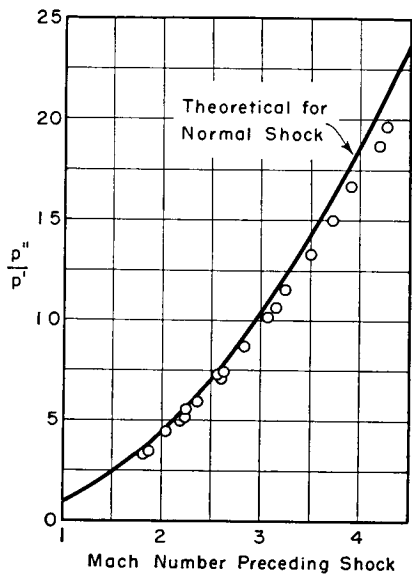
(a)



(b)



(c)



(d)

FIG. 28.29. Measured parameters for normal shock in duct (after Neumann and Lustwerk).

(a) Nomenclature.

(b) Effect of boundary-layer thickness on shock length.

(c) Effect of Mach Number on shock length (with thick boundary layer).

(d) Comparison of measured with theoretical pressure rise.

the  $L/D$  of the shock to vary from about 8 at  $M = 1.8$  to about 13 at  $M = 4.2$ .

**PRESSURE RISE THROUGH SHOCK.** We have just seen that the normal shock in a duct may extend over many duct diameters because of boundary-layer separation and that it may have a very different appearance from a true normal shock. However, when the governing physical equations of the normal shock are reviewed, and when we also remember that the skin-friction forces in a separated boundary layer are very small, it is to be expected that the over-all rise in pressure through

the shock should be substantially the same as for the idealized normal discontinuity. Experimental data<sup>(9)</sup> confirm this reasoning (Fig. 28.29d).

**SUPersonic DIFFUSERS.** An understanding of the actual configurations of normal shocks in ducts proves to be of considerable practical significance. For example, Fig. 28.30<sup>(9)</sup> shows how normal-shock diffusers may be improved in efficiency by providing a sufficient length of constant-area duct in which the "normal" shock may occur. Without this length, the stream does not fill the cross section as it enters the diverging subsonic diffuser. This may either produce inefficient subsonic diffusion, or it may produce locally a supersonic stream of even higher Mach Number than the one which originally entered the diffuser.

FIG. 28.30. Improvement of supersonic diffuser efficiency by incorporating a constant-diameter section of sufficient length to allow the normal shock to be completed (after Neumann and Lustwerk).

Fig. 28.31 shows the complicated nature of the flow in the converging portion of a supersonic diffuser.



FIG. 28.31. Schlieren photograph of flow in converging portion of supersonic diffuser. Flow left to right (Krenkel, M.I.T. Gas Turbine Laboratory).

## 28.6. Boundary-Layer Separation Produced by Shock Waves

Many of the shock-boundary layer interactions for the different configurations discussed in this chapter display a common feature, namely, a separation of the boundary layer as a result of the pressure rise across a shock which is generated because of the separation itself (Fig. 28.32a). Examples include (i) the generation of such a separation and shock upstream of the point of incidence of an oblique shock of the other family, as in Figs. 28.11a and 28.11c; (ii) a similar generation at

the bifurcated base of a normal shock, as in Fig. 28.16, Fig. 28.27, and Fig. 28.29a; and (iii) a similar generation upstream of a large corner angle in the wall, as in Fig. 28.20c.

**Critical Pressure Rise for Separation.** Donaldson and Lange<sup>(13)</sup> have correlated the pressure rise at such a separation point by means of parameters based on the following physical argument. Assuming that

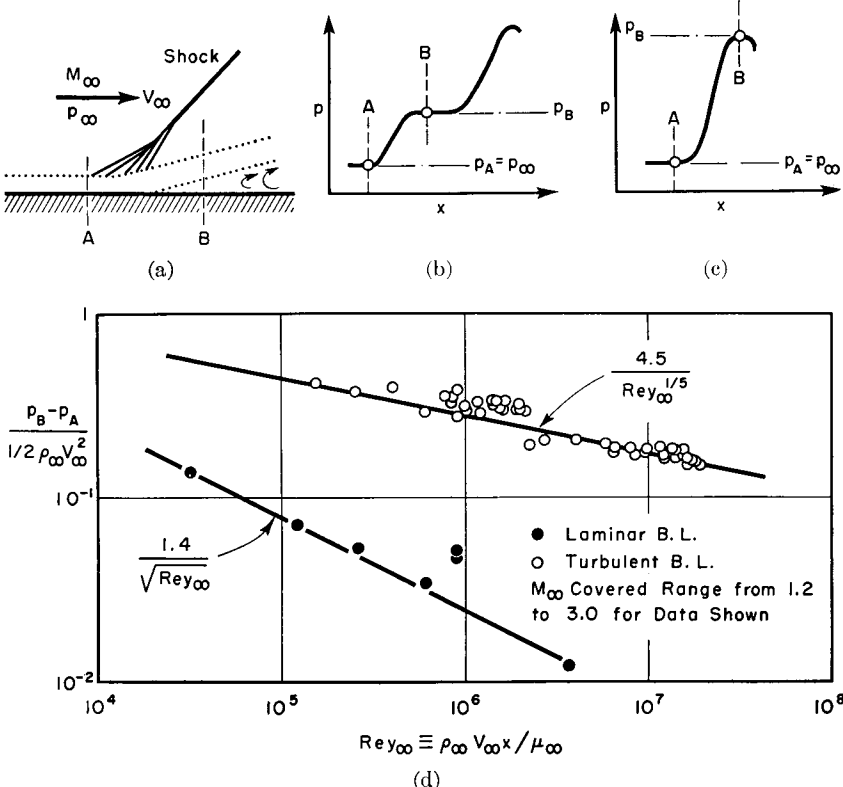


FIG. 28.32. Pressure rise across shock required to separate boundary layer (after Donaldson).

- Schematic sketch of flow pattern, showing separated zone.
- Definition of pressure rise for laminar layer.
- Definition of pressure rise for turbulent layer.
- Correlation of experimental data for many different experiments.

the boundary layer upstream of the pressure rise (point *A* of Fig. 28.32a) is either a laminar or turbulent layer such as prevails in a zero pressure gradient, a consideration of the physical phenomena (viscous, pressure, and inertia effects) between point *A* and the point of separation *B* indicate that the pressure rise should be controlled by the wall shear

stress  $\tau_0$  at  $A$ , by the boundary-layer thickness  $\delta$  at  $A$ , and by the free-stream properties  $M_\infty$ ,  $\rho_\infty$ , and  $V_\infty$ . That is,

$$p_B - p_A = \text{function}(\tau_0, \delta, M_\infty, \rho_\infty, V_\infty)$$

By means of the principle of dimensional homogeneity, this physical relationship may be replaced by a simpler physical relationship in terms of dimensionless groups, namely,

$$\frac{p_B - p_A}{\frac{1}{2} \rho_\infty V_\infty^2} = \text{function}\left(\frac{\tau_0}{\frac{1}{2} \rho_\infty V_\infty^2}, M_\infty\right) = \text{function}(C_f, M_\infty)$$

where  $C_f$  is the skin-friction coefficient at point  $A$ . But  $C_f$  depends only on the length Reynolds Number at point  $A$ , and so we may write

$$\frac{p_B - p_A}{\frac{1}{2} \rho_\infty V_\infty^2} = \text{function}\left(\frac{\rho_\infty V_\infty x}{\mu_\infty}, M_\infty\right)$$

Experimental data from many sources and for several different types of experiments are plotted in this manner in Fig. 28.32d. The correlation obtained is gratifying, considering the simplicity of this approach. There is clearly a laminar branch and a turbulent branch, with the turbulent layer able to support a much greater pressure rise than a separating laminar layer. The effect of Mach Number is quite small in the range between 1.2 and 3.0. Since the slopes of the curves follow the skin-friction laws for laminar and turbulent layers respectively, it follows that the pressure-rise coefficient is proportional to the skin-friction coefficient at point  $A$ . In the case of laminar flow the pressure-rise coefficient is about twice as large as the laminar skin-friction coefficient; for the turbulent layer it is approximately nine times as large as the turbulent skin-friction coefficient.

For turbulent flow the measurements of Fig. 28.32d can be approximately predicted by assuming that the events occur so rapidly that the change to a separating velocity profile occurs with negligible wall friction and negligible entrainment of free-stream flow.<sup>(15)</sup>

These results go far toward explaining many of the complex interactions discussed in this chapter. They show clearly that the shock-boundary layer interaction is of greater consequence for thick boundary layers than for thin ones, and of greater consequence for laminar layers than for turbulent ones.

**APPLICATION TO SUPERSONIC DIFFUSERS.** As an example of the practical utility of such results, Donaldson and Lange<sup>(13)</sup> suggest the following considerations for the design of supersonic diffusers:

(i) It is desirable to keep the Reynolds Number of the supersonic part of the diffuser low. Thus in some cases it might prove advisable

to replace a single large diffuser by an assembly in parallel of several small short diffusers of the same shape.

(ii) Artificial transition (by boundary-layer trips or vortex generators) may be useful unless the Reynolds Number is so low that the laminar layer will tolerate almost as large a pressure rise as a turbulent layer.

(iii) When compression waves are generated at a curved wall, it is desirable to keep the total pressure rise less than the critical value, and to impinge the coalesced wave on another surface at as low a Reynolds Number as possible.

(iv) Unless the supersonic Mach Number entering the normal shock in the diffuser is very low, the critical pressure rise of even a turbulent layer will be exceeded.

#### REFERENCES AND SELECTED BIBLIOGRAPHY

1. KEENAN, J. H., and NEUMANN, E. P. Measurements of Friction in a Pipe for Subsonic and Supersonic Flow of Air, *Jour. App. Mech.*, Vol. 13 (1946), p. A91.
2. DEISSLER, R. G. Analytical and Experimental Investigation of Adiabatic Turbulent Flow in Smooth Tubes, *NACA Tech. Note*, No. 2138 (1950).
3. KAYE, J., KEENAN, J. H., and SHOULBERG, R. H. Measurement of Recovery Factors and Friction Coefficients for Supersonic Flow of Air in a Tube, presented at General Discussion on Heat Transmission in London, September, 1951.
4. LELCHUK, V. L. Heat Transfer and Hydraulic Flow Resistance for Streams of High Velocity, *NACA Tech. Memo.*, No. 1054 (1943).
5. MCADAMS, W. H., NICOLAI, L. A., and KEENAN, J. H. Measurements of Recovery Factors and Coefficients of Heat Transfer in a Tube for Subsonic Flow of Air, *Trans. Amer. Inst. of Chem. Eng.*, Vol. 42, Nos. 5-6 (1946), p. 907.
6. ACKERET, J., FELDMANN, F., and ROTT, N. Investigations of Compression Shocks and Boundary Layers in Gases Moving at High Speed, *NACA Tech. Memo.*, No. 1113 (1947).
7. LIEPMANN, H. W. The Interaction Between Boundary Layer and Shock Waves in Transonic Flow, *Jour. Aero. Sci.*, Vol. 13, No. 12 (1946), p. 623.
8. BARRY, F. W., SHAPIRO, A. H., and NEUMANN, E. P. The Interaction of Shock Waves with Boundary Layers on a Flat Surface, *Jour. Aero. Sci.*, Vol. 18, No. 4 (1951), p. 229.
9. NEUMANN, E. P., and LUSTWERK, F. Supersonic Diffusers for Wind Tunnels, *Jour. App. Mech.*, Vol. 16, No. 2 (1949), p. 195.
10. LUSTWERK, F. The Influence of Boundary Layer on the "Normal" Shock Configuration, *Meteor Report*, No. 61 (1950), M.I.T. Guided Missiles Program.
11. TOONG, T. Y. *The Laminar Boundary Layer of a Steady, Compressible Flow in the Entrance Region of a Tube*, Sc.D. Thesis, Dept. of Mech. Eng., Mass. Inst. of Tech., Cambridge, 1952.
12. LIEPMANN, H. W., ROSHKO, A., and DHAWAN, S. On Reflection of Shock Waves from Boundary Layers, *NACA Tech. Note*, No. 2334 (1951).
13. DONALDSON, C. D.U.P., and LANGE, R. H. Study of the Pressure Rise Across Shock Waves Required to Separate Laminar and Turbulent Boundary Layers, *NACA Tech. Note*, No. 2770 (1952).
14. LEE, J. D. The Influence of High Adverse Pressure Gradients on Boundary Layers in Supersonic Flow, *UTIA Report*, No. 21 (1952), Univ. of Toronto.
15. TYLER, R. D., and SHAPIRO, A. H. Pressure Rise Required for Separation in Interaction Between Turbulent Boundary Layer and Shock Wave, *Jour. Aero. Sci.*, Vol. 20, No. 12 (1953), p. 858.

## INDEX

(Volume I—pages 1 to 647. Volume II—pages 649 to 1159.)

- Absolute temperature scale, 32  
Accelerating flows, 507  
Acoustics, 48  
Action, zone of, 500  
Adiabatic ellipse, 58-59  
Adiabatic flow  
    critical velocity for, 79-81  
    dimensionless velocity  $M^*$  of, 81-82  
    energy equation of, 80-81  
    flow per unit area of, 82  
    maximum velocity for, 79-81  
    one-dimensional, 160-78  
    of perfect gas, 78-82  
        at constant area, 162-73  
    stagnation-temperature ratio for, 80  
Adiabatic process  
    definition of, 29  
    entropy change for, 34  
Adiabatic wall  
    temperature, 211-12, 1036  
    turbulent flow past, 1089  
Affine transformation, 319  
Air, properties of, 612  
Airfoils; *see also* Profiles; Wings  
    biconvex, 568, 849, 858  
    camber effects in transonic flow, 872  
    completely symmetrical, 574  
    double-wedge, 444, 446, 568  
    flow patterns in transonic flow, 866  
    lift-drag polars of, 446, 571  
    lift-drag ratio in transonic flow, 872  
    low-drag in transonic flow, 874  
    optimum for transonic flow, 876  
    pressure drag in transonic flow, 871  
    shock-characteristic theory of, 566  
    skin-friction drag of, 1066  
    subsonic  
        pressure distributions for, 379-81  
        at supersonic speeds, 571  
        thickness of, 384-87  
        in wind tunnel, 378  
        without stagnation points; *see*  
            Bump  
    supersonic  
        aerodynamically optimum, 575  
        biplane, 579  
        center of pressure of, 444, 446, 574  
        downwash of, 576  
        drag of, 442, 446, 572  
        experimental data for, 447-48  
        flow past, 501  
        induced drag of, 442  
        lift of, 441, 445, 472  
lift-drag polar of, 446  
lift-drag ratio of, 443  
linearized theory of, 440-49  
of minimum thickness drag, 575  
moment of, 444, 572  
performance of, 445  
pressure drag of, 442  
second-order theory of, 571-78  
shape of, 571  
skin-friction drag of, 443  
theory vs. experiment, 575  
thickness drag of, 443; *see also*  
    Pressure drag  
trailing-edge flow of, 584  
two-dimensional, 567-80  
types of, 575  
wake of, 578  
wave drag of, 443  
thickness effects in transonic flow, 870  
thin, supersonic flow for, 427  
in transonic flow, 812, 822-25, 840,  
    842-50, 858, 865, 866, 870-78, 888,  
    894; *see also* Transonic flow  
transonic similarity law for, 825  
triangular profile, 574  
two-dimensional, 567-80  
uniqueness in transonic flow, 894  
Analogue techniques, 289  
Angular velocity, 269  
Apparent friction coefficient, 1131, 1135  
Apparent heat flux, in turbulent flow,  
    1086  
Apparent mass flow, in turbulent flow,  
    1084  
Apple curve, 659  
Area change  
    flow with, 219-55  
    unsteady flow with, 972  
Area change and friction, flow with,  
    241-42  
Area discontinuity, interaction with  
    moving shock, 1026  
Area ratio, for isentropic flow, 85-86  
Arrowhead wing  
    of constant chord, 725  
    sweptback, 725  
Aspect ratio  
    effect on compressibility, 400, 411-  
        15  
    effects in transonic flow, 878  
    generalized correlation of, 422  
Atmosphere, properties of, 612  
Atomic explosion, 211

Attached shocks  
for cone, 662  
for wedge, 662  
Axially symmetric body of low pressure drag, 688  
Axially symmetric boundary layer; *see* Boundary layer  
Axially symmetric flow, 291, 294-95, 299, 596  
conical-shock-expansion theory for, 675  
hypersonic, 761-66  
hypersonic similarity law for, 751  
laminar boundary layer of, 1066-67; *see also* Laminar boundary layer, axi-symmetric  
Mangler transformation for, 1066  
method of characteristics for, 676-96; *see also* Method of characteristics  
graphical, 682-84  
with rotation, 684; *see also* Rotation; Vorticity  
supersonic, 651-702  
approximate method for, 696  
Kármán-Moore theory of, 668-76; *see also* Kármán-Moore theory  
linear theory for, 663-76; *see also* Linearized theory  
second-order theory of, 675; *see also* Second-order theory  
tangent-cone method for, 675  
transonic similarity law of, 812; *see also* Transonic similarity law  
Ballistics, 49  
Barotropic fluid, 278  
Barrier  
sonic, 1044  
thermal, 1044  
Base pressure, 697  
Bend, concave, 583  
Bernoulli constant, 276  
Bernoulli's equation, 276, 278  
Biconvex airfoil, 568; *see also* Airfoils in transonic flow, 849, 858  
Biplane, supersonic, 455, 579  
Body  
free, 11  
isolated, 11  
Body forces, 18  
Body of revolution; *see* Revolution, body of  
Bomb, drag of, 408; *see also* Drag; Revolution, body of  
Borda re-entrant orifice, 111  
Boundary layer, 10, 265-66, 282, 379; *see also* Laminar boundary layer; Turbulent boundary layer  
assumptions of, 1037  
axi-symmetric, 1066-67  
differential equations of, 1066  
integral equations of, 1067

(Volume I—pages 1 to 647.)

Mangler transformation for, 1066  
concept of, 1033  
continuity equation of, 1039  
differential equations of, 1036-43, 1082-89  
displacement thickness of, 266, 1062, 1090  
energy equation of, 1040, 1085  
friction and heat transfer in, 1034  
integral energy equation of, 1063, 1092  
integral equations of, 1089-96  
integral method for, 1060-66  
velocity and temperature profiles of, 1063  
integral momentum equation of, 1061, 1089  
interaction with potential flow, 1033  
and interaction with shocks, 135-37, 266, 381-82, 580-84, 897-902, 1033, 1138-50; *see also* Shock-boundary layer interaction  
laminar, 1033-77; *see also* Laminar boundary layer  
momentum equation of, 1039, 1084  
momentum thickness of, 1062, 1090  
possible instability in supersonic flow, 893  
and pressure distribution, 308  
recovery factor for, 1117-24; *see also* Recovery factor  
on flat plate, 1122  
separation of, 379, 380, 415  
pressure rise for shock interaction, 1157  
produced by shock wave, 1156-59  
stability of, effect of heat transfer on, 1127  
stagnation-temperature thickness of, 1063, 1092  
temperature, 1061  
temperature distribution in, 1035  
thermal, 1035, 1061  
transition of, effect of heat transfer on, 1127  
in transonic flow, 893  
in tube flow, 1130-38; *see also* Ducts; Pipe; Tube  
turbulent, 1080-1129; *see also* Turbulent boundary layer  
on body of revolution, 1124-27  
velocity, 1061  
velocity and temperature profiles of, 1063  
viscous shear work in, 1034  
Boundary of system, 11  
Bump, flow past, 350, 372-74, 826  
Burning, slow, 207-11  
Busemann solution for cone, 657-60  
Camber  
in subsonic flow, 384-87  
in transonic flow, 872  
Cancellation of waves, 450, 452, 493; *see also* Wave  
Cauchy-Riemann equations, 351  
Cavitation, 475  
Center of pressure, of supersonic airfoils, 446, 572; *see also* Airfoils  
Centered simple wave, 945; *see also* Simple waves; Wave  
Centered waves, 474, 945; *see also* Corner flow; Prandtl-Meyer wave; Simple waves  
streamlines of, 525  
Chapman-Jouguet rule, 210-11  
Characteristic coordinates, 478, 938; *see also* Method of characteristics  
Characteristic curves, 482-86, 598, 677, 918, 925, 938, 974; *see also* Method of characteristics  
for axi-symmetric flow with rotation, 684  
equations of, 602  
geometry of, 938  
hodograph, 599, 678  
initial-value theorem of, 603-6  
method of constructing, 603-6  
orthogonality relation for, 485, 603  
physical, 599, 678  
properties of, 601  
and shocks, 601  
as solutions, 601  
Characteristic function  
series expression of, 561  
table of, 632  
Characteristic net, construction of, 953; *see also* Method of characteristics  
Characteristic quadrilateral, 498, 499  
Characteristics, 933; *see also* Hodograph characteristic; Method of characteristics  
hodograph, 467-68, 478, 485, 678, 684, 919, 935; *see also* Hodograph characteristic; Hodograph characteristic curves  
table of, 468  
working chart of, 467  
method of, 462-523; *see also* Characteristic curves; Method of characteristics  
illustrative example of, 479, 486-89, 680  
rules for using, 478  
unit processes for, 492-94, 678-82  
physical, 484, 678, 684, 912, 918, 976  
physical significance of, 499  
state, 919, 934, 976  
theory of, 482-91, 595-608  
Chemical reaction, flow with, 206-11, 219-55; *see also* Simple  $T_0$ -Change  
Choking, 234-36, 257  
due to heating, 192-93, 201-3, 205  
due to Simple  $T_0$ -Change, 192-93, 201-3, 205  
in explosion wave, 210-11  
frictional, 162, 170-78  
for isentropic flow, 89-94  
for isothermal flow, 183  
rules of, 235-36  
thermal, 192-93, 201-3, 205  
Circular-arc profile, in subsonic flow, 375; *see also* Airfoils  
Circular cylinder  
recovery factor for, 1071  
in subsonic flow, 367  
in free jet, 368; *see also* Subsonic wind tunnel; Wind tunnel, subsonic  
in wind tunnel, 357-58, 367  
Circulation, 267-69, 278-80, 284  
Clausius, inequality of, 32  
Coefficient  
of discharge; *see* Discharge coefficient  
of friction; *see* Drag; Friction coefficient; Skin-friction coefficient  
of heat transfer, 212-13, 1046; *see also* Boundary layer; Heat transfer  
for turbulent boundary layer, 1089; *see also* Turbulent boundary layer  
influence; *see* Influence coefficients  
pressure; *see* Pressure coefficient  
Combustion  
choking in, 198, 201-2; *see also* Choking  
example of, 197-98  
flow with, 206-11; *see also* Simple  $T_0$ -Change  
unsteady flow with, 972  
Combustion chamber, 219  
Complete simple wave, 945  
Compressibility bubble, 326, 384  
effect of aspect ratio on, 400  
Compressibility of liquid, 69  
Compressible flow  
classification of, 58-59  
hypersonic, 59; *see also* Hypersonic flow  
subsonic, 59; *see also* Subsonic flow  
supersonic, 59; *see also* Supersonic flow  
transonic, 59; *see also* Transonic flow  
Compressible source and sink, 665-68  
Compression shock; *see* Shocks  
Compression wave  
development to shock, 1025  
steepening of, 127-31, 915; *see also* Wave  
Compressor, interference in, 315  
Compressor cascades, 427, 462  
supersonic, 505  
Comprex, 907  
Concave bend, 583  
Condensation  
flow with, 219-55  
moisture, flow with; *see* Simple  $T_0$ -Change

(Volume II—pages 649 to 1159.)

Condensation—Continued  
 shock, moisture, 203-5  
 Conduction of heat, Fourier law of, 36; *see also* Heat transfer  
 Conductivity, thermal, definition of, 36  
 Cone  
 apple curve for, 659  
 attached shocks for, 662  
 Busemann solution for, 657-60  
 charts for supersonic flow, 660-62  
 compared with wedge, 662  
 comparison of theories for, 672-76  
 detached shock for, 662, 886, 887  
 experimental results for, 663-64  
 heat transfer for, 1067, 1073, 1125, 1126  
 in hypersonic flow, 763, 767  
 hypersonic similarity for, 672  
 laminar boundary layer on, 1067, 1125  
 Mach, 706  
 Newtonian theory for, 672  
 pressure drag of, 662  
 recovery factor for, 1070-71, 1126  
 turbulent, 1123  
 second-order theory for, 672-76  
 skin friction on, 1067, 1125  
 strong solution for, 662  
 in supersonic flow, 653-63, 670-71  
 in supersonic inlet, 662-63  
 tables for supersonic flow, 661  
 Taylor-Maccoll solution for, 656-57  
 transition of laminar boundary layer on, 1076  
 turbulent boundary layer on, 1124  
 weak solution for, 662  
 yawing, 663  
 Cone-cylinder, in hypersonic flow, 769  
 Cone-expansion method, 766  
 Configuration of moving shocks, 998; *see also* Moving shocks; Shocks  
 Conical field, 729  
 method of, 716, 729-35  
 Conical flow, 653  
 Conical-shock-expansion theory, 675  
 Conservation of mass; *see also* Continuity equation  
 principle of, 12  
 for control volume, 13  
 Contact discontinuity, 970; *see also* Slip line; Vortex sheet  
 shock incident on, 1024  
 Continuity equation, 14, 283-84; *see also* Conservation of mass  
 in cylindrical coordinates, 290  
 in spherical coordinates, 299  
 in steady flow, 15  
 for turbulent flow, 1082  
 time-mean, 1083  
 Continuum  
 concept of, 4, 23  
 domain of, 56-58  
 Euler's description of, 11  
 Lagrange's description of, 11

(Volume I—pages 1 to 647.)

limitations of, 56-58  
 mathematical description of, 10  
 properties of, 5, 35  
 Control surface, 12  
 Control volume, 12  
 First Law of thermodynamics for, 39  
 Second Law of thermodynamics for, 40  
 Converging-diverging nozzle  
 operating characteristics of, 139-43; *see also* Nozzle  
 with varying pressure ratio, 93-94  
 Converging nozzle  
 discharge coefficient of, 93; *see also* Nozzle  
 as flow meter, 93  
 as flow regulator, 93  
 with varying pressure ratio, 91-93  
 Cooling, flow with; *see also* Simple  $T_o$ -Change  
 Corner  
 flow, supersonic, 463-64; *see also* Prandtl-Meyer wave; Simple waves; Centered waves  
 generation of shock in, 1142  
 Corpulsular flow, Newtonian theory of, 675  
 Corpulsular theory, Newton's, 746, 753, 755  
 Correlation coefficient, 1101; *see also* Turbulent flow  
 Critical Mach Number, 874; *see also* Lower critical Mach Number  
 lower, 797  
 in transonic similarity form, 826; *see also* Transonic similarity law  
 upper, 797; *see also* Limit line  
 Critical point, 258  
 Critical pressure ratio, 76; *see also* Nozzle  
 Critical speed, 79-81  
 Critical state, 83  
 Critical velocity, in adiabatic flow, 79-81  
 Crocco's temperature-velocity relationship, 1097; *see also* Boundary layer  
 Crocco's theorem, 281-82  
 Crossing of moving shocks; *see also* Moving shocks; Shocks  
 Crossing of waves; *see also* Intersection of waves; Wave  
 Curved shocks, 549, 559-61, 908; *see also* Shocks  
 Curved wall, supersonic flow past, 464  
 Curves, characteristic, 598; *see also* Characteristic curves; Method of characteristics  
 Cusped profile, lower critical Mach Number of, 826; *see also* Bump  
 Cycle, 24  
 First Law for a, 28  
 Cylinder, recovery factor for, turbulent, 1123  
 d'Alembert's Paradox, 449, 708  
 d'Arcy's formula, 189  
 Decelerating flows, 507  
 Deflagration, 207-11  
 Delta wing  
 lift of, 738  
 supersonic, 719-24  
 Dependence, domain of, 499<sup>y</sup>  
 Detached shocks, 548, 881-88; *see also* Shocks  
 for cone, 662  
 location of, 884-88  
 shape of, 886  
 for wedge, 662  
 Detonation, 207-11  
 Detonation wave, 219  
 Diffuser  
 isentropic flow in, 73  
 oblique-shock, 566, 691  
 supersonic, 143-152, 651, 689-94, 1156, 1158; *see also* Inlet, supersonic of air-breathing engines, 147-51, 689-94  
 allowable contraction for, 144-51  
 devices for starting of, 147  
 efficiency of, 151-52, 691-92  
 of fixed geometry, 143-52  
 friction in, 147  
 limiting contraction ratio of, 149  
 one-dimensional, 143-52  
 operating conditions of, 146-47  
 overspeeding of, 150  
 plug type, 691  
 special problems of, 143-44  
 starting of, 144-51  
 of variable geometry, 147-52, 693  
 for wind tunnels, 144-47; *see also* Wind tunnel  
 Dimensional analysis, 315  
 of inviscid flow, 308-9  
 Dimensions, of dynamical quantities, 20  
 Direction index, 450  
 Discharge coefficient  
 of Borda orifice, 111  
 of nozzle, 99-100  
 of orifice, 359  
 of sharp-edged orifice, 100  
 Discharge duct, unsteady flow in, 986; *see also* Unsteady flow  
 Discharge from reservoir, starting of, 986; *see also* Unsteady flow  
 Discontinuity  
 contact, shock incident on, 1024  
 surface of; *see* Contact discontinuity; Slip line; Vortex sheets  
 temperature, 969; *see also* Discontinuity, surface of  
 Disk, recovery factor for, turbulent, 1123  
 Displacement thickness, 266, 1062, 1090  
 Distorted models, 315  
 theory of, 803  
 Disturbances, propagation of, 499; *see also* Mach wave; Shocks; Wave  
 Domain of dependence, 499  
 Domain of influence, 499  
 Double-cone body, supersonic flow past, 685  
 Double wedge  
 lift-drag ratio of, 446  
 supersonic flow past, 444, 568  
 Doublet  
 compressible, 798  
 supersonic, 716  
 Doublet distributions, for calculation of lift, 729  
 Downwash of supersonic airfoil, 576; *see also* Wake  
 Drag, 449; *see also* Airfoils; Drag coefficient; Induced drag; Pressure drag; Skin friction; Thickness drag; Wave drag  
 of airfoils, 442, 446, 572, 757-61, 1066  
 in hypersonic flow, 757-61  
 in supersonic flow, 443  
 and aspect ratio, 401  
 axi-symmetric body of low, 688  
 base pressure, 697  
 of bomb, 408  
 of cone, 662  
 of cone-cylinder, 769  
 of flat plate; *see also* Boundary layer; Laminar boundary layer; Turbulent boundary layer  
 frictional, 1107-17  
 normal to stream, 360  
 in hypersonic flow, 766  
 induced, 442  
 due to lift, 708  
 of wings, 412  
 internal, flow with, 219-55  
 and Mach Number, 383  
 at Mach Number unity, 843  
 nose, 766  
 and oblique shocks, 569  
 pressure, 442, 549; *see also* Induced drag; Pressure drag; Thickness drag; Wave drag  
 of parabolic bodies, 673  
 of swept wings, 725-29  
 of projectiles, 697  
 projectiles of minimum, 674  
 skin friction  
 effect of pressure gradient on, 1066  
 on flat plate, 1059  
 of spheres, 410  
 for subsonic flow, 386  
 of supersonic airfoils, 442, 446, 572  
 thickness, 443  
 in transonic flow, 846-50  
 wave, 443  
 Drag-break, 875  
 (Volume II—pages 649 to 1159.)

Drag coefficient, 163, 379; *see also* Drag; Friction coefficient; Skin friction coefficient

relation to skin-friction coefficient, 1107

Drag divergence, 874

Mach Number of, 384-87

Duct

- flow in; *see also* Pipe, flow in; Tube, flow in
- fed by converging-diverging nozzle, 175-78
- fed by converging nozzle, 173-75
- with friction, 159-86
- isothermal, 178-83; *see also* Isothermal flow in ducts
- shock-boundary layer interaction in, 1153-56
- with varying pressure ratio, 173-78

Eddy heat conductivity, 1086; *see also* Turbulent boundary layer; Turbulent flow

Eddy thermal conductivity, 1086; *see also* Turbulent boundary layer; Turbulent flow

Eddy viscosity, 1086; *see also* Shear stress, apparent; Reynolds stress; Turbulent boundary layer; Turbulent flow

Efficiency

- of nozzle, 98-99, 110; *see also* Nozzle of supersonic diffuser, 151-52; *see also* Diffuser
- thermal, of heat engines, 29

Ejector, 219

Elbow

- for accelerated flow, 359-60
- supersonic, 504

Ellipse

- adiabatic, 58-59
- steady-state, 962

Ellipsoid

- subsonic flow past, 398-401

Ellipsoid of revolution

- lower critical Mach Number of, 407
- subsonic flow past, 405

Elliptic cylinder

- lift of, 376
- lower critical Mach Number of, 407, 826
- subsonic flow past, 354-56, 358, 369

Elliptic differential equation, 429, 600

Energy

- internal, 27
- for perfect gas, 41
- U*, for pure substance, 35
- kinetic, 36
- flux of, 39
- potential, 36

Energy effects, flow with; *see also* Simple  $T_0$ -Change

(Volume I—pages 1 to 647.)

Film coefficient of heat transfer, 212-13, 1046; *see also* Heat transfer

Finite wings, lift of, 735-41; *see also* Lift; Wings

First Law of thermodynamics, 26

- for control volume, 37-39
- for a cycle, 28

First-order theory; *see* Linearized theory

Flame front, 219

- propagation speed of, 207, 209-11

Flat plate

- friction on; *see also* Boundary layer; Laminar boundary layer; Turbulent boundary layer
- friction drag on, 1059
- heat transfer for, 1060, 1066; *see also* Boundary layer; Heat transfer; Laminar boundary layer; Turbulent boundary layer
- turbulent, 1096-1107, 1103, 1106

in hypersonic flow, 758

Kármán's mixing-length formulation for, 1110

- laminar boundary layer on, 1056-60
- laminar skin friction on, 1057
- nonadiabatic, turbulent skin friction and heat transfer, 1117
- normal to subsonic stream, 360

Prandtl's mixing-length formulation for, 1110

- recovery factor for, 1071, 1099
- laminar, 1122
- turbulent, 1096-1107, 1118-23

reflection of shock from, 1139

shock-boundary layer interaction on, 1139

- skin friction on, 1066, 1068
- turbulent, 1095-1117

stagnation-temperature profile on, turbulent, 1115

- subsonic flow past, 448, 707
- supersonic flow past, 444, 448, 707
- lift-drag ratio of, 446

transition of laminar boundary layer on, 1076

- in transonic flow, 822-25
- turbulent boundary layer on, 1089
- turbulent skin friction on, 1109, 1110
- experimental, 1111
- velocity profile on, turbulent, 1115

Fliegner's formula, 85

Flow; *see also* One-dimensional flow

- accelerating, 507
- adiabatic; *see* Adiabatic flow
- decelerating, 507
- irrotational; *see* Irrotational motion
- isentropic; *see* Isentropic flow
- mass rate of, 14
- one-dimensional
- adiabatic, 160-78; *see also* Friction, one-dimensional flow with, adiabatic
- in long ducts, 173-78
- of perfect gas, 162-73

(Volume II—pages 649 to 1159.)

Friction—Continued  
 tables for, 169, 626  
 unsteady, 972; *see also* Unsteady flow  
 simple, 159-78; *see also* Fanno line; Friction, one-dimensional flow with in tube flow, 1130-38  
 Friction and area change, flow with, 241-42  
 Friction coefficient; *see also* Drag coefficient; Skin friction coefficient apparent, 1131, 1135  
 definition of, 163  
 experimental, 184-86  
 for subsonic flow, 184-85  
 for supersonic flow, 185-86  
 for tube flow, 1131-35  
 Friction factor; *see* Friction coefficient  
 Friction and heat transfer in boundary layer, 1034  
 flow with, 242-55  
 Reynolds analogy for, 1047  
 Friction length, 1094  
 Friction velocity, 1094  
 Frictional effects on gas flow; *see* Friction, one-dimensional flow with Frictional flow, table of, 626  
 Frictional heating, 211-12; *see also* Boundary layer  
 Frictional shear work, 1034; *see also* Boundary layer  
 Frictionless flow, dimensional analysis of, 308-9  
 Fuselage  
 of minimum drag, 674  
 in supersonic flow, 651  
 transonic drag of, 879  
 Gas, perfect; *see* Perfect gas  
 Gas constant, definition of, 41  
 and molecular weight, 41  
 universal, 41  
 Gas constants, relations among, 42  
 Gas dynamics, 49  
 Generation of shock in concave corner, 1142  
 Generation of wave, 449, 463, 493  
 Geometry of moving shocks, 998  
 Gladstone-Dale equation, 63  
 Goertler's rule, 316-21, 336  
 for bodies of revolution, 402-5  
 for one-dimensional flow, 331-32  
 for spheres, 409  
 for sweptback wings, 416  
 for three-dimensional flow, 394-99  
 for two-dimensional passages, 330-32  
 for wind tunnels, 327-30  
 for wings, 410  
 Green's theorem, 268-69  
 Heat  
 definition of, 27  
 mechanical equivalent of, 28

(Volume I—pages 1 to 647.)

in reversible processes, 33  
 specific, 36  
 of perfect gas, 42  
 Heat conduction, Fourier law of, 36  
 Heat conductivity  
 coefficient of, 1086  
 eddy, 1086; *see also* Turbulent boundary layer; Turbulent flow molecular, 1086  
 Heat engines, 29  
 thermal efficiency of, 29  
 Heat exchanger, 214-55; *see also* Heat transfer  
 approximate method for low Mach Numbers, 249-51  
 with constant heat flux, 246-47, 251-52  
 with constant wall temperature, 243-51  
 graphical integration for, 244-48  
 in nuclear reactor, 252-55  
 numerical integration for, 244-48  
 Heat flow  
 apparent, in turbulent flow, 1086; *see also* Heat transfer; Turbulent boundary layer; Turbulent flow in laminar boundary layer, 1046  
 Heat transfer; *see also* Heat exchanger for bodies of revolution, 1074  
 coefficient of, 212-13, 1046  
 choice of definition for, 1136  
 for turbulent boundary layer, 1089  
 for turbulent flow, 1100  
 for cone, 1067, 1125, 1126  
 effect on stability of laminar boundary layer, 1075  
 experimental correlation of, 213  
 on flat plate, 1060, 1066  
 turbulent, 1096-1107, 1117  
 flow with, 219-55; *see also* Simple  $T_0$ -Change  
 in laminar boundary layer, 1053, 1060, 1066, 1074  
 Reynolds' analogy for, 1100  
 in tube flow, 1130-38  
 unsteady flow with, 972  
 Heat transfer and friction  
 in boundary layer, 1034; *see also* Boundary layer  
 flow with, 242-55  
 Reynolds' analogy for, 1047  
 Heating  
 flow with, *see* Simple  $T_0$ -Change  
 frictional, 211-12  
 Hodograph characteristic, 468, 478, 485, 678, 684, 919, 935  
 related to shock polar, 552  
 Hodograph characteristic curves, 599  
 Hodograph characteristic function, 467  
 chart of, 467  
 table of, 468, 632  
 Hodograph coordinates, 338  
 Hodograph equations, 338-41  
 Hodograph method, 288, 336, 773  
 Hodograph plane, 336, 465, 934  
 equation of stream function in, 341  
 Hodograph shock polars, 542, 552  
 Hodograph streamlines, 336-37  
 and physical streamlines, 336-37, 341  
 Holzwarth turbine, 907  
 Homogeneous fluid, 278  
 Hyperbolic differential equation, 429, 600  
 Hypergeometric functions, 798  
 Hypersonic boundary layer, 746  
 Hypersonic flow, 59, 745-70  
 axi-symmetric, 761-66  
 cone-cylinder in, 769  
 cones in, 763, 767  
 corpuscular theory of, 746, 753  
 experimental results for, 766-70  
 with large disturbances, 753  
 oblique shock relations of, 753-55  
 past ogive-cylinders, 763-65  
 Prandtl-Meyer expansion in, 755-57  
 simple wave in, 755-57  
 for two-dimensional profiles, 757-61  
 wings in, 766  
 Hypersonic similarity law, 651-52, 747-53  
 for axi-symmetric flow, 751  
 combined with supersonic, 752  
 for finite wings, 752  
 for plane flow, 750  
 range of, applicability of, 763  
 for supersonic flow, 751  
 Hypersonic similarity parameter, 651, 749  
 Impulse function  
 definition of, 86  
 for isentropic flow, 86-87  
 Impulse turbine blade, 504  
 Inclined body of revolution, 675  
 Incompressible flow  
 Bernoulli's equation for, 278  
 flat-plate drag coefficient for, 1107  
 similarity law for, 321-22  
 square network for, 297  
 velocity potential for, 289  
 Index of refraction, 63  
 Induced drag, 442; *see also* Drag; Pressure drag  
 due to lift, 708  
 of wings, 412  
 Influence  
 domain of, 499  
 range of, 500  
 Influence coefficients, 226-31  
 table of, 228, 231, 237-38, 630  
 Initial-value theorem  
 for hyperbolic equations, 603-6, 982  
 for supersonic flow, 497-500, 603-6  
 Injector, 219  
 Inlet, supersonic, 506, 689-94; *see also* Diffuser, supersonic  
 with cone plug, 662-63  
 efficiency of, 691-92  
 of fixed geometry, 148-51  
 limiting contraction ratio for, 149  
 overspeeding of, 150  
 starting of, 147-51  
 of variable geometry, 150-51, 693  
 Insulated wall, turbulent flow past, 1089  
 Integral energy equation, 1063, 1092  
 Integral equations, for axi-symmetric boundary layer, 1067  
 Integral method  
 for axi-symmetric boundary layer, 1067  
 for boundary layer, 1060-66  
 calculation procedure for, 1064-66  
 example of, 1065  
 heat transfer by, 1066  
 skin-friction coefficient by, 1066  
 for turbulent boundary layer, 1089-96  
 velocity and temperature profiles for, 1063  
 Integral momentum equation, 1061  
 Integral surface, 598  
 Interface of laminar sublayer, 1094  
 Interference in wind tunnel, 315, 335, 403; *see also* Wind tunnel  
 Interference pressure coefficient, 329  
 Interferogram  
 evaluation of, 62-65  
 fringe-displacement, 63-65  
 infinite-fringe, 61-63  
 Interferometer, 60-65  
 Intermittent-jet engine, 907  
 Internal energy, 27  
 of perfect gas, 41, 43  
 $U$ , for pure substance, 35  
 Intersection of oblique shocks, 553-59; *see also* Shocks; Wave  
 of same family, 558  
 Intersection of waves, 450, 453, 494, 922, 958; *see also* Wave  
 Inviscid flow, dimensional analysis of, 308-9  
 Inviscid fluid, definition of, 10  
 Irreversibility, 30  
 and perpetual motion, 31  
 and Second Law, 31  
 Irrotational flow; *see* Irrotational motion  
 Irrotational motion, 266, 267-73, 280, 282, 284, 286  
 in axially symmetric flow, 294  
 in cylindrical coordinates, 290  
 example of, 271-73  
 in spherical coordinates, 299  
 Isentropic flow  
 applications of, 73  
 charts for, 87  
 choking in, 89-94; *see also* Choking  
 of compressible liquid, 11  
 with deviations from perfect gas laws, 95-97  
 (Volume II—pages 649 to 1159.)

Isentropic flow—Continued  
 in diffuser, 73; *see also* Diffuser  
 formulas in powers of Mach Number, 95  
 general features of, 74–78  
 illustrative example of, 88  
 for low Mach Numbers, 94–95  
 Mach Number relations for, 83–86  
 in nozzle, 73; *see also* Nozzle  
 one-dimensional, 74–78, 239  
 of perfect gas, 83–88  
 in stream tube, 73  
 tables for, 88, 614  
 with van der Waals gas, 96–97  
 with variable specific heat, 96–97  
 Isentropic process  
 enthalpy change in, 43  
 of perfect gas, 43  
 Isentropic stagnation pressure, 75  
 Isentropic stagnation state, 83  
 Isothermal flow in ducts, 178–83  
 charts for, 181  
 choking effects for, 183  
 formulas for, 180–81  
 at low Mach Number, 182–83  
 variation of fluid properties for, 179–80

Jet  
 contraction ratio of, 358–59  
 free, 368  
 overexpanded, 454, 565  
 turbine nozzle, 566  
 underexpanded, 454, 479–81, 501

Joukowski profile  
 lift of, 370  
 lower critical Mach Number of, 370  
 in subsonic flow, 369

Joule's constant, 28

Kadenacy effect, 924

Kármán hypothesis of mechanical similitude, 1101

Kármán mixing length formulation, 1110

Kármán-Moore theory  
 for body of revolution, 668–76; *see also* Linearized theory  
 parabolic, 671–74  
 for cone, 670–71

Kármán-Tsien coordinate correction formula, 353

Kármán-Tsien method, 344–51  
 for flow with circulation, 357  
 with polygonal approximation, 357  
 profile correction for, 351–56

Kármán-Tsien pressure correction formula, 323, 327, 341; *see also* Kármán-Tsien rule

Kármán-Tsien rule, 370, 374, 375  
 accuracy of, 349–50  
 chart for, 348  
 comparison with experiment, 350

(Volume I—pages 1 to 647.)

comparison with Prandtl-Glauert rule, 349  
 Kelvin temperature scale, 32  
 Kelvin's theorem, 278–80, 282  
 Kinetic energy, 36  
 flux of, 39  
 Lagrange, method of, 11  
 Laitone's modification of Prandtl-Glauert rule, 324–27  
 Lambda shock, 381, 866  
 Laminar boundary layer, 1033–77; *see also* Boundary layer for adiabatic wall, 1043; *see also* Flat plate  
 for arbitrary Prandtl Number, 1056–60  
 axi-symmetric, 1066–67; *see also* Axi-symmetric flow  
 integral equations of, 1067  
 Mangler transformation for, 1066  
 on cone, 1067, 1125  
 for constant wall temperature, 1044–56  
 differential equations of, 1036–43  
 effect of heat transfer on, 1058–59  
 effect of Prandtl Number on, 1057  
 effect of pressure gradient on, 1055  
 effects of viscosity variation on, 1055  
 experimental, results for, 1067–74  
 heat transfer in, 1045, 1053, 1060, 1066, 1074  
 on insulated flat plate, 1052, 1054, 1055, 1056–58  
 integral equations of, 1060–66  
 integral method for, 1060–66  
 calculation procedure of, 1064–66  
 example of, 1065  
 and interaction with shocks, 1141, 1150; *see also* Shock-boundary layer interaction  
 Mach Number profile in, 1058  
 Nusselt Number for, 1053; *see also* Heat transfer  
 for Prandtl Number unity, 1043–56  
 recovery factor for, 1056, 1070, 1122; *see also* Recovery factor  
 summary of, 1071  
 results based on wall properties, 1053  
 Reynolds analogy for, 1047; *see also* Reynolds analogy  
 skin friction in 1053, 1057–60, 1066, 1068; *see also* Skin friction  
 stability of, 1127; *see also* Stability, boundary layer  
 temperature profile in, 1052–54, 1056–60, 1096  
 temperature-velocity relationship in, 1045  
 temperature-viscosity relationship in, linear, 1049  
 theoretical results for, 1052–60  
 thickness of, 1059  
 transition of  
 effect of heat transfer on, 1127  
 effect of wall temperature on, 1076  
 in transonic flow, 900  
 velocity profile in, 1052–54, 1056–60, 1067, 1096  
 von Mises transformation for, 1048  
 for zero pressure gradient, 1044–56  
 Laminar flow, compared with turbulent, 1080  
 Laminar sublayer, 1080, 1093  
 interface of, 1094  
 Laplace's equation, 289, 294, 297  
 Lattice-point method, 491, 924, 955; *see also* Method of characteristics  
 Layer, boundary; *see* Boundary layer; Laminar boundary layer; Turbulent boundary layer  
 Leading edge  
 subsonic, 706  
 suction force on, 708  
 supersonic, 706  
 swept, 707  
 Length  
 friction, 1094  
 mixing, 1101  
 units of, 20–21  
 Lift; *see also* Airfoils; Wings  
 calculation by doublet distribution, 729  
 of finite wings, 735–41  
 in hypersonic flow, 766  
 at Mach Number unity, 845  
 of profile in hypersonic flow, 757–61  
 of supersonic airfoils, 441, 445, 472, 572; *see also* Airfoils; Lift coefficient  
 in transonic flow, 846–50  
 Lift-break, 875  
 Lift coefficient; *see also* Airfoils; Lift; Wings  
 of circular-arc profile, 375  
 Goert's rule for, 321  
 and Mach Number, 315, 326, 376, 383  
 Prandtl-Glauert rule for, 322–23  
 for subsonic flow, 385  
 of supersonic airfoils, 441, 445, 472  
 Lift-curve slope, effect of Mach Number on, 326  
 Lift-divergence Mach Number, 384–87  
 Lift-drag polar  
 of subsonic profiles in supersonic flow, 571  
 of supersonic profile, 446  
 Lift-drag ratio  
 of supersonic airfoil, 443  
 in transonic flow, 872  
 Limit line, 540, 773, 778, 787, 790, 950, 992; *see also* Critical Mach Number, upper  
 Linear differential equation, 288, 289  
 Linearized theory; *see also* Goert's rule; Kármán-Moore theory; Prandtl-Glauert rule  
 assumptions of, 308  
 axi-symmetric  
 comparison of theory and experiment, 674  
 supersonic, 663–76; *see also* Kármán-Moore theory  
 for cone, 670–71  
 for parabolic body of revolution, 671–74  
 pressure coefficient in, 309–10  
 and second-order theory, 561–63  
 subsonic, 303  
 supersonic, 426–56  
 for bodies of revolution, 663–76  
 compared with experiment, 447–48  
 general solution for, 429  
 geometrical interpretation of, 434–37  
 modified, 463, 477  
 and shock theory, 553  
 for three-dimensional subsonic flow, 394–99  
 Liquid  
 change in wave shape for, 131  
 shock wave in, 155  
 Low-drag profile in transonic flow, 874  
 Lower critical Mach Number, 348, 349, 797  
 of bump, 372–74  
 of circular-arc profile, 375  
 of circular cylinder, 367  
 of circular cylinder in wind tunnel, 358, 368  
 of ellipsoid, 398–400  
 of ellipsoid of revolution, 407  
 of elliptic cylinder, 358, 369, 407  
 of Joukowski profile, 370  
 of profile, 387  
 of sphere, 409  
 and sweepback, 418  
 Mach angle, 54, 432  
 Mach cone, 51–54, 706  
 Mach line, 463, 484, 499, 678, 684, 976; *see also* Mach wave  
 Mach Number  
 constant, flow with, 241–42  
 definition of, 54  
 influence of independent variables on, 233  
 lower critical; *see* Lower critical Mach Number  
 profile, in laminar boundary layer, 1058  
 relation to  $M^*$ , 81–82  
 as similarity parameter, 56  
 Mach quadrilateral, 477, 498  
 Mach reflection, 555–57, 1140, 1146  
 Mach wave, 601; *see also* Mach line; Pressure wave; Wave  
 compared with oblique shock, 531

(Volume II—pages 649 to 1159.)

Mach wave—Continued  
 four basic types of, 436  
 interaction with oblique shock, 541  
 left-running, 432, 678  
 as limit of oblique shock, 551  
 pressure-deflection relation for, 435  
 right-running, 433, 678  
 Mangler transformation for axi-symmetric boundary layer, 1066  
 Mass  
 conservation of; *see* Conservation of mass; Continuity equation  
 flux of, 14  
 units of, 20-21  
 Mass flow, apparent, in turbulent flow, 1084; *see also* Turbulent boundary layer; Turbulent flow  
 Mass flow parameter, for adiabatic flow, 82  
 Mass rate of flow, 14  
 Maximum velocity, for adiabatic flow, 79-81  
 Mean effective pressure, 907  
 Mechanical equivalent of heat, 28  
 Mechanical similitude, Kármán's hypothesis of, 1101  
 Method of characteristics, 462-528; *see also* Characteristic curves; Characteristics, method of  
 for axi-symmetric flow, 676-96; *see also* Axially symmetric flow  
 with rotation, 684  
 compared with experiment, 514  
 details of working, 979-82  
 graphical, 494, 682-84  
 graphical vs. numerical procedures, 979  
 grid size vs. accuracy of, 497, 685  
 illustrative example of, 479, 486-89, 680  
 initial-value theorem of, 497-500, 603-6  
 numerical, 494-97, 603  
 for rotational flow, 516-23  
 rules for using, 478  
 and shock theory, 553  
 theory of, 595-608  
 unit processes for, 492-94, 495, 678-82  
 for unsteady flow, 972  
 Minimum critical Reynolds Number, 1075  
 Missiles  
 of minimum drag, 674  
 in supersonic flow, 651  
 Mixed flow, 773, 881; *see also* Transonic flow  
 Mixing  
 flow with, 239; *see also* Simple gas injection  
 one-dimensional flow with, 219-55  
 Mixing length, constant for, 1106  
 Kármán's formulation of, 1110

(Volume I—pages 1 to 647.)

Nonlinear differential equation, 288  
 Normal shock, 112-54, 199-200; *see also* Shocks; Wave  
 curves for, 122  
 development of, 125-31, 131-32  
 direction of, 120-21  
 in ducts, 135-37, 583  
 interaction with boundary layer, 1153-56  
 with energy effects, 203-11  
 entropy increase in, 119-20  
 example of, 123  
 formation of, 125-31  
 formulas for, 118-20  
 governing equations of, 114-16  
 impossibility of rarefaction, 120-21  
 interaction with boundary layer, 135-37, 583  
 in liquid, 155  
 moving, 137-39; *see also* Moving shocks  
 in perfect gas, 116-22  
 Prandtl's equation of, 118  
 Rankine-Hugoniot equation of, 121-22  
 stagnation-pressure loss in, 119  
 strength of, 123-24  
 tables for, 123, 621  
 thickness of, 131-34  
 transformed from oblique shock, 530; *see also* Shocks, oblique  
 of vanishing strength, 124  
 velocity of, 124  
 weak, 123-25  
 Normal shock wave; *see* Normal shock; Wave  
 Normal stresses, 18  
 work done by, 38  
 Nozzle; *see also* Isentropic flow  
 asymmetric flow in throat of, 830  
 converging  
 discharge coefficient of, 93  
 as flow meter, 93  
 as flow regulator, 93  
 with varying pressure ratio, 91-93  
 converging-diverging  
 flow in throat of, 839-40  
 operating characteristics of, 139-43  
 with varying pressure ratio, 93-94  
 discharge coefficient of, 99-100  
 efficiency of, 98-99, 110  
 flow in throat of, 826-36  
 isentropic flow in, 73  
 overexpanded, 454, 565  
 performance of, 98-100  
 rocket, 219  
 shape of sonic line in, 830-34  
 sharp-cornered, 412  
 supersonic  
 axi-symmetric, 694  
 sonic line in, 834  
 two-dimensional, 507-16  
 supersonic flow in, 651  
 supersonic wind tunnel, 427, 507-16, 694, 834  
 symmetric flow in throat of, 828  
 transition from subsonic to subsonic-supersonic flow, 834  
 turbine, 566  
 underexpanded, 454, 479-81, 501  
 velocity coefficient of, 99  
 wind tunnel, 502  
 Nuclear reactor, 219  
 heat transfer in, 252-55  
 Nusselt Number, 213, 1047; *see also* Boundary layer; Heat transfer for laminar boundary layer, 1053  
 Oblique shocks, 529-84; *see also* Shocks  
 approximate treatment of, 552  
 charts for, 536-38  
 compared with Mach waves, 531; *see also* Wave  
 crossing of, 555  
 crossing slip line, 561, 592  
 curved, 549, 559-61  
 detached, 548  
 equations of, 532-39  
 formation of, 540, 563  
 formulas for, 535  
 generation at concave bend, 583  
 geometry of, 539-41  
 in hypersonic flow, 753-55  
 hypersonic similarity law for, 754  
 impossibility of rarefaction, 539  
 interaction with shocks, 541  
 interaction with waves, 541, 559, 563  
 intersection of, 553-59  
 limit of as Mach wave, 551  
 maximum deflection for, 548, 586  
 minimum Mach Number for, 548  
 nearly normal, 550  
 Prandtl relation for, 534  
 Rankine-Hugoniot law for, 533  
 reflection of, 553-59; *see also* Reflection  
 from boundary layer, 582  
 from flat plate, 1139  
 from free boundary, 554  
 from wall, 554  
 and Second Law of thermodynamics, 539  
 series solution of, 562  
 sonic flow after, 550, 586  
 streamline turning in, 539  
 strong, 544-48  
 tables for, 536  
 transformed from normal shock, 530  
 transonic similarity law for, 815-19  
 and wave drag, 569  
 weak, 544-48, 551-53, 587  
 Ogive-cylinder  
 in hypersonic flow, 763-65  
 turbulent recovery factor for, 1123  
 One-dimensional approximation, 73-74

(Volume II—pages 649 to 1159.)

One-dimensional flow; *see also* Flow with area change, 219-55; *see also* Isentropic flow with chemical reaction, 219-55; *see also* Simple  $T_0$ -Change with evaporation or condensation, 219-55; *see also* Simple  $T_0$ -Change with friction, 159-86; *see also* Boundary layer; Fanno line; Friction, flow with with friction and area change, 241-42 with friction and heat transfer, 242-55; *see also* Heat exchanger general method of solution, 236-37 Goertler's rule for, 331-32 with heat transfer, 219-55; *see also* Heat transfer; Simple  $T_0$ -Change influence coefficients of, 237-38 influence of independent variables on, 232-36 with internal drag, 219-55 with mixing, 219-55 simple types of, 238-41 table for, 239 transition through sonic speed, 235-36 unsteady, 596; *see also* Unsteady flow with wall friction, 219-55; *see also* Boundary layer; Duct; Tube Open-nosed body external supersonic flow past, 687 internal supersonic flow in, 688 of revolution, 674 Optical methods, 59-68 comparison of, 59-60 Optimum airfoils, supersonic, 575 Orifice, discharge coefficient of, 100, 359 Orthogonal network of equipotential and streamlines, 296-97 Overexpanded nozzle, 454, 565 Overtaking of moving shock, 1023

Parabolic bodies comparison of incompressible and supersonic flow, 673 comparison of two- and three-dimensional flow, 673 Parabolic differential equation, 600 Paraboloid recovery factor for, 1071 turbulent, 1123 Patching curves, 482, 601 Path lines, 912, 976; *see also* Unsteady flow Perfect fluid, 1033 definition of, 10 Perfect gas adiabatic flow of, 78-82 change in wave shape for, 131 constants of, 42 definition of, 41

(Volume I—pages 1 to 647.)

Prandtl mixing length, 1086, 1106, 1110 Prandtl Number, 1042 laminar, 1087 as similarity parameter, 56 turbulent, 1087 Prandtl's equation for normal shock, 118 for oblique shock, 534 Pressure base, 697 center of; *see* Center of pressure mean effective, 907 stagnation, 75 total, 75; *see also* Isentropic stagnation pressure; Stagnation pressure Pressure coefficient, 107, 309 dimensional analysis of, 308-9 effect of Mach Number on, 309, 314-15, 327 for elliptic cylinder, 369 Goertler's rule for, 320 interference, 329 Kármán-Tsien rule for, 347 lateral decay of, 314 linearized, 309-10, 428 Prandtl-Glauert rule for, 322-23 for small perturbations, 428 Pressure distribution and boundary layer, 308 and Mach Number, 327 for subsonic airfoils, 379-81 on subsonic flat plate, 707 for supersonic airfoils, 571 on supersonic flat plate, 707 in transonic flow, 846-50 on wing profiles, 379-81 Pressure drag, 442; *see also* Drag; Induced drag; Thickness drag of airfoils in supersonic flow, 442 of airfoils in transonic flow, 871 of cone, 662 nose, 766 and oblique shocks, 569 of parabolic bodies, 673 projectiles of minimum, 674 of swept wings, 725-29 Pressure gradient, effect on laminar boundary layer, 1055 effect on skin friction, 1066 in tube flow, 1131-35 Pressure index, 450 Pressure probe, static, 696 Pressure pulses, 915 Pressure ratio, critical, 76 Pressure stresses, work done by, 38 Pressure wave, 433, 463; *see also* Mach wave; Shocks; Unsteady flow; Wave Probe, stagnation-temperature, 1123 Process, adiabatic; *see* Adiabatic process definition of, 24 equal-temperature, 25

irreversible, 30 reversible, 30 Profiles; *see also* Airfoils biconvex, in transonic flow, 849, 858 drag in transonic flow, 865 hypersonic performance of, 757-61 at Mach Number unity, 842-46 in transonic flow, 840, 866-76 Projectiles detached shock for, 886, 887 drag of, 697 in transonic flow, 879 of minimum wave drag, 674 in supersonic flow, 651, 685 Prolate spheroid, subsonic flow past, 406 Propagation of disturbances, 499; *see also* Pressure wave; Wave Properties, thermodynamic, units of, 37 Property specific value of, 35 of a system, 24 per unit mass, 35 Pulse, pressure, 915 Pure substance, definition of, 34 internal energy of, 35-36 Quasi-linear equation, 597 Ram jet, 219 combustion in, 201-2 in supersonic flow, 651 Rankine-Hugoniot curve, 125; *see also* Shocks Rankine-Hugoniot equation, 121-22, 533, 552 Rankine temperature scale, 32 Rarefaction wave, 915; *see also* Unsteady flow; Wave Rarefaction wave, spreading of, 128-31 Rayleigh-Janzen method, 336, 365-67, 371 for spheres, 409 Rayleigh line, 115-16, 191-93, 240 equation of, 155 table of, 628 Rayleigh pitot-tube formula, 153-54 Reactor, nuclear, 219 Reciprocating engines, unsteady motion in, 907 unsteady flow in ducts of, 986 Recovery factor, 211-13, 1036; *see also* Boundary layer; Laminar boundary layer; Laminar flow; Turbulent boundary layer; Turbulent flow for circular cylinder, 1071 for cone, 1070-71, 1126 effect of Mach Number on, 1071 effect of Reynolds Number on, 1071 for flat plate, 1056, 1071, 1096-1107, 1118-23 for laminar boundary layer, 1070 for paraboloid, 1071

(Volume II—pages 649 to 1159.)

Recovery factor—Continued  
 for tube flow, 1135-36  
 turbulent  
 for cone, 1123  
 for cone-cylinder, 1123  
 for disk normal to flow, 1123  
 experimental summary of, 1123  
 for flat plate, 1123  
 for ogive-cylinder, 1123  
 for paraboloid, 1123  
 for wire normal to flow, 1123  
 for wire parallel to flow, 1123  
 for turbulent boundary layer, 1099  
 for turbulent flow, 1117-24  
 for wire, 1070

Rectangular wing, 735; *see also* Wings  
 Reference temperature, 1108

Reflection  
 Mach, 555-57; *see also* Shocks  
 of moving shock  
 from closed end, 1019; *see also*  
 Moving shocks  
 from open end, 1021  
 from piston, 1022  
 of oblique shock, 553-59; *see also*  
 Oblique shocks  
 from boundary layer, 582  
 from free boundary, 493, 554  
 from wall, 554  
 regular, 555  
 of wave, 922, 959-72; *see also* Un-  
 steady flow; Wave; Wave reflec-  
 tion  
 from free boundary, 450, 452  
 from surface of discontinuity, 461  
 from wall, 450, 451, 493

Refraction, index of, 63

Regular reflection, 555

Relaxation method, 297, 336, 377-79,  
 836-41

Relief effect, three-dimensional, 399,  
 400, 414, 416

Reservoir, starting of discharge from,  
 986

Reversibility, 30

Revolution

body of; *see also* Axially symmetric  
 flow  
 disturbance of, 402

drag of, 408  
 experimental results for, 404, 407

Gothert's rule for, 402-5  
 heat transfer for, 1074

in hypersonic flow, 761-66  
 inclined, 675

Kármán-Moore theory for, 668-  
 76

in linearized supersonic flow, 663-  
 76

open-nosed, 674  
 parabolic, 671-74

pressure coefficient for, 402  
 pressure distribution on, 766

(Volume I—pages 1 to 647.)

recovery factor for, 1123  
 subsonic flow past, 401-10  
 supersonic flow past, 663-76  
 thin, 405-6  
 transonic drag of, 879-81  
 turbulent boundary layer on, 1124-  
 27  
 ellipsoid of, subsonic flow past, 405  
 Reynolds' analogy, 213, 243, 1047  
 for turbulent boundary layer, 1100  
 for turbulent flow, 1089  
 Reynolds Number  
 minimum critical, 1075  
 of shock wave, 132-34  
 as similarity parameter, 56  
 of supersonic wind tunnel, 103-4  
 Reynolds stress, 1081, 1085  
 Reynolds stress, Kármán's formulation  
 of, 1101  
 Ringleb flow, 783  
 Rocket motor, thrust of, 100-3  
 Rocket nozzle, 219; *see also* Nozzle  
 Rocket in supersonic flow, 651  
 Rotation, 267, 269-71; *see also* Vor-  
 iosity  
 axi-symmetric flow with, 684  
 flow with; *see* Rotational flow  
 in streamline coordinates, 280-81  
 supersonic flow with, 516-23  
 and thermodynamic properties 280-  
 82  
 Rotational flow, 266, 271, 282, 516-  
 23  
 Saddle point; *see* Critical point  
 Schlieren method, 59-60, 65-67  
 analysis of, 66-67  
 Second Law of thermodynamics, 30  
 in analytical form, 34  
 for control volume, 40  
 corollaries of, 31  
 and irreversibility, 31  
 Second-order theory  
 for axi-symmetric supersonic flow,  
 675  
 coefficients of, 562  
 table of, 633  
 compared with experiment, 575  
 supersonic, 561-63, 571-78  
 Separation of boundary layer, 379, 380,  
 415; *see also* Shock-boundary layer  
 interaction  
 pressure rise in shock interaction,  
 1157  
 produced by shock wave, 1156-59  
 Shadowgraph, 59-60, 67-68  
 Shaft work, 39  
 Sharp-cornered nozzle, 512  
 experiments on, 514  
 Shear deformation, rate of, 270-71  
 Shear stress, 18  
 apparent, 1085  
 definition of, 9

Reynolds, 1085  
 turbulent, 1085  
 Kármán's formulation of, 1101  
 Shear stresses, work done by, 38, 1034  
 Shear work, 38-39  
 in boundary layer, 1034  
 Shock-boundary layer interaction, 507,  
 576, 580-84  
 in concave corner, 1142  
 effect of Mach Number on, 1151-53  
 effect of Reynolds Number on, 1153  
 laminar, 1141, 1150  
 for normal shocks in ducts, 1153-56  
 at nose of wedge, 1149  
 pressure rise for separation, 1157  
 for reflection of oblique shock, 1139  
 separation in, 1156-59  
 in supersonic flow, 1138-50  
 in transonic flow, 1150-53  
 turbulent, 1141, 1153  
 Shock-characteristic theory, 575  
 for airfoils, 566  
 Shock polars, 542-44; *see also* Moving  
 shocks; Shocks; Unsteady flow  
 hodograph, 542, 552  
 and characteristic curve, 552  
 pressure-deflection, 544  
 unsteady flow, 1004  
 Shock stall, 866  
 correlation of, 875  
 Shock tube, 1007-11  
 comparison of theory and experi-  
 ment, 1027  
 Shock wave, 992; *see* Normal shock;  
 Oblique shocks; Shocks; Wave  
 normal; *see* Normal shock  
 oblique; *see* Oblique shocks  
 Shocks, 266; *see also* Normal shock;  
 Oblique shocks; Wave  
 analysis of, 994-1007  
 attached  
 for cone, 662  
 for wedge, 662  
 attachment of, 881  
 back side of, 995  
 change from detached to attached,  
 881  
 and characteristics, 601  
 compared with simple wave, 1012-  
 1014  
 configuration of, 998  
 curved, 282, 549, 559-61, 908  
 detached, 548, 881-88  
 for cone, 662  
 location of, 884-88  
 shape of, 886  
 for wedge, 662  
 development of, 125-32  
 direction of, 116  
 as discontinuities, 112  
 dissipative effects in, 131-32  
 entropy increase of, 119-20  
 for weak shock, 124-25  
 Silence, zone of, 500  
 Similarity laws, 303, 315-17; *see also*  
 Gothert's rule; Hypersonic similar-  
 ity law; Prandtl-Glauert rule;

(Volume II—pages 649 to 1159.)

Similarity laws—*Continued*  
 Subsonic similarity law; Supersonic similarity law; Transonic similarity law  
 combined supersonic-hypersonic, 752  
 for flow far from profile, 324  
 general remarks on, 803  
 hypersonic, 651–52, 747–53  
   for axi-symmetric flow, 751  
   for finite wings, 752  
   for plane flow, 750  
   range of applicability of, 763  
   for supersonic flow, 751  
 for incompressible flow, 321–22  
 subsonic, 303–32  
   compared with experiment, 326–27  
   for one-dimensional flow, 331–32  
   for two-dimensional passages, 330–32  
   for wind tunnels, 327–30, 335  
 for supersonic wings, 714–16  
 transonic, 802  
   for axi-symmetric flow, 812  
   for flow with rotation, 814  
   for plane flow, 808–12  
   for wings, 812  
 for two-dimensional subsonic flow, Goertler's, 315–21  
 Laitone, 324–26  
 Prandtl-Glauert, 321–24  
 summary of, 323  
 for wings, 410–15  
 Similarity parameters, 54–56  
 hypersonic, 651, 749  
 transonic, 808  
 Simple Area Change; *see* Isentropic flow  
 Simple friction; *see* Friction, one-dimensional flow with  
 Simple gas injection, 239–41  
 Simple heating; *see* Simple  $T_a$ -Change  
 Simple  $T_a$ -Change, 190–211, 239  
   chart for, 196  
   choking due to, 192–93, 201–3  
   example of, 197–98  
   formulas for, 195–96  
   of perfect gas, 193–203  
   tables for, 196, 628  
   variations of fluid properties in, 198–99  
 Simple types of flow, 238–41  
   table of, 239  
 Simple wave flow; *see* Simple waves  
 Simple waves, 431, 464, 489–91, 602, 606–8, 913, 940–52; *see also* Centered waves; Corner flow; Method of characteristics; Prandtl-Meyer wave  
   calculation rules of, 467  
   cavitation in, 475  
   centered; *see* Centered waves  
   change in form of, 948  
   compared with shock, 1012–14  
   complete, 474, 475, 946  
   definition of, 940  
   exact solution for, 465–77  
   examples of, 468, 470, 944  
   features of, 471  
   flow, axi-symmetric, 653  
   four classes of, 948  
   generation of, 940  
   hodograph of, 607  
   in hypersonic flow, 755–57  
   left-running, 472  
   patching of, 608  
   path lines in, 947  
   in physical plane, 607  
   right-running, 473  
   streamlines of, 475–77  
   tables for, 468  
   transonic similarity law for, 819–22  
 Skin friction  
   of airfoils, 1066  
   on cone, 1067  
   effect of pressure gradient on, 1066  
   on flat plate  
    incompressible turbulent, 1107  
    turbulent, 1096–1117  
   in laminar boundary layer, 1057–60, 1068  
   turbulent  
    based on Kármán's mixing-length formulation, 1110  
    based on Prandtl's mixing-length formulation, 1110  
   effect of Mach Number on, 1109  
   Frankl and Voishel method for, 1109  
   by reference temperature hypothesis, 1108  
 Skin-friction coefficient, 379; *see also* Friction coefficient; Drag coefficient; Skin friction  
   for circular cylinder parallel to flow, 1126  
   for cone, 1125  
   by integral method, 1066  
   integrated, 1107  
   for laminar boundary layer, 1053  
   relations to drag coefficient, 1107  
   for tube flow, 1131–35  
 Skin-friction drag of airfoils, 443, 1066; *see also* Drag  
 Skin-friction law for turbulent flow, 1095  
 Slender bodies, flow past; *see* Linearized theory  
 Slip line, 519, 544, 555  
   crossed by oblique shocks, 561, 592  
 Slow burning, 207–11  
 Slug, definition of, 20–21  
   and pound force, 21  
   and pound mass, 21  
 Small perturbations; *see* Linearized theory  
   Sonic barrier, 852, 1044

Sonic line in nozzle, 830–34  
 Sonic point  
   passage through, 258  
   stability of, 260  
   special conditions at, 255  
 Sound, velocity of, 45–49; *see also* Velocity of sound  
   in air, 48  
   in incompressible fluid, 48  
   in liquid, 69  
   in perfect gas, 47  
   transition through, 235–36  
 Source  
   compressible, 665–68  
   incompressible, 665  
   subsonic, 666  
   supersonic, 666  
    superposition of, 668  
 Source distribution, supersonic, method of, 716–29  
 Source flow, 776  
 Source-vortex flow, 776, 780  
 Sources and sinks, method of, 401  
 Specific heat  
   definition of, 36  
   of perfect gas, 42  
 Speed, escape, 946  
   flame propagation, 207, 209–11  
 Speed of sound; *see* Velocity of sound; Sound, velocity of  
 Spheres  
   detached shock for, 886, 887  
   drag of, 410  
   subsonic flow past, 409–10  
   in transonic flow, 881  
 Spherical coordinate system, 299  
 Stability, boundary layer, 1075–76  
   effect of heat transfer on, 1075, 1127  
   effect of Mach Number on, 1075  
 Stagnation enthalpy, 75  
 Stagnation pressure, 75  
   loss of, in normal shock, 119  
 Stagnation state, 83  
 Stagnation temperature, 79  
   measurement of, 1123  
 Stagnation-temperature probe, 1123  
 Stagnation-temperature profile on turbulent flat plate, 1115  
 Stagnation-temperature ratio, 80  
 Stagnation-temperature thickness, 1063, 1092  
 Stagnation velocity of sound, 79–81  
 Stall, shock, 866  
   correlation of, 875  
 Stanton number, 1047  
 Starting vortex, 707  
 State, change of, 24  
   equation of, for perfect gas, 41  
   equilibrium, 40  
   nonequilibrium, 40  
   of a system, 24  
 State characteristics, 919, 934, 976  
 State plane, 934  
 Static pressure probe, 696  
 Steady flow  
   continuity equation for, 15  
   definition of, 11  
   energy equation of, 39–40  
   one-dimensional, 15  
 Steady-state ellipse, 962  
 Stokes' theorem, 269  
 Stream function, 1048  
   for axially symmetric flow, 294  
   definition of, 291–92  
   differential equations of, 291–92  
   equation of  
    for incompressible flow, 293  
    in Cartesian coordinates, 292–94  
    in cylindrical coordinates, 294–95  
    in hodograph plane, 341  
   physical meaning of, 292  
   of plane source, 299  
   and velocity potential, 295–97  
 Stream tube, isentropic flow in, 73  
 Streamline coordinates, 280  
 Streamline curvature method, 387–91  
 Streamlines  
   and equipotential lines, 295–97  
   for flow past circular cylinder, 297  
   hodograph, 336–37, 341  
 Strength of shock, 123–24, 551  
 Stress  
   apparent shear, 1085  
   Mohr's circle of, 9  
   normal, 18  
   work done by, 38  
 Reynolds, 1085  
   Kármán's formulation of, 1101  
 shear, 9, 18  
   work done by, 38  
 state of, 9  
   hydrostatic, 9  
   in inviscid fluid, 9  
   in viscous fluid, 9  
 surface, 18  
 turbulent, 1085  
 viscous, 18  
 Strong solution for cone, 662  
 Sublayer, laminar, 1080, 1093  
   interface of, 1094  
 Subsonic flow, 59  
   in accelerating elbow, 359–60  
   for airfoil in wind tunnel, 378  
   angle of attack in, 410–34  
   for bodies of revolution, 401–10  
    drag of, 408  
   for bump, 372–74  
   for circular arc profile, 375  
   for circular cylinder, 367  
    in free jet, 368  
    in wind tunnel, 357–58, 367  
   compared with supersonic, 76–78, 429, 448, 500  
 (Volume II—pages 649 to 1159.)

Subsonic flow—Continued  
 effect of camber in, 384-87  
 effect of Mach Number on flow far from profile, 324  
 effect of thickness in, 384-87  
 for ellipsoids, 398-401  
 for elliptic cylinder, 354-56, 369  
 at angle of attack, 358, 376  
 experimental results for, 326-27, 350, 379-87  
 for flat plate normal to stream, 360  
 influence of compressibility in, 400  
 for Joukowski profile, 369  
 Kármán-Tsien method for, 344-60  
 lift coefficient for, 376  
 pressure distributions in, 379-81  
 similarity laws for, 303-32  
 for spheres, 409-10  
 for sweptback wings; *see* Sweptback wings  
 for thin bodies of revolution, 405-6  
 three-dimensional, 394-99  
 wind tunnel corrections for, 327-30  
 for wings, 410-15  
 generalized correlation of, 422  
 Subsonic leading edge, 706  
 Subsonic pitot-tube, 154  
 Subsonic source, 666  
 Subsonic-supersonic flow, 773  
 Subsonic trailing edge, 706  
 Subsonic wind tunnel, airfoils in, 357, 368, 378  
 Substance, pure  
 definition of, 34  
 internal energy of, 35-36  
 Suction force, leading edge, 708  
 Suction pressure, at nose of airfoil, 449  
 Super-aerodynamics, 745  
 Superposition of effects, 709  
 Superposition of solutions, 289  
 Superposition of sources, 668  
 Supersaturation, 203  
 Supersonic airfoils, optimum, 575; *see also* Airfoils, supersonic; Wings, supersonic  
 Supersonic biplane, 579  
 Supersonic diffuser; *see* Diffuser, supersonic  
 Supersonic doublet, 716  
 Supersonic flow, 59  
 axi-symmetric, 651-702  
 Kármán-Moore theory of, 668-76  
 linear theory for, 663-76  
 compared with subsonic, 76-78, 429, 448, 500  
 in duct with friction, 104-5  
 Kármán's rules of, 51  
 linearized, 427-56  
 general solution for, 429  
 method of characteristics for, 482-91  
 parabolic body of revolution in, 671-74

(Volume I—pages 1 to 647.)

compared with incompressible flow, 673  
 compared with plane flow, 673  
 past cones, 653-63; 670-71; *see also* Cone  
 yawing, 663  
 with rotation, 516-23  
 with small perturbations, 427-56  
 Supersonic inlet; *see* Diffuser, supersonic; Inlet, supersonic  
 Supersonic leading edge, 706  
 Supersonic nozzle, 426, 507-16, 694; *see also* Supersonic flow  
 axisymmetric, 694  
 two-dimensional, 507-16  
 Supersonic pitot tube, 153-54  
 Supersonic similarity law, combined with hypersonic, 752  
 Supersonic source, 666, 716  
 superposition of, 668  
 Supersonic source distribution, method of, 716-29  
 Supersonic-subsonic flow, 773  
 Supersonic trailing edge, 706  
 Supersonic wind tunnel, 459, 502  
 Supersonic zones  
 in transonic flow, 889  
 stability of, 897  
 Surface  
 control, 12  
 integral, 598  
 Surface forces, definition of, 18  
 Surface of discontinuity; *see* Slip line; Vortex sheets  
 Surface stresses, 18  
 Surroundings, definition of, 11  
 Sutherland viscosity law, 1059  
 Sweepback, effects in transonic flow, 878; *see also* Sweptback wings  
 Swept leading edge, 707  
 Sweptback wings  
 arrowhead, 725  
 compressibility effects for, 417  
 drag of, 421  
 experimental results for, 419-22  
 generalized correlation of, 422  
 Goertler's rule for, 416  
 lift of, 420, 421  
 lower critical Mach Number of, 418  
 pressure drag of, 725-29  
 subsonic flow past, 415-22  
 in supersonic flow, 709-14  
 System  
 boundary of, 11  
 definition of, 11  
 property of, 24  
 state of, 24  
 Tangent-cone method, 675  
 Tangent gas, 336  
 definition of, 342  
 limitations of, 343-44  
 polygonal extension of, 357  
 properties of, 342-43  
 Tangent-gas approximation, 341-44  
 Taylor-Maccoll solution for cone, 656-57  
 Temperature  
 absolute scale of, 32  
 adiabatic wall, 211-12, 1036  
 equality of, 24  
 ratio of stagnation to static, 80  
 reference, 1108  
 scale of, 24  
 stagnation, 79  
 measurement of, 1123  
 total, 79  
 Temperature boundary layer, 1061  
 Temperature discontinuity, 969  
 Temperature distribution in boundary layer, 1035; *see also* Temperature profile  
 Temperature profile, 1063  
 in laminar boundary layer, 1052-54, 1056-60  
 in laminar sublayer, 1096  
 in turbulent boundary layer, 1097  
 Temperature recovery factor; *see* Recovery factor  
 Temperature scale  
 absolute, 32  
 Kelvin, 32  
 Rankine, 32  
 Temperature-entropy diagram, 34  
 Temperature-velocity relationship in laminar boundary layer, 1045  
 Temperature-viscosity law, 1049  
 Temporal mean value in turbulent flow, 1083  
 Thermal barrier, 1044  
 Thermal boundary layer, 1061  
 Thermal choking, 192-93, 201-3, 205  
 Thermal conductivity  
 coefficient of, 1086  
 definition of, 36  
 eddy, 1086  
 molecular, 1086  
 Thermal efficiency of heat engines, 29  
 Thermodynamic properties, units of, 37  
 Thermodynamics  
 First Law of, 26  
 for a cycle, 28  
 laws of  
 for irrotational frictionless flow, 284  
 of nonequilibrium states, 40  
 Second Law of, 30  
 in analytical form, 34  
 for control volume, 40  
 corollaries of, 31  
 Zeroth law of, 25  
 Thickness, boundary layer, 1090  
 displacement  
 of boundary layer, 266, 1062, 1090  
 effects of  
 in subsonic flow, 384-87  
 in transonic flow, 865, 870  
 of laminar boundary layer, 1059  
 momentum, 1062, 1090  
 stagnation-temperature, 1063, 1092  
 Thickness drag, 443, 575  
 Thickness ratio, effects of  
 in subsonic flow, 384-87  
 in transonic flow, 870  
 Thickness of normal shock, 112  
 Thin airfoil, supersonic flow past, 434; *see also* Linearized theory  
 Thin bodies, flow past; *see* Linearized theory  
 Thomson's theorem, 278-80, 282  
 Three-dimensional flow, supersonic, past wings, 703-43  
 Three-dimensional relief effect, 399, 400, 414, 416  
 Thrust of rocket motor, 100-3  
 Time, units of, 20-21  
 Time-mean properties, 1083  
 Tollmien-Schlichting waves, 1075  
 Total pressure, 75  
 Total temperature, 79  
 Trailing edge  
 subsonic, 706  
 supersonic, 706  
 flow at, 584  
 Trajectory, time-space, 913  
 Transformation, affine, 319  
 Transient processes, 907  
 Transition of boundary layer  
 effect of heat transfer on, 1127  
 effect of wall temperature on, 1076  
 Transition through speed of sound, 235-36  
 Transmission of waves, 960-72  
 Transonic differential equation, 806  
 Transonic flow, 59, 378, 773, 800  
 airfoil camber effects in, 872  
 airfoil lift-drag in, 872  
 airfoil pressure drag in, 871  
 airfoil thickness effects in, 870  
 airfoils in, 812, 822-25, 840, 842-50, 858, 865, 866, 870-78, 888, 894  
 approximate equation of, 804  
 aspect ratio effects in, 878  
 biconvex profile in, 849, 858  
 bodies of revolution in, 879-81  
 boundary layer in, 893  
 camber in, 872  
 change from symmetrical to asymmetrical pattern, 891  
 drag vs. Mach Number in, 848  
 drag of wings in, 866  
 flat plate in, 822-25  
 fuselage drag in, 879  
 lift vs. Mach Number in, 848  
 low-drag airfoils for, 874

(Volume II—pages 649 to 1159.)

Transonic flow—*Continued*  
 at Mach Number unity, 812, 842–46,  
 846–50  
 in nozzle throat, 826–36  
 optimum profiles for, 876  
 profile drag in, 865  
 projectile drag in, 879  
 shock-boundary layer interaction in,  
 897–902, 1150–53  
 shockfree, 888  
 stability of, 897  
 uniqueness of profile, 894  
 spheres in, 881  
 stability of imbedded supersonic zone  
 in, 897  
 supersonic zones in, 889  
 sweepback effects in, 878  
 thickness effects in, 865, 870  
 two-dimensional profiles in, 840  
 uniqueness of profile in, 894  
 viscous effects in, 893  
 wavy wall in, 841  
 wedge nose in, 850, 862  
 wind tunnel tests for, 849  
 wings in, 876–79

Transonic similarity law, 802  
 for airfoils, 825  
 applications of, 815–26  
 for axi-symmetric flow, 812  
 for critical Mach Number, 826  
 experimental validity of, 858–66  
 for flat plate, 822–25  
 for flow with rotation, 814  
 for oblique shocks, 815–19  
 for plane flow, 808–12  
 for Prandtl-Meyer expansion, 819–22  
 validity of, 814  
 for wedge airfoil, 825  
 for wings, 812

Transonic similarity parameter, 808

Transonic wind tunnel, 800

Tricomi equation, 856

Tube  
 flow in, 1130–38; *see also* Ducts, flow  
 in  
 heat transfer for, 1136–38  
 recovery factor for, 1135–36  
 friction coefficient for, 1131–35  
 subsonic turbulent, 1131  
 supersonic, 1131  
 shock, 1007–11  
 comparison of theory and experiment, 1027  
 shock-boundary layer interaction in, 1153–56

“Tuning” of ducts, 907

Turbine, blade cascades of, 427  
 impulse blade of, 504  
 interference in, 315  
 nozzle jet of, 566

Turbulent boundary layer, 1080–1129;  
*see also* Boundary layer; Turbulent flow

(Volume I—pages 1 to 647.)

velocity profile in, 1092, 1094, 1097,  
 1115  
 calculated, 1095  
 universal, 1094  
 universal mixing-length constant for,  
 1106  
 Turbulent exchange coefficients, 1086  
 Turbulent flow; *see also* Turbulent boundary layer  
 apparent heat flux in, 1086  
 apparent mass flow in, 1084  
 apparent shear stress in, 1085  
 compared with laminar, 1080  
 continuity equation for, 1082  
 correlation coefficient for, 1101  
 exchange coefficients for, 1086  
 fluctuating components of, 1083  
 heat flux in, apparent, 1086  
 physical description of, 1080  
 Prandtl mixing length of, 1086  
 recovery factor for; *see also* Recovery factor  
 experimental summary of, 1123  
 Reynolds stress in, 1085  
 “steady,” 1080  
 time-mean properties of, 1082  
 Turbulent Prandtl Number, 1087  
 Turbulent shear stress, Kármán's formulation of, 1101  
 Turn, 180°, 783  
 Two-dimensional airfoils; *see* Airfoils, two-dimensional  
 Two-dimensional passages, subsonic similarity rule for, 330–32  
 Two-dimensional profile in hypersonic flow, 757–61

Underexpanded jet, 454, 479–81, 501  
 Underexpanded nozzle, 454, 479–81, 501

Unit processes, for waves, 450, 492–94  
 Units of dynamic quantities, 20–21  
 Units of thermodynamic quantities, 37  
 Universal velocity profile, 1094

Unsteady flow  
 accelerating, 926  
 with area change, 925  
 characteristic curves for, 918  
 decelerating, 926  
 equations of motion for, 908–11  
 example of, 919, 986  
 governing equations of, 931  
 linearized theory of, 931  
 method of characteristics for, 972  
 shock waves in, 992–1027  
 of small amplitude, 911–17

Unsteady one-dimensional flow, 596

Upper critical Mach Number, 797  
 for bump, 372–74  
 definition of, 372

Velocity  
 critical, 79–81

dimensionless,  $M^*$ , 81–82  
 flame propagation, 207, 209–11  
 fluid, 6  
 friction, 1094  
 line integral of, 267  
 maximum, for adiabatic flow, 79–81  
 perturbation, 305  
 of shock wave, 48  
 of sound, 45–49  
 in air, 48  
 in incompressible fluid, 48  
 in liquid, 69  
 passage through, 258  
 stability of, 260  
 in perfect gas, 47  
 special conditions at, 255  
 stagnation, 79–81  
 transition through, 235–36

Velocity boundary layer, 1061

Velocity plane, 465

Velocity potential, 909, 931  
 definition of, 285  
 equation of, 284–91  
 for axially symmetric flow, 291  
 in Cartesian coordinates, 286–89  
 in cylindrical coordinates, 289–91  
 for incompressible flow, 289  
 linearized, 304–8  
 mathematical features of, 288  
 in polar coordinates, 291  
 solution of, 288  
 for two-dimensional flow, 289  
 of line vortex, 299  
 lines of; *see* Equipotential lines  
 perturbation, 305, 426, 428  
 and stream function, 295–97

Velocity profile, 1063  
 on flat plate, turbulent, 1115  
 in laminar boundary layer, 1052–54, 1056–60, 1067  
 in laminar sublayer, 1096  
 power law for, 1092  
 in turbulent boundary layer, 1092, 1094, 1097  
 calculated, 1095  
 universal, 1094

Velocity-temperature relationship in laminar boundary layer, 1045

Viscosity  
 coefficient of, 9, 1086  
 eddy, 1086  
 effects of, in design, 506  
 variation with temperature, 1049

Viscosity law, Sutherland, 1059

Viscosity variation, effects on laminar boundary layer, 1055

Viscous stresses, 18

Volume, control, 12

Volumetric efficiency, 907

von Mises transformation for boundary layer, 1048

Vortex  
 potential, 271–73

(Volume II—pages 649 to 1159.)

Vortex—*Continued*  
 starting, 707  
 Vortex flow, 778  
 Vortex sheets, 519, 544, 555  
 Vortex-source flow, 776, 780  
 Vorticity; *see also* Rotation  
 axi-symmetric flow with, 684  
 error in ignoring, 685

Wake  
 of supersonic airfoils, 578  
 wave system in, 578  
 Wake losses, effect of Mach Number on, 383

Wall  
 curved, supersonic flow past, 464  
 wave-shaped, flow past, 310-15

Wall properties, boundary layer results for, 1053

Wave, 912, 914; *see also* Mach wave; Pressure wave; Shocks  
 of both families, 477-89, 952-58  
 calculation rules for, 915  
 cancellation of, 450, 452, 493  
 centered; *see* Centered waves  
 compression, 915  
 steepening of, 127-31  
 detonation, 219  
 development of, 158  
 analysis of, 128-31  
 expansion, 915  
 spreading of, 128-31  
 explosion, 206-11  
 generation of, 449, 463, 493  
 interaction with moving shocks, 1026  
 interaction with oblique shocks, 559  
 intersection with wave, 450, 453, 494, 922, 958  
 left-running, 465  
 lumped, 449  
 Mach; *see* Mach wave  
 normal shock, 112-54; *see also* Normal shock  
 of one family, 431  
 physical analysis of, 917  
 rarefaction, 915  
 spreading of, 128-31  
 reflection of, 922, 959-72  
 from free boundary, 450, 452, 493  
 from surface of discontinuity, 461  
 from wall, 450, 451, 493  
 right-running, 467  
 shock  
 with energy effects, 203-11  
 oblique, 529-84; *see also* Oblique shocks  
 thickness of, 131-34  
 velocity of, 48  
 simple, 913, 940-52; *see also* Simple wave  
 of small amplitude, 911-17  
 steepness of, rate of change of, 158  
 transmission of, 960-72

(Volume I—pages 1 to 647.)

delta  
 lift of, 738  
 supersonic, 719-24  
 diamond planform, 739  
 drag of, in transonic flow, 866  
 effect of aspect ratio on, 411-15  
 experimental results for, 412-15  
 finite, lift of, 735-41  
 lift-curve slope for, 411-12  
 regions of two-dimensional flow in, 704  
 similarity rule for, 714-16  
 subsonic flow past, 410-15  
 in supersonic flow, 703-43  
 generalized correlation of, 422  
 in hypersonic flow, 766  
 hypersonic similarity law for, 752  
 induced drag of, 412  
 lift of, generalized correlation of, 422  
 lift-curve slope of, 425  
 quadrilateral, 739  
 rectangular, 735  
 supersonic; *see also* Airfoils, supersonic  
 similarity rule for, 714-16

Wire  
 recovery factor for, 1070  
 turbulent, 1123

Work  
 definition of, 25  
 done by normal stresses, 38  
 done by shear stresses, 38  
 measurement of, 26  
 recognition of, 25  
 shaft, 38-39  
 shear, 38-39

Yawing cone, 663

Zeroth law of thermodynamics, 25  
 Zone of action, 500  
 Zone of silence, 500

(Volume II—pages 649 to 1159.)